Challa S.S.R. Kumar *Editor*

In-situ Characterization Techniques for Nanomaterials

MATERIALS.SPRINGER.COM

Springer

In-situ Characterization Techniques for Nanomaterials

Challa S. S. R. Kumar
Editor

In-situ Characterization Techniques for Nanomaterials

With 210 Figures and 8 Tables

Springer

Editor
Challa S. S. R. Kumar
Integrated Mesoscale Architectures for Sustainable Catalysis (IMASC)
Rowland Institute of Science
Harvard University
Cambridge, MA, USA

ISBN 978-3-662-56321-2 ISBN 978-3-662-56322-9 (eBook)
https://doi.org/10.1007/978-3-662-56322-9

Library of Congress Control Number: 2018932039

© Springer-Verlag GmbH Germany, part of Springer Nature 2018
This work is subject to copyright. All rights are reserved by the Publisher, whether the whole or part of the material is concerned, specifically the rights of translation, reprinting, reuse of illustrations, recitation, broadcasting, reproduction on microfilms or in any other physical way, and transmission or information storage and retrieval, electronic adaptation, computer software, or by similar or dissimilar methodology now known or hereafter developed.
The use of general descriptive names, registered names, trademarks, service marks, etc. in this publication does not imply, even in the absence of a specific statement, that such names are exempt from the relevant protective laws and regulations and therefore free for general use.
The publisher, the authors and the editors are safe to assume that the advice and information in this book are believed to be true and accurate at the date of publication. Neither the publisher nor the authors or the editors give a warranty, express or implied, with respect to the material contained herein or for any errors or omissions that may have been made. The publisher remains neutral with regard to jurisdictional claims in published maps and institutional affiliations.

Printed on acid-free paper

This Springer imprint is published by the registered company Springer-Verlag GmbH, DE part of Springer Nature.
The registered company address is: Heidelberger Platz 3, 14197 Berlin, Germany

Contents

Contributors

Patricia Abellan SuperSTEM Laboratory, SciTech Daresbury Campus, Daresbury, UK

Luis Armando Carvajal Ahumada Centro de tecnología Biomédica (CTB), Universidad Politécnica de Madrid (UPM), Madrid, Spain

Facultad de Ingeniería y Ciencias Básicas, Universidad Central, Bogotá, Colombia

Centro de investigación y desarrollo tecnológico de la industria electro electrónica y TIC, Bogotá, Colombia

Mireia Baeza Departament de Química, Facultat de Ciències, Carrer dels Til·lers, Edifici C-Entrada Nord, Bellaterra, Barcelona, Spain

Julio Bastos-Arrieta Department of Chemical Engineering, Universitat Politècnica de Catalunya, Barcelona, Spain

Barcelona Research Center in Multiscale Science and Engineering, Barcelona, Spain

Physical Chemistry, Technische Universität Dresden, Dresden, Germany

Dibyendu Bhattacharyya Atomic and Molecular Physics Division, Bhabha Atomic Research Centre, Trombay, Mumbai, India

K. Boniface Kokoh IC2MP UMR 7285 CNRS University of Poitiers, Poitiers, France

A. Brinkman Faculty of Science and Technology and MESA+, Institute for Nanotechnology, University of Twente, Enschede, The Netherlands

Mariana R. Camilo IQSC, University of São Paulo, São Carlos, SP, Brazil

Soma Chattopadhyay Elgin Community College, Elgin, IL, USA

Laetitia Dubau University of Grenoble Alpes, Grenoble, France

CNRS, Grenoble, France

Julien Durst University of Grenoble Alpes, Grenoble, France

CNRS, Grenoble, France

Marisol Espinoza Department of Chemistry, Universidad Autónoma Metropolitana, México, D. F., México

Mariano Alberto García-Vellisca Centro de tecnología Biomédica (CTB), Universidad Politécnica de Madrid (UPM), Madrid, Spain

David B. Geohegan Center for Nanophase Materials Sciences, Oak Ridge National Laboratory, Oak Ridge, TN, USA

Felipe Andrés Silva Gómez Corporación de Alta Tecnología para la Defensa (CODALTEC), Villavicencio, Colombia

Steve M. Heald Advanced Photon Source, Argonne National Laboratory, Argonne, IL, USA

S. N. Jha Atomic and Molecular Physics Division, Bhabha Atomic Research Centre, Trombay, Mumbai, India

Jong K. Keum Center for Nanophase Materials Sciences, Oak Ridge National Laboratory, Oak Ridge, TN, USA

Neutron Scattering Division, Oak Ridge National Laboratory, Oak Ridge, TN, USA

G. Koster Faculty of Science and Technology and MESA+, Institute for Nanotechnology, University of Twente, Enschede, The Netherlands

Soon Gu Kwon Center for Nanoparticle Research, Institute for Basic Science and Seoul National University, Seoul, Republic of Korea

Fabio H. B. Lima IQSC, University of São Paulo, São Carlos, SP, Brazil

Frédéric Maillard University of Grenoble Alpes, Grenoble, France

CNRS, Grenoble, France

Jeffrey T. Miller School of Chemical Engineering, Purdue University, West Lafayette, IN, USA

Vladimir M. Mirsky Institute of Biotechnology, Department of Nanobiotechnology, Brandenburg University of Technology Cottbus-Senftenberg, Senftenberg, Germany

Raquel Montes Departament d'Enginyeria Química, Biològica i Ambiental, Escola d'Enginyeria, Universitat Autònoma de Barcelona, Barcelona, Spain

Departament d'Enginyeria Química, Biològica i Ambiental, Carrer de les Sitges S/N, Edifici Q, Escola d'Enginyeria Bellaterra, Barcelona, Spain

Claudia Morais IC2MP UMR 7285 CNRS University of Poitiers, Poitiers, France

Maria Muñoz Departament de Química, Facultat de Ciències, Carrer dels Til·lers, Edifici C-Entrada Nord, Bellaterra, Barcelona, Spain

Têko W. Napporn IC2MP UMR 7285 CNRS University of Poitiers, Poitiers, France

Chandrani Nayak Atomic and Molecular Physics Division, Bhabha Atomic Research Centre, Trombay, Mumbai, India

P. Ngabonziza Faculty of Science and Technology and MESA+, Institute for Nanotechnology, University of Twente, Enschede, The Netherlands

Department of Physics, University of Johannesburg, Johannesburg, South Africa

Shavkat Nizamov Institute of Biotechnology, Department of Nanobiotechnology, Brandenburg University of Technology Cottbus-Senftenberg, Senftenberg, Germany

Cristina Ocaña Departament Micronano Sistemes, CSIC, Institute of Microelectronics of Barcelona IMB CNM, Bellaterra, Spain

Johan Gadolin Process Chemistry Centre, c/o Laboratory of Analytical Chemistry, Abo Akademi University, Turku, Finland

José Javier Serrano Olmedo Centro de tecnología Biomédica (CTB), Universidad Politécnica de Madrid (UPM), Madrid, Spain

Nuria Peña Perez Centro de tecnología Biomédica (CTB), Universidad Politécnica de Madrid (UPM), Madrid, Spain

Victor S. Popov Department of advanced research and development, Polyus Research Institute of M.F.Stelmakh, Moscow, Russia

Sector for high-temperature and sensor materials, Kurnakov Institute of General and Inorganic Chemistry, The Russian Academy of Sciences, Moscow, Russia

Oscar Leonardo Herrera Sandoval Facultad de Ingeniería y Ciencias Básicas, Universidad Central, Bogotá, Colombia

Centro de investigación y desarrollo tecnológico de la industria electro electrónica y TIC, Bogotá, Colombia

Elena V. Shevchenko Nanoscience and Technology division, Argonne National Laboratory, Argonne, IL, USA

Alexander Sopilniak The Institute of Chemistry, The Hebrew University of Jerusalem, Jerusalem, Israel

M. P. Stehno Faculty of Science and Technology and MESA+, Institute for Nanotechnology, University of Twente, Enschede, The Netherlands

Bin Tang National Engineering Laboratory for Advanced Yarn and Fabric Formation and Clean Production, Wuhan Textile University, Wuhan, China

Institute for Frontier Materials, Deakin University, Geelong, VIC, Australia

Taylor J. Woehl Department of Chemical and Biomolecular Engineering, University of Maryland, College Park, MD, USA

Kai Xiao Center for Nanophase Materials Sciences, Oak Ridge National Laboratory, Oak Ridge, TN, USA

Department of Electrical Engineering and Computer Science, University of Tennessee, Knoxville, TN, USA

Bin Yang Center for Nanophase Materials Sciences, Oak Ridge National Laboratory, Oak Ridge, TN, USA

The Molecular Foundry, Lawrence Berkeley National Laboratory, Berkeley, CA, USA

Ji Zhou Hubei Collaborative Innovation Center for Advanced Organic Chemical Materials and Key Laboratory for the Synthesis and Application of Organic Functional Molecules, Ministry of Education and College of Chemistry and Chemical Engineering, Hubei University, Wuhan, China

1 Liquid Cell Electron Microscopy for the Study of Growth Dynamics of Nanomaterials and Structure of Soft Matter

Patricia Abellan and Taylor J. Woehl

Contents

Patricia Abellan and Taylor J. Woehl contributed equally to this work.

P. Abellan (✉)
SuperSTEM Laboratory, SciTech Daresbury Campus, Daresbury, UK
e-mail: pabellan@superstem.org

T. J. Woehl (✉)
Department of Chemical and Biomolecular Engineering, University of Maryland, College Park, MD, USA
e-mail: tjwoehl@umd.edu

© Springer-Verlag GmbH Germany, part of Springer Nature 2018

C. S. S. R. Kumar (ed.), *In-situ Characterization Techniques for Nanomaterials*,
https://doi.org/10.1007/978-3-662-56322-9_1

1 Definition of the Topic

This chapter lays out experimental evidence from the field of liquid cell electron microscopy, related concepts from radiation chemistry, and models explaining particle growth, diffusion, and electron beam charging during experiments. We present an overview of main results regarding particle growth, observation of low contrast systems such as proteins, and operando experiments using nonaqueous solutions.

2 Overview

Using liquid cell transmission electron microscopy (TEM) stages, in situ observations of dynamic processes in liquids can be made with (sub)nanometer spatial resolution. This approach allows for a large variety of experiments to be implemented; the main reasons being: (1) stages can be used in any TEM and thus benefit from any specific capability available, and (2) newly designed stages and microfabricated chips provide an increasing number of stimuli, substrates, and experiment-control capabilities for the study of liquid phase reactions. To fully exploit the myriad of experiences that this relatively new technique offers, knowledge on the different effects of the beam on the liquid and how to control them is needed.

In this chapter we present an overview of the main results obtained regarding various experiments that are possible in liquid cells and discuss methodologies, concepts, and best practices related to each of them. We will discuss results on in situ radiation chemistry–induced growth of metallic particles from solution, methods to avoid artifacts and damage of low-contrast objects (e.g., proteins), relevant effects related to the presence of membranes and the use of ionizing radiation during the experiments, and the use of organic solvents and operando methodologies for observation of electrochemical processes. Important concepts from radiation chemistry and useful models on particles diffusion and electrostatic charging effects are introduced.

3 Introduction

From the advent of the first transmission electron microscope (TEM) by Ruska and Knoll in 1931, there has been a sustained interest in using TEM to image hydrated samples in their native environment. This is not a trivial problem as a high vacuum must be maintained in the electron microscope. Initially, researchers approached the problem in two ways [1]: (1) preservation of samples in vitreous ice (i.e., cryo-TEM) [2, 3] and (2) maintaining liquid water in the sample using either a high humidity environment via differential pumping [4] or hermetic sealing via thin carbon windows [5]. While the technical challenges associated with achieving high spatial and energy resolution electron beams, differential pumping, and reliable membrane

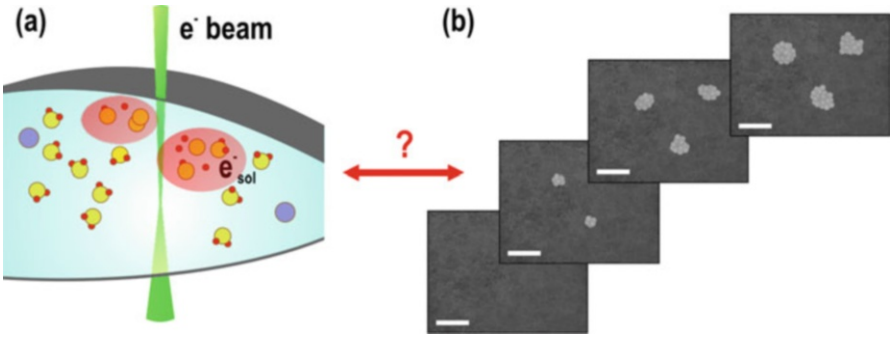

Fig. 1.1 A main challenge in LCEM is to establish a relationship between the incident electron beam and the in situ observations. (**a**) Schematic of a sample for LCEM, where two thin membranes "sandwich" a small – overall electron transparent – liquid sample and separate it from the high vacuum of the microscope column. The electron beam probes the sample in transmission. Radiolysis of the solution will occur. Note the different parts of the drawing are not to scale for illustrative purposes. (**b**) Observations in LCEM mainly consist of a set of time-resolved TEM/STEM micrographs with nanometer scale resolution

fabrication inhibited early efforts to image samples in liquid water in the TEM, the advent of microfabrication and micromachining techniques for producing strong robust thin film membranes and sealed sample cells revitalized an interest in electron microscopy of liquid samples, now termed liquid cell electron microscopy, LCEM [6–9].

During a LCEM experiment, the microscope settings can be tuned, thus changing the incident electron-beam characteristics. Changes in the beam current, irradiation time (pixel dwell time in scanning TEM (STEM) or exposure time in conventional TEM), or irradiation area determine the electron dosage delivered. Higher doses can increase image contrast and signal-to-noise ratio as well as nominal pixel resolution in STEM, but will also accelerate the breakdown of molecules in the solution via radiation damage. Changing the electron-beam energy (kV) will ultimately either produce slower or more rapid recombination of species. The thickness and material properties of the membranes, especially electrical resistance, will also have important consequences that are only starting to be understood. In this chapter we will highlight some of the general trends that have been observed and that describe the effect of each individual parameter. A schematic of a sample for LCEM experiments is shown in Fig. 1.1a. Experiments in a (S)TEM are performed in transmission and thus the interaction volume (combined thickness and density of membranes and solution) must be electron transparent. The high-energy electrons (80–300 kV) used for imaging will also induce radiolysis of the solution as they interact with the sample.

Experimental observations in LCEM consist of a sequence of in situ data (typically images, but also spectra) that are collected and subsequently analyzed (see Fig. 1.1b for a cartoon example). A main challenge that the LCEM community has faced since the advent of this field is whether the characteristics of the primary

incident beam can be directly correlated with the process observed. Indeed, this direct correlation would provide means for quantification, in situ control, and reproducibility. To make this important connection, the chemical effects of the incident electrons on the solution must be known, which will enable elimination of confounding variables. Ideally, as will be discussed in Sect. 5.1, these effects must be anticipated and predetermined.

As mentioned above, changes in the microscope settings (imaging electron beam) and encapsulating membranes have important effects on the experiments and will be a main topic of this chapter. The crucial role of the chemistry of the solution irradiated will be also discussed. For more details on the effect of microscope settings and membranes, we redirect the reader to the following manuscripts and reviews written by the authors [10–13], and for the chemical effects of the incident electrons in a solution in the (S)TEM, to the following works [13–15]. The overall effect of ionizing radiation in a solution is the production of a number of chemical species. Many LCEM in situ growth experiments that trigger particle growth using the incident electron beam have interpreted observations based on the main interactions driving the process and often ignore other secondary interactions and back reactions that alter the kinetics of the process. In general, radiation chemical methods used outside the electron microscope for growth of nanostructures include an important step aimed at dealing with back reactions and which consists of purposely tuning the primary radicals produced in the solvent into a completely different pool of radicals/molecules by adding a small amount of an additive to the initial solution. Whether in situ growth and observations in the STEM are done following one approach or the other (using scavenged or unscavenged solutions), the chemical effects of the incident electrons must be understood to achieve reproducibility and to understand any phenomena observed in the liquid cell. Once established the LCEM methodology can be a powerful tool for chemical and materials sciences experimentation in the microscope.

As mentioned above, electron beam-sample interactions can be harnessed to investigate important dynamic nanoscale phenomena, such as electron beam–induced nanoparticle growth, [12, 16] nanoparticle manipulation and motion, [10, 17] and self-assembly and aggregation [10, 18–20]. On the other hand, experiments involving the application of external stimuli or requiring the preservation of native structure, such as in situ electrochemistry [21] and live cell imaging [7, 22–24], require electron-beam interactions to be minimized. These two types of experiments represent a bifurcation in the experimental approach taken by liquid cell electron microscopy researchers; on the one hand, electron beam effects are desirable, while on the other hand they would ideally be eliminated. Both approaches have yielded extraordinary fundamental insights into various nanoscale systems and require an in-depth understanding of the underlying physics and chemistry of electron beam-sample interactions; however, each requires a distinct experimental approach. The knowledge presented in this chapter could be used for either of these purposes. Finally, we will review different fundamental processes that can be investigated by LCEM and discuss recommended practices and methods, see Sects. 5.1.2, 5.2, and 5.4.3.

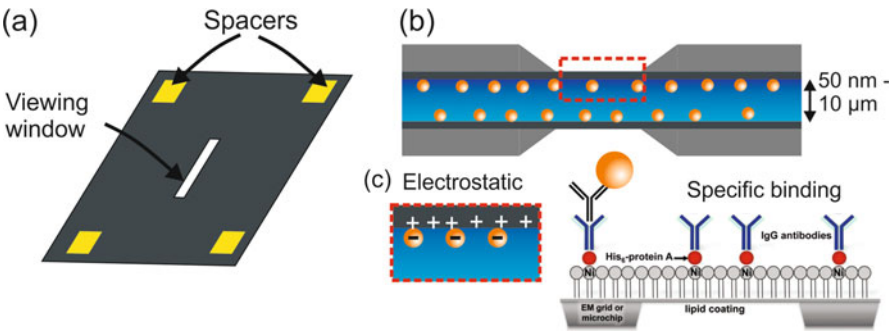

Fig. 1.2 (**a**) Silicon nitride liquid cell membrane. (**b**) Side view of the thin liquid layer between two liquid cell membranes. Nanomaterials are attached to the membrane surface by various mechanisms shown in (**c**) (Figure 2c adapted with permission from Ref. [26] copyright Royal Society of Chemistry 2015)

4 Experimental and Instrumental Methodology

4.1 General Sample and Microscope Preparation Considerations

Preparation of a liquid cell electron microscopy sample consists of three aspects: preparation of the liquid cell membranes, the liquid cell sample holder, and the liquid sample (Fig. 1.2). Sample preparation for liquid cell electron microscopy is a critical experimental aspect to enable reproducible experiments, high spatial resolution, and probing of native structure of nanomaterials. Liquid cell membrane preparation should be consistent and may include cleaning with solvents to remove protective photoresist followed by plasma cleaning to remove residual organics and render the surface hydrophilic. Adventitious organics in the solution can lead to sample contamination [11] or act as radical scavengers that alter the radiation chemistry of the solution, which will be discussed in Sect. 5.1.3. In most cases, it is ideal for the nanomaterial sample to adhere to the liquid cell membranes instead of freely diffusing in the liquid layer, such that it can be imaged without severe image blur due to diffusion (Fig. 1.2b; see Sects. 5.2 and 5.3.3). Several methods can be used to adhere the sample to the membrane, including electrostatic binding, antibody-antigen binding [25], or physical adsorption via Van der Waals forces (Fig. 1.2c). Electrostatic binding can be achieved by functionalizing the liquid cell membranes with a surface chemistry of opposite surface charge compared to the nanomaterial sample: functionalized liquid cell membranes are currently commercially available. It is worth noting that coating the liquid cell chips with poly-l-lysine or (3-aminopropyl)triethoxysilane (APTES) will create a positively charged surface that promotes cell adhesion [23, 24] and adhesion of negatively charged nanoparticles. Prior to experiments, liquid flow lines should be flushed with ethanol and DI water to remove organics and salts. For electron beam–induced growth experiments, flushing the lines with a strong reducing agent, such as sodium

borohydride, will react away any residual metal ions that could potentially compete with the intended reaction.

Calibrating the electron dose rate of the (S)TEM is key to mitigating beam damage and performing reproducible electron beam–induced nanomaterial nucleation, growth, and degradation experiments [27]. Practical considerations include whether an aberration corrected or uncorrected instrument is being used, as Cs-corrected STEM generally employs large condenser apertures and electron beam currents, which should be considered in designing experiments. If electron beam–induced growth experiments are being performed, electron beam current should be measured for a variety of aperture sizes and electron beam spot sizes. The electron dose rate is a key parameter to measure for imaging and depends on magnification, beam current, and beam size for TEM. For STEM, the frame average electron dose rate is typically employed, which is determined by the size of the scan area, pixel dwell time, and beam current (for calculation examples of electron dose rate see methods sections in refs [12, 27]). Radiation chemistry literature typically expresses the electron dose in units of grays, which takes into account the energy deposited by the electron beam in the material (for an example of direct conversion between units used in the STEM and in radiation chemistry see Ref. [28]).

4.2 Lessons Learned from the Development of Cryo-EM

The motivations for and origins of cryo-EM and liquid cell electron microscopy are unmistakably similar. The history of cryo-EM development, one of the most prolific techniques for determining near-native macromolecule structure, can thus be compared to the current trajectory of technique development for liquid cell electron microscopy. The development of cryo-EM was faced with difficulties familiar to liquid cell electron microscopy researchers [9, 11], such as issues with sample reproducibility [29, 30], electron beam damage [31–33], and sample preparation and manipulation [1, 34]. Cryo-EM sample preparation involves depositing a very thin liquid layer onto a carbon TEM grid and freezing it rapidly enough to render it vitreous, which creates a low contrast background for imaging. Initial attempts utilized liquid nitrogen but were plagued by crystallization of the ice. Not until the utilization of liquid ethane were quenching rates rapid enough to consistently form vitreous ice. Cryo-EM faced criticism as a technique because the physics of water vitrification were still not well understood. Similarly, early liquid cell electron microscopy experiments suffered from uncontrolled electron beam interactions with the sample and surrounding fluid, confinement effects, and experimental repeatability. Consistent treatment of liquid cell membranes with plasma and new cell designs that limit membrane bulging are enabling more repeatable experiments. These similarities indicate that liquid cell microscopy researchers stand to learn much from the development and popularization of cryo-EM as a mainstream microscopy technique.

One of the main obstacles for cryo-EM imaging during its initial development was avoiding beam damage to the biological samples [29, 33]. Low dose imaging

techniques were devised to minimize the amount of dose received by the sample during imaging [1]. This method involves shifting the electron beam off the area of interest for focusing and stigmation, and then quickly shifting back to the area to acquire an image. To preserve secondary and tertiary structure of biological macromolecules, the electron dose must be kept below ~1 $e^{-}/Å^2$; however, for lower resolution a tolerable dose is typically between 10 and 50 $e^{-}/Å^2$. Bubbling of the area surrounding the sample begins to occur at 2000–5000 $e^{-}/Å^2$, and mass loss will occur at much higher electron doses. Similar threshold electron doses should be developed for liquid cell electron microscopy, for instance, to limit alteration of ionic strength, pH, dissolved gas, and electron beam charging. Currently, cryo-EM has implemented dose fractionation techniques and direct electron cameras to reduce the dose per image and enable higher resolution. Similar techniques will find importance in liquid cell electron microscopy to reduce total dose and dose per image; direct electron cameras are already being utilized in LCEM experiments [35, 36].

5 Key Research Findings

5.1 Growth of Particles from Aqueous Solutions

In the last decades, radiolytic synthesis routes have exploited the chemical effects of the absorption of high-energy radiation on precursor solutions to form nanostructures in a selective reducing/oxidizing environment. Radiation chemical synthesis provides a powerful means to form nuclei which are homogeneously distributed in the whole volume and where the growth rate can be easily controlled [37–40]. The latter has recently been achieved using liquid cell electron microscopy, with examples of formation kinetics of particles in polar (water) [28] and nonpolar (toluene) [14] solvents following a linear relation with applied dose rate. Thus far, most experiments in the liquid cell involved the use of water as a solvent, which explains the large amount of work dedicated to understanding the effects of the electron beam in aqueous conditions. We will discuss the radiation chemistry of water next.

5.1.1 Radiation Chemistry of Water

All liquids partially decompose during high-energy electron beam irradiation; understanding electron-beam interactions is key to successful and reproducible liquid cell experiments in a TEM. Radiation chemistry is the chemistry initiated by the interaction of incident high-energy electrons – the so-called ionizing radiation – with the liquid. In this section, we will present an overview of the radiation chemistry of various solvents, the effect of tuning different parameters during data acquisition, and some of the main observations in LCEM. We note that the energy involved when the primary electrons interact with the solution under investigation is much larger than the energy needed to break any bond in the molecules. A main reason all bonds in the solution molecules are not instantly broken is that the interaction duration is less than 10^{-15} s, indicating that the immediate direct effect of the incident electron

beam is to ionize solution molecules, which produces electronic excitations. The bond scissions only take place further on in the process, during the relaxation of the system [41].

An important characteristic of radiation chemistry is that solution phase species are ionized per their relative abundance. Thus, for dilute solutions ([Solute] $\leq$ 0.1 M), the ionized molecules are essentially those of the solvent [40]. This means that for dilute solutions in the STEM, knowledge of the radiation chemistry of the solvent is of paramount importance to understand the chemical processes initiated by the electron beam during liquid cell electron microscopy. LCEM experiments typically employ dilute solutions, except for battery materials (e.g., electrolytes solutions) and operando experiments in batteries, for which solution concentrations are typically 1 M (see Sect. 5.4.2).

From the possible solvents that are available for radiation chemistry outside the electron microscope, water is by far the most commonly used. Some reasons include (1) the simplicity of the radicals formed as compared to organic solvents; (2) the high reactivity of the species produced as well as their large G-values (high concentrations), which means that a large pool of radicals can be produced with relatively low dosages; and (3) the fact that the radiolysis of water has been broadly studied and therefore much information is available to be used for applications. The radiolysis of water produces the breakdown of molecules into the following primary radicals and several other molecular species [42]:

$$H_2O \rightarrow H_3O^+, OH^{\cdot}, e_{aq}^-, H^{\cdot}, OH^-, H_2O_2, H_2, HO_2. \tag{1.1}$$

The species in Eq. 1.1 are listed in descending order of their G-value for 300 keV electrons, which is the rate of generation per 100 eV of energy deposited in the solvent [42]. Several properties of the solvent can alter the G-values of radiolysis species [43], which determines the concentration of species created. The most relevant factors are (1) additional competing reactions due to high solute concentrations [44], (2) the presence of molecular scavengers, and (3) the alteration of the solution pH. A more complete discussion of these points and further references can be found in Ref. [15]

For the case of pure DI water, if the irradiation ceases and the system is allowed to evolve freely, it will eventually equilibrate back to the nonirradiated steady state of water. This is in principle not the case when solutes are present. Figure 1.3 shows a diagram illustrating different kinetic paths during radiolysis and provides the approximate timescales for each process [41]. In fact, in the presence of additives, the chemistry of the solution is irreversibly changed following irradiation and does not equilibrate back to the original state. The effect of additives in aqueous solutions will be the topic of Sect. 5.1.3. Generally, the generation of products for low LET radiation (e.g., high energy electrons) is very inhomogeneous and typically occurs in spurs, i.e., small pockets in the solvent where most ionization events occur (non-homogeneous kinetics range in Fig. 1.3) [41]. Only for timescales longer than 10^{-7} s, the concentration of radicals will reach steady state and the reaction kinetics will be within the "homogeneous kinetics" regime.

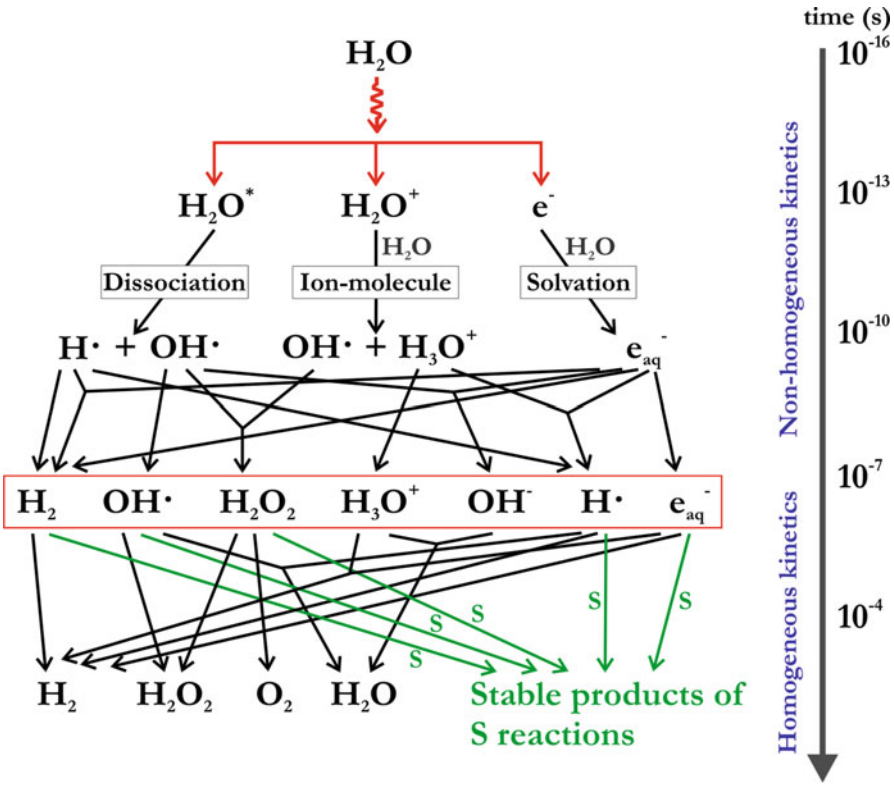

Fig. 1.3 Diagram showing the radiolysis of water and timescales involved with and without solutes. Data, diagram, and processes explained in [45]

We note here that while both TEM and STEM images are recorded within milliseconds, the irradiation time for TEM ($\sim 10^{-3}$ s) and STEM ($\sim 10^{-6}$ s) differs by several orders of magnitude. In the case of STEM, signal collection at each pixel occurs within microseconds. In principle, production of primary radicals and steady-state conditions should occur during data collection for both imaging modes; however, for the case of applying steady-state conditions to simulate the reaction products formed, STEM is expected to have larger errors.

Three primary species of particular importance in the radiation chemistry of water are the aqueous electron (e_{aq}^{-}), the hydroxyl radical ($OH^{\cdot}$), and the hydrogen radical ($H^{\cdot}$), which have standard reduction potentials of −2.9 V, 1.8 V, and −2.3 V at neutral pH [46] respectively, indicating that they are strongly reducing ($e_{aq}^{-}, H^{\cdot}$) and oxidizing ($OH^{\cdot}$) species. Aqueous electrons, or solvated electrons for the case of nonaqueous solutions, are a particularly interesting species. Following the simplest model used to describe the properties of solvated electrons, namely the cavity model, aqueous/solvated electrons can be envisioned as a delocalized negative elementary charge surrounded by water molecules (or solvent for solvated electrons).

Their properties are not well known even after decades of research: the delocalized negative charge effectively creates a cavity of 2.5 Å of radius, but the reason for this is unknown. It is a thermodynamically stable radical and has a short lifetime (~50 μs in neat water) due to its high chemical reactivity [47].

5.1.2 In Situ Particles Growth in Unscavenged Aqueous Solutions

Metallic nanoparticles formed by the effect of electron beam irradiation inducing chemical reduction of metal ions (or metal complexes), are mainly due to the interaction of these with aqueous electrons via the following general reaction [40]:

$$e_{aq}^{-} + M^{n} \rightarrow M^{n-1}. \tag{1.2}$$

Here M represents a metal cation species with an oxidation state of n. As an example, the first order reaction rate for reduction of Ag^{+} into Ag^{0} by aqueous electrons is $k = 4.5 \cdot 10^{10}\ M^{-1}s^{-1}$. Such a high reaction rate suggests diffusion limited reaction conditions in most cases of metal cation reduction [46, 48]. We note that in unscavenged solutions, there will also be competing oxidation reactions that might have similarly high reaction rates. For the case of silver, the competing reaction $OH^{\cdot} + Ag^{+} \rightarrow AgOH^{+}$ occurs with a large reaction rate of $k = 1.4 \cdot 10^{10}\ M^{-1}s^{-1}$, indicating it will counteract the metal ion reduction process, where the $AgOH^{+}$ species react with aqueous electrons to decrease the rate of Ag^{0} precipitation.

Figure 1.4a shows the effect of electron dose rate on the nucleation rate of silver nanoparticles under STEM irradiation [12]. The power law dependence of radical concentration on electron dose rate enables systematic control over the nanoparticle reduction reaction conditions. Typical dose rates for (S)TEM imaging are 10^{5}–10^{7} Grays/s, allowing for steady-state concentrations of aqueous electrons of $\left[e_{aq}^{-}\right] \approx 10^{-6} - 10^{-7}$ M . The nucleation rate increased as a function of electron dose rate (Fig. 1.4a); however, the total threshold electron dose necessary to initiate nucleation remained constant [12]. A similar threshold electron dose was observed by Park et al. for beam-induced growth of gold nanoparticles in water [49]. The existence of a threshold to nanoparticle nucleation suggests a solution chemistry–dependent activation energy for nucleation during electron beam–induced nanoparticle growth that is not determined by electron beam parameters.

Further investigation of the effect of dose rate on beam-induced nanoparticle growth revealed the electron dose rate determined the nanoparticle growth mechanism (Fig. 1.4b) [12]. At relatively low dose rates growth was reaction limited, while at high dose rates growth was diffusion limited. Park et al. found that the nanocrystal volume increased approximately linearly with time for reaction limited growth conditions (Fig. 1.4c) [49]. Thermodynamic growth (i.e., reaction limited) of faceted gold nanoparticles was observed to occur below a critical supply rate of precursor to the nanoparticle surface, corresponding to a critical dose rate of $4 \cdot 10^{6}$ Gy/s (Fig. 1.4d) [28]. Fast diffusion limited reaction kinetics above this critical dose rate led to the loss of nanoparticle faceting. This experimental evidence shown

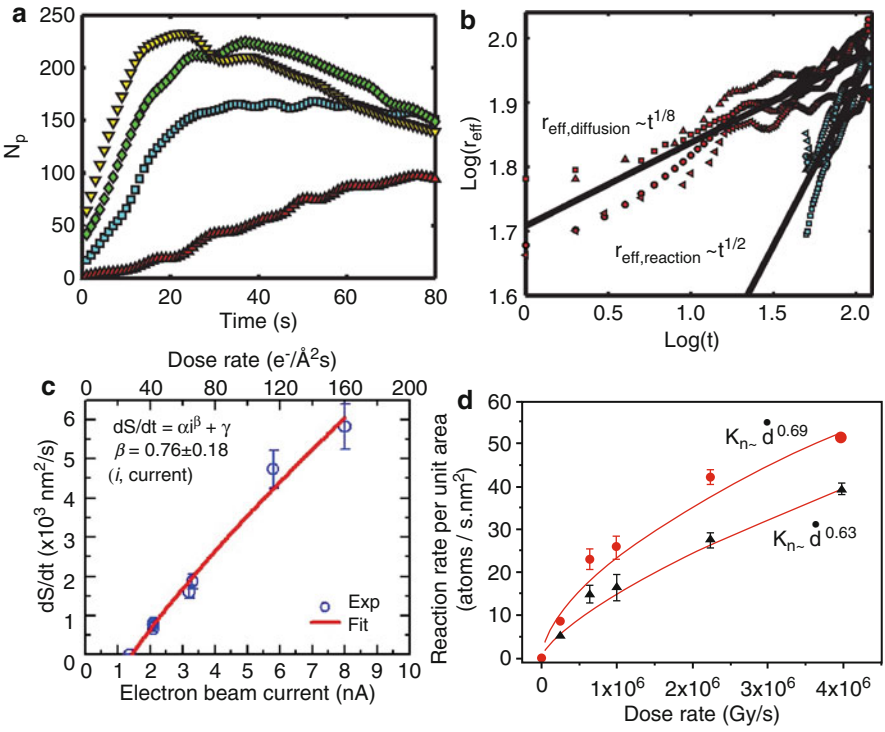

Fig. 1.4 (**a**) Number of particles nucleating as a function of time for four different electron dose rates. Yellow triangle: electron dose per frame of 6.65 $e^-/Å^2$; green diamond: 4.43 $e^-/Å^2$; blue square: 2.22 $e^-/Å^2$; red triangle: 0.89 $e^-/Å^2$. (**b**) Effect of electron beam current on the mechanism for electron beam–induced silver nanoparticle growth (Figures reproduced with permission from Woehl et al. [12] Copyright 2012 American Chemical Society). (**c**) Growth rate of gold nanoparticles increases linearly with electron dose rate for reaction limited growth (Figure reproduced with permission from Park et al. [49] Copyright 2014 American Chemical Society). (**d**) Dependence of growth rate of faceted gold nanoprisms (triangles) and planar nanohexagons (hexagons) on electron dose rate (Figure reproduced with permission from Alloyeau et al. [28] Copyright 2015 American Chemical Society)

across several research groups indicates that minimizing the electron dose rate sufficiently can result in reaction limited kinetics even though radical reactions are generally considered to be diffusion limited.

5.1.3 Creating Net Reducing Conditions for Particle Growth

The general approach for nanomaterial synthesis in conventional radiation chemistry is to convert primary radicals, consisting of both oxidizing and reducing species, to either net reducing or oxidizing conditions to simplify reaction kinetics and prevent back reactions. Species such as secondary alcohols, for instance, are highly reactive with ·OH and H·, while they do not strongly interact with aqueous electrons.

Table 1.1 Relative reactivity of primary radicals with organic functional groups[a] (Adapted from Ref. [51] with permission)

Functional group	Relative reactivity		
	e^-_{aq}	H·	·OH
H^+	***	–	–
O_2	***	***	–
Halide ions (Br^-, Cl^-, I^-)[b]	–	–, *	***
Saturated carbon (–CH_2–)	–	**	***
Unsaturation			
Alkene	–	***	***
Aromatic	*	***	***
Pyrimidine	***	**	***
Nitrile (–C ≡ N)	**	*	**
Carbonyl (>C═O)	***	*	**
Carboxylic acid (–CO_2H)[c]	**	*	**
Ester (–CO_2R)	**	*	**
Amide (–$CONH_2$)	**	*	**
Amine (–CH_2)[c]	*	*	***
Nitro (–NO_2)	***	**	–
Alcohol (–CH_2OH)	–	**	***
Ether (–O–)	–	**	***
Chloro (–Cl)	**	*	
Bromo (–Br)	***	**	
Iodo (–I)	***	***	
Thiol (–SH)[c]	***	**	***
Disulfide (–S–S–)	***	**	***

[a]Approximate rate constants for reactions between the primary radical products from water and organic compounds containing the functional groups displayed. Oxygen, hydrogen ion, and halide ions are included for comparison. Symbols used to represent rate constant ranges ($dm^3\ mol^{-1}\ s^{-1}$) are ***, $k > 10^9$; **, $k = 10^7$–10^9; *, $k = 10^5$–10^7; –, $k < 10^5$

[b]$H\cdot + I^-$ and $\cdot OH + Cl^-$ only occur in acidic solution

[c]pH dependent

In general, species that react specifically and strongly with a certain radical product are referred to as radical scavengers. As a guideline, Table 1.1 outlines values of the reaction rates of the most reactive primary radicals in water with typical organic functional groups that would act in some cases as radical scavengers for the primary radical of water indicated. Recently, we have detailed this information in a review article and provided a number of methodologies and relevant references about the use of additives in radiation chemistry and, in particular, in the (S)TEM (see Woehl and Abellan [15]).

Growth of metal nanoparticles by radiation chemistry has typically employed net reducing conditions by adding OH^- radical scavengers such as alcohols or formate anions [40, 46]. Generally, this method either converts ·OH to a relatively inert secondary radical or to a reducing species. A commonly used method is the addition of isopropanol to the aqueous solution. The following reaction thus occurs:

$$OH^{\cdot} + CH_3CHOHCH_3 \rightarrow H_2O + CH_3C^{\cdot}OHCH_3 \quad (1.3)$$

Note that isopropanol reacts with ·OH radicals to form the reducing radical ($(CH_3)_2 \cdot COH$).

In the electron microscope, growth of palladium on the surface of silver nanoparticles (seeds) was achieved by following this methodology. A comparison of the seeded particle growth from a $PdCl_2$ solution with and without the use of isopropanol showed that while a hollow silver nanocage is generated in the former case, due to the oxidation and dissolution of silver, adding isopropanol results in growth of a homogeneous palladium shell on the silver seed [52].

Radical scavengers can also be used to establish oxidizing conditions during radiolysis as well (cf. Table 1.1). For general methods we redirect the reader to the book chapter [45] and to the recent review focused on radiolysis during LCEM [15] and references therein.

5.2 Dose, Motion, and Contrast Limited Resolution for Imaging (Bio)macromolecules

Resolution and contrast for imaging proteins and macromolecules with liquid cell TEM should be comparable to cryo-EM: the liquid layer thicknesses achieved for LCEM and cryo-EM are similar and low dose imaging can be employed for both techniques as well. The key differences between the two techniques are radical diffusion, molecule mobility, and sample membranes. Proteins are frozen into a single conformation during cryo-EM, meaning essentially no motion blur during imaging. However, during liquid cell electron microscopy, proteins in free solution rotate and translate by Brownian motion in the liquid layer, making imaging impossible without high temporal resolution (microseconds) imaging, which is not achievable even with high-speed direct electron detectors. One strategy to image protein and biomolecules with liquid cell electron microscopy is to attach them to the liquid cell membranes using nonspecific physical interactions such as Van der Waals or electrostatic forces; or specific biochemical interactions, such as antibody-antigen interaction [25]; or other specific binding chemistries (e.g., biotin-streptavadin, DNA hybridization) (cf. Fig. 1.2). We note, however, that binding of a protein to a surface using nonspecific or specific interactions can change its inherent structure. Antibody-antigen binding has been shown to successfully fix rotavirus particles, enabling liquid cell TEM imaging at resolutions of ~2 nm. Similar spatial resolutions were obtained for crystalline acrosomal bundles [53]. However, this is still approximately an order of magnitude worse spatial resolution than achieved by the best cryo-EM techniques. The reduced spatial resolution is likely due to various factors. Experiments comparing cryo-EM directly to liquid cell TEM images are helpful in determining the predominant factors limiting resolution for liquid cell imaging (Fig. 1.5). Spontaneously self-assembled star miktoarm polymers were synthesized and imaged using cryo-EM and liquid cell TEM to determine their size and

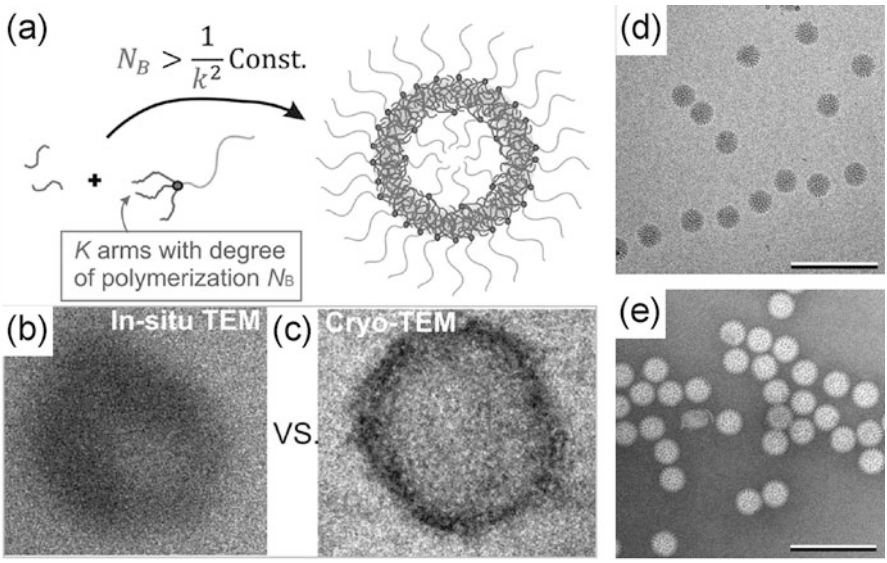

Fig. 1.5 Comparison of images obtained from cryo-EM (**b** and **d**) to LCEM images of the same samples. (**a**) Schematic cartoon of the structure of miktoarm star polymer. (**b**) LCEM image of the polymer acquired using most probably loss energy filtered TEM (EFTEM) imaging. (**c**) Cryo-EM of the same polymer. (**d**) Cryo-EM image of rotavirus double-layered particles. (**e**) LCEM image of the same virus particles. Scale bars in (**d**) and (**e**) are 300 nm; the polymer in (**b**) and (**c**) is approximately 20 nm in diameter. (**a**–**c**) reproduced with permission from Ref. [54]. (**d**) and (**e**) reproduced with permission from Ref. [25]

morphology (Fig. 1.5a–c) [54]. The cryo-EM images had approximate spatial resolutions of single nanometers, while liquid cell TEM images had resolutions on the order of tens of nanometers. The authors suggest the main cause of low spatial resolution in liquid cell TEM images was increased sample thickness. While this is likely a major effect, molecular mobility likely also contributes to decreases in spatial resolution as well. Energy filtered TEM and most probable loss imaging increased resolution and contrast of liquid cell TEM images, by reducing chromatic aberrations [54]. Comparison of cryo-EM and liquid cell TEM images of rotavirus particles revealed similar spatial resolutions due to preparation of liquid cell samples with very thin liquid layers (Fig. 1.5d, e) [25]. Relatively thick silicon nitride membranes, compared to the thickness of cryo-EM samples, enclose the liquid cell and reduce spatial resolution by introducing additional chromatic aberration in TEM mode, beam broadening in STEM mode, and increase the amount of radiation damage due to their higher density and atomic number compared to the water layer. This is evidenced by recent examples of liquid cell TEM protein imaging using graphene as an alternative membrane material. Increased sample tolerances to radiation damage [55] and higher spatial resolution [56] were achieved using graphene membranes, suggesting experimental conditions more closely resembling cryo-EM.

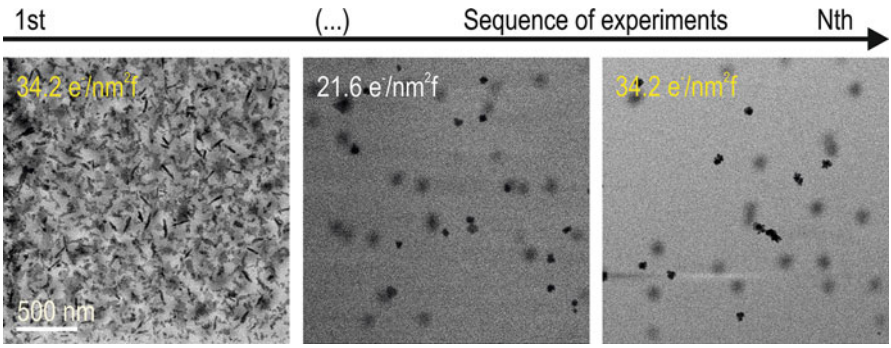

Fig. 1.6 Three frames from different datasets recorded consecutively during the same microscope session and recorded after increasing number of experiments. Despite using the same irradiation conditions, the growth of particles observed in the first experiment could not be reproduced after several additional observations. From left to right, BF STEM images from different sample areas recorded using $M = 40{,}000\times$ magnification, 3 μs pixel-dwell time (frame time accounting for flyback was 3.78 s), and beam currents of 6.2 pA (left and right) and 3.9 pA (middle). Corresponding dose rate values are indicated on the images (Images reprinted with permission from Abellan et al. [27] Copyright 2014 Royal Society of Chemistry)

5.3 Other Effects of the Electron Beam in LCEM Experiments

5.3.1 Depletion of Precursor Solution

Unlike the study of solid samples in the electron microscope, the observation of processes in liquids requires different methodologies for low dose image acquisition. The main reason behind these new requirements is that observation of liquids by means of an ionizing radiation source, particularly for the case of small experimental volumes and the presence of membranes and layer-like geometries of liquid cells, is that the sample retains a *memory* of previous irradiations. This has been previously termed the *history of dose delivery* [27]. For beam-induced nanoparticle growth, sample *history* is typically manifested as reduced nanoparticle growth rates and differences in nanoparticle shape to more rounded and agglomerated structures and is due to depletion of precursor ions. Figure 1.6 illustrates the effect of precursor solution depletion and other changes in the solution chemistry upon accumulation of radicals over consecutive Ag nanoparticle growth experiments recorded in different *pristine* areas during the same microscope session.

As discussed elsewhere [27], precursor depletion and the increasing number of excess unreacted radicals in solution likely altered the growth rates measured and modified the experiments over time. Figure 1.6 demonstrates that sample *history* can have a large effect on in situ experiments and, if not prevented, may limit reproducibility in the growth rates. The rapid diffusion of radicals away from the viewing area during LCEM experiments, which has been proposed in several recent works to explain particles growth rate observations [14, 49], contributes to the rapid depletion of radicals and solution chemistry changes. This is especially evident when high doses are used, such as during in situ growth of dendritic gold nanostructures [57, 58].

5.3.2 Electron Beam Charging

Predominant electron-beam sample interactions during liquid cell electron microscopy stem from inelastic electron scattering in the membrane windows and thin liquid layer. Typical membrane windows are 10 – 50 nm amorphous silicon nitride or silicon dioxide. Ultra-thin graphene based windows are also used in liquid cells, providing minimal electron scattering for high-resolution applications but less control of specimen thickness and experimental reproducibility. In this section, we review electron beam charging effects for silicon nitride and silicon dioxide membranes. Inelastic scattering of high energy electrons, typically 100–300 keV for liquid cell electron microscopy in a TEM, induces secondary and Auger electron emission into the liquid layer and vacuum of the TEM [59]. Loss of negative charge renders the thin membranes positively charged because the membrane windows are highly insulating [11, 60]. An electrostatic model developed by *Cazaux* provides estimates of the amount of charging that occurs in an isolated thin insulating membrane under TEM illumination [59]. The total charge induced by irradiating an isolated thin insulating membrane with high energy electrons (>100 keV) is as follows:

$$Q(\infty) = \frac{I_0(\delta^{\mathrm{x}} + y^{\mathrm{x}})\varepsilon_{\mathrm{m}}\varepsilon_0}{\sigma} \tag{1.4}$$

Here $Q(\infty)$ is the steady-state charge in the irradiated area of the film, I_0 is the incident electron beam current, δ^{x} is the secondary electron (SE) yield, y^{x} is the Auger electron yield, ε_{m} is the relative permittivity of the membrane, ε_0 is the vacuum permittivity, and σ is the electrical conductivity of the membrane. The SE yield δ^{x} is assumed to be insignificant as the foil potential will be >50 V (SEs are defined as having energies <50 eV). The Auger electron yield of an insulating 100 nm SiO_2 membrane is estimated to be $y^{\mathrm{x}} = 10^{-4}$ for 100 keV electrons [61]. Assuming a uniform distribution of charges throughout the irradiated area, the following expression for the maximum electric potential in the foil is obtained.

$$V_{\mathrm{m}} = \frac{Q(\infty)}{4\pi\varepsilon_{\mathrm{m}}\varepsilon_0}\left(1 + 2\ln\frac{r_0}{a}\right) = \frac{I_0(\delta^{\mathrm{x}} + y^{\mathrm{x}})}{4\pi\sigma}\left(1 + 2\ln\frac{r_0}{a}\right). \tag{1.5}$$

Here V_{m} is the steady-state electric potential in the thin film, r_0 is the path length to electrical ground, and a is the radius of the electron beam. Note that the electric potential and charge are both linearly proportional to the electron beam current. Electron irradiation of two parallel membranes separated by a liquid layer will induce an electric field between the membranes. Both membranes will acquire charge; however, beam broadening due to beam divergence and elastic scattering [62] in the liquid layer causes a larger potential in the top window compared to the bottom, and induces a potential drop and electric field normal to the two parallel windows, directed toward the bottom membrane. Additionally, a divergent tangential electric field will be induced due to the potential difference between the irradiated and nonirradiated areas. We estimate the magnitude of the potential drop between the

two windows by simply subtracting the electric potential of the top window from that of the bottom window.

$$\Delta\varphi = V_{\mathrm{m,t}} - V_{\mathrm{m,b}} = \frac{I_0 y^{\mathrm{x}}}{2\pi d\sigma} \ln \frac{a_{\mathrm{b}}}{a_{\mathrm{t}}} \tag{1.6}$$

Here $\Delta\varphi$ is the potential difference between the top and bottom membranes, $V_{\mathrm{m,\,t}}$ is the potential of the top membrane, $V_{\mathrm{m,\,b}}$ is the potential of the bottom membrane, a_{b} is the electron beam radius at the bottom membrane, and a_{t} is the electron beam radius at the top membrane. The electric field is estimated by dividing the potential difference by the thickness of the liquid layer, $E_n \approx \Delta\varphi/t$. Calculation of the membrane potential and electric field strength for parameters typical for TEM and STEM imaging yields unrealistically large electric field strengths exceeding the dielectric breakdown strength of water (> 70 MV/m). Obviously, naïve application of models developed for isolated membranes does not capture the complex physics associated with the liquid layer between the two membranes. In fact, Glaesar and Downing suggested that electron beam charging of thin insulating films in contact with a conducting layer likely involves complex charge compensation via capacitive charging and the formation of a "dipole sheet" at the conductor-insulator interface [63]. For the case of liquid cell electron microscopy, this effect is likely manifested as an induced electrical double layer in the liquid at the membrane/liquid interface. Describing specimen charging in the liquid cell will likely require more intricate modeling that is out of the scope of this chapter. Regardless, *Cazaux's* model (Eq. 1.4) and empirical evidence [19, 60, 64] demonstrate that the amount of electron beam charging can be controlled with the electron beam current.

5.3.3 Diffusion of Nanoparticles in the Liquid Cell

Diffusion is ubiquitous to all liquid phase nanoscale systems, including synthetic nanomaterials, naturally occurring biomineral nanocrystals, and biomolecules. Diffusion controls the collision rate of nanophase materials, colloidal stability, assembly, and aggregation mechanisms that dictate growth. Numerous reports have experimentally shown that diffusion during liquid cell (S)TEM imaging is severely hindered, where measured diffusion coefficients are typically 10^7–10^9 orders of magnitude smaller than the Stokes-Einstein prediction for Brownian motion [10, 17, 18, 35, 65–69]. Understanding the predominant diffusion mechanisms during liquid cell electron microscopy is important to compare in situ observations in the TEM to processes outside of the TEM. During liquid cell electron microscopy experiments, nanoparticles are typically confined between two solid membranes (silicon nitride or graphene) in a liquid layer that is hundreds of nanometers thick. The increased hydrodynamic drag due to the presence of the solid wall seems an attractive explanation for the retarded diffusion; however, it only accounts for a $5\times$ decrease in the expected diffusion coefficient [70].

There are currently several proposed mechanisms for the retarded diffusion during liquid cell (S)TEM experiments (Fig. 1.7): Verch et al. have suggested local ordering and thus increased viscosity of the liquid layer near the window

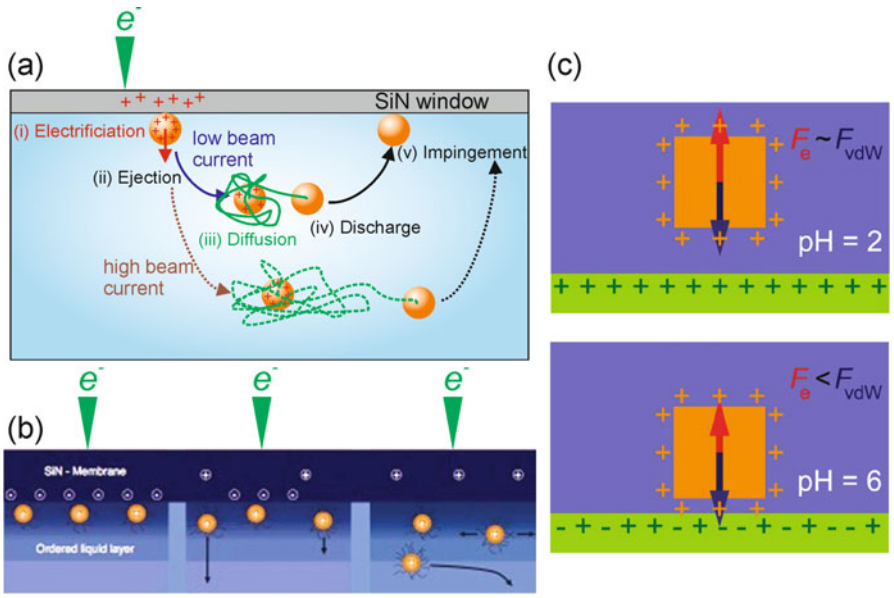

Fig. 1.7 Current models for explaining slow diffusion of nanomaterials during liquid cell electron microscopy. (**a**) Electrostatically mediated hopping-induced surface diffusion. Image reproduced with permission from Woehl and Prozorov [10]. (**b**) Liquid ordering near the membrane surface increases local viscosity and decreases diffusion coefficient. Image reproduced from permission Verch et al. [17] (**c**) pH-meditated desorptive diffusion of nanoparticles during LCEM (Images reproduced with permission from Chee et al. [35])

surface [17], Chee et al. have proposed a Levy flight model based on heterogeneous window charge distribution and significant beam-induced pH effects, [35] and Woehl and Prozorov proposed electrostatically induced hopping diffusion of nanoparticles mediated by the electron beam [10]. Van der Waals attraction between nanoparticles and the silicon nitride membrane is typically stronger than double layer repulsion, especially in the presence of buffer, causing nanoparticles to physically adhere to the membrane prior to imaging, as predicted by the particle-membrane interaction potential of mean force (Fig. 1.8). Imaging of the nanoparticles with TEM or STEM irradiation induces subsequent diffusion of the nanoparticles, often with a lag time between the initial irradiation and the beginning of movement [17]. Under moderate beam currents, diffusion is two dimensional and occurs parallel to the membrane surface; large beam currents ($>$ 1 nA) cause complete ejection of nanoparticles from the field of view [11].

Both Woehl and Prozorov and Chee et al. showed an increase in diffusion coefficient with electron beam current but proposed different models to explain the ensuing behavior. Woehl and Prozorov explained the hindered diffusion and increase in diffusion coefficient with beam current in terms of increased electron

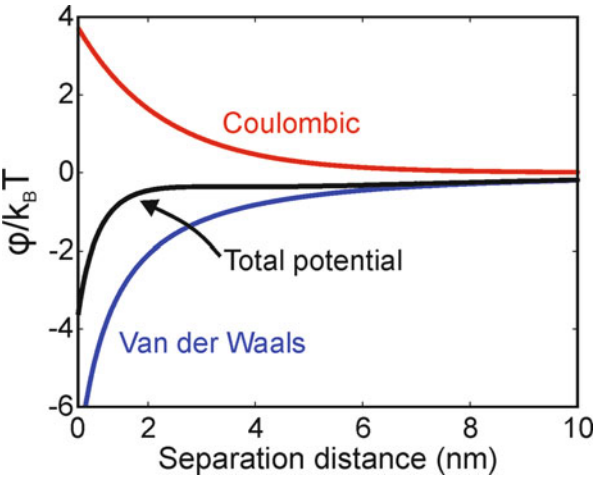

Fig. 1.8 Total interaction potential of mean force between the liquid cell membrane with a zeta potential of −15 mV and a 30 nm gold nanoparticle with a zeta potential of −15 mV dispersed in a 29 mM acetate buffer. The primary minimum at a separation distance of 0 nm indicated nanoparticles will physically adhere to the membrane due to strong Van der Waals interactions

beam–induced charging ejecting the nanoparticles from the silicon nitride membrane for longer times (Fig. 1.7a). Ejection of secondary and Auger electrons into the vacuum during irradiation of the silicon nitride membrane causes positive charge to be acquired on membrane [59]. Physically adhered nanoparticles acquire the positive charge via contact electrification over a 1–10 s timescale and are subsequently repelled from the membrane via coulomb interactions. After ejection, nanoparticles diffuse in the liquid via Brownian motion for a short time (~ns), during which they lose their acquired charge to the conducting buffer solution. The uncharged nanoparticles then fall back into the potential well at the surface of the membrane and the process begins again. Because the imaging timescales are much longer than the nanosecond diffusion timescales, this desorption-adsorption-mediated diffusion appears as continuous diffusion with intermittent sticking. Importantly, scaling estimates of the charging and discharging times associated with contact electrification and charge leakage in the liquid layer agreed with the order of magnitude of the experimentally measured diffusion coefficients. This mechanism draws a direct comparison to classical surface diffusion of adatoms induced by thermal forces; however, in this case it is electrostatic forces that imbue the surface adsorbed nanoparticles with the energy to overcome the activation barrier. Hence, this mechanism has been termed electrostatically induced surface diffusion [10].

Chee et al. offered an alternative explanation based on a heterogeneous charge distribution on the silicon nitride window surface and electron beam–induced pH change (Fig. 1.7b) [35]. The authors observed nanoparticle diffusion during liquid cell TEM at high frames rates on the order of 100 fps and found that diffusion occurred via a combination of sustained sticking sequences in which nanoparticles rotated rapidly but did not translate, intermittently dispersed with large sporadic flights where the nanoparticle would travel 10–100 nm at a time. This diffusion

behavior is consistent with a Levy flight model, which can be described as a random walk diffusion process with a heavy tail on the jump distance distribution, corresponding to the large flights taken by the particles. The wait time distribution between flights followed a power law behavior, suggesting a distribution of adsorption binding energies and a heterogeneous charge distribution on the silicon nitride membrane. The increase in mobility with beam current was attributed to electron beam–induced decreases in solution pH, which decreases the binding energies between the nanoparticles and membrane, allowing for more rapid diffusion. While the models of Woehl and Prozorov and Chee et al. offer scaling estimates and/or qualitative explanations of nanoparticle diffusion, quantitative agreement between experiment and theory has yet to be achieved in either case.

Verch et al. found that electron beam current did not affect the mobility of gold nanoparticle during liquid cell electron microscopy but did influence the lag time from initial irradiation to when nanoparticles became mobile [17]. As with the model of Woehl and Prozorov, this suggests that electron beam–induced charging is responsible for the nanoparticle mobility, where the initial lag time corresponds to the time it takes for a sufficient amount of charging to occur to induce nanoparticle desorption. As opposed to the desorption-mediated mechanisms proposed by Woehl and Prozorov and Chee et al., Verch et al. proposed that after charging induced desorption, nanoparticles diffuse by Brownian motion near the membrane surface, but in an ordered liquid layer (Fig. 1.7c). This model requires that this ordered liquid layer has a viscosity 10^7 times higher than water.

Differing experimental conditions could lead to the various diffusion behaviors described here, meaning each of these proposed mechanisms could in principle be correct. However, we note that models that do not impose specific restrictions on the experimental system will be more generally applicable for different types of liquid cell membranes (silicon nitride, silicon oxide, graphene), various buffer conditions, and different classes of nanophase materials. More systematic experiments varying each of these parameters are needed to develop more quantitative models of diffusion during LCEM.

The overwhelming experimental evidence points toward surface diffusion controlling mobility of nanoparticles during liquid cell electron microscopy. This has advantages and disadvantages for imaging nanoscale growth and assembly processes in situ. The obvious advantage is that nanomaterial mobility is low enough to capture images at high resolution without significant image blur due to motion. Understanding the effect of electron beam current on diffusion is important in that it allows researchers to optimize imaging conditions to minimize movement and image blur. On the other hand, many nanoscale liquid phase growth and assembly processes rely on rapid three-dimensional diffusion to enable kinetics that are accessible over experimental timescales. Reproducing the transport phenomena conditions of bulk experiments while obtaining useful in situ images of these fast processes in liquid cell electron microscopy is currently a limitation of the technique. Dynamic TEM (DTEM) may offer a solution for imaging fast diffusive processes at timescales over which there is no image blur.

5.4 In Situ Observations in Nonaqueous Solutions

5.4.1 Radiation Chemistry of Organic Solvents

Organic solvents, while giving us access to a broader range of experimental conditions, are not as commonly used in radiation chemistry as water and thus less information can be found about them. Radiolysis of nonaqueous systems typically generates a complex mixture of species including molecular hydrogen, small molecules, dimeric species, and even larger polymeric molecules. Furthermore, the G-values for organic materials are not well established compared to water. The main reason for this is that they are strongly influenced by irradiation conditions and the presence of impurities [71].

The free-ions G-values of nonpolar solvents (e.g., hydrocarbons) are generally lower than those of polar solvents. Abellan et al. proposed the use of polar solvents including in general any solvent that also allows for smaller production of radicals for similar amount of incident irradiation as water, as an alternative for synthesis in LCEM [14]. In fact, dose rates in LCEM are orders of magnitude higher than for typical radiation chemistry synthesis and alternative methodologies allowing for lower production of radicals are desirable. As an illustrative example exposed in that work, the G-values of H_2 from the radiolysis of toluene is $G(H_2) = 0.14$ molecules/100 eV, which is much lower than production yields of radicals from the radiolysis of water ($G(e_{aq}^-) = 2.7$ molecules/100 eV for water). Experimentally, it has been estimated that in the liquid cell the number of incident electrons required to form each Pd^0 atom incorporated into a Pd nanoparticle is at least one order of magnitude higher than those needed for production of one Au^0 in unscavenged water (we note that in a solution where the oxidizing radicals were scavenged this difference would be even higher). This observation supports the fact that a lower production of radicals is formed in hydrocarbon solvents as compared to more polar solvents (e.g., water). Palladium particles with homogeneous 2–3 nm size were grown by molecular hydrogen in toluene, see Fig. 1.9.

5.4.2 Radiolysis of Highly Concentrated Electrolyte Solutions – Degradation and Aging Studies

While most examples in this chapter relate to solutions with solute concentrations of <0.1 M, electrolyte mixtures for Li-ion battery applications are in the 1 M range. This difference means that radiolysis of solvent molecules will not necessarily dominate the radiation chemistry of the solutions; solute molecule radiolysis will also have a significant impact. Indeed, the specific salt-solvent combination dictates the specifics of the breakdown products [13]. Note the different breakdown behavior in Fig. 1.10c, d, corresponding to two different salts, $LiPF_6$ and $LiAsF_6$, dissolved in the same solvent, EC:DMC. Importantly, in the same work, a qualitative correlation between degradation kinetics and the biomolecular rate constants of the salt was observed. In that work, Abellan et al. proposed to use radiation chemistry in the electron microscope as a fast and efficient method for studying and directly probing

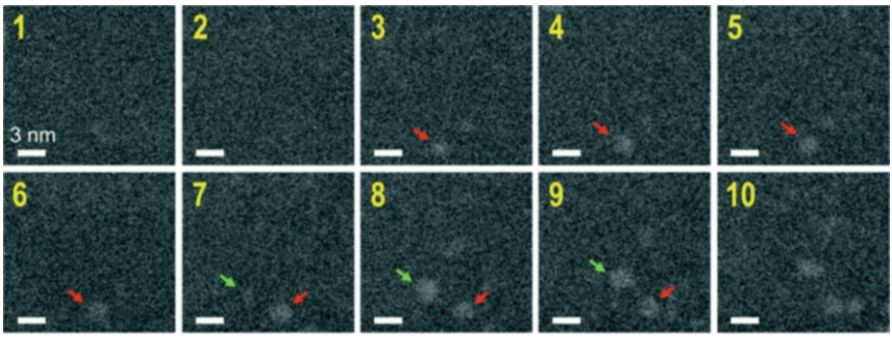

Fig. 1.9 We recently introduced the use of aromatic hydrocarbons (toluene) as solvents that are very resistant to high-energy electron irradiation and achieved synthesis with tunable kinetics for sub-3 nm particles by creating net reducing conditions (with no addition of scavengers for oxidizing radicals) and very low yields of reactive species for a given incident electron dose. Dihydrogen (H_2) was proposed as the main primary species involved in the reduction process leading to Pd^0 particle formation, which is a widely used reductant in the synthesis of supported metal catalysts (Image reprinted with permission from Ref. [14] with permission, copyright 2016 American Chemical Society)

the degradation mechanisms of electrolyte solutions upon reduction. More recently, different timescales have been used to investigate electrolyte aging and degradation using radiation chemistry outside the electron microscope, [72] thus confirming the validity of the method proposed.

Interestingly, an electrolyte solution containing 1 M lithium triflate (LiTf) dissolved in DMSO was observed to be stable (no signs of structural degradation observed) for extended period of times (see Fig. 1.10e), while the other electrolyte mixtures degraded when exposed to much lower cumulative electron doses (Fig. 1.10b).

5.4.3 Imaging Electrochemical Processes In Situ

Liquid cell electron microscopy is a powerful technique for operando characterization of electrochemical processes, such as understanding the effects of lithiation/delithiation on electrode structure and solid electrolyte interphase formation [73]. The electron beam can create similar effects as electrochemical reactions, namely oxidation and reduction reactions due to radiolysis of the solvent (Sect. 5.1). As electron beam effects have similar chemical mechanisms (i.e., redox reactions) to electrochemical reactions, they must be fundamentally understood and accounted for during experiments.

Various strategies can be used to account for and mitigate electron beam–induced artifacts during in situ electrochemistry experiments. Unlike reversible electrochemical processes, radiation damage is typically irreversible and independent of electrochemical charge state [74] and beam current dependent [12, 75–77], so observing an electrochemical process as a function of electron dose will reveal any imaging artifacts. It is worth mentioning, however, that there are reports of reversible redox reactions where the electron-beam drives reversible deposition/dissolution cycles of copper shells over gold nanoparticles which show aparrent similarities with

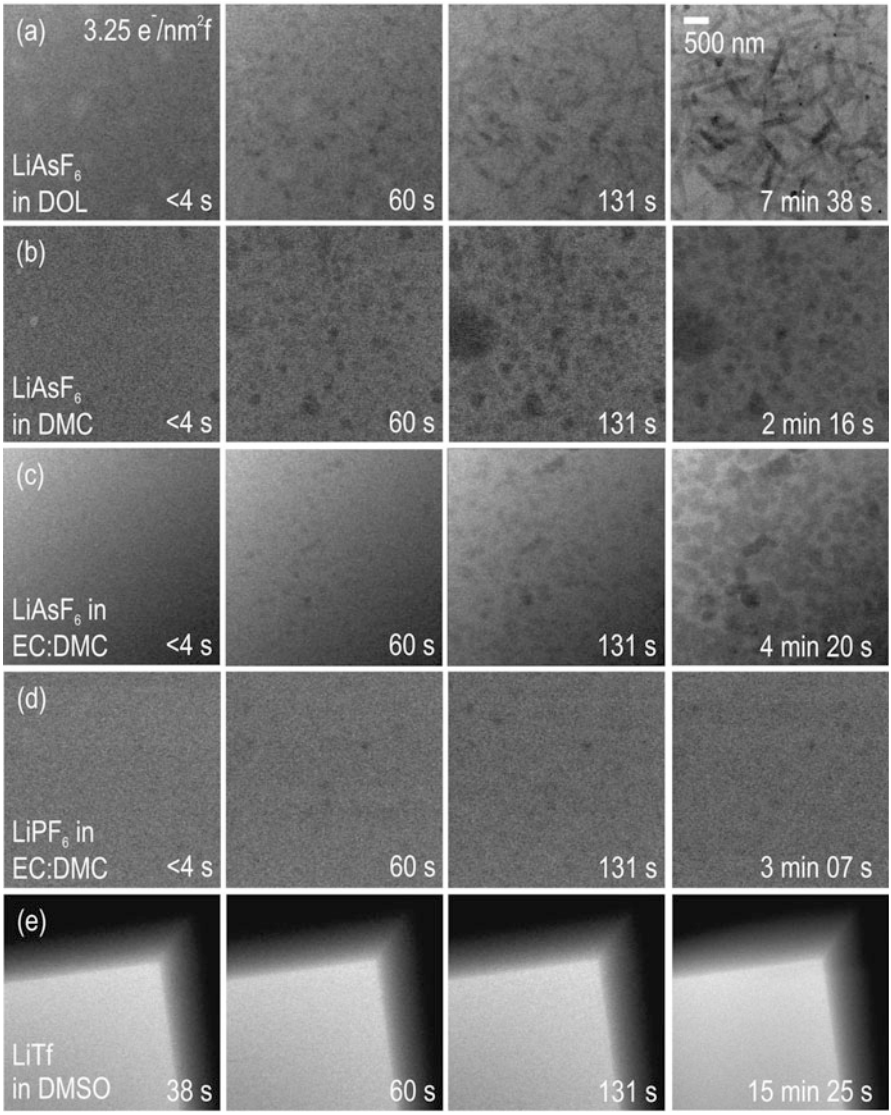

Fig. 1.10 Electron beam degradation of different electrolyte mixtures when exposed to the same electron dose rate. Images are compared to one another after the same irradiation time, thus after the same electron dose. While inorganic particle formation and polymerization are observed for most of the mixtures, the LiTf:DMSO solution remains stable. This electrolyte mixture was thus proposed as a good candidate for in situ Li-air experiments in the (S)TEM (Image reprinted with permission from Ref. [13] Copyright 2014 American Chemical Society)

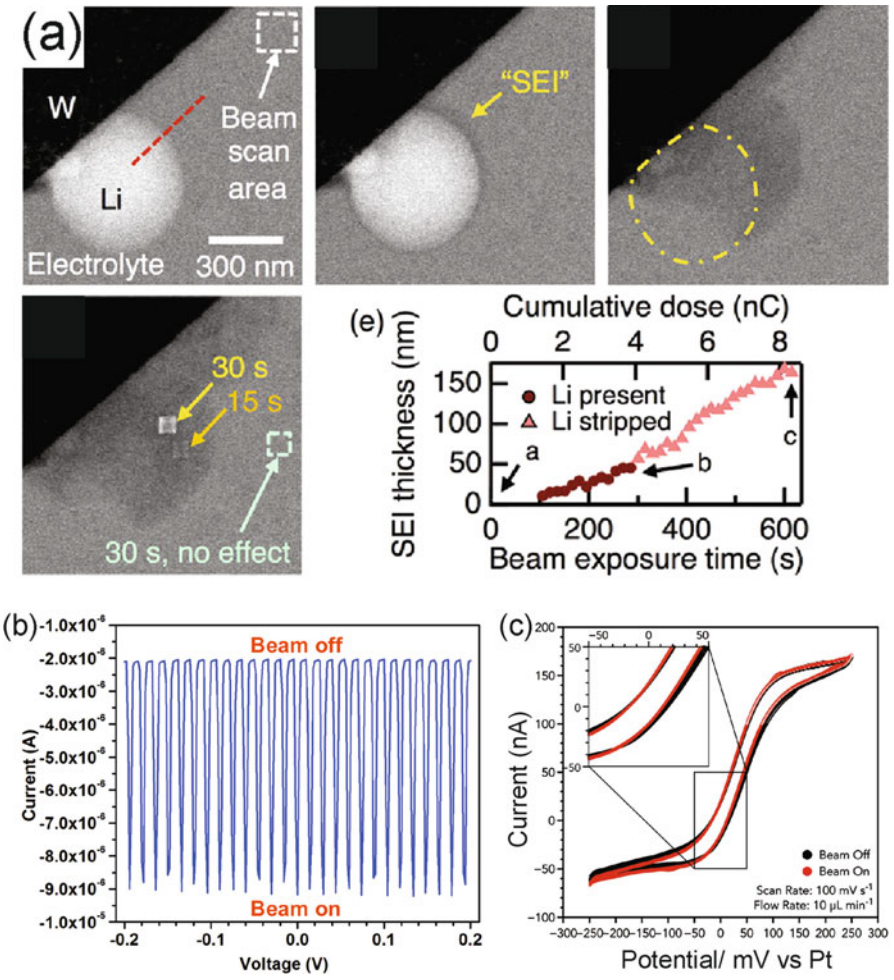

Fig. 1.11 (**a**) Electron beam–induced solid electrolyte interphase growth on a tungsten electrode (Images reproduced with permission from Leenheer et al. [79]). (**b**) TEM electron beam–induced electrochemical charging of a gold electrode. Plot reproduced with permission from Sun et al. [84]. (**c**) Minimal effect of STEM electron beam irradiation on a cyclic voltammogram (Plot reproduced with permission from Unocic and Sacci [21])

structural changes and kinetic speeds observed in electrochemical experiments [78]. Leenheer et al. used this method recently to determine the effect of the electron beam on the morphology of a solid electrolyte interphase formed during charging of a lithium battery inside a TEM [79]. The authors observed electron beam–induced solid electrolyte interphase layer growth and investigated the growth as a function of total electron dose delivered to understand the process and separate it from electrochemically induced SEI formation (Fig. 1.11a). In situ microscopists can

learn lessons from radiation damage mitigation strategies for cryo-EM, such as acquiring a reference image at very low electron dose [3, 80]. Specific to in situ electrochemistry, this could mean performing an initial experiment, such as a cyclic voltammetry scan, with the electron beam blanked to form a reference structure relatively free from imaging artifacts. Low dose imaging can be used for electrodeposition experiments with solutions containing reactive metal ion precursors to slow [75] or stop beam-induced crystal growth in aqueous or organic solutions [11, 12]. The stability of battery electrolytes can be tested empirically with systematic irradiation experiments to determine the most electron beam–resistant battery electrolytes for an in situ electrochemical system [13] (see Sect. 5.4.2).

Measuring and reporting electron beam imaging parameters is imperative for designing a successful in situ electrochemistry experiment as well as correctly interpreting the results. Many radiolysis-induced processes, such as beam-induced nanocrystal growth [12, 81] and nanobubble formation, [77, 82] have threshold electron dose rates or beam currents below which they do not occur. Using kinetic modeling and liquid cell STEM experiments, Grogan et al. demonstrated there was a threshold beam current for radiolytic H_2 bubble nucleation and growth [77]. Similarly, Woehl et al. showed that there was an inherent electron dose below which beam-induced nucleation of silver nanocrystals did not occur (see Sect. 5.1.2) [12]. Establishing threshold electron doses for the imaging artifacts found specifically in in situ electrochemistry experiments will set limitations on useable (S)TEM imaging parameters, e.g., a dose-limited resolution [83], at which images and electrochemical data can be faithfully interpreted free from artifacts. The well-known radiation damage threshold of ~10 electrons/$Å^2$ established for cryo-EM [3] (see Sect. 4.2) exemplifies the type of electron dose threshold that must be set for in situ electrochemistry and liquid cell electron microscopy for these techniques to become well established across multiple research fields. Other beam-induced processes that we suspect will have unique electron dose thresholds are pH changes, formation of passive layer (solid electrolyte interface, SEI), and beam-induced amorphization of materials.

Electron beam charging has been shown to induce current in in situ electrochemical measurements: positive charge induced by secondary electron emission from the electrode causes flow of electrons from ground to neutralize the charge. The determining factors as to whether electron beam charging will be observed in electrochemical data is (1) the amount of active electrode area being imaged relative to the amount of unirradiated electrode, (2) the electron dose rate, and (3) the atomic number and density of the electrode material. Two recent in situ electrochemistry studies demonstrate the effects of these factors in determining whether there is significant electron beam–induced electrochemical current. Sun et al. showed that electron beam charging of a gold electrode in a closed in situ electrochemical cell (200 kV TEM, dose rate of 500 electrons/$Å^2$s) increased the current flow in the cell by ~5 times (Fig. 1.11b) [84]. In a separate study, irradiation of a glassy carbon electrode (300 kV STEM, dose rate of 1.54 electrons/$Å^2$s) in a similar closed electrochemical cell showed no significant effect on the cyclic voltammogram [21]. The significant beam-induced electrochemical charging observed by Sun et al. is likely

due to the strongly scattering gold electrode, which has very high secondary electron emission yields, in combination with irradiation of nearly the entire electrochemically active area [84]. On the other hand, irradiation of a weakly scattering material, such as glassy carbon, over a small region of the electrochemically active area does not produce significant electrochemical charging. The custom fabricated electrochemical cell developed by Leenheer et al. isolates the electrochemically active area to a micron sized region using atomic layer deposition (ALD) to mask the majority of the electrode area with a passivating layer [79]. Thus, electron beam–induced electrochemical charging can be clearly seen in their electrochemical data when images are taken and must be accounted for. Accelerating voltage will also contribute to electron beam–induced charging, where higher voltages should decrease charging effects due to decreased scattering cross sections. Calibrating image artifacts and radiation damage dose thresholds between different imaging modes, accelerating voltages, and electrode materials will allow for reproduction of in situ electrochemistry experiments between different electron microscopes and liquid cells and help microscopists identify optimal imaging conditions and techniques for each experiment.

6 Conclusions and Future Perspective

The focus of this chapter has been to provide an overview of methods and concepts relevant to various experiments that are possible using liquid cell transmission electron microscopy. Imaging liquids in the electron microscope requires means of separating the solution from the high vacuum in the microscope column. This is done by using specially designed holders (commercial holders for the most part) using a three o-ring sealing system and microfabricated chips that maintain the liquid in an encapsulated volume. Different considerations for preparing these membranes for experiments have been overviewed. The most important imaging parameters to consider in a LCEM experiment are the dose rate and the total dose. For this reason, we have discussed the evolution of cryo-EM, which faced relatively similar challenges and found creative solutions and methodologies to overcome them.

Experiments that are possible now in the liquid cell span from in situ particle growth and dissolution, imaging of biological objects in their native environment, to experiments where more than one solution is mixed in situ, and electrochemistry at the nanoscale. We have selected some of these different aims of LCEM and presented important observations, models, and concepts that we believe provide important information. We discussed the main findings on electron beam–induced growth of metallic particles from aqueous solutions. Knowledge of the radiation chemistry of water is particularly relevant for these experiments, since it describes the effect of the incident electrons in a solvent and in particular explains which species trigger the reduction reactions. We have also discussed competing and back reactions during radiolytic growth processes and explained that these chemical effects can ultimately be “directed” for general chemistry and materials science applications.

Besides the effect of dose rate and dose, contrast, spatial, and temporal resolution can be an important factor for some structures, such as biological and organic materials. We discuss LCEM observations of proteins and macromolecules and the main challenges faced during these experiments. Important considerations for successful experiments and/or for interpretation of in situ images have been described. Among them, irreversible solution chemistry changes, precursor depletion, electron beam charging, and the diffusion of particles at membranes surface have been discussed. Finally, we have covered a range of in situ experiments that employed organic solvents. A complex mixture of species, more complex than for the case of water, is formed upon irradiation of organic solvents. While this has disadvantages, like the lack of knowledge on radiolysis of organic solvents as compared to the radiolysis of water and that control of the experiments is more difficult due to the complexity of the reactions, some clear advantages stand out. We have discussed how nonpolar solvents produce lower concentrations of reactive species upon irradiation and the prospects of different types of experiments, such as the investigation of the degradation mechanisms and aging of electrolyte solutions. The use of these solvents also allows for performing electrochemistry and we have reviewed some of the main findings in this field with a focus on the influence of the incident electron beam in the results and how to overcome it.

While huge progress in the field of liquid cell electron microscopy has been made in the last decade, a main challenge in the field is still ruling out the effect of the electron beam and reproducibility. The large diffusion gradients and effect of membranes makes quantitative kinetic modeling of radiolysis in the liquid cell very challenging. The development of experimental sensors for detecting in situ pH variations or the concentration of radicals could provide valuable information on radiolysis. New acquisition methods in combination with image processing allowing for lower dose and more sensitive detection schemes will provide further control of the experiments. We anticipate that the application of the concepts of radiation chemistry for modifying the environment for specific purposes will have a huge impact in the field, as we have recently described in an extensive review on this topic [15].

References

1. Taylor KA, Glaeser RM (2008) Retrospective on the early development of cryoelectron microscopy of macromolecules and a prospective on opportunities for the future. J Struct Biol 163:214–223
2. Taylor KA, Glaeser RM (1974) Electron-diffraction of frozen, hydrayed protein crystals. Science 186:1036–1037
3. Dubochet J, Adrian M, Chang JJ, Homo JC, Lepault J, McDowall AW, Schultz P (1988) Cryo-electron microscopy of vitrified specimens. Q Rev Biophys 21:129–228
4. Parsons DF (1974) Structure of wet specimens in electron microscopy. Science 186:407–414
5. Abrams IM, McBain JW (1944) A closed cell for electron microscopy. Science 100:273–274
6. Williamson MJ, Tromp RM, Vereecken PM, Hull R, Ross FM (2003) Dynamic microscopy of nanoscale cluster growth at the solid-liquid interface. Nat Mater 2:532–536

7. Peckys DB, Veith GM, Joy DC, de Jonge N (2009) Nanoscale imaging of whole cells using a liquid enclosure and a scanning transmission electron microscope. PLoS One 4:e8214
8. Ross FM (2015) Opportunities and challenges in liquid cell electron microscopy. Science 350: aaa9886
9. Jonge N, Ross FM (2011) Electron microscopy of specimens in liquid. Nat Nanotechnol 6:695
10. Woehl TJ, Prozorov T (2015) The mechanisms for nanoparticle surface diffusion and chain self-assembly determined from real-time nanoscale kinetics in liquid. J Phys Chem C 119:21261–21269
11. Woehl TJ, Jungjohann KL, Evans JE, Arslan I, Ristenpart WD, Browning ND (2013) Experimental procedures to mitigate electron beam induced artifacts during in situ fluid imaging of nanomaterials. Ultramicroscopy 127:53–63
12. Woehl TJ, Evans JE, Arslan L, Ristenpart WD, Browning ND (2012) Direct in situ determination of the mechanisms controlling nanoparticle nucleation and growth. ACS Nano 6:8599–8610
13. Abellan P, Mehdi BL, Parent LR, Gu M, Park C, Xu W, Zhang YH, Arslan I, Zhang JG, Wang CM, Evans JE, Browning ND (2014) Probing the degradation mechanisms in electrolyte solutions for Li-ion batteries by in situ transmission electron microscopy. Nano Lett 14:1293–1299
14. Abellan P, Parent LR, Al Hasan N, Park C, Arslan I, Karim AM, Evans JE, Browning ND (2016) Gaining control over radiolytic synthesis of uniform sub-3-nanometer palladium nanoparticles: use of aromatic liquids in the electron microscope. Langmuir 32:1468–1477
15. Woehl TJ, Abellan P (2016) Defining the radiation chemistry during liquid cell electron microscopy to enable visualization of nanomaterial growth and degradation dynamics. J Microsc 265:135
16. Zheng HM, Smith RK, Jun YW, Kisielowski C, Dahmen U, Alivisatos AP (2009) Observation of single colloidal platinum nanocrystal growth trajectories. Science 324:1309–1312
17. Verch A, Pfaff M, de Jonge N (2015) Exceptionally slow movement of gold nanoparticles at a solid/liquid interface investigated by scanning transmission electron microscopy. Langmuir 31:6956–6964
18. Powers AS, Liao H-G, Raja SN, Bronstein ND, Alivisatos AP, Zheng H (2016) Tracking nanoparticle diffusion and interaction during self-assembly in a liquid cell. Nano Lett 17:15
19. Liu YZ, Lin XM, Sun YG, Rajh T (2013) In situ visualization of self-assembly of charged gold nanoparticles. J Am Chem Soc 135:3764–3767
20. Grogan JM, Rotkina L, Bau HH (2011) In situ liquid-cell electron microscopy of colloid aggregation and growth dynamics. Phys Rev E 83:061405
21. Unocic RR, Sacci RL, Brown GM, Veith GM, Dudney NJ, More KL, Walden FS, Gardiner DS, Damiano J, Nackashi DP (2014) Quantitative electrochemical measurements using in situ ec-S/TEM devices. Microsc Microanal 20:452–461
22. Dukes MJ, Peckys DB, de Jonge N (2010) Correlative fluorescence microscopy and scanning transmission electron microscopy of quantum-dot-labeled proteins in whole cells in liquid. ACS Nano 4:4110–4116
23. Peckys DB, Mazur P, Gould KL, de Jonge N (2011) Fully hydrated yeast cells imaged with electron microscopy. Biophys J 100:2522–2529
24. Woehl TJ, Kashyap S, Firlar E, Perez-Gonzalez T, Faivre D, Trubitsyn D, Bazylinski DA, Prozorov T (2014) Correlative electron and fluorescence microscopy of magnetotactic bacteria in liquid: toward in vivo imaging. Sci Rep 4:6854
25. Gilmore BL, Showalter SP, Dukes MJ, Tanner JR, Demmert AC, McDonald SM, Kelly DF (2013) Visualizing viral assemblies in a nanoscale biosphere. Lab Chip 13:216–219
26. Varano AC, Rahimi A, Dukes MJ, Poelzing S, McDonald SM, Kelly DF (2015) Visualizing virus particle mobility in liquid at the nanoscale. Chem Commun 51:16176–16179
27. Abellan P, Woehl TJ, Parent LR, Browning ND, Evans JE, Arslan I (2014) Factors influencing quantitative liquid (scanning) transmission electron microscopy. Chem Commun 50:4873–4880

28. Alloyeau D, Dachraoui W, Javed Y, Belkahla H, Wang G, Lecoq H, Ammar S, Ersen O, Wisnet A, Gazeau F, Ricolleau C (2015) Unravelling kinetic and thermodynamic effects on the growth of gold nanoplates by liquid transmission electron microscopy. Nano Lett 15:2574
29. Talmon Y (1982) Thermal and radiation-damage to frozen hydrated speciments. J Microsc Oxford 125:227–237
30. Jaffe JS, Glaeser RM (1984) Preparation of frozen-hydrated speciments for high-resolution electron-microscopy. Ultramicroscopy 13:373–377
31. Glaeser RM (1971) Limitations to significant information in biological electron microscopy as a result of radiation damage. J Ultrastruct Res 36:466–482
32. Glaeser RM, Taylor KA (1978) Radiation-damage relative to transmission electron-microscopy of biological specimans at low-temperature – review. J Microsc Oxford 112:127–138
33. Talmon Y, Adrian M, Dubochet J (1986) Electron-beam radiation-damage to organic inclusions in vitreous, cubic, and hexagonal ice. J Microsc Oxford 141:375–384
34. Dubochet J, Lepault J, Freeman R, Berriman JA, Homo JC (1982) Electron-microscopy of frozen water and aqueous-solutions. J Microsc Oxford 128:219–237
35. Chee SW, Baraissov Z, Loh ND, Matsudaira PT, Mirsaidov U (2016) Desorption-mediated motion of nanoparticles at the liquid-solid interface. J Phys Chem C 120:20462–20470
36. Park J, Elmlund H, Ercius P, Yuk JM, Limmer DT, Chen Q, Kim K, Han SH, Weitz DA, Zettl A, Alivisatos AP (2015) 3D structure of individual nanocrystals in solution by electron microscopy. Science 349:290–295
37. Belloni J (2006) Nucleation, growth and properties of nanoclusters studied by radiation chemistry – application to catalysis. Catal Today 113:141–156
38. Choi SH, Zhang YP, Gopalan A, Lee KP, Kang HD (2005) Preparation of catalytically efficient precious metallic colloids by gamma-irradiation and characterization. Colloids Surf A Physicochem Eng Asp 256:165–170
39. Farhataziz, Rodgers MAJ (1987) Radiation chemistry, principles and applications. VCH, New York
40. Belloni J, Mostafavi M, Remita H, Marignier JL, Delcourt MO (1998) Radiation-induced synthesis of mono- and multi-metallic clusters and nanocolloids. New J Chem 22:1239–1255
41. Buxton GV (1987) Radiation chemistry of the liquid state. In: Farhataziz, Rodger MAJ (eds) Radiation chemistry: principles and applications. VCH, New York
42. Allen AO (1961) The radiation chemistry of water and aqueous solutions. Van Nostrand, New York
43. Dispenza C, Grimaldi N, Sabatino MA, Soroka IL, Jonsson M (2015) Radiation-engineered functional nanoparticles in aqueous systems. J Nanosci Nanotechnol 15:3445–3467
44. Pastina B, LaVerne JA (1999) Scavenging of the precursor to the hydrated electron by the selenate ion. J Phys Chem A 103:209–212
45. Buxton GV (2008) Radiation chemistry of the liquid state. In: Mostafavi MM, Douki T, Belloni J (eds) Radiation chemistry: principles and applications. EDP Sciences, Orsay
46. Buxton GV, Mulazzani QG, Ross AB (1995) Critical-review of rate constants for reactions of transients from metal-ions and metal-complexes in aqueous-solution. J Phys Chem Ref Data 24:1055–1349
47. Mostafavi M (2008) Lampre, the solvated electron: a singular chemical species. In: Rizot SM, Mostafavi M, Douki T, Rigny P (eds) Radiation chemistry: from basics to applications in material and life sciences. EDP Sciences, Les Ulis
48. Hart EJ (1964) Hydrated electron. Science 146:19–25
49. Park JH, Schneider NM, Grogan JM, Reuter MC, Bau HH, Kodambaka S, Ross FM (2015) Control of electron beam-induced Au nanocrystal growth kinetics through solution chemistry. Nano Lett 15:5314–5320
50. Abellan P, Woehl TJ, Evans JE, Browning ND (2014) Calibrated in situ transmission electron microscopy for the study of nanoscale processes in liquids, in chapter one – CISCEM 2014: proceedings of the second conference on in situ and correlative electron microscopy,

Saarbrücken, Germany, October 14–15. In: Hawkes PW (ed) Advances in imaging and electron physics, vol 190. Elsevier Ltd, San Diego, USA pp 43–45
51. Spinks JWT, Woods RJ (1964) An introduction to radiation chemistry. Wiley, New York
52. Sutter E, Jungjohann K, Bliznakov S, Courty A, Maisonhaute E, Tenney S, Sutter P (2014) In situ liquid-cell electron microscopy of silver-palladium galvanic replacement reactions on silver nanoparticles. Nat Commun 5:4946
53. Mirsaidov UM, Zheng H, Casana Y, Matsudaira P (2012) Imaging protein structure in water at 2.7 nm resolution by transmission electron microscopy. Biophys J 102:L15–L17
54. Plamper FA, Gelissen AP, Timper J, Wolf A, Zezin AB, Richtering W, Tenhu H, Simon U, Mayer J, Borisov OV, Pergushov DV (2013) Spontaneous assembly of Miktoarm stars into vesicular interpolyelectrolyte complexes. Macromol Rapid Commun 34:855–860
55. Wang CM, Qiao Q, Shokuhfar T, Klie RF (2014) High-resolution electron microscopy and spectroscopy of ferritin in biocompatible graphene liquid cells and graphene sandwiches. Adv Mater 26:3410–3414
56. Park J, Park H, Ercius P, Pegoraro AF, Xu C, Kim JW, Han SH, Weitz DA (2015) Direct observation of wet biological samples by graphene liquid cell transmission electron microscopy. Nano Lett 15:4737–4744
57. Kraus T, Jonge N (2013) Dendritic gold nanowire growth observed in liquid with transmission electron microscopy. Langmuir 29:8427
58. Ahmad N, Le Bouar Y, Ricolleau C, Alloyeau D (2016) Growth of dendritic nanostructures by liquid-cell transmission electron microscopy: a reflection of the electron-irradiation history. Adv Struct Chem Imaging 2:9
59. Cazaux J (1995) Correlations between ionization radiation-damage and charging effects in transmission electron-microscopy. Ultramicroscopy 60:411–425
60. White ER, Mecklenburg M, Shevitski B, Singer SB, Regan BC (2012) Charged nanoparticle dynamics in water induced by scanning transmission electron microscopy. Langmuir 28:3695–3698
61. Humphreys CJ, Bullough TJ, Maher RW, Turner PS (1990) Electron beam nano-etching in oxides, fluorides, metals and semiconductors. Fundamental electron and ion beam interactions with solids for microscopy, microanalysis and microlithography, scanning microscopy supplement, 4:185–192
62. Egerton RF (2007) Limits to the spatial, energy and momentum resolution of electron energy-loss spectroscopy. Ultramicroscopy 107:575–586
63. Downing KH, McCartney MR, Glaeser RM (2004) Experimental characterization and mitigation of specimen charging on thin films with one conducting layer. Microsc Microanal 10:783–789
64. Chen YT, Wang CY, Hong YJ, Kang YT, Lai SE, Chang P, Yew TR (2014) Electron beam manipulation of gold nanoparticles external to the beam. RSC Adv 4:31652–31656
65. Zheng HM, Claridge SA, Minor AM, Alivisatos AP, Dahmen U (2009) Nanocrystal diffusion in a liquid thin film observed by in situ transmission electron microscopy. Nano Lett 9:2460–2465
66. Yuk JM, Park J, Ercius P, Kim K, Hellebusch DJ, Crommie MF, Lee JY, Zettl A, Alivisatos AP (2012) High-resolution EM of colloidal nanocrystal growth using graphene liquid cells. Science 336:61–64
67. Lu JY, Aabdin Z, Loh ND, Bhattacharya D, Mirsaidov U (2014) Nanoparticle dynamics in a nanodroplet. Nano Lett 14:2111–2115
68. Woehl TJ, Park C, Evans JE, Arslan I, Ristenpart WD, Browning ND (2013) Direct observation of aggregative nanoparticle growth: kinetic modeling of the size distribution and growth rate. Nano Lett 14:373–378
69. Chen Q, Smith JM, Park J, Kim K, Ho D, Rasool HI, Zettl A, Alivisatos AP (2013) 3D motion of DNA-au nanoconjugates in graphene liquid cell electron microscopy. Nano Lett 13:4556–4561
70. Brenner H (1961) The slow motion of a sphere through a viscous fluid towards a plane surface. Chem Eng Sci 16:242–251

71. Woods RJ, Pikaev AK (1994) Applied radiation chemistry: radiation processing. Wiley, New York
72. Ortiz D, Steinmetz V, Durand D, Legand S, Dauvois V, Maitre P, Le Caer S (2015) Radiolysis as a solution for accelerated ageing studies of electrolytes in Lithium-ion batteries. Nat Commun 6:6950
73. Wang CM (2015) In situ transmission electron microscopy and spectroscopy studies of rechargeable batteries under dynamic operating conditions: a retrospective and perspective view. J Mater Res 30:326–339
74. Holtz ME, Yu YC, Gunceler D, Gao J, Sundararaman R, Schwarz KA, Arias TA, Abruna HD, Muller DA (2014) Nanoscale imaging of Lithium ion distribution during in situ operation of battery electrode and electrolyte. Nano Lett 14:1453–1459
75. Park J, Kodambaka S, Ross FM, Grogan JM, Bau HH (2012) In situ liquid cell transmission electron microscopic observation of electron beam induced Au crystal growth in a solution. Microsc Microanal 18:1098–1099
76. Schneider NM, Norton MM, Mendel BJ, Grogan JM, Ross FM, Bau HH (2014) Electron–water interactions and implications for liquid cell electron microscopy. J Phys Chem C 118:22373
77. Grogan JM, Schneider NM, Ross FM, Bau HH (2014) Bubble and pattern formation in liquid induced by an electron beam. Nano Lett 14:359–364
78. Ahmad N, Wang G, Nelayah J, Ricolleau C, Alloyeau D (2018) Driving reversible redox reactions at solid-liquid interfaces with the electron beam of a transmission electron microscope. J Microsc 269(2):127–133
79. Leenheer AJ, Jungjohann KL, Zavadil KR, Sullivan JP, Harris CT (2015) Lithium electrodeposition dynamics in aprotic electrolyte observed in situ via transmission electron microscopy. ACS Nano 9:4379–4389
80. Pierson J, Sani M, Tomova C, Godsave S, Peters PJ (2009) Toward visualization of nanomachines in their native cellular environment. Histochem Cell Biol 132:253–262
81. Evans JE, Jungjohann KL, Browning ND, Arslan I (2011) Controlled growth of nanoparticles from solution with in situ liquid transmission electron microscopy. Nano Lett 11:2809–2813
82. White ER, Mecklenburg M, Singer SB, Aloni S, Regan BC (2011) Imaging nanobubbles in water with scanning transmission electron microscopy. Appl Phys Express 4:055201
83. Egerton RF (2013) Control of radiation damage in the TEM. Ultramicroscopy 127:100–108
84. Sun M, Liao H-G, Niu K, Zheng H (2013) Structural and morphological evolution of lead dendrites during electrochemical migration. Sci Rep 3:3227

In Situ X-Ray Studies of Crystallization Kinetics and Ordering in Functional Organic and Hybrid Materials

2

Bin Yang, Jong K. Keum, David B. Geohegan, and Kai Xiao

Contents

B. Yang
Center for Nanophase Materials Sciences, Oak Ridge National Laboratory, Oak Ridge, TN, USA

The Molecular Foundry, Lawrence Berkeley National Laboratory, Berkeley, CA, USA

J. K. Keum
Center for Nanophase Materials Sciences, Oak Ridge National Laboratory, Oak Ridge, TN, USA

Neutron Scattering Division, Oak Ridge National Laboratory, Oak Ridge, TN, USA

D. B. Geohegan
Center for Nanophase Materials Sciences, Oak Ridge National Laboratory, Oak Ridge, TN, USA

K. Xiao (✉)
Center for Nanophase Materials Sciences, Oak Ridge National Laboratory, Oak Ridge, TN, USA

Department of Electrical Engineering and Computer Science, University of Tennessee, Knoxville, TN, USA
e-mail: Xiaok@ornl.gov

© Springer-Verlag GmbH Germany, part of Springer Nature 2018

C. S. S. R. Kumar (ed.), *In-situ Characterization Techniques for Nanomaterials*,
https://doi.org/10.1007/978-3-662-56322-9_2

1 Definition of the Topic

In Situ and time-resolved X-ray scattering and diffraction is dedicated to yielding the change of structural information as the materials are processed or grown in a controlled environment. In this chapter, we introduce the use of in situ and time-resolved X-ray techniques to understand molecular packing, crystal orientation, and phase transformation during the synthesis and processing of functional organic semiconductors, organic nanowires, and hybrid perovskite materials.

2 Overview

Understanding the fundamental structural information of organic and hybrid organic-inorganic materials is the basis for developing high-performance functional electronic devices such as organic photovoltaics, perovskite solar cells, organic thin film transistors, organic photodetectors, and organic light-emitting diodes. These materials and devices are particularly intriguing because they can be highly flexible, light in weight, and provide a wide range of tunability over structure and optoelectronic properties. The optoelectronic performance of functional materials is largely determined by the molecular packing, crystal orientation, and phase transformations that evolve kinetically and thermodynamically during growth and subsequent processing that, in turn, generally govern the charge transport properties and charge recombination processes when operated as devices.

Despite rapid progress in the design and application of functional organic and hybrid optoelectronic materials in recent years, understanding the molecular interactions and kinetics that govern their synthesis and assembly during processing lags far behind, mainly due to a lack of time-resolved, in situ diagnostic techniques. Compared to post-processing ex situ structural characterizations of functional materials by conventional X-ray diffraction, advanced in situ and time-resolved X-ray measurements offer a more in-depth understanding of how structural phases evolve in real time during the synthesis and growth of materials, yielding valuable insights of chemical reactions, solvent interactions, and interactions with substrates. Such real-time kinetic information provides the input for models of growth, and feedback to guide improvements in materials design. Here, we first describe the use of in situ and time-resolved X-ray scattering/diffraction techniques to understand molecular

packing and ordering during organic film processing, and then how crystallization kinetics and ordering can be revealed during the synthesis and growth of organic nanowires and hybrid perovskite thin films.

3 Introduction

Functional materials, especially functional organic soft materials and hybrid organic-inorganic materials, are currently the subject of intensive investigations due to their promising applications in the multiple fields including electronics [1–5], photonics [6–10], and magnetics [11–13]. The family of π-conjugated organic materials [14] is a versatile class of carbon-based soft matter sharing molecular designs that often result in appealing optoelectronic properties such as enhanced electronic conductivity [15] and photoresponsivity [16]. Conjugated molecular materials are of highly desired for applications in flexible electronic devices [17, 18], such as building integrated photovoltaics [19], high-definition ultra-thin organic light-emitting diode (OLED) displays and televisions [20], and radio frequency identification tags [21]. Compared to conventional inorganic semiconductors such as silicon, gallium arsenide, and conjugated organic materials have a number of unique attractive characteristics such as flexibility and light weight, and hold the promise of large-scale synthesis and processing, resulting in low fabrication cost [22]. As a result of this flexibility, organic materials can be processed onto a variety of surfaces and shapes including plastic (e.g., PET, PEN) substrates for flexible electronic devices [23].

The performance of organic electronic devices is strongly influenced by the charge transport properties of their constituent conjugated materials and is greatly affected by the orientation and ordering of the organic molecules on substrates [15]. In general, preferential charge carrier transport occurs along the π-π stacking direction of the aromatic rings of the organic molecules. Therefore, it is of critical importance to find a reliable approach to control molecular orientation, packing behavior, and crystallinity during organic thin film processing. Since molecular orientation and crystallinity are determined not only thermodynamically but kinetically, it is essential to understand the kinetics of molecular ordering and crystallization of organic materials on various substrates as they occur during processing.

Organic photovoltaics (OPVs) harvest solar energy by converting solar photons to electricity and are one important class of organic electronics that have received intensive attention during the past decade [24–27]. In particular, building-integrated organic photovoltaics offer high market potential due to their advantageous features that include colorable, semitransparent features, and the ability to easily print organic photovoltaic modules, which could enable savings for construction and materials costs [28]. However, the ultimate application of OPVs still relies on the steady improvement of their power conversion efficiency (PCE) in devices, which measures how efficiently photons can be converted to electrons. Past efforts on organic photovoltaics have focused primarily on the design and synthesis of new organic polymeric or small molecular materials to enable a broader range of light absorption, and the understanding of the molecular packing, i.e., crystallization and orientation

behavior of organic molecules in the donor/acceptor bulk heterojunction layer for improved charge transport and collection efficiencies, leading to PCE of ~12% at the current stage according to literature [29]. In order to further improve PCE, beside resorting new materials design and synthesis, it is also essential to tune the molecular orientation and molecular packing through processing control during the organic thin film growth and/or post-treatments of as-cast organic thin films. In situ and time-resolved X-ray diffraction allow the detection of possible time-dependent/transient film structures and for monitoring the evolution of these structures during growth.

Another representative application is organic thin-film transistors (OTFTs) which are devoted to acting as a complementary or replacing the silicon-based integrated circuits in next-generation flexible consumer electronics [30]. To obtain high charge mobilities in OTFTs, it is a crucial step to obtain organic thin films with desirable charge transport properties, which is dependent on the fundamental understanding of the molecular orientation and packing behavior in the organic semiconductor channel layer. Such molecular level understanding and tuning of molecular packing could be realized by in situ and time-resolved high flux synchrotron X-ray scattering and diffraction [31].

Compared to the abovementioned 3D organic bulk films, 1D crystalline organic nanowires, which is assembled from small molecules to incorporate functionalities arising from nanoscale and microscale ordering, can offer a more promising approach to develop high-performance OPVs and OTFTs [32]. These 1D organic nanowires systems hold unique advantages as compared with amorphous or disordered domain structures in the regular bulk films [33]. Their 1D assembled structures promise unidirectional charge transport which is superior to anisotropic transport in bulk film. More importantly, controllable growth of organic nanowires enables the packing of donor/acceptor heterojunctions through the π-π interaction force along the axial direction or normal to the axial direction, which could be more efficient than conventional bulk heterojunction OPVs due to longer exciton diffusion length, more efficient exciton dissociation, and faster charge transport [32]. Recent studies have shown that OPVs [34] and OTFTs [35] could be efficient based on vertically or parallely aligned nanowires on substrates, respectively. To further improve the performance of organic nanowire electronic devices, a critical step is gaining the fundamental understanding of growth mechanism and kinetics of these nanostructures to tailor their molecular orientations and packing behavior.

Recently, a class of functional hybrid organic-inorganic materials, organometallic trihalide perovskites (OTPs), invigorated a tremendous research effort to understand their fundamental material properties, how they operate and assemble as thin films, and their ultimate limitations as electronic devices [36–41]. Perovskite solar cells relatively quickly achieved PCEs of around 22%, which is comparable or better than the current state-of-the-art inorganic thin film photovoltaic technologies [42–44]. These organic hybrid perovskite materials have many appealing properties such as strong light absorption [45, 46], excellent carrier transport [47, 48], tunable electronic structure [43], and feature defect-tolerance [48, 49], although both environmental stability and thermal stability are still an issue [50–53]. These appealing optoelectronic properties result from the nanoscopic packing and orientation of

inorganic frameworks and organic moieties in organic-inorganic hybrid systems, which in turn governs charge transport [48]. In order to further improve OTP device performance, again it is imperative to study how organic and inorganic precursors interact to determine the synthesis and assembly of these hybrid perovskite materials. Furthermore, to minimize grain boundaries and enable long-range carrier transport, it is of great significance to understand the kinetics and orientation of crystal growth during the controlled chemical reactions of the precursors, and during any subsequent post-processing of the perovskite films [47, 54, 55].

Recently, Kowarik has briefly reviewed the development of in situ X-ray diffraction analysis of thin film growth [56]. In situ X-ray is a powerful tool for the fundamental understanding of a large variety of materials systems and further for the optimization of materials processing for enhanced materials performance [56]. However, to the best of our knowledge, a more specific and deeper survey has not yet performed about frontier organic and hybrid functional materials and associated thin films using in situ X-ray to reveal the chemical reaction kinetics, phase transformation, and crystal nucleation and growth. Here we focus on nondestructive in situ and time-resolved X-ray diffraction/scattering techniques, which not only offer the flexibility of operation in different sample environments (vacuum/air/liquids/penetration of thin solids) but also offer access to relatively deep penetration depths in organic soft materials [32, 57, 58]. Real-time X-ray diffraction measurements therefore offer the potential to reveal the key fundamental information about the crystallization kinetics and ordering in the abovementioned functional organic [59, 60] and hybrid materials [56]. In particular, this technique not only offers the capability to probe the molecular orientations and packing structures during the growth of organic thin films [61], but also provides the detailed information for the diffusion-controlled reactions and crystal growth kinetics in the growth of organic nanowires and organic-inorganic hybrid perovskites [62].

In this chapter, we introduce how to use in situ and time-resolved X-ray diffraction techniques to understand the molecular packing behavior during film processing and reveal crystallization kinetics and ordering during the growth and/or post-treatments of organic thin films [63–65]. By directly monitoring the growth of organic nanowires [32, 62] and hybrid perovskites film [62] on substrates using real-time X-ray diffraction, insights into the vapor-solid growth process will be discussed to understand and explain how crystals grow through atomistic modeling. Such fundamental understanding of the growth process should lead to processing insights for more effective incorporation of these functional materials into electronic devices.

4 Experimental Methodology

4.1 Fabrication of Organic Thin Films

Organic thin films are fabricated on substrates by multiple methods including ink-based solution processes [1, 17, 29] or thermal vacuum processes [66–68]. For the solution processes, thin films are deposited by a variety of spin-coating [69],

spray-coating [70], roll-to-roll coating [57], Gravure printing [71], and inkjet printing processes [72]. To make electronic ink solutions, organic materials are dissolved in organic solvents such as dichlorobenzene, toluene, and chloroform. The thickness of the films can be tuned by changing solution concentrations. For some organic materials, the as-cast films were thermally annealed above the glass transition temperature to facilitate the reorganization of molecular chains and enhance the crystallinity [73]. The pentacene films (introduced later) were deposited with a vacuum thermal evaporation method under two different conditions: room temperature (RT) and 75 °C. The P1 and P2 polymer films (introduced later) were spin-casted at RT. The P3HT films were fabricated with a roll-to-roll printing. In situ X-ray diffraction (XRD) was used to monitor the growth of these films during processing.

4.2 Growth of Organic Nanowires

The metal-$TCNQF_4$ organic nanowires were synthesized from reactions between the metal film (e.g., Ag, Cu) and $TCNQF_4$ vapor at 150–170 °C. The metal films were deposited on precleaned silicon Si substrates with e-beam evaporation method. The metal film samples were placed on a ceramic holder and surrounded by $TCNQF_4$ powders. Flow of N_2 gas was applied during the synthesis of organic nanowires.

4.3 Growth of Perovskite Thin Films

Lead halides (e.g., PbI_2, $PbBr_2$, $PbCl_2$) were dissolved in polar solvents dimethylformamide (DMF) and dimethyl sulfoxide (DMSO) to make precursor solutions with different concentrations (550 mg/mL in this study). To make (I, Br)-based mixed halides solution, mixture of PbI_2 and $PbBr_2$ with 1:1 weight ratio was dissolved in DMF or DMSO. As for the (I, Cl)-based mixed halides solution, mixtures of PbI_2 and $PbCl_2$ with 1:1 weight ratios were also dissolved in DMF or DMSO. All the lead halide precursor films were grown on glass substrates by spin coating solutions at spin speed of 6000 rpm for 30 s in an N_2-filled glovebox. The lead halide precursor films were then placed on a ceramic substrate in the Anton Paar XRK-900 chamber and were surrounded with methylammonium iodide (CH_3NH_3I) powder. When the CH_3NH_3I was heated up 70 °C, materials transform from solid state to the vapor state, and the CH_3NH_3I vapor diffuses into the lead halide films to facilitate the chemical reaction between them. Such reaction process was monitored by in situ X-ray diffraction.

4.4 In Situ Grazing Incidence Wide Angle X-Ray Scattering Using Synchrotron X-Ray Source

A schematic diagram is shown in Fig. 2.1a to depict the in situ synchrotron grazing incidence X-ray scattering measurement setup to probe the in situ crystallization

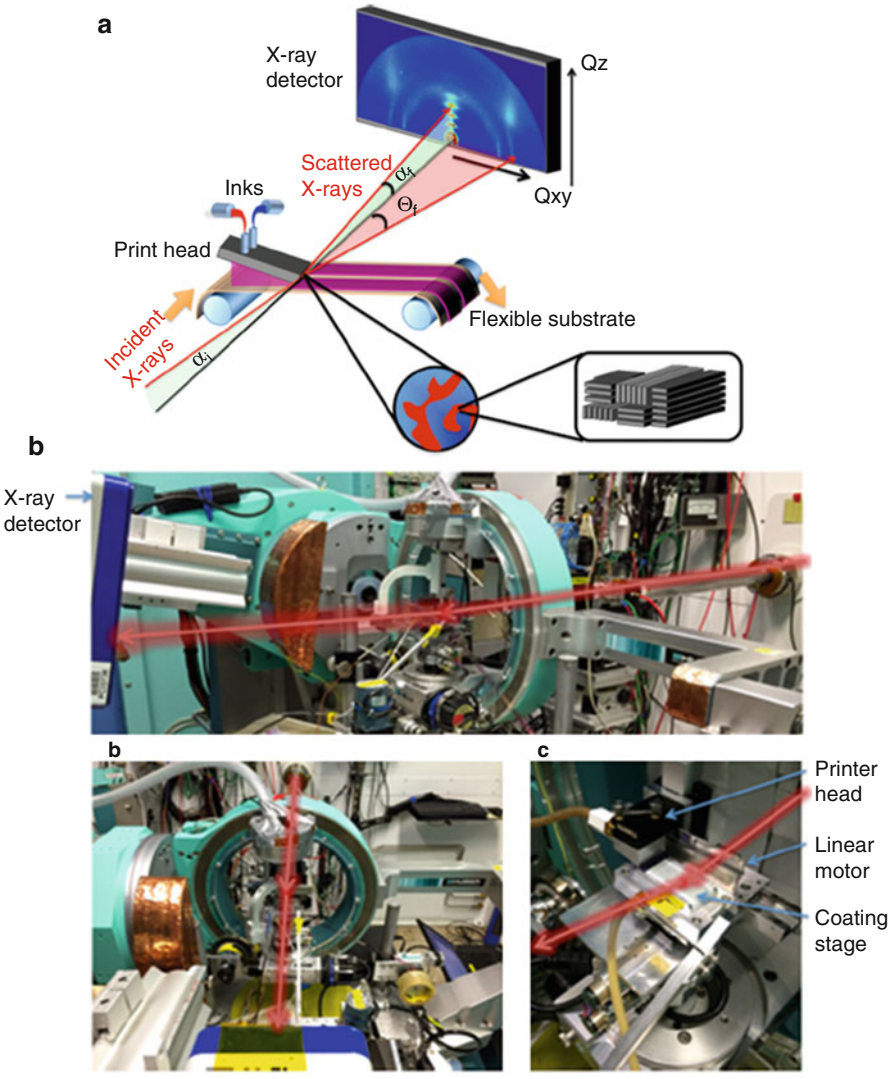

Fig. 2.1 In situ GIWAXS of P3HT:PCBM films during roll-to-roll printing. (**a**) Schematic representation of the setup of to track crystallization dynamics and morphology evolution, and (**b**) shows the real setup with different viewing angle (Reprint with permission from Gu et al. [57], Copyright © 2016, American Chemical Society)

process occurring during the fabrication of OPV P3HT:PCBM blend films by ink-based roll-to-roll printing technology. In this case, the intense and fine collimated state-of-the-art synchrotron X-ray source combined with high-speed and high-sensitivity 2D X-ray detectors ensure the reliable real-time investigation of the orientation and crystallization process of P3HT and characterization of the molecular

structure. Figure 2.1b shows the real experimental setup of combination of roll-to-roll printing machine with GIWAXS instruments which was designed by Gu et al. at high-flux synchrotron X-ray radiation facility, Beamline 7–2 at the Stanford Synchrotron Radiation Laboratory SSRL Beamline 7–2 [57]. As seen in Fig. 2.1a, b, the roll-to-roll printing stage was mounted onto a goniometer to align the substrate to the X-ray beam. A Dectris 300k Pilatus detector was used to collect the 2D GIWAXS images with sample–detector distance of 260 mm and the grazing incidence angle of 0.14°. In order to reduce absorption of X-rays through the electron-rich chlorinated solvent, the X-ray energy was set to be 15 keV, which gives rise to the X-ray wavelength of 0.8270 Å. The bay-annulated indigo-based polymer P1 and P2 films were examined at Beamline 7.3.3 at Advanced Light Source of the Lawrence Berkeley National Laboratory by He et al. [69, 74]. In the study, in order to investigate the structural evolution occurring upon elevating temperature in greater detail, in situ GIWAXS measurements were carried out, where thin film samples were mounted on a heating stage inside a helium box along the X-ray beam path. The X-ray energy was set to be 10 keV yielding the X-ray wavelength of 1.25 Å. In the in situ GIWAXS measurements during heating and cooling, the applied heating rate was 10 °C/min, while natural cooling was used for the investigation of structure change during cooling.

4.5 Time-Resolved, In Situ X-Ray Diffraction

Powder X-ray diffractometer (PANAlytical X'Pert MPD Pro) equipped with a silicon-based position-sensitive 1D solid-state detector, i.e., X'Celerator detector and X-ray tube generating Cu-Kα radiation ($\lambda = 1.54050$ Å) was used to characterize the reaction process and crystallization kinetics of the hybrid perovskite films. Since X'Celerator detector can speed up XRD measurement time up to 100 times much faster than a traditional point detector and the entire reaction time, using the detector with excellent counting rate and statistics is critical to in situ X-ray studies to catch up with the fast process of chemical reaction, crystallization kinetics, and phase transition of hybrid perovskite in real time. Also, an Anton Paar XRK-900 reaction chamber was used to induce the reaction and the reaction-induced crystallization of lead halide perovskite and acquire the X-ray diffraction (XRD) patterns during the entire reaction and crystallization process of the perovskites. For the XRD measurements, X-ray was generated at the tension of 45 kV and tube current of 40 mA, and the measurement step size and scan rate were 0.0167113° and 0.107815°/s, respectively. For the reaction, the spun-cast lead halide precursor (e.g., PbI_2) films were placed on the ceramic sample holder and the lead halide samples were surrounded with CH_3NH_3I powder as depicted in Fig. 2.2. For the reaction to occur, both lead halide precursors and CH_3NH_3I powder were heated up to 100, 120, and 140 °C by surrounding heater coils in the XRK-900 reaction chamber under N_2 or He inert gas environment. As the temperature reached to the desired reaction temperature, i.e., the isothermal reaction and reaction-induced crystallization kinetics were monitored in real time by collecting in situ XRD patterns. The specific diffraction geometry is shown in Fig. 2.2.

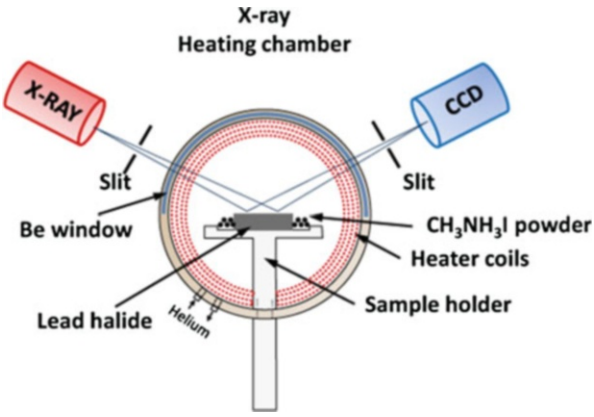

Fig. 2.2 Schematic representation of the in situ X-ray diffraction measurement setup and XRK-900 reaction chamber. The chemical reaction is PbX_2 (X = I, Br, Cl) + $CH_3NH_3I \rightarrow CH_3NH_3PbX_3$ (X = I, Br, Cl) (Reprint with permission from Yang et al. [62], Copyright © 2016, American Chemical Society)

5 Key Research Findings

5.1 Molecular Packing and Orientation of Organic Molecules Revealed by In Situ GIWAXS

Charge transport properties of organic molecules are determined by their orientation and ordering with respect to substrates. In principal, the preferential charge transport is along the direction of π-π stacking of the aromatic rings of the organic molecules. Understanding how organic molecules align and further finding a controllable approach to tune molecular orientation and packing behavior during the deposition of thin films by thermal vacuum evaporation method or solution-based processing method is essentially important for the improvement in performance of organic electronic devices.

Vacuum thermal evaporation has been widely employed as a method to fabricate highly uniform organic thin films for high-performance electronic device such as OLEDs, OPVs, and OTFTs, especially for the commercially available AMOLED displays and TVs. To further improve device performance, it is urgently required to understand the molecular crystallization kinetics during the growth stages of organic thin films. The real-time measurement of GIWAXS is an excellent tool to reach this goal. Watanabe et al. developed an in-house-built thermal evaporation chamber coupled with in situ and time-resolved 2D GIWAXS to track the real-time growth of pentacene thin films [58].

Well-defined conjugated small molecular materials, such as pentacene, prove relatively easy to process by simple synthetic and processing control to achieve reproducible device performance. Vacuum thermal evaporation has been widely applied to deposit such small molecules into thin films. Real-time GIWAXS is one of the major tools to probe thin films as they grow and has been used to analyze the structural evolution of pentacene thin films. The GIWAXS patterns were collected from the pentacene films grown at room temperature and 75 °C. Two diffraction peaks

along the q_z out-of-plane direction are assigned to (001) and (002) planes. The diffraction peaks along the in-plane direction are assigned to (11 L), (02 L), (12 L) planes. The thickness dependence of growth mechanism was studied with in situ GIWAXS. The diffraction peaks transform from streaks to spots with increasing thickness of the pentacene films, suggesting the transformation of 2D layer growth to 3D bulk island growth behavior with increasing film thickness. It is mentioned that the $(00\ L)_B$ represents the bulk-phase of pentacene films. Since these diffraction peaks are off the q_z axis, indicating that the bulk phase plane is tilted with the respect to the substrate. In addition to the thickness effect, the growth temperature also makes an impact on the orientation and packing of pentacene molecules. The discrete diffraction spots appear in the case of a 1 nm-thick film at 75 °C, which is invisible for the room temperature growth conditions. This suggests that the pentacene film formed a textured polycrystalline structure when the organic film is as thin as 1 nm. Since such in situ X-ray diffraction analysis only offers average structural information and lacks the microscopic local structure details, it is still possible that the film is noncontinuous at an elevated growth temperature of 75 °C and the pentacene shrinks into individual domains at such high-temperature growth condition. It is anticipated that the combination of in situ microscopy measurements (e.g., SEM) with in situ X-ray diffraction analysis would offer a more complete understanding of the growth mechanism. Moreover, the diffraction intensities of (11 L), (02 L), and (12 L) planes increase with increasing film thickness. The $(001)_B$ diffraction peak of the bulk-phase appeared on the q_z axis, indicating (001) plane of bulk phase orients parallel to the substrate when it was grown at 75 °C. Further reading can be found in Ref. [58].

While vacuum thermal evaporation thus has proven to be a reliable approach to deposit uniform and reproducible organic thin films, this method requires expensive high-vacuum instrumentation that may increase the ultimate cost of organic electronic devices. Therefore, much effort has been devoted to developing solution-based processing approaches such as spin-coating and roll-to-roll printing. Despite of the large amount of effort expended to date, the understanding of the morphological evolution and structural change during the assembly of thin films from solution is far from understood.

Spin-coating methods have been used to process a broad variety of organic materials, including recently intensively studied low bandgap polymers. In order to develop efficient low bandgap organic semiconductors, recent efforts have focused on the design and synthesis of alternating donor and acceptor structures within the backbone of the organic molecular materials, where the donor unit and the acceptor unit is electron-rich and electron-poor, respectively [75–78]. Bo et al. report an electron accepting unit, bay-annulated indigo (BAI) [69], which was applied to design a series of high-performance donor-acceptor organic materials (e.g., P1 and P2 polymers). Organic thin film transistors (OTFTs) based on these materials show ambipolar behavior with a mobility of around 1 cm^2/Vs. The success of the P1 and P2 polymers is based on a number of good features of the BAI unit, including strong planarity, high conjugation, and high solubility. To understand the molecular packing and ordering of the spin-coated thin P1 and P2 films, GIWAXS data was collected as shown in Fig. 2.3. The as-cast P1 film exhibits a strong (100) scattering

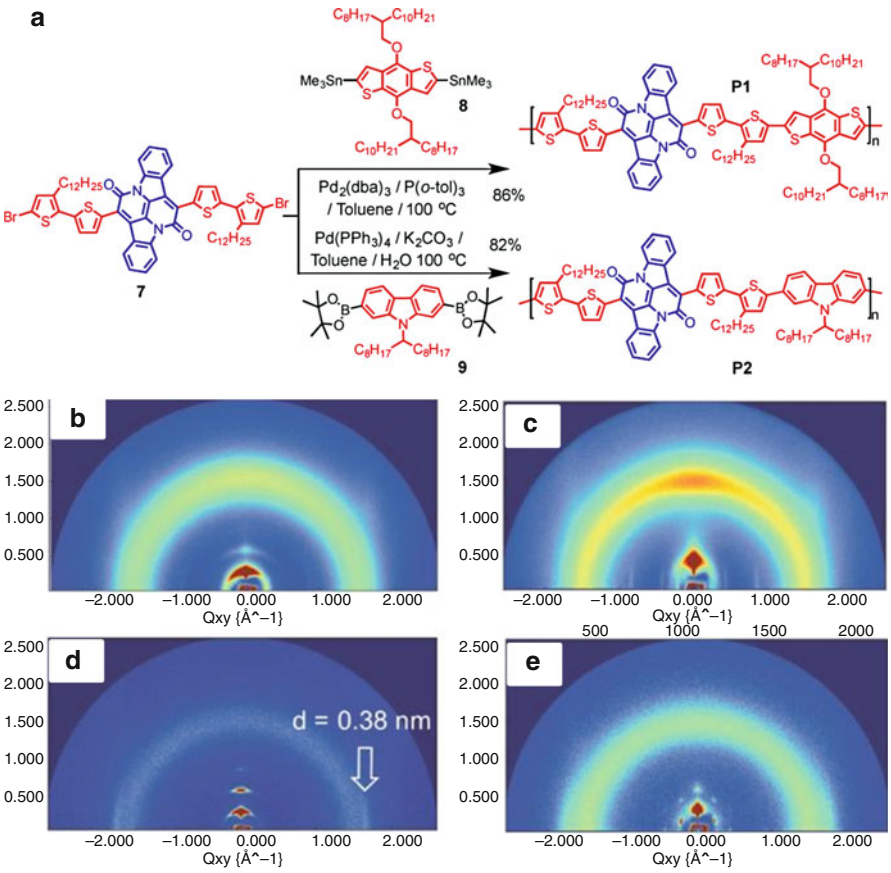

Fig. 2.3 (**a**) The synthesis routes of P1 and P2 polymers. Ex situ GIWAXS patterns collected from P1 thin films (**b** and **c**) and P2 thin films (**d** and **e**); **b** and **d** were both as-cast films while **c** and **e** were films after thermally annealed at 100 °C for 10 min (Reprint with permission from He et al. [69], Copyright © 2014, American Chemical Society)

peak along the out-of-plane direction with respect to the substrates. In addition, the edge-on orientation is suggested by the second-order diffraction peaks along the out-of-plane direction (100) as shown in Fig. 2.3b. It should be mentioned the thermal annealing treatment offers positive effect on the original as-cast films. The thermal annealing increases the overall crystallinity and edge-on stacking as indicated by the enhanced scattering intensity and sharper peak of the (100) plane. Moreover, the narrower (010) peak suggests the enhanced π-π stacking, i.e., increased crystal size along the in-plane direction (Fig. 2.3c). However, with a reduction of the number of side chains (from P1 to P2), the crystallinity is significantly decreased as shown in Fig. 2.3d, e. As for the as-cast P2 film, (100) peak is weak due to the lower degree of orientation along the out-of-plane direction. Both edge-on and face-on molecular

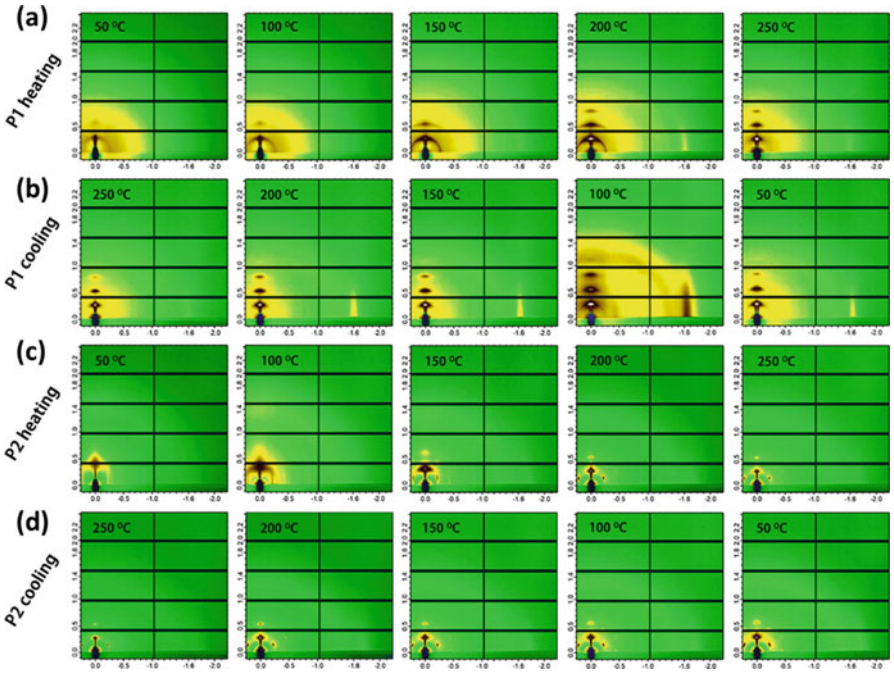

Fig. 2.4 In situ GIWAXS patterns collected from P1 and P2 polymer thin films during heating (a,c) and cooling (b,d) cycles (Reprint with permission from He et al. [69], Copyright © 2014, American Chemical Society)

orientation of the P2 are reflected by the presence of the strong reflections along both in-plane and out-of-plane directions.

In general, thermal annealing provides energy to induce the reorganization of polymer chains for promoting molecular packing and ordering. To understand how P1 and P2 polymers orient with respect to substrates with changing temperatures, in situ GIWAXS measurements were conducted. The temperature ramp rate was 10 °C/min during the heating circle, which was followed by a cooling circle. As shown in Fig. 2.4a during the heating circle, the (100) peak associated lamellar stacking increased with increasing temperature while the strong, (010) peak originated from the π-π stacking of aromatic ring showed up at 200 °C, indicating the initiation of an edge-on molecular orientation on the substrate. The π-π stacking was observed to reduce with further increase in temperature to 250 °C. It is not surprising that the edge-on orientation on the substrate was maintained during cooling of the sample as shown in Fig. 2.4b. The P2 polymer crystallized at 100 °C and exhibited hexagonal packing structure at 150 °C (Fig. 2.4c), which was also maintained during the cooling process (Fig. 2.4d).

The abovementioned organic films for GIWAXS studies were deposited by the spin-coating method. However, it is generally believed that the morphology of the films is highly dependent on the processing methods and conditions. For example,

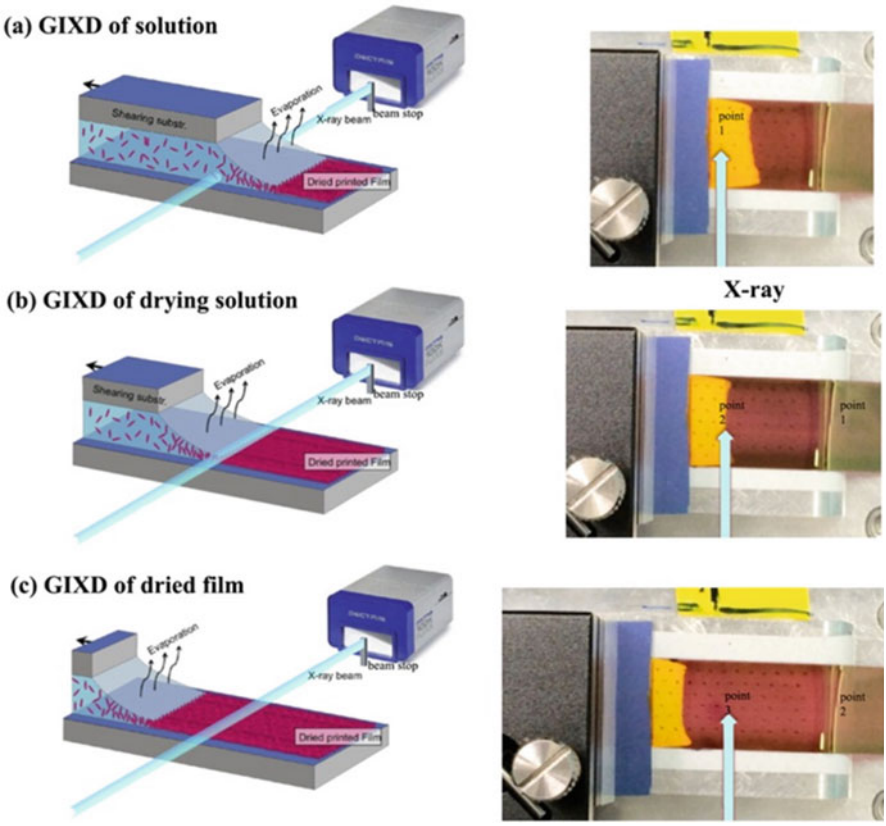

Fig. 2.5 Schematic representation to show the in situ GIWAXS characterization at multiple stages: (**a**) wet film after printing, (**b**) drying film, and (**c**) dried film (Reprint with permission from Gu et al. [57], Copyright © 2016, American Chemical Society)

the morphology of the films processed by roll-to-roll printing and spin-coating could be different due to different drying speeds of the as-cast wet films. This results in different molecular packing and crystallinity for the two different processing techniques. Moreover, roll-to-roll printing is a high-throughput production method to make large-scale electronic devices. Therefore, fully understanding the evolution in the molecular structure, morphology and the associated molecular ordering and crystallization processes of organic thin films fabricated by roll-to-roll methods are of great importance. Recently, Gu et al. have applied in situ GIWAXS to monitor the crystallization dynamics of P3HT:PCBM bulk heterojunction blend films during the roll-to-roll printing process [57]. Figure 2.5 shows the in situ diagnostic setup used in the roll-to-roll printing to track the crystallization dynamics and morphology evolution at multiple stages: (a) wet film after printing, (b) drying film, and (c) dried film.

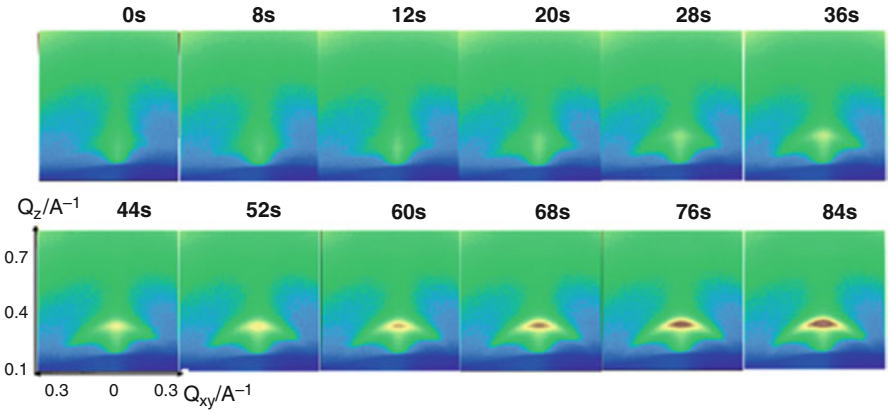

Fig. 2.6 Real-time evolution of GIWAXS images of the out-of-plane (100) peak of the P3HT thin film (Reprint with permission from Gu et al. [57], Copyright © 2016, American Chemical Society)

Using in situ setup, Gu et al., obtained the real-time evolution of the out-of-plane (100) patterns, which could be ascribed to the diffraction of P3HT lamella packed normal to the substrate [57]. It was pointed out that the (010) peak, which is a signature of π-π stacking of P3HT main chains, was not observed, and was most likely masked due to strong scattering from the PET substrate used for this roll-to-roll printing study. Figure 2.6 shows the time evolution of GIWAXS images of out-of-plane (100) peak of the P3HT thin film. It was shown that the diffraction intensity of (100) peak increased with time during the drying process. From these measurements, Gu et al., showed that the drying and crystallization process can be divided into three stages: (1) dissolved state, (2) nucleation and growth, and (3) vitrification. During stage 1 (dissolved state), no diffraction was observed since the molecules were disordered in the wet state. During stage 2 (nucleation and growth), the out-of-plane (100) diffraction peak shows up and its intensity increases with time, as a result of the nucleation and packing behavior of P3HT molecules. During this stage, the P3HT molecules start to align and order to form crystalline domains. In stage 3 (vitrification), after the film dried, the vitrification of P3HT polymers initiates, and during this stage, the side chains of P3HT polymers become more closely packed along the out-of-plane direction.

5.2 Understanding the Metal-Direct Growth of Single-Crystal Organic Nanowires

It is still a challenge to obtain fully-crystallized organic thin films, especially via solution-based processing methods [79, 80]. Most organic thin films have a certain amount of morphological disorder in addition to well-ordered domains [81]. These features lead to anisotropic charge transport and low charge mobilities [82–84]. This challenge can be potentially overcome by assembling organic materials into single

crystalline organic nanowires, or organic nanorods, or other nanostructured forms [86]. In this case, strong π-π interactions are a driving force toward the growth of the one-dimensional structures, which could have excellent unidirectional charge transport behavior with high charge mobilities [85–87]. More importantly, both exciton dissociation and charge separations could be potentially improved by constructing donor/acceptor heterostructure-type organic building blocks along the axial direction or normal to the axial direction [88, 89]. In order to design and fabricate organic nanowires-based electronic devices, it is essential to understand the synthesis and processing process, i.e., controllable growth of organic nanostructure with well-defined molecular orientations and alignment and packing motif, etc.

A typical approach to grow oriented crystalline organic nanowires is the vapor-solid chemical reaction (VSCR) [90, 91], e.g., the reaction between organic vapor molecules with solid thin films. One example of VSCR is the growth of M-$TCNQF_4$ nanowires (M = Cu, Ag), where the metal film (e.g., Cu, Ag) is used to localize and direct the growth of organic nanowires [91]. By replenishing metal reactants to maintain the chemical reaction between metal atoms with the organic small molecules along the π-π stacking direction, the metal atoms are directly incorporated into the structure of organic crystalline nanowires during the reaction process. With such directional growth and spatial confinement of chemical reactions, a mechanism exists to tune the nanowire size, molecular structure, and crystal orientation. For example, by using optical lithography to pattern the metal reactant in combination with the VSCR method, researchers have grown vertically or horizontally aligned organic nanowires [34, 35]. Further controllable growth of organic nanowires between electrodes has also been realized to build transistor and memory devices [35, 92]. The fundamental understanding of nucleation and growth mechanisms of organic nanowires with VSCR method is of fundamental importance to obtain a more precise control of structure, orientation, position, and size of crystalline organic nanowires [92–94].

X-ray diffraction allows for the real-time characterization of the crystallization kinetics of organic nanowires during their growth process. Xiao et al. applied in situ and time-resolved XRD to probe the growth kinetics during the VSCR process [32]. In particular, the nucleation and growth mechanism of M-$TCNQF_4$ nanowires (M = Cu, Ag) was studied with in situ XRD to understand how metals direct the assembly of small-molecules into nanowires, and further reveal what governs the selectivity of which metal that an organic vapor prefers to react with.

Xiao et al. studied the growth kinetics of highly crystalline Ag- and Cu-$TCNQF_4$ nanowires at different temperatures (i.e., 160 °C, 170 °C, 180 °C, and 190 °C). For the growth of Ag-$TCNQF_4$, the time-resolved XRD patterns were collected at growth temperature of 170 °C (Fig. 2.7). To monitor the growth kinetics, scattering windows of 27–30° and 37–39° were chosen to trace the X-ray reflection from Ag-$TCNQF_4$ (222) and Ag (111) peaks. After reaction for 15 min, the (222) peak for Ag-$TCNQF_4$ nanowires became detectable while the Ag (111) peak decreased simultaneously, suggesting the continuous growth of Ag-$TCNQF_4$ nanowires and the simultaneous consumption of the Ag film due to the chemical reaction with the $TCNQF_4$ vapor. The (222) peak of Ag-$TCNQF_4$ and (111) peak of Ag were

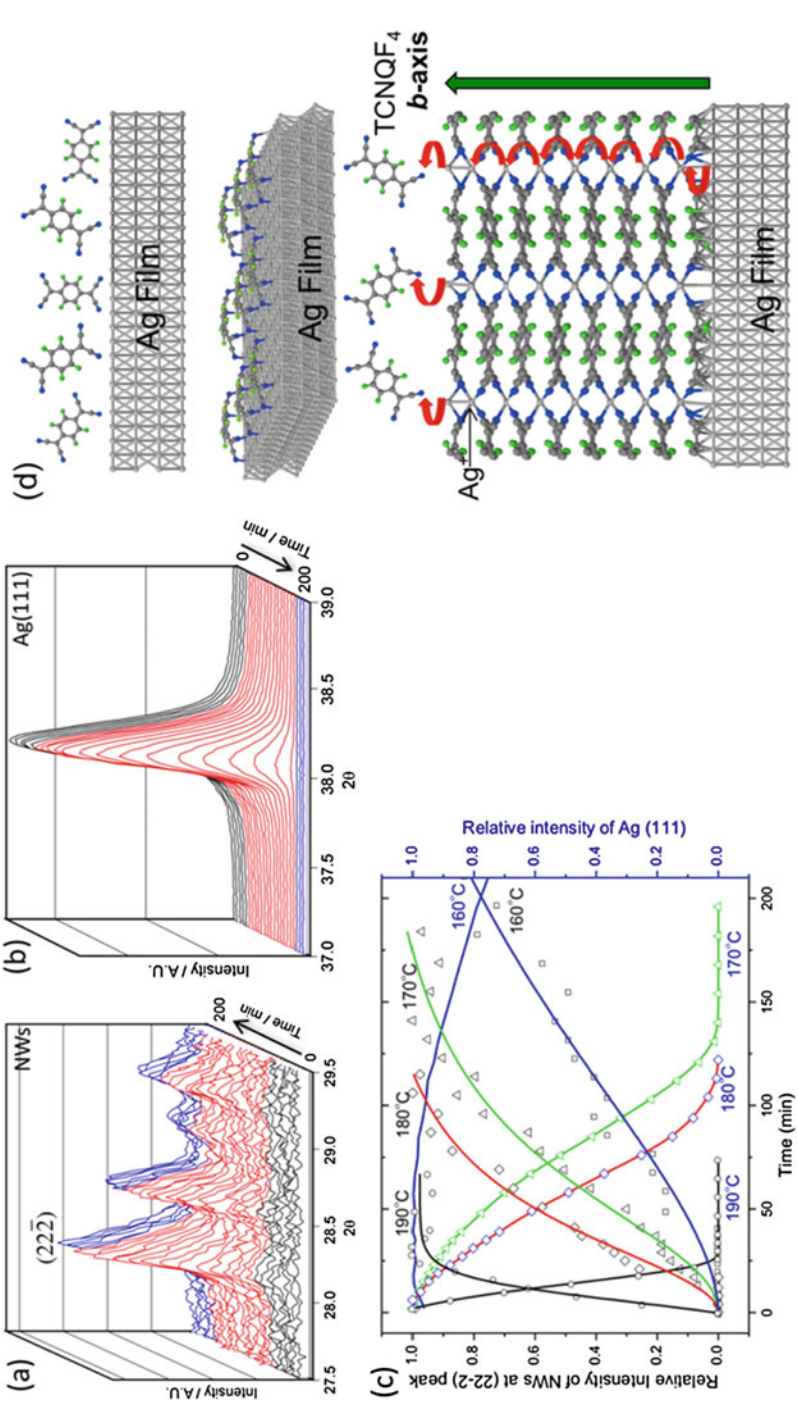

Fig. 2.7 Real-time XRD patterns during the synthesis and growth of Ag-$TCNQF_4$ NWs by a VSCR method at growth temperature of 170 °C. (**a**) $(22\bar{2})$ X-ray reflection of Ag-$TCNQF_4$ NWs and (**b**) Ag (111) reflection with time. (**c**) Normalized integrated intensities of in situ XRD of Ag-$TCNQF_4$ nanowire growth

integrated and then the peak areal intensity was plotted as a function of time to show the dynamic process of growth of nanowires and consumption of Ag metal, respectively. The normalized integrated X-ray peak intensities were shown in Fig. 2.7c. The modified Avrami model was used to fit the growth kinetic curves, and it was found that the Avrami exponents (n) at four growth temperatures were between 1.1 and 1.7, which indicates the growth mechanism of Ag-$TCNQF_4$ nanowire is one dimensional, diffusion-controlled growth behavior. Additionally, Xiao et al. also found that the growth rate of Ag-$TCNQF_4$ nanowires increases with increasing temperature, as suggested by the higher kinetic constant at higher temperatures. The growth kinetics of the organic nanowire probed using in situ XRD combined with theory calculations and modeling suggested that the metal ions from the film diffuse along the nanowires to their tips where they react with the organic vapor to continue the growth, an energetically favorable process (Fig. 2.7d).

Xiao et al. also conducted another in situ X-ray diffraction experiment to test the above- proposed growth mechanism and to investigate the long-range migration behavior of the metal ions (such as Ag^+ in the abovementioned case) during the ionic exchange reaction process. Real-time X-ray diffraction was again applied to monitor the chemical reaction between $TCNQF_4$ vapor molecules and Cu/Ag double layers to study the growth kinetics of nanowires involving a competition between Ag and Cu with $TCNQF_4$. Here, the Ag layer is on top of Cu layer. The Ag layer thickness varies whereas the bottom Cu layer thickness was maintained at 50 nm. The reaction temperature was set at 170 °C. XRD peaks at 15.5° and 16.8° were monitored to obtain the growth kinetics of Ag-$TCNQF_4$ and Cu-$TCNQF_4$, respectively (Fig. 2.8a). Interestingly, when the thickness of Ag layer was less than 200 nm, only the Cu was involved into the reaction with $TCNQF_4$ vapor molecules and only Cu-$TCNQF_4$ nanowires were formed (red and green); however, when the Ag thickness was larger than 200 nm, the $TCNQF_4$ vapor molecules initially reacted with Ag to form the intermediate state Ag-$TCNQF_4$, which was then transformed into Cu-$TCNQF_4$ due to ion exchange reactions where Ag^+ ions were replaced by Cu^+ ions (dark and blue). The SEM images show the consumption of Cu and remaining of Ag after the growth process of nanowires (Fig. 2.8b–d). This result confirmed that the metal ion migration over long distances along the 1D channel of nanowires is possible during the ionic exchange reaction process. The selectivity of a metal for the vapor reactant is quite distinct. For example, the deposition of nickel (Ni) film on top of Cu film may block the diffusion of Cu, preventing the growth of nanowires.

Fig. 2.7 (continued) from Ag metal at four different temperatures (160 °C, 170 °C, 180 °C, and 190 °C) to describe the growth kinetics of the nanowires: rise in the Ag-$TCNQF_4$ $(22\bar{2})$ peak reflection and consumption in Ag (111) peak reflection of Ag metal. The curves were fitted with a modified Avrami model. (**d**) Illustration of ionic diffusion tip growth process with three steps: Top: $TCNQF_4$ vapor molecules adsorbed on the Ag film surface; middle: an electron migrates from Ag to $TCNQF_4$ to form a $TCNQF_4^-$ ion, and Ag^+ interacts with $TCNQF_4^-$ ion form Ag-$TCNQF_4$; bottom: face-to-face stacking of $TCNQF_4$ molecules to form periodic 1D channels for Ag^+ diffusion normal to the substrate. (Blue, N; gray, C; green, F; light gray, Ag) (Reprint with permission from Xiao et al. [32], Copyright © 2012, American Chemical Society)

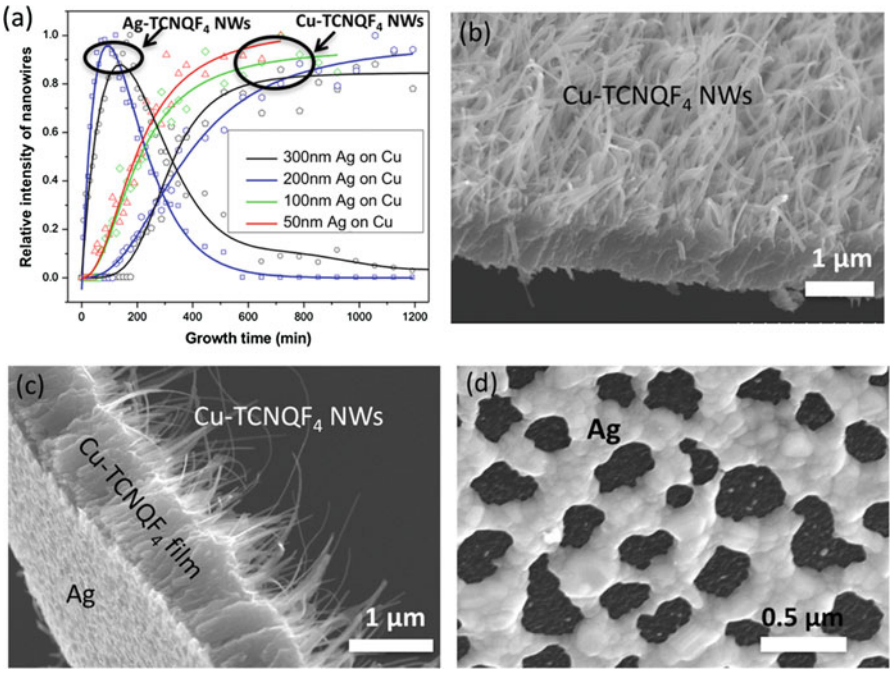

Fig. 2.8 Growth mechanism of $TCNQF_4$ on a substrate coated with Cu/Ag double metal layers. (**a**) Variation of normalized XRD peak intensities of organic nanowires grown under Ag films with different thickness (50 nm, 100 nm, 200 nm, and 300 nm), where the bottom Cu layer thickness was kept at 50 nm and growth temperature was 170 °C. The curves were fitted with an Avrami model. (**b**–**c**) SEM image showing morphology of the typical organic nanowires by this method: (**b**) surface morphology and (**c**) side view. (**d**) SEM image showing the rear of nanowire array, which suggests the consumption of Cu and remaining of Ag after the growth process of nanowires (Reprint with permission from Xiao et al. [32], Copyright © 2012, American Chemical Society)

5.3 Crystallization Mechanism of Organic-Inorganic Hybrid Perovskites

During the past several years, a group of functional organic-inorganic hybrid perovskites have drawn considerable attention for promising optoelectronic applications including photovoltaics [9, 45, 55], LEDs [95], lasers [96, 97], photodetectors [98–100], etc. To achieve superior device performance, it is essential to understand the controllable synthesis and processing of the perovskites film from their chemical precursors, including the crystal growth kinetics and morphology evolution under the specific choice of film growth conditions [95, 101, 102]. Depending on materials synthesis and film growth conditions, hybrid perovskites not only exhibit *n*- or *p*-type semiconducting behavior [103], but also differing the degrees of defects and traps [104], which may cause significant energy loss as a result of nonradiative recombination [47, 105]. Moreover, understanding how crystallization of perovskites can result in large crystallites within thin films appears to be one key to fabricate high-efficiency perovskite solar cells [106–109].

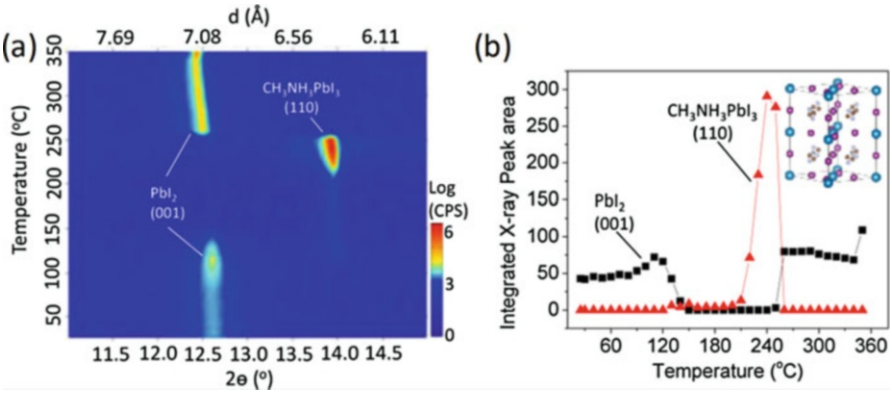

Fig. 2.9 (**a**) Temperature ramp study of XRD to show the transformation from PbI_2 to $CH_3NH_3PbI_3$ perovskites. (**b**) Temperature dependent of variation of integrated peak areal intensity of PbI_2 and $CH_3NH_3PbI_3$ perovskites. The inset of (**b**) displays the illustration of crystal structure of $CH_3NH_3PbI_3$ (Reprint with permission from Yang et al. [62], Copyright © 2016, American Chemical Society)

Recently, Yang et al. applied in situ X-ray diffraction to monitor the whole transformation process from lead halide PbX_2 (PbX_2, X = Cl, Br, I) precursors to final $CH_3NH_3PbX_3$ (X = Cl, Br, I) perovskites in a sealed chamber which was filled with methylammonium iodide (CH_3NH_3I) vapor [62]. A lead halide precursor (e.g., PbI_2) film was surrounded with CH_3NH_3I powder. The reaction and growth temperature was controlled by a heater coil, and the reaction and growth of the perovskite films occurred in the helium or nitrogen gas environment. First, a temperature ramp study was conducted to track the chemical reaction ($PbI_2 + CH_3NH_3I \rightarrow CH_3NH_3PbI_3$) to find suitable growth temperatures for the subsequent isothermal studies. Figure 2.9a shows the temperature ramp study of the transformation from PbI_2 to $CH_3NH_3PbI_3$ perovskites, and the temperature dependence of variation of integrated intensity of (001) peak of PbI_2 and (110) peak of $CH_3NH_3PbI_3$ perovskites was also exhibited in Fig. 2.9b. The (110) of $CH_3NH_3PbI_3$ perovskite appeared at around 120 °C while the (001) plane of PbI_2 decreased significantly. It should be noted that, since the $CH_3NH_3PbI_3$ perovskites experience a phase transition from tetragonal to cubic at around 327 K, the peak at 14.05° is indexed as (100) when temperature is higher than 327 K. Based on the temperature ramp study results, three growth temperatures (i.e., 100 °C, 120 °C, and 140 °C) were selected to study growth kinetics by monitoring XRD reflections at $2\theta = 12.65°$ and 14.05° to track the evolution of structure transformation between PbI_2 and $CH_3NH_3PbI_3$.

The growth kinetics are shown in Fig. 2.10a–c. The chemical reaction and crystallization of perovskites were highly temperature dependent. At 100 °C, the PbI_2 still remained even after reaction for about 760 min in the CH_3NH_3I vapor environment. However, the same amount of PbI_2 was quickly consumed in the CH_3NH_3I vapor environment even with reaction for only about 30 min at 140 °C. By integrating the peak area of PbI_2 (001) and $CH_3NH_3PbI_3$ (110) at the three growth temperatures, the

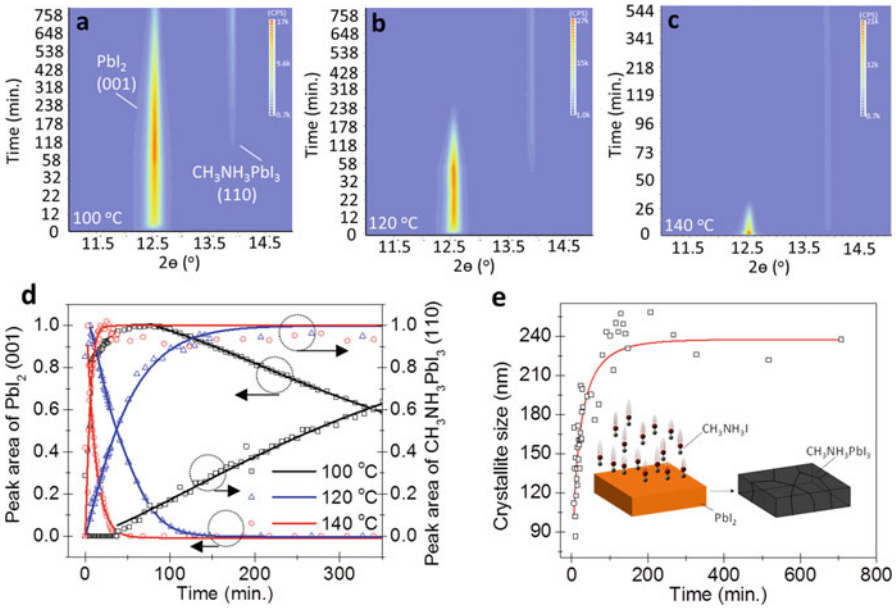

Fig. 2.10 Isothermal crystallization kinetics of $CH_3NH_3PbI_3$ at three different temperatures: (**a**) 100 °C, (**b**) 120 °C, and (**c**) 140 °C. (**d**) Variations of normalized peak areal density of PbI_2 (001) and $CH_3NH_3PbI_3$ (110) at different temperatures. The corresponding solid lines are a result of Avrami model fits. (**e**) The crystallite size as a function of growth time. Inset of (**e**) shows a schematic representation of the PbI_2 film reacting with CH_3NH_3I vapor to form $CH_3NH_3PbI_3$ (Reprint with permission from Yang et al. [62], Copyright © 2016, American Chemical Society)

time-resolved evolution of peak intensity is shown in Fig. 2.10d, and these curves were fitted with an Avrami model. The Avrami exponents are between 1 and 2, suggesting a diffusion-controlled, one-dimensional mechanism governs the growth of perovskite films. Based on the in situ XRD results, Yang et al. proposed a growth process of perovskite films (Fig. 2.10e) [62] wherein the $CH_3NH_3PbI_3$ perovskite crystal nuclei is initially generated on top surface of the PbI_2 film as the CH_3NH_3I vapor contacts with the PbI_2 precursors, and afterwards the additional CH_3NH_3I vapor molecules diffuse into the underneath PbI_2 layer to facilitate the top-down reaction. During this top-down nucleation process, the $CH_3NH_3PbI_3$ crystals grow along the direction normal to the PbI_2 film. Finally, the perovskite grains coalescence laterally to increase the lateral dimension of grains [61, 111].

Recent studies have shown that incorporating multiple halogen ion species into the perovskite structure can tune optical bandgap, defect, ion migration, and film morphology [110, 111]. However, how these halogen ion species compete with each other during the chemical reaction process has not been clear [112]. Recently, Yang et al. applied in situ XRD to reveal such completion [62], where it was revealed that bromine ions were gradually substituted by iodine ions in the perovskite lattice. Figure 2.11a, b shows the transformation of perovskite structure from $CH_3NH_3PbI_{1.5}Br_{1.5}$ to $CH_3NH_3PbI_3$ in the presence of an excess of CH_3NH_3I vapor. Yang et al. also studied

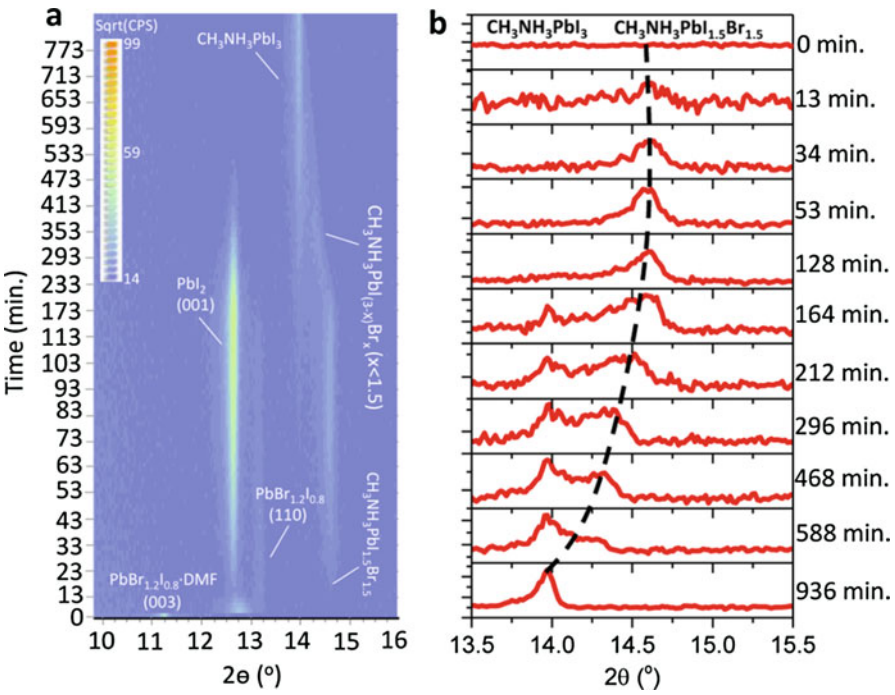

Fig. 2.11 In situ powder X-ray diffraction to reveal the competition between I^- and Br^- ions during the vapor-assisted synthesis and growth of perovskites. (**a**) Time-dependent variation of Bragg peaks at 11.24° for $PbBr_{1.2}I_{0.8}$·DMF (003), 13.18° for $PbBr_{1.2}I_{0.8}$ (110), 12.64° for PbI_2 (001), 13.95° for $CH_3NH_3PbI_3$, and 14.59° for $CH_3NH_3PbI_{1.5}Br_{1.5}$ grown at 120 °C. (**b**) Time-dependent phase transformation from $CH_3NH_3PbI_{1.5}Br_{1.5}$ to $CH_3NH_3PbI_3$ in the excess of CH_3NH_3I vapor environment (Reprint with permission from Yang et al. [62], Copyright © 2016, American Chemical Society)

the competition between iodine and chorine ions during the formation of perovskites. Interestingly, in the presence of excess of CH_3NH_3I vapor, the chlorine was found to reside in the grain boundaries of perovskite films, rather than in the perovskite crystal lattice. Although in situ XRD revealed that neither Br^- nor Cl^- was incorporated into the perovskite crystal lattice in the presence of more reactive I^-, the evolving of Br^- or Cl^- ions in the synthesis and growth of perovskite was found to promote crystal growth and achieve larger crystals in films, which could improve the carrier transport in $CH_3NH_3PbI_3$ perovskite films [62, 113].

6 Conclusions and Future Perspective

In situ GIWAXS and XRD both provide promising nondestructive, real-time diagnostics that reveal important reaction or crystallization mechanism and structural information crucial to the assembly of organic small molecules and polymers, as well as

complex organic/inorganic hybrid structures, that are emerging for commercially important flexible electronics today. The employment of in situ GIWAXS to investigate molecular orientation and packing behavior during the deposition of organic thin films with either vacuum thermal evaporation or solution-based coating has been discussed in this chapter. These studies showed that the processing conditions significantly affect the morphological features at molecular level. Molecular chain can orient along the direction either parallel to the substrate or perpendicular to the substrate, depending on the interfacial properties, substrate temperatures, processing methods, etc.

Starting with thermally evaporated small molecules, we showed that both film thickness and growth temperature impacted molecular orientation and packing behavior of pentacene during the vacuum thermal evaporation deposition process. It was found that only 1 nm-thick-pentacene film could exhibit highly oriented discrete diffraction spots at an elevated growth temperature of 75 °C. GIWAXS results also indicated the crystal orientation, where the (001) crystal plane of bulk phase was parallel to the substrate.

In addition to thermally evaporated films, in situ GIWAXS reveals the molecular level evolution of morphology during solution-processing, as was shown for annealing of bay-annulated indigo based donor−acceptor polymer films. There GIWAXS revealed how the polymer chains in the as-cast film formed a (100) plane, edge-on orientation with respect to the substrate that increased during annealing, while the aromatic π-π stacking along the (010) plane reduced. In another example, GIWAXS revealed the kinetics and dynamics of three stages in the drying and crystallization from wet P3HT:PCBM films processed by large-scale roll-to-roll methods: [1] a disordered "dissolved" state, [2] nucleation and growth of P3HT domains, and [3] vitrification with packing (interdigitation) of aliphatic side chains. Such studies are invaluable to provide understanding and real-time feedback in large-scale solution processing of organic electronics.

In situ and time-resolved powder X-ray characterization can be applied to monitor the overall crystallization processes of films and nanostructures, as in the example of the M-$TCNQF_4$ NWs (M = Cu, Ag) organic nanowire growth kinetics measured during the VSCR process. This technique enabled the understanding of the one-dimensional diffusion-controlled growth kinetics, revealed how metals direct the assembly of small-molecules into nanowires, and revealed the selectivity of between two metals competing for an organic vapor reactant during the VSCR growth process.

Finally, in situ powder X-ray diffraction was shown to achieve fundamental understanding of crystal growth kinetics and mechanisms for complex organic/inorganic hybrid perovskites by monitoring the whole transformation process from lead halide PbX_2 (X = Cl, Br, I) precursors to final $CH_3NH_3PbI_3$ perovskites in a sealed chamber which was filled with CH_3NH_3I vapor. Starting with $CH_3NH_3PbI_3$ perovskite crystal nuclei initially generated on the top surface of the PbI_2 film by the CH_3NH_3I vapor, the $CH_3NH_3PbI_3$ crystals grow along the direction perpendicular to the PbI_2 film and substrates, eventually forming grains that coalesce laterally to increase the lateral dimension. Revealing this one-dimensional, diffusion-controlled growth mechanism could provide guidance to facilitate large crystallite size perovskite thin films.

In situ X-ray diffraction analysis is a powerful tool for the fundamental understanding of a large variety of materials systems and further for the optimization of materials processing for enhanced materials performance [56]. As introduced in this chapter, this tool has been widely recognized and applied to reveal the chemical reaction kinetics, phase transformation, and crystal nucleation and growth [114]. However, the in situ X-ray diffraction analysis only provides average information and lacks the microscopic local structure details. The combination of in situ microscopy measurements (e.g., SEM/AFM) with in situ X-ray diffraction analysis would offer a more complete understanding of the materials system during the in situ growth for future studies. In addition, understanding the relationship between the structure and properties of functional materials is of fundamental interest because they often couple together. Therefore, developing in situ real-time measurements of both properties and structure directly and simultaneously in functional materials to study the correlation between them during processing and growth are highly desirable.

Acknowledgments This research was conducted at the Center for Nanophase Materials Sciences (CNMS), which is a DOE Office of Science User Facility. B.Y. acknowledges support for the writing of this chapter while at LBNL from the Office of Science, Office of Basic Energy Sciences, of the US Department of Energy under Contract No. DE-AC02-05CH11231.

References

1. Chen JD et al (2015) Single-junction polymer solar cells exceeding 10% power conversion efficiency. Adv Mater 27:1035–1041
2. Dou L, Liu Y, Hong Z, Li G, Yang Y (2015) Low-bandgap near-IR conjugated polymers/molecules for organic electronics. Chem Rev 115:12633–12665
3. Guo X, Baumgarten M, Müllen K (2013) Designing π-conjugated polymers for organic electronics. Prog Polym Sci 38:1832–1908
4. Bujak P et al (2013) Polymers for electronics and spintronics. Chem Soc Rev 42:8895–8999
5. Yuan Y, Xiao Z, Yang B, Huang J (2014) Arising applications of ferroelectric materials in photovoltaic devices. J Mater Chem A 2:6027–6041
6. Yau CP et al (2014) Influence of the electron deficient co-monomer on the optoelectronic properties and photovoltaic performance of dithienogermole-based co-polymers. Adv Funct Mater 24:678–687
7. Tan WY et al (2014) Lending triarylphosphine oxide to phenanthroline: a facile approach to high-performance organic small-molecule cathode interfacial material for organic photovoltaics utilizing air-stable cathodes. Adv Funct Mater 24:6540–6547
8. Wang Y, Yang X, Li H, Sheng C (2016) Bright single-mode random laser from a concentrated solution of π-conjugated polymers. Opt Lett 41:269–272
9. Lin Q, Armin A, Nagiri RCR, Burn PL, Meredith P (2015) Electro-optics of perovskite solar cells. Nat Photon 9:106–112
10. Yao D, Zhang X, Mongin O, Paul F, Paul-Roth CO (2016) Synthesis and characterization of new conjugated fluorenyl-porphyrin dendrimers for optics. Chem Eur J 22:5583–5597
11. Ramadan KS, Sameoto D, Evoy S (2014) A review of piezoelectric polymers as functional materials for electromechanical transducers. Smart Mater Struct 23:033001
12. Sriplai N et al (2015) Ferromagnetism in metal-free polymers. IEEE Magn Lett 6:1–4

13. Yang B et al (2013) Room-temperature organic ferromagnetism in the crystalline poly (3-hexylthiophene): phenyl-C61-butyric acid methyl ester blend film. Polymer 54:490–494
14. Zhen S, Lu B, Xu J, Zhang S, Li Y (2014) Poly (mono-, bi-or trifuran): effect of oligomer chain length on the electropolymerization performances and polymer properties. RSC Adv 4:14001–14012
15. Yang B, Shao M, Keum J, Geohegan D, Xiao K (2016) Semiconductor materials for solar photovoltaic cells. Springer, Cham, pp 197–228
16. Guo F et al (2012) A nanocomposite ultraviolet photodetector based on interfacial trap-controlled charge injection. Nat Nanotechnol 7:798–802
17. Caironi M, Anthopoulos TD, Noh YY, Zaumseil J (2013) Organic and hybrid materials for flexible electronics. Adv Mater 25:4208–4209
18. Fujisaki Y et al (2014) Transparent nanopaper-based flexible organic thin-film transistor array. Adv Funct Mater 24:1657–1663
19. Kettle J et al (2015) Three dimensional corrugated organic photovoltaics for building integration; improving the efficiency, oblique angle and diffuse performance of solar cells. Energy Environ Sci 8:3266–3273
20. Li ZR (2015) Organic light-emitting materials and devices. CRC Press, Boca Raton
21. Chiba A, Nara T (2014) 2-D localization of radio frequency identification tags from measurements of the weighted integrals of the magnetic flux density. IEEE Trans Magn 50:1–8
22. Sekine C, Tsubata Y, Yamada T, Kitano M, Doi S (2014) Recent progress of high performance polymer OLED and OPV materials for organic printed electronics. Sci Technol Adv Mater 15:034203
23. Das S et al (2016) Low thermal budget, photonic-cured compact TiO_2 layers for high-efficiency perovskite solar cells. J Mater Chem A 4:9685–9690
24. Yang B et al (2012) Tuning the energy level offset between donor and acceptor with ferroelectric dipole layers for increased efficiency in bilayer organic photovoltaic cells. Adv Mater 24:1455–1460
25. Yang B et al (2013) Solution-processed fullerene-based organic Schottky junction devices for large-open-circuit-voltage organic solar cells. Adv Mater 25(4):571
26. Yang B, Cox J, Yuan Y, Guo F, Huang J (2011) Increased efficiency of low band gap polymer solar cells at elevated temperature and its origins. Appl Phys Lett 99:206
27. Yang B, Xiao Z, Huang J (2014) Polymer aggregation correlated transition from Schottky-junction to bulk heterojunction organic solar cells. Appl Phys Lett 104:143304
28. https://www.wbdg.org/resources/building-integrated-photovoltaics-bipv
29. Li M et al (2017) Solution-processed organic tandem solar cells with power conversion efficiencies >12%. Nat Photonics 11:85–90
30. Yuan Y et al (2014) Ultra-high mobility transparent organic thin film transistors grown by an off-centre spin-coating method. Nat Commun 5:3005
31. Keum JK, Zuo F, Hsiao BS (2008) Formation and stability of shear-induced shish-kebab structure in highly entangled melts of UHMWPE/HDPE blends. Macromolecules 41:4766–4776
32. Xiao K, Yoon M, Rondinone AJ, Payzant EA, Geohegan DB (2012) Understanding the metal-directed growth of single-crystal M-$TCNQF_4$ organic nanowires with time-resolved, in situ X-ray diffraction and first-principles theoretical studies. J Am Chem Soc 134:14353–14361
33. Yang B, Yuan Y, Huang J (2014) Reduced bimolecular charge recombination loss in thermally annealed bilayer heterojunction photovoltaic devices with large external quantum efficiency and fill factor. J Phys Chem C 118:5196–5202
34. Yang F, Shtein M, Forrest SR (2005) Controlled growth of a molecular bulk heterojunction photovoltaic cell. Nat Mater 4:37–41
35. Xiao K et al (2009) Metastable copper-phthalocyanine single-crystal nanowires and their use in fabricating high-performance field-effect transistors. Adv Funct Mater 19:3776–3780
36. Dar MI et al (2016) Origin of unusual bandgap shift and dual emission in organic-inorganic lead halide perovskites. Sci Adv 2:e1601156

37. Dou L et al (2015) Atomically thin two-dimensional organic-inorganic hybrid perovskites. Science 349:1518–1521
38. Eperon GE et al (2016) Perovskite-perovskite tandem photovoltaics with optimized band gaps. Science 354:861–865
39. Jeon NJ et al (2015) Compositional engineering of perovskite materials for high-performance solar cells. Nature 517:476–480
40. Tsai H et al (2016) High-efficiency two-dimensional Ruddlesden–Popper perovskite solar cells. Nature 536:312–316
41. Zhou H et al (2014) Interface engineering of highly efficient perovskite solar cells. Science 345:542–546
42. Bella F et al (2016) Improving efficiency and stability of perovskite solar cells with photocurable fluoropolymers. Science 354:203–206
43. Frost JM et al (2014) Atomistic origins of high-performance in hybrid halide perovskite solar cells. Nano Lett 14:2584–2590
44. Green MA, Ho-Baillie A, Snaith HJ (2014) The emergence of perovskite solar cells. Nat Photonics 8:506–514
45. Nie W et al (2015) High-efficiency solution-processed perovskite solar cells with millimeter-scale grains. Science 347:522–525
46. Yang B, Mahjouri-Samani M, Rouleau CM, Geohegan DB, Xiao K (2016) Low temperature synthesis of hierarchical TiO_2 nanostructures for high performance perovskite solar cells by pulsed laser deposition. Phys Chem Chem Phys 18:27067–27072
47. Yang B et al (2015) Perovskite solar cells with near 100% internal quantum efficiency based on large single crystalline grains and vertical bulk heterojunctions. J Am Chem Soc 137:9210–9213
48. Du M-H (2014) Efficient carrier transport in halide perovskites: theoretical perspectives. J Mater Chem A 2:9091–9098
49. Yang B et al (2015) Controllable growth of perovskite films by room-temperature air exposure for efficient planar heterojunction photovoltaic cells. Angew Chem Int Ed 54: 14862–14865
50. Yang B et al (2016) Observation of nanoscale morphological and structural degradation in perovskite solar cells by in situ TEM. ACS Appl Mater Interfaces 8:32333–32340
51. Divitini G et al (2016) In situ observation of heat-induced degradation of perovskite solar cells. Nat Energy 1:15012
52. Wang D, Wright M, Elumalai NK, Uddin A (2016) Stability of perovskite solar cells. Sol Energy Mater Sol Cells 147:255–275
53. Yang J, Siempelkamp BD, Mosconi E, De Angelis F, Kelly TL (2015) Origin of the thermal instability in $CH_3NH_3PbI_3$ thin films deposited on ZnO. Chem Mater 27:4229–4236
54. Kim J et al (2016) Nucleation and growth control of $HC(NH_2)_2PbI_3$ for planar perovskite solar cell. J Phys Chem C 120:11262–11267
55. Saparov B, Mitzi DB (2016) Organic–inorganic perovskites: structural versatility for functional materials design. Chem Rev 116:4558–4596
56. Kowarik S (2016) Thin film growth studies using time-resolved x-ray scattering. J Phys Condens Matter 29:043003
57. Gu X et al (2016) Compact roll-to-roll coater for in situ X-ray diffraction characterization of organic electronics printing. ACS Appl Mater Interfaces 8:1687–1694
58. Watanabe T, Hosokai T, Koganezawa T, Yoshimoto N (2012) In situ real-time X-ray diffraction during thin film growth of pentacene. Mol Cryst Liq Cryst 566:18–21
59. Smilgies DM et al (2013) Look fast: crystallization of conjugated molecules during solution shearing probed in situ and in real time by X-ray scattering. Phys Status Solidi RRL 7:177–179
60. Nahm R, Engstrom J (2017) Who's on first? Tracking in real time the growth of multiple crystalline phases of an organic semiconductor: tetracene on SiO_2. J Chem Phys 146:052815

61. Beyer P et al (2014) Lattice matching as the determining factor for molecular tilt and multilayer growth mode of the nanographene hexa-peri-hexabenzocoronene. ACS Appl Mater Interfaces 6:21484–21493
62. Yang B et al (2016) Deciphering halogen competition in organometallic halide perovskite growth. J Am Chem Soc 138:5028–5035
63. Zykov A et al (2017) Diffusion and nucleation in multilayer growth of PTCDI-C8 studied with in situ X-ray growth oscillations and real-time small angle X-ray scattering. J Chem Phys 146:052803
64. Yoshimoto N, Watanabe T, Kikuchi M, Koganezawa T, Hirosawa I (2014) In-situ observation of 2-dimensional X-ray diffraction of organic thin-film growth by synchrotron radiation. Hyomen Kagaku 35:190–195
65. Frank C et al (2013) Real-time X-ray scattering studies on temperature dependence of perfluoropentacene thin film growth. J Appl Phys 114:043515
66. Lin Y-Y, Gundlach D, Nelson SF, Jackson TN (1997) Pentacene-based organic thin-film transistors. IEEE Trans Electron Dev 44:1325–1331
67. Zhang M, Irfan, Ding H, Gao Y, Tang CW (2010) Organic Schottky barrier photovoltaic cells based on MoO_x/C60. Appl Phys Lett 96:87
68. Chen W-B et al (2007) Improving efficiency of organic photovoltaic cells with pentacene-doped CuPc layer. Appl Phys Lett 91:191109
69. He B et al (2014) New form of an old natural dye: bay-annulated indigo (BAI) as an excellent electron accepting unit for high performance organic semiconductors. J Am Chem Soc 136:15093–15101
70. Das S et al (2015) High-performance flexible perovskite solar cells by using a combination of ultrasonic spray-coating and low thermal budget photonic curing. ACS Photon 2:680–686
71. Pudas M, Halonen N, Granat P, Vähäkangas J (2005) Gravure printing of conductive particulate polymer inks on flexible substrates. Prog Org Coat 54:310–316
72. Sirringhaus H et al (2000) High-resolution inkjet printing of all-polymer transistor circuits. Science 290:2123–2126
73. Kim Y et al (2005) Device annealing effect in organic solar cells with blends of regioregular poly (3-hexylthiophene) and soluble fullerene. Appl Phys Lett 86:063502
74. Hexemer A et al (2010) J Phys Conf Ser 247:012007
75. Müllen K, Pisula W (2015) Donor-acceptor polymers. J Am Chem Soc 137:9503–9505
76. Kronemeijer AJ et al (2012) A selenophene-based low-bandgap donor–acceptor polymer leading to fast ambipolar logic. Adv Mater 24:1558–1565
77. Sonar P et al (2011) High mobility organic thin film transistor and efficient photovoltaic devices using versatile donor–acceptor polymer semiconductor by molecular design. Energy Environ Sci 4:2288–2296
78. Ajayaghosh A (2003) Donor–acceptor type low band gap polymers: polysquaraines and related systems. Chem Soc Rev 32:181–191
79. Rivnay J et al (2009) Large modulation of carrier transport by grain-boundary molecular packing and microstructure in organic thin films. Nat Mater 8:952–958
80. Madec M-B et al (2010) Enhanced reproducibility of inkjet printed organic thin film transistors based on solution processable polymer-small molecule blends. J Mater Chem 20:9155–9160
81. Peisert H et al (2001) Order on disorder: copper phthalocyanine thin films on technical substrates. J Appl Phys 90:466–469
82. Crossland EJ et al (2012) Anisotropic charge transport in spherulitic poly (3-hexylthiophene) films. Adv Mater 24:839–844
83. O'Connor B et al (2011) Anisotropic structure and charge transport in highly strain-aligned regioregular poly (3-hexylthiophene). Adv Funct Mater 21:3697–3705
84. Fraboni B et al (2009) Solution-grown, macroscopic organic single crystals exhibiting three-dimensional anisotropic charge-transport properties. Adv Mater 21:1835–1839

85. Jang K, Jung IG, Nam HJ, Jung D-Y, Son SU (2009) One-dimensional organometallic molecular wires via assembly of $Rh(CO)_2Cl$(amine): chemical control of Interchain distances and optical properties. J Am Chem Soc 131:12046–12047
86. Palmer LC, Stupp SI (2008) Molecular self-assembly into one-dimensional nanostructures. Acc Chem Res 41:1674–1684
87. Palmer LC et al (2014) Long-range ordering of highly charged self-assembled nanofilaments. J Am Chem Soc 136:14377–14380
88. Lee J et al (2014) Donor–acceptor alternating copolymer nanowires for highly efficient organic solar cells. Adv Mater 26:6706–6714
89. Lei Y et al (2016) Solution-processed donor-acceptor polymer nanowire network semiconductors for high-performance field-effect transistors. Sci Rep 6:24476
90. Liu H et al (2005) Field emission properties of large-area nanowires of organic charge-transfer complexes. J Am Chem Soc 127:1120–1121
91. Xiao K et al (2007) Single-crystal organic nanowires of copper–tetracyanoquinodimethane: synthesis, patterning, characterization, and device applications. Angew Chem Int Ed 46:2650–2654
92. Xiao K et al (2008) Selective patterned growth of single-crystal ag–TCNQ nanowires for devices by vapor–solid chemical reaction. Adv Funct Mater 18:3043–3048
93. Xiao K et al (2009) Growth, patterning, and one-dimensional electron-transport properties of self-assembled Ag-$TCNQF_4$ organic nanowires. Chem Mater 21:4275–4281
94. Xiao K, Ivanov IN, Puretzky AA, Liu Z, Geohegan DB (2006) Directed integration of tetracyanoquinodimethane-Cu organic nanowires into prefabricated device architectures. Adv Mater 18:2184–2188
95. Cho H et al (2015) Overcoming the electroluminescence efficiency limitations of perovskite light-emitting diodes. Science 350:1222–1225
96. Zhu H et al (2015) Lead halide perovskite nanowire lasers with low lasing thresholds and high quality factors. Nat Mater 14:636–642
97. Fu A, Yang P (2015) Organic-inorganic perovskites: lower threshold for nanowire lasers. Nat Mater 14:557–558
98. Dou L et al (2014) Solution-processed hybrid perovskite photodetectors with high detectivity. Nat Commun 5:5404
99. Hu X et al (2014) High-performance flexible broadband photodetector based on organolead halide perovskite. Adv Funct Mater 24:7373–7380
100. Fang Y, Huang J (2015) Resolving weak light of sub-picowatt per square centimeter by hybrid perovskite photodetectors enabled by noise reduction. Adv Mater 27:2804–2810
101. Chen Q et al (2013) Planar heterojunction perovskite solar cells via vapor-assisted solution process. J Am Chem Soc 136:622–625
102. Liu M, Johnston MB, Snaith HJ (2013) Efficient planar heterojunction perovskite solar cells by vapour deposition. Nature 501:395–398
103. Wang Q et al (2014) Qualifying composition dependent p and n self-doping in $CH_3NH_3PbI_3$. Appl Phys Lett 105:163508
104. Simpson MJ, Doughty B, Yang B, Xiao K, Ma Y-Z (2016) Imaging electronic trap states in perovskite thin films with combined fluorescence and femtosecond transient absorption microscopy. J Phys Chem Lett 7:1725–1731
105. Simpson MJ, Doughty B, Yang B, Xiao K, Ma Y-Z (2015) Spatial localization of excitons and charge carriers in hybrid perovskite thin films. J Phys Chem Lett 6:3041–3047
106. Pistor P, Borchert J, Fränzel W, Csuk R, Scheer R (2014) Monitoring the phase formation of coevaporated lead halide perovskite thin films by in situ x-ray diffraction. J Phys Chem Lett 5:3308–3312
107. Pool VL et al (2017) Thermal engineering of $FAPbI_3$ perovskite material via radiative thermal annealing and in situ XRD. Nat Commun 8:14075
108. Schelhas LT et al (2016) Monitoring a silent phase transition in $CH_3NH_3PbI_3$ solar cells via operando X-ray diffraction. ACS Energy Lett 1:1007–1012

109. Miyadera T et al (2015) Crystallization dynamics of organolead halide perovskite by real-time X-ray diffraction. Nano Lett 15:5630–5634
110. Eperon GE et al (2014) Formamidinium lead trihalide: a broadly tunable perovskite for efficient planar heterojunction solar cells. Energy Environ Sci 7:982–988
111. Jacobsson TJ et al (2016) Exploration of the compositional space for mixed lead halogen perovskites for high efficiency solar cells. Energy Environ Sci 9:1706–1724
112. Kim YC et al (2016) Beneficial effects of PbI_2 incorporated in organo-lead halide perovskite solar cells. Adv Energy Mater 6:1502104
113. Yang B, Geohegan DB, Xiao K (2017) Encyclopedia of inorganic and bioinorganic chemistry. In: Perovskite materials: solar cell and optoelectronic applications. John Wiley & Sons, Ltd, Hoboken, NJ
114. Rossander LH et al (2016) In situ X-ray scattering of perovskite solar cell active layers roll-to-roll coated on flexible substrates. CrystEngComm 18:5083–5088

Wide-Field Surface Plasmon Resonance Microscopy for In-Situ Characterization of Nanoparticle Suspensions

3

Shavkat Nizamov and Vladimir M. Mirsky

Contents

1 Introduction

During the past two decades, nanomaterials have had an enormous diversity of applications in different industrial fields and fundamental research. Some of these nanomaterials are specifically engineered to exhibit unique optical, electrical, or other physical or chemical characteristics. Owing to these attributes, the products containing various engineered nanoparticles (NP) cover large segments of the

S. Nizamov · V. M. Mirsky (✉)
Institute of Biotechnology, Department of Nanobiotechnology, Brandenburg University of Technology Cottbus-Senftenberg, Senftenberg, Germany
e-mail: Vladimir.Mirsky@B-TU.De

© Springer-Verlag GmbH Germany, part of Springer Nature 2018

C. S. S. R. Kumar (ed.), *In-situ Characterization Techniques for Nanomaterials*,
https://doi.org/10.1007/978-3-662-56322-9_3

market from clothing to electronics and healthcare products [1]. The rapid development of nanotechnologies, their industrial applications, and related nanosafety concerns demand sensitive analytical methods for identification and analysis of nanoparticles (NPs) in very different media [2]. In the same time, there are serious concerns on possible toxicity of nanoparticles for humans and environment [3]. Engineered NPs (ENPs) have to be analyzed not only during their production, in pure and concentrated form, but also at trace concentrations in environment, drinking water and food, healthcare and pharmacological products, biological fluids, etc. Ideally, such a technique should provide a possibility to detect NPs at the level of single particles and deliver information on their concentration, core and surface chemical composition, size, and shape [2–4].

The environment, in which nanoparticles are present, defines and restricts the measurement technique that can be used for their characterization. In-situ characterizations of nanoparticles in solid, liquid, or gaseous media have their own specifics. Unlike the solids, where nanomaterials are immobilized within its structure and cannot be easily or unintentionally altered, nanomaterials in liquids can freely move in the media. Unlike the gases, where the media density is so sparse that its effect is usually negligible, the density of liquids as well as the amount of solute can be comparable to solids. Moreover, the range of the materials, which can be dispersed or solved in liquids, is much broader than that for gases or solids. Together with a high mobility of the solutes, it complicates the analytics of the liquid dispersions of NPs. Indeed, conventional transmission or scanning electron microscopies (TEM/SEM) for characterization of nanomaterials are applied for solid samples in vacuum [2]. At the same time, such techniques as the differential electrical mobility analysis, which can be used for characterization of aerosols [2], can be hardly applied for liquids. Similarly, the widely used characterization of specific surface area based on the BET (Brunauer, Emmett, and Teller) isotherms of gas adsorption is intrinsically applicable only for investigation of solid nanomaterials in gas media.

At the same time, liquid suspensions of nanomaterials (having the size in at least one dimension mainly between 1 and 100 nm according to EU definition [4]) or broadly, colloidal particles (with the size in at least one dimension between 1 and 1000 nm, according the IUPAC definition [5]), are of the great practical and scientific interest. Therefore, the characterization of liquid suspensions is the hot topic in analytical sciences. A lot of various techniques have been suggested for this purpose. Some of these methods suppose a conversion of liquid suspensions into another phase state and further ex-situ characterization (e.g., an application of TEM/SEM after drying or freezing). Such approaches are almost always confronted with the question, whether obtained results still represent the state of the original nanomaterial in the liquid phase, or should be considered as a phase transition artifact. Due to lability of liquids and colloidal instability of suspensions, the in-situ characterization of liquid suspensions of nanomaterials is less susceptible to artifacts. It makes such techniques highly preferable. An overview of such techniques (Table 3.1) is given in the next section. Further, surface plasmon resonance (SPR) sensors and, particularly, wide-wield surface plasmon resonance microscopy (SPRM) for detection and characterization of nanoparticles in liquid suspensions are

Table 3.1 Selected state-of-the-art analytical techniques for characterization of nanoparticles in liquid suspensions

Domain		In the bulk liquid		On the interface (surface)		
Principle		Various	Optical			Various
Characterization level	Cumulative analysis	Mass-spectrometry (ICP-MS, TI-MS, GD-MS,. . .) Atomic absorption / emission spectroscopy (ICP-AES, ICP-OES, . . .) Laser-induced breakdown spectroscopy (LIBS) Small angle X-ray (or neutron) scattering (SAXS, SANS)	Dynamic light scattering Static (multiangle) light scattering Differential dynamic microscopy Photon density wave spectroscopy (Fig. 3.1)	UV-Vis spectroscopy	Surface plasmon resonance Ellipsometry Interferometry Waveguide sensors	Electrochemistry Quartz crystal microbalance
	Single particles	sp-ICP-MS Resistive pulse sensing (Fig. 3.2)	Nanoparticle tracking analysis (Fig. 3.1)	Photo-thermal optical microscopy UV-Vis spectroscopy of single particles Dark field optical microscopy	Evanescent wave, surface plasmon resonance, interferometric microscopies (Fig. 3.3)	Liquid cell TEM (LCTEM) Scanning probe microscopy (AFM) Scanning electrochemical microscopy (SECM) Ultramicro- and nano-electrodes Nanoimpact electrochemistry

described. This novel approach was intensively developed within the EU FP7 funded project "Nanodetector" during 2012–2015. The present chapter is the first review of this analytical technique and summarization of main obtained results.

2 An Overview of Analytical Techniques for In-Situ Characterization of Nanoparticle Suspensions

An overview of the selected analytical techniques that can be applied for characterization of liquid samples is given in Table 3.1. The techniques are grouped and shortly described according to three classifiers:

- Measurement principle (optical vs. others)
- Localization of the analyzed nanomaterial (in bulk suspension and/or on the sensor surface)
- Analysis level (at the level of single particles or cumulative over the sample)

The main attention in this overview is given to optical methods which form the largest group, are in intensive development, and provide contactless nondestructive measurements.

2.1 Characterization of Nanoparticles in Bulk Suspension

Dynamic light scattering (DLS) is probably the most popular analytical technique in this regard. It is unobtrusive and nondestructive method with low acquisition and operation costs. DLS is based on the analysis of fluctuations of the light scattered by moving particles (see Fig. 3.1). The particles in the illuminated volume scatter light in all directions. The fluctuation spectrum depends on the velocities of particles. Since the scattered light is many orders of magnitude weaker than the incident light, the photodetector is placed outside its propagation path. Applying the autocorrelation function to the signal from photodetector, one can calculate the diffusion coefficient of particles. For this reason DLS is also known as photon correlation spectroscopy. On the other side, the diffusion coefficient of a particle is directly related to its hydrodynamic radius. For spherical particles this is described by Stokes-Einstein equation [6]:

$$D = \frac{k_B T}{6\pi\eta r}$$

where D is the diffusion coefficient, k_B is the Boltzmann constant, T is the absolute temperature, η is the dynamic viscosity, and r is the radius of the particle.

Thus, DLS can be used for characterization of the size of particles in mono- and polydisperse suspensions [7, 8]. It is to note that determination of diffusion coefficient from light fluctuations in DLS assumes that each photon is scattered only once.

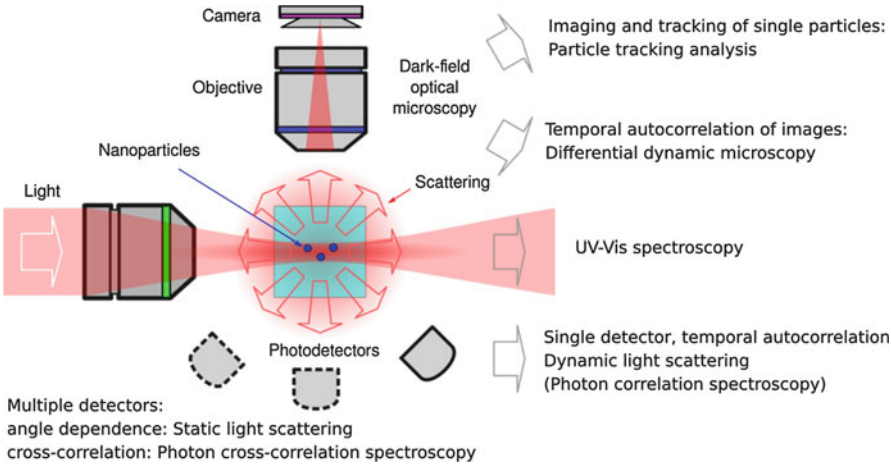

Fig. 3.1 Optical techniques for characterization of nanomaterials in the bulk suspension

Therefore, DLS cannot be applied at high particles concentration, where a multiple scattering can occur. The multiple scattering can be minimized by the design of the measurement cell [9]. On the other side, the multiple scattering in turbid colloidal suspensions is addressed by extension of DLS to photon cross-correlation spectroscopy [10, 11] or diffusing wave spectroscopy [12]. Also, the photon density wave, a novel optical measurement technique specifically addressing highly concentrated turbid colloidal suspensions, was introduced recently [13]. All these scattering techniques are used for characterization of an average size and size distribution of particles in the whole sample without recognition of individual particles. Therefore, these techniques are not able to determine concentration of particles by directly counting them. However, the concentration can be estimated from the scattering intensity, e.g., a concentration of virus particles was determined by the scattering intensity using a calibration by organic nanoparticles [14].

In contrast to the dynamic light scattering, where fluctuations of the scattered light are analyzed by photodetector at fixed single angle, in the static light scattering an intensity of the light is measured at multiple angles. Then, using the obtained angular dependency of the scattering intensity, the size of particles can be determined from Mie theory [15].

Instead of capturing scattered photons by a simple photodetector, the volume illuminated by an incident light can be projected onto the image sensor. Since the imaging optics avoids capturing the illuminating light and selects the scattered light only, it represents a regular dark-field optical microscopy. Single nanoparticles with a strong enough scattering can be then detected in images captured by camera. This technique was called ultramicroscopy [16]. The dark-field optical microscopy is capable to image and even characterize an angular orientation of single high-aspect ratio NPs [17]. Tracking the position of the detected particles in the illumination volume, one can measure directly their diffusion, and, using the Stokes-Einstein equation, determine the hydrodynamic radii of these particles [18]. The approach,

known generally as a particle tracking analysis (PTA, commercialized also as the nanoparticle tracking analysis – NTA), allows fast and uncomplicated quantification of nanoparticle suspensions. PTA is used for characterization of engineered nanomaterials [18, 19] as well as NPs of biologic origin [20–22], in polydisperse samples and in complex media [23]. However, the light scattered by a single particle is not always strong enough to be distinguished from the scattering by solvent molecules. Unlike DLS, which can be applied for characterization of particles and even molecules with sizes down to ~1 nm, PTA can be used for characterization of much larger particles only: above 20 nm in diameter for very dense metallic or oxide particles or above 40–60 nm for the particles with a smaller optical contrast relative to the bulk of suspension (organic particles, SiO_2). Therefore, depending on the sample composition, both techniques can be used complementarily. An "intermediate" technology that combines the principles of both PTA and DLS was suggested [24, 25]. This technique, called differential dynamic microscopy, applies the principle of DLS – a determination of autocorrelation function of the signal from photodetector – to the pixels in differential images obtained by dark-field microscopy [26, 27]. However, due to competition with well-established analytical techniques DLS and PTA, the differential dynamic microscopy have not found so far wide applications for characterization of nanomaterials.

The above described analytical techniques, suggested for characterization of nanomaterials in liquid suspensions, are based on the detection of light scattering. The scattering effect is the intrinsic property of a particle with refractive index different from that of its environment. In air, the Rayleigh scattering cross section σ_S, which characterizes the scattering of light by a particle with refractive index n and diameter d much less than the wavelength of the light λ, is:

$$\sigma_s = \frac{2\pi^5}{3}\frac{d^6}{\lambda^4}\frac{\left(n^2-1\right)^2}{\left(n^2+2\right)}.$$

Notably, at the same wavelength the scattering increases as the 6th power of the diameter. Oppositely, the scattering of small particles is a very weak effect.

The nanoparticles that have an intrinsic structural optical absorption or emission bands (plasmonic nanoparticles possessing localized SPR, quantum dots) can be characterized by appropriate application of UV/VIS spectroscopy. Absorption and emission properties of such NPs are strongly dependent on their size, shape, and chemical composition. Using UV-VIS adsorption spectra the size and concentration of gold and silver nanoparticles can be determined [28, 29]. Also in the case of quantum dots the fluorescence spectroscopy can be used for particle sizing [30]. The principle of UV-VIS spectroscopy can be extended to the characterization of a single nanoparticle using the dark-field optical microscopy [31]. The strong absorption of plasmonic particles can be used for the excitation of photothermal effect. Basing on this principle, the photothermal detection of nanoparticles can be performed (photothermal microscopy) [32, 33].

The described optical techniques are unobtrusive and nondestructive – the particle(s) are studied contactless and are impacted only by optical irradiation. The impact of optical irradiation in most cases is negligible (excluding the cases where such impact is desired, e.g., photothermal microscopy). Since many of these optical

techniques for characterization of nanomaterials rely on the detection of the scattered light, these techniques cannot be used directly for the determination of the chemical composition of nanomaterials or their shape. Such questions have to be addressed separately. Mainly, the size distribution and concentration of particles are determined.

The techniques are based on the detection and characterization of particles freely moving in the volume phase (in case of DLS and NTA this is an intrinsic requirement of measurement principles). After leaving the measurement focus volume, the NPs cannot be identified subsequently; this complicates a combination of these methods with other approaches for further analysis of these NPs.

The described methods are not well-suited for chemical characterization of nanoparticles suspensions. For such a characterization, methods based on other principles are more appropriate. A number of analytical techniques which are based on the atomization/ionization of the small liquid volumes and subsequent analysis of the plasma components have been established. Several methods were suggested for the atomization of a sample and generation of plasma: inductively coupled plasma (ICP), thermal ionization (TI), glow discharge (GD), flame (F) or microwaves (MPT). The analysis of the plasma components can be done using mass spectrometry (MS), atomic absorption (AAS), or emission spectroscopy (AES). Correspondingly, a broad range of combinations like ICP-MS, ICP-OES (optical emission spectroscopy), ICP-AES, F-AAS, GD-AAS, TI-MS, GD-MS, F-AES, MPT-AES, etc. have been reported. An intense laser beam is used in laser-induced breakdown spectroscopy (LIBS) [34, 35]. Since the small volume of the nanomaterial suspension is analyzed independently and instantly, the artifacts caused by the phase transfer of nanomaterials from liquid phase to solid or gaseous can be neglected. However, the atomization of sample is performed at the level of small but finite amounts of suspension. Correspondingly, the subsequent analysis results are cumulative for this finite volume. For ICP-MS a single particle resolution was achieved (sp-ICP-MS) [36, 37]. The technique allows one a detection and accurate chemical and physical characterization of single nanoparticles extracted from complex media like biological tissues.

In comparison with optical methods, these techniques are destructive and have a lower throughput. Besides, they are sophisticated and expensive. In the same league are the techniques based on the small angle X-ray (or neutron) scattering (SAXS or SANS) [38–40]. The application of high energy irradiation like X-rays or neutrons makes these techniques even more complex and expensive. Due to the much higher energy (and correspondingly shorter wavelength) compared to the visible light, the scattering of X-rays or neutrons provides more information on the physical properties of nanoparticles. The size distribution and determination of shape of nanomaterials can be performed. The high energy of irradiation allows a deep penetration into the sample making possible also a direct characterization of particle suspensions. However, despite a much higher resolution, SAXS/SANS are inherently not particle specific. The determination of size and shape of particles can be done only assuming that all particles in the irradiated volume have the same properties.

For physical characterization of nanomaterial suspensions (size, concentration, shape), the above described optical methods are simpler and less expensive but their

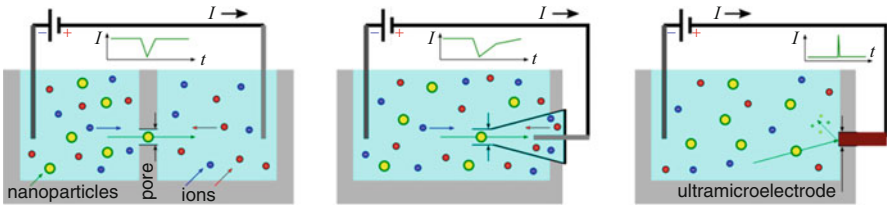

Fig. 3.2 Electrochemical sensing for characterization of nanoparticles in suspension

analytical performance is competitive to the nonoptical ones. However, for the chemical characterization of nanomaterial composition, the optical methods can be applied only in few particular cases, while the techniques based on MS have a very wide application field.

Most of the above described techniques represent an accommodation of the well-established analytical techniques for characterization of nanomaterials. In the same time, there are also nanotechnology-based methods which were developed intentionally for characterization of nanoparticles. In tunable resistive pulse sensing (RPS) a passage of nanoparticles through a small nanosized aperture in the septum separating two electrode compartments is detected (Fig. 3.2, left) [41, 42]. Instead of using a nanosized aperture, one can place one electrode into the nanopipette (Fig. 3.2, middle) [43]. The detection is based on the fact that the electrical resistance between two electrodes is mainly defined by the electrical resistance of the aperture. The nanoparticle, passing through the aperture, occludes it and hinders electrical current carried by electrolyte ions (Fig. 3.2). For this reason, the technique is also known as scanning ion occlusion sensing (SIOS) [41]. Correspondingly, the electrical resistance increases during the passage of nanoparticles for the value which is characteristic for the size of the particle. Calibrating the size of aperture and measuring these resistive pulses, it is possible to characterize the concentration and size of engineered NPs in the suspension [44, 45]. The method can be applied also for viruses [46].

2.2 Surface Sensing of Particles in Bulk Suspension

Looking at the principle of TRPS (Fig. 3.2), one can note that not arbitrary nanoparticles in suspension are detected but only those passing through the aperture. So the aperture represents some virtual detection plane. This is even more obvious in case of nanopipette: the detection of nanoparticles is done at the moment they are crossing the entrance of nanopipette [43]. Replacing this imaginary liquid orifice of a pore or nanopipette with a solid electrode, one gets a powerful electrochemical approach for detection, counting, and analysis of single nanoparticles – impact electrochemistry [47–49].

The principle of the nanoimpact electrochemistry is based on the measurement of current spikes due to collision of single nanoparticles with the surface of

microelectrode. The charge transfer, occurred, e.g., due to the electrochemical oxidation or reduction of NP, characterizes the NP size. Whereas the conditions, at which such reaction occur, determine its composition.

The described technique can be considered as surface sensing. The detection limit of this approach is ~10^9 particles per mL. The value is mainly defined by the time, which is needed for a nanoparticle freely diffusing in bulk suspension, to hit the sensing surface. Correspondingly, the diffusion coefficient of nanoparticles influences greatly the frequency of their collisions with a sensor surface. This peculiarity shows one of the main challenges of the surface sensing – only those particles that collide with the sensing surface can be detected and characterized. Principally, even a single particle in the bulk suspension can eventually collide with a sensing surface; however, the expectation time may be prohibitively large. Therefore, an improvement of the detection limit requires an increase of the sensing area, thus increasing the probability of collision events. In the case of microelectrodes, the randomized array of electrodes was suggested [50]. However, the total electrode area is limited by electrotechnical reasons: an increase of the area leads to an increase of the electrode capacitance and corresponding increase of the time constant of the current amplifier and its noise. In the case of RPS, the flow of particles towards the orifice can be forced by applying of a difference in hydrostatic pressure. This results in the directed flow of bulk suspension through the orifice. It allows one not only to increase the probability of particle passing through the pore but also to calculate the concentration of particles. Since the flow volume is known, the concentration is simply proportional to the detection rate [51]. However, in the case of nanoimpacts, the directed flow of particles from the bulk suspension towards the sensor surface cannot be realized as the suspension flow. Moreover, the electrochemical dissolution of particles on the sensor surface creates a concentration gradient of particles from bulk suspension towards sensor surface. Correspondingly, the determination of absolute concentration in bulk is tricky, since the detection rate characterizes the concentration in the depleted volume and the concentration gradient is defined also by the diffusion coefficient.

On the other side, sensing on the surface has also a number of important advantages. The surface can be designed in a way that prefers some particular analytes to be detected. Surface sensing is also less susceptible to the influence of the matrix components of the probe (e.g., majority of optical bulk sensing methods fail in turbid or strongly inhomogeneous media). It is also important that the nanoparticles that have been strongly adsorbed on the sensor surface are immobilized. Therefore, they can be subsequently identified and analyzed by another analytical technique. For instance, scanning probe microscopies (SPM, e.g., AFM [52]) operating in liquid media can be used for characterization of nanomaterials adsorbed on the sensor surface. It is to note that SPM can be used for dry surfaces too, but the drying of samples for ex-situ characterization of suspensions may lead to possible artifacts that have to be addressed properly [53, 54].

An application of the ultramicroelectrode as a scanning probe (scanning electrochemical microscopy SECM [55–57]) provides visualization of electrochemical reactions on/of the nanomaterials. Thus, an electrochemical analysis of nanomaterial

composition is possible. Unfortunately, most of SPMs (and especially SECM [58]) are notoriously slow due to the mechanical scanning principle and deliver only a static snapshot image of the surface. Much faster imaging rate has an extension of the transmission electron microscopy for applications in liquid media: liquid cell electron microscopy (LCEM) [59, 60]. This sophisticated technique is able to image in real time the cluster growth at the solid–liquid interface in electrochemical reaction. The sensing area is comparable to that of TEM, whereas the spatial resolution is much lower (5–30 nm). Moreover, due to effects of a high energy electron beam, tightly constrained reaction volumes and inhomogeneity caused by the geometry of reference electrode, the results obtained by these techniques are disputable [61]. Finally, the SECM and LCEM techniques are quite sophisticated and expensive; therefore, their application areas are limited mainly to the basic research.

The general electrochemistry techniques, like cyclic and differential pulse voltammetry [62, 63], can be used for cumulative analysis of nanoparticles. Unfortunately, the range of nanomaterials that can be characterized by electrochemical approaches is limited by the necessity to make electrochemical conversions of this material within electrochemical stability window of water and electrode material. It can be extended by using of other solvents (e.g., acetonitrile or ionic liquid) but requires a transfer of nanomaterials into this solvent which can lead to corresponding artifacts. Besides, the electrochemical approaches are also at least partially destructive: they characterize nanomaterials by inducing their electrochemical conversions.

For the cumulative analysis of particles adsorbing to the sensor surface nonspecific approaches, well known as transducing principles for affinity chemical sensors and biosensors can be used: electrochemical impedance spectroscopy (EIS), [64] quartz crystal microbalance (QCM, sometimes QMB), surface plasmon resonance (SPR), reflectometric interference spectroscopy, [65–67] or other optical, electrochemical, or acoustomechanic techniques. An application of impedance spectroscopy is complicated by the shape of the analyte which contacts the sensor surface by only a small part of its surface [68].

The principle of QCM is that the resonance of miniaturized quartz crystal is strongly influenced by the matter which adsorbs to its surface. An increase of the adsorbate mass leads to lower resonance frequencies. Since the measurement of the quartz resonance frequency can be implemented electronically very easily, the method has found wide adoption for bio- and chemosensors. Long year implementation of this transducing principle in chemo- and biosensors demonstrated that it provides quantitative results in the gas phase, but the data obtained in liquids requires an analysis of possible contribution of changes in surface microviscosity. Such effects are addressed by using of QCM with dissipation monitoring (QCM-D) which is certainly preferable for investigation of binding of nanoparticles. It was reported in Refs [69, 70]. It is to note that the QCM-method is intrinsically cumulative and in case of adsorption of colloidal particles it requires a particular analysis of data [71].

A lot of optical techniques for characterization of adsorption to sensor surface, which are also applicable for detection of adsorption of nanoparticles, have been proposed so far. Typically, surface plasmon resonance, reflectometric interference

spectroscopy, general ellipsometry, and interferometry are considered. Most of these techniques determine optical properties of a thin adsorbate layer. The ellipsometry relies on the change in the polarization of the incident light upon reflection from the adsorbed layer. In interferometry the phase of the reflected or transmitted light is measured using the incidence light as a reference. Both optical methods are fast and nonintrusive and have found numerous applications for the characterization of thin adsorbed films. Surface plasmon resonance and waveguide refractometry are based on generation of an evanescent wave in the conditions of total internal reflection (TIR). In waveguides the incident light is guided along its core by a multiple reflections at waveguide cladding. As a result of TIR, the evanescent wave is generated which penetrates into the free space. An adsorption of nanoparticles onto the waveguide surface alters the effective refractive index thus changing the reflection conditions. An application of plain waveguide for detection and characterization of nanoparticles has been shown [72]. Waveguides can be formed in the shape of ring resonators and utilize the principle of whispering gallery modes for the detection of nanoparticles [73, 74]. This approach was used for detection of colored nanoparticles [75] but can be applied even for viruses [76]. Despite that the waveguide-based sensors are able to detect single nanoparticles, these methods are inherently cumulative: the whole sensor surface is characterized by an integral optical signal, like the change in intensity, phase, or spectra of the transmitted light. The waveguide sensors also suffer from the small sensing area; however, this limitation is less stringent than in nanoimpact electrochemistry, TRPS, or nanowire sensors.

Surface plasmon resonance (SPR) [77, 78] is detected as a deviation from total internal reflection observed for *p*-polarized light for the reflection from thin layers of highly conducting metals (usually silver or gold) deposited on glass substrate (plasmonic layer). At resonance conditions the energy of the incident light can be almost completely coupled to the surface plasmons thus achieving manifold increase in the intensity of evanescent wave. Small changes of the refractive index within the penetration depth of the evanescent wave change resonance conditions. This provides a way to make extremely sensitive measurements of adsorption of nanoparticles or any species onto resonant surface: just a few angstrom change in the mean thickness of the adsorbed layer leads to the measurable signal.

An intensity, phase, or spectra of the reflected light is usually measured in SPR sensors. The measured value represents averaged values over the whole sensor area; therefore, such sensors belong to the integral sensing techniques. SPR conditions are dependent on the refractive index on both sides of the plasmonic layer. The refractive indices of both substrate and aqueous media (effective refractive index can be used if the composition of media is not homogenous [79]) are considered. An application of such sensors for detection of nanoparticles extracted from food or environmental samples was reported [80]. A functionalization of the surface of SPR sensors with a receptor layer is a way to achieve selective detection of analytes. This approach was applied for selective detection of protein nanoparticles [81]. The method was applied also for quantification of biosensing properties of engineered nanoparticles [82]. Using SPR, the size and concentration of exosomes was determined [83, 84].

The sensing scope of SPR sensor is intrinsically limited to the surface and adjacent media. Evanescent wave is excited in the thin volume adjacent to the interface of two mediums with different refractive indices in condition of total internal reflection. In visible range the intensity of the evanescent wave drops rapidly within 100–300 nm [85]. This feature of evanescent wave–based sensors is exploited by many techniques. The most prominent example is the total internal reflection fluorescence microscopy TIRFM [86]. In TIRFM, this evanescent wave excites fluorophores, whose emission (fluorescence) can be then registered by ordinary optical microscopy (Fig. 3.3). TIRFM can be used for sizing and characterization of particles of different origin within the biological samples [87, 88]. The evanescent wave is, however, also intensely scattered by inhomogeneity. In TIRFM the scattered light is filtered out by color filters. The scattered light can be imaged as well, and in the absence of fluorophores, delivers an optical image of the sample. This is the principle of the novel evanescent wave scattering microscopy [89, 90]. The approach allows one a detection and characterization of single biological vesicles and engineered nanoparticles. As one can see from Fig. 3.3, the main difference with the dark-field optical microscopy is that as the excitation source serves not the propagating incidence light but the evanescent wave created by it.

The peculiarity of the evanescent wave approaches is that the reflected light can also serve for imaging purposes (total internal reflection microscopy [91]). An advantage of this approach is that the sample thickness and turbidity do not play much role in this case. Moreover, the single high numerical aperture objective can be used for both illumination and imaging purposes, thus greatly simplifying the overall measurement setup [92]. The approach, however, has not found a wide acceptance and is mostly used to study biological processes.

All three described techniques can be also applied in SPR conditions. The principal difference in this case is the presence of the thin plasmonic layer on the top of substrate. Due to the manifold increase of the evanescent wave intensity, the light scattered by nanoparticles on the sensor surface is also more intense. This can be registered in the reflected light – surface plasmon resonance microscopy

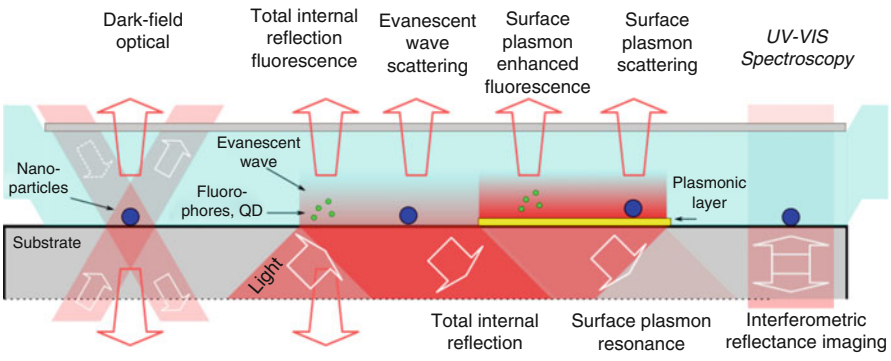

Fig. 3.3 Various optical approaches for sensing of single nanoparticles on the surface

(similar to TIRM) [93, 94]. However, the detection of scattered light like in evanescent wave scattering microscopy is also possible – surface plasmon scattering microscopy [95, 96] (or transmission SPR [97]). Due to the amplification of evanescent wave intensity, the combination of simultaneous SPR and SERS measurement is possible; [98] this can be as well implemented as microscopy [99]. Similarly, the intense evanescent wave can be used for fluorescence excitation [100]. The fluorescence can be imaged like in a typical TIRFM [101]. The simultaneous SPRM and SPREFM is also possible [102].

Interferometric approaches for detection and characterization of a thin adsorbate layers are presented by reflectometric interference spectroscopy, [65–67] interferometric reflectance imaging sensor (IRIS) [103, 104] and interferometric scattering microscopy (iSCAT) [105, 106]. These interferometric techniques have different capabilities covering a wide range of applications: starting from integral characterization of thin adsorbate films till the detection and characterization of single protein molecules. Unfortunately, the compromise between size and concentration detection limits requires a small sensing area in case of detection of single nanoparticles.

Many of the mentioned optical surface sensing techniques, which are based on the evanescent wave or interferometry approaches, were introduced in recent few years and have not yet been fully established. Despite this, all of them have already shown their potential for the detection and characterization of nanoparticle suspensions. It is also to note that many authors use contradicting definitions for evanescent wave microscopies – e.g., TIRM is described as a microscopy in reflected light or in scattered light (like evanescent wave scattering). An overview of described surface measurement techniques is shown in Fig. 3.3.

2.3 Hyphenated Technologies

From the description of various mass-spectroscopy and atomic absorption/emission spectroscopies the hyphenation pattern in modern analytics can be recognized [107]. The broad choice of such analytical techniques is basically the result of a combination of one of ionization/atomization techniques (e.g., ICP, GD, TI) with one of detection/characterization techniques (e.g., MS, AES, AAS). Not all such combinations are possible, viable or reasonable, but the range of the relevant combinations is still very large and covers a broad range of analytical requirements and capabilities.

Therefore, the hyphenation of analytical techniques (also referred to as tandem techniques) – application of several otherwise unrelated with each other techniques in succession – is one of the popular solutions for solving complex analytical tasks. Due to the different operational principles, a combination of analytical techniques can effectively solve shortcomings of its constituents. For instance, the characterization of nanoparticle suspensions can be done as a combination of separation/fractionation technique, which sorts the nanoparticles according to their physical properties, and detection technique that detects the presence of nanoparticles. This basic principle is widely used in analytical chromatography [108]. It is to note that

detector specificity to analyte is not required, the specificity is achieved by separation technique. For instance, a combination of the flow-field-fractionation (FFF) [109] with a simple light scattering or absorption detector can be used for characterization of nanomaterials [110]. Thus, the characterization of detected particles is done retrospectively: the detector signal quantifies only the amount of particles vs. their retention time in FFF channel. Therefore, despite that the detector does not determine the particle properties but only its presence, its physicochemical properties (e.g., size, shape, or composition) can be deduced from the retention time. An interesting example of such approach is the differential centrifugal sedimentation (DCS) [111, 112]: it actually hyphenates an analytical ultracentrifugation of analyte sample (which separates the analyte constituents along the density gradient along disk radius from the inner side towards the outer edge) with subsequent photodetection. The photodetector near the outer edge detects a presence of the analyte. So, this method can be described as analytical ultracentrifugation hyphenated with photodetection. DCS was suggested for detection and characterization of nanoparticles in suspensions [113]. The sizing accuracy of DCS is much better than that of DLS/NTA and reaches the accuracy of TEM [114].

One can imagine that chromatographic separation (FFF in particular) can be hyphenated with any of the detection/characterization technique described above. For instance, FFF with subsequent sp-ICP-MS allows the characterization of nanoparticles in very complex environment [115]. Being coupled to multiangle static light scattering, FFF forms FFF-MALLS [116], hyphenated further to TEM: FFF-MALLS-TEM [54]. The main advantage of FFF for characterization of nanoparticle suspensions in comparison with classical liquid chromatography approaches is that the separation occurs under the physical field (thermal, flow, electrical, gravitational) rather than due to chemical interaction with separation media which can lead to a substantial loss of NPs.

Hyphenation is not restricted to a combination of separation with detection/characterization. Also characterization techniques can be hyphenated with each other. This is especially true for surface sensing: for instance, the analyte adsorbed in SPR sensor can be subjected further to SEM/TEM, AFM, or to mass-spectrometry, or to electrochemistry (SECM, or even in-situ electrochemistry using the plasmonic layer as a working electrode).

3 Surface Plasmon Resonance Microscopy

The implementation of SPR sensors where the image of the sensor area is focused on the image sensor (camera) is known as SPR imaging (SPRi) or SPR microscopy (SPRM) [117]. The difference in SPRi vs. SPRM terms reflects the difference in magnification and resolution only. Originally, the approach was called as a surface plasmon microscopy, [117] but to avoid confusion with more frequently mentioned scanning probe microscopy (abbreviated as well as SPM), SPRM is a more appropriate term. SPRi is applied mainly for characterization of homogenous films where a high resolution is not required [118]. Simultaneous and instantaneous imaging of

the full sensor surface in SPRM/SPRi has a lot of advantages: e.g., it provides high-throughput, multiplexed or self-referencing sensors [119, 120]. The low lateral optical resolution which is complicated by plasmon propagation is outweighted by extremely high sensitivity in transversal direction. Since the plasmon propagation and resonance conditions are influenced mainly by the complex refractive index of medium contacting metallic layer within the volume of penetration of evanescent wave, SPRi provides an exceptional sensitivity for the nanoscale changes on this interface. Due to these properties SPRi is widely used in surface science and in bioanalytical chemistry, particularly in chemo- and biosensors [78, 118, 119, 121]. In most applications of SPRi, however, adsorbates are considered as thin homogenous films whose imaging serves merely multiplexing purposes. In other words, SPRi is used as a multichannel integral SPR sensor.

Recently, another application of SPRM has attracted a great attention from several scientific groups. A complex interaction of propagating surface plasmons with nanoscale objects on the sensor interface leads to the scattering which can be detected optically. This effect allows one to use SPRM for detection of single nanoparticles adsorbed on the sensor surface. It was shown that SPRM can be used for ultrasensitive detection and characterization of single nanoparticles adsorbing to the sensor surface from the bulk suspension [93, 94, 122–125]. While the underlying principle is the same, the SPRM setups, designed for imaging sensor surface with a high magnification and resolution and used for imaging single colloidal particles, can be divided into two distinct groups: (i) the wide-field prism-based SPRM configuration (with a separate illumination and imaging optics as originally suggested [117]) and (ii) a high numerical aperture (NA) objective configuration [126] (Fig. 3.4). It is to note, that the high-NA objective configuration is basically the same approach which is used for TIRM, [92] but adapted for SPR conditions.

An essential difference between these two SPRM approaches originates in the NA of the objective which is required to collect the reflected light. Surface plasmon resonance occurs when *p*-polarized light is incident at some defined angle Θ in TIR conditions. This angle range and refractive index of substrate define the minimally

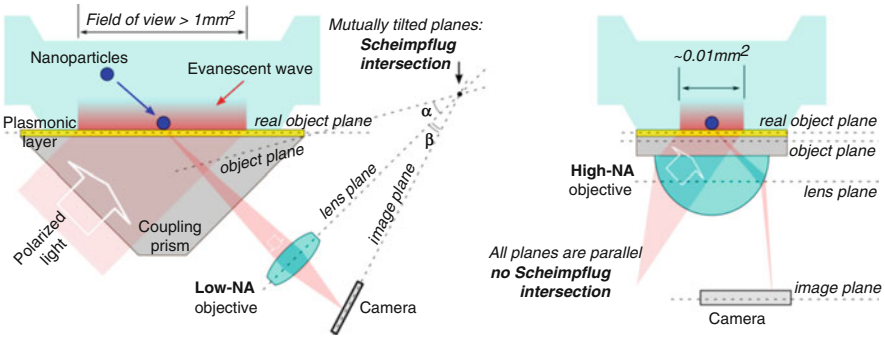

Fig. 3.4 Two optical configuration of SPRM: wide-field prism-based SPRM (left) and high-NA objective based SPRM (right)

required NA for SPRM [126]. At a thickness of gold layer 50 nm on the typical glass substrate with $n = 1.5$ in contact with aqueous media, SPR resonance angle is ~70° at 630 nm wavelength. Correspondingly, $NA_{SPR} = n^*\sin(\Theta) \sim 1.41$. If the objective and image (camera) planes are parallel to the object plane (sensor surface), the objective applied for imaging in conditions close to SPR must have a numerical aperture of at least 1.4, preferably >1.45. Application of higher RI substrates can be used to decrease the SPR angle; however, regular microscopy objectives with high NA can reach their optimal resolution only for the particular cover slides with a given thickness and refractive index. Another viable solution is the application of longer wavelengths, shifting from red to near-infrared region (814 nm) [122]. However, high-NA microscopy objectives are designed generally for visible light and their performance in NIR decreases. Besides, SPR curve becomes narrower in infrared making the approach very sensitive to the incidence angle, which is difficult to maintain constant over the entire field of view. Also the *s/p* polarization ratio of the incident light varies over the field of view: even if the linearly polarized light source is actually used, due to the ray geometry in objective, the resulting incidence polarization is mixed *s/p* polarization [127, 128]. For such reasons, the quantitative analysis of SPRM images is complicated [129]. Notably, high NA objectives are also typically high magnification objectives with relatively small field of view: most of literature data on application of high-NA-based SPRM were obtained using objectives with NA > 1.4, magnification >×60 and field of view ~80 × 100μm. So small field of view restricts strongly the detection limit in analysis of nanoparticle suspensions (see Sect. 4.3 for details).

On the other side, the high-NA SPRM is very effective and has a high resolution approaching the diffraction limits [130]. Its main optical component is just a commercially available objective. The polarized and collimated beam is focused on the off-axis point in the back focal plane of the objective. The focus offset defines the incidence angle. The reflected light collected by objective forms an image on the camera. For many scientific applications the efficiency and resolution of high-NA SPRM overweight its shortcomings. Using this approach, a detection of single organic (polymer, hydrogel, liposomes, viruses, large DNA molecules) and metallic nanoparticles as well as of electrochemical reactions on single nanoparticles were demonstrated [93, 122–125, 131–137].

The strict requirements for the high NA as well as intrinsic limitations of field-of-view/magnification encouraged other approaches to SPRM. The requirement for the high NA of objective follows from the desire of parallel object, lens, and image planes. Using the objective, whose NA is lower than NA_{SPR}, the SPRM microscopy is still possible. However, to fit the light outgoing from the SPR sensor surface, it has to be tilted (see Fig. 3.4). Thus, the lens plane and object plane are not parallel anymore and have a crossing somewhere in space: Scheimpflug intersection [138, 139]. According to the Scheimpflug principle, the image plane crosses with object and lens planes as well in this intersection. Thus, there is also a tilt between camera and an objective. In typical SPRi, where the image is smaller than the object (absolute magnification <1), these tilts are not essential: such applications do not imply a high optical resolution and tolerate defocused/distorted images. Defocusing

is the result of the camera plane not coinciding with the actual image plane, the notable image distortion in this case is the keystone distortion [138]. However, with an increase in magnification, the Scheimpflug principle becomes the largest obstacle in the optical design of SPRM. The situation is complicated by the displacement of the specular object plane – it does not coincide with the physical plane of sensor surface and depends on the incidence angle. Optical aberrations in prism-based SPRM are also nontrivial [140]. However, many of these problems can be minimized by selection of glass substrate with a high refractive index; this reduces greatly the SPR angle. The prism geometry in which the reflected light leaves the prism facet at the right angle also has a positive effect on the optical performance.

For these reasons, an optical design and implementation of the prism-based SPRM is more challenging than that of the high-NA objective-based SPRM. Despite that there is principally no limitation on the achievable magnification in prism-based SPRM, the Scheimpflug principle complicates the design for magnifications above 4–5. Fortunately, there is no reason to do so: modern cameras have pixel sizes down to 2–3 μm; this results in the correspondence of one pixel to 400–800 nm of the sensor surface. Taking into account that the propagation of surface plasmons decreases the resolution limit at least in the propagation direction and that for gold coated sensors the red/NIR light is used, such magnifications and resolutions are reasonable. On the other side, the field of view in prism based SPRi/SPRM can be very large. In commercial SPRi instruments the typical surface area of imaged sensor surface can be up to square centimeters [141]. In prism-based SPRM, the imaged area of 1.2 mm^2 can be imaged at magnification ~5, [142–145] but this can be easily increased manifold. Thus, this approach can be called as a wide field (of view) SPRM in contrast to high-NA-based SPRM whose field of view is ~0.01 mm^2 [93].

Another important difference between high-NA-based SPRM and prism-based SPRM is the illumination optics. Contrary to the high-NA approach, where the same objective is used for the excitation and registration of SPR, in prism-based SPRM with tilted objective it is simply not possible due to the lower NA of objective. So the illumination optics must be made separately. However, this is not a drawback but rather a huge advantage. In prism-based SPRI the collimated light beam simply passes through the prism facet to the plasmonic layer. Thus, homogenous SPR conditions (incidence angle, polarization state; to a lesser extent an intensity) over the entire field of view can be achieved. The small deviations of polarization or incidence angle are caused mainly by the divergence of the incident light beam. Coupled with the large surface area, this makes the approach an attractive option for analytics. In prism-based SPRM the plasmonic layer can be deposited directly on the surface of the glass prism. This eliminates the application of immersion oil for optical coupling of plasmonic substrate to the glass prism (or objective in high-NA SPRM), making the instrument more user-friendly.

Therefore, being principally based on the same effect of surface plasmon resonance in Kretschmann configuration, several SPRi/SPRM configurations differing by their performance are known (Table 3.2). Correspondingly, these approaches have very different application areas. High-NA SPRM tends more to the basic science applications whereas typical SPRi tends more to the applied sciences and industrial applications. In

Table 3.2 Comparison of approximate capabilities of different SPRi/SPRM approaches

	Typical SPRi	Wide-field prism-based SPRM	High-NA-based SPRM
Required numerical aperture (50 nm Au, 650 nm illumination)	Unrestricted	Unrestricted	>1.4
Magnification	<1	~3–5	>60
Resolution	> 2–5 μm	~2 μm	~300 nm
Field of view	> 10 mm^2	0.3–1.5 mm^2	0.01 mm^2
Main application area	Commercial bio- and chemosensors	Basic and applied research, analytics	Basic research

following section the application of wide-field prism-based SPRM for analytical task of in-situ detection and characterization of nanoparticle suspensions will be discussed.

4 In-Situ Characterization of Nanoparticle Suspensions Using Wide-Field Surface Plasmon Resonance Microscopy

4.1 Experimental and Instrumental Methodology of Wide-Field SPRM

The principle of the detection of nanoparticles using the surface plasmon microscopy and the initial measurement setup based on wide-angle photolens is described elsewhere [94]. The further development within the EU FP7 project "Nanodetector" resulted in several prototypes of wide-field SPRMs being built and distributed among project partners.

In the wide-field SPRM setup, used for obtaining experimental data discussed in the present chapter, 642 nm SM-fiber coupled laser diode with current and temperature controllers (LP642-SF20, LDC205C and TED200C correspondingly, www.thorlabs.com) was used as a light source. The light was collimated to a parallel beam by the 16 mm focus length objective (MVL16, Thorlabs, www.thorlabs.de). The linear polarization of beam was assured by 14 mm free aperture Glan polarizer (EksmaOptics, www.eksmaoptics.com). The collimated light beam with diameter of ~ 3 mm was directed with the help of rotating mirror and 4F relay lens system onto the gold coated plasmonic sensor prepared from SF-10 prism ($n = 1.72$) with ~ 43–47 nm gold layer and ~3 nm Ti adhesion layer (Phasis, Switzerland, www.phasis.ch). Incidence polarization was set to *p*-polarization. Proprietary optical system with input aperture 18 mm and focal distance 23 mm ($NA = 0.39$), designed and manufactured by Optolita UAB (Lituania, Vilnius), was used for imaging the gold sensor surface onto the MT9P031 monochrome CMOS image sensor (ON Semiconductor). The image sensor has 2592 × 1944 square pixels with 2.2 μm size. The total magnification of the optical system is ~4.5, thus each pixel corresponds to ~0.5 μm of SPR-sensor surface. Optical resolution of the setup is limited by diffraction being ~2 μm. Images were read by Beagleboard-XM board at maximal possible pixel frequency of ~15 frames per second at full resolution,

averaged over 16 consecutive frames and transferred to PC. Correspondingly, the frame time at full resolution is ~1.08 s. The measurements were performed at fixed wavelength and incidence angle (~0.1–0.3° smaller than the SPR minima). After setting of the SPR incidence angle, the light intensity of the laser diode and an exposition time of the image sensor were adjusted to maximize the mean image intensity but avoiding an overexposure of an essential part of the image.

Prior to functionalization, the gold coated sensor prisms were cleaned by freshly prepared "piranha solution" (1:3 v: v mixture of 32 % H_2O_2/H_2SO_4), rinsed thoroughly with water, ethanol and dried at room temperature. *Caution: piranha solution reacts violently with most organic materials and must be handled with extreme care.* The functionalization of the gold film was done by self-assembled monolayers of alkan thiols with chain length 11–16 and various ω-terminated groups. Functionalized thiols were purchased from Sigma-Aldrich or ProChimia Surfaces (www.prochimia.com).

All solutions and suspensions were prepared using deionized water additionally purified by ELGA-Classic system (elgalabwater.com) and filtered using 200 nm cellulose acetate syringe filters from VWR International (www.wvr.com). 100 nm latex beads (polystyrene nanoparticles), citrate stabilized gold and silver nanoparticles (20, 30, 40, 60, 80, and 100 nm in diameter), and TiO_2-NP (<150 nm in diameter) were from Sigma Aldrich (www.sigmaaldrich.com). The size of nanoparticles was proved by dynamic light scattering (DLS) using Nano-ZS ZEN3600 (www.malvern.com). Concentrations of stock nanoparticle suspensions were proved using nanoparticle tracking analyzer NTA300 with 532 nm laser module (Nanosight, www.malvern.com). Aqueous suspensions of nanoparticles were prepared at final concentrations 10^6–10^{10} NPs/mL by dilution. Except long time repeatability measurements, each probe before injection was treated for few seconds with vortex shaker Lab Dancer S40 (VWR International). All solutions and suspensions were pumped by a solenoid operated micro-pump (Biochem Valve, 130SP1220-1TP) at flow rate of 0.5–2 ml/min. After flashing the flow cell, 1.5–2 ml suspensions of nanoparticles in the same solution were injected. Experimental and instrumental details for particular measurements can be found in respective publications [142–147].

4.2 Data Analysis in Wide-Field SPRM

Analytical applications of the wide-field prism-based SPRM are based on the fact that the adsorbed NPs disturb the propagation conditions of surface plasmons. The scattering of surface plasmon waves can be registered optically by specifically designed microscopy instrument. The regular image sensor (CMOS or CCD camera) are used for the image acquisition. However, the light scattered by a single nanoparticle is weak compared to the inevitable image background and noise. Most essential sources of noise are the shot noise (Poisson noise) and the noise related to the readout electronics of image sensor. These can be reduced by frame averaging. The background is caused by the residual light reflected from the sensor surface. It can be caused by the roughness of the sensor surface (which itself scatters surface

plasmons), incomplete fulfillment of the resonance conditions caused by variations of incidence angle, wavelength, or polarization of illumination light. The thickness of the sensor plasmonic layer plays also a major role; this defines the residual reflectivity in the SPR dip [148]. To minimize the level of the background light, the measurement is performed near SPR minimum, while the illumination is performed using a monochromatic well collimated and polarized light beam [142, 143]. To suppress the static background and to detect image changes due to adsorption of NPs only, a detection of changes in SPRM images is performed. For this, the straightforward arithmetical subtraction can be applied to subtract the background [122, 149]. However, the changes between two images can be calculated also by other ways [150]. The pixel-to-pixel ratio of two frames combines a determination of the image changes and their normalization to the local light intensity [142, 143, 148]. This compensates an illumination inhomogeneity over the field of view. Due to vibrations and drift of optical elements, the illumination (and correspondingly the background image) changes over the time. Therefore, to account for a slowly changing background the detection of image changes by taking the ratio of a two subsequent frames ($frame_N$/$frame_{N+1}$) is beneficial. However, this may lead to the underestimation of the image intensity contribution from a single nanoparticle. The time required for the diffusing NP to cross the penetration depth of the evanescent wave (~150–300 nm) is much smaller than the averaged frame time (~1 s). Therefore, the NPs adsorbed within the frame N contribute to the measured light for only a part of the frame time, and the full contribution of these NPs into the image intensity is spread over two differential frames: $frame_N$ / $frame_{N+1}$ and $frame_{N-1}$/$frame_N$. To capture the full contribution of NPs adsorbed within the frame N, the differential frames are calculated not as the ratio $frame_N$ / $frame_{N+1}$ but as $frame_{N+1}$/$frame_{N-1}$ (skipping the frame N). In differential frames obtained by such a dynamically sliding ratiometric image referencing, the pixel values close to unity (~1, gray) denote no changes in this pixel in raw SPRM images, whereas an intensity changes within the considered frame N result in values higher (>1, white) or lower than the unity (<1, black). It is to note that the scattering image of NP on image sensor is formed in the presence of high amount of residually reflected light. The monochromaticity of the light and the sharp phase change of the surface plasmon near the resonance conditions result in the constructive/destructive interference. An adsorption of a NP is then represented as a characteristic black-and-white image pattern, which has typical size of $5 \times 10\ \mu m^2$ because of limited optical resolution. The typical images, obtained by wide-field SPRM are shown in Fig. 3.5, left (images obtained by a high-NA SPRM are shown on the right for comparison).

As expected, the images obtained by wide-field SPRM have a lower resolution than those in high-NA SPRM. Still, the same image pattern can be recognized – the image has an asymmetric X shape, with longer and more intensive tails in the direction of propagation of surface plasmons. The cross of X shape denotes the position of NP.

Analytical application of wide-field SPRM for in-situ detection and characterization of nanomaterial suspensions is based on the detection and characterization of such images. It can be principally done using manual image processing (e.g. using ImageJ/FIJI and similar software packages). However, this is slow, tedious, and

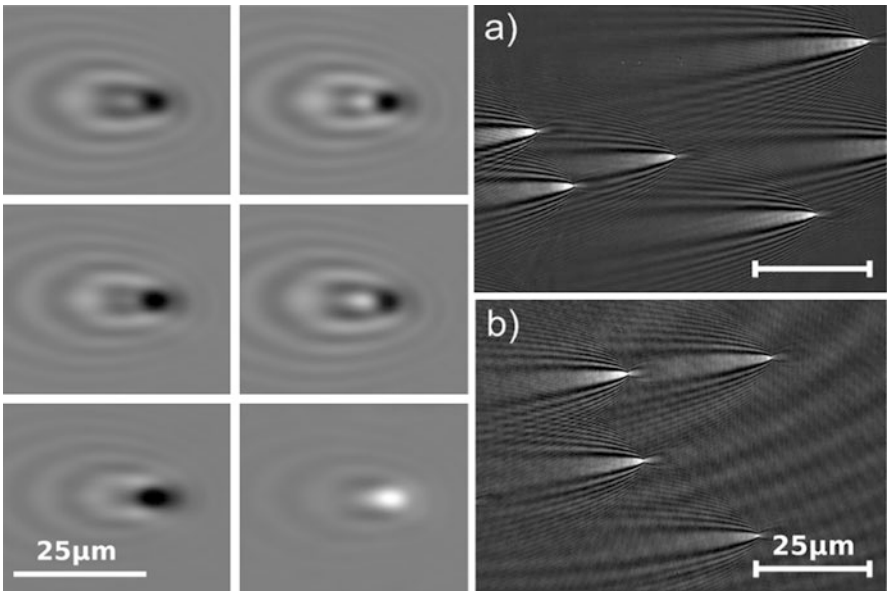

Fig. 3.5 Nanoparticle images, obtained by wide-field SPRM (left) and high-NA SPRM (right, adapted with permission from [122]. Copyright 2013 American Chemical Society.)

susceptible to a personal perception. The large sensor surface of the wide-field SPRM can adsorb millions of nanoparticles without reaching noticeable surface coverage. The area occupied by a single 60 nm NP in densely packed hexagonal monolayer is ~3×10^{-9} mm^2, correspondingly, a million of nanoparticles occupy ~3×10^{-3} mm^2 or less than 0.3 % of the 1.2 mm^2 sensor surface. In our typical measurement, a number of adsorbed nanoparticles were one-two orders of magnitude less. At so low surface coverage a random binding of new NPs on the top of the formerly adsorbed ones or in their closest vicinity is almost improbable.

The large sensor surface of wide-field SPRM enables a wide dynamic range. However, this important sensor feature cannot be fully exploited in manual image analysis. The wide-field SPRM was developed having analytical applications in mind. This assumes that the measurements are done with a high throughput, may result in large amount of data to get a statistically representative data, and the characterization and/or quantification is reproducible and operator independent. Moreover, the analyzed samples may be present as a real media of a complex composition, such as industrial wastes, environmental waters, food and drinks, biological liquids and tissues. Therefore, to establish the wide-field SPRM as an analytical technique, it must be supplemented by a robust image processing.

An automated data analysis of wide-field SPRM records can be implemented in a straightforward manner by application of image filtration succeeded by detection of a local spatiotemporal intensity changes [143, 149]. Assuming that the adsorption of a NP causes stepwise intensity change in a group of pixels with some predetermined

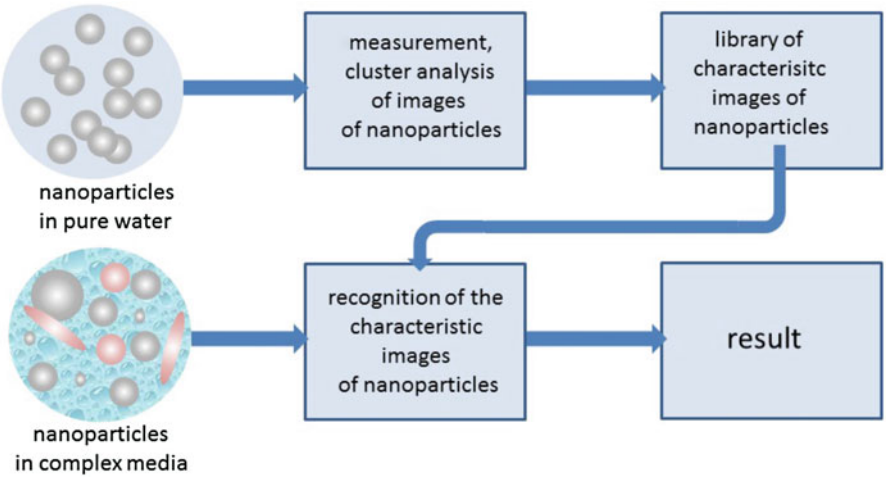

Fig. 3.6 The principle of nanoparticles detection in complex media using image template matching

spot size, the detection mechanism ignores most of the fine structure of the image pattern. This may lead to false identification of unrelated image noise as an adsorbed NP. Adsorbed particle with intense scattering also has a larger specular size of the image pattern (because the scattered light level overcomes noise over the larger group of pixels). This may be neglected entirely or identified falsely as a bunch of NPs. This complicates an application of the wide-field SPRM for complex samples with interfering matrix components. Extraction of nanoparticles from such complex media to make a subsequent analysis is a widely accepted approach [109, 151, 152]. However, the extraction procedure may change the concentration and properties of nanomaterials in comparison to their original state in the sample. In the case of moderately complex samples, the more advanced image processing of SPRM images was suggested (Fig. 3.6) [142].

In this approach, the template matching (based on the calculation of normalized correlation coefficient of two images [153]) is used. Using the distinctive shape of NP images as a template, the adsorbed NPs are recognized in differential SPRM images. This suppresses interference from matrix elements and provides a reliable analysis of SPRM records with a low signal-to-noise ratio. The required image templates can be gathered in different ways. Aqueous suspensions of NPs of the same size and composition can be characterized to find out the typical NP images. These images can be averaged to increase the signal-to-noise ratio (examples are shown on Fig. 3.5) and later be used as a template (Fig. 3.6). In this case the possible influence of the media on the resulting NP images is neglected. An extraction of NP images from the SPRM record obtained directly in the complex analytical probes spiked intentionally by NPs is more reliable. Analogously to the technique of standard additions, this can be as well used for estimation of a rate of false positives in original media. The developed approach was tested using a wide range of

consumer products as a matrix, starting from simple aqueous media to such complex as wines, fruit juices, or suncream. Except suncream, explicitly containing NPs according to its formulation, other probes were spiked with known amount of engineered NPs shortly before the measurement. These known concentrations were considered as the reference values for calibration curve and validation of the proposed technique.

Using the described approach, the SPRM records were processed and the adsorption of NPs was recognized based on their image templates. For the quantitative results, a number of the detected adsorbed nanoparticles was normalized to the frame duration and the sensor area. Therefore, the unit for the adsorption rate is the mean count of adsorbing nanoparticles per unit time and surface. To get a total number of adsorbed NPs the adsorption rate is integrated. From the adsorption rate the concentration of NPs in bulk suspension is determined, while each detected NPs is characterized by its image [142, 145].

4.3 Surface Properties and Adsorption of Nanoparticles

Since the evanescent wave penetrates to some extent into the liquid suspension, SPRM can be used for imaging of not only stickily adsorbed NPs but also those moving within the evanescent wave. However, the evanescent wave decays exponentially from the sensor surface with exponential factor of ~200 nm for $\lambda = 650$ nm. Therefore, NPs passing at some distance from the sensor surface have much weaker scattering than those adsorbed on the surfaces. The diffusion coefficient of 20 nm NPs in aqueous suspensions at 20 °C is ~20 $\mu m^2/s$. Therefore, NP can cross the penetration depth of the evanescent wave and adsorb to the sensor surface within milliseconds. Thus, for the time-resolved imaging of an adsorption of a NP, a very high frame rate of image acquisition is needed [154]. Therefore, the adsorption of a NP can be considered as occurring instantly within the single image frame time. As described above, to achieve the high signal-to-noise ratio, a frame averaging is used which can be only effective when the position of NP does not change substantially within the averaging time. Therefore, only the NPs remaining adsorbed and immobilized for this time can be detected and analyzed. For the maximal image intensity, the adsorbed NPs must stay at the surface during one averaged frame acquisition (for our wide-field SPRM ~1 s). For determination of bulk concentration of nanoparticles, described in next section, the assumption is made that the adsorption of nanoparticle is irreversible.

For the prolonged adsorption of a NP, the sensor surface should be properly functionalized. This was done by formation of self-assembled monolayers of thiol-derivative compounds [155]. A further functionalization of terminating groups is also possible (e.g., by chemical immobilization of antibodies for selective adsorption of biological NPs) [81, 156, 157]. Using the microspotting procedure, [144, 146] the surface of SPR gold layer was functionalized by various terminal groups – COOH, NH_2, $N(CH_3)$, OH, olygo-EG, CH_3. Using a noncontact dispenser, an array of droplets of organic solvent containing ω-terminated thiolated compound with a dot

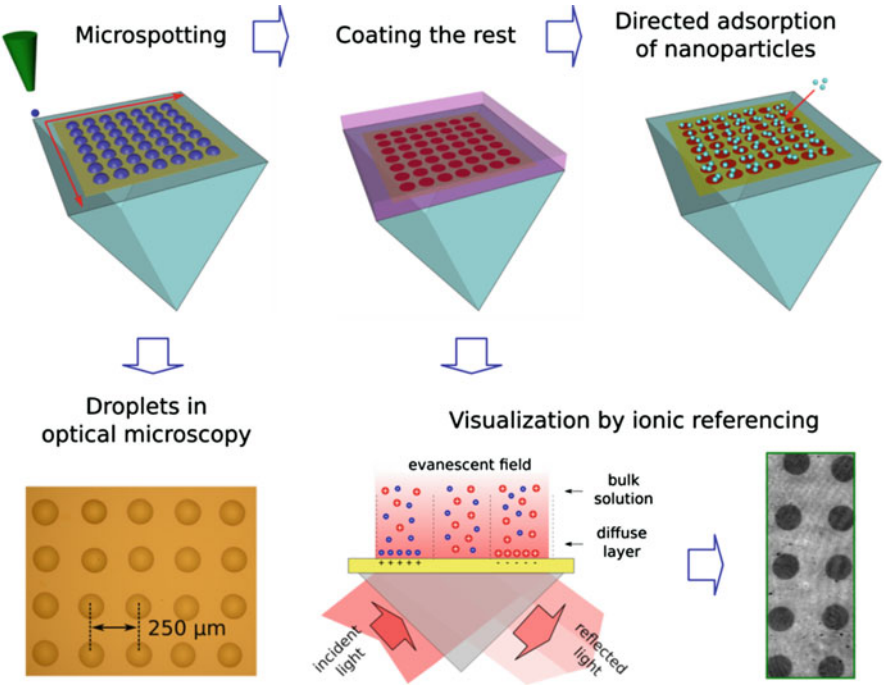

Fig. 3.7 Formation, characterization, and application of the micropatterned sensor surfaces in wide-field prism-based SPRM (Partially adapted from Ref. [147])

pitch of 200–300 µm is deposited on the surface (Fig. 3.7). Then the rest of the gold area was functionalized by another ω-terminated thiol. The formation of a patterned sensor surface with different surface properties was confirmed using the ionic referencing [147]. The prepared micropatterned surface was then installed into SPRM, and an adsorption of various NPS was studied.

For discrimination of NPs with different polarity of surface charges, a micropatterned sensor surface consisting of the negatively charged spots on the positively charged surface was used [144]. The results of adsorption of different negatively charged NPs to such patterned surface are shown in Fig. 3.8. It is evident, that the negatively charged citrate capped gold (cit-Au) and sulfonate terminated polystyrene (sPS) NPs adsorb to the positively charged sensor areas. In order to prove that this is caused by electrostatic interactions (sticky adsorption to a sensor surface with opposite sign of surface charge and repulsion from the surface with the same sign of charge), a positively charged branched polyimine coated silver (bPEI-Ag) NPs were subsequently injected into the flow cell. The results are shown in Fig. 3.9. Due to electrostatic interactions, the adsorption of charged nanoparticles occurs predominantly to the sensor areas of the opposite charge. It is to note, that the electrostatic interactions can be influenced by the change of pH and ionic strength of suspensions. With increase of the ionic strength from 1–2 mM to 100–200 mM, the electrostatic

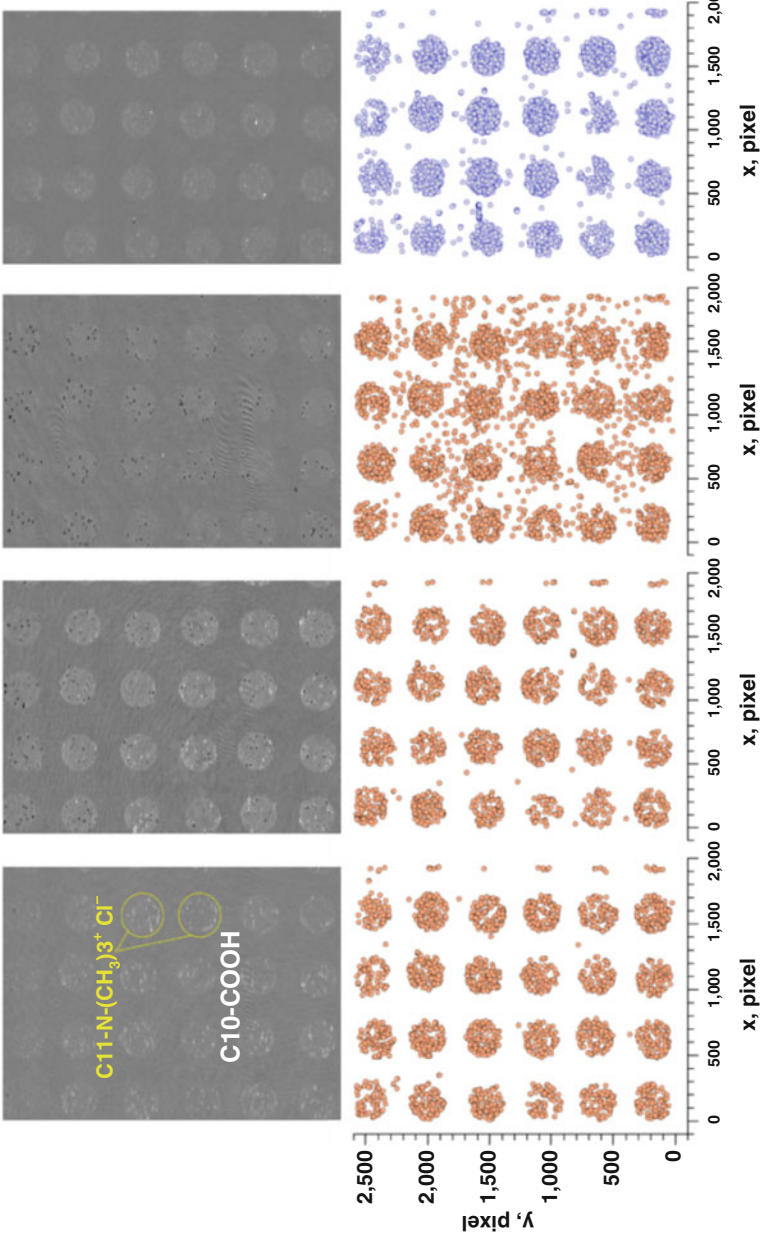

Fig. 3.8 Visualization of selective adsorption of negatively charged nanoparticles without addition of sodium chloride on a surface coated by spots with C_{11}-$N^{+}(CH_3)_3$ Cl^{-} (120–130 µm spot diameter) surrounded by a coating with C_{10}-COOH alkyl thiol. Upper panel: Differential SPRM images. Bottom panel: Visualization of nanoparticles adsorbed within 90 s. Visible area is ~ 1.3 mm^2 (Reproduced from Ref. [144])

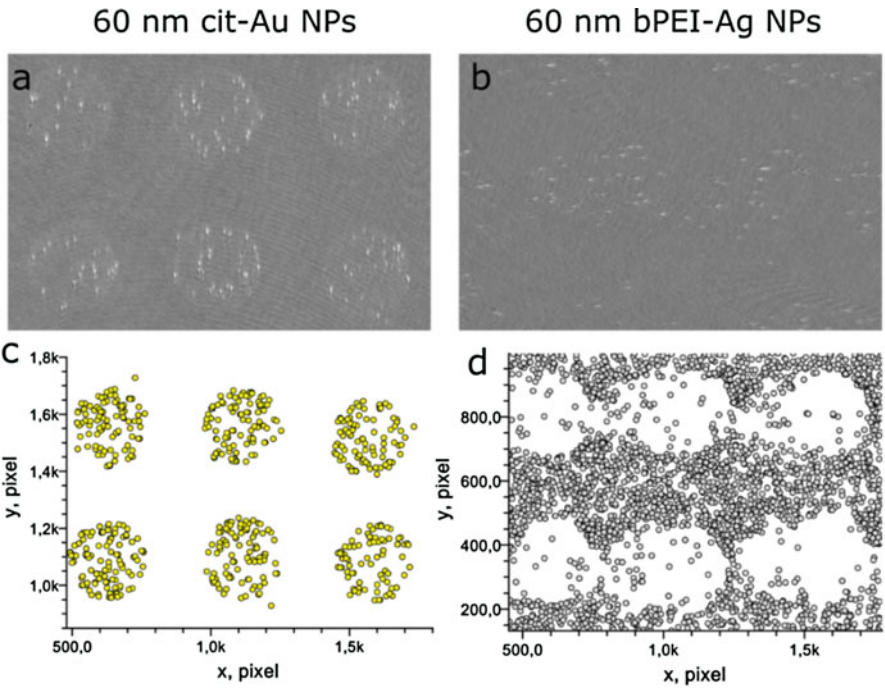

Fig. 3.9 Visualization of selective adsorption of negatively charged citrate stabilized gold nanoparticles (**a**, **c**) and positively charged branched polyethylenimine coated silver nanoparticles (**b**, **d**) at low ionic strength onto the surface coated by spots of HS-$(CH_2)_{11}$-$N(CH_3)_3^+$ Cl^- (120–130 μm spot diameter) with HS-$(CH_2)_{10}$-COOH coated area in-between. Differential SPRM images (**a**, **b**). Visualization of single nanoparticles adsorbed within 90 s (**c**, **d**). Visible area is ~ 0.3 mm^2 (Reproduced from Ref. [144])

interaction was screened and its influence on the adsorption of NPs decreased. Similar to the adsorption of proteins, the adsorption of NPs can be decreased by application of –OH and –olygoEG coatings.

4.4 Determination of Concentration of Nanoparticles in Liquid Suspensions

According to the Fick's law for one-dimensional case (the coordinate x is normal to the surface), the diffusion flux of NPs J is proportional to the sensor surface area A, diffusion coefficient D, and gradient of NPs concentration $C(x)$:

$$J = -A\,D\,\frac{dC}{dx}$$

As shown in the section above, the appropriate functionalization of the sensor surface enhances strongly the adsorption of NPs. Experimental data suggest that the

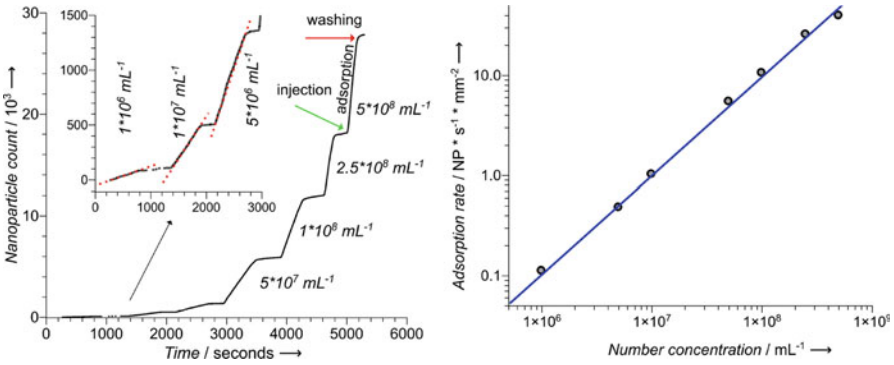

Fig. 3.10 Adsorption kinetics for 60 nm Ag nanoparticles during subsequent injections of their suspensions with different concentrations (left) and corresponding concentration dependence of the adsorption rate (right) (Reproduced from Ref. [145])

desorption of NPs in many cases can be neglected. Therefore, assuming that NPs adsorb fast and irreversibly to the sensor surface, $C(0) = 0$. Assuming that the concentration of NPs in the bulk suspension (at a distance beyond unstirred layer with thickness δ) is constant: $C(x>\delta) = C_0$, we get $\frac{\partial C}{\partial x} \approx \frac{C_0}{\delta}$ and $J \sim A\ D\ C_0$.

Therefore, the concentration of nanoparticles in SPRM can be characterized by the detected adsorption rate of nanoparticles. In the wide-field SPRM, the linear dependence of the adsorption rate on the concentration of NPs in the bulk suspensions holds true over 3 orders of magnitude of concentrations, from 10^6 to 10^9 NPs/ml [142, 145] (Fig. 3.10).

The concentration range can be extended in both directions. At number concentration of 10^6 NPs/mL, the adsorption rate of 60 nm Ag NPs to the sensor surface of 1 mm^2 is ~1 NP per 10 s (note that it depends on the flow conditions). Scaling down the concentration to 10^3 NPs/mL the adsorption rate would proportionally decrease to 1 NP per 10,000 s (almost 3 h). So the limitation of the minimal concentration is imposed by the measurement time which is required for the detection of a randomly diffusing nanoparticle that eventually adsorbs to the sensor surface. For the concentrations of 10^5–10^6 NPs/mL, the measurement time required for the acquisition of statistically representative amount of data is still acceptable. The concentration range can be as well scaled down at the same measurement time by increasing the sensor surface area A. This emphasizes the benefits of the wide-field SPRM for analytical applications involving samples with a very low concentration of NPs.

The limitation on the maximal concentration is as well imposed by the detectable adsorption rate. At high concentrations (above 10^9–10^{10} NPs/mL), the amount of NPs adsorbed during the single image frame is so high that their images start overlapping. This complicates the reliable recognition of NP images. The problem can be probably alleviated by increasing the frame rate while maintaining the same signal-to-noise ratio of SPRM images. However, at so high number concentrations of NPs (above 10^{10} NPs/mL), not only wide-field SPRM but also many other analytical techniques for detection and characterization of NP suspensions become applicable.

The adsorption rate of NPs to the sensor surface with a constant surface area A is governed by two independent unknown variables: the diffusion coefficient of nanoparticles D and their bulk concentration C_0. Therefore, a calibration is required for determination of concentration of nanoparticles from the adsorption rate. For this calibration, the samples with a known concentration of NPs of the same size (to retain the same diffusion coefficient) were characterized. To maintain the same thickness of the unstirred layer, this should be done at the same flow conditions (viscosity, temperature, and flow rate). Thus the calibration curve of an adsorption rate for given NPs and experimental conditions can be obtained. Using such approach, the detection and characterization of nanoparticles in samples was performed [142]. In Fig. 3.11 the detection and characterization of TiO_2 NPs in suncream is shown. For the calibration, TiO_2 suspensions with known size distribution and weight concentration 1–1000 ng/mL were used (covering the full part per billion range). To match the concentration range of the wide-field SPRM, the suncream with 5% w/w concentration of TiO_2 was diluted $1{:}10^5$ and $1{:}10^6$ times. Then the adsorption rates for these samples were measured, and from the calibration curve the concentration of TiO_2 NPs in suncream was determined. As it can be seen from Fig. 3.11, the measured adsorption rate fits very well the calibration curve and corresponds to the actual concentration of ~4%.

Similar measurements were also performed for gold and silver NPs in various beverages like mineral water, juices, or wines. Notably, except extremely turbid orange juice, most of these measurements were performed directly in the media without any pretreatment. These examples show the applicability of wide-field SPRM for detection and characterization of NPs in real samples with complex composition.

The determination of the concentration of NPs in liquid samples was done using a calibration by known samples. However, the calibration free approaches can be as well implemented. Using the high-frame rate imaging for the visualization of adsorption of single NPs, their diffusion coefficients and the concentration in bulk suspensions can be determined [154]. Our results show that the separate determination of diffusion coefficient and concentration from the kinetics of adsorption rate is also possible without application of high-frame rate imaging (will be published elsewhere).

4.5 Determination of the Size and Size Distribution of Single Nanoparticles

The common way of characterizing each detected NP is based on the peak intensity of NP image [94, 122, 142, 143, 145, 148, 149, 156]. However, there are differences in the calculation of NP images: in earlier works the absolute intensity was taken, later differential images were referenced to the image intensity. Despite the differences in optical resolution and NP image calculation between wide-field SPRM and high-NA SPRM, the observed NP images share common image features (Fig. 3.5).

Experimental data of various authors undoubtedly demonstrate that the NP image intensity increases with the size of NP. Therefore, the relation between NP properties

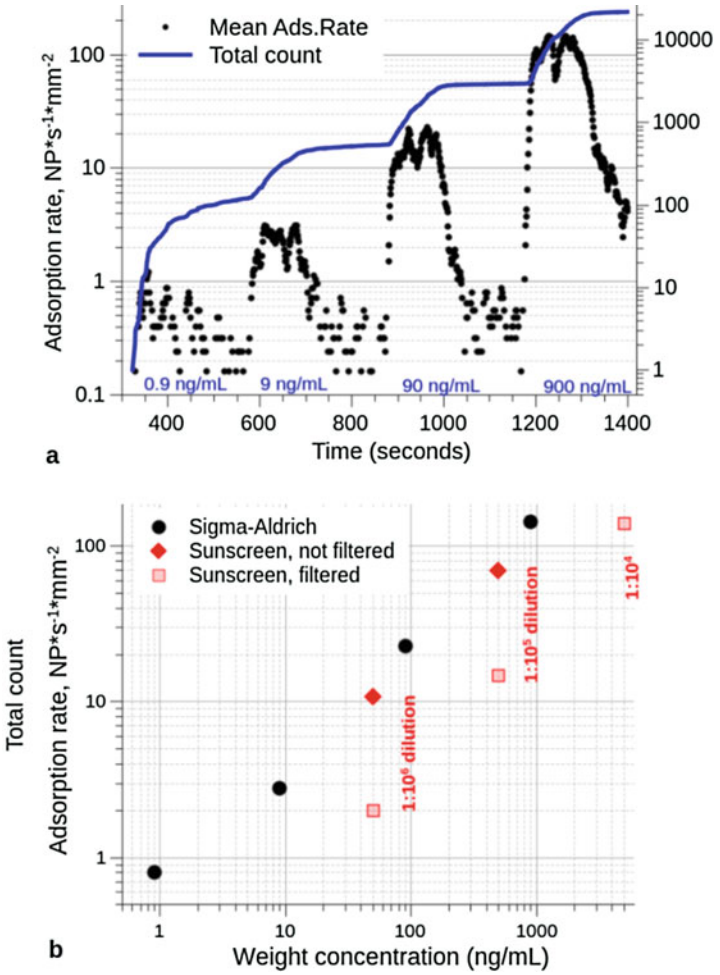

Fig. 3.11 Analysis of content of TiO_2 NPs in the suncream. The sample was diluted by water $1{:}10^4$, $1{:}10^5$, or $1{:}10^6$ to match the optimal working range of the device. The weight concentrations were calculated using supplier data on the content of TiO_2 (5 % w/w). For comparison, the aqueous suspension of TiO_2 from Sigma-Aldrich was studied (Reproduced from Ref. [142])

and its image in the far-field has an enormous importance for analytical applications of SPRM. Several theoretical approaches for establishing such a relation have been described. The most rigorous theoretical analysis, supported by numerical simulation using finite difference time domain (FDTD), is given in Refs [158, 159]. A good match between NP images in high-NA SPRM and numerical simulation was shown [125]. The same was confirmed by using rigorous coupled wave analysis (RCWA) [160]. RCWA also confirmed that the maximal intensity of image is expected at conditions close to the resonance (near the SPR dip) [148]. Such result is expectable since the light reflected from the SPR sensor surface in such conditions is minimal and creates least

background illumination level in image. At the same time, intensities of evanescent wave and, correspondingly, of scattered light are maximal. Theoretical analysis suggests that the image intensity is linearly dependent on the NP radius as long as the distance between the plasmonic layer and the particle is small [161]. This is in line with experimental observations obtained using wide-field SPRM [94, 162]. With high-NA SPRM a linear dependence between image intensity and volume of NP was shown [122, 125]. So, the determination of optical response (SPRM image) to the adsorption of a single NP with determined size and material is possible using different theoretical and numerical approaches. However, the inverse task – a determination of NP properties from its image – is much more difficult. In fact, various nanoparticles have quite similar SPRM images (note that these images have low signal-to-noise ratio due to weak scattering). Moreover, the NP images are dependent on the optical conditions (incidence angle of light, image focus) [163]. This complicates the recognition of distinct properties of the image of a single NP. Therefore, the main information is the image intensity which can be equal for different nanoparticles: large but lower RI NPs have similar image as small NPs composed of a material with a high RI.

The size dependence of the image intensity of Au NPs measured by a wide-field prism-based SPRM is shown in Fig. 3.12a. This dependency is approximately linear in the 30–100 nm size range. It is in good agreement with theoretical analysis [158–161] and with previous report for polystyrene particles [94, 162]. It is to note that the differential image intensity is dimensionless and cannot be quantified directly. Indeed, this is the ratio of the reflected light intensities before and after adsorption of NP. To convert this dimensionless value into some representative physical value, a calibration of the sensor response to the changes of the effective refractive index has been done. This was performed by addition of 20 mM NaCl to the medium: this changes the RI of the dilute aqueous solutions by ~180 μRIU [85, 164]. Using such a calibration, the differential image intensity (peak-to-peak value) can be expressed in terms of RI. Thus the maximum image intensity for 30 nm Au NPs corresponds to $\sim 10^{-4}$ RIU. In SPR sensors the RI resolution lies typically in the range of 10^{-5}–10^{-6} RIU. Therefore, for the application of SPRi/SPRM for detection of single NPs not the RI resolution but rather the optical resolution of the instrument and image analysis have the key importance. The low spatial resolution blurs otherwise detectable signal from a single NP over a large surface area.

The RI calibration enables a quantitative analysis and comparison of images obtained in different conditions. The histograms of image intensities of Ag and Au NPs, obtained in various media (water, wine, juice) in independent measurements, are shown in Fig. 3.12b. It is to note that the detection of Ag and Au NPs is not based on the detection of their plasmonic adsorption bands (which are caused by LSPR and lie in a shorter wavelength range than the wavelength of illumination light in wide-field SPRM). Since the optical properties of bulk Ag and Au at the SPRM wavelength (~640 nm) are very similar, the normalized histograms for Ag and Au NPs display a good coincidence as well.

The distribution of image intensities was used for analysis of polydisperse samples. The histograms for 40/60, 40/80, 40/100, 30/60, 30/80, 30/100 nm mixtures of Au NPs (with the nominally equal number concentration of NPs in mixture)

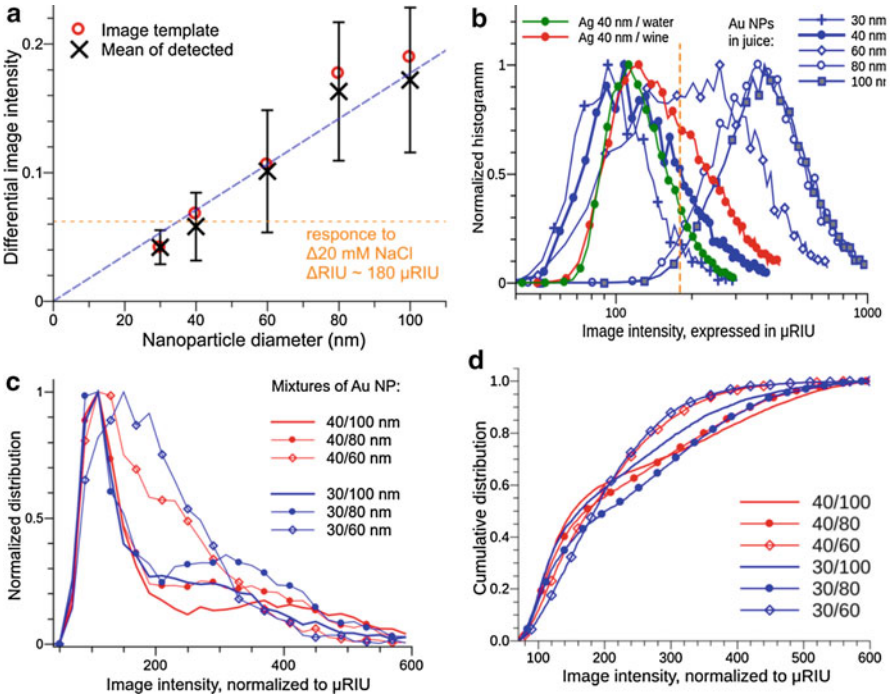

Fig. 3.12 Characterization of size of nanoparticles in complex media. (**a**) Image intensity of Au NPs of different size in apple juice. (**b**) Histograms of image intensities of NPs normalized to the RI response. Ag 40 nm NPs were measured separately in water and wine, Au NPs were measured in apple juice. (**c**) Histograms of image intensities mixed suspensions of Au NPs. (**d**) Cumulative histogram of image intensities. All the plots were normalized to RI units by calibration with 20 mM NaCl (Reproduced from Ref. [142])

are shown in Fig. 3.12c. As expected, the histograms for the mixtures show bimodal distributions. The discrepancy in the adsorption rates between smaller 30 and 40 nm Au NPs and larger NPs in mixtures may be explained by two reasons. First, the smaller NPs diffuse faster through the unstirred layer near the sensor surface. Thus, it leads to a higher adsorption rate of smaller NPs at the same concentration in the volume. The second reason is that the narrower distribution of image intensities for smaller NPs makes the mode value of the histogram apparently higher. The number of NPs corresponding to the particular size population can be obtained by integration of the area under distribution curve. For the mixed suspensions consisting of 40/60, 40/100, 30/80, and 30/100 nm NPs, clear two-phase curves with the ratio of the components between 1:1 and 2:1 were obtained (Fig. 3.12d).

The data demonstrate that the distribution of image intensities relates to the size distribution of nanoparticles. However, one cannot exclude also a contribution of other effects, such as thickness variations of the gold layer throughout the sensor surface, incomplete compensation of inhomogeneous light distribution during the calibration step, or an influence of impurities on the distance between adsorbed NPs

and gold layer. These effects contribute to the image intensity variations causing broadening of the distribution of image intensities; however, this influence is difficult to quantify. Compared to the evanescent wave, the adsorbed NPs are subwavelength objects. Therefore, a noticeable influence of the shape of nanoparticle can be expected only for large aspect ratio NPs (e.g., rods longer than 1 μm). For the long stretched DNA molecules (~15 μm), the SPRM images have been shown to be of the same length [133].

4.6 Hyphenation with Electrochemical Analysis

The functionalization of the sensor arrays enables a determination of the surface charge (to a some extent, of the surface chemistry as well) of NPs. Counting adsorbed NPs and making kinetic analysis, the concentration of NPs can be determined, whereas the images of NPs characterize their size/compositions. However, as mentioned in the previous section, the size and material composition cannot be resolved independently. In general, purely optical determination of the size and composition (refractive index) of a subwavelength particle is not easy. Therefore, for addressing the chemical composition of NPs, we suggested to hyphenate the wide-field SPRM by in-situ electrochemical analysis.

The principle of electrochemistry combined surface plasmon resonance (EC-SPR) is based on the simultaneous application of the plasmonic layer as a conductive electrode for electrochemical approaches and as plasmonic transducer of occurring electrochemical processes to optical signals. Importantly, SPR measures the light reflected by plasmonic layer from the backside leaving its front side freely usable by electrochemistry cell. In EC-SPR many of electrochemical techniques, applicable to the flat thin electrodes, can be applied. The approach can be implemented as a microscopy (EC-SPRM) [131, 132, 134, 136, 145], making it a powerful analytic technique which can compete with purely electrochemical scanning probe microscopy (SECM).

The principle of wide-field EC-SPRM is shown in Fig. 3.13. Controlling electrical potential of the gold sensor surface it is also possible to control the potential of NPs adsorbed on it. Changing the potential of the gold sensor, the nanoparticle of certain composition can be forced to dissolve. The potential, which is required for dissolution, is mainly defined by the composition of nanoparticle, but is also influenced by their size [145]. In the electrochemical analysis of single NPs using wide-field EC-SPRM, the NPs are first adsorbed at some potential value which excludes their dissolution. The adsorption of NPs to the sensor surface is monitored, the positions and adsorption images of NPs are determined.

It is to expect that the adsorption of a NP to the sensor surface and its desorption manifest themselves as differential SPRM images of the same shape and intensity but of opposing signs (similarly to photopositive and photonegative of the same scene image; Fig. 3.13 right) [122]. The same applies for adsorption and electrochemical dissolution. Therefore, the regression coefficient (RC) and normalized correlation coefficient (NCC) between two images of the same NP, corresponding

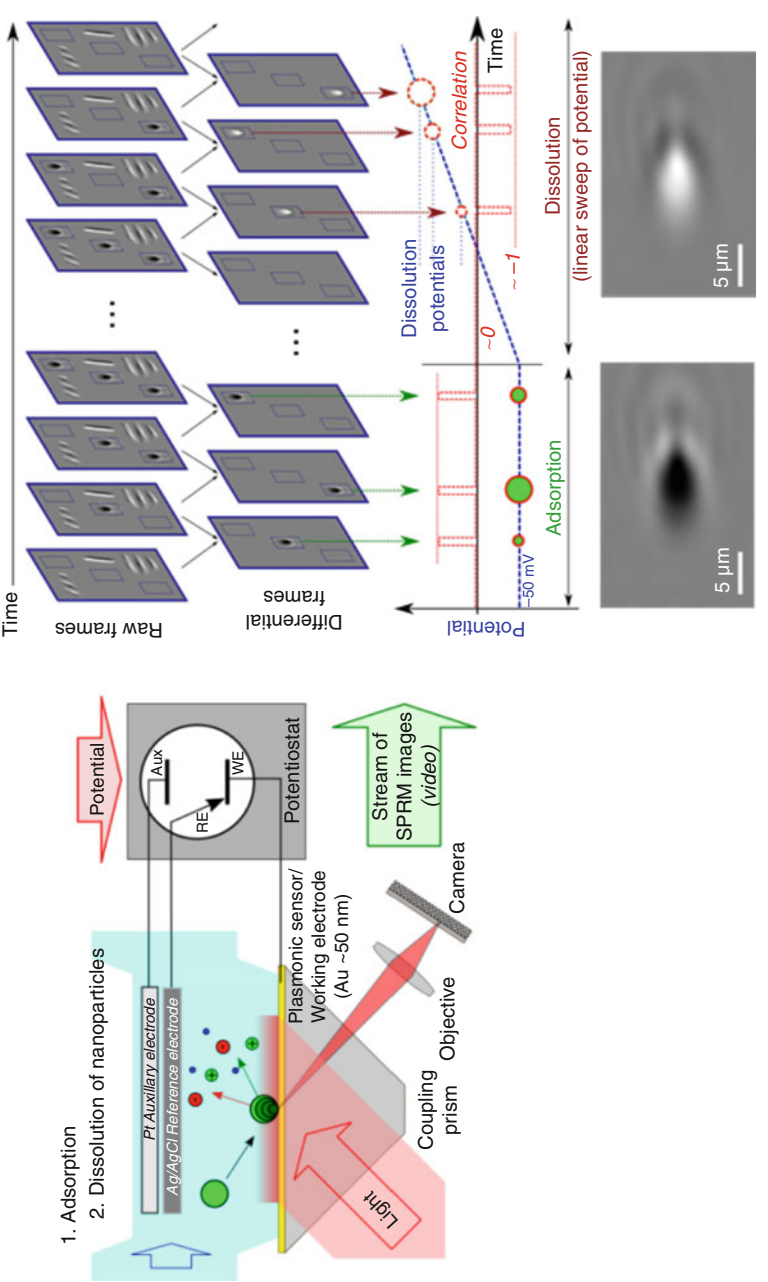

Fig. 3.13 Wide-field SPRM for detecting, tracking, and in-situ electrochemical treating of adsorbed nanoparticles. The gold layer has two functions: a plasmonic sensing surface and a working electrode which controls redox state of adsorbed nanoparticles (Reproduced from Ref. [145]). Determination of dissolution potential of single nanoparticles. Adsorption and dissolution of nanoparticles in differential frames are revealed by "positive" and "negative" images of nanoparticle (bottom, for 60 nm Ag NP)

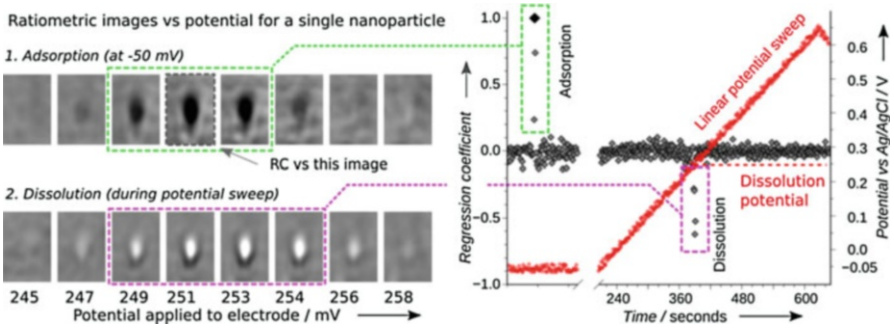

Fig. 3.14 Determination of dissolution potential of single 60 nm Ag nanoparticle in wide-field EC-SPRM. Differential images corresponding to adsorption (left, top) and dissolution (left, bottom) of the same nanoparticle and corresponding changes in the regression coefficient (right) (Adapted from Ref. [145])

to its adsorption and desorption/dissolution, are close to −1. For analysis, the positions of adsorbed nanoparticles are monitored and the SPRM differential images at these positions are continuously checked using RC/NCC vs. the adsorption image of NPs. As long as at that position the image with opposite intensity occurs (in other words, the RC and/or NCC give the value ~−1), the nanoparticle can be considered as desorbed/dissolved (Figs. 3.13b and 3.14). Adsorption is performed at such cathodic potentials that this happens very rarely and can be ascribed to desorption. During the electrochemical analysis, the electrode potential is scanned to the anodic direction and such events occur very frequently (Fig. 3.15). This is certainly caused by electrochemical oxidation of NPs and their dissolution.

The exemplary sequence of differential SPRM images, corresponding to the adsorption and electrochemical dissolution of the same single Ag NP, is shown in Fig. 3.14. An adsorption of this NP leads to an appearance of the dark spot in differential frames. Increasing the electrode potential this NP can be dissolved, this is observed as an image with inverse intensity appearing in the same place. This can be as well detected by plotting RC/NCC vs. applied potential (time in the case of linear sweep of potential). The positive spike corresponds to the adsorption event. Then most of the time NCC and RC fluctuate around zero indicating no changes of the adsorbed NP. The dissolution/desorption of NPs can be detected as a spike of RC/NCC in negative direction. It is to note that the electrode potential controls the potential of all adsorbed NPs. Thus, the electrode potential, at which a NP dissolves and which is characteristic for its size and composition, can be determined simultaneously for each adsorbed NP. Notably, the characteristic potentials of electrochemical dissolution are determined without electrochemical measurements of the dissolution current (but at high surface concentrations of adsorbed nanoparticles it can be done as well).

The results of such analysis for sequential measurements of 40, 60, and 100 nm Ag NPs, as well as for 50 nm Cu NPs, are shown in Fig. 3.15. For these plots, the RC for all monitored NPs is determined and the value at 5th percentile is taken [145]. At

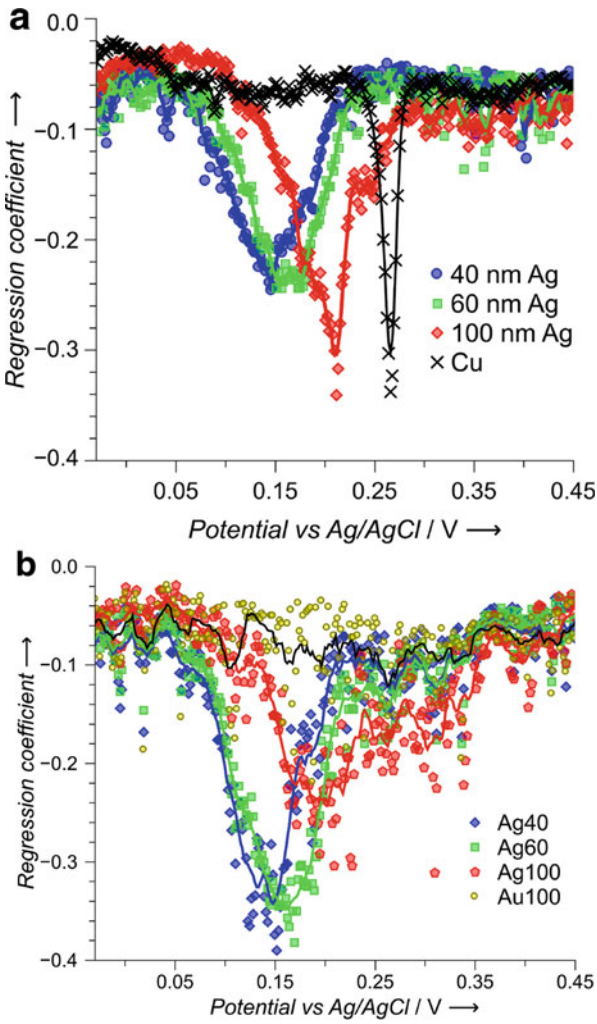

Fig. 3.15 Regression coefficient for different types of nanoparticles vs. applied potential sweep: when analyzed separately (**a**) or adsorbed sequentially but analyzed altogether within a single potential sweep (**b**) (Reproduced from Ref. [145])

the beginning of the potential sweep, the percentile value of RC, which describes all detected NPs, fluctuates around some constant value. This indicates that no dissolution happens. After reaching some defined value of the electrode potential, a strong shift of the RC in negative direction is observed. It means that at the positions of adsorbed NPs images, inversed to their adsorption image, were observed. This indicates clearly that the NPs disappeared from the sensor surface due to electrochemical dissolution. Because of thermodynamic reasons, once NP starts dissolving and shrinking at some particular potential, this process should continue till the complete dissolution of the NP or loss of electrical contact to the electrode. The expected difference between dissolution potentials of Ag- and Cu-NPs is clearly visible (Fig. 3.15). The exact values of dissolution potential vary for different NPs of

the same nominal size and material. The reasons could be size variations, impurities, and inhomogeneity of electrochemical conditions. Dissolution potential decreases with the size of NP; however, the variability of dissolution potential hinders the determination of the NP size from its dissolution potential. Therefore, it is more reliable to determine the size of NPs from the image intensity whereas the composition of NPs can be identified by electrochemical analysis.

A simultaneous analysis of different NPs was shown (Fig. 3.15b). For this, various Ag NPs were adsorbed sequentially on the sensor surface. Then all adsorbed NPs were subjected to electrochemical dissolution during a single potential sweep to anodic direction. Au NPs, used as a negative control, do not display any dissolution potential peak. Whereas the RC plots for dissolution of Ag NPs of different size exhibit the same behavior like in individual measurements of Ag NPs.

5 Conclusion and Future Perspective

In-situ detection and characterization of nanoparticles in liquid media is still a challenge for the state-of-the-art analytical methods, especially in real complex samples. A broad overview and classification of such methods is given. Due to the large amount of analytical techniques, broad extension capabilities, and a rapid development, this overview does not pretend to be complete and accurate. It underlines the complexity of such analytical task and shows the possible benefits of the surface plasmon resonance microscopy with a wide field of view.

Wide-field SPRM is a label-free and cost-effective analytical method for detection of nanoparticles in the broad concentration range 10^6–10^{10} NPs/ml. This corresponds to the weight concentration covering the full part-per-billion range. It is able to detect and count adsorbing nanoparticles individually, totally up to the hundreds of thousands of NPs on the sensor surface reaching ~1.3 mm^2. At constant diffusion conditions, the detection rate is proportional to the number concentration of NPs; this provides an approach to determine the NPs concentration. The adsorption of nanoparticles can be manipulated by surface functionalization, pH, and electrolyte concentration of suspensions. Detected NPs are characterized individually based on their plasmonic images. The image intensity grows quasi-linearly with nanoparticle size for the given material. For Ag and Au NPs the smallest reliably detected NP size was ~20 nm, whereas for polystyrene NPs ~40 nm. However, the size and material of nanoparticle cannot be resolved directly from the image. For determination of chemical composition, SPRM can be assisted by electrochemical analysis. In this case, the gold sensor surface is used both as the resonant media for plasmon microscopy and as the working electrode. Under potential sweep, the adsorbed NPs are subjected to electrochemical dissolution, which is detected optically. The potential of this conversion characterizes the material of NPs.

The unique features, capabilities, and benefits of the wide-field SPRM make it a perspective analytical technique for solving complex analytical tasks. This technique, intrinsically sensing the phenomena on the sensor surface, doing it in reflected

light and enhanced by plasmonic amplification, has a large application potential. Moreover, it can be hyphenated with a broad range of other analytical techniques.

Contrary to the SPR imaging, SPR microscopy is a very young technique – in its current shape, it is known for less than a decade. Still, a great progress during this short period of time can be observed. The potential of SPRM is not yet fully exploited; hence, it is to expect that it is going to be improved in many directions. The future developments of this technique will undoubtedly include bioanalytical applications. For instance, SPRM was already shown for individual detection of single large DNA molecules [133], viruses [125, 157], virus-like particles [157], liposomes and microvesicles [123, 156], bacteria, and cells [165, 166]. Manifold improvement of the size detection limits can be expected: for example, by changing the principle of optical registration to the surface plasmon enhanced scattering [95, 96] or by reducing the level of background light (off-axis illumination or polarization control). The concentration detection limits can be improved as well. However, unless the diffusion of particles towards sensor surface is not somehow enhanced, the main improvement in this regard will be related to the increase of the imaged sensor area. Some interesting opportunities are opened by application of a high frame rate imaging cameras [154]. The hyphenation of SPRM with surface enhanced Raman spectroscopy [99] or with chromatographical separation techniques [108] can be as well imagined.

Acknowledgments The work was supported by FP7 EC Project "NANODETECTOR" (FP7-NMP-2011-SME-5, #280478) and Thermo-SPR (MWFK). We are grateful to all project partners for discussions and suggestions. An assistance of Dr. K. Tonder and V. Scherbahn is acknowledged.

References

1. Stark WJ, Stoessel PR, Wohlleben W, Hafner A (2015) Industrial applications of nanoparticles. Chem Soc Rev 44:5793–5805
2. Babick F, Mielke J, Wohlleben W, Weigel S, Hodoroaba V-D (2016) How reliably can a material be classified as a nanomaterial? Available particle-sizing techniques at work. J Nanopart Res 18:158
3. Love SA, Maurer-Jones MA, Thompson JW, Lin YS, Haynes CL (2012) Assessing nanoparticle toxicity. Annu Rev Anal Chem 5:181–205
4. Bleeker EAJ, de Jong WH, Geertsma RE, Groenewold M, Heugens EHW, Koers-Jacquemijns M et al (2013) Considerations on the EU definition of a nanomaterial: science to support policy making. Regul Toxicol Pharmacol 65:119–125
5. Nič M, Jirát J, Košata B, Jenkins A, McNaught A (eds) (2009) IUPAC compendium of chemical terminology: gold book. 2.1.0. IUPAC, Research Triagle Park
6. Berne BJ, Pecora R (2000) Dynamic light scattering: with applications to chemistry, biology, and physics. Dover Publications, Mineola
7. Jiang J, Oberdörster G, Biswas P (2008) Characterization of size, surface charge, and agglomeration state of nanoparticle dispersions for toxicological studies. J Nanopart Res 11:77–89
8. Murdock RC, Braydich-Stolle L, Schrand AM, Schlager JJ, Hussain SM (2008) Characterization of nanomaterial dispersion in solution prior to in vitro exposure using dynamic light scattering technique. Toxicol Sci 101:239–253

9. Medebach M, Moitzi C, Freiberger N, Glatter O (2007) Dynamic light scattering in turbid colloidal dispersions: a comparison between the modified flat-cell light-scattering instrument and 3D dynamic light-scattering instrument. J Colloid Interface Sci 305:88–93
10. Urban C, Schurtenberger P (1998) Characterization of turbid colloidal suspensions using light scattering techniques combined with cross-correlation methods. J Colloid Interface Sci 207:150–158
11. Pusey PN (1999) Suppression of multiple scattering by photon cross-correlation techniques. Curr Opin Colloid Interface Sci 4:177–185
12. Pine DJ, Weitz DA, Chaikin PM, Herbolzheimer E (1988) Diffusing wave spectroscopy. Phys Rev Lett 60:1134
13. Bressel L, Hass R, Reich O (2013) Particle sizing in highly turbid dispersions by photon density wave spectroscopy. J Quant Spectrosc Radiat Transf 126:122–129
14. Makra I, Terejánszky P, Gyurcsányi RE (2015) A method based on light scattering to estimate the concentration of virus particles without the need for virus particle standards. MethodsX 2:91–99
15. Quinten M (2011) Optical properties of nanoparticle systems: Mie and beyond. Wiley-VCH, Weinheim
16. Mappes T, Jahr N, Csaki A, Vogler N, Popp J, Fritzsche W (2012) The invention of immersion ultramicroscopy in 1912-the birth of nanotechnology? Angew Chem Int Ed 51:11208–11212
17. Xiao L, Qiao Y, He Y, Yeung ES (2010) Three dimensional orientational imaging of nanoparticles with darkfield microscopy. Anal Chem 82:5268–5274
18. Hole P, Sillence K, Hannell C, Maguire CM, Roesslein M, Suarez G et al (2013) Interlaboratory comparison of size measurements on nanoparticles using nanoparticle tracking analysis (NTA). J Nanopart Res 15:2101
19. Filipe V, Hawe A, Jiskoot W (2010) Critical evaluation of nanoparticle tracking analysis (NTA) by nanosight for the measurement of nanoparticles and protein aggregates. Pharm Res 27:796–810
20. Gardiner C, Ferreira YJ, Dragovic RA, Redman CWG, Sargent IL (2013) Extracellular vesicle sizing and enumeration by nanoparticle tracking analysis. J Extracell Vesicles 2:19671
21. Kramberger P, Ciringer M, Štrancar A, Peterka M (2012) Evaluation of nanoparticle tracking analysis for total virus particle determination. Virol J 9:265
22. Tian X, Nejadnik MR, Baunsgaard D, Henriksen A, Rischel C, Jiskoot W (2016) A comprehensive evaluation of nanoparticle tracking analysis (nanosight) for characterization of proteinaceous submicron particles. J Pharm Sci 105:3366–3375
23. Gallego-Urrea JA, Tuoriniemi J, Hassellöv M (2011) Applications of particle-tracking analysis to the determination of size distributions and concentrations of nanoparticles in environmental, biological and food samples. TrAC Trends Anal Chem 30:473–483
24. Giavazzi F, Brogioli D, Trappe V, Bellini T, Cerbino R (2009) Scattering information obtained by optical microscopy: differential dynamic microscopy and beyond. Phys Rev E 80:031403
25. Cerbino R, Trappe V (2008) Differential dynamic microscopy: probing wave vector dependent dynamics with a microscope. Phys Rev Lett 100:188102
26. Martinez VA, Besseling R, Croze OA, Tailleur J, Reufer M, Schwarz-Linek J et al (2012) Differential dynamic microscopy: a high-throughput method for characterizing the motility of microorganisms. Biophys J 103:1637–1647
27. Wilson LG, Martinez VA, Schwarz-Linek J, Tailleur J, Bryant G, Pusey PN et al (2011) Differential dynamic microscopy of bacterial motility. Phys Rev Lett 106:018101
28. Haiss W, Thanh NTK, Aveyard J, Fernig DG (2007) Determination of size and concentration of gold nanoparticles from UV−vis spectra. Anal Chem 79:4215–4221
29. Paramelle D, Sadovoy A, Gorelik S, Free P, Hobley J, Fernig DG (2014) A rapid method to estimate the concentration of citrate capped silver nanoparticles from UV-visible light spectra. Analyst 139:4855
30. Mutavdžić D, Xu J, Thakur G, Triulzi R, Kasas S, Jeremić M et al (2011) Determination of the size of quantum dots by fluorescence spectroscopy. Analyst 136:2391

31. Yim S-Y, Park J-H, Kim M-G (2015) Dark-field spectral imaging microscope for localized surface plasmon resonance-based biosensing. Proc SPIE 9523:952307
32. Boyer D (2002) Photothermal imaging of nanometer-sized metal particles among scatterers. Science 297:1160–1163
33. Gaiduk A, Ruijgrok PV, Yorulmaz M, Orrit M (2010) Detection limits in photothermal microscopy. Chem Sci 1:343
34. Diwakar PK, Loper KH, Matiaske A-M, Hahn DW (2012) Laser-induced breakdown spectroscopy for analysis of micro and nanoparticles. J Anal At Spectrom 27:1110
35. Gimenez Y, Busser B, Trichard F, Kulesza A, Laurent JM, Zaun V et al (2016) 3D imaging of nanoparticle distribution in biological tissue by laser-induced breakdown spectroscopy. Sci Rep 6:29936
36. Schwertfeger DM, Velicogna JR, Jesmer AH, Scroggins RP, Princz JI (2016) Single particle-inductively coupled plasma mass spectroscopy analysis of metallic nanoparticles in environmental samples with large dissolved analyte fractions. Anal Chem 88:9908–9914
37. Laborda F, Bolea E, Jiménez-Lamana J (2014) Single particle inductively coupled plasma mass spectrometry: a powerful tool for nanoanalysis. Anal Chem 86:2270–2278
38. Agbabiaka A, Wiltfong M, Park C (2013) Small angle X-ray scattering technique for the particle size distribution of nonporous nanoparticles. J Nanopart 2013:1–11
39. Li T, Senesi AJ, Lee B (2016) Small angle X-ray scattering for nanoparticle research. Chem Rev 116:11128–11180
40. Chu B, Liu T (2000) Characterization of nanoparticles by scattering techniques. J Nanopart Res 2:29–41
41. Roberts GS, Kozak D, Anderson W, Broom MF, Vogel R, Trau M (2010) Tunable nano/micropores for particle detection and discrimination: scanning ion occlusion spectroscopy. Small 6:2653–2658
42. Roberts GS, Yu S, Zeng Q, Chan LCL, Anderson W, Colby AH et al (2012) Tunable pores for measuring concentrations of synthetic and biological nanoparticle dispersions. Biosens Bioelectron 31:17–25
43. Wang Y, Kececi K, Mirkin MV, Mani V, Sardesai N, Rusling JF (2013) Resistive-pulse measurements with nanopipettes: detection of Au nanoparticles and nanoparticle-bound anti-peanut IgY. Chem Sci 4:655–663
44. Makra I, Gyurcsányi RE (2014) Electrochemical sensing with nanopores: a mini review. Electrochem Commun 43:55–59
45. Weatherall E, Willmott GR (2015) Applications of tunable resistive pulse sensing. Analyst 140:3318–3334
46. Yang L, Yamamoto T (2016) Quantification of virus particles using nanopore-based resistive-pulse sensing techniques. Front Microbiol 7:1500
47. Cheng W, Compton RG (2014) Electrochemical detection of nanoparticles by 'nano-impact' methods. TrAC Trends Anal Chem 58:79–89
48. Rees NV (2014) Electrochemical insight from nanoparticle collisions with electrodes: a mini-review. Electrochem Commun 43:83–86
49. Sokolov SV, Eloul S, Kätelhön E, Batchelor-McAuley C, Compton RG (2017) Electrode–particle impacts: a users guide. Phys Chem Chem Phys 19:28–43
50. Sokolov SV, Bartlett TR, Fair P, Fletcher S, Compton RG (2016) Femtomolar detection of silver nanoparticles by flow-enhanced direct-impact voltammetry at a microelectrode array. Anal Chem 88:8908–8912
51. DeBlois RW, Bean CP, Wesley RK (1977) Electrokinetic measurements with submicron particles and pores by the resistive pulse technique. J Colloid Interface Sci 61:323–335
52. Aliano A, Cicero G, Nili H, Green NG, García-Sánchez P, Ramos A et al (2012) AFM in liquids. In: Bhushan B (ed) Encyclopedia of nanotechnology. Springer, Dordrecht, pp 83–89
53. Baalousha M, Prasad A, Lead JR (2014) Quantitative measurement of the nanoparticle size and number concentration from liquid suspensions by atomic force microscopy. Environ Sci: Processes Impacts 16:1338

54. Baalousha M, Kammer FVD, Motelica-Heino M, Le Coustumer P (2005) Natural sample fractionation by FlFFF–MALLS–TEM: sample stabilization, preparation, pre-concentration and fractionation. J Chromatogr A 1093:156–166
55. Takahashi Y, Kumatani A, Shiku H, Matsue T (2017) Scanning probe microscopy for nanoscale electrochemical imaging. Anal Chem 89:342–357
56. Polcari D, Dauphin-Ducharme P, Mauzeroll J (2016) Scanning electrochemical microscopy: a comprehensive review of experimental parameters from 1989 to 2015. Chem Rev 116:13234–13278
57. Sun P, Laforge FO, Mirkin MV (2007) Scanning electrochemical microscopy in the 21st century. Phys Chem Chem Phys 9:802–823
58. Momotenko D, Byers JC, McKelvey K, Kang M, Unwin PR (2015) High-speed electrochemical imaging. ACS Nano 9:8942–8952
59. Williamson MJ, Tromp RM, Vereecken PM, Hull R, Ross FM (2003) Dynamic microscopy of nanoscale cluster growth at the solid–liquid interface. Nat Mater 2:532–536
60. Radisic A, Vereecken PM, Hannon JB, Searson PC, Ross FM (2006) Quantifying electrochemical nucleation and growth of nanoscale clusters using real-time kinetic data. Nano Lett 6:238–242
61. Hodnik N, Dehm G, Mayrhofer KJJ (2016) Importance and challenges of electrochemical in situ liquid cell electron microscopy for energy conversion research. Acc Chem Res 49:2015–2022
62. Stuart EJE, Tschulik K, Omanović D, Cullen JT, Jurkschat K, Crossley A et al (2013) Electrochemical detection of commercial silver nanoparticles: identification, sizing and detection in environmental media. Nanotechnology 24:444002
63. Moretto LM, Kalcher K (eds) (2015) Environmental analysis by electrochemical sensors and biosensors. Springer, New York
64. Wagner T, Lazar J, Schnakenberg U, Böker A (2016) In situ electrochemical impedance spectroscopy of electrostatically driven selective gold nanoparticle adsorption on block copolymer lamellae. ACS Appl Mater Interfaces 8:27282–27290
65. Proll G, Markovic G, Fechner P, Proell F, Gauglitz G (2017) Reflectometric interference spectroscopy. In: Rasooly A, Prickril B (eds) Biosensors and biodetection. Springer, New York, pp 207–220
66. Hänel C, Gauglitz G (2002) Comparison of reflectometric interference spectroscopy with other instruments for label-free optical detection. Anal Bioanal Chem 372:91–100
67. Gauglitz G (2005) Multiple reflectance interference spectroscopy measurements made in parallel for binding studies. Rev Sci Instrum 76:062224
68. Terrettaz S, Stora T, Duschl C, Vogel H (1993) Protein binding to supported lipid membranes: investigation of the cholera toxin-ganglioside interaction by simultaneous impedance spectroscopy and surface plasmon resonance. Langmuir 9:1361–1369
69. Olsson ALJ, Quevedo IR, He D, Basnet M, Tufenkji N (2013) Using the quartz crystal microbalance with dissipation monitoring to evaluate the size of nanoparticles deposited on surfaces. ACS Nano 7:7833–7843
70. Chen Q, Xu S, Liu Q, Masliyah J, Xu Z (2016) QCM-D study of nanoparticle interactions. Adv Colloid Interf Sci 233:94–114
71. Tellechea E, Johannsmann D, Steinmetz NF, Richter RP, Reviakine I (2009) Model-independent analysis of QCM data on colloidal particle adsorption. Langmuir 25:5177–5184
72. Teigell Beneitez N, Missinne J, Schleipen J, Orsel J, Prins MWJ, Van Steenberge G (2014) Polymer slab waveguides for the optical detection of nanoparticles in evanescent field based biosensors. Proc SPIE 8954:89540Q
73. Özdemir ŞK, Zhu J, Yang X, Peng B, Yilmaz H, He L et al (2014) Highly sensitive detection of nanoparticles with a self-referenced and self-heterodyned whispering-gallery Raman microlaser. Proc Natl Acad Sci 111:E3836–E3844
74. Baaske M, Vollmer F (2012) Optical resonator biosensors: molecular diagnostic and nanoparticle detection on an integrated platform. ChemPhysChem 13:427–436

75. Fujimaki M, Nomura K, Sato K, Kato T, Gopinath SCB, Wang X et al (2010) Detection of colored nanomaterials using evanescent field-based waveguide sensors. Opt Express 18:15732
76. Gopinath SCB, Awazu K, Fujimaki M (2010) Detection of influenza viruses by a waveguide-mode sensor. Anal Methods 2:1880
77. Liedberg B, Nylander C, Lunstrom I (1983) Surface plasmon resonance for gas detection and biosensing. Sensors Actuators 4:299–304
78. Homola J (2008) Surface plasmon resonance sensors for detection of chemical and biological species. Chem Rev 108:462–493
79. Jung LS, Campbell CT, Chinowsky TM, Mar MN, Yee SS (1998) Quantitative interpretation of the response of surface plasmon resonance sensors to adsorbed films. Langmuir 14:5636–5648
80. Rebe Raz S, Leontaridou M, Bremer MGEG, Peters R, Weigel S (2012) Development of surface plasmon resonance-based sensor for detection of silver nanoparticles in food and the environment. Anal Bioanal Chem 403:2843–2850
81. Klemm F, Johnson R, Mirsky VM (2015) Binding of protein nanoparticles to immobilized receptors. Sensors Actuators B Chem 208:616–621
82. Canovi M, Lucchetti J, Stravalaci M, Re F, Moscatelli D, Bigini P et al (2012) Applications of surface plasmon resonance (SPR) for the characterization of nanoparticles developed for biomedical purposes. Sensors 12:16420–16432
83. Rupert DLM, Lässer C, Eldh M, Block S, Zhdanov VP, Lotvall JO et al (2014) Determination of exosome concentration in solution using surface plasmon resonance spectroscopy. Anal Chem 86:5929–5936
84. Rupert DLM, Shelke GV, Emilsson G, Claudio V, Block S, Lässer C et al (2016) Dual-wavelength surface plasmon resonance for determining the size and concentration of sub-populations of extracellular vesicles. Anal Chem 88:9980–9988
85. Nizamov S, Mirsky VM (2011) Self-referencing SPR-biosensors based on penetration difference of evanescent waves. Biosens Bioelectron 28:263–269
86. Axelrod D (1989) Chapter 9. Total internal reflection fluorescence microscopy. In: Methods in cell biology. Elsevier, Imprint: Academic Press, pp 245–270
87. Block S, Fast BJ, Lundgren A, Zhdanov VP, Höök F (2016) Two-dimensional flow nanometry of biological nanoparticles for accurate determination of their size and emission intensity. Nat Commun 7:12956
88. Olsson T, Zhdanov VP, Höök F (2015) Total internal reflection fluorescence microscopy for determination of size of individual immobilized vesicles: theory and experiment. J Appl Phys 118:064702
89. Agnarsson B, Wayment-Steele HK, Höök F, Kunze A (2016) Monitoring of single and double lipid membrane formation with high spatiotemporal resolution using evanescent light scattering microscopy. Nanoscale 8:19219–19223
90. Agnarsson B, Lundgren A, Gunnarsson A, Rabe M, Kunze A, Mapar M et al (2015) Evanescent light-scattering microscopy for label-free interfacial imaging: from single Sub-100 nm vesicles to live cells. ACS Nano 9:11849–11862
91. Byrne GD, Pitter MC, Zhang J, Falcone FH, Stolnik S, Somekh MG (2008) Total internal reflection microscopy for live imaging of cellular uptake of sub-micron non-fluorescent particles. J Microsc 231:168–179
92. Velinov T, Asenovska Y, Marinkova D, Yotova L, Stoicova S, Bivolarska M et al (2011) Total internal reflection imaging of microorganism adhesion using an oil immersion objective. Colloids and Surfaces B: Biointerfaces 88(1):407–412
93. Wang W, Tao N (2014) Detection, counting, and imaging of single nanoparticles. Anal Chem 86:2–14
94. Zybin A, Kuritsyn YA, Gurevich EL, Temchura VV, Überla K, Niemax K (2009) Real-time detection of single immobilized nanoparticles by surface plasmon resonance imaging. Plasmonics 5:31–35

95. Yang C-T, Wu L, Liu X, Tran NT, Bai P, Liedberg B et al (2016) Exploiting surface-plasmon-enhanced light scattering for the design of ultrasensitive biosensing modality. Anal Chem 88:11924–11930
96. Rengevych OV, Beketov GV, Ushenin YV (2014) Visualization of submicron Si-rods by SPR-enhanced total internal reflection microscopy. Semicond Phys Quantum Electron Optoelectron 17(4):368–373
97. Loison O, Fort E (2013) Transmission surface plasmon resonance microscopy. Appl Phys Lett 103:133110
98. Meyer SA, Le REC, Etchegoin PG (2011) Combining surface plasmon resonance (SPR) spectroscopy with surface-enhanced Raman scattering (SERS). Anal Chem 83:2337–2344
99. Meyer SA, Auguié B, Le Ru EC, Etchegoin PG (2012) Combined SPR and SERS microscopy in the Kretschmann configuration. J Phys Chem A 116:1000–1007
100. Roy S, Kim J-H, Kellis JT, Poulose AJ, Robertson CR, Gast AP (2002) Surface plasmon resonance/surface plasmon enhanced fluorescence: an optical technique for the detection of multicomponent macromolecular adsorption at the solid/liquid interface. Langmuir 18:6319–6323
101. Balaa K, Devauges V, Goulam Y, Studer V, Lévêque-Fort S, Fort E (2009) Live cell imaging with surface plasmon-mediated fluorescence microscopy. SPIE-OSA 7367:736710
102. Thariani R, Yager P (2010) Imaging of surfaces by concurrent surface plasmon resonance and surface plasmon resonance-enhanced fluorescence. Peccoud J, editor. PLoS One 5:e9833
103. Avci O, Ünlü N, Özkumur A, Ünlü M (2015) Interferometric reflectance imaging sensor (IRIS) – a platform technology for multiplexed diagnostics and digital detection. Sensors 15:17649–17665
104. Sevenler D, Ünlü NL, Ünlü MS (2015) Nanoparticle biosensing with interferometric reflectance imaging. In: Vestergaard MC, Kerman K, Hsing I-M, Tamiya E (eds) Nanobiosensors and nanobioanalyses. Springer, Tokyo, pp 81–95
105. Ortega-Arroyo J, Kukura P (2012) Interferometric scattering microscopy (iSCAT): new frontiers in ultrafast and ultrasensitive optical microscopy. Phys Chem Chem Phys 14:15625
106. Piliarik M, Sandoghdar V (2014) Direct optical sensing of single unlabelled proteins and super-resolution imaging of their binding sites. Nat Commun 5:4495
107. Lobinski R, Szpunar J (eds) (2003) Hyphenated techniques in speciation analysis. Royal Society of Chemistry, Cambridge
108. Cazes J (ed) (2010) Encyclopedia of chromatography, 3rd edn. CRC Press, Boca Raton
109. Messaud FA, Sanderson RD, Runyon JR, Otte T, Pasch H, Williams SKR (2009) An overview on field-flow fractionation techniques and their applications in the separation and characterization of polymers. Prog Polym Sci 34:351–368
110. Baalousha M, Stolpe B, Lead JR (2011) Flow field-flow fractionation for the analysis and characterization of natural colloids and manufactured nanoparticles in environmental systems: a critical review. J Chromatogr A 1218:4078–4103
111. Scott D, Harding SE, Rowe A (eds) (2005) Introduction to differential sedimentation. analytical ultracentrifugation. Royal Society of Chemistry, Cambridge, pp 270–290
112. Scott DJ, Harding SE, Rowe AJ, Royal Society of Chemistry (Great Britain) (eds) (2005) Analytical ultracentrifugation: techniques and methods. RSC Publishing, Cambridge
113. Krpetić Ž, Davidson AM, Volk M, Lévy R, Brust M, Cooper DL (2013) High-resolution sizing of monolayer-protected gold clusters by differential centrifugal sedimentation. ACS Nano 7:8881–8890
114. Anderson W, Kozak D, Coleman VA, Jämting ÅK, Trau M (2013) A comparative study of submicron particle sizing platforms: accuracy, precision and resolution analysis of polydisperse particle size distributions. J Colloid Interface Sci 405:322–330
115. Poda AR, Bednar AJ, Kennedy AJ, Harmon A, Hull M, Mitrano DM et al (2011) Characterization of silver nanoparticles using flow-field flow fractionation interfaced to inductively coupled plasma mass spectrometry. J Chromatogr A 1218:4219–4225

116. Baalousha M, Kammer FVD, Motelica-Heino M, Hilal HS, Le Coustumer P (2006) Size fractionation and characterization of natural colloids by flow-field flow fractionation coupled to multi-angle laser light scattering. J Chromatogr A 1104:272–281
117. Rothenhauesler B, Knoll W (1988) Surface plasmon microscopy. Lett Nat 332:615–617
118. Brockman JM, Nelson BP, Corn RM (2000) Surface plasmon resonance imaging measurements of ultrathin organic films. Annu Rev Phys Chem 51:41–63
119. Campbell C, Kim G (2007) SPR microscopy and its applications to high-throughput analyses of biomolecular binding events and their kinetics. Biomaterials 28:2380–2392
120. Boecker D, Zybin A, Niemax K, Grunwald C, Mirsky VM (2008) Noise reduction by multiple referencing in surface plasmon resonance imaging. Rev Sci Instrum 79:023110
121. Rich RL, Cannon MJ, Jenkins J, Pandian P, Sundaram S, Magyar R et al (2008) Extracting kinetic rate constants from surface plasmon resonance array systems. Anal Biochem 373:112–120
122. Halpern AR, Wood JB, Wang Y, Corn RM (2014) Single-nanoparticle near-infrared surface plasmon resonance microscopy for real-time measurements of DNA hybridization adsorption. ACS Nano 8:1022
123. Viitala L, Maley AM, Fung HWM, Corn RM, Viitala T, Murtomäki L (2016) Surface plasmon resonance imaging microscopy of liposomes and liposome-encapsulated gold nanoparticles. J Phys Chem C 120:25958–25966
124. Cho K, Fasoli JB, Yoshimatsu K, Shea KJ, Corn RM (2015) Measuring Melittin uptake into hydrogel nanoparticles with near-infrared single nanoparticle surface plasmon resonance microscopy. Anal Chem 87:4973–4979
125. Wang S, Shan X, Patel U, Huang X, Lu J, Li J et al (2010) Label-free imaging, detection, and mass measurement of single viruses by surface plasmon resonance. Proc Natl Acad Sci 107:16028–16032
126. Huang B, Yu F, Zare RN (2007) Surface plasmon resonance imaging using a high numerical aperture microscope objective. Anal Chem 79:2979–2983
127. Somekh MG, Liu S, Velinov TS, See CW (2000) High-resolution scanning surface-plasmon microscopy. Appl Opt 39:6279–6287
128. Peterson AW, Halter M, Tona A, Plant AL (2014) High resolution surface plasmon resonance imaging for single cells. BMC Cell Biol 15:35
129. Peterson AW, Halter M, Plant AL, Elliott JT (2016) Surface plasmon resonance microscopy: achieving a quantitative optical response. Rev Sci Instrum 87:093703
130. Vander R, Lipson SG (2009) High-resolution surface-plasmon resonance real-time imaging. Opt Lett 34:37–39
131. Shan X, Díez-Pérez I, Wang L, Wiktor P, Gu Y, Zhang L et al (2012) Imaging the electrocatalytic activity of single nanoparticles. Nat Nanotechnol 7:668–672
132. Fang Y, Wang W, Wo X, Luo Y, Yin S, Wang Y et al (2014) Plasmonic imaging of electrochemical oxidation of single nanoparticles. J Am Chem Soc 136:12584–12587
133. Yu H, Shan X, Wang S, Chen H, Tao N (2014) Plasmonic imaging and detection of single DNA molecules. ACS Nano 8:3427–3433
134. Fang Y, Wang H, Yu H, Liu X, Wang W, Chen H-Y et al (2016) Plasmonic imaging of electrochemical reactions of single nanoparticles. Acc Chem Res 49:2614–2624
135. Wo X, Luo Y, Tao N, Wang W, Chen H-Y (2016) Measuring the number concentration of arbitrarily-shaped gold nanoparticles with surface plasmon resonance microscopy. SCIENCE CHINA Chem 59:843–847
136. Wang Y, Shan X, Wang H, Wang S, Tao N (2017) Plasmonic imaging of surface electrochemical reactions of single gold nanowires. J Am Chem Soc 139:1376–1379
137. Maley AM, Terada Y, Onogi S, Shea KJ, Miura Y, Corn RM (2016) Measuring protein binding to individual hydrogel nanoparticles with single-nanoparticle surface plasmon resonance imaging microscopy. J Phys Chem C 120:16843–16849
138. Sasian JM (1992) Image plane tilt in optical systems. Opt Eng 31:527–532
139. Smith WJ (2000) Modern optical engineering: the design of optical systems, 3rd edn. McGraw-Hill, New York

140. Laplatine L, Leroy L, Calemczuk R, Baganizi D, Marche PN, Roupioz Y et al (2014) Spatial resolution in prism-based surface plasmon resonance microscopy. Opt Express 22:22771
141. Schasfoort RBM, Tudos AJ (2008) Handbook of surface plasmon resonance. RSC Publishing, Cambridge
142. Nizamov S, Scherbahn V, Mirsky VM (2016) Detection and quantification of single engineered nanoparticles in complex samples using template matching in wide-field surface plasmon microscopy. Anal Chem 88:10206–10214
143. Sidorenko I, Nizamov S, Hergenröder R, Zybin A, Kuzmichev A, Kiwull B et al (2016) Computer assisted detection and quantification of single adsorbing nanoparticles by differential surface plasmon microscopy. Microchim Acta 183:101–109
144. Scherbahn V, Nizamov S, Mirsky VM (2016) Plasmonic detection and visualization of directed adsorption of charged single nanoparticles to patterned surfaces. Microchim Acta 183:2837–2845
145. Nizamov S, Kasian O, Mirsky VM (2016) Individual detection and electrochemically assisted identification of adsorbed nanoparticles by using surface plasmon microscopy. Angew Chem Int Ed 55:7247–7251
146. Nizamov S, Scherbahn V, Mirsky VM (2015) Self-referencing SPR-sensor based on integral measurements of light intensity reflected by arbitrarily distributed sensing and referencing spots. Sensors Actuators B Chem 207:740–747
147. Nizamov S, Scherbahn V, Mirsky VM (2017) Ionic referencing in surface plasmon microscopy: visualization of the difference in surface properties of patterned monomolecular layers. Anal Chem 89:3873–3878
148. Zybin A, Shpacovitch V, Skolnik J, Hergenröder R (2017) Optimal conditions for SPR-imaging of nano-objects. Sensors Actuators B Chem 239:338–342
149. Weichert F, Gaspar M, Timm C, Zybin A, Gurevich EL, Engel M et al (2010) Signal analysis and classification for surface plasmon assisted microscopy of nanoobjects. Sensors Actuators B Chem 151:281–290
150. Radke RJ, Andra S, Al-Kofahi O, Roysam B (2005) Image change detection algorithms: a systematic survey. IEEE Trans Image Process 14:294–307
151. Lapresta-Fernández A, Salinas-Castillo A, Anderson de la Llana S, Costa-Fernández JM, Domínguez-Meister S, Cecchini R et al (2014) A general perspective of the characterization and quantification of nanoparticles: imaging, spectroscopic, and separation techniques. Crit Rev Solid State Mater Sci 39:423–458
152. von der Kammer F, Legros S, Hofmann T, Larsen EH, Loeschner K (2011) Separation and characterization of nanoparticles in complex food and environmental samples by field-flow fractionation. TrAC Trends Anal Chem 30:425–436
153. Lewis JP (1995) Fast template matching. Vision interface. Canadian Image Processing and Pattern Recognition Society, Quebec, pp 15–19
154. Wo X, Li Z, Jiang Y, Li M, Su Y, Wang W et al (2016) Determining the absolute concentration of nanoparticles without calibration factor by visualizing the dynamic processes of interfacial adsorption. Anal Chem 88:2380–2385
155. Love JC, Estroff LA, Kriebel JK, Nuzzo RG, Whitesides GM (2005) Self-assembled monolayers of thiolates on metals as a form of nanotechnology. Chem Rev 105:1103–1170
156. Shpacovitch V, Sidorenko I, Lenssen J, Temchura V, Weichert F, Müller H et al (2017) Application of the PAMONO-sensor for quantification of microvesicles and determination of nano-particle size distribution. Sensors 17:244
157. Shpacovitch V, Temchura V, Matrosovich M, Hamacher J, Skolnik J, Libuschewski P et al (2015) Application of surface plasmon resonance imaging technique for the detection of single spherical biological submicrometer particles. Anal Biochem 486:62–69
158. Demetriadou A, Kornyshev AA (2015) Principles of nanoparticle imaging using surface plasmons. New J Phys 17:013041
159. Demetriadou A (2015) The impact of natural modes in plasmonic imaging. Sci Rep 5:18247

160. Son T, Kim D (2015) Theoretical approach to surface plasmon scattering microscopy for single nanoparticle detection in near infrared region. Proc SPIE 9340:93400W
161. Lozovski V (2012) Visualization of Nano-sized objects by scattering of surface plasmon polariton theoretical aspects of the problem. J Comput Theor Nanosci 9:859–863
162. Gurevich EL, Temchura VV, Überla K, Zybin A (2011) Analytical features of particle counting sensor based on plasmon assisted microscopy of nano objects. Sensors Actuators B Chem 160:1210–1215
163. Yu H, Shan X, Wang S, Chen H, Tao N (2014) Molecular scale origin of surface plasmon resonance biosensors. Anal Chem 86:8992–8997
164. Concentrative properties of aqueous solutions: density, refractive index, freezing point depression, and viscosity. In: CRC Handbook of Chemistry and Physics, 87th ed Editor-in-Chief: David R. Lide (NIST). CRC Press/Taylor and Francis Group: Boca Raton, FL. 2006. 2608 pp. ISBN 0-8493-0487-3.
165. Syal K, Wang W, Shan X, Wang S, Chen H-Y, Tao N (2015) Plasmonic imaging of protein interactions with single bacterial cells. Biosens Bioelectron 63:131–137
166. Yang Y, Yu H, Shan X, Wang W, Liu X, Wang S et al (2015) Label-free tracking of single organelle transportation in cells with nanometer precision using a plasmonic imaging technique. Small 11:2878–2884

4 In Situ Localized Surface Plasmon Resonance Spectroscopy for Gold and Silver Nanoparticles

Ji Zhou and Bin Tang

Contents

J. Zhou
Hubei Collaborative Innovation Center for Advanced Organic Chemical Materials and Key Laboratory for the Synthesis and Application of Organic Functional Molecules, Ministry of Education and College of Chemistry and Chemical Engineering, Hubei University, Wuhan, China

B. Tang (✉)
National Engineering Laboratory for Advanced Yarn and Fabric Formation and Clean Production, Wuhan Textile University, Wuhan, China

Institute for Frontier Materials, Deakin University, Geelong, VIC, Australia
e-mail: bin.tang@deakin.edu.au

© Springer-Verlag GmbH Germany, part of Springer Nature 2018

C. S. S. R. Kumar (ed.), *In-situ Characterization Techniques for Nanomaterials*,
https://doi.org/10.1007/978-3-662-56322-9_4

1 Definition of the Topic

Localized surface plasmon resonance (LSPR) spectroscopy of metallic nanoparticles (NPs) is a powerful technique for chemical and biological sensing experiments. LSPR is responsible for the electromagnetic field enhancement that leads to surface-enhanced Raman scattering (SERS) and other surface-enhanced spectroscopic processes [1].

2 Introduction

Nanoparticles have been the subject of intense research over the last two decades. A large variety of shapes, sizes, and materials can now be synthesized, thus broadening the range of the chemical and physical properties accessible. Among them, metallic nanoparticles have been extensively studied for over 100 years due to their unique optical properties. Fundamentally, electromagnetic wave incident on the metallic nanoparticles induces a collective oscillation of free electrons at a resonant frequency, a phenomenon known as localized surface plasmon resonance (LSPR), which depends on the size, shape, and composition of the nanoparticle and relates sensitively to the refractive index of the surrounding environment. As a result of the LSPR, the absorption and scattering of light by nanoparticles, as well as the local electromagnetic field around the nanoparticles, will be strongly enhanced. The extremely intense and highly localized electromagnetic (EM) fields induced by LSPR make nanoparticles highly sensitive transducers of small changes in the local refractive index. These changes are exhibited in spectral shifts of extinction (absorption plus elastic light-scattering) and scattering spectra.

In general, LSPR instruments consist of three main components: a light source (white light or laser), the sample, and a detector. Common LSPR detection techniques are ultraviolet-visible (UV-vis) spectroscopy and dark-field scattering microscopy. The extinction spectrum of the nanoparticles is measured using UV-vis spectroscopy with excitation relying on a white light source. For transparent samples, light is passed directly through the sample. For nontransparent samples, an optical geometry suitable to study reflection is used. Imaging is achieved with dark-field microscopy where small regions, as well as single nanoparticles, are studied.

LSPR can be determined and measured by an extinction spectrum (scattering and absorption) at visible and near-infrared (NIR) wavelengths and in particular the peak wavelength (λ_{max}). Similar to the surface plasmon resonance (SPR), the LSPR is sensitive to changes in the local dielectric environment. Typically, an LSPR wavelength shift is measured for sensing changes in the local environment by researchers. The LSPR spectral shift has been implemented as a transduction strategy to investigate the molecular binding events and conformational changes and can provide steady-state and kinetic data.

In this chapter, we give a brief introduction on the influencing factors of LSPR. Subsequently, we present a comprehensive review on in situ characterization methods based on LSPR, including spectral monitoring, sensing, and imaging.

3 Influencing Factors of LSRP

LSPR extinction spectra including absorption and scattering spectra of gold and silver nanoparticles are strongly sensitive to their shape, size, surrounding medium, composition, and ensemble form, with wavelengths in the UV-vis and NIR regions. The applications based on LSPR promote the shape-controlled synthesis of noble metal nanoparticles and precise assembly of particles, which can tune deliberately LSPR features of plasmonic materials and eventually acquire desired plasmonic structures. In contrast, a relation between LSPR and influencing factors can provide people a simple and effective route to probe the information involved in noble metal nanoparticles, including shape, size, component, surrounding, and assembly state.

Noble metal nanoparticles are widely used in enhancing spectroscopies, biological sensing, and chemical sensing, because of the LSPR features. The size and shape of noble metal nanoparticles determine and control their unique plasmonic properties. Many strategies have been developed to fabricate the gold and silver nanoparticles with different shapes, such as spheres, triangular plates, hexagonal plates, bars, rods/wires, right bipyramids, concave cubes, cubes and tetrahedrons, octahedrons, decahedrons. The routes to synthesize gold and silver nanoparticles include chemical synthesis [2–4], seed-mediated growth [5–8], template-assisted synthesis, lithographic fabrication [9], and photo-mediated synthesis [10, 11].

3.1 Effect of Shape

LSPR features can be simulated and predicted by calculation methods, such as Mie theory, discrete dipole approximation (DDA) method, finite-difference time-domain (FDTD) method. The LSPR spectra of polygonal silver nanoparticles with equal volume but different shapes, including cubes, and truncated cubes (TC), spheres, icosahedrons, were calculated using DDA method by Cecilia Noguez [12]. Nanocubes exhibit multiple resonances with high multipolar order charge distributions. The dipolar resonance band of the nanocube blue-shifts as truncation increases. An intense and broad LSPR band produces when a blue-shifting dipolar resonance is overlapped the quadrupolar one. Compared with cubes, nanospheres shows a dipolar resonance band around 400 nm. Silver nanoplates including triangular, hexagonal, and circular plates generally display multiple LSPR bands due to their anisotropy. For example, triangular silver nanoplates synthesized by photoinduction of silver seeds present four LSPR bands at 770, 470, 410, and 340 nm, ascribed to in-plane dipole, in-plane quadrupole, out-of-plane dipole, and out-of-plane quadrupole plasmon resonance modes [11].

Nanorods made of noble metal exhibit two LSPR bands that are longitudinal plasmon band and transverse plasmon band, which are attributed to electron oscillation along the long and short axes of nanorods, respectively [6, 13]. For gold nanorods (Au NRs), the transverse plasmon band is located around 520 nm, insensitive to the changes of the rod size, and the surrounding refractive index [6, 14, 15], whereas the longitudinal plasmon band of Au nanorods is strongly sensitive to the

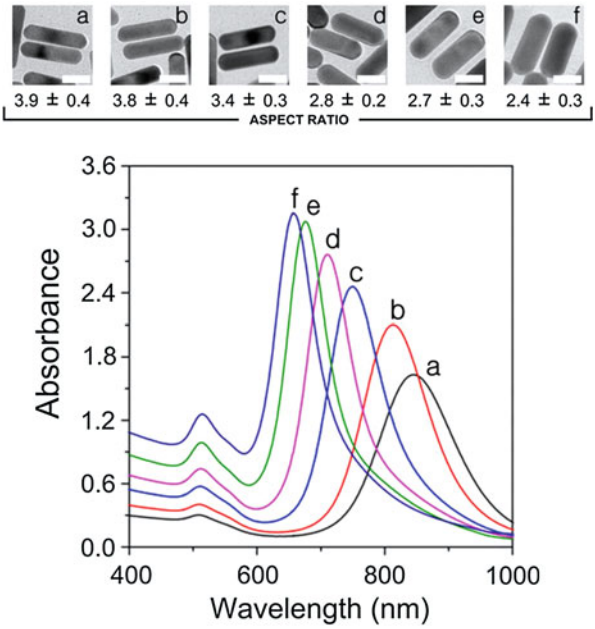

Fig. 4.1 TEM images of Au nanorods with different aspect ratios and their corresponding LSPR spectra (Reproduced with permission from Ref. [17]. Copyright 2013 American Chemical Society)

aspect ratio of nanorods. The changes of the aspect ratio of rods would make longitudinal plasmon band of AuNR vary. There is a linear coloration between the wavelength of longitudinal plasmon band (λ_{max}) and aspect ratio (AR) for AuNR, which is given as followed: [16]

$$\lambda_{max} = 95AR + 420 \tag{4.1}$$

LSPR of gold nanorods can be effectively tuned by controlling aspect the ratio of nanorods. Liz-Marzán et al. proposed a bimodal reducing agent system comprising salicylic acid and ascorbic acid to tailor the morphology and the optical properties of Au NRs. The longitudinal LSPR change to 650 from 850 nm when the AR values of Au NRs varied from 3.9 to 2.4, respectively (Fig. 4.1) [17].

Gold nanocubes, concave nanocubes, nanorods, and triangular nanoprisms were prepared by wet chemical seed-mediated approaches. Remarkably different dominated LSPR bands were observed corresponding to gold nanostructures with different shapes [18]. In a photochemically synthesis of silver nanodecahedra by LED irradiation, the corners of the silver nanodecahedra were round at early stage and sharpened as light irradiation prolonged, with a red-shift of LSPR band [19]. Combining experimental and simulated data, Qu et al. attributed the LSPR red-shift of silver nanodecahedra to the enhancement of corner sharpness. Through DDA simulation, Bansal and Verma brought up the same conclusion that sharp corner noble metal nanostructures present enhanced plasmonic features in comparison to rounded counterparts [20].

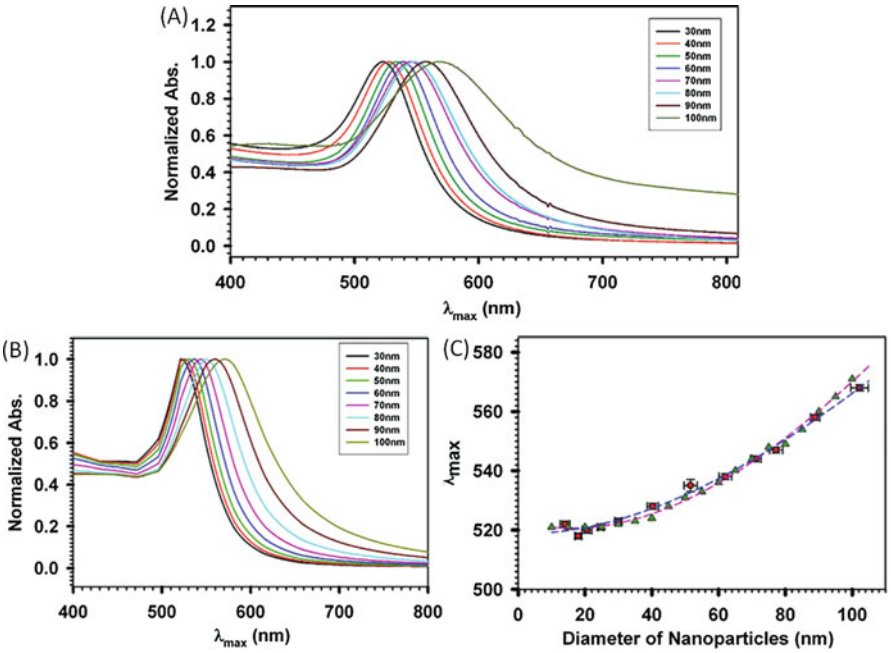

Fig. 4.2 (**a**) UV-vis spectra (normalized) and (**b**) simulated spectra of SP band (normalized) for Au nanoparticles with different particle sizes in aqueous solution. (**c**) Comparison between experimental and theoretical relationships for SPR band wavelength (λ_{max}) versus diameter of the nanoparticles (nm). Simulation data (triangles) and experimental data (circles) are taken from panel **a** and **b**. Dashed lines are fitting curves (Reproduced with permission from Ref. [21]. Copyright 2007 American Chemical Society)

3.2 Effect of Size

Dependence of LSPR on particle size was clearly reflected by a systematic study of the various trends. Zhong et al. investigated a correlation between the size of gold nanoparticles and their LSPR band properties [21]. The gold nanoparticles Au NPs with different diameters in aqueous solutions were synthesized and their UV-vis extinction spectra were recorded (Fig. 4.2a). The LSPR band red-shifted from 519 to 569 nm as the particle size increased from 30 to 100 nm, with a small broadening of the band at long wavelength. Simulated LSPR spectra of gold nanoparticles corresponding to different sizes were calculated through Mie theory (Fig. 4.2b). As the same as experimental data, the wavelength of SPR band increased with particle size. In comparison with the varying trend of LSPR wavelength, the correlation of size and LSPR from the theoretical data agreed with that from experimental data (Fig. 4.2c). The magnitude of LSPR extinction, as well as the relative contribution of scattering to the extinction, dramatically increases with an increase in gold nanosphere size from 20 to 80 nm, accompanying with a variation in the LSPR peaks of nanospheres from ~ 520 to 550 [22].

The size-dependent LSRP optical properties of sub-10-nm gold nanoparticles were investigated. Highly monodisperse and sub-10-nm gold nanoparticles (Au NPs) with a size range of 3.5 to 10 nm were synthesized by a kinetically controlled seed-growth method (Fig. 4.3a) [5]. LSPR band narrows and the peak position red-shifts from 505 to 517 nm as particle size increased from 3.6 to 11.3 nm (Fig. 4.3b, c). However, an inflection point appeared in the plot of LSPR wavelength of Au nanoparticles via particle size, corresponding to 8 nm of particles. In comparison with larger Au NPs, LSPR of the particles smaller than 8 nm showed higher sensitivity to size. Surface phenomena with a high percentage of surface atoms can contribute to the higher susceptibility of the gold nanoparticles with small size.

We also employed Mie theory to simulate the LSPR extinction spectra of silver seeds with different sizes [23]. It is supposed that silver seeds are spherical in shape. We modified the fitting program of the Mie model in the literature [24] to make it suitable for silver nanospheres. The simulated LSPR extinction spectra of silver spheres with radii from 1.0 to 10 nm were obtained, and the relationship between the LSPR wavelength and relative intensity and the silver nanoparticle size was disclosed. The results indicate that the LSPR peak of the silver nanospheres red-shifts in position and increases in intensity as increasing particle size.

A large quantity of well-defined silver nanodisks were prepared from nanoprisms through heat treatment [25]. The diameter of silver nanodisks decreased as heating time prolonged (Fig. 4.4a). Thicknesses of these nanodisks were similar around 13 nm. The in-plane dipole resonance band of silver nanodisks at long wavelength blue-shifted from 604 to 472 nm when the diameter of disks varied from 73.2 to 39.3 nm (Fig. 4.4b). In addition, circular gold nanodisks were obtained by etching nanoprisms using $HAuCl_4$ in the presence of CTAB [26]. The diameter of the nanodisk was tuned by changing sizes of starting triangular prism. LSPR bands ranged from 650 to 1000 nm as the diameters of circular disks were changed from 30 to 125 nm. Simulation of disk extinction spectra with DDA demonstrated the LSPR change trends of nanodisks as a function of disk diameter.

Silver nanocubes with different edge lengths in the range of 36 ~ 172 nm were obtained during a polyol synthesis process [27]. The dipole peak in the extinction spectra of the silver nanocubes exhibited a continuous red-shift as the increase in edge length increased. The wavelength of LSPR peak had a nearly linear relationship with the edge length of nanocubes. It was suggested that the extinction spectra could be used to monitor and control the size of nanocubes during a synthesis process [28].

3.3 Effect of Component

Compositions of nanoparticles determine the intrinsic optical properties. Gold and silver nanoparticles are the most widely used as plasmonic materials with LSPR lying in the visible region. Van Duyne et al. firstly compared experimentally the LSPR of Cu, Ag, and Au nanoparticles with similar size and shape [29]. These nanoparticles were fabricated by nanosphere lithography (NSL) with the parameters of $D = 390$ nm, $d_m = 50$ nm and displayed the maximum LSRP extinction bands at

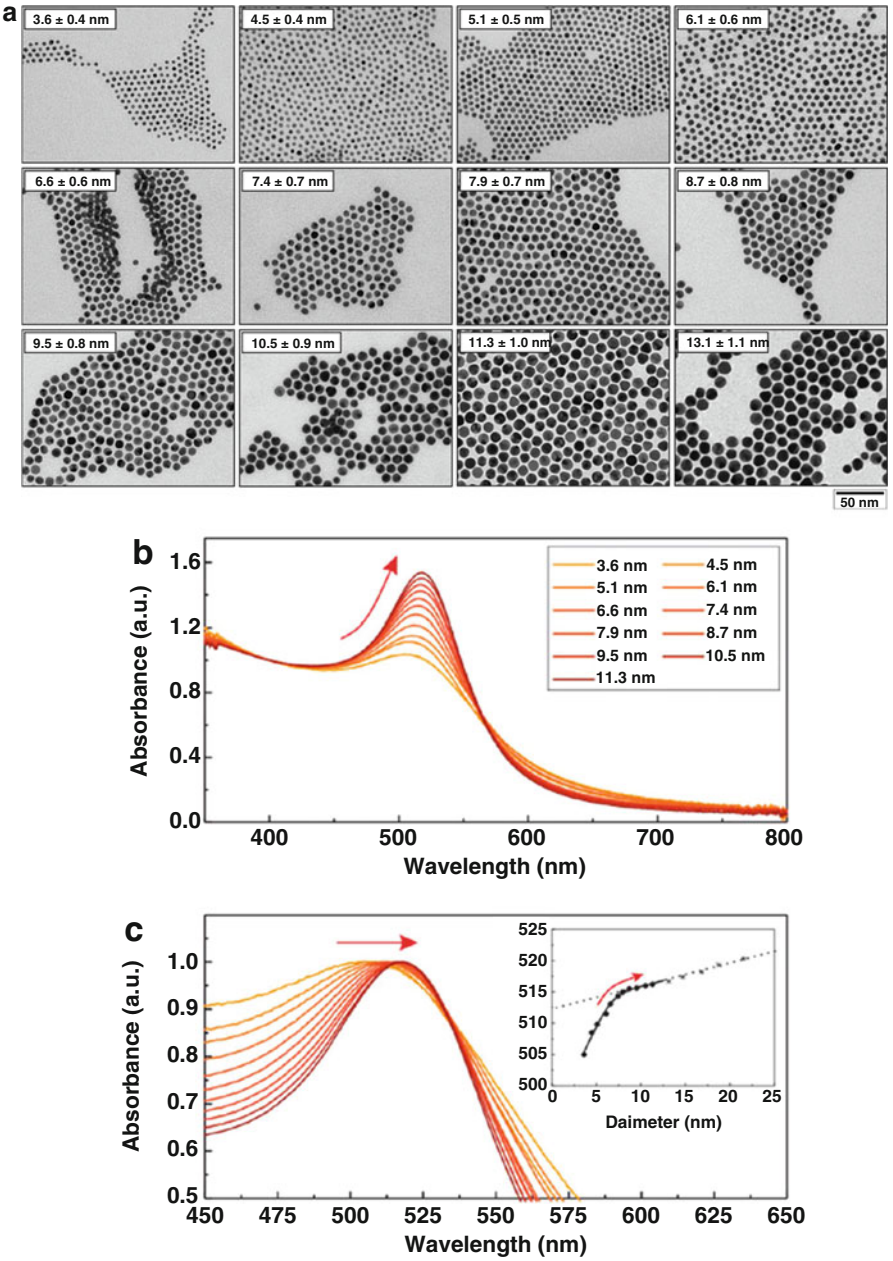

Fig. 4.3 (**a**) TEM images of Au seed particles and those obtained after different growth steps. Optical properties of selected Au colloids obtained after different growth steps. (**b**) normalized at 400 nm and (**c**) normalized at the LSPR peak maximum. Arrows indicate evolution of the LSPR peak as increasing the size of the Au NPs. Inset graph is a plot of the position of the LSPR peak as a function of particle size (Reproduced with permission from Ref. [5]. Copyright 2016 American Chemical Society)

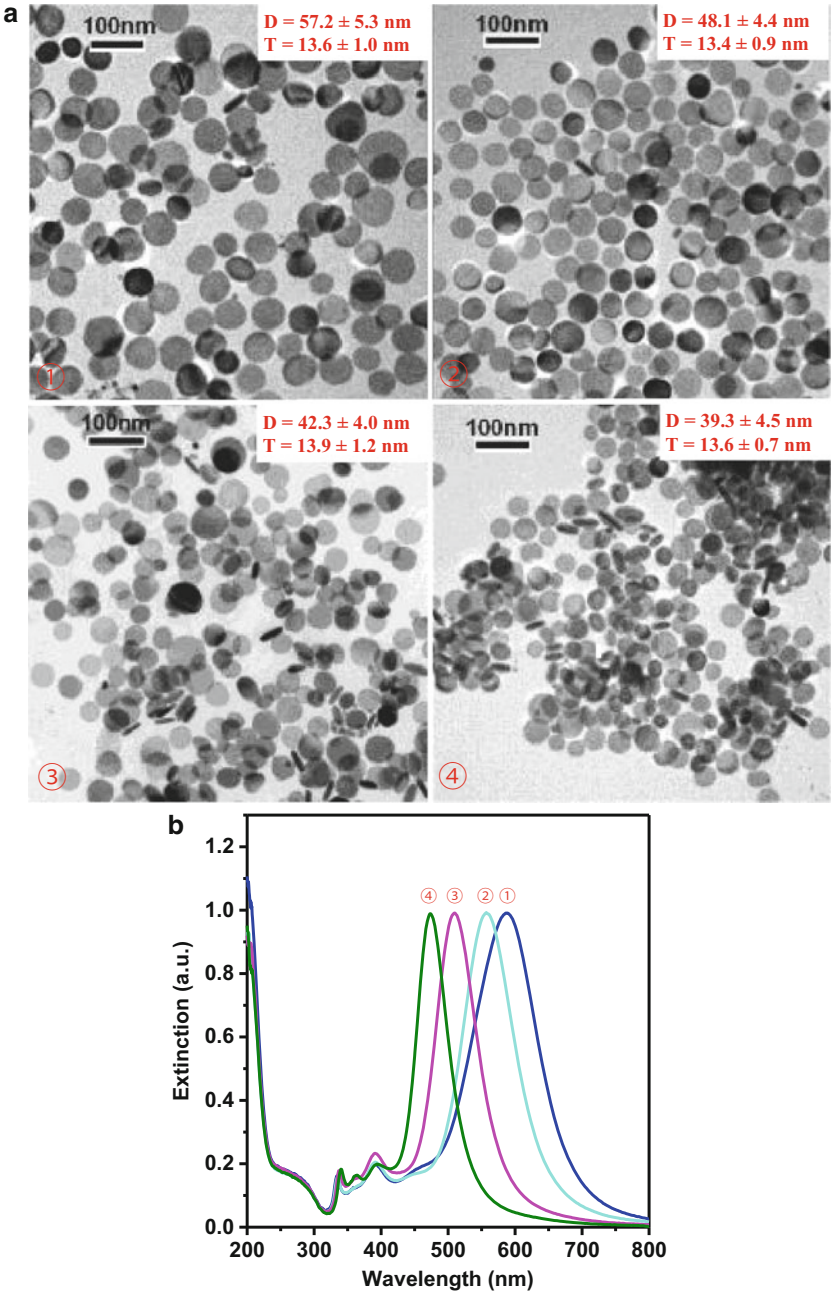

Fig. 4.4 (**a**) TEM images and (**b**) normalized UV-vis spectra of silver nanodisks with different diameters. D and T denote diameter and thickness of nanodisk, respectively (Reproduced with permission from Ref. [25]. Copyright 2008 American Chemical Society)

698, 639, and 787 nm, according to Cu, Ag, and Au, respectively. Cu and Au exhibit longer maximum LSPR wavelength than Ag nanoparticle arrays of similar geometry. The experimental results are consisted with trends from DDA calculations. In addition to Cu, Al nanostructures as promising plasmonic materials have extensive interests. Different from gold and silver nanoparticles, small Al nanoparticles can show sharp LSPR bands with high intensity in UV and deep-UV (DUV) regions. Tang and coworkers fabricated large-scale Al nanoparticle arrays (≈1.2 cm^2) using the AAO template technique [30]. The LSPR bands were tuned by changing the out-of-plane height of nanoparticle arrays. Combining with the wet chemical etching, they tuned LSPR peak of Al nanoparticles to 234 from 292 nm.

Bimetallic nanostructures can extend the range of LSPR bands from a single composition. Calculation studies based on DDA method have predicted the change trend of LSPR as the component of one metal varied [31]. It is found that LSPR is sensitive to the surrounding medium refractive index, showing a distinct redshift with increasing the surrounding medium refractive index. Au-Ag core-shell nanostructure exhibits a strong coupling between the core and shell plasmon resonance modes. The coupled resonance mode wavelengths show dependence on the layer thickness and the composition of core and shell metal. LSPR can be tuned over an extended wavelength range by adjusting the ratio of core to shell.

Alloying of different noble metals is believed to be an optional strategy for tuning the LSPR wavelength. Verbruggen and coworkers proposed a semiempirical model to study the plasmonic band wavelength of water-suspended gold-silver alloy nanoparticles by insights into the combined effect of alloy composition and particle size [32]. The LSPR wavelength is derived from the extinction spectra of monodisperse spherical nanoparticles that were simulated based on available experimental dielectric constant data and accounts for particle size by using Mie theory with the software package MiePlot (v4300). A mesh plot was provided to display the range of the plasmonic band wavelengths for different sizes and compositions based on simulated results. The LSPR wavelength can effectively be tuned by changing the $Au_xAg_{(1-x)}$ alloy composition (gold fraction termed by x) and particle size. The LSPR wavelength red-shifts as increasing particle size, mainly due to retardation effects for particles larger than 20–30 nm, whereas the effect of alloy composition dominates the LSPR wavelength of nanoparticles.

Yin et al. investigated systematically the plasmonic property of fully alloyed Ag/Au nanospheres through a practical experimental process [33]. First, Au nanoparticles of a desired size were synthesized by a seed-mediated growth method as a starting material. Subsequently, silver was deposited on Au nanoparticles to produce Au@Ag core/shell nanoparticles, with suppressing self-nucleation of Ag by acetonitrile. After silica coating, Au@Ag nanoparticles were annealed around 1000 °C in a nitrogen atmosphere to accelerate diffusion efficiency of the Ag and Au atoms, with complete alloying of Ag and Au. Final alloyed Ag/Au nanospheres were obtained after removing the silica with NaOH solution and then being transferred to water. The UV-vis extinction spectra of the Ag/Au alloy nanospheres with different compositions were measured (Fig. 4.5). The overall spectra of Au@Ag core-shell nanoparticles with a thin layer of Ag exhibited a relatively broad peak, due

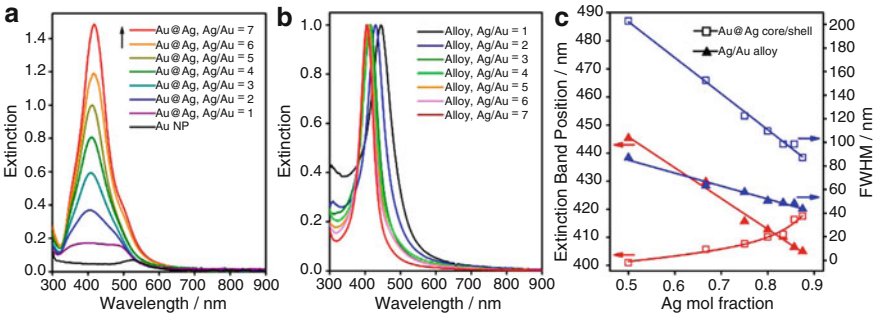

Fig. 4.5 Spectroscopic study of the core/shell and alloy nanoparticles. (**a**) Optical evolution of the Au@Ag core/shell nanoparticles during seeded growth of Ag on Au nanoparticles. The spectra have been normalized relative to the maximum of the Au@Ag (Ag/Au = 5) spectrum. (**b**) UV-vis extinction spectra of Ag/Au alloy nanospheres with different Ag/Au ratios, which have been normalized relative to their respective maxima. (**c**) Dependence of the band position and full-width at half-maximum (FWHM) of extinction peaks of the Au@Ag core/shell and Ag/Au alloy nanoparticles on the Ag mole fraction (Reproduced with permission from Ref. [33]. Copyright 2014 American Chemical Society)

to an emergence of a shoulder peak analogous to a combination of the spectra from the respective Au and Ag. The spectral change of nanoparticles indicates that the LSPR of a noble metal nanoparticle is very sensitive to its outer shell composition. The scattering effect of the Ag-Au boundary on the conduction electrons leads to damping of the surface plasmons, which results in the broadening of LSPR band. LSPR spectra of Au@Ag nanoparticles is approximating to that of single-composition Ag nanoparticles as the Ag layer is thickening (Fig. 4.5a). After annealing, the Ag/Au alloy nanospheres displayed a nearly symmetric and much narrower compared with core/shell nanoparticles (Fig. 4.5b). The particular features of Ag/Au alloy nanospheres, including the monodispersity and the uniform spherical shape, single crystals containing no crystallographic defects and homogeneously distribution without compositional interface, contribute to their distinguishing spectral properties. The mole fraction of Ag in alloy nanospheres resulted in a blue-shift of LSPR extinction spectra. The Ag/Au ratio was suggested to dominate the band shift of the alloy nanospheres. It was found that the bandwidth of the alloy nanospheres depended linearly on the mole fraction of Ag and much narrower than that of their core/shell counterparts.

3.4 Effect of Surrounding

Dielectric medium around nanoparticles influences the LSPR properties of noble metal nanoparticles. Spectral changes caused by a change in refractive index (Δn) of the surrounding dielectric medium are the primary mechanism of LSPR-based sensing. The subtle change in local dielectric environment can be reflected by the wavelength shift of LSPR. Tuersun investigated the effect of the refractive index of

ambient medium on LSPR extinction spectra of single gold and silver nanobars with length of 100 nm and width of 40 nm, using DDA method [34]. A series of simulated LSPR spectra of gold and silver nanobars were obtained for different refractive indexes at an incident angle. The plasmon resonance wavelengths of gold and silver nanobars red-shifts with the increase of the refractive index of ambient medium.

The rapid decay of amplitude of electromagnetic (EM) near-field from metal surface along the direction brings about the evanescent wave character to EM near-field. The characteristic EM decay length can be used to describe the decay of the evanescent EM field. Poly(styrene sulfonate) (PSS) and poly(allyl amine hydrochloride) (PAH) were coated on the surface of gold nanorods by layer-by-layer (LBL) electrostatic assembly method and the influence of gold nanorod dimensions on distance-dependent LSPR sensitivity and electromagnetic (EM) decay length were investigated [16]. LSPR wavelength red-shifted and intensity of LSPR increased as the layer number of polyelectrolytes, because of the increase in the refractive index after LBL coating. EM decay length increased linearly with an increase in length and diameter of the gold nanorods (AuNRs) with similar aspect ratio. Relation of LSPR wavelength shift and EM decay length is described by the following equation.

$$R = \eta B(\Delta\eta)\left(1 - \exp\left(-\frac{2d}{l}\right)\right) \tag{4.2}$$

where R is LSPR shift, ηB is the refractive index (RI) sensitivity, $\Delta\eta$ is the RI change of the surrounding medium, d is the thickness of the adsorbed molecular layer, and l is the EM decay length [16, 18]. LSPR changes of noble metal nanoparticles with a certain morphology related to dielectric changes can be estimated by Eq. 4.2. Dependence of the sensitivity for the RI changes (ηB) on the magnitude of the spectral change (i.e., LSPR shift) was investigated by Mirkin and Aili [18]. The RI sensitivity values for gold nanocubes, concave nanocubes, nanorods, and nanoprisms were compared. Their experimental results demonstrated a linear relationship between the bulk RI sensitivity and the wavelength of the LSPR peak (Fig. 4.6). The lowest and highest RI sensitivity values were obtained from nanocubes ($<$100 nm RIU^{-1}) and nanorods ($\approx$400 nm RIU^{-1}), respectively. The RI sensitivity of nanoparticle not only associates with particle morphology, but also depends on the LSPR wavelength.

3.5 Coupling Effect

A strong coupling plasmon resonance modes appeared between the core and shell in Au-Ag core-shell nanostructure. The coupled resonance mode wavelength depends on the layer thickness and the metal composition of core and shell, leading to tunning of wavelength of LSPR for nanoparticles in an extended range. The extinction and absorption efficiencies of Au-Ag core-shell were calculated. For fixed outer Ag shell ($r_2 = 20$ nm) and water medium ($n = 1.00$), the extinction and absorption spectra at long wavelength red-shift from 420 nm ($r_1 = 8$ nm) to 515 nm ($r_1 = 19$ nm) with an

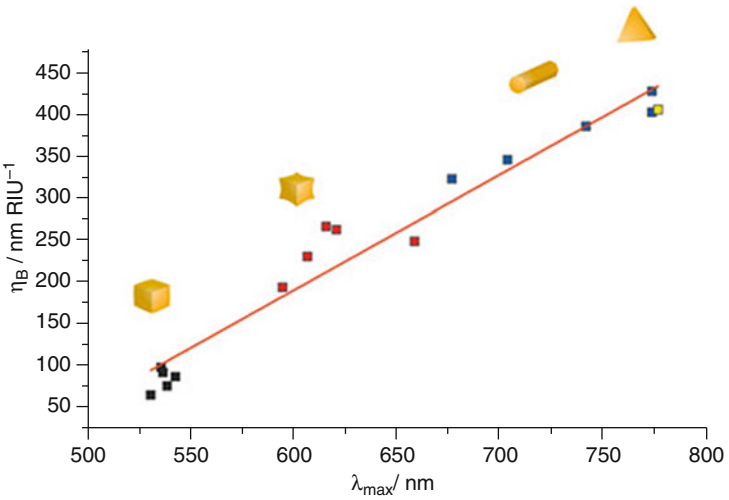

Fig. 4.6 Experimental bulk RI sensitivity (η_B) for the different gold nanoparticles plotted against their corresponding spectral plasmon peak position (λ_{max}). A linear regression (red line) shows the linear relationship between the bulk RI sensitivity and the LSPR peak position (Reprinted with permission from Ref. [18]. Copyright 2016 John Wiley & Sons, Inc)

increase in inner core radius. The hybridization (coupling) between the sphere and cavity plasmon controlled by the shell thickness resulted to red-shift of LSPR of core-shell nanostructures. Compared with the bare nanosphere of the same size, bimetallic core-shell nanostructures show additional tunability of longer LSPR band wavelength. Particle shape also affects notably the coupling of LSPR from core-shell nanostructures. Gao and Yin investigated the LSPR properties of spherical and plate-like Ag-Au core-shell nanostructures through theoretical and experimental methods [35]. Using finite element method (FEM), Ag nanospheres as typical isotropic plasmonic nanoparticles showed a strong LSPR band at 410 nm, whereas the corresponding Ag-Au core-shell nanoparticles displayed a new LSPR band at 510 nm. Also the electric field intensity of Ag-Au core-shell nanoparticles in their proximity decreased dramatically in comparison with the Ag nanospheres at their respective resonance wavelengths. However, the LSPR properties of the Ag-Au core-shell nanoplates were similar to those of the pure Au nanoplates, due to very close extinction efficiency and local electric field enhancement of the nanocrystals. Ag core in core-shell nanoplates resulted in a redshift of the LSPR band relative to that of the pure Au ones, revealing that the Ag core affected the overall LSPR properties to a small extent. The Ag-Au core-shell nanoplates exhibited the same LSPR property as that of pure Au nanoplates when a thick shell of Au is fabricated on particle surfaces. Compared with the pure Ag nanoplates, Ag@Au core/shell nanoplates showed lower electric field intensity. The plasmonic features of the core-shell nanostructures are strongly dependent on particle shape anisotropy.

In addition to core-shell nanoparticles, the LSPR bands of gold nanoshells present optical cross-sections comparable to and even higher than the nanospheres, tending

to the NIR region [22]. Increasing the total nanoshell size or the ratio of the core-shell increased sharply the LSPR wavelength. A linear relation between the total extinction of nanoshells and their total size was observed. Increasing the nanoshell size or decreasing the ratio of the core/shell radius increased rapidly the relative scattering contribution to the extinction spectra.

Dimers and trimers of noble metal nanoparticles are common plasmon coupling examples. Coupling between particles generates new LSPR features and creates hot spots with strong electric field in the gap between the particles [36]. Zhao et al. studied the plasmonic properties of single Ag nanospheres and the plasmon interactions in assemblies of Ag nanosphere dimers and trimers [37]. Silver nanospheres were synthesized by etching prefabricated silver nanocubes and deposited silver nanospheres on coverglass. Single silver nanospheres presented a major scattering peak around 453 nm due to the interaction of electromagnetic waves with the free electrons of Ag nanospheres and a side peak at 625 nm from coupling between nanosphere and substrate. The assemblies of Ag nanosphere dimers displayed two scattering peaks located at ~460 nm and ~644 nm. Based on the theoretical simulation using the T-matrix method, the shorter peak generated from the weakly coupled dipoles arranged shoulder by shoulder and the peak at longer wavelength rises from the strongly interacting dipoles arranged head to tail. The scattering spectra showed three peaks located at 486, 545, and 658 nm, respectively. Compared to the scattering spectra of the dimers, a new peak at 545 nm appears in the scattering spectra of the trimer, attributed to the symmetry breaking of the system. LSPR properties of metal nanoparticles rely on the coupling effect between nanoparticles. Halas et al. discussed the influence of coupling on plasmonic properties of noble metal nanoparticles in their review [38]. Coupled LSPR spectra of assemblies of plasmonic nanoparticles can serve as indicators and rulers for measuring nanoscale distances and dynamic distance changes in biological and macromolecular systems. The optical features for assemblies consisting of a Au nanosphere attached to an Au nanoplate were investigated by correlating scattering spectra with morphologies for a large set of individual constructs [39]. Attachment of the nanosphere resulted in considerable change of the LSPR spectrum of the nanoplate under optimized condition. Dark-field spectroscopy was employed to measure the scattering spectra of single nanoplate and nanoplate/nanosphere assemblies. After nanosphere attachment, a large redshift was observed in the dipolar LSPR mode of the nanoplate rising from strong coupling between the nanoplate and the nanosphere (Fig. 4.7). These spectral changes can be used as the optical readout for measuring distance changes occurring in the molecular linker of the nanoplate/nanosphere dimer. Quantitative comparison of the sensor response of individual constructs can be achieved by using the magnitude of this readout, for application in plasmon rulers and coupling-based sensors.

Plasmonic properties for the end-to-end and side-by-side assemblies of Au nanorods were studied by Shi et al. [40] A water-soluble poly (ethylene glycol) dithiol (HS-PEG-SH) linked Au NRs to form side-by-side (S-S) assembly. During assembly process, the transverse LSPR band of Au NRs red-shifted slightly from ~515 nm to ~525 nm, whereas the longitudinal SPR band blue-shifted gradually

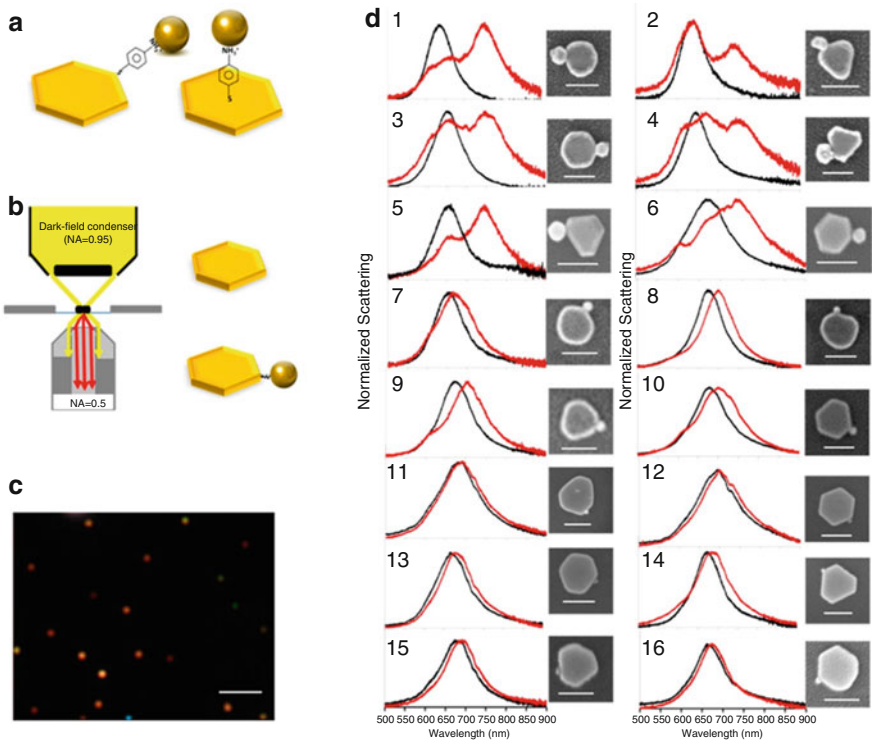

Fig. 4.7 Construction and optical characterization of individual constructs composed of nanoplate/nanosphere dimers. (**a**) First, nanoplates were synthesized on a glass substrate by a method optimized to have an area density for addressing individual nanoplates. Then, via ligand place-exchange reactions, a nanosphere is attached regioselectively either to a vertex on the side of the nanoplate (left) or on the terrace of the nanoplate (right). Schematic is not to scale. (**b**) Principle of transmission dark-field optical microscopy (left) used for characterizing a single nanoplate (right, top) and a coupled nanoplate/nanosphere dimer (right, bottom). (**c**) Representative dark-field scattering image of several single Au nanoplates on a glass slide. (**d**) Scattering spectra of 16 single Au nanoplates before (black line) and after (red line) attachment of an Au nanosphere on a vertex/edge site, as shown in the corresponding SEM images to the right. Scale bars are 100 nm in all SEM images and 5 μm in the dark-field image. The scattering intensity of the nanospheres is much weaker than that of the nanoplate, and therefore the nanosphere LSPR mode does not contribute to the overall scattering spectrum of the dimer (Reprinted with permission from Ref. [39]. Copyright 2015 American Chemical Society)

and decreased in intensity. The end-to-end (E-E) assembly of Au NRs was achieved by linking of cysteine (Cys). The E-E assembly led to red-shifting of longitudinal LSPR band, due to a strong electromagnetic coupling effect. The slight change of transverse LSPR band implied the absence of coupling along the transversal direction. Reinhard and Chen utilized directed self-assembly approach to generate plasmonic cluster pixels, i.e., 1D nanoparticle chains, containing silver nanoparticles with a diameter of 35 nm. The spectral properties of plasmonic clusters can be

systematically tuned through adjusting the size and aspect ratio of the contained plasmonic nanoparticles [41]. The plasmon resonance wavelength red-shifted with the length of the binding site in the investigated range of 35~250 nm. The peak resonance wavelength increases continuously. Plasmon coupling gave rise to a strong increase of the scattering intensity with growing cluster size [41].

Alivisatos et al. investigated the evolution of the coupling behavior of plasmonic hexamers and heptamers with varying interparticle gap distance from 130 to 20 nm [42]. An isolated gold nanoparticle displayed a single dipolar resonance band around 700 nm. The heptamer with a large interparticle gap distance of 130 nm shows approximately the same plasmonic behavior as the isolated nanoparticle because of the well-separated nanoparticle configuration (Fig. 4.8). A new peak appeared around 800 nm as the interparticle gap distance is reduced to 60 nm. The two peaks are separated by a pronounced dip. The LSPR bands of the heptamer red-shifted successively as the interparticle gap distance further decreased. In comparison to the heptamers, the ringlike hexamer presented a shorter-wavelength peak around 700 nm, without pronounced dip. Additionally, the experimental data agreed well with the numerical simulation.

4 Monitoring Based on LSPR

4.1 Spectroscopic Measurements

LSPR spectroscopy can be done with either a large ensemble of colloids/substrate or individual particles. Typically, the extinction spectrum of nanoparticles colloids/substrate is measured using UV-Vis-NIR spectroscopy with excitation relying on a white light source. For transparent samples, light passes directly through the sample and the scattered plus absorbed light is collected by the spectrometer detector. For nontransparent samples such as the films-over-nanosphere (FON) structures substrates, an optical fiber suitable to collect reflection is used. Here, a fiber is usually used both to direct the excitation light to the sample (center fiber) and to collect the light reflected from the surface (radial array of fibers). While the transmission mode yields the LSPR wavelength as a maximum value in the extinction curve, the reflected mode yields the LSPR wavelength as a minimum value. Indeed, UV-Vis-NIR spectroscopy is a relatively simple method for measuring the LSPR spectrum of metal nanoparticles, but it reflects the metal nanoparticles as a whole (ensemble) properties.

Obviously, ensemble measurements may not reflect the properties of individual components. For samples in which small regions or even single nanoparticles are considered, dark-field LSPR spectroscopy or imaging measurements are extremely powerful. Single-particle LSPR instruments are typically homemade and are designed to handle a particular experiment or application. In this case, the incident white light strikes the surface at a high angle and scattered light is collected at the low angle. A two-aperture set-up would rely on a high numerical aperture objective lens to bring incident light obliquely to a surface, and an objective selected for

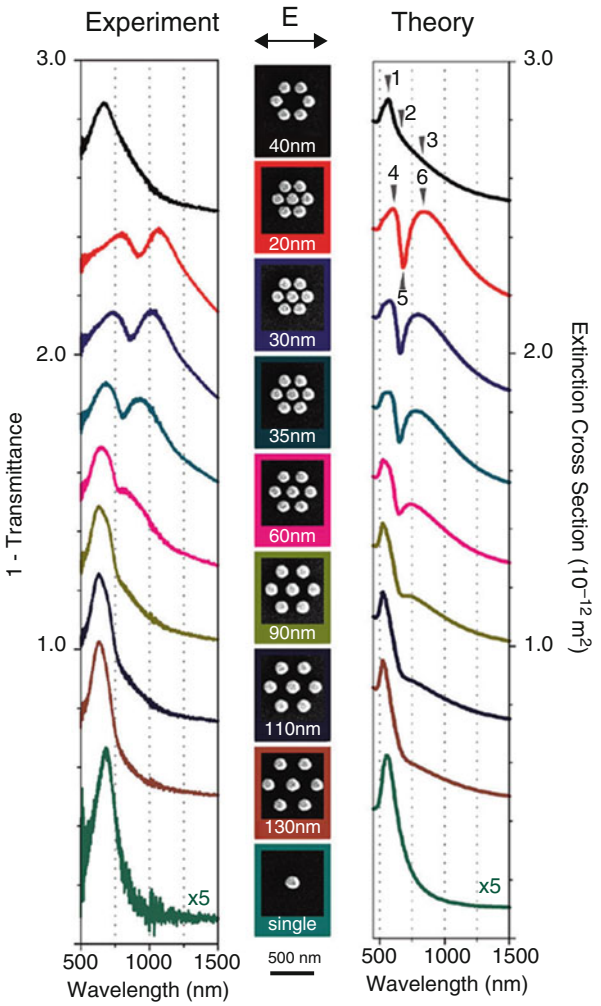

Fig. 4.8 Extinction spectra of a gold monomer, a gold hexamer, and gold hepatmers with different interparticle gap separations. Spectra are shifted upward for clarity. (left column) The experimental extinction spectra (1-transmittance). (middle column) SEM images of the corresponding samples with indicated interparticle gap distances. The scale bar dimension is 500 nm. (right column) Simulated extinction cross-section spectra using the multiple multipole method. The gold structures are embedded in air. The difference between the experimental and simulated spectra is due to the presence of the glass substrate in the experiment, and it is also partially due to the assumption of a nanosphere shape for the trapezoidal nanoparticles in the simulation. In the gold monomer and hexamer, dipolar plasmon resonances are observed. The transition from isolated to collective modes is clearly visible in the different heptamers when decreasing the interparticle gap distance (Reprinted with permission from Ref. [42]. Copyright 2010 American Chemical Society)

suitable numerical aperture would be used to collect the scattered light. A dark field objective can also be used in reflection mode where incident and collected light travel through the same objective. The scattered light is then sent to the spectrometer and detector, where the most common spectrum/imaging detector is a spectroscopy or CCD camera. The advent of dark-field LSPR measurement enables observing the dynamic changes in LSPR scattered light of single nanoparticles without blinking or photo-bleaching. Therefore, a broad perspective of single nanoparticle in situ LSPR spectroscopy can be seen from lots of review articles.

4.2 In Situ Macroscale UV-Vis-NIR Extinction Spectroscopy

4.2.1 Monitoring Growth of Nanoparticles

Nanoparticles with a large variety of shapes (from "spheres" to complex anisotropic particles), sizes (from a few to >100 nm), and materials (Ag, Au, Cu) can now be prepared through numerous chemical and physical methods. Meanwhile, experimental and theoretical studies of LSPR properties have highlighted how they relate to the structure. Therefore, the geometrical dependence of the LSPR extinction spectrum of nanoparticles to monitor the growth kinetics was exploited. In particular, macroscale LSPR extinction spectroscopy and TEM/AFM have been simultaneously used for deeply correlated studies on the synthesis kinetics of nanoparticles.

Synthesis of gold nanoparticles by citrate reduction is a good model system, and the synthetic scheme has been widely studied. Frens clearly demonstrated that the size variation of the gold nanoparticles can be readily realized by simply changing the concentration of sodium citrate. It was suggested that gold nanoparticles were grown through a fast nucleation process followed by a diffusion controlled growth. However, this nucleation-growth mechanism was found to be contradictory with the temporal evolution of the nanoparticle sizes under certain conditions. To better examine the role of sodium citrate and address the synthetic scheme, an interesting illustration of the structure-LSPR correlation has been performed by Peng et al. who performed macroscale UV-Vis extinction and TEM measurements (Fig. 4.9) [43]. In their research, the temporal evolution of the size and shape of gold nanoparticles was examined with selected $Na_3Ct/HAuCl_4$ ratios using TEM. There are two distinguishable evolution patterns (Fig. 4.9a). Consistent with the shape evolution observed by TEM, the temporal evolution of UV-vis absorption spectra of the reaction solutions also possessed two different patterns (Fig. 4.9b). Although only four sets of LSPR spectra are shown, the spectroscopic differences between the reactions with a low and a high $Na_3Ct/HAuCl_4$ ratio can be observed directly. The integrated absorbance in the 600–800 nm, as well as the absorbance at the absorption peak, is summarized. They found that gold nanoparticles with a high $Na_3Ct/HAuCl_4$ ratio grew through a nucleation-growth pathway more or less without aggregation, while serious aggregation of primary particles occurred for the reactions with a low

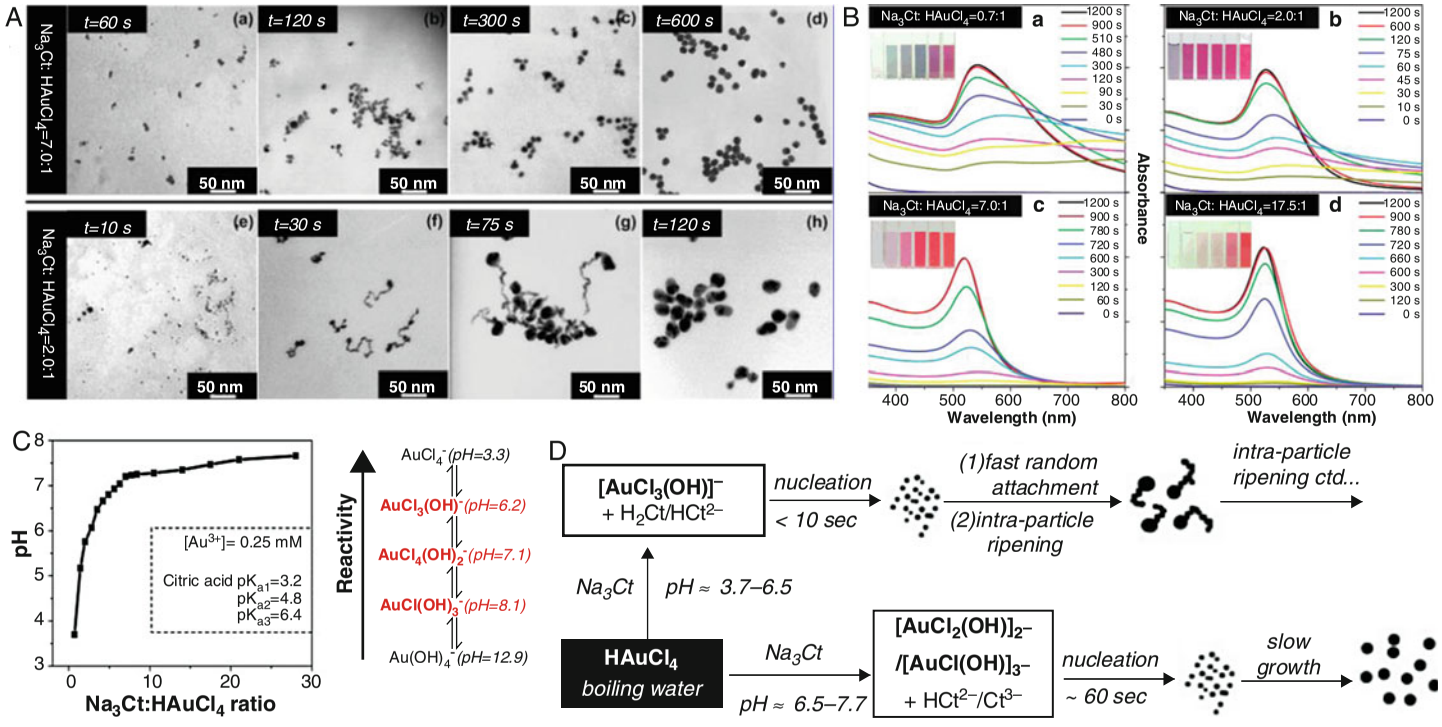

Fig. 4.9 (**a**) Temporal size/shape evolution of gold nanocrystals using two different precursor ratios as labeled. Note: the timescale is different for the two cases. (**b**) Temporal evolution of UV-vis spectra of four reactions with different precursor ratios as labeled. Inset: photographs of the color evolution for each reaction. (**c**) Left: pH variation upon the addition of Na_3Ct in the precursor ratio range. Right: Structure and reactivity variations of Au(III) complexes upon changing the solution pH. Three dominating species associated with this work are shown in red. (**d**) Schematic Illustration of Two Reaction Pathways for Synthesis of Gold Nanocrystals by Citrate Reduction (Reproduced with permission from Ref. [43]. Copyright 2007 American Chemical Society)

$Na_3Ct/HAuCl_4$ ratio in the initial stage. To further clarify the growth mechanism of nanoparticles, temporal evolutions of the Au(III) complexes concentration and the pH-dependent reactivity of the Au(III) complex by UV-Vis extinction spectra were discussed. Meanwhile, sodium citrate known as a weak base should also change the solution pH in a certain extent if its concentration varies. Based on these results, they declared that the reactivity of the Au(III) complexes and the molecular forces between citrate protection groups and gold surfaces were also strongly dependent on pH. After systematical and quantitative studies of the growth process of gold nanocrystals in citrate reduction, they confirmed that citrate plays a determining role as the pH mediator in the reaction system. Dependent on the reaction pH, gold nanocrystals could be formed through either the nucleation growth pathway or nucleation-aggregation-smoothing pathway, with pH roughly being 6.2–6.5 as the switching point. With this understanding, nearly monodisperse gold nanocrystals in the size range from about 20 nm to 40 nm were synthesized by simply varying the solution pH.

For the chemical synthesis of nanoparticles, surfactants are commonly used to direct the growth of nanoparticles to create anisotropic structures in high yield, while the exact roles of surfactants and other reactants are not entirely understood. Usually, ex situ TEM observation and spectroscopic measurements were employed to obtain the information on length and diameter of gold nanorods and estimate the nanorod aspect ratio for most kinetic studies. Gulati et al. have demonstrated a simple LSPR spectroscopic method to determine the microscopic length and diameter of gold nanorods during synthesis by comparing their plasmon resonant extinction spectra to those calculated by Gans' theory for prolate spheroids [44]. Nanorod length and diameter were then monitored to follow the kinetics of seed mediated. By means of this method, the nanorod structure could be detected and analyzed by UV-Vis extinction spectra for sizes as small as 6 nm diameter and 20 nm length.

LSPR spectroscopy can be also applied to monitor the in situ kinetics of early stage growth of liquid phase chemical bath deposition (CBD) [45] and electroless (EL) deposition [46]. As is known, CBD has become an important technique to deposit metal, semiconductor, and dielectric thin films over large areas due to its low cost and scalability. However, understanding the CBD process has primarily been through a postdeposition analysis of film microstructure. LSPR is a well-established technique to sense refractive index changes with extremely high, molecular-level sensitivity. On the basis of electromagnetic field calculations, the shift in the wavelength position of the LSPR peak can be quantified.

4.2.2 Monitoring Reaction Kinetics Involving Nanoparticles

It has been noticed that certain shapes with a higher Gibbs energy can reshape into more stable ones as the growth of nanoparticles with various morphologies was achieved. Tuning of LSPR along with the plasmonic properties of metal nanostructures is a promising research subject due to the potential applications in sensing, optoelectronics, and photonics. Thus, understanding the mechanisms into morphological transformations in noble metal NPs is of great interest for both fundamental studies and practical applications.

It has been described that the addition of small amount of halide ions can drastically change or rebuild silver nanoparticles in colloidal system. However, conventional micro−/nanocharacterization techniques such as TEM, AFM, and SEM can only provide the shape and size information of a small portion from a sample at a certain moment, which are limited in investigation of reaction kinetics. As is known to all, the fingerprints of the LSPR bands allow us to obtain information about the shape and size of noble metal nanoparticles with the combination of calculations including DDA and FDTD. The LSPR spectroscopy featuring the ensemble information of the colloid can easily realize the temporal resolution, which is a necessary approach for performing in situ and real time measurements. Additionally, optical characterization is nondestructive. In situ LSPR extinction spectroscopy is employed to study the reaction kinetics in the shape-conversion reaction silver nanoplates from halide etching [47]. A series of time-resolved extinction spectra are obtained during the in situ etching process, and the evolution of LSPR extinction spectra of the silver nanoparticles is analyzed (Fig. 4.10). The 2D correlation analysis proves that the decreasing of nanoprisms concentration was synchronous with increasing of nanodisks concentration in the shape conversion process. The etching rate of different halide ions was evaluated through the in-plane dipole resonance peak intensity of silver nanoplates vs. the reaction time (dI/dt). The relationship between the etching rate and the halide ion concentration shows that the halide ion etching reaction can be considered as a pseudo-first-order reaction. According to the Arrhenius equation, the activation energy (E_a) of the etching reaction was calculated using the rate constants the of halide ion etching reaction at different temperatures, which indicates that the etching ability of different halide ions is on the order of $Cl^- < I^- < Br^-$. Significantly, in situ LSPR spectroscopy assisted with 2D correlation analysis provides an effective approach for obtaining more detailed information in rapid nanoreactions.

Another similar reshaping system by simply adding a small amount of cationic surfactants-cetrimonium bromide (CTAB) was also studied by Luis M. Liz-Marz [48]. They found that the Au nanostars morphology was dramatically affected when minute amounts of CTAB were added, eventually leading to complete loss of the sharp tips. Unlike the halide system, the process was slow enough, so that reshaping can be blocked at any stage, thus allowing fine-tuning of the LSPR tip-mode in the colloid. By comparing the time evolution of the LSPR tip-mode for the three CTAB concentrations (0.1, 0.3, and 0.5 mM) (Fig. 4.11), the role of CTAB used for the etching of nanostars was confirmed. To further examine the individual roles of CTA^+ and Br^-, control experiments were carried out and showed in Fig. 4.12. On the basis of these findings, they demonstrated a strong dependence of the reshaping process with the presence of different chemical moieties in solution, which points toward an Ostwald ripening mechanism ("dissolution/re-deposition"), which is consistent with the morphology evolution observed in TEM images. Besides, Kumar et al. performed a similar research [49]. They discussed that the addition of a simple base (such as NaOH) to the precursor reaction mixture enhances the fine tuning/reshaping of the 3D star/flower-like gold nanostars with controlled precision right from the nucleation stage.

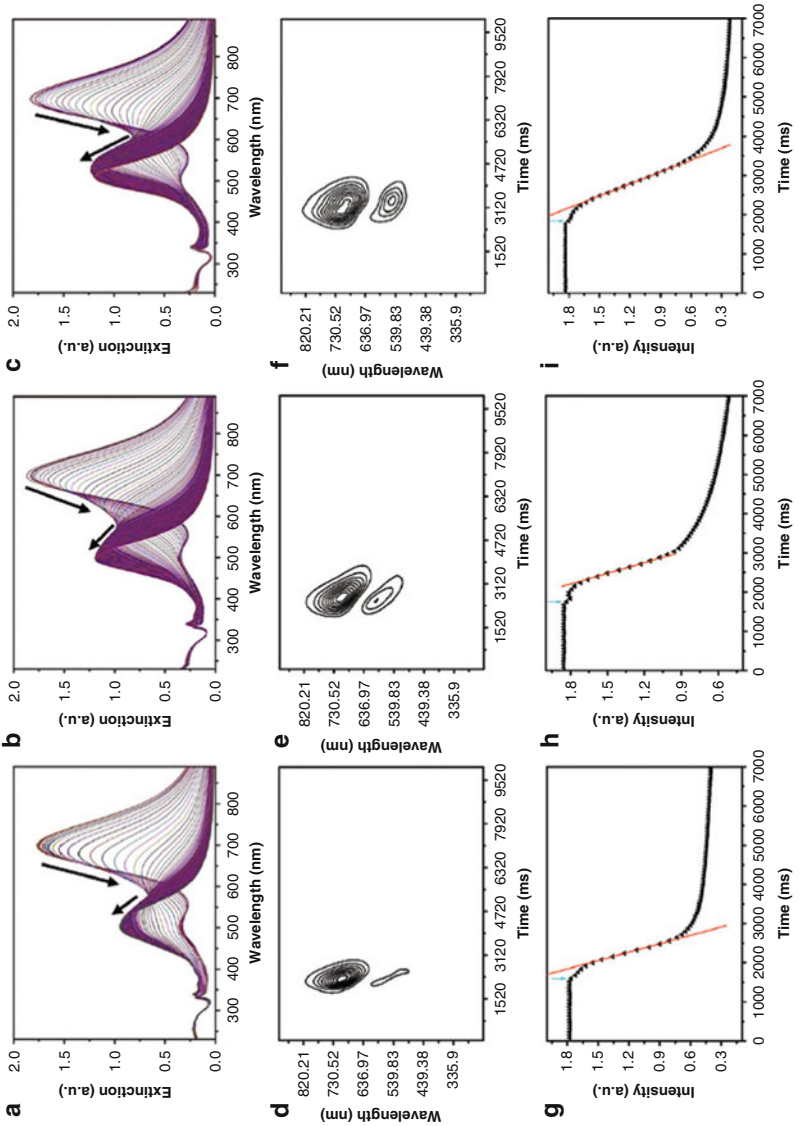

Fig. 4.10 Time-resolved extinction spectra of silver nanoplates etched by the chloride ions (100 mM, 20 mL) (**a**), bromide ions (0.750 mM, 20 mL) (**b**), and iodide ions (0.750 mM, 20 mL) (**c**). The time interval is 80 ms. (**d**–**f**): MW2D correlation spectra based on auto-correlation calculated from the time-resolved

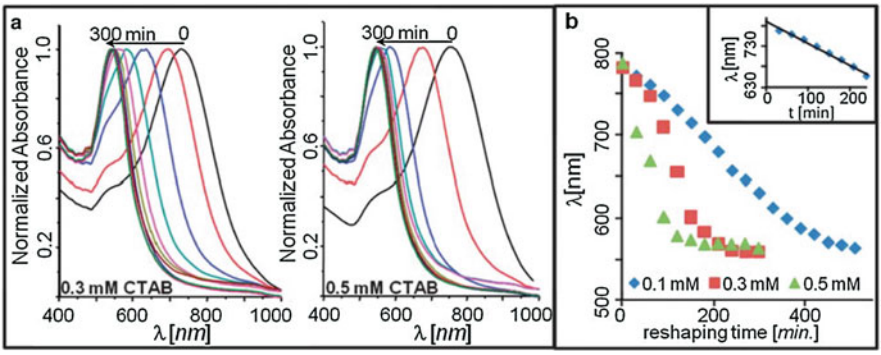

Fig. 4.11 (**a**) Spectral evolution of gold nanostar colloids in the presence of 0.3 and 0.5 mM CTAB, as labeled. (**b**) Position of the tip plasmon mode as a function of reshaping time for 0.1, 0.3 and 0.5 mM CTAB. The inset shows a linear fit to the data between 30 and 240 min ($\lambda = 0.546\ t + 792.96$; $r^2 = 0.9914$) for the case of 0.1 mM CTAB (Reprinted with permission from Ref. [48]. Copyright 2011 Royal Society of Chemistry)

4.2.3 Monitoring Interaction Between Nanoparticles and Protein

Studies on noble metal nanoparticles (NPs) and protein complexes have attracted considerable interest because of their extensive applications in immunoassay, optical imaging, nuclear targeting, sensing, and diagnosing. Among many techniques for investigation into the metal-protein interactions, LSPR spectroscopic characterization is one of the convenient and efficient approaches because of its temporal resolution detection, in situ collection, and nondestructive measurement. To inspect further the correlation of the LSPR spectral regions along the temporal axis and the changes of extinction spectra, two-dimensional correlation spectroscopy (2DCOS) analysis and principal component analysis (PCA) were employed to investigate the interaction between them [50]. Tang and coworkers firstly reported the combination of the 2DCOS/PCA analysis and LSPR spectroscopy to analyze the spectra to elucidate the interaction between noble metal NPs and bovine serum albumin (BSA). They obtained a series of LSPR spectra of silver (gold) NPs just after a small amount of BSA was added into metal colloids (Fig. 4.13a). The 2DCOS maps disclosed that the silver NPs were facile to interact with the BSA, resulting in aggregation (Fig. 4.13b, c). Interaction of gold NPs and BSA was weaker than that of silver NPs. Interestingly, the gold NPs could weaken the interaction of silver NPs and BSA after the addition of BSA in a gold/silver mixed system. All the result revealed that the 2DCOS analysis of LSPR spectra not only is powerful in extracting weak signals from a complicated

Fig. 4.10 (continued) spectra recorded in range of 0–1000 ms in (**a**–**c**), respectively. (**g**–**i**): plots of the intensity of in-plane dipole resonance peak versus the etching time. The red lines are the fitting curves. The slopes of the fitting curves present the reaction rates. Green arrows point out the moment at which halide ions are added (Reprinted with permission from Ref. [47]. Copyright 2009 Royal Society of Chemistry)

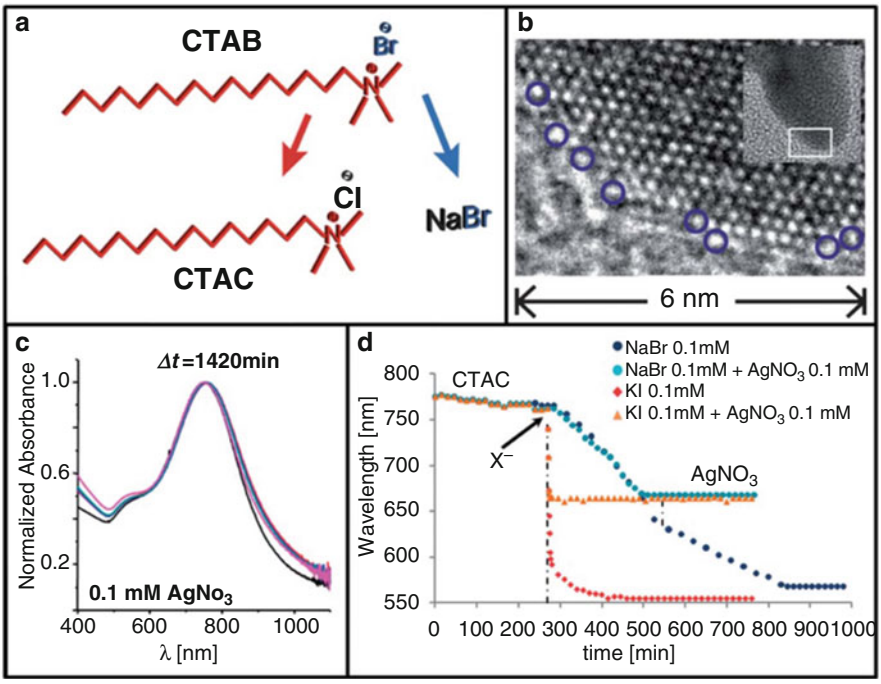

Fig. 4.12 (**a**) Molecular structures of the various chemicals used in control experiments to test the role of the reshaping agents. (**b**) HRTEM image of the end of a sharp tip illustrating the high density of reactive Au atoms (less bound to the lattice) imposed by its high convex curvature. (**c**) Spectral evolution of Au NSs in the presence of CTAB and 0.1 mM silver nitrate. (**d**) Time evolution of the LSPR tip-mode during four different experiments, demonstrating the role of halide counterions (Cl, Br or I) and the role of $AgNO_3$ as blocking agent (Reprinted with permission from Ref. [48]. Copyright 2011 Royal Society of Chemistry)

metal colloid system but also simplifies comparison of a large number of spectral data. It will be very useful for obtaining detailed information about the interaction and conversion process with the metal NPs involved.

4.2.4 Monitoring Catalysis Process

In the recent 10 years, lots of nanoplasmonic application via a versatile in situ spectroscopy platform for catalysis applications was reported rapidly. The optical indirect nanoplasmonic sensing (INPS) was presented. The LSPR excitation in gold nanoparticles at visible light frequencies was utilized to probe processes and changes on/in adjacent catalyst nanoparticles via the locally enhanced plasmonic near field. The INPS with high temporal resolution and compatibility with high temperatures and pressure in a harsh chemical environment turn it into a very promising emerging in situ spectroscopy technique for catalysis applications [51]. The INPS chip features a dielectric spacer layer (several to tens of nanometers thick) that physically separates the plasmonic Au sensor nanoparticles from the probed nanomaterial deposited on top (Fig. 4.14a). For the in situ LSPR experiment, the INPS chip with the sample

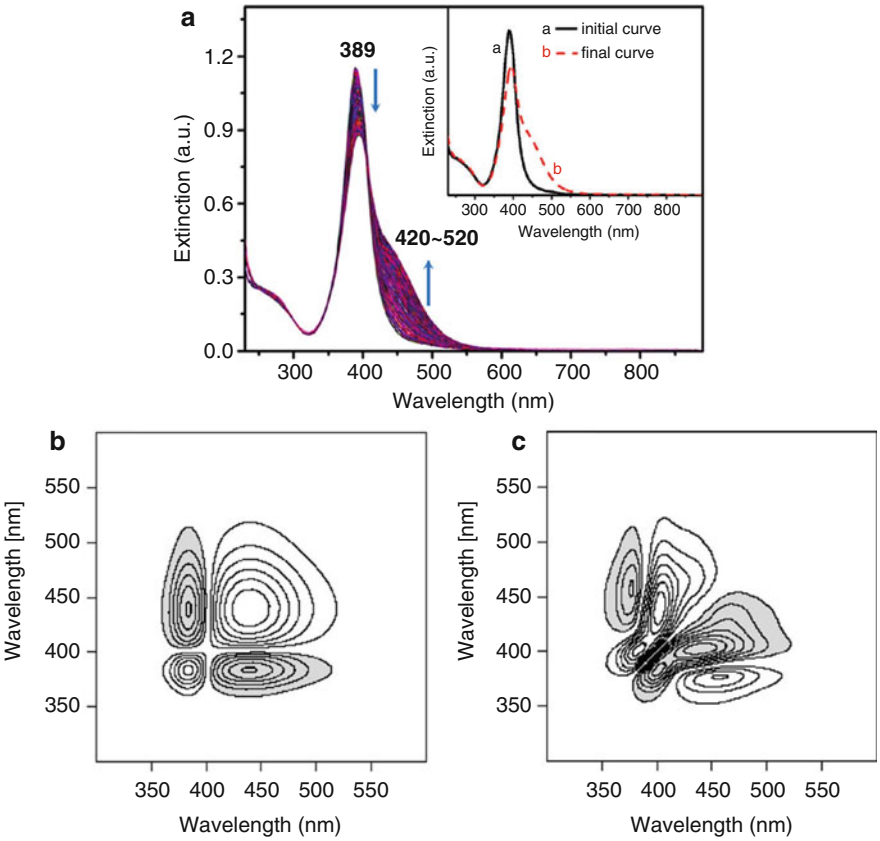

Fig. 4.13 (**a**) Time-resolved extinction spectra of the LSPR of the silver NPs (0.1 mM Ag, 1.0 mL) measured after BSA (0.1 mg/mL, 20 μL) was added. The time interval was 40 ms. The spectra contain 250 curves. Inset: initial and final extinction spectra of the silver NPs before and after BSA was added. (**b**) Synchronous and (**c**) asynchronous maps of 2D correlation spectra derived from the time-resolved spectra in Fig. 4.13a (Reproduced with permission from Ref. [50]. Copyright 2010 American Chemical Society)

material is mounted in a suitable reaction chamber, which allows for either optical transmission or reflection measurements in combination with control of the chip environment (Fig. 4.14d). As mentioned, it is the shift of λ_{max} that provides the sensing function (Fig. 4.14e). It can be efficiently measured with a resolution of 0.01 nm under optimal conditions and by means of a simple pixel array spectrometer. As additional observables to the shifts of the spectral peak position ($\Delta\lambda_{max}$), changes in the peak full-width-at-half-maximum ($\Delta fhwm$, inversely proportional to the lifetime of the LSPR excitation) and in the extinction at peak (ΔE_{max}) can also be used.

INPS can be used to monitor changes in adsorbed species on catalyst nanoparticles, which was illustrated on the Pt-catalyzed CO oxidation reaction by Larsson

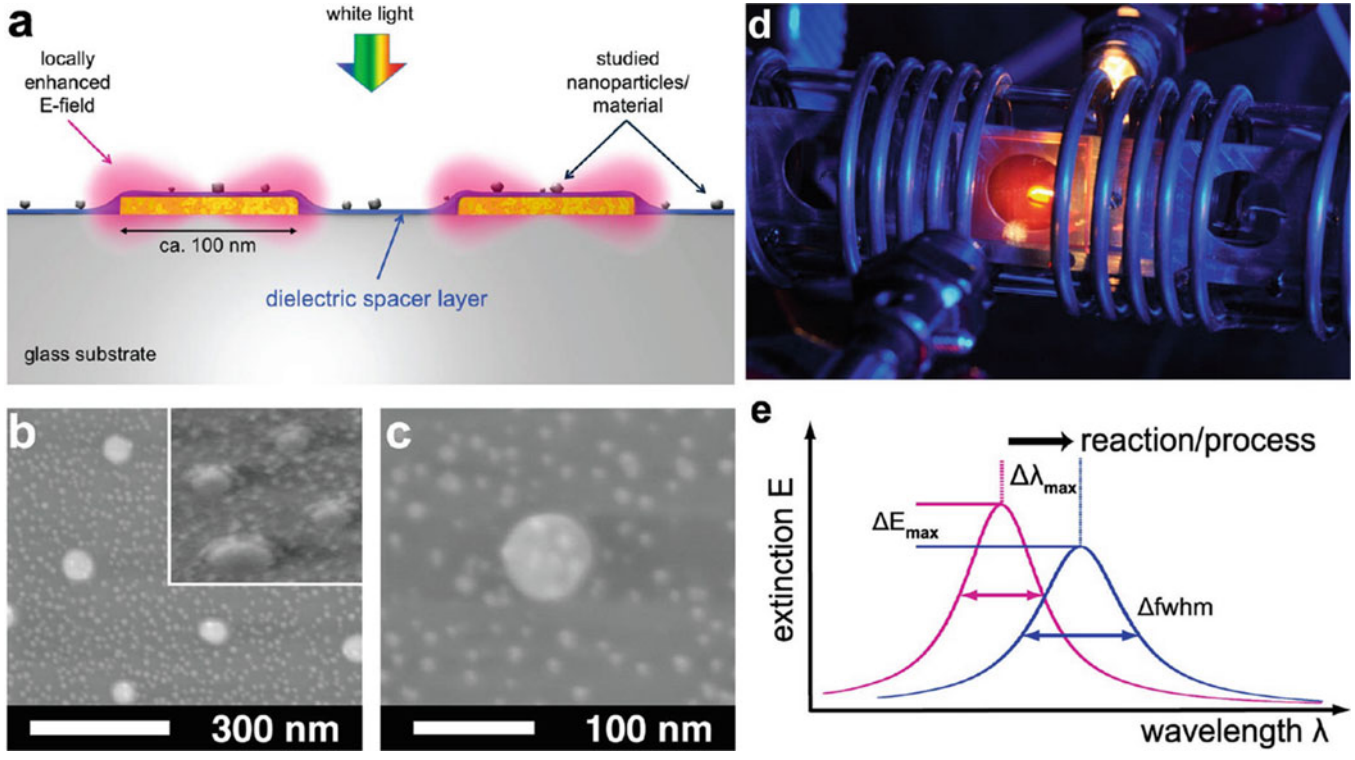

Fig. 4.14 (**a**) Schematic depiction of the INPS sensing platform. (**b**, **c**) SEM micrographs of an INPS sensor showing the amorphous array of Au nanodisk sensors and small (~10 nm) Pt nanoparticles (the sample material) on top. (**d**) Photograph of a possible arrangement for an INPS experiment in catalysis featuring a quartz tube flow reactor with a mounted INPS chip (red) and optical fibers for illumination and readout. (**e**) Schematic illustration of the readout from an INPS experiment (Reprinted with permission from Ref. [51]. Copyright 2012 American Chemical Society)

et al. [52] In their study, the INPS chip arrangement was constructed with a 10 nm of SiO_2 spacer layer and Pt catalyst nanoparticles in the 5–20 nm size range. The sample was exposed to mixtures of CO and O_2 in Ar carrier gas at atmospheric pressure with the total reactant concentration kept constant at 8%. The relative CO concentration, $\alpha^{CO} = [CO]/([CO] + [O_2])$, was scanned from CO-rich to O_2-rich and back while continuously recording the spectral position of the LSPR peak maximum, $\Delta\lambda_{max}$. The sample temperature was measured to 506 K in the absence of a reaction with a thermocouple in contact with the sample surface. When scanning the relative CO concentration, discontinuous steps up and down of ~1 nm in $\Delta\lambda_{max}$ at a critical reactant mixture of α^{CO} around 0.07 were observed. The $\Delta\lambda_{max}$ step was assigned to the kinetic phase transition in the CO + O_2 reaction, occurring at a critical gas mixture, where a sudden transition occurs from an oxygen-covered surface at low α^{CO} to a CO-covered surface at high α^{CO}. The asymmetry of the temperature versus α profile around α^{CO} is due to the well-known poisoning effect of CO for oxygen adsorption, preventing O_2 from dissociating and reacting. The capacity of the method was demonstrated for other two catalytic reactions, H_2 oxidation on Pt, and NO_x conversion to N_2 on Pt/BaO.

Catalyst deactivation by sintering significantly reduces productivity and energy efficiency of the chemical industry and the effectiveness of environmental cleanup processes. The use of experimental techniques that allow the scrutiny of sintering in situ at high temperatures and pressures in reactive environments is a key to alleviate this situation. Larsson et al. demonstrated indirect nanoplasmonic sensing (INPS) has the potential to fill this gap [53]. A Pt/SiO_2 model catalyst was applied, and a simple and robust experimental setup and platform (optical transmission measurement through a nanofabricated sensor chip) was used for in situ INPS with high resolution and throughput, which is suitable for realistic catalyst operation conditions and does not affect sintering kinetics. The correlation between the optical response of the INPS sensor and catalyst sintering is read out as a spectral shift of the Au nanoparticle LSPR peak, which is caused by a change in the local dielectric environment due to the rearrangement of the Pt nanoparticles on the sensor (Fig. 4.15). The obtained data are then analyzed via a kinetic model accounting for the particle-size-dependent activation energy of the Pt detachment, and Ostwald ripening is identified as the main sintering mechanism.

4.3 In Situ LSPR Spectroscopy of Single Nanoparticle

In the field of nano-plasmonic sensing, the introduction of dark field scattering spectroscopy (DFSS) has made it possible to study the optical properties of single nanoparticles and analyze the effects of size and shape of nanoparticles as well as the refractive index of the surrounding medium on the LSPR in single Au and Ag nanoparticles. Single nanoparticle measurements have multiple advantages over ensemble-averaged measurements. Firstly, single nanoparticles are easily implemented in multiplexed detection schemes since each unique nanoparticle possesses a distinguishable LSPR maximum. The second advantage is that the absolute detection limit

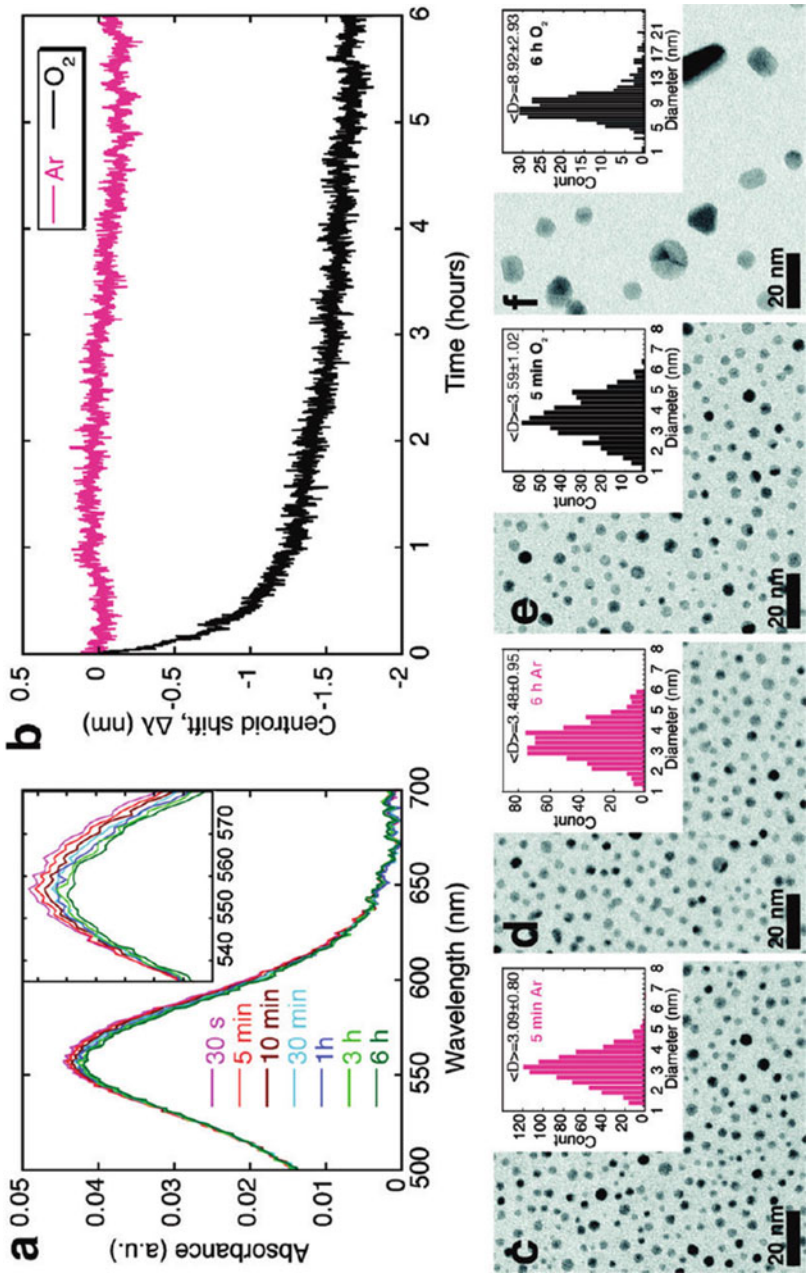

Fig. 4.15 INPS sensor response to model catalyst sintering: real time kinetics and TEM. (**a**) Absorbance spectra obtained at different times during the sintering of the Pt model catalyst in 4% O_2/Ar at 610 °C. The LSPR peak of the INPS sensor spectrally shifts to the blue, and simultaneously, a decrease in the optical

(number of analyte molecules per nanoparticle) is significantly reduced, leading to the ultimate sensing limit: the single molecule. The third advantage of single nanoparticle spectroscopy is the ability to measure the LSPR spectrum of individual particles with a high signal-to-noise ratio. Finally, single nanoparticle spectroscopy allows us to examine exactly spectral properties from different structures [54].

4.3.1 Monitoring Growth and Morphological Evolution

Techniques employed for monitoring of the growth and morphologic evolution of nanoparticles mainly include small-angle X-ray scattering (SAXS), time-resolved X-ray diffraction (XRD), atomic force microscopy (AFM), and liquid cell transmission electron microscopy (TEM). In practice, SAXS and XRD are often performed by sequentially collect the signals of an ensemble of nanoparticles to reveal the whole growth process. But both the two techniques hardly provide direct growth information. AFM is a powerful tool to fulfill this task by providing 3D surface profiles of single nanoparticles, whereas AFM is not a real-time method and it always performs intermittently by disturbing the growth. In this case, the measuring process significantly interrupts the reaction, and the important phenomenon of intermediate growth is not observed. Recently, developed liquid cell TEM has been proven as a useful tool for real-time monitoring of the in situ growth of single nanoparticles. However, the instrument is too expensive to afford this technique in common laboratories. Therefore, an alternative method is urgently required. It is well known that changes in the refractive index of the surrounding medium influence the LSPR spectra of metallic nanoparticles. It is reasonable to explore the growth mechanism of single nanoparticles by real-time monitoring of the LSPR changes during growth.

A comprehensive understanding of the growth mechanism of nanoalloys is beneficial in designing and synthesizing nanoalloys with precisely tailored properties to extend their applications. Huang et al. employed dark-field scattering microscopy to real-time monitor the in situ growth of single Ag@Hg nanoalloys, produced by direct amalgamation of Ag nanoparticles with elemental mercury [55]. On exposure to growth solution, the scattered light of differently shaped single Ag nanoparticles exhibited a noticeable blue-shift followed by a red-shift. A growth mechanism of single Ag@Hg nanoalloys from typically shaped Ag nanoparticles was proposed according to the time-dependent spectral data and shape changes of

Fig. 4.15 (continued) absorbance is observed. (**b**) Diagram showing the LSPR peak centroid shift versus sintering time in 4% O_2/Ar (black) and 100% Ar (pink) atmosphere. Clearly, in O_2, which is known to promote the sintering of supported Pt catalysts, the centroid shifts fast in the beginning and then more slowly, almost linearly, toward the end. In contrast, in pure Ar, only a very small centroid shift is seen. TEM pictures and corresponding PSD histograms of the Pt nanoparticles after 5 min (**c**) and 6 h (**d**) in pure Ar at 610 °C reveal an almost constant particle size, indicating almost total absence of sintering. TEM images and PSD histograms after 5 min (**e**) and 6 h (**f**) in 4% O_2/Ar at 610 °C clearly show significant Pt catalyst particle sintering, in agreement with the INPS sintering kinetic curve (Reprinted with permission from Ref. [53]. Copyright 2012 American Chemical Society)

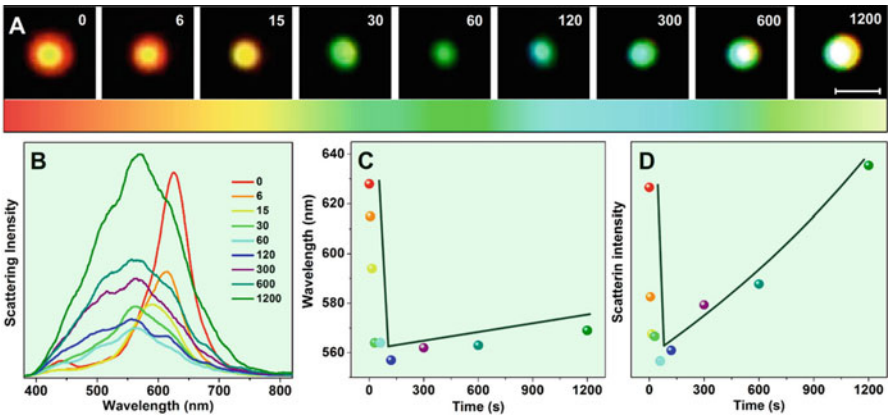

Fig. 4.16 Real-time monitoring of the in situ growth of a single Ag@Hg nanoalloy from a Ag nanorod by dark-field scattering microscopy and spectroscopy. (**a**) Time-dependent dark-field light scattering images and (**b**) corresponding spectra of a representative Ag nanorod after its exposure to growth solution. (**c** and **d**) Scattering wavelength peak and intensity changes of the Ag nanorod as a function of growth time. The color bar in (**a**) and the lines in (**c**) and (**d**) are guides to the eye. The scale bar is 1 μm for all images (Reprinted with permission from Ref. [55]. Copyright 2013 American Chemical Society)

single nanoparticles (Fig. 4.16). As can be inferred from these results, Ag@Hg nanoalloys with given optical properties can be synthesized. Moreover, dark-field scattering microscopy is expected to be a powerful tool used for real-time monitoring of the in situ growth of other metal nanoparticles.

The galvanic replacement reaction has recently been become a standard protocol to create complex hollow structures with various compositions and morphologies. The formation mechanism of this reaction was elucidated through a change in the morphology as observed in TEM images during the reaction progress. Due to the complex process involving multiple steps with a large particle-to-particle variation, many researchers have shifted toward high-resolution measurements with in situ techniques. Song et al. suggested a detailed mechanism of the formation of hollow structures by means of both ex situ and in situ techniques at a single-particle resolution [56]. For the ex situ reaction monitoring, the samples were taken out at various stages of the reaction process and were directly characterized by SEM, TEM, and dark-field microscopy (DFM). For in situ reaction monitoring, a flow cell setup was combined with DFM to maintain a constant reaction environment, and the changes of the LSPR signals at an individual particle were continuously monitored as the reaction proceeded. Importantly, the reaction behaviors at distinct temperatures (25 and 60 °C) were successfully analyzed at the single-particle level (Fig. 4.17). They exhibited two important features distinct from previous observations: (1) at a late stage of the reaction, the LSPR peak shift reaches a steady state, but the evolution of the morphology continuously occurs, leading to the generation of the nanobox structure; and (2) the room-temperature reaction forms granules on the surface, whereas the high-temperature reaction provides flat and even surfaces with complex intermediate structures, mainly due to the high

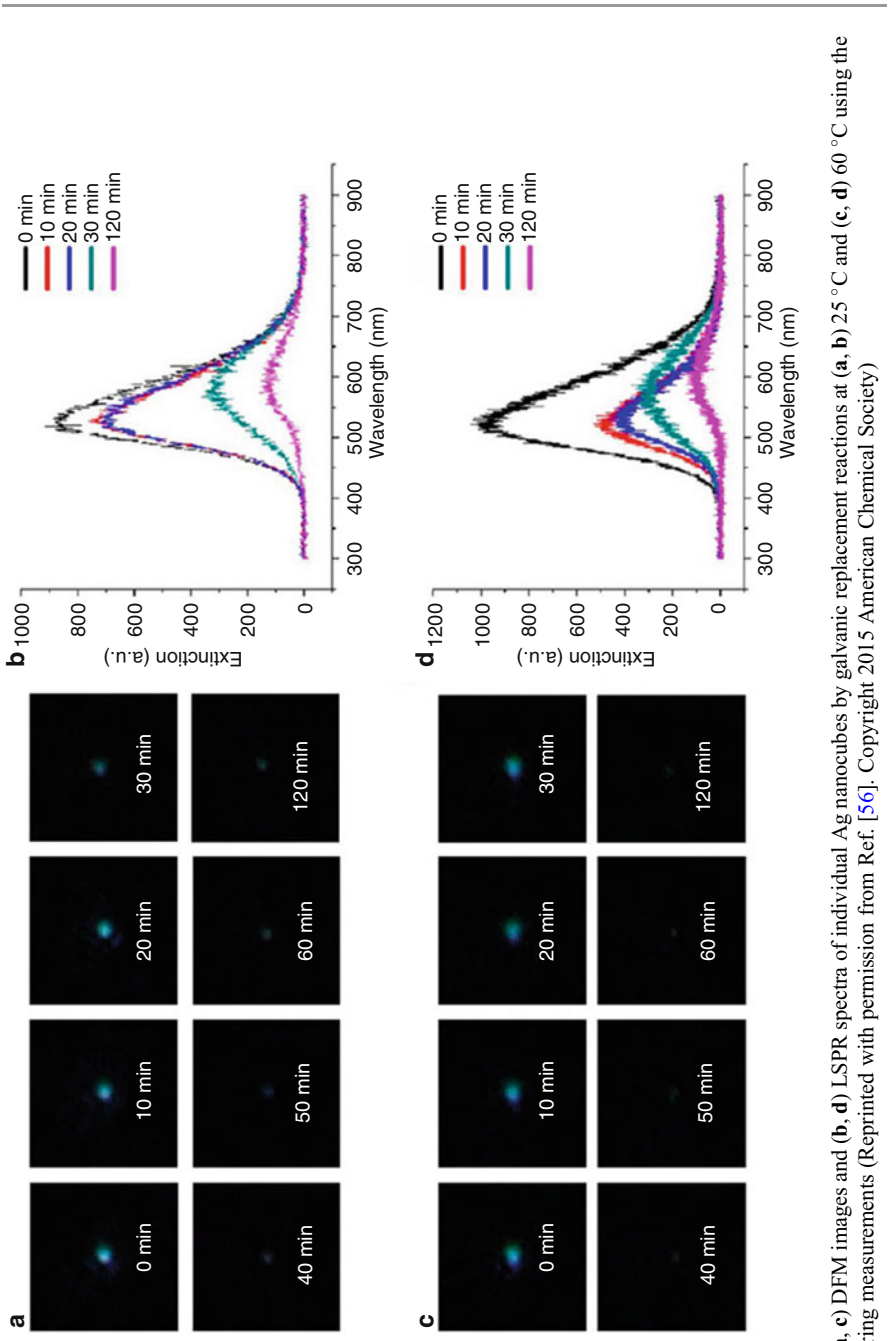

Fig. 4.17 (**a**, **c**) DFM images and (**b**, **d**) LSPR spectra of individual Ag nanocubes by galvanic replacement reactions at (**a**, **b**) 25 °C and (**c**, **d**) 60 °C using the in situ scattering measurements (Reprinted with permission from Ref. [56]. Copyright 2015 American Chemical Society)

diffusion rate of the Ag atoms in Au at a high temperature. In situ monitoring displays rapid peak shifts at the early stages of the reaction at both temperatures. It follows that these plasmon-based monitoring techniques have great potentials to investigate various heterogeneous reaction mechanisms at the single-particle level.

An oxidative etching reaction was reported by Huang et al. [57] In their research, a low-cost and easily conducted light-scattering dark-field microscopy imaging (iDFM) technique for real-time and in situ monitoring of the oxidative etching on a single Ag nanocube was presented. Their results indicated that the oxidative etching of the AgNCs is a thermodynamics-dependent process, which started from the corners of the nanocube due to the relatively high energy at these sites. The cubic AgNPs evolved finally into isotropic spheres along with the decrease of particle size.

Notably, all the research works reported above were focused on plasmonic nanoparticles. As single particles with size of <30 nm or made of dielectric materials do not support LSPR, plasmonic DFSS measurements were demonstrated to be infeasible. To solve this problem, Langhammer et al. reported for the first time that DFSS on single-particle nano-plasmonic sensors was used for in situ and in real-time study of the formation of a new phase in a single nanoparticle [58]. Hydride formation thermodynamics in single Pd and Mg nanoparticles was investigated systematically, which was achieved exploiting HCl-nanofabricated single and truncated Au nanocones as nano-plasmonic sensors.

4.3.2 Monitoring of Chemical Reactions at the Single-Particle Level

Traditionally, most of these studies are carried out by monitoring the reaction-induced spectral variations of plasmonic nanoparticles using UV-visible spectroscopy along with electron microscopy characterization. However, the averaged signals obtained from multiple nanoparticles cannot provide accurate information on the nanoscale level compared to the signals obtained from a single nanoparticle. To gain more insights into the behavior of metal NPs during reactions, it is both of fundamental and practical importance to measure plasmonic spectral shifts of metal NPs at the single particle level. With a simple and high-throughput single-molecule dark field spectral imaging technique, oxidation reaction-induced spectral shifts and intensity changes of either multiple single gold nanorods immobilized on the glass substrate or single gold nanorods moving in solution have been monitored in situ and in real time [59]. Heterogeneous reaction rates and pathways were recorded and a previously unnoticed self-catalysis mechanism was discovered. This high-throughput single particle spectral imaging technique has wide potential applications in chemical reaction kinetics studies and heterogeneous catalysis studies of other metal nanoparticles.

Recently, click chemistry has already become a powerful, highly reliable, and selective method in synthesis chemistry. Among them, Cu^{+}-catalyzed azide–alkyne 1,3-dipolar cycloaddition (CuAAC) is considered as a typical click reaction with very high yields and good region selectivity and has been widely applied in polymer and material science, discovery, biochemistry, pharmaceutical science. A novel method to monitor a Cu^{+}-catalyzed click reaction at the single-nanoparticle level by using plasmon resonance Rayleigh scattering (PRRS) spectroscopy and DFM

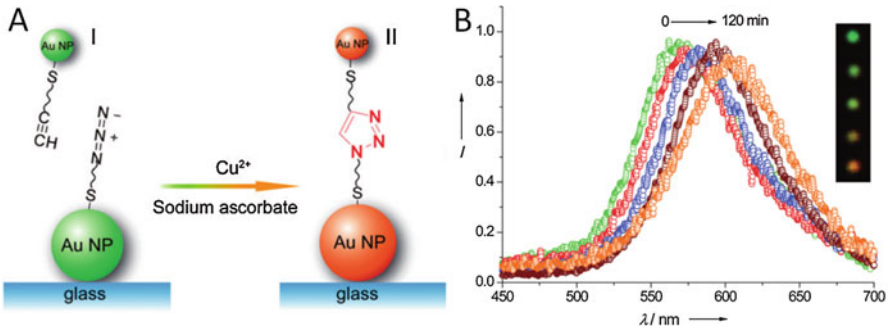

Fig. 4.18 (**a**) Cu^{+}-catalyzed click reaction at the single-particle level. (**b**) Representative scattering spectra of single azide-function-alized GNPs (60 nm) obtained at different times after treatment with Cu^{2+} (1 μm), sodium ascorbate (10 μm), and alkyne-functionalized gold nanoparticles (14 nm), showing that the λ_{max} of the PRRS spectra is red shifted. Inset: Corresponding dark-field images of individual nanoparticles after treatment with Cu^{2+} and sodium ascorbate, showing a color change from green (control) to orange (120 min) (Reproduced with permission from Ref. 60. Copyright 2013 John Wiley & Sons, Inc)

was described by Long et al. [60] Their strategy is shown in Fig. 4.18. The method involves the interparticle coupling by CuAAC. The click reaction on the surface of single gold NPs results in interparticle cross-linking, leading to a red-shift of PRRS spectra and a color change in DFM. Time-dependent $\Delta\lambda_{max}$ changes of a selected single gold nanoparticle are shown in Fig. 4.18a. A single gold nanoparticle with green color in the DFM image gradually changed to orange after the addition of Cu^{2+} and sodium ascorbate. The scattering peak red-shift to increasingly longer wavelengths. The red-shifting with time, in the spectra of the gold nanoparticle, may be attributed to the inhomogeneous diffusion of Cu^{2+} ions and the diffusion of 14 nm gold nanoparticles. It is believed that the strategy will be a valuable technique for the real-time monitoring of chemical reactions in organic chemistry.

An investigation into the nature of metal-sulfur bond is meaningful but challenging in life science. Although there have been several applications of silver-dithiocarbamate (Ag-DTC), essential characteristics of Ag-DTC bond have been researched rarely. The photosensitivity of the covalently linked Ag-DTC bond was real-time monitored by using both the spherical and rod shaped silver nano-probes (Fig. 4.19) [61]. The degradation of the DTC followed by the bond breakage leads to the formation of HS^{-} in neutral condition. The formed HS^{-} can induce the formation of an Ag_2S shell on the surface of the silver nano-probes, leading to a red-shift of the LSPR scattering signal. The imaging data confirmed that the scattering intensity of the spherical nano-probes firstly increased and then decrease until disappearing, which was consistent with the single nanoparticle scattering spectra. This photosensitivity is not existing in the case of gold. These findings suggested a visualization strategy at single plasmonic nanoparticle level, which can be applied to explore new stimulus-triggered reactions and might open a new way to understand traditional organic reaction mechanisms.

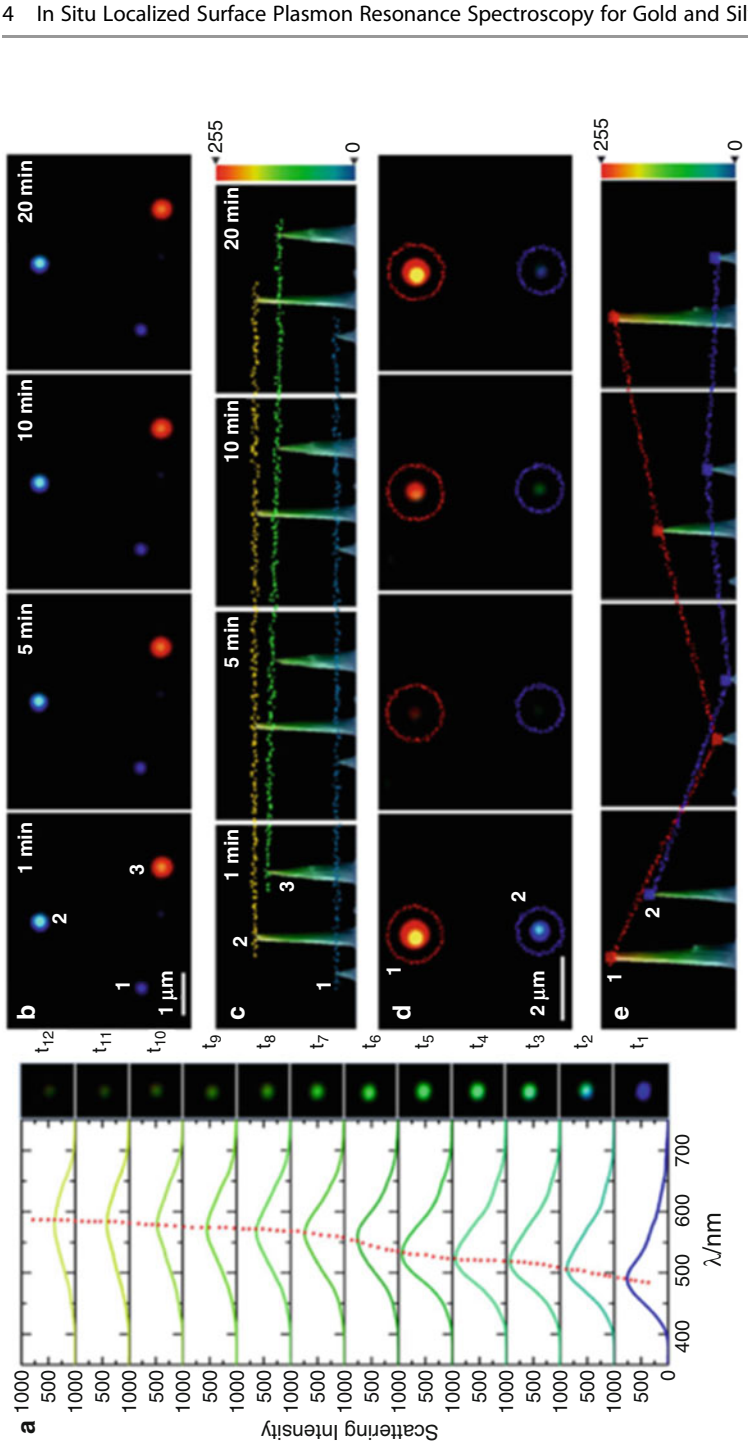

Fig. 4.19 iDFM and spectra of silver nanospheres during the light-driven Ag-DTC breakage and the inhibition of sulfidation process with sodium ascorbate (SA) and the reverse reaction with $NaBH_4$. (**a**) Simultaneous iDFM and spectroscopic measurements of a single nanosphere during the light-driven reaction. (**b**) The iDFM image of treatment with 100 mM SA. (**c**) The scattering intensity of the nanoparticles in (b). (**d**) From left to right are images before the reaction, after the reaction, treated with 100 mM $NaBH_4$ for 15 min and further treated with 500 mM $NaBH_4$ for 15 minutes. (**e**) The corresponding scattering intensities of the four situations in (**d**) [61]

4.3.3 Monitoring the Heterogeneous Catalysis Process at Single-Particle Level

Heterogeneous catalysts made of various materials play a crucial role in modern chemistry, ranging from fine chemical synthesis, energy conversions to pollutant removals. Characterizing their catalytic properties is essential for understanding the fundamental principles governing their activities, but is challenging in ensemble measurements due to their particle-specific heterogeneity from their individual differences in size, shape, and surface sites. In order to truly understand the controlling effects of such catalytic events, studies of catalytic reactions in real time and at the single-particle level are needed to address these key challenges.

For gold/silver nanoparticles that play an important role in heterogeneous catalysis, their LSPR spectra can be measured directly to monitor the catalytic reactions occurring on their surfaces. The advent of dark-field microscopy (DFM) has enabled us to study the optical properties of single nanoparticles and to analyze the changes of the local environment on the catalyst surfaces. These facilitate locally probing catalytic reactions in real time by either direct or indirect strategy. As pioneered by Mulvaney's groups using this strategy, the kinetics of atomic deposition onto a single gold nanocrystal were directly observed, and the electron injection and extraction of a single Au decahedron nanoparticle were monitored during an oxidation of ascorbic acid by dissolved oxygen [62]. The oxidation of ascorbic acid molecules caused electron injection into the Au nanoparticle, resulting in a ~20 nm blue-shift of the nanoparticle's LSPR spectrum in the first 3 min. The subsequent reaction of the Au nanoparticle with O_2 depopulated the accumulated electrons, and concurrently the LSPR spectrum red-shifted back to the initial state (Fig. 4.20). They calculated the electron injected rate was 4600 electrons per second. The kinetics of atomic deposition onto a single Au nanorod was also studied by using this strategy.

Optical shifts in Au NPs/metal oxide are often considered to be the consequence of electron exchange on the metal at the metal/oxide interface, as well as an effect of dielectric changes in the support. It is therefore crucial to understand the separate contributions that modify the free electron density on the plasmonic particles and the dielectric function of the supporting medium on LSPR changes. Recent investigations by Mulvaney's group have capitalized on the flexibility of DFM to measure electron transport and catalysis mechanisms in colloidal thin films at the single particle level [63]. Individual gold nanorods were monitored in real time to reveal the peak position, the full width at half-maximum, and the relative intensity of the surface plasmon resonances during repeated N_2-H_2-N_2 and air-H_2-air cycles. Shifts in the spectra were shown to be due to changes in electron density and not to refractive index shifts in the environment. Then the dissociation of hydrogen on single gold nanoparticles embedded in different metal oxide supports was also monitored. By measuring electron transfer at the single particle level, they showed that the H_2 adsorption mechanism on Au and Pt NPs strongly depends on the metal oxide support (TiO_2, ZnO, and SiO_2) (Fig. 4.21). They have demonstrated that it is possible for electrons to be transported from Pt NPs during hydrogen dissociation to single Au NRs via a semiconducting matrix. The matrix also greatly enhanced the number of electrons transferred and also accelerates the kinetics of forward and back electron transfer.

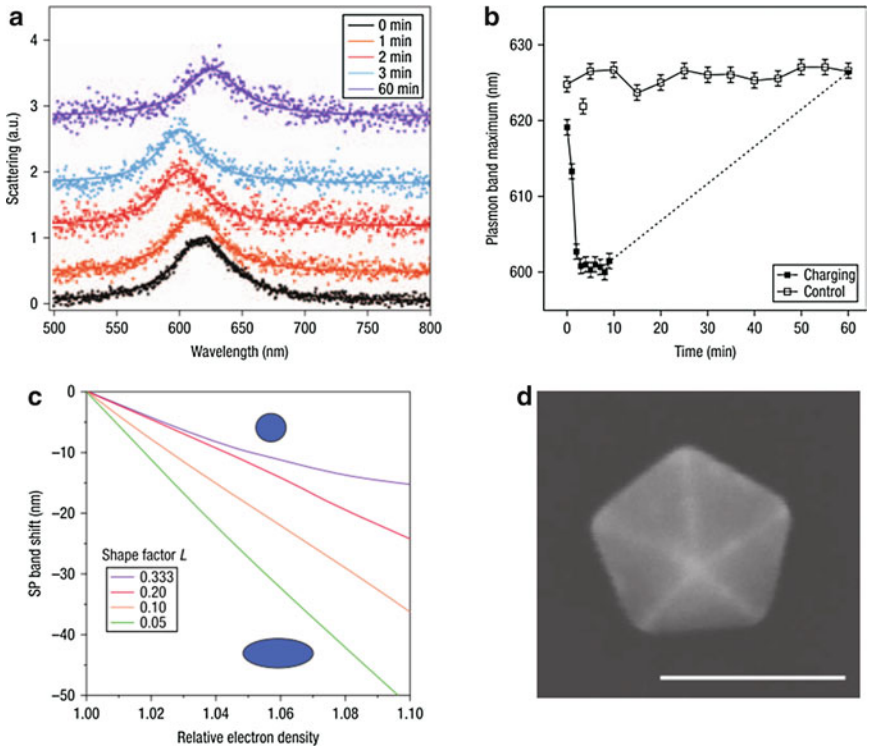

Fig. 4.20 Gold-catalyzed oxidation of ascorbic acid. (**a**) Scattering spectra of the decahedron before and at 1, 2, 3, and 60 min after electron injection by ascorbate ions. (**b**) Spectral shift as a function of time for the catalysis reaction and for the control experiment. The error bars represent the error in determining the peak position from the Lorentzian fitting procedure. (**c**) Plot of the sensitivity of the SP resonance to changes in electron density for different shaped gold nanocrystals. (**d**) SEM image of the gold decahedron used in the catalysis experiments. Scale bar, 100 nm (Reprinted with permission from Ref. [62]. Copyright 2008, Rights Managed by Nature Publishing Group)

Unlike Au or Ag, many materials do not support a measurable LSPR signal. To solve this problem, several indirect LSPR sensing strategies have been developed. Alivisatos and coworkers developed an Au nanoantenna-based strategy to study the chemical properties at a single arbitrary nanoparticle [64]. They used electron beam lithography to position an Au nanostructure at nanometer distances away from a Pd nanoparticle. Pd nanoparticles could absorb hydrogen strongly and react with it to form PdH, which changes their electrical properties in a reversible manner. Meanwhile, Au nanoparticles are sensitive to dielectric environment and exhibit the best plasmonic scattering features in visible region. Hydrogen gas uptake of Pd nanoparticle changed the dielectric of the single Au nanostructure, causing a shift in its LSPR spectrum. They suggested that the presence of 33 Torr hydrogen gas induced a 10 nm shift in the maximum LSPR wavelength and the sensitivity was highly dependent on the spatial distance between Pd and Au, as well as the geometry of the Au

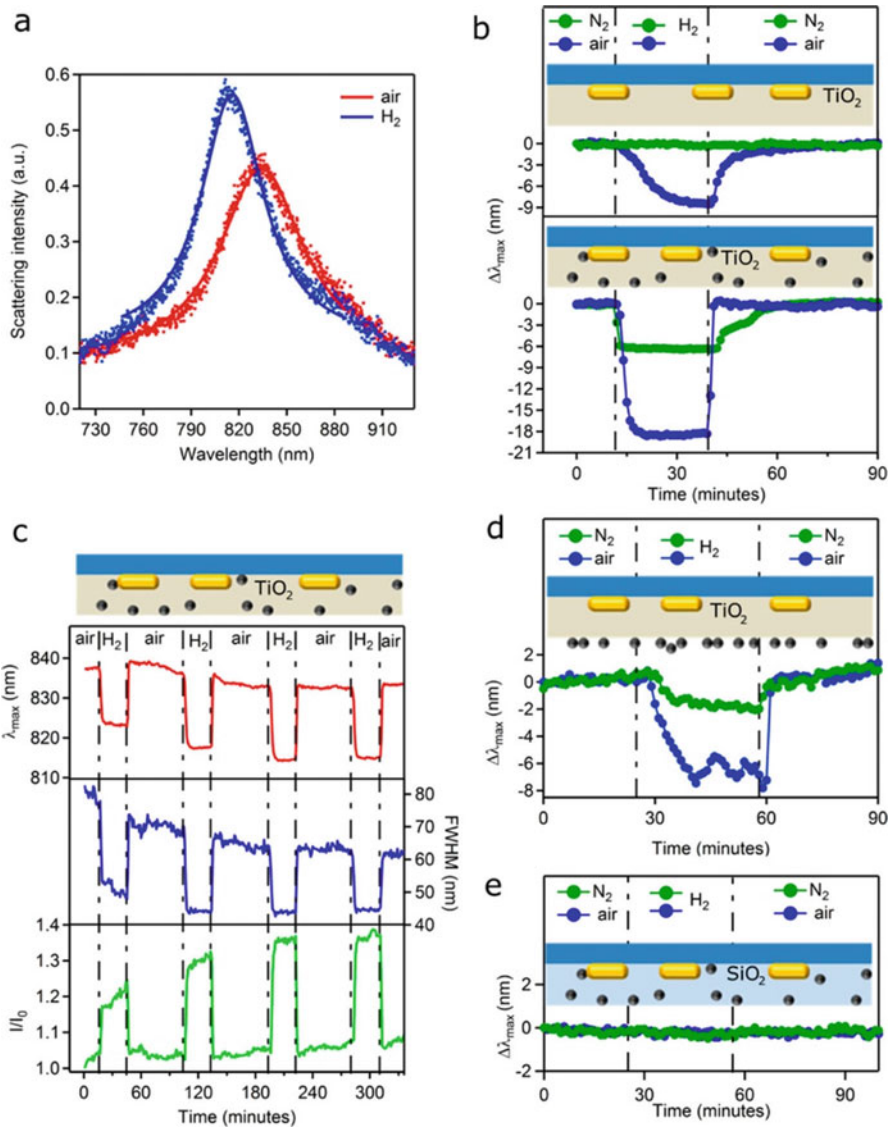

Fig. 4.21 Gas interaction results for a typical single particle in the 30 nm thick Au/TiO_2, 30 nm thick Au/TiO_2-Pt, 30 nm thick Au/TiO_2/Pt, and 100 nm thick Au/SiO_2-Pt samples. (**a**) Comparison of scattering spectra for a single Au NR in the Au/TiO_2-Pt sample on the fourth air-H_2-air cycle in air (red) and H_2 (blue) after 30 min. (**b**) Comparison of $\Delta\lambda_{max}$ for a single Au NR in the Au/TiO_2 sample (top) and a single Au NR in the Au/TiO_2-Pt sample (bottom) in the fourth N_2-H_2-N_2 (green) and air-H_2-air (blue) cycle. (**c**) Full temporal and spectral analysis of λ_{max} (red), fwhm (blue), and I/I_0 (green) of a single Au NR in the Au/TiO_2-Pt sample during repeated cycles of air-H_2-air at rt. Comparison of $\Delta\lambda_{max}$ for a single Au NR in the Au/TiO_2/Pt sample (**d**) and in the Au/SiO_2-Pt sample (**e**) in the fourth N_2-H_2-N_2 (green) and air-H_2-air (blue) cycle (Reprinted with permission from Ref. [63]. Copyright 2015 American Chemical Society)

nanostructures. Using a similar strategy, Song and coworkers investigated the decomposition of lactic acid into hydrogen on a single chemically synthesized Au nanostructure capsulated by a platinized CdS shell [65]. The kinetic analysis of the LSPR wavelength shift allowed for calculation of the rate constant and diffusion coefficient, as well as average distance between active sites of Pt/CdS and the Au domains. Liu et al. studied the dissociation and uptake of hydrogen on 15-nm Pd films on individual Au nanostructures coated with a thin SiO_2 shell as plasmonic reporters [66].

Due to the unique physical and chemical properties, plasmonic gold nanoparticles have also been widely applied in electrochemical catalysis as functional substrates. A novel method was devised by Long and coworkers to monitor electrochemical redox events on single gold nanoparticles from the optical insight using a developed spectroelectrochemistry technique which combines DFM and electrochemistry [67]. Indium tin oxide (ITO) was modified by electrostatically adhering gold nanorods (GNR), and this acted as a working electrode. Two Pt wires were immersed in the electrolyte and acted as counter electrode and quasi-reference electrode, respectively. The applied potential was calibrated via potassium ferricyanide solution. The time-dependent dark-field scattering spectra of the single GNR during the triangular wave potential scanning reveal the information about surface of a single GNR during the electrocatalytic process (Fig. 4.22). Data analysis demonstrated that the electrochemical catalytic oxidation of H_2O_2 at a single gold nanorod can be investigated, and the presence of chloride ions could block the catalytic activity of nanorods for the oxidation of H_2O_2. Moreover, it was discovered that different nanoparticles exhibited various catalytic activities. This method offers a unique way for monitoring electrochemical processes and catalysis reaction at single particle level, which would improve the understanding of the mechanism of electrochemistry and catalysis of metal nanoplasmonics including electron transfer, substance exchanging, and catalyst poisoning.

5 Sensing and Imaging

Gold and silver nanoparticles are highly sensitive to the refractive index of their surface bound molecules and surrounding environment, which is the basis of using LSPR for molecular sensing. LSPR-based sensors have been used as effective platforms to quantitatively detect biological or chemical molecules.

5.1 Design Principles for LSPR Sensing

The LSPR spectral shift ($\Delta\lambda_{max}$) in response to changes in the refractive index of the bulk can be approximated as:

$$\Delta\lambda_{max} = m(n_2 - n_1)\left(1 - e^{-2d/l_d}\right) \tag{4.3}$$

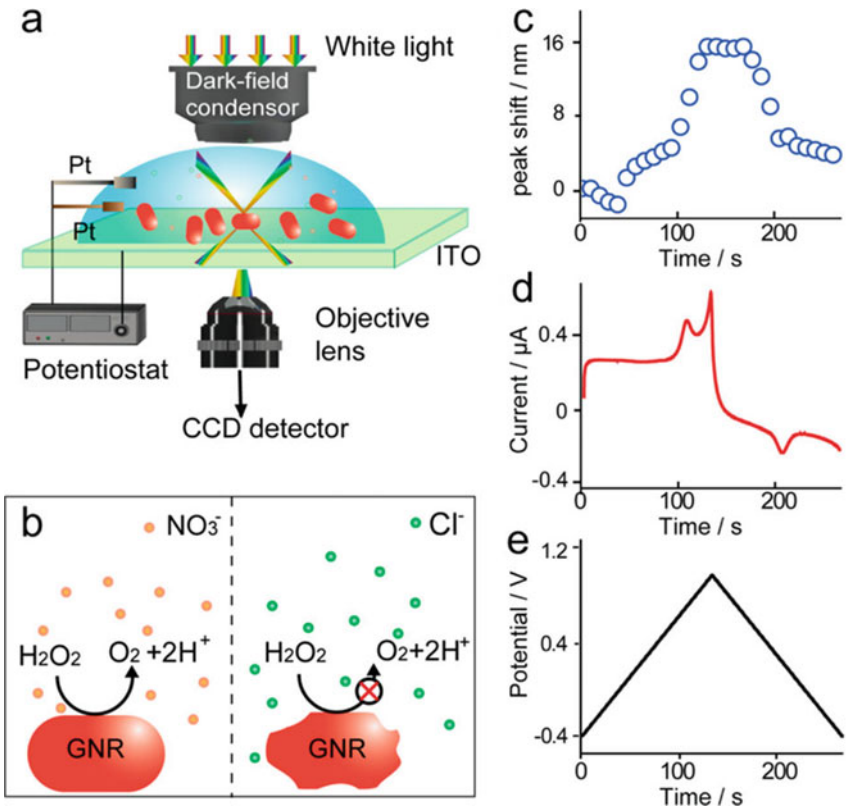

Fig. 4.22 (**a**) Setup of dark-field microscopy integrated with an electrochemical workstation. (**b**) Scheme of electrocatalytic oxidation of H_2O_2 on the surface of gold nanorods in KNO_3 and KCl solutions, respectively. (**c**–**e**) Simultaneous plasmonic scattering spectra peak shift of single nanorod (**c**) and electrochemical current of entire samples (**d**) under the applied triangular wave potential (**e**) on the GNRs (Reprinted with permission from Ref. [67]. Copyright 2014 American Chemical Society)

where m is the refractive index sensitivity (RIS) [in nm/RI unit (RIU)], n_2 and n_1 are the refractive indexes of the dielectric local environment of the nanostructures post and prior to the sensing event, respectively, d is the thickness of the dielectric layer (in nm) and l_d is the electromagnetic field decay lengths (in nm).

The bulk refractive index sensitivity of LSPR-based sensor depends mainly on the morphology and geometry of the surface linked metallic nanostructures. The useful method to improve sensitivity is to increase the nanostructures polarizability via multipolar resonance, such as nanostars [68], nanoprisms [69], nanocrescents [70]. Obviously, a nanosphere exhibits dipolar resonance with degenerated longitudinal and transverse modes due to its spherical symmetry. Though it is the simplest nanostructure, it has low sensitivity at around 76 nm/RIU [71]. In general, both transverse and longitudinal modes are segregated by increasing the aspect ratio

(width/height) of the nanoparticle. Due to the anisotropy property, the nanorod exhibits two plasmon resonant peaks corresponds to longitudinal and transverse plasmon modes, respectively, which leads to a red shift of λ_{max}, with longer electromagnetic field decay lengths and higher sensitivities [72]. Au nanorods excited with the near-infrared light source show greater sensitivity (366 nm/RIU) than nanosphere [70]. The higher aspect ratio results in stronger dipole moment and more sensitive to the surrounding materials.

Another promising approach for increasing the sensitivity is using the plasmon hybridization. The plasmon hybridization theory originates from the hybridization of essentially fixed-frequency plasmon resonances of individual nanostructures in a complicated nanostructure. Plasmon hybridization for LSPR sensing can be formed by symmetrical coupling and asymmetrical coupling in a nanostructure, respectively [72]. The highly geometry-dependent plasmon response can be seen as an interaction between two conjugated physical modes.

Notably, interaction with incident light, gold disk trimers can be employed as dual wavelength chemical sensing. The gold disk trimers show the intra- and inter-trimer interactions allow the generation of visible and near-infrared surface plasmon resonances associated with highly localized electric near-fields. Moreover, for the interacting gold disk trimers, the change of the infrared resonance wavelength with optical index (373.9 nm/RIU) is nearly three times larger than that of the visible resonance (130.3 nm/RIU) [73].

Furthermore, in plasmonic structures with broken symmetry, Fano resonances can emerge due to the interaction of narrow dark modes with broad bright modes and own tunability of line width of the LSPR band. It has been proven that plasmonic Fano resonances are more sensitive to the local dielectric environment than the primitive plasmon modes of the nanostructure. So introducing a coupling between dark and bright modes can create an anisotropic environment, such as depositing a nanoparticle or nanoarrys or fabricating a nanostructure by deposition methods, onto a dielectric (flexible) substrate [74–76]. For a nanocube, a nearby dielectric mediates an interaction between bright dipolar and dark quadrupolar modes (Fig. 4.23), with the LSPR sensitivity of around 1.3 eV per RIU for both modes with different figure of merits.

Typically, gold nanoparticles with various size and shape have been widely reported, while the silver nanostructure can also act as sensing units in LSPR-based sensing [77–79]. It is possible to fabricate new types of sensing materials by combining two kinds of noble metal nanoparticles. Huang et al. developed an optical sensing probe of silver/gold nanocages (Ag/Au NCs) for the detection of Hg^{2+} ions [80]. Sugawa et al. recently reported that the Pd nanoparticle is a promising candidate of "the third plasmonic sensing material." It was reported that Au nanoparticle core/Pd-shell nanospheres (Au/PdNSs, ca. 73 nm in diameter) show higher sensitivity than those of Au (AuNSs) and Ag nanospheres (AgNSs) with similar diameters [81].

The refractive index sensitivity is by far the most typical characteristic of LSPR sensors. It is not the only design principle for nanoparticle sensors. The changes of bulk refractive index sensitivity and the peak line-width of precision in the refractive index should be comprehensively taken account. As a useful parameter in verifying LSPR nanosensor, the figure of merit (FOM) is defined as:

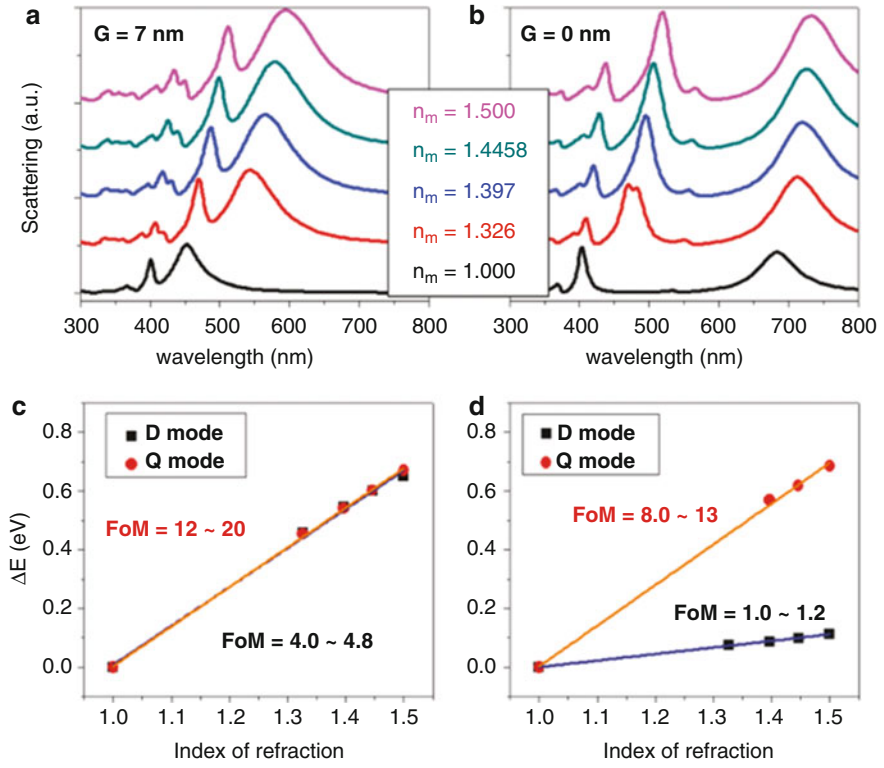

Fig. 4.23 LSPR sensing of the nanocube-on-substrate system. (**a**, **b**) Scattering cross section of a 60 nm silver nanocube on ZnSe substrate, in the weak coupling regime with $G = 7$ nm (**a**) and in the strong coupling regime with $G = 0$ nm (**b**). The index of refraction of the embedding media, nm, is 1.000 (air, black), 1.326 (methanol, red), 1.397 (butanol, blue), 1.4458 (chloroform, green), and 1.500 (oil, magenta). (**c**, **d**) Linear plot of the LSPR shifts of the D (black) and Q (red) mode as a function of refractive index nm, corresponding to (**a**) and (**b**), respectively (Reprinted with permission from Ref. [75]. Copyright 2011 American Chemical Society)

$$\mathrm{FOM} = \frac{m(\mathrm{nm/RIU})}{\mathrm{FWHM(nm)}} \tag{4.4}$$

where m is the bulk refractive index sensitivity of the LSPR transducer and FWHM is the full width at half-maximum (FWHM) of the extinction peak [82, 83]. The FOMs of gold nanodisks and pairs of gold disks are shown in Fig. 4.24 [83]. As an indication for good sensor performance, the higher FOM can be achieved with increasing refractive index sensitivity while narrowing line widths, which also results in reduced detection limit. Here another major principle which is introduced to judge sensing performance is the resolution. Many approaches have been attempted to improve the spectral resolution of LSPR chemical sensor.

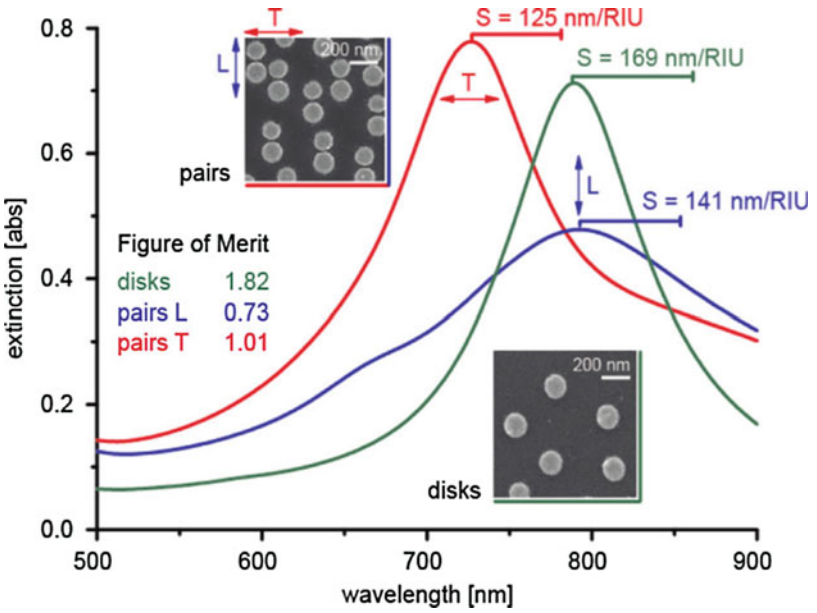

Fig. 4.24 Extinction spectra (in absorption units (abs)) in water are shown for disks (green) and pairs, the latter measured in longitudinal (L; blue) and transverse (T; red) polarization. The bulk sensitivity is indicated with horizontal bars of proportional lengths for the different systems. Values for the figure of merit (FOM) are obtained by dividing the bulk sensitivity by the full width at half-maximum (fwhm). The insets are scanning electron microscopy (SEM) micrographs of the disks and the pairs samples (Reprinted with permission from Ref. [83]. Copyright 2012 American Chemical Society)

Traditional LSPR sensors typically monitor shifts in the peak position or extinction in response to local refractive index changes in the close vicinity of the nanoparticle surface. The ability to resolve minute shifts or extinction changes is to a large extent limited by instrumental noise. A new strategy to evaluate LSPR responses utilizing changes in the shape of the extinction spectrum (the curvature) is proposed. It has been proposed that the curvature (K) related to the sharpness of the peak is superior over peak shift and extinction both in terms of signal-to-noise (S/N) ratio and reliability of LSPR sensors [84]. In addition, as an intrinsic property, the phase change of a plasmon resonance can be extracted by performing phase-sensitive measurements. Around the center frequency of the LSPR, the electron cloud makes the transition of in- to out-of-phase oscillation with respect to the driving field, which is an intrinsic property of a plasmon resonance. This phase difference shows a much smaller spectral footprint than the intensity-based reflection measurements, resulting in much narrower line widths and largely increased values of the FOM. It has been demonstrated that the FOM for reflection-based refractive index sensing can be largely increased by measuring the phase of the reflected beam instead of its intensity only [85].

The LSPR-based sensors have mostly been used to detect the solution-based binding reactions [77, 86]. Ho et al. suggested that the diffusion, absorption, and

saturation processes of hexadecyltrimethylammonium bromide (C_{16}TAB) both in the water and on the nanorod can be monitored by the peak shifts of absorption spectrum based on the LSPR of gold nanorods. This sensing technique is expected to investigate the chemical mixing or reaction process [86]. Moreover, the application of plasmonic nanosensor has been significantly expanded to the research of gaseous analytes by demonstrating the ability of inert gases sensing such as He, N_2, and Ar [78]. It is valuable to expand the detection of volatile organic molecules with highly toxic. However, The LSPR sensing is not well suited to the identification of unknown species as LSPR-based sensors are not inherently selective. To solve this problem, several methods have been proposed. Liu et al. developed a nanoprobe of polyamine-capped AuNRs for LSPR-based simple, selective, and sensitive detection of Cu^{2+} ions. The specific PEI-Cu^{2+} chelation gives a chance to eliminate the interference from other metal ions [87]. Huang et al. utilized the redox reaction between Hg^{2+} ions and Ag atoms existing in silver/gold nanocages (Ag/Au NCs) to detect Hg^{2+} ions based on the blue-shift of LSPR peak of Ag/Au NCs. This sensor showed good selectivity and high sensitivity for detection of Hg^{2+} ions [80].

5.2 Colorimetric Assay

Depending on the changing of LSPR properties, the color shift of the noble metal nanoparticles can be read out simply by naked eyes. It makes colorimetric sensing, one of the easiest and most powerful methods, be possible. When the distance between NPs decreases, the enhancement of strong localized electric field within the interparticle spacing can be achieved based on the near-field coupling. Typically, gold nanostructure can be used as LSPR-based recognizer and indicator for its distinguishable color change caused by particle aggregation. The surface of Au NPs functionalization with recognition elements allows analyte-programmed Au NPs aggregation or Au NPs aggregate dispersion. Another metal nanoparticle nonaggregation based-method has been studied. It relies on the chemical redox occurring on nanoparticle surfaces. Wang et al. demonstrated a nonaggregation-based colorimetric assay of ascorbic acid by tailoring the optical properties of mesoporous silica-coated gold nanorods (MS GNRs) via silver overcoating (Fig. 4.25) [88]. The resulting LSPR absorption band of MS GNRs is observed to exhibit regular blue shift behavior with increasing amount of ascorbic acid (AA). A very good linear dependence between the peak shift and AA concentration is attained within a certain range, and the limit of detection is determined to be 49 nM which is lower than many other typical techniques for AA analysis.

5.3 Refractive Index Assay

LSPR sensors can be also used for affinity-based sensing in which changes in the dielectric environment of metallic nanostructures result in measurable shift of the LSPR position and amplitude. The refractive index changes caused by those

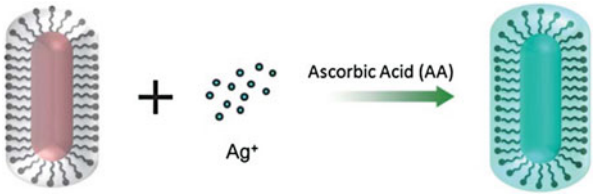

Fig. 4.25 Schematic representation of the LSPR sensing mechanism of AA using MS GNR probes in the presence of Ag^+ (Reprinted with permission from Ref. [88]. Copyright 2011 Royal Society of Chemistry)

molecular interactions near the noble metal nanoparticle surface can be recorded by the LSPR spectra. When the noble metal nanoparticles immersed in solvents of different refractive indexes, the effect from changing solvents and ligands on the LSPR band was studied. Typically, the increase of refractive index would lead to the red-shift of LSPR position in the extinction spectra, while the decrease of refractive index would lead to the blue-shift.

In addition, changes of solvents or ligands on the LSPR band of plasmonic nanoparticles dispersed in solution can be used to obtain information about the sensing performance. The change of refractive index at the single-particles level makes LSPR sensors competitive with propagating SPR interfaces. Notably, an individual nanoparticle analysis can yield unique target information. The next-generation biosensor is revolutionary for end-point detection (single or multiplex) and can be functionally extended to biological phenomena monitoring. Sim and coworkers presented a single nanoplasmonic sensing technology based on LSPR for label-free and real-time detection of highly reliable cancer markers (mutant gene and telomerase) in clinical samples (Fig. 4.26) [89]. The entire detection process was performed on an optimized platform using a ~50 nm single AuNP. This single-nanoparticle spectroscopic technique can specifically indicate mutant DNA and could detect telomerase from as few as 10 HeLa cells. This approach can be easily translated to detect other pathological targets with high sensitivity and specificity and monitor key interactions between biomolecules such as nucleic acids and proteins during disease development in real time.

5.4 LSPR Imaging

The use of the localized surface plasmon resonance (LSPR) observed in metallic nanostructures has been widely used for designing sensitive optical sensors. Recently, advances in instrumentation and analysis now allow many of these measurements to be performed on individual nanostructures, opening the door for new imaging applications in which hundreds or thousands of nanostructures are measured in parallel. LSPR imaging (LSPRi) enables high-throughput, multiplexed measurements by simultaneously probing multiple individually addressable sensors on a single sample surface. Each spatially distinct sensor can be tailored to provide

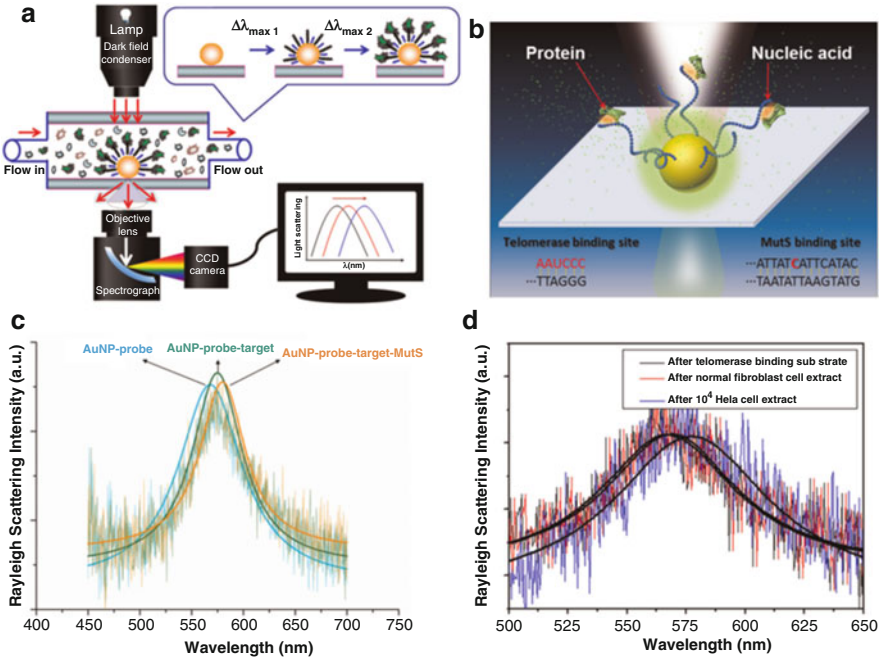

Fig. 4.26 Illustrations for (**a**) the system of dark-field microscope in combination with Rayleigh light scattering spectroscope, and (**b**) the interactions between nucleic acids and proteins in the sensor. The spectra for the detection of (**c**) mutant gene and (**d**) telomerase extracted from clinical cells were recorded by measuring the scattering spectra of an individual nanoparticle and fitted by Lorentzian algorithm in the same wavelength range to eliminate the noise from the system (Reprinted with permission from Ref. [89]. Copyright 2014 Elsevier B.V.)

data regarding different surface functionalities or reaction environments. Thus, LSPR imaging has the potential to take advantage of each sensor's nanoscale dimensions to map complex spatiotemporal variations in analyte concentration, such as those encountered in live-cell applications.

Full spectral imaging of macroscale LSPR sensor arrays based on discrete LSPR sensors composed of surface-confined nanoparticle arrays was demonstrated by Van Duyne (Fig. 4.27) [90]. Defined macroscale arrays of nanoparticles were created by hole-mask colloidal lithography (HCL). Then the LSPR sensor arrays are illuminated with white light filtered through a liquid crystal tunable filter (LCTF), which allows full access to either the visible or near-IR spectral range. As the LCTF scans through a wavelength sequence, a camera takes a series of images that are later analyzed for intensity information. These intensity maps are then correlated back to illumination wavelength in order to construct a spectrum for each nanoparticle array region in the image. They reported the first demonstration of multiplexed LSPR imaging and showed that the increased throughput of the instrument enables the collection of a complete Langmuir binding curve on a single sensor surface.

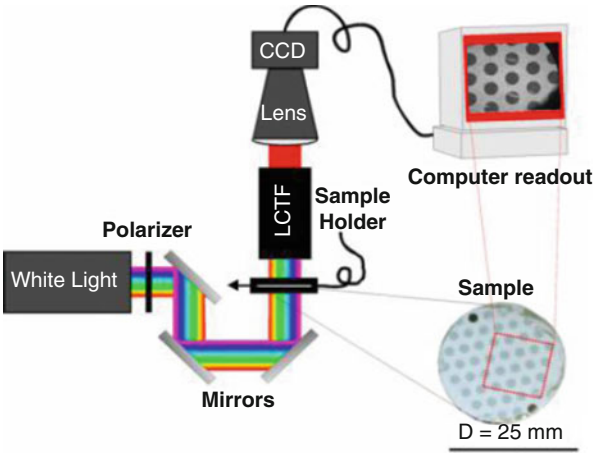

Fig. 4.27 Schematic of LSPR imaging instrument. Collimated white light from the light source is sent through a polarizer and then directed via three mirrors through the sample into a liquid crystal tunable filter (LCTF). A single selected wavelength is sent through a lens to the CCD camera, which collects a single-wavelength black-and-white image. The computer cycles the LCTF through all the wavelengths of interest and triggers the CCD to take an image at each wavelength (Reprinted with permission from Ref. [90]. Copyright 2013 American Chemical Society)

In addition, the multiplexed LSPR sensor is highly selective, as demonstrated by the hybridization of single-stranded DNA to complementary sequences immobilized on the sensor surface. The LSPR arrays exhibit uniform sensitivity and tailorable optical properties, making them an ideal platform for high-throughput and label-free analysis of a variety of molecular binding interactions.

The use of the LSPR observed in metallic nanostructures for label-free biosensing is a relatively recent research field, but its applicability has already proven to be far-reaching. Kurabayashi et al. have developed a label-free LSPR microarray immunoassay that enables the high-throughput analysis of multiple immune biomarkers rapidly, accurately, and sensitively, which is attributed to synergistically employing microfluidics-enabled patterning and dark-field imaging (Fig. 4.28) [91]. The device was fabricated using easy-to-implement, one-step microfluidic patterning and antibody conjugation of AuNRs. Scanning the scattering light intensity across the microarrays of AuNR ensembles with dark-field imaging optics, allowing for quantitative cytokine measurements at concentrations ranging from 10 to 10,000 pg/mL in a 1 μL sample of serum. A whole parallel on-chip assays were completed within 40 min, which involved the manual loading, incubation, and washing of 8 different samples, and multianalyte detection repeated 10 times for each sample using the entire 480 LSPR biosensor arrays [91]. The study has taken the first significant step toward translating nano-plasmonic biosensing technology to its practical use in serum cytokine based on immune status monitoring.

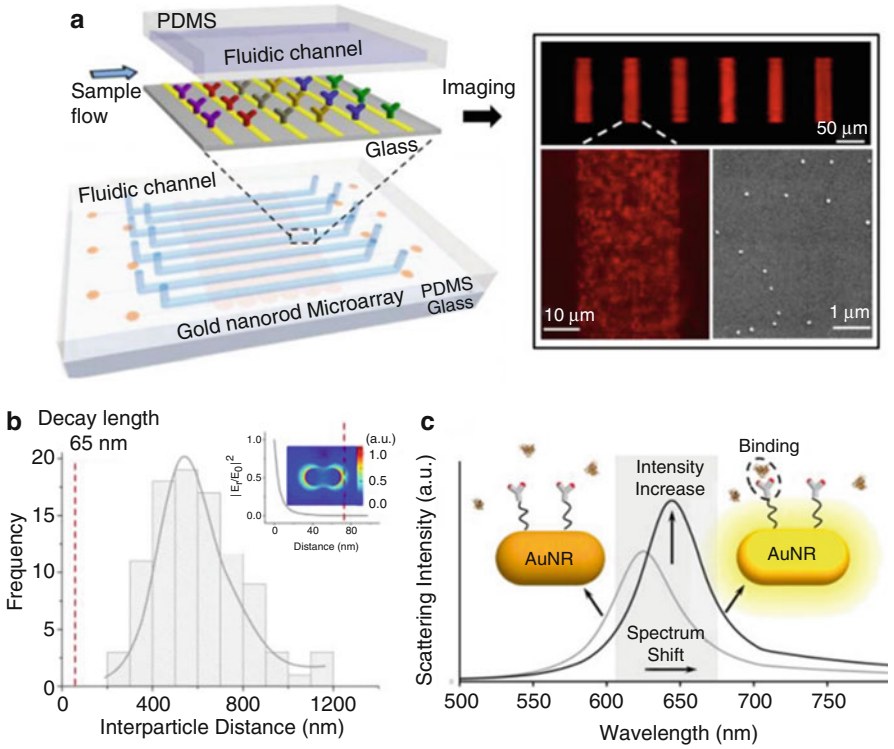

Fig. 4.28 Schematic and principle of the method. (**a**) Schematic of the LSPR microarray chip and the image under dark-field microscopy and scanning electron microscopy (SEM). (**b**) Histograms of the particle-to-particle distance of the AuNRs on the LSPR microarray chip. (**c**) The principle of the LSPR microarray method. This intensity change is imaged via the characteristic frequency (gray area) using EMCCD coupled dark-field microscopy (Reprinted with permission from Ref. [90]. Copyright 2015 American Chemical Society)

6 Conclusions and Future Perspective

This chapter has highlighted the theory and applications of in situ LSPR for monitoring the changes around the nanoparticles, sensing and imaging. A survey of the real time spectroscopy techniques and nanoparticle engineering approaches for application has been presented to indicate the potential and challenges for the "old" spectroscopy. An appreciation of fundamentals of LSPR offers opportunities to tune and control optical behavior. The strong dependence of LSPR on NP shape, size and composition provides methods to improve the sensitivity of sensor. Despite the challenges that LSPR faces in terms of implementation of practical applications, the scientific literature indicates that interest in assay development continues to grow at an exponential rate. LSPR provides rapid, easy and cost-effective experimental designs with at least comparable analytical performance. Additionally, LSPR

enables single nanoparticle detection and probing extremely small volumes. The understanding of the plasmonic response of nanoparticles would be extended and these LSPR-based sensing experiments will be optimized, leading to higher sensitivity, faster and more reversible responses and an ever-broadening scope of applicability. In the near future, the research focus of in situ LSPR based analytical techniques will continuously concern with the following aspects.

1. Real-time tracking dynamic events using single plasmonic nanoparticles. In situ spectroscopy of single NPs undergoing chemical reaction allows us to capture the rich dynamic structural evolution of the nanostructure in the course of reaction exchange. Such single-nanoparticle-level insights into the complex dynamics of a seemingly simple reaction, which would otherwise be masked by heterogeneity in ensemble studies, may enable more the understanding and control of catalyst restructuring in corrosive/reactive environments.
2. Real-time monitoring biochemical reaction in vivo. Biochemical reactions play a critical role in the metabolism, energy generation and exchange in the biosystem. By real-time monitoring the scattering feature changes of single plasmonic nanoparticles in vivo, the critical biochemical reaction in biosystem can be investigated, which may in turn provide a new opportunity for drug screening, disease diagnosis, and cancer therapy. A single-nanoparticle LSPR spectroscopy is an important tool for understanding the relationship between local structure and spectra. Such experiments will be able to provide information of local RI changes inside cells and tissues for tracking in vivo chemical reactions.
3. Miniaturization of point-of-care and microfluidic devices. LSPR can provide a platform for multiplexed analysis, which is crucial for clinical diagnostics and proteomics. At the same time, recent interest has grown enormously towards multiplexed and microfluidic LSPR biosensing platforms, leading to advances in fabrication and microscopy. Undoubtedly drug-screening devices will also benefit from these advances. Future point-of-care devices will most likely require interfacing LSPR technologies with cell lysing and separation platforms for true lab-on-a-chip applications.

References

1. Willets KA, Van Duyne RP (2007) Localized surface plasmon resonance spectroscopy and sensing. Annu Rev Phys Chem 58:267–297
2. Turkevich J, Stevenson PC, Hillier J (1951) A study of the nucleation and growth processes in the synthesis of colloidal gold. Discuss Faraday Soc 11:55–75
3. Lee PC, Meisel D (1982) Adsorption and surface-enhanced Raman of dyes on silver and gold sols. J Phys Chem 86:3391–3395
4. Frens G (1973) Controlled nucleation for the regulation of the particle size in monodisperse gold suspensions. Nature 241:20–22
5. Piella J, Bastus NG, Puntes V (2016) Size-controlled synthesis of sub-10-nanometer citrate-stabilized gold nanoparticles and related optical properties. Chem Mater 28:1066–1075

6. Luo M, Huang H, Choi S-I, Zhang C, da Silva RR, Peng H-C, Li Z-Y, Liu J, He Z, Xia Y (2015) Facile synthesis of Ag nanorods with no plasmon resonance peak in the visible region by using pd decahedra of 16 nm in size as seeds. ACS Nano 9:10523–10532
7. Wang W, Yan Y, Zhou N, Zhang H, Li D, Yang D (2016) Seed-mediated growth of Au nanorings with size control on Pd ultrathin nanosheets and their tunable surface plasmonic properties. Nanoscale 8:3704–3710
8. Chao Y-J, Lyu Y-P, Wu Z-W, Lee C-L (2016) Seed-mediated growth of Ag nanocubes and their size-dependent activities toward oxygen reduction reaction. Int J Hydrog Energy 41:3896–3903
9. Zhang X, Hicks EM, Zhao J, Schatz GC, Van Duyne RP (2005) Electrochemical tuning of silver nanoparticles fabricated by nanosphere lithography. Nano Lett 5:1503–1507
10. Jin RC, Cao YC, Hao EC, Metraux GS, Schatz GC, Mirkin CA (2003) Controlling anisotropic nanoparticle growth through plasmon excitation. Nature 425:487–490
11. Jin RC, Cao YW, Mirkin CA, Kelly KL, Schatz GC, Zheng JG (2001) Photoinduced conversion of silver nanospheres to nanoprisms. Science 294:1901–1903
12. Noguez C (2007) Surface plasmons on metal nanoparticles: the influence of shape and physical environment. J Phys Chem C 111:3806–3819
13. Cao J, Sun T, Grattan KTV (2014) Gold nanorod-based localized surface plasmon resonance biosensors: a review. Sens Actuators B Chem 195:332–351
14. Zhang Q, Zhou Y, Villarreal E, Lin Y, Zou S, Wang H (2015) Faceted gold nanorods: nanocuboids, convex nanocuboids, and concave nanocuboids. Nano Lett 15:4161–4169
15. Nikoobakht B, El-Sayed MA (2003) Preparation and growth mechanism of gold nanorods (NRs) using seed-mediated growth method. Chem Mater 15:1957–1962
16. Tian L, Chen E, Gandra N, Abbas A, Singamaneni S (2012) Gold nanorods as plasmonic nanotransducers: distance-dependent refractive index sensitivity. Langmuir 28:17435–17442
17. Scarabelli L, Grzelczak M, Liz-Marzán LM (2013) Tuning gold nanorod synthesis through prereduction with salicylic acid. Chem Mater 25:4232–4238
18. Martinsson E, Shahjamali MM, Large N, Zaraee N, Zhou Y, Schatz GC, Mirkin CA, Aili D (2016) Influence of surfactant bilayers on the refractive index sensitivity and catalytic properties of anisotropic gold nanoparticles. Small 12:330–342
19. Ye S, Song J, Tian Y, Chen L, Wang D, Niu H, Qu J (2015) Photochemically grown silver nanodecahedra with precise tuning of plasmonic resonance. Nanoscale 7:12706–12712
20. Bansal A, Verma SS (2015) Optical response of noble metal alloy nanostructures. Phys Lett A 379:163–169
21. Njoki PN, Lim IIS, Mott D, Park H-Y, Khan B, Mishra S, Sujakumar R, Luo J, Zhong C-J (2007) Size correlation of optical and spectroscopic properties for gold nanoparticles. J Phys Chem C 111:14664–14669
22. Jain PK, Lee KS, El-Sayed IH, El-Sayed MA (2006) Calculated absorption and scattering properties of gold nanoparticles of different size, shape, and composition: applications in biological imaging and biomedicine. J Phys Chem B 110:7238–7248
23. Tang B, Xu S, Jian X, Tao J, Xu W (2010) Real-time, in-situ, extinction spectroscopy studies on silver-nanoseed formation. Appl Spectrosc 64:1407–1415
24. Amendola V, Meneghetti M (2009) Size evaluation of gold nanoparticles by UV−vis spectroscopy. J Phys Chem C 113:4277–4285
25. Tang B, An J, Zheng X, Xu S, Li D, Zhou J, Zhao B, Xu W (2008) Silver nanodisks with tunable size by heat aging. J Phys Chem C 112:18361–18367
26. O'Brien MN, Jones MR, Kohlstedt KL, Schatz GC, Mirkin CA (2015) Uniform circular disks with synthetically tailorable diameters: two-dimensional nanoparticles for plasmonics. Nano Lett 15:1012–1017
27. Zhang Q, Li W, Moran C, Zeng J, Chen J, Wen L-P, Xia Y (2010) Seed-mediated synthesis of Ag nanocubes with controllable edge lengths in the range of 30−200 nm and comparison of their optical properties. J Am Chem Soc 132:11372–11378

28. Rycenga M, Cobley CM, Zeng J, Li W, Moran CH, Zhang Q, Qin D, Xia Y (2011) Controlling the synthesis and assembly of silver nanostructures for plasmonic applications. Chem Rev 111:3669–3712
29. Chan GH, Zhao J, Hicks EM, Schatz GC, Van Duyne RP (2007) Plasmonic properties of copper nanoparticles fabricated by nanosphere lithography. Nano Lett 7:1947–1952
30. Zhao C, Zhu Y, Su Y, Guan Z, Chen A, Ji X, Gui X, Xiang R, Tang Z (2015) Tailoring plasmon resonances in aluminium nanoparticle arrays fabricated using anodic aluminium oxide. Adv Opt Mater 3:248–256
31. Ma YW, Zhang LH, Wu ZW, Yi MF, Zhang J, Jian GS (2015) The study of tunable local surface plasmon resonances on Au-Ag and Ag-Au core-shell alloy nanostructure particles with DDA method. Plasmonics 10:1791–1800
32. Verbruggen SW, Keulemans M, Martens JA, Lenaerts S (2013) Predicting the surface plasmon resonance wavelength of gold-silver alloy nanoparticles. J Phys Chem C 117:19142–19145
33. Gao C, Hu Y, Wang M, Chi M, Yin Y (2014) Fully alloyed Ag/Au nanospheres: combining the plasmonic property of Ag with the stability of Au. J Am Chem Soc 136:7474–7479
34. Tuersun P (2016) Simulated localized surface plasmon spectra of single gold and silver nanobars. Optik 127:3466–3470
35. Liu H, Liu T, Zhang L, Han L, Gao C, Yin Y (2015) Etching-free epitaxial growth of gold on silver nanostructures for high chemical stability and plasmonic activity. Adv Funct Mater 25:5435–5443
36. Zohar N, Chuntonov L, Haran G (2014) The simplest plasmonic molecules: metal nanoparticle dimers and trimers. J Photochem Photobiol C Photochem Rev 21:26–39
37. Tian XD, Zhou YD, Thota S, Zou SL, Zhao J (2014) Plasmonic coupling in single silver nanosphere assemblies by polarization-dependent dark-field scattering spectroscopy. J Phys Chem C 118:13801–13808
38. Halas NJ, Lal S, Chang W-S, Link S, Nordlander P (2011) Plasmons in strongly coupled metallic nanostructures. Chem Rev 111:3913–3961
39. Fang A, White SL, Masitas RA, Zamborini FP, Jain PK (2015) One-to-one correlation between structure and optical response in a heterogeneous distribution of plasmonic constructs. J Phys Chem C 119:24086–24094
40. Liu J, Kan C, Li Y, Xu H, Ni Y, Shi D (2015) Plasmonic properties of the end-to-end and side-by-side assembled Au nanorods. Plasmonics 10:117–124
41. Chen TH, Reinhard BM (2016) Assembling color on the nanoscale: multichromatic switchable pixels from plasmonic atoms and molecules. Adv Mater 28:3522–3527
42. Hentschel M, Saliba M, Vogelgesang R, Giessen H, Alivisatos AP, Liu N (2010) Transition from isolated to collective modes in plasmonic oligomers. Nano Lett 10:2721–2726
43. Tang Y, Zhang W, Liu J, Zhang L, Huang W, Huo F, Tian D (2015) A plasmonic nanosensor for lipase activity based on enzyme-controlled gold nanoparticles growth in situ. Nanoscale 7:6039–6044
44. Gulati A, Liao H, Hafner JH (2006) Monitoring gold nanorod synthesis by localized surface plasmon resonance. J Phys Chem B 110:22323–22327
45. Taz H, Ruther R, Malasi A, Yadavali S, Carr C, Nanda J, Kalyanaraman R (2015) In situ localized surface plasmon resonance (LSPR) spectroscopy to investigate kinetics of chemical bath deposition of CdS thin films. J Phys Chem C 119:5033–5039
46. Jang GG, Blake P, Roper DK (2013) Rate-limited electroless gold thin film growth: a real-time study. Langmuir 29:5476–5486
47. Tang B, Xu S, An J, Zhao B, Xu W, Lombardi JR (2009) Kinetic effects of halide ions on the morphological evolution of silver nanoplates. Phys Chem Chem Phys 11:10286–10292
48. Rodriguez-Lorenzo L, Romo-Herrera JM, Perez-Juste J, Alvarez-Puebla RA, Liz-Marzan LM (2011) Reshaping and LSPR tuning of Au nanostars in the presence of CTAB. J Mater Chem 21:11544–11549
49. Kedia A, Kumar PS (2013) Controlled reshaping and plasmon tuning mechanism of gold nanostars. J Mater Chem C 1:4540–4549

50. Tang B, Xu S, Tao J, Wu Y, Xu W, Ozaki Y (2010) Two-dimensional correlation localized surface plasmon resonance spectroscopy for analysis of the interaction between metal nanoparticles and bovine serum albumin. J Phys Chem C 114:20990–20996
51. Langhammer C, Larsson EM (2012) Nanoplasmonic in situ spectroscopy for catalysis applications. ACS Catal 2:2036–2045
52. Larsson EM, Langhammer C, Zoric I, Kasemo B (2009) Nanoplasmonic probes of catalytic reactions. Science 326:1091–1094
53. Larsson EM, Millet J, Gustafsson S, Skoglundh M, Zhdanov VP, Langhammer C (2012) Real time indirect nanoplasmonic in situ spectroscopy of catalyst nanoparticle sintering. ACS Catal 2:238–245
54. Henry A-I, Bingham JM, Ringe E, Marks LD, Schatz GC, Van Duyne RP (2011) Correlated structure and optical property studies of plasmonic nanoparticles. J Phys Chem C 115:9291–9305
55. Liu Y, Huang CZ (2013) Real-time dark-field scattering microscopic monitoring of the in situ growth of single ag@hg nanoalloys. ACS Nano 7:11026–11034
56. Park Y, Lee C, Ryu S, Song H (2015) Ex situ and in situ surface plasmon monitoring of temperature-dependent structural evolution in galvanic replacement reactions at a single-particle level. J Phys Chem C 119:20125–20135
57. Wang Y, Zou HY, Huang CZ (2015) Real-time monitoring of oxidative etching on single Ag nanocubes via light-scattering dark-field microscopy imaging. Nanoscale 7:15209–15213
58. Shegai T, Langhammer C (2011) Hydride formation in single palladium and magnesium nanoparticles studied by nanoplasmonic dark-field scattering spectroscopy. Adv Mater 23:4409–4414
59. Cheng J, Liu Y, Cheng X, He Y, Yeung ES (2010) Real time observation of chemical reactions of individual metal nanoparticles with high-throughput single molecule spectral microscopy. Anal Chem 82:8744–8749
60. Shi L, Jing C, Ma W, Li D-W, Halls JE, Marken F, Long Y-T (2013) Plasmon resonance scattering spectroscopy at the single-nanoparticle level: real-time monitoring of a click reaction. Angew Chem Int Ed 52:6011–6014
61. Gao PF, Yuan BF, Gao MX, Li RS, Ma J, Zou HY, Li YF, Li M, Huang CZ (2015) Visual identification of light-driven breakage of the silver-dithiocarbamate bond by single plasmonic nanoprobes. Sci Rep 5:15427
62. Novo C, Funston AM, Mulvaney P (2008) Direct observation of chemical reactions on single gold nanocrystals using surface plasmon spectroscopy. Nat Nanotechnol 3:598–602
63. Collins SSE, Cittadini M, Pecharroman C, Martucci A, Mulvaney P (2015) Hydrogen spillover between single gold nanorods and metal oxide supports: a surface plasmon spectroscopy study. ACS Nano 9:7846–7856
64. Liu N, Tang ML, Hentschel M, Giessen H, Alivisatos AP (2011) Nanoantenna-enhanced gas sensing in a single tailored nanofocus. Nat Mater 10:631–636
65. Seo D, Park G, Song H (2012) Plasmonic monitoring of catalytic hydrogen generation by a single nanoparticle probe. J Am Chem Soc 134:1221–1227
66. Tittl A, Yin X, Giessen H, Tian X-D, Tian Z-Q, Kremers C, Chigrin DN, Liu N (2013) Plasmonic smart dust for probing local chemical reactions. Nano Lett 13:1816–1821
67. Jing C, Rawson FJ, Zhou H, Shi X, Li W-H, Li D-W, Long Y-T (2014) New insights into electrocatalysis based on plasmon resonance for the real-time monitoring of catalytic events on single gold nanorods. Anal Chem 86:5513–5518
68. Cennamo N, D'Agostino G, Dona A, Dacarro G, Pallavicini P, Pesavento M, Zeni L (2013) Localized surface plasmon resonance with five-branched gold nanostars in a plastic optical fiber for bio-chemical sensor implementation. Sensors 13:14676–14686
69. Sherry LJ, Jin RC, Mirkin CA, Schatz GC, Van Duyne RP (2006) Localized surface plasmon resonance spectroscopy of single silver triangular nanoprisms. Nano Lett 6:2060–2065
70. Bukasov R, Ali TA, Nordlander P, Shumaker-Parry JS (2010) Probing the plasmonic near-field of gold nanocrescent antennas. ACS Nano 4:6639–6650

71. Bolduc OR, Masson J-F (2011) Advances in surface plasmon resonance sensing with nanoparticles and thin films: nanomaterials, surface chemistry, and hybrid plasmonic techniques. Anal Chem 83:8057–8062
72. Chung T, Lee S-Y, Song EY, Chun H, Lee B (2011) Plasmonic nanostructures for nano-scale bio-sensing. Sensors 11:10907–10929
73. Lin VK, Teo SL, Marty R, Arbouet A, Girard C, Alarcon-Llado E, Liu SH, Han MY, Tripathy S, Mlayah A (2010) Dual wavelength sensing based on interacting gold nanodisk trimers. Nanotechnology 21:305501
74. Hao F, Nordlander P, Sonnefraud Y, Dorpe PV, Maier SA (2009) Tunability of subradiant dipolar and fano-type plasmon resonances in metallic ring/disk cavities: implications for nanoscale optical sensing. ACS Nano 3:643–652
75. Zhang S, Bao K, Halas NJ, Xu H, Nordlander P (2011) Substrate-induced fano resonances of a plasmonic nanocube: a route to increased-sensitivity localized surface plasmon resonance sensors revealed. Nano Lett 11:1657–1663
76. Polavarapu L, Liz-Marzan LM (2013) Towards low-cost flexible substrates for nanoplasmonic sensing. Phys Chem Chem Phys 15:5288–5300
77. Wang H, Chen D, Wei Y, Yu L, Zhang P, Zhao J (2011) A localized surface plasmon resonance light scattering-based sensing of hydroquinone via the formed silver nanoparticles in system. Spectrochim Acta A Mol Biomol Spectrosc 79:2012–2016
78. Bingham JM, Anker JN, Kreno LE, Van Duyne RP (2010) Gas sensing with high-resolution localized surface plasmon resonance spectroscopy. J Am Chem Soc 132:17358–17359
79. Kazuma E, Tatsuma T (2014) Localized surface plasmon resonance sensors based on wavelength-tunable spectral dips. Nanoscale 6:2397–2405
80. Huang D, Hu T, Chen N, Zhang W, Di J (2014) Development of silver/gold nanocages onto indium tin oxide glass as a reagentless plasmonic mercury sensor. Anal Chim Acta 825:51–56
81. Sugawa K, Tahara H, Yamashita A, Otsuki J, Sagara T, Harumoto T, Yanagida S (2015) Refractive index susceptibility of the plasmonic palladium nanoparticle: potential as the third plasmonic sensing material. ACS Nano 9:1895–1904
82. Szunerits S, Boukherroub R (2012) Sensing using localised surface plasmon resonance sensors. Chem Commun 48:8999–9010
83. Feuz L, Jonsson MP, Hook F (2012) Material-selective surface chemistry for nanoplasmonic sensors: optimizing sensitivity and controlling binding to local hot spots. Nano Lett 12:873–879
84. Chen P, Liedberg B (2014) Curvature of the localized surface plasmon resonance peak. Anal Chem 86:7399–7405
85. Lodewijks K, Van Roy W, Borghs G, Lagae L, Van Dorpe P (2012) Boosting the figure-of-merit of LSPR-based refractive index sensing by phase-sensitive measurements. Nano Lett 12:1655–1659
86. Ho FH, Wu Y-H, Ujihara M, Imae T (2012) A solution-based nano-plasmonic sensing technique by using gold nanorods. Analyst 137:2545–2548
87. Liu Y, Zhao Y, Wang Y, Li CM (2015) Polyamine-capped gold nanorod as a localized surface Plasmon resonance probe for rapid and sensitive copper(II) ion detection. J Colloid Interface Sci 439:7–11
88. Wang G, Chen Z, Chen L (2011) Mesoporous silica-coated gold nanorods: towards sensitive colorimetric sensing of ascorbic acid via target-induced silver overcoating. Nanoscale 3:1756–1759
89. Ma X, Truong PL, Anh NH, Sim SJ (2015) Single gold nanoplasmonic sensor for clinical cancer diagnosis based on specific interaction between nucleic acids and protein. Biosens Bioelectron 67:59–65
90. Ruemmele JA, Hall WP, Ruvuna LK, Van Duyne RP (2013) A localized surface plasmon resonance imaging instrument for multiplexed biosensing. Anal Chem 85:4560–4566
91. Chen P, Chung MT, McHugh W, Nidetz R, Li Y, Fu J, Cornell TT, Shanley TP, Kurabayashi K (2015) Multiplex serum cytokine immunoassay using nanoplasmonic biosensor microarrays. ACS Nano 9:4173–4181

In Situ X-Ray Absorption Spectroscopy Studies of Functional Nanomaterials

5

Soma Chattopadhyay, Soon Gu Kwon, Elena V. Shevchenko, Jeffrey T. Miller, and Steve M. Heald

Contents

S. Chattopadhyay (✉)
Elgin Community College, Elgin, IL, USA
e-mail: soma.tifr@gmail.com

S. G. Kwon
Center for Nanoparticle Research, Institute for Basic Science and Seoul National University, Seoul, Republic of Korea

E. V. Shevchenko
Nanoscience and Technology division, Argonne National Laboratory, Argonne, IL, USA

J. T. Miller
School of Chemical Engineering, Purdue University, West Lafayette, IN, USA

S. M. Heald
Advanced Photon Source, Argonne National Laboratory, Argonne, IL, USA

© Springer-Verlag GmbH Germany, part of Springer Nature 2018

C. S. S. R. Kumar (ed.), *In-situ Characterization Techniques for Nanomaterials*,
https://doi.org/10.1007/978-3-662-56322-9_5

1 Definition of the Topic

X-ray absorption spectroscopy (XAS) is a powerful technique to study the unoccupied states and the local structure around an excited species of atoms from an element present in a material. Recently, in situ XAS is being used to study catalytic transformations, synthesis of nanoparticles and thin films, kinetics of potential battery materials, etc. Such studies can explain the mechanisms associated with the formation of chemical species during various types of reactions. In this chapter, we shall describe how XAS has proved to be a powerful characterization tool for nanomaterials with potential applications by determining the variation in interatomic distances, coordination numbers, and the type of neighboring atoms within the first few coordination shells of the atom of interest in nanoparticles.

2 Overview

Nanomaterials defined as materials with at least one dimension in the nanometer ($1\ \text{nm} = 10^{-9}$ m) range have been found to possess structure and properties that are significantly different from those of the corresponding bulk material. The large surface-to-volume ratio of nanoparticles (NP) makes their surface play a key role in tailoring their physical and chemical properties. Hence, they have been found to possess unique characteristics making them suitable for many novel applications related to energy storage, catalysis, electronic devices, drug delivery, etc. Studying such unique materials, so as to harness their properties for suitable applications, would need powerful characterization techniques.

Synchrotron-based X-ray absorption spectroscopy comprising of EXAFS (extended X-ray absorption fine structure) and XANES (X-ray absorption near edge structure) are exquisite characterization tools since they can study local structure around atoms in crystalline as well as amorphous and disordered materials and also in all states of matter. Hence, XAS is applicable and useful for nanomaterials related to condensed matter physics, engineering sciences, chemistry, biology, and environmental and geological sciences. Quick-XAS, i.e., Quick-EXAFS (QEXAFS) and Quick-XANES (QXANES) combined together, enables time-resolved spectroscopic studies down to millisecond regime and can provide information related to chemical changes and phase transitions taking place during the formation of NPs, cycling of batteries, catalytic reactions, physical transformations, and biological changes.

In this chapter, we shall describe how QEXAFS and QXANES have been successfully used to study mechanisms of chemical reactions and kinetics related to different types of NPs.

3 Introduction

The present century has seen a tremendous growth in the field of Nanotechnology. The ability to drastically change the physical and chemical properties of nanomaterials by changing their size and shape has increased their potential for many unique and useful applications relevant to modern times: high energy density batteries, catalysts for cars with high fuel efficiency, medical implants and drug delivery systems, computer chips related to miniaturization, materials for low-cost flat panel displays, elimination of environmental pollutants, etc. The growth of this emerging field has been possible due to novel synthesis routes that have been developed by scientists and engineers in the past decades. This coupled with the development of novel characterization tools and techniques that were initiated by the invention of the scanning tunneling microscope (STM) in the 1980s have further enriched the studies of nanomaterials of different types. Especially important for these nanomaterials have been the techniques based on synchrotron sources with a strong X-ray beam of high luminosity, which has made time-dependent studies possible in the fields of spectroscopy, scattering, diffraction, and imaging.

Standard X-ray absorption spectroscopy (XAS) scans at synchrotron sources were developed in the 1970s to study the detailed local structure around individual atoms from an element present in a compound [1]. These scans consist of step scans where the monochromator used to select the energy range is moved by a small amount in energy. Data are collected from the beginning to the end of the energy range till the entire spectrum for a particular element has been generated. Each of these scans generally takes 15–20 min. Quick-XAS measurements were developed in the mid-1990s at several synchrotron sources where data are collected on the fly, i.e., the monochromator motors are encoded and the crystals selecting the beam energy are moved with constant velocity from the beginning to the end of the energy range as the data are collected [2–7]. These scans have reduced the overhead time associated with moving the monochromator motor during step scans. Hence, a QEXAFS scan can be completed in 1–3 min and in some cases in several seconds. QXANES scans be collected in few seconds and sometimes in milli- and microseconds. Hence, time-resolved XAS studies have become possible and are becoming popular due to the unique combination of high penetration depth of hard X-ray beam and element sensitivity with time resolution. Apart from this, a new type of XAS called energy dispersive EXAFS (EDE) has been developed where a bent polychromator and a position-sensitive detector are used to collect data. The beam position is related to energy and the entire spectrum is collected in parallel. Here, the XAS spectrum can be collected in milliseconds, thereby making it extremely useful for studying catalytic reactions. Presently, research is being conducted to introduce ultrafast EXAFS and XANES also using pump probe methods [5].

Such developments related to QXAS have been extremely useful for in situ studies of various systems from different branches of science and engineering,

especially those related to the evolving field of nanotechnology. Nanomaterials have broad X-ray diffraction (XRD) peaks, and hence only limited structural information is available from XRD. In situ spectroscopy by itself as well as coupled with in situ scattering, imaging, and XRD can throw light on the pathways associated with synthesis of NPs and thereby help to produce tailor-made nano-systems in future for novel applications. In this chapter, we shall focus on how QXAS has already been used to study the local structural changes associated with (a) colloidal synthesis of NPs, (b) chemical reactions associated with homogeneous and heterogeneous catalysis, (c) synthesis of metallic NPs in nano-reactors, and (d) chemical changes occurring during cycling of battery materials.

4 EXAFS and XANES: Theory and Instrumentation

XAS is a powerful technique to study the local structure around an excited species of atoms. XAS in general consists of two regimes: (a) X-ray absorption near edge structure (XANES) and (b) extended X-ray absorption fine structure (EXAFS) [1, 8–12]. In general, EXAFS refers to the sinusoidal oscillations observed over a wide energy range extending to 1000 eV above the edge, while XANES refers to fine structure around an absorption edge extending typically 50 eV. XANES is strongly sensitive to the electronic levels around the Fermi level and hence provides information about the oxidation states and coordination geometries. EXAFS is used to determine the interatomic distances, variation in interatomic distances, coordination number, and the type of neighboring atoms within the first few coordination shells of the atom that is being studied by tuning the incident X-ray energy to the absorption edge of the atom.

A typical EXAFS spectrum is shown in Fig. 5.1a. X-ray photons of the specific energy chosen to interact with the atoms under study produce photoelectrons that are scattered by the neighboring atoms. The interference between the outgoing photoelectron wave and the scattered photoelectron wave at the probe atom causes oscillations in the absorption coefficient. EXAFS is defined as the normalized oscillatory part of the absorption coefficient above the absorption edge of the excited atoms in a material. Figure 5.1b shows the background subtracted data $\chi(k)$ in k-space. The Fourier transform of the normal oscillatory signal has peaks whose intensity depends on the type and number of atoms at a particular distance, and whose width depends on the structural disorder of the same atoms (Fig. 5.1c). The peak position represents the distance between the excited atom and the neighboring atom but occurs at slightly shorter distances than the corresponding theoretical bond length due to a phase shift, φ_j, between the incident and scattered waves. EXAFS spectra are modeled to obtain the average number, type, and distance of atoms around the probe atom, as well as mean square displacement of the average distance (σ^2). Figure 5.1d shows the pre-edge region of the EXAFS spectrum: the energy change is referred to as the edge jump. This region between −50 eV and +50 eV around the edge region is called XANES.

When the energy of incident X-rays photons (E) is scanned across the binding energy of a core shell electron, there is a sharp increase in the probability for X-ray to

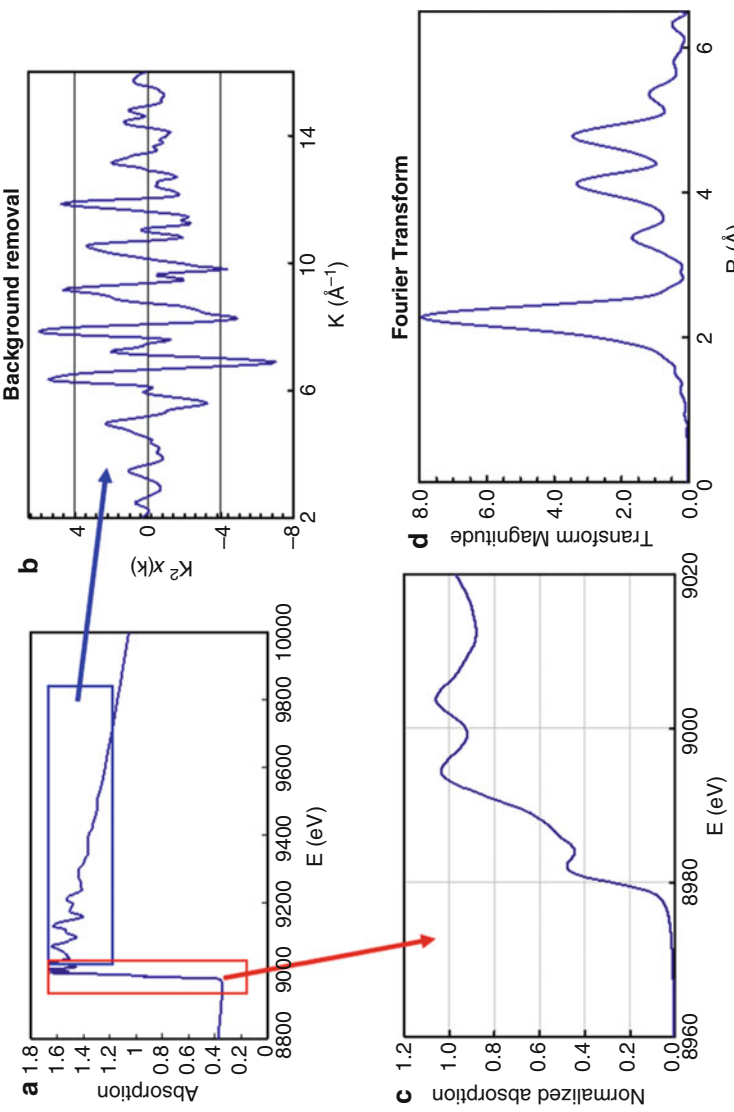

Fig. 5.1 (**a**) A typical EXAFS spectrum. (**b**) The background subtracted data in reciprocal space. (**c**) XANES region of the spectrum and (**d**) Fourier transformed EXAFS spectrum

be absorbed (μ), resulting in an absorption edge. The absorbed X-ray results in an excited atomic state consisting of a core hole and photoelectron. The photoelectron propagates as a wave with the wave number k,

$$k = \sqrt{2m(E - E_0)/\hbar^2} \tag{5.1}$$

where $\hbar = h/2\pi$ with h being the Planck constant, E_0 is at the absorption edge, and m is the electron mass. If the absorbing atoms are isolated (such as in an inert gas), μ has a relatively smooth atomic background (μ_0). On the other hand, if surrounding atoms exist as in solids, the photoelectron wave is scattered by them, and the outgoing and backscattered electron waves interfere, resulting a modulation of the absorption coefficient μ written as

$$\mu = \mu_0[1 + \chi(k)] \tag{5.2}$$

These modulations in $\chi(k)$ are called EXAFS and expressed as a sum of the sinusoidal functions from the scattering paths from all the neighboring atoms as

$$\chi(k) = \sum_{j=1} A_j(k) \sin\left(2kR_j + \varphi_j\right) \tag{5.3}$$

$$A_j(k) = \frac{N_j}{kR_j^2} S_0^2 F_j(k) e^{-2R_j/\lambda} e^{-2k^2\sigma_j^2} \tag{5.4}$$

and φ_j being the phase shift from the potentials of the absorber and backscattering atoms. These phase shifts are approximately linear and thus, the individual contributions maintain their sinusoidal character.

EXAFS analysis gives structural information around the absorbing atoms including number of neighbors (N_j), bond length (R_j), and the bond length distribution characterized by a Debye-Waller factor (σ_j^2). Since the mean free paths (λ) of the electrons are usually short, information is limited to a few Å around absorbing atoms; therefore, EXAFS is a local structural probe. Particularly important are the backscattering functions $F_j(k)$ and phase shift φ_j, which are characteristic of the atomic species of the scattering atoms; thus, EXAFS analysis can distinguish between several types of atoms which may be present in a compound. The Fourier transform of k-weighted $\chi(k)$ separates the signal in terms of the radial distances (R_j) between the absorbing atom and its neighbors. The peak height depends on the type and number of atoms at a particular distance and the peak width depends on the structural disorder (σ_j^2) of the atoms at that distance. EXAFS data can be modeled to obtain N_j, R_j, and σ_j^2 for the first few coordination shells.

A typical setup for performing QXAS measurements is shown in Fig. 5.2. The X-ray beam from the synchrotron source goes through a double a crystal monochromator which selects the energy range needed for the element of interest. The beam then passes through filters and a harmonic rejection (HR) mirror. The latter is used to eliminate higher energy X-rays. Most HR mirrors consist of Rhodium, Platinum, and

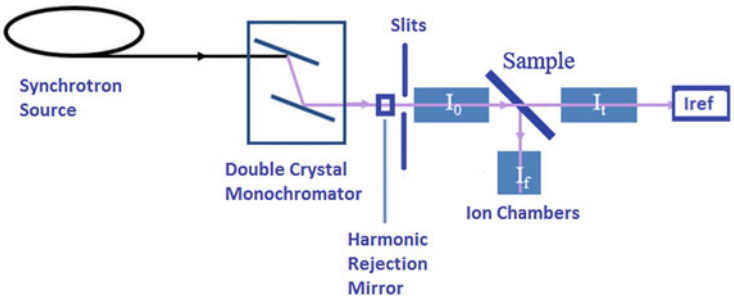

Fig. 5.2 A typical XAS setup in a beamline

glass stripes for use in different energy ranges. The beam is then defined with the help of mechanical slits and passes through the incident ion chamber (I_0) that counts the number of photons falling on the sample. Size of incident beam is always kept smaller than the size of the sample. Concentrated samples are placed perpendicular to the beam, whereas dilute samples are placed at 45° to the path of the beam to allow for fluorescence detection. For homogenous, highly concentrated samples, μ is measured with transmission geometry and obtained from Beer's law as

$$\mu x = \ln(I_0/I_t) \tag{5.5}$$

where x is thickness of the sample, and I_0 and I_t are incident and transmitted X-ray intensity, respectively. For diluted samples, the fluorescence signal is used to obtain μ since the fluorescence intensity is proportional to the number of core-holes created by X-ray absorption and thus proportional to the absorption coefficient. It is more sensitive than transmission mode because fluorescence comes only from the element of interest. The transmission ion chamber (I_t) counts the number of photons in the beam after passing through the sample. Fluorescence X-ray from dilute samples is detected with an ion chamber (I_f) placed at 90° to the incident beam. These ion chambers are equipped with filters and Soller slits to minimize the background. I_{ref} is the reference ion chamber placed after the transmission ion chamber.

A metal foil of the element which is being probed is placed on this ion chamber so as to verify the calibration of the edge energies before merging the scans. The foil scans are important since the amplitude $\left(S_0^2\right)$ needed to fit the data for a particular element is obtained by fitting the EXAFS data from the respective foil. $\left(S_0^2\right)$ can depend on chemical environment and is energy dependent. However, it mainly comes from the atomic nature of the central atom, and these dependencies are small. The gases in the ionization chamber were optimized on the basis of the X-ray energy so that 1–5% of the X-ray gets absorbed in I_0, 70% in I_t, and the rest in I_{ref}. Energy calibration is done before data are taken at each edge energy. Solid samples are ground to fine powder with the particle size much less than one absorption length ($1/\mu \sim 40$ μm) to avoid the pinhole effect. The powder can be

rubbed on Kapton® tapes and stacked with the number of layers optimized so that the edge step ($\Delta\mu x$) at a particular edge energy becomes 0.5 ~ 1, the total absorption by the entire sample ($\mu_{total}x$) is less than 2.5, and absorption by the respective atom ($\mu_{element}x$) is about unity. Powder can also be mixed with the correct amount of fine powder of boron nitride and pressed into pellets so as to have the right edge step and absorption. Over 10 scans are recorded for each edge energy measured for a sample to ensure repeatability and averaged to improve statistics.

The data are processed using Athena [13]. Conventional EXAFS analysis consists of extracting the oscillations, $\chi(k)$, as a function of the photoelectron wave number (k) from the background-subtracted absorption spectrum, $\mu(E)$, and Fourier-transforming $\chi(k)$ into real space, $\chi(R)$. The measured absorption spectrum below the pre-edge region is fitted to a straight line. The background contribution above the postedge region is fitted to a cubic spline (a segmented third order polynomial). The fitted polynomials are extrapolated through the total energy region and subtracted from the total absorption spectra. The theoretical paths are generated using FEFF6 [14], and the models are constructed in the conventional way using the fitting program Artemis [13] to refine the fitting parameters. The background subtracted $\chi(R)$ data are fitted to models based on the FEFF-based calculations of the scattering paths using the relevant coordination numbers, Debye-Waller factor (σ^2), and bond lengths as parameters. Various scattering models and different fit ranges are tried using the Artemis fitting program, before arriving at the best fit.

5 Key Research Findings

Nanometer-sized particles in the form of loose aggregates, wires, spheres, and various other shapes and sizes have been found to possess superior structural, optical, electronic, and magnetic properties in many cases making them suitable candidates for versatile applications in new technological devices. Progress in instrumentation and detectors at the synchrotron sources in the last two decades has led to new and powerful characterization tools to probe the structure of materials. Especially novel and useful has been the invention of the time-resolved techniques in the field of high-resolution X-ray diffraction (HRXRD), small-angle X-ray scattering (SAXS), pair distribution function (PDF), imaging, and quick X-ray absorption spectroscopy (QXAS). These techniques have become critical to the research efforts in the field of nanomaterials. They have the ability to generate real-time structural data and can help to identify how structure influences the functional properties and performance of devices made from these nanomaterials. Hence, these advanced characterization methods have led to the development of new synthesis techniques for NPs and thin films. They have also helped in studying chemical and physical processes occurring in catalysis, energy storage in batteries, protein formations, mechanically stressed nano-alloys, etc. We shall describe how QXAS, either alone or in combination with HRXRD, SAXS, PDF, and other techniques, can help to enhance the study of advanced materials in various fields and their performance.

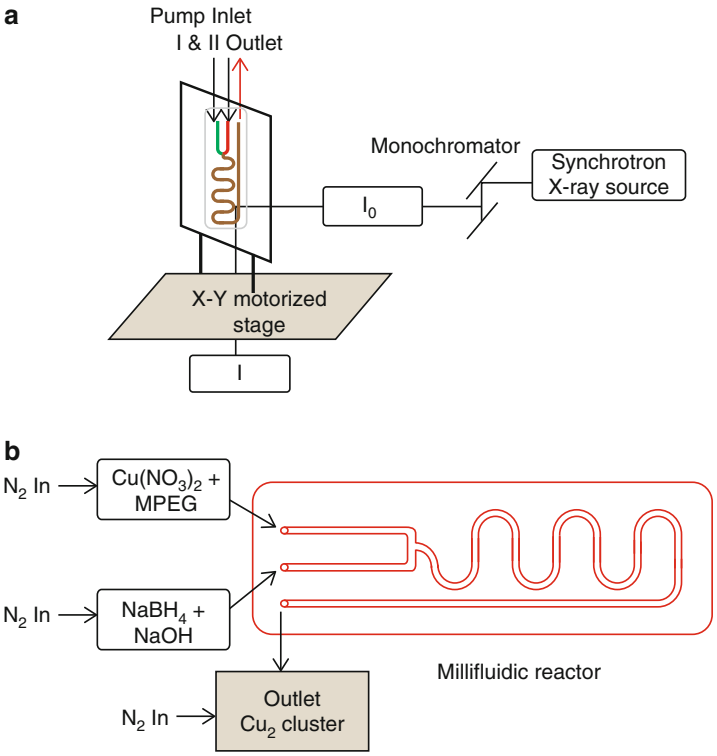

Fig. 5.3 (**a**) QXAS setup for microfluidic chip reactor in the beam with the beam coming from the right and the Stern-Heald detector placed at 90° to the beam. (**b**) The microfluidic chip reactor with the inlet tubes to introduce the precursors and the outlet tube for the clusters to come out and get collected for further characterization

5.1 Using In Situ XAS to Study Synthesis of Nanoclusters and Nanoparticles in the Beam

5.1.1 Metal Nanoclusters Using Milli−/Micro-Fluidic Chip Reactors

Recently, millifluid and microfluid reactors are being used for the preparation of NPs [15–21]. These lab-on-a-chip reactors consisting of small channels with micrometer diameter have liquid precursors flowing through them. They are allowed to react and produce NPs or nanoclusters. The use of time-resolved QXAS in conjunction with microfluidic lab-on-a-chip reactor has helped in studying the reaction dynamics of a chemical reaction at every stage during the formation of NPs.

A typical QXAS setup for chip-based microfluidic experiment on the beamline to produce copper nanoclusters [18] is shown in Fig. 5.3a, where the beam is scanned in a raster fashion over the microfluidic reactor while data are being collected at different points of the reactor with serpentine channels shown in Fig. 5.3b from the time of introducing the precursors to the end of the reaction where Cu nanoclusters come out

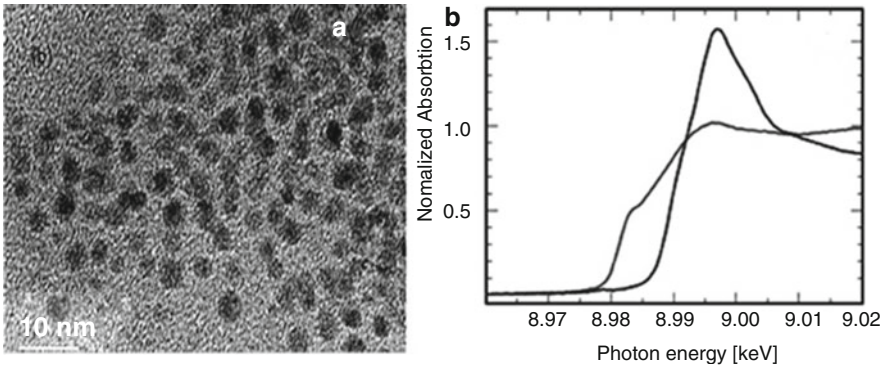

Fig. 5.4 (**a**) TEM image of ultra-small copper nanometer-sized clusters collected at the outlet of a millifluidic reactor. (**b**) QXANES spectra of Cu precursor (peak with higher absorption) versus Cu nanoclusters (peak with lower absorption) [18]

of the reactor. The nanoclusters are further characterized by transmission electron microscopy (TEM) and UV-vis absorption spectroscopy.

Figure 5.4a shows a TEM image of ultra-small Cu nanoclusters (UCNCs). Figure 5.4b compares the QXANES spectrum taken for $Cu(NO_3)_2.xH_2O$ precursor at the inlet to the spectrum for UCNCs at the outlet. EXAFS spectrum was taken every 30 s and at several positions along the path of the chip reactor to track the nanocluster formation process. Analysis of QXAS data helped in the determination of size, oxidation state, coordination number, and bond length of the UCNCs at various stages of their formation in the reactor and confirmed that oxidative impurities were not present in the sample collected from the outlet. These clusters, smallest ever produced using a lab-on-a-chip reactor, have been found to efficiently catalyze C-H oxidation reactions when supported on silica. In situ QXAS, proved to be an useful tool to study the controlled synthesis of Cu nanoclusters that were found to catalyze C-H oxidation for the first time, later was used successfully to study the formation of Au and Pt nanocluster also [19, 21]. Such studies will provide fundamental insights into formation of novel nanoclusters and NPs which will help to develop the next generation of high-performance advanced materials.

5.1.2 Synthesis of Colloidal Metal, Metal-Oxide, and Doped Metal-Oxide Nanoparticles

The exponential growth in the field of nanotechnology in the past two decades has led to the development of novel synthesis techniques in this field. One of them is the colloidal route which has helped to produce stable nanocrystals of metals, semiconductors, and insulators with uniform size distribution and of different shapes and sizes for a variety of applications [22–26]. Colloidal NPs generally possess an inorganic core surrounded by surfactants or ligands which are used in stabilizing them. Each individual colloidal nanocrystal is a freestanding nanoparticle in solution. Though the process of doping has been known for a long time, doping the

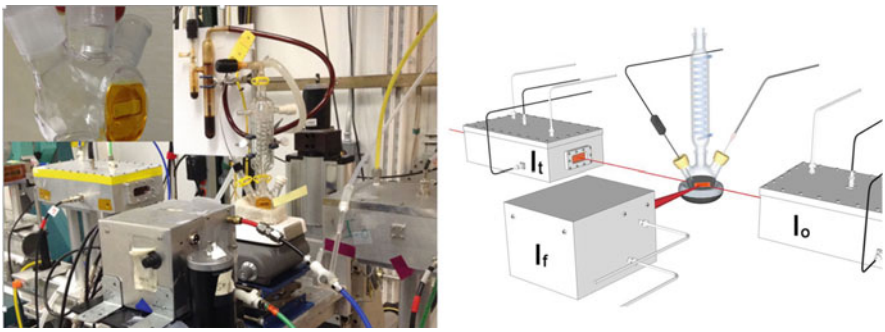

Fig. 5.5 QXAS setup for in situ X-ray absorption spectroscopy measurement of the synthesis of pure and Mo-doped hollow iron oxide NPs. The picture on the left shows the actual Schlenk-line setup installed at the beamline located at Advanced Photon Source, USA. The schematic diagram on the right shows the path of the X-ray beam and the arrangement of the detectors: I_o, I_t, and I_f for measuring intensities of incident, transmitted, and fluorescent X-rays, respectively [27]

colloidal nanocrystals has been challenging. The synthesis process of pure and doped nanocrystals involves several steps [24] and heating the solution to higher temperatures. Controlling each of these steps is crucial for obtaining the right size and shape for the desired NPs. Though there has been substantial progress in the synthesis of doped NPs, the doping mechanisms have been mainly studied by ex situ techniques, including TEM, Fourier transform infrared spectroscopy (FTIR), UV-vis absorption spectroscopy, Raman, etc., that do not provide detailed information on the kinetics of the doping mechanism. Successful synthesis of doped NPs requires studying the correlation of various kinetic parameters. Therefore, time-resolved studies of the doping processes are critical to resolve the doping mechanism in colloidal NPs.

Recently, the entire process of Mo-doped and un-doped iron oxide NPs synthesis was studied in real time by synchrotron in situ X-ray absorption spectroscopy done in QXAS mode [27]. The actual and schematic setup for this experiment is shown in Fig. 5.5. Mo-doped iron oxide NPs have been chosen since it is a promising electrode material to improve Li^+ ion capacity of rechargeable battery. XAS being a unique characterization technique, the QXAS measurements done at Fe edge as well as at Mo edge during the synthesis allowed simultaneous monitoring of reaction kinetics of the precursors, compositional changes of the NPs during the synthesis, the chemical state (valency and coordination geometry) and position (whether it is in the solution or in the host lattice) of the dopant. TEM images of the colloidal metallic iron NPs before oxidation to hollow iron oxide NPs and the Mo-doped iron oxide NPs produced in the beamline at the end of the synthesis are shown in Fig. 5.6.

The QXANES data along with the linear combination fit results are shown in Fig. 5.7. The analysis of the time-resolved XAS studies coupled with TEM measurements revealed for the first time an *oxidation induced doping mechanism* which is illustrated in Fig. 5.8b corresponding to the chemical reaction shown in Fig. 5.8a. The reaction mechanism from QXAS results predicts that the mass transport of the

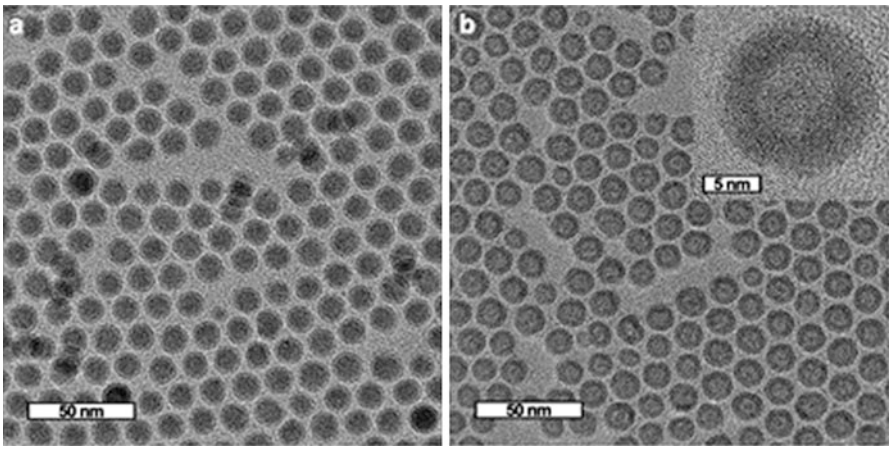

Fig. 5.6 (**a**) TEM image of the iron NPs before oxidation, (**b**) TEM image of Mo-doped iron oxide NPs after oxidation [27]

host (iron and oxygen) atoms induces the incorporation and internalization of the dopant atoms (molybdenum) into the lattice of oxidized hollow NPs of γ-Fe_2O_3. Time-resolved QXANES/QEXAFS study revealed that the reaction kinetics of the nucleation, growth, and oxidation of the host NPs are significantly affected by the dopant precursor, and the latter can substantially change the reaction kinetics of formation of iron and iron oxide NPs. Thus, in the presence of dopant precursor, we observed significantly faster decomposition rate of iron precursors and substantial resistance and higher stability of iron NPs against oxidation. The same doping mechanism and higher stability of host metal NPs against oxidation was observed for cobalt-based systems also. Since the internalization of the adsorbed dopant at the surface of the host NPs is driven by the mass transport of the host, this mechanism can be potentially applied to introduce dopants into different oxidized forms of metal and metal alloy NPs providing the extra degree of compositional control in material design. This is the first time that an entire synthetic colloidal chemistry was done successfully at a beamline demonstrating and proving that NPs can be synthesized in organic solutions with only inorganic capping ligands. We believe that oxidation-induced doping mechanism can be applied to a number of other NP systems where the mass transport can be induced chemically (e.g., oxidation) or electrochemically. This in situ measurement technique is generally applicable for time-resolved mechanism study of various doped NPs synthesis using the conventional reaction setups that are generally used in the laboratory, and it proves the strength of QXAS in being able to provide insight into chemical reactions. It should be possible to use QXAS to monitor synthesis of NPs by sol-gel, microemulsion, and other wet chemical techniques also.

Apart from these, there have been reports of QXANES being used successfully to study the in situ growth of ZnO nanowires from zinc nitrate and HMTA (hexamethylenetetramine) precursors during chemical bath deposition (CBD) for a fundamental

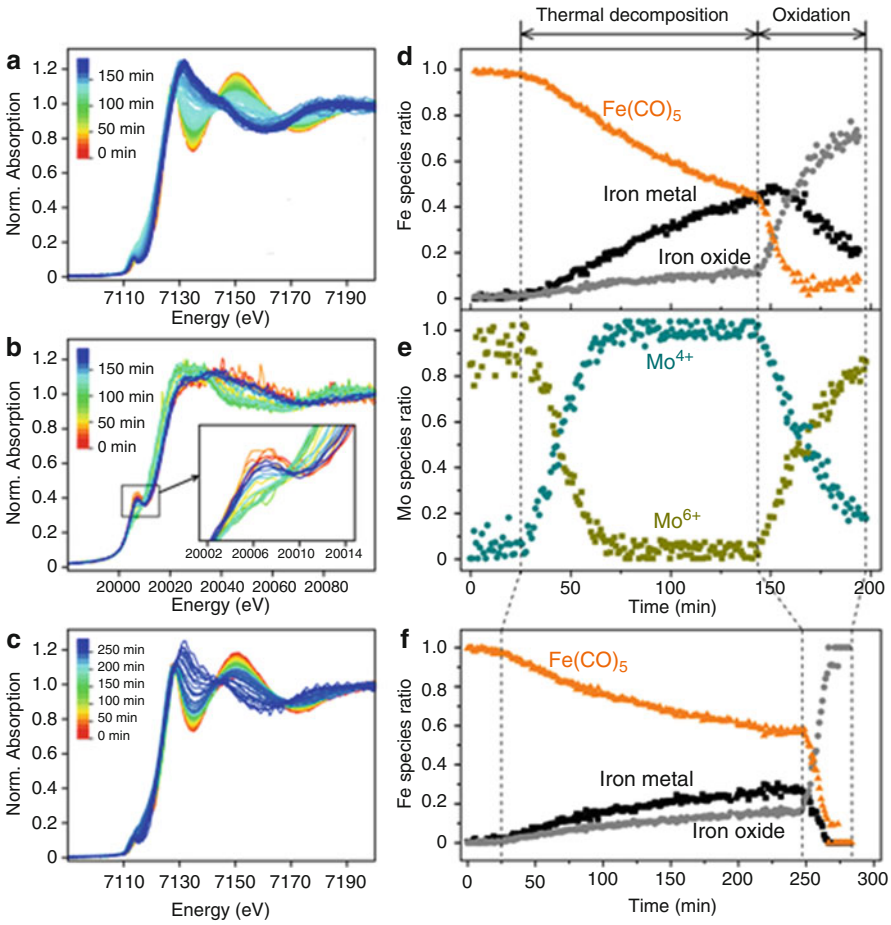

Fig. 5.7 Time-dependent changes of Fe and Mo XANES spectra and the ratio of iron and molybdenum species during the synthesis of Mo-doped and un-doped hollow iron oxide NPs. (**a**, **b**): Fe-QXANES and Mo-QXANES spectra, respectively, taken during the synthesis of Mo-doped hollow iron oxide NPs. The inset in panel b shows the magnified pre-edge peak range. (**c**) Fe *K*-edge QXANES spectra acquired during the synthesis of un-doped hollow iron oxide NPs. (**d**, **e**) Linear combination fit results obtained from the time-dependent XANES spectra (**a**) and (**b**), respectively, showing the changes in the ratio of iron and molybdenum species, in the reaction mixture as a function of time during the synthesis of Mo-doped hollow iron oxide NPs. The reaction temperature reached 180 °C at 37 min. (**f**) Time-dependent change of iron species obtained from linear combination fits of QXANES spectra taken during the synthesis of un-doped hollow iron oxide NPs. The reaction temperature reached 180 °C at 32 min (More details of the experiments and analysis can be found in Ref. 27)

understanding of the reaction mechanisms and kinetics associated with the underlying chemical processes [28]. In situ QXAS has been used to study the 2-stage growth mechanism associated with the aqueous synthesis of glutathione (GSH) capped ZnSe quantum dots [29]. It has also been used to monitor the adsorption of Co^{2+} on the

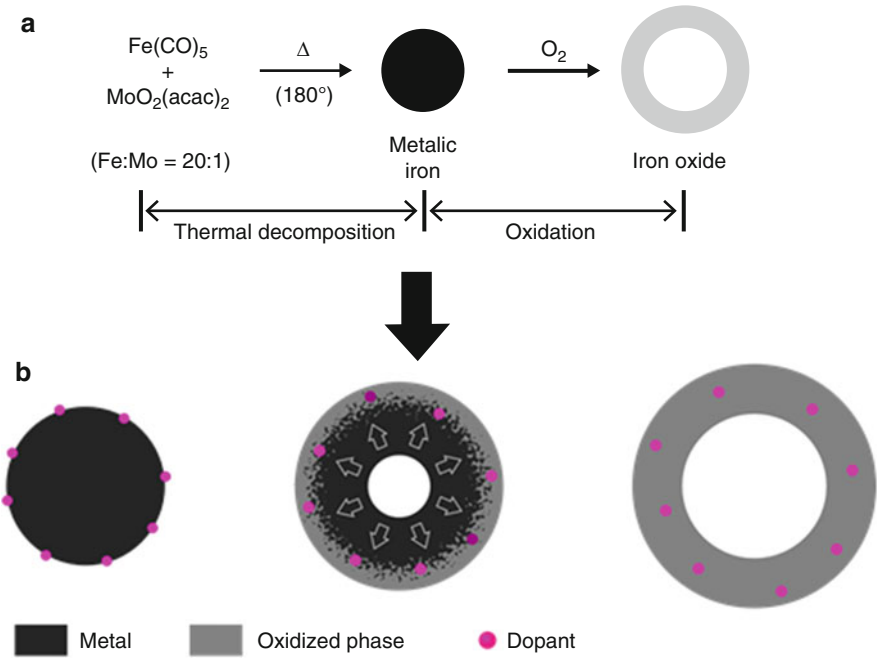

Fig. 5.8 (**a**) Synthesis of Mo-doped iron oxide hollow shell NPs. (**b**) Modeling of the chemistry associated with oxidation-induced doping mechanism as predicted from QXAS results. A metallic iron NP with dopant ions adsorbed on the surface (left); early stage of the oxidation of metallic Fe NP and capturing of Mo-dopant ions inside of the oxidized layer (middle); doped hollow shell NP after full oxidation (right)

surface of Fe_3O_4 NPs in high temperature aqueous fluids [30]. The results have indicated that QXAS with its capability to determine the coordination environment around individual atoms, will enable discovery of novel synthesis routes for new materials in future.

5.2 In Situ QXAS Studies of Nanomaterials for Battery Applications

The enormous energy need of our civilization is the driving force behind the intensive research of materials related to energy-storage. There has been huge progress in the field of battery materials in the last two decades due to the growing demand of modern technology. Since their discovery in the early1990s, Lithium ion batteries have become popular since they possess the highest energy density of all rechargeable batteries available in the market and hence have become standard power source for many electronic devices like cell phones, laptops, etc. Further research to improve the properties of these batteries has been ongoing since they may be the source of power for a future generation electric vehicles and large-scale

electrical grid storage also. XAS especially QEXAFS and QXANES have proved to be powerful and ideal tools to study batteries. Together, they have the capability to correlate the changes in the electronic state of an atom to the structural changes occurring in the neighborhood of an atom during electrochemical changes, i.e., charging and discharging of batteries. QXAS can provide valuable insight about the mechanisms in electrochemical reactions when one of the transition metal constituents is removed or changed in the electrode materials, which is needed to achieve high specific capacity and long-term stability in Li-ion batteries. Hence, they have been used for past 20 years to probe the structure and composition of various types of electrode materials used in batteries [31–50]. These studies have thrown light on the charge compensation process during cycling of batteries and the response of cathodes to Li ion insertion and extraction. It has been observed that for transition metal doped $LiCoO_2$ (a) capacity fading is closely related to the J-T distortion of the NiO6 octahedron when Ni is doped at Co sites in $LiCoO_2$ and (b) during electrochemical delithiation process, all the charge compensation occurs at the Ni site which changes oxidation state from 3+ to 4+ during charging, thereby causing reduction of J-T effects. Co atoms oxidize towards the end of charging process [37–40]. Studies of $LiMn_2O_4$ layered compounds have shown that Li de-intercalation leads to oxidation of Mn^{3+} to Mn^{4+} to MnO_2, and there are local structural changes around Mn atoms which can cause cyclic instability of the battery material [32, 34, 36]. The active role of oxygen atoms during cycling of batteries is confirmed. This research has proved that with proper design of electrodes and choice of active materials, lithium-ion batteries can function at high rates and with higher utilization of the active material. These studies have opened the path for development of lithium-iron phosphate [46] and other high capacity cathode materials [47, 48] and also intermetallic-phase-based anode materials with the zinc blende structure [35].

Significant improvement is still needed in this field to produce electrode materials which are cheap, safe-to-use, and possess higher capacity and higher rate performance. Use of nanomaterials as electrodes for batteries is being probed since NPs have more surface area which will give them higher charge and discharge rates, short path length for electron and Li ion transport, and higher strain accommodation capacity. In situ XAS on nanometer-sized materials were reported as early as 2010 when the Cu *K*-edge of 20 nm sized 85 wt% CuF_2–15 wt% MoO_3 nanocomposite was investigated [51] to study the electrochemical conversion reaction in metal fluorides which have demonstrated high energy density. The nanocomposite, prepared by high energy milling, resulted in the formation of highly dispersed metallic Cu NPs with size 2–3 nm as a result of the lithiation reaction, i.e., conversion of CuF_2 into Cu and LiF during discharge of the battery. In situ XAS studies of batteries with NPs of metallic Sn, SnO_2, and hybrid $Sn_3O_2(OH)_2$/graphite as anode material show segregation of tin and formation of SnLi and Li_2O phases within the electrodes. Though SnO_2 has been found to be a more promising candidate than metallic tin, QXAS studies of the tin atoms during the battery cycling process helped to explain the poor electrochemical performance and rapid capacity decline of the batteries using both Sn and SnO_2 [52, 53]. In situ QXAS measurements to track structural changes during Li intercalation/de-intercalation of nanometer-sized

$LiCoO_2$ demonstrated enhanced capacity fading and irreversible losses due to high surface area of the NPs [54]. In situ XANES studies of Ni edge and Mo edge of MoO_2 NPs doped with 2 atomic percent of Ni showed the nucleation of the ternary Ni:MoO_2 compound formed by substitution of Mo atoms by divalent Ni atoms. Doubling of the initial discharge capacity has been observed in these Ni-doped nanometer-sized MoO_2 due to relaxation of local structure. An increase of capacity for both pure and Ni doped MoO_2 anodes also occurred upon cycling with increasing cycling rate [47]. Nanocomposites of LiF/V_2O_5 (0–20 wt% of V_2O_5) prepared by high energy ball-milling showed stable capacity over a period of 20 cycles for the sample with 15 wt% of V_2O_5. In situ Fe and V edge XAS data helped to diagnose the oxidation states of V and Fe atoms and identify the new phases and the mechanism of their formation during the battery cycling [48]. In situ XAS demonstrated that Cu^{2+} copper ions in 2D–layered copper birnessite NP electrodes get reduced to amorphous nanosized copper metal which can get oxidized to Cu^{2+} ions during lithium insertion and de-insertion cycle leading to enhanced discharge capacity of these layered Mn oxide compounds when compared with the compounds without copper [55].

Research using in situ XAS has been extended to hollow iron-oxide NPs whose electrochemical properties have been investigated to probe their usefulness as an anode and a cathode material in Li ion batteries [56, 57]. The aim was to study if changing the morphology of NPs to something other than solid NPs can lead to enhanced properties of the batteries constructed from them. Better performance was observed for the smaller sized hollow iron oxide NPs compared to the bigger sized NPs with the same high stability when cycled in high voltage ranges [56]. Cation vacancies in octahedral sites of hollow γ-Fe_2O_3 NPs can serve as hosts for Li ions at high voltage range and possess high capacity, excellent Coulombic efficiency, good capacity retention, and superior rate performance demonstrating that this material can be successfully used as a cathode material for Li ion batteries. The studies of Koo et al. showed that hollow core-shell NPs can be used efficiently for reversible Li ion intercalation without causing structural changes in the material and provided a clear understanding of the lithium intercalation processes during electrochemical cycling. Cation vacancies in hollow γ-Fe_2O_3 NPs can be utilized for fast transport of sodium ions also and produce low-cost rechargeable cathodes with excellent charge transport properties [58]. Figure 5.9a shows a TEM image of hollow γ-Fe_2O_3 NPs after annealing of Fe/Fe_3O_4 core-shell NPs for 12 h at 200 °C. Figure 5.9b depicts the fabrication of light-weight, binder-free, flexible, and stable electrodes with carbon nanotubes (CNTs). Figure 5.10 shows the in situ QEXAFS measurements done at Fe k-edge during charging and discharging of the battery several times and over a period of few hours in the beam. Figure 5.10a shows the voltage profile of the first electrode discharge versus metallic sodium counter electrode. The points marked in Fig. 5.10a correspond to the in situ QXANES data collected at Fe edge during charging and discharging of the battery. Figure 5.10c shows the Fourier transformed QEXAFS data and depicts the changes in Fe-O and Fe-Fe bond distances during intercalation of Na ions into the hollow iron oxide NPs. Linear combination of the QXANES data was used to generate the plot of Fig. 5.10d showing the Fe-oxidation state during the cycling of the battery. This study proved

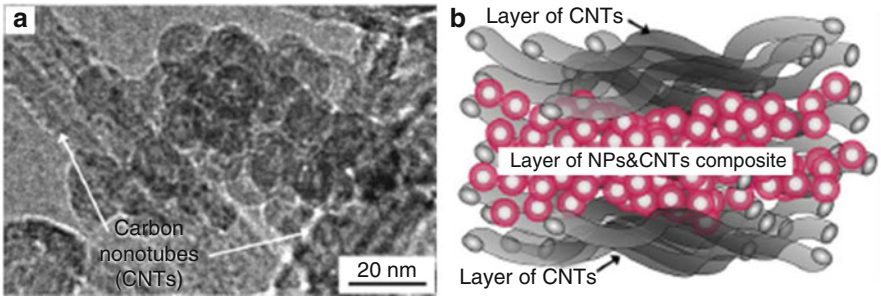

Fig. 5.9 (**a**) TEM image of showing formation of hollow γ-Fe_2O_3 NPs, (**b**) fabrication of low- cost, stable electrodes with NPs and CNTs [58]

that CNTs are successful as a conductive matrix for NPs, which can be used as high performance cathodes with Na + ions. Thus, we see that QXAS with its unique ability to probe local structure around individual atoms and the oxidation state of the element has proved to be extremely useful in understanding structure-property correlations in energy related materials. It has helped to discover new materials with enhanced electrical properties, thereby expanding the ongoing research of NPs as potential materials for next generation batteries.

5.3 In Situ QXAS Studies of Reactions in Catalytic Nanomaterials

Catalysts are compounds that affect the pathway and mechanism of a chemical reaction but do not enter the overall stoichiometry of the reaction. From the time of its discovery by Berzelius in 1835, catalysis has been known to play an important role in chemistry as many chemical processes involve catalysts at some step. The exponential growth in the field of nanotechnology has led to the discovery of novel synthesis techniques in the last two decades. This has not only initiated the research for advanced characterization techniques but has also revolutionized the field of catalysis since catalytic properties depend strongly on the number of surface atoms, which are enhanced in nanometer-sized particles. Nanocatalysts in the form of metals, metal oxides, metal complexes, biocatalysts, as well as other types of compounds have played a major role in water gas shift reactions, CO oxidation, hydrogenation, etc., as well as in fuel cells, energy conversion, and storage technologies. The catalytic properties of materials are determined not only by their size and shape but also by their composition and structure, the type of organic capping agent, the properties of inorganic support, etc. When a catalyst is active, there are changes in its physical and electronic properties. In order to be able to control the functions of engineered NP catalysts, detailed understanding of the relationships between the physical and electronic structure and the catalytic activity is essential. XAS has proved to be an ideal tool for catalysts since the powerful X-ray beam can penetrate matter in all three states as well as both amorphous and crystalline materials. It can

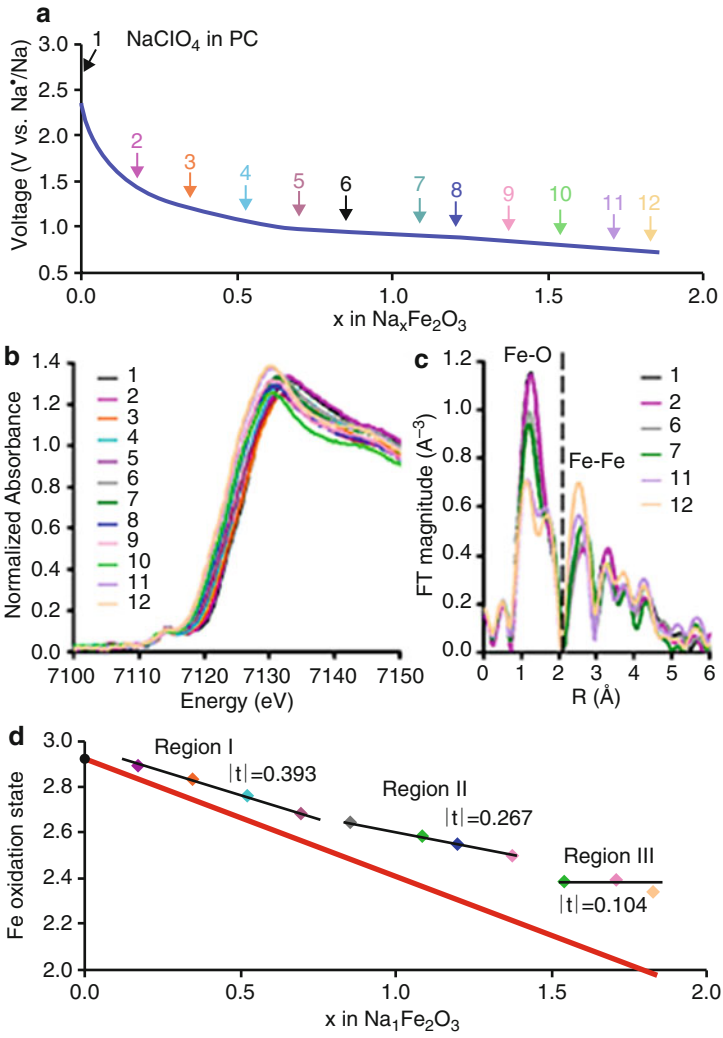

Fig. 5.10 (**a**) Voltage profile of first electrode discharge versus metallic sodium counter electrode; (**b**) QXANES data corresponding to the points shown in (**a**); (**c**) Fourier transformed QEXAFS data and (**d**) oxidation state of Fe obtained from the QXANES plots in (**b**) [58]

provide information about physical and electronic property changes occurring during reactions under changing conditions of pressure, temperature, and the flow of a multitude of gases needed for catalytic reactions. With fluorescence measurements, it can also detect species present at very low concentrations. Hereby, we shall present how results generated from in situ XAS research has helped to study homogeneous and heterogeneous catalysts of nanometer-sized metals, metal-oxides, etc., and paved the road for designing nanocatalysts with novel properties.

Though XAS has been used since the 1980s for studying catalysts [59], in operando studies were started during the late 1990s. Mukerjee et al. reported one of the earliest in operando XAS studies done on Pt and Sn edges to study the effects of Sn substitution during voltage cycling of carbon-supported Pt electro-catalysts [60]. Since then, there have been several review articles [61–82] on in situ XAS experiments that were conducted successfully at different synchrotron sources to study electro-catalysts, homogeneous, and heterogeneous catalysts that include metallic, bi–metallic NPs and nanoclusters, zeolites, oxides, and supported catalysts. These experiments have helped in identifying reaction intermediates and catalysis active sites. In situ XAS studies have worked successfully for fuel cells, water-gas experiments, and in operando cells. Researchers have developed theories (DFT) to explain the behavior of the catalysts and have designed catalysis setups [67, 68, 83–88] for re-enacting conditions that exist in industries. In order to do in situ measurements of catalysts similar to industrial atmosphere, Bare et al. [84] developed and implemented a four-channel ionization chamber with two different in situ cells. This setup shown in Fig. 5.11 helps in collecting QXAS data from 4 samples simultaneously in transmission geometry, thereby eliminating scan-to-scan uncertainties. In addition to increased productivity and time-saving, this setup has enabled in situ XAS data collection axially at four different positions in a catalyst bed and decipher small differences in the behavior of similarly prepared catalysts. Apart from that, catalysts can be subjected to same conditions of temperature and gas pressure and reference spectra can be collected in four channels simultaneously. This setup is easy-to-use and can be used in bending magnet and wiggler beamlines with a horizontal fan of radiation.

Rochet et al. have developed a cell to conduct in situ and operando experiments to improve cycle length, catalytic activity, and selectivity towards heavy paraffin of Fischer-Tropsch supported cobalt nanometer-sized catalysts [86]. They have been successful in doing QXAS under realistic working conditions at high pressure (18 bar of syngas) and reaction temperature (250 °C) under pure hydrogen at 400 °C, thereby proving that it is possible to mimic harsh conditions in a real catalytic fixed bed reactor. An operando QXAS cell has been developed by O'Neill et al. to measure simultaneous changes in catalyst structure and catalytic activity during liquid phase hydrogenation of furfural over supported copper catalysts [87]. This setup allowed continuous monitoring of the size of the copper NPs whose sintering has been proved to be predominant mode of catalyst deactivation for a $Cu/\gamma\text{-}Al_2O_3$ catalyst. Detailed description of several catalysis cells has been given by Bare and Ressler in their chapter on catalysis [67]. The developments in instrumentation related to in situ QAS at various beamlines all over the world have immensely helped the catalysis community. Kumar et al. have studied multicomponent NiFeCu catalyst using in situ XAS coupled with scanning electron microscopy (SEM), FTIR, and X-ray photoelectron spectroscopy (XPS) [89]. The results demonstrate that though the NiFeCu catalyst appears homogeneous at the mesoscale, it is highly heterogeneous at the nanoscale. There are changes in the oxidation states of Ni, Fe, and Cu during reaction. Cu was fully reduced before reaction and later became partly oxidized upon exposure to ethanol and oxygen. Ni is mostly (75%) reduced and does

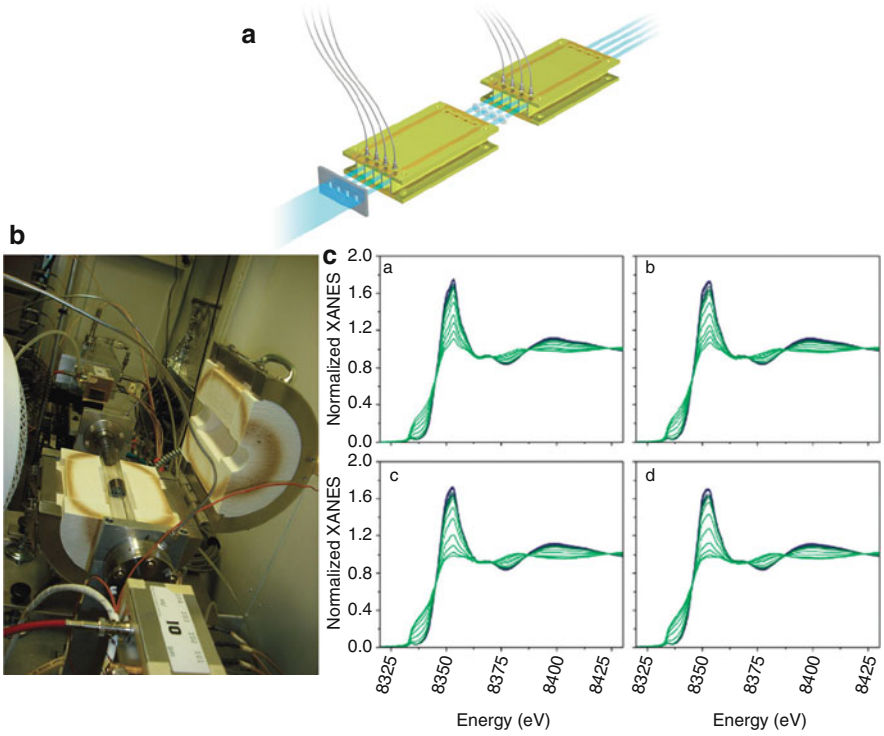

Fig. 5.11 (**a**) Schematic diagram of the experimental setup showing the X-ray beam from the left going through the beam defining aperture, the four samples that are in the path of the four X-ray beams, and the four ionization chambers collecting data. (**b**) Actual experimental setup in the beamline using the quartz tube reactor with the sample holder inside it. The prototype four-channel ion chamber is labeled I0 and is at the front. (**c**) Normalized Ni K-edge temperature-programmed-reduction XANES data collected simultaneously on four Ni-containing catalysts [84]

not change its oxidation state during the reaction. Fe is not present in its metallic form after reduction and during the reaction, but changes in the oxidation state from Fe(II) to Fe(III) occurred during the reaction. QXAS studies were performed to study the real-time transformation of silver species over alumina [90] with a spectrum being collected every second for 30 s. The data taken at Ag K-edge demonstrated the sensitivity of silver to gaseous ethanol. While the reduction of silver occurs at room temperature under air/ethanol flow, it gets accelerated when it is heated to a temperature of 78 °C, the boiling point of ethanol, making Ag-Al_2O_3 catalysts useful for selective catalytic reduction of NO_x in the presence of ethanol. A combination of TPR (temperature programmed reduction) QEXAFS and QXANES along with high resolution TEM, XRD, and diffuse reflectance Fourier transform infrared spectroscopy was used to study water gas shift. It involved detailed characterization and testing of nanoscale ZrO_2 and YSZ supported Pt catalysts [91]. EXAFS results demonstrated that Pt clusters were highly dispersed and similar in size and that Y

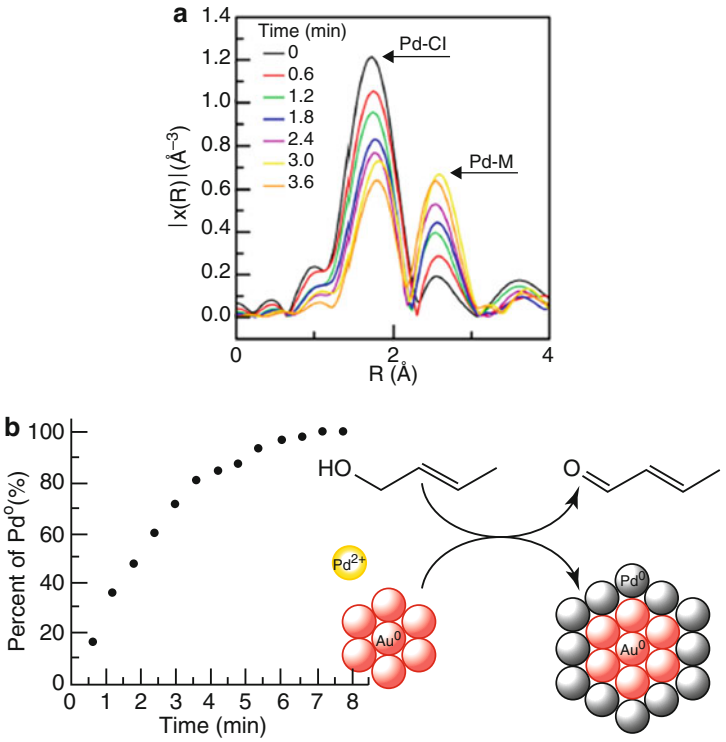

Fig. 5.12 (**a**) Time-resolved Pd K-edge EXAFS data in R-space for the NPs that formed in situ during oxidation of crotyl alcohol in water. (**b**) Growth of Pd shell around Au core with increase in time forming Au core-Pd shell bimetallic catalysts in presence of crotyl alcohol [92]

addition enhanced surface reduction especially in samples with more Zr. Y doped Pt catalysts displayed higher water gas-gas-shift activity relative to the 0.5%Pt/ZrO_2 catalyst when the Y content was below 50%.

In situ Pd K-edge and Pd-L3 edge XAS was used successfully to study the formation of gold core – Pd shell bimetallic NPs from Pd(II) salts in situ in the beam in the presence of crotyl alcohol [92]. Figure 5.12a, b gives time-resolved Pd speciation information which was used to predict the reaction mechanism and kinetics of Pd reducing on the Au NPs and forming Au Core- Pd shell bimetallic nanoparticle catalysts in the presence of crotyl alcohol. These studies also explained the role of Au atoms, which prevented the re-oxidation of the catalytically active Pd atoms present on the surface of the Pd shell around Au core. Thus, we observe that in situ QXAS studies have enriched the field of catalysis immensely. Different types of new cells have been designed in different beamlines around the world, which has in the course of time helped researchers from academics and industry investigate different types of oxidation and reduction mechanisms and the kinetics of the growth of catalysts, thereby accelerating the evolution of novel catalytic materials with tailor made properties.

5.4 In Situ XAS Studies in Nanomaterials with In Situ SAXS and Other Techniques

Construction of next generation synchrotron sources producing beams with enhanced photon flux and the development of faster detectors has led to the growth of many synchrotron-based measurement techniques. Novel experiments have been designed and executed producing unique results in different fields. We have seen so far how in situ XAS characterization techniques have contributed to the fields of catalysis, battery, and in situ chemistry-on-the-beamline for nanomaterials. There have been large-scale developments in the fields of in situ scattering (SAXS) [93, 94], in situ imaging [95], in situ high resolution XRD (HRXRD) [96], and in situ pair distribution function (PDF) measurements also [97, 98]. This initially led to the coupling of ex situ XAS measurements with some of these techniques [99–104]. In the last decade, the efforts to couple in situ XAS measurements with other in situ synchrotron-based techniques have been successful, and this has opened the doors to novel discoveries in various fields, which we shall highlight in this section.

Sasaki et al. have used in situ XRD and in situ XAS to study the synthesis and catalytic activities of carbon supported Ir-Ni core-shell NPs [105]. The NPs, synthesized using chemical reduction followed by thermal annealing, are composed of IrNi alloy cores covered by 2 shells of Ir that protect the Ni core from getting oxidized or modified by the acid electrolyte under elevated potentials. The Ni cores have been found to lead to contraction of the Ir shell, thereby suppressing formation of IrOH on the surface and resulting in a NP system possessing higher H_2 reduction capacity than commercial Pt/C catalysts. The combination of in situ XRD and in situ XAS studies have proved that IrNi core-shell NPs can be a potential candidate for hydrogen anode fuel cell electro-catalysts.

A combination of in situ PDF (pair distribution function) along with XAS was applied to study the structure and nature of PdO-Pd transformation in a 4 wt% Pd/Al_2O_3 catalyst by Keating et al. [106]. Pd phases within the catalyst could be established at various temperatures till 850 °C, above which most of the PdO converted to metallic Pd. Complete re-oxidation of Pd to PdO occurred between 650 °C and 580 °C.

Structural evolution during solid-state formation of Li_2MnO_3, a primary material for Li ion batteries, was investigated by in situ high-energy X-ray diffraction and in situ X-ray absorption spectroscopy [107]. In situ XAS helped to capture formation of an intermediate MnO_2 phase, whereas anisotropic crystallization of Li_2MnO_3 during sintering above 600 °C was observed for in situ diffraction. Without these state-of-the-art techniques, it would not have been possible to study materials for future devices.

In situ XRD and in situ XAS were also used to study the synthesis and oxidation of Co cores of Co-SiO_2 core-shell NPs prepared by sol-gel method [108]. The oxidation was carried out till 800 °C in the presence of air as well as nitrogen. Metallic cobalt as well as a small amount Co in the 2+ state was observed till 200 °C. With an increase in temperature to 300 °C, oxygen from air diffused through SiO_2 and the interface between Co and SiO_2 oxidized to CoO. With further increase in

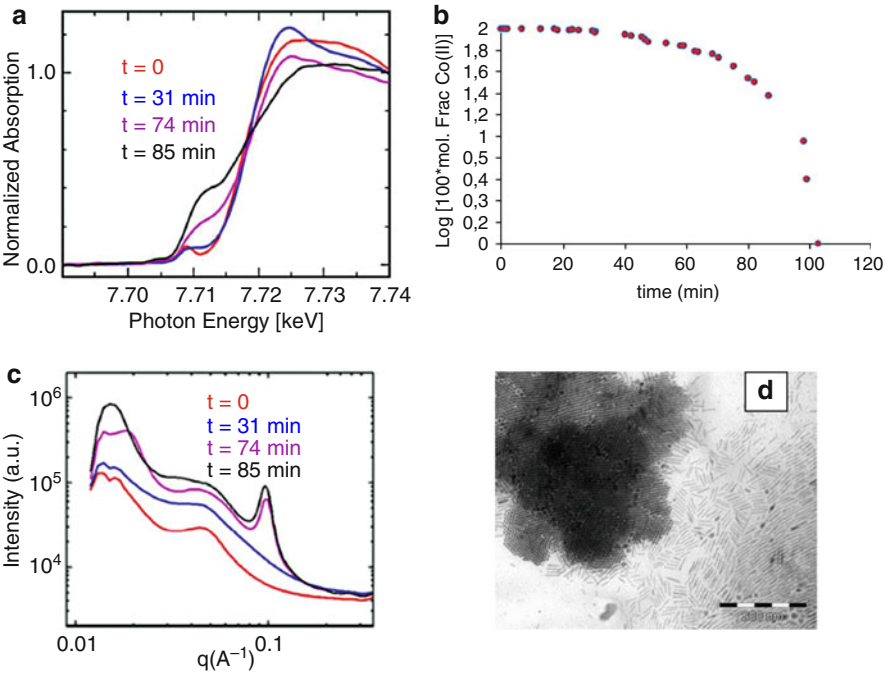

Fig. 5.13 (**a**) Time-dependent Co K-edge QXANES spectra taken at different time intervals during in situ formation of Co nanorods in the beam at 130 °C and 50 psi of H_2, starting with precursor (red) and ending with Co metallic nanorods (black). (**b**) Reduction of Co (II) to Co(0) in the beam. (**c**) In situ SAXS spectra taken during reduction of Co precursor to Co-metallic nanorods in the beam at 130 °C and 50 psi of H_2 and at an energy of 8979 eV. Time intervals for these spectra are same as that for the QXANES spectra. (**d**) TEM image of a superlattice obtained after 3 h of reaction at 130 °C

temperature to 800 °C, Co_3O_4 or a mixture of CoO and Co_3O_4 was formed. Similar phenomenon was observed in the presence of N_2 gas also where the oxygen was procured by Co atoms from the SiO_2 shell. This experiment helped to study the behavior of core-shell NPs at high temperature.

A very unique experiment was done by Cormary et al. [109] to study the detailed growth mechanism and kinetics of cobalt nanorods using in situ SAXS (small angle X-ray scattering) and in situ QXAS measurements. Figure 5.13a, c shows the in situ QXANES and SAXS data taken when the Co (II) precursor reduced to metallic Co nanorods in the presence of a long chain amine and a long chain carboxylic acid. The reaction took place at 130 °C and 50 psi of H_2. Figure 5.13b shows the reduction of Co (+2) to Co(0) with progress in time. Figure 5.13d shows the TEM image of the nanorods produced by the reaction. The growth mechanism starts with a fast nucleation followed by a fast growth brought about by monomer addition. The latter happens during reduction of Co(2+) precursor to Co(0). The last step consists of a slower ripening that occurs after the reduction is complete and the nanorods organized into 3D smectic-like superlattices. An in-depth understanding of the dynamic

processes associated with the nanorod formation could be obtained by these experiments. This will open the gate to synthesize different types of nanomaterial superlattices with tailor made properties.

6 Conclusions and Future Perspective

We have observed that in situ XAS solo and in conjunction with other techniques has developed into a unique tool and has been applied to study local structural changes and mechanisms associated with different types of reactions involving NPs for various applications. In the last couple of years, lots of advancements have occurred in the field of XFEL (X-ray free electron laser) to do XAS measurements in the scale of nano- and picoseconds to study ultrafast reactions happening in nature [110, 111]. Such studies will be extremely beneficial to scientists and engineers to develop novel materials for future generation devices. It has been found that biological samples often get degraded with hard x-rays from an undulator beamline where QXAS is generally done. Efforts should be made so that biological samples can be studied with in situ QXAS to observe reactions occurring in biological organs, organisms and cells [112]. Progress in detector science and enhancement in the design of sample cells will enable in situ QXAS studies along with other in situ techniques to contribute further in the development of nanoscience and nanotechnology.

References

1. Koningsberger DC, Prins R (1988) X-ray absorption, principles, applications, techniques of EXAFS, SEXAFS, XANES. Wiley, New York
2. Müller O, Nachtegaal M, Just J, Lützenkirchen-Hecht D, Frahm R (2016) Quick-EXAFS setup at the SuperXAS beamline for in situ X-ray absorption spectroscopy with 10 ms time resolution. J Synchrotron Radiat 23(1):260–266
3. Prestipino C, Mathon O, Hino R, Beteva A, Pascarelli S (2011) Quick-EXAFS implementation on the general purpose EXAFS beamline at ESRF. J Synchrotron Radiat 18(2):176–182
4. Mathon O, Beteva A, Borrel J, Bugnazet D, Gatla S, Hino R, Kantor I, Mairs T, Munoz M, Pasternak S, Perrin F, Pascarelli S (2015) The time-resolved and extreme condition XAS (TEXAS) facility at the European Synchrotron Radiation Facility: the general-purpose EXAFS bending-magnet beamline BM23. J Synchrotron Radiat 22(6):1548–1554
5. Koide A, Fujikawa T, Ichikuni N (2014) Recent progress in EXAFS/NEXAFS spectroscopy. J Electron Spectrosc Relat Phenom 195:375–381
6. Dent AJ (2002) Development of time-resolved XAFS instrumentation for quick EXAFS and energy-dispersive EXAFS measurements of catalyst systems. Top Catal 18(1–2):14–22
7. Segre CU, Leyarovska NE, Chapman LD, Lavender WM, Plag PW, King AS, Kropf AJ, Bunker BA, Kemner KM, Dutta P, Duran RS, Kaduk J (2000) The MRCAT insertion device beamline at the advanced photon source. AIP Conf Proc 521(1):419–422
8. Newville M (2004) Fundamentals of XAFS. Consortium for advanced radiation sources, University of Chicago, Chicago. http://XAFS.org/
9. Lee PA, Citrin PH, Eisenberger P, Kincaid BM (1981) Extended X-ray absorption fine structure – its strengths and limitations as a structural tool. Rev Mod Phys 53(4):769
10. Rehr JJ, Albers RC (2000) Theoretical approaches to X-ray absorption fine structure. Rev Mod Phys 72(3):621

11. Bunker G (2010) Introduction to XAFS: a practical guide to X-ray absorption fine structure spectroscopy, 1st edn. Cambridge University Press, Cambridge
12. Kelly SD, Hesterberg D, Ravel B (2008) Chapter 14 Analysis of soils and minerals using X-ray absorption spectroscopy. In: Methods of soil analysis Part 5 – Mineralogical methods. Soil Science Society of America, Madison, pp 387–463
13. Ravel B, Newville M (2005) ATHENA, ARTEMIS, HEPHAESTUS: data analysis for X-ray absorption spectroscopy using IFEFFIT. J Synchrotron Radiat 12(4):537–541
14. Zabinsky SI, Rehr JJ, Andukinov A, Albers RC, Ellen MJ (1995) Multiple-scattering calculations of X-ray absorption spectra. Phys Rev B 52(4):2995
15. Kumar CSSR (ed) (2010) Microfluidic devices in nanotechnology – fundamental concepts. Wiley, Hoboken
16. Kumar CSSR (ed) (2010) Microfluidic devices in nanotechnology – applications. Wiley, Hoboken
17. Gaur S, Miller JT, Stellwagen DR, Sanampudi A, Kumar CSSR, Spivey JJ (2012) Synthesis, characterization and testing of supported Au catalysts prepared from atomically-tailored $Au_{38}(SC_{12}H_{25})_{24}$ clusters. Phys Chem Chem Phys 14(5):1627–1634
18. Biswas S, Miller JT, Li Y, Nandakumar K, Kumar CSSR (2012) Developing a millifluidic platform for the synthesis of ultra-small nano-clusters: ultra-small copper nano-clusters as a case study. Small 8(5):688–698
19. Krishna KS, Navin CV, Biswas S, Singh V, Ham K, Bovenkamp GL, Theegala CS, Miller JT, Spivey J, Kumar CSSR (2013) Milli-fluidics for time-resolved mapping of the growth of gold nanostructures. J Am Chem Soc 135(14):5450–5456
20. Krishna KS, Biswas S, Navin CV, Yamane DG, Miller JT, Kumar CSSR (2013) Millifluidics for chemical synthesis and time-resolved mechanistic studies. J Vis Exp 81:e50711
21. Navin CV, Krishna KS, Bovenkamp GL, Miller JT, Chattopadhyay S, Shibata T, Losovyj Y, Singh V, Theegala C, Kumar CSSR (2015) Investigation of the synthesis and characterization of platinum-DMSA nanoparticles using millifluidic chip reactor. Chem Eng J 281:81–86
22. Yin Y, Alivisatos AP (2005) Colloidal nanocrystal synthesis and the organic–inorganic interface. Nature 437(7059):664–670
23. Pellegrino T, Kudera S, Liedl T, Javier AM, Manna L, Parak WJ (2005) On the development of colloidal nanoparticles towards multifunctional structures and their possible use for biological applications. Small 1(1):48–63
24. Talapin DV, Lee J-S, Kovalenko MV, Shevchenko EV (2010) Prospects of colloidal nanocrystals for electronic and optoelectronic applications. Chem Rev 110(1):389–458
25. Park J, Joo J, Kwon SG, Jang Y, Hyeon T (2007) Synthesis of monodisperse spherical nanocrystals. Angew Chem Int Ed 46(25):4630–4660
26. Kwon SG, Krylova G, Phillips PJ, Klie RF, Chattopadhyay S, Shibata T, Bunel EE, Liu Y, Prakapenka VB, Lee B, Shevchenko EV (2015) Heterogeneous nucleation and shape transformation of multicomponent metallic nanostructures. Nat Mater 14(2):215–223
27. Kwon SG, Chattopadhyay S, Koo B, dos Santos Claro PC, Shibata T, Requejo FG, Giovanetti LJ, Johnson C, Prakapenka V, Lee B, Shevchenko EV (2016) Oxidation induced doping of nanoparticles revealed by in situ X-ray adsorption studies. Nano Lett 16(6):3738–3747
28. McPeak KM, Becker MA, Britton NG, Majidi H, Bunker BA, Baxter JB (2010) In situ X-ray absorption near-edge structure spectroscopy of ZnO nanowire growth during chemical bath deposition. Chem Mater 22(22):6162–6170
29. Song J, Zhang J, Xie Z, Wei S, Pan Z, Hu T, Xie Y (2010) In situ XAFS studies on the growth of ZnSe quantum dots. Nucl Instrum Methods Phys Res, Sect A 619(1–3):280–282
30. Yan H, Mayanovic RA, Demster JW, Anderson AJ (2013) In situ monitoring of the adsorption of Co^{2+} on the surface of Fe_3O_4 nanoparticles in high-temperature aqueous fluids. J Supercrit Fluids 81:175–182
31. Tryk DA, Bae IT, Hu Y, Kim S, Antonio MR, Schersona DA (1995) In situ X-ray absorption fine structure measurements of $LaNi_5$ electrodes in alkaline electrolytes. J Electrochem Soc 142(3):824–828

32. Shiraishi Y, Nakai I, Tsubata T, Himeda T, Nishikawa F (1997) In situ transmission X-ray absorption fine structure analysis of the charge–discharge process in $LiMn_2O_4$, a rechargeable lithium battery material. J Solid State Chem 133(2):587–590
33. Balasubramanian M, Sun X, Yang XQ, McBreen J (2001) In situ X-ray diffraction and X-ray absorption studies of high-rate lithium-ion batteries. J Power Sources 92(1–2):1–8
34. Terada Y, Yasaka K, Nishikawa F, Konishi T, Yoshio M, Nakai I (2001) In situ XAFS analysis of $Li(Mn,M)_2O_4$ (M = Cr, Co, Ni) 5V cathode materials for lithium-ion secondary batteries. J Solid State Chem 156(2):286–291
35. Kropf AJ, Tostmann H, Johnson CS, Vaughey JT, Thackeray MM (2001) An in situ X-ray absorption spectroscopy study of InSb electrodes in lithium batteries. Electrochem Commun 3 (5):244–251
36. Balasubramanian M, McBreen J, Davidson IJ, Whitfield PS, Kargina I (2002) In situ X-ray absorption study of a layered manganese-chromium oxide-based cathode material. J Electrochem Soc 149(2):A176–A184
37. Johnson CS, Kropf AJ (2002) In situ XAFS analysis of the $Li_xNi_{0.8}Co_{0.2}O_2$ cathode during cycling in lithium batteries. Electrochim Acta 47(19):3187
38. Holzapfel M, Proux O, Strobel P, Darie C, Borowski M, Morcrette M (2004) Effect of iron on delithiation in $Li_xCo_{1-y}Fe_yO_2$: part 2, in-situ XANES and EXAFS upon electrochemical cycling. J Mater Chem 14(1):102–110
39. Yoon W-S, Balasubramanian M, Chung KY, Yang X-Q, McBreen J, Grey CP, Fischer DA (2005) Investigation of the charge compensation mechanism on the electrochemically Li-ion deintercalated $Li_{1-x}Co_{1/3}Ni_{1/3}Mn_{1/3}O_2$ electrode system by combination of soft and hard X-ray absorption spectroscopy. J Am Chem Soc 127(49):17479–17487
40. Deb A, Bergmann U, Cramer SP, Cairns EJ (2005) In-situ X-ray absorption spectroscopic study of the Li $[Ni_{1/3}Co_{1/3}Mn_{1/3}]O_2$ cathode material. J Appl Phys 97(11):113523
41. Deb A, Cairns EJ (2006) In situ X-ray absorption spectroscopy – a probe of cathode materials for Li-ion cells. Fluid Phase Equilib 241(1–2):4–19
42. Dominko R, Arčon I, Kodre A, Hanžel D, Gaberšček M (2009) In-situ XAS study on Li_2MnSiO_4 and Li_2FeSiO_4 cathode materials. J Power Sources 189(1):51–58
43. Nedoseykina T, Kim MG, Park S-A, Kim H-S, Kim S-B, Cho J, Lee Y (2010) In situ X-ray absorption spectroscopic study for the electrochemical delithiation of a cathode $LiFe_{0.4}Mn_{0.6}PO_4$ material. Electrochim Acta 55(28):8876–8882
44. Ito A, Sato Y, Sanada T, Hatano M, Horie H, Ohsawa Y (2011) In situ X-ray absorption spectroscopic study of Li-rich layered cathode material $Li[Ni_{0.17}Li_{0.2}Co_{0.07}Mn_{0.56}]O_2$. J Power Sources 196(16):6828–6834
45. Simonin L, Colin J-F, Ranieri V, Canévet E, Martin J-F, Bourbon C, Baehtz C, Strobel P, Daniel L, Patoux S (2012) In-situ investigations of a Li-rich Mn-Ni layered oxide for Li-ion batteries. J Mater Chem 22(22):11316–11322
46. Love CT, Korovina A, Patridge CJ, Swider-Lyons KE, Twigg ME, Ramaker DE (2013) Review of $LiFePO_4$ phase transition mechanisms and new observations from X-ray absorption spectroscopy. J Electrochem Soc 160(5):A3153–A3161
47. Pohl AH, Guda AA, Shapovalov VV, Witte R, Das B, Scheiba F, Rothe J, Soldatov AV, Fichtner M (2014) Oxidation state and local structure of a high-capacity $LiF/Fe(V_2O_5)$ conversion cathode for Li-ion batteries. Acta Mater 68:179–188
48. Hirsch O, Zeng G, Luo L, Staniuk M, Abdala PM, van Beek W, Rechberger F, Süess MJ, Niederberger M, Koziej D (2014) Aliovalent Ni in MoO lattice – probing the structure and valence of Ni and its implication on the electrochemical performance. Chem Mater 26 (15):4505–4513
49. Pelliccione CJ, Ding Y, Timofeeva EV, Segre CU (2015) In situ XAFS study of the capacity fading mechanisms in ZnO anodes for lithium-ion batteries. J Electrochem Soc 162(10): A1935–A1939

50. Li B, Shao R, Yan H, An L, Zhang B, Wei H, Ma J, Xia D, Han X (2016) Understanding the stability for Li-rich layered oxide Li_2RuO_3 cathode. Adv Funct Mater 26(9):1330–1337
51. Mansour AN, Badway F, Yoon WS, Chung KY, Amatucci GG (2010) In situ X-ray absorption spectroscopic investigation of the electrochemical conversion reactions of CuF_2-MoO_3 nanocomposite. J Solid State Chem 183(12):3029–3038
52. Pelliccione CJ, Timofeeva EV, Segre CU (2016) Potential-resolved in situ X-ray absorption spectroscopy study of Sn and SnO nanomaterial anodes for lithium-ion batteries. J Phys Chem C 120(10):5331–5339
53. Pellicione CJ, Timofeeva EV, Segre CU (2015) In situ X-ray absorption spectroscopy study of the capacity fading mechanism in hybrid $Sn_3O_2(OH)_2$/graphite battery anode nanomaterials. Chem Mater 27(2):574–580
54. Patridge CJ, Love CT, Swider-Lyons KE, Twigg ME, Ramaker DE (2013) In-situ X-ray absorption spectroscopy analysis of capacity fade in nanoscale-$LiCoO_2$. J Solid State Chem 203:134–144
55. Pelliccione CJ, Li YR, Marschilok AC, Takeuchi KJ, Takeuchi ES (2016) X-ray absorption spectroscopy of lithium insertion and de-insertion in copper birnessite nanoparticle electrodes. Phys Chem Chem Phys 18(4):2959–2967
56. Koo B, Xiong H, Slater MD, Prakapenka VB, Balasubramanian M, Podsiadlo P, Johnson CS, Rajh T, Shevchenko EV (2012) Hollow iron oxide nanoparticles for application in lithium ion batteries. Nano Lett 12(5):2429–2435
57. Koo B, Goli P, Sumant AV, dos Santos Claro PC, Rajh T, Johnson CS, Balandin AA, Shevchenko EV (2014) Toward lithium ion batteries with enhanced thermal conductivity. ACS Nano 8(7):7202–7207
58. Koo B, Chattopadhyay S, Shibata T, Prakapenka VB, Johnson CS, Rajh T, Shevchenko EV (2013) Intercalation of sodium ions into hollow iron oxide nanoparticles. Chem Mater 25 (2):245–252
59. Iwasawa Y (1997) Applications of X-ray absorption fine structure to catalysts and model surfaces. J Phys IV 7(C2):67–81
60. Mukerjee S, McGreen J (1999) An in-situ X-ray absorption spectroscopy investigation of the effect of Sn additions to carbon-supported Pt electrocatalysts, part 1. J Electrochem Soc 146 (2):600–606
61. Bazin D, Mottet C, Tréglia G, Lynch J (2000) New trends in heterogeneous catalysis processes on metallic clusters from synchrotron radiation and theoretical studies. Appl Surf Sci 164 (1–4):140–146
62. Bazin D, Mottet C, Tréglia G (2000) New opportunities to understand heterogeneous catalysis processes on nanoscale bimetallic particles through synchrotron radiation and theoretical studies. Appl Catal A Gen 200:47–54
63. Lee JS, Park ED (2002) In-situ XAFS characterization of supported homogeneous catalysts. Top Catal 18(1–2):67–72
64. Bazin D (2002) Solid state concepts to understand catalysis using nanoscale metallic particles. Top Catal 18(1–2):79–84
65. Grunwaldt JD, Wandeler R, Baiker A (2003) Supercritical fluids in catalysis: opportunities of in-situ spectroscopic studies and monitoring phase behavior. Catal Rev Sci Eng 45(1):1–96
66. Bazin D, Rehr J (2003) Soft X-ray absorption spectroscopy at the cutting edge for nanomaterials used in heterogeneous catalysis: the state of the art. Catal Lett 87(1–2):85–90
67. Bare SR, Ressler T (2009) Chapter 6 characterization of catalysts in reactive atmospheres by X-ray absorption spectroscopy. Adv Catal 52:339–465
68. Grunwaldt JD (2009) Shining X-rays on catalysts at work. J Phys Conf Ser 190(1):012151
69. Andrew J, Lobo RF (2010) Identifying reaction intermediates and catalytic active sites through in situ characterization techniques. Chem Soc Rev 39(12):4783–4793

70. Singh J, Lamberti C, van Bokhoven JA (2010) Advanced X-ray absorption and emission spectroscopy: in situ catalytic studies. Chem Soc Rev 39(12):4754–4766
71. Pascarelli S, Mathon O (2010) Advances in high brilliance energy dispersive X-ray absorption spectroscopy. Phys Chem Chem Phys 12(21):5535–5546
72. Ferri D, Newton MA, Nachtegaal M (2011) Modulation excitation X-ray absorption spectroscopy to probe surface species on heterogeneous catalysts. Top Catal 54(16–18):1070–1078
73. Fechetea I, Wangb Y, Vedrinec JC (2012) The past, present and future of heterogeneous catalysis. Catal Today 189(1):2–27
74. Frenkel AI (2012) Applications of extended X-ray absorption fine-structure spectroscopy to studies of bimetallic nanoparticle catalysts. Chem Soc Rev 41(24):8163–8178
75. Wachs IE (2013) Catalysis science of supported vanadium oxide catalysts. Dalton Trans 42(33):11762–11769
76. Ehteshami SMM, Chan SH (2013) A review of electrocatalysts with enhanced CO tolerance and stability for polymer electrolyte membrane fuel cells. Electrochim Acta 93:334–345
77. Grunwaldt J-D, Wagner JB, Dunin-Barkowski RE (2013) Imaging catalysts at work: a hierarchical approach from the macro-to the meso- and nano-scale. ChemCatChem 5(1):62–80
78. Nemeth L, Bare SR (2014) Science and technology of framework metal containing zeotype catalysts. Adv Catal 57:1–97
79. Garino C, Borfecchia E, Gobetto R, van Bokhoven JA, Lamberti C (2014) Determination of the electronic and structural configuration of coordination compounds by synchrotron-radiation techniques. Coord Chem Rev 277:130–186
80. Tielens F, Bazin D (2015) Operando characterization and DFT modelling of nanospinels: some examples showing the relationship with catalytic activity. Appl Catal A Gen 504:631–641
81. Sherborne GJ, Nguyen BN (2015) Recent XAS studies into homogeneous metal catalyst in fine chemical and pharmaceutical syntheses. Chem Cent J 9(1):37
82. Zhu M, Wachs IE (2015) Iron-based catalysts for the high-temperature water gas shift (HT-WGS) reaction: a review. ACS Catal 6(2):722–732
83. Meneses CT, Flores WH, Sotero AP, Tamura E, Garcia F, Sasaki JM (2006) In situ system for X-ray absorption spectroscopy experiments to investigate nanoparticle crystallization. J Synchrotron Radiat 13(6):468–470
84. Bare SR, Kelly SD, Ravel B, Greenlay N, King L, Mickelson GE (2010) Characterizing industrial catalysts using in situ XAFS under identical conditions. Phys Chem Chem Phys 12(27):7702–7711
85. Nelson RC, Miller JT (2012) An introduction to X-ray absorption spectroscopy and its in situ application to organometallic compounds and homogeneous catalysts. Catal Sci Technol 2(3):461–470
86. Rochet A, Moizan V, Pichon C, Diehl F, Berliet A, Briois V (2011) In situ and operando structural characterization of a Fischer-Tropsch supported cobalt catalyst. Catal Today 171(1):186–191
87. O'Neill BJ, Miller JT, Dietrich PJ, Sollberger FG, Ribeiro FH, Dumesic JA (2014) Operando X-ray absorption spectroscopy studies of sintering for supported copper catalysts during liquid-phase reaction. ChemCatChem 6(9):2493–2496
88. Grunwaldt J-D, Caravati M, Hannemann S, Baiker A (2004) X-ray absorption spectroscopy under reaction conditions: suitability of different reaction cells for combined catalyst characterization and time-resolved studies. Phys Chem Chem Phys 6:3037–3047
89. Kumar A, Miller JT, Mukasyan AS, Wolf EE (2013) In situ XAS and FTIR studies of a multicomponent Ni/Fe/Cu catalyst for hydrogen production from ethanol. Appl Catal A Gen 467:593–603
90. Sayah E, Fontaine CL, Briois V, Brouri D, Massiani P (2012) Silver species reduction upon exposure of Ag/Al_2O_3 catalyst to gaseous ethanol: an in situ quick-XANES study. Catal Today 189(1):155–159

91. Martinelli M, Jocabs G, Graham UM, Shafer WD, Cronauer DC, Kropf AJ, Marshall CL, Khalid S, Visconti CG, Letti L, Davis BH (2015) Water-gas shift: characterization and testing of nanoscale YSZ supported Pt catalysts. Appl Catal A Gen 497:184–197
92. Maclennan A, Banerjee A, Hu Y, Miller JT, Scott RWJ (2013) In situ X-ray absorption spectroscopic analysis of gold–palladium bimetallic nanoparticle catalysts. ACS Catal 3(6):1411–1419
93. Craievich AF (2002) Synchrotron SAXS studies of nanostructured materials and colloidal solutions. A review. Mater Res 5(1):1–11
94. Abécassis B, Testard F, Spalla O, Barboux P (2007) Probing in situ the nucleation and growth of gold nanoparticles by small-angle X-ray scattering. Nano Lett 7(6):1723–1727
95. Susini J, Salome M, Fayward B, Ortega R, Kaulich B (2002) The scanning X-ray microprobe at the ESRF X-ray microscopy beamline. Surf Rev Lett 9(1):203–211
96. Wu J, Shan S, Petkov V, Prasai B, Cronk H, Joseph P, Luo J, Zhong C-J (2015) Composition-structure-activity relationships for palladium-alloyed nanocatalysts in oxygen reduction reaction: an ex-situ/in-situ high energy X-ray diffraction study. ACS Catal 5(9):5317–5327
97. Beyer KA, Zhao H, Borkiewicz OJ, Newton MA, Chupas PJ, Chapman KW (2014) Simultaneous diffuse reflection infrared spectroscopy and X-ray pair distribution function measurements. J Appl Crystallogr 47(1):95–101
98. Chapman KW (2016) Emerging operando and X-ray pair distribution function methods for energy materials developments. MRS Bull 41(3):231–240
99. Oxford SM, Lee PL, Chupas PJ, Chapman KW, Kung MC, Kung HH (2010) Study of supported PtCu and PdAu bimetallic nanoparticles using in-situ X-ray tools. J Phys Chem 114(40):17085–17091
100. Newton MA, van Beek W (2010) Combining synchrotron-based X-ray techniques with vibrational spectroscopies for the in situ study of heterogeneous catalysts: a view from a bridge. Chem Soc Rev 39(12):4845–4863
101. Ehrlich SN, Henson JC, Camara AL, Bariio L, Estralla M, Zhou G, Si R, Khalid S, Wang Q (2011) Combined XRD and XAS. Nucl Inst Methods Phys Res A 649(1):213–215
102. Gallagher JR, Li T, Zhao H, Liu J, Lei Y, Zhang X, Ren Y, Elam JW, Meyer RJ, Winans RE, Miller JT (2014) In situ diffraction of highly dispersed supported platinum nanoparticle. Catal Sci Technol 4(9):3053–3063
103. Gallagher JR, Childers DJ, Zhao H, Winans RE, Meyer RJ, Miller JT (2015) Structural evolution of an intermetallic Pd-Zn catalyst selective for propane dehydrogenation. Phys Chem Chem Phys 17(42):28144–28153
104. Muñoz FF, Cabezas MD, Acuña LM, Leyva AG, Baker RT, Fuentes RO (2011) Structural properties and reduction behavior of novel nanostructured Pd/gadolinia-doped ceria catalysts with tubular morphology. J Phys Chem C 115(17):8744–8752
105. Sasaki K, Kuttiyiel KA, Barrio L, Su D, Frenkel AI, Marinkovic N, Mahajan D, Adzic RR (2011) Carbon-supported IrNi core-shell nanoparticles: synthesis, characterization, and catalytic activity. J Phys Chem C 115(20):9894–9902
106. Keating J, Sankar G, Hyde TI, Kohara S, Ohara K (2013) Elucidation of structure and nature of the PdO–Pd transformation using in situ PDF and XAS techniques. Phys Chem Chem Phys 15(22):8555–8565
107. Kan Y, Hu Y, Croy J, Ren Y, Sun C-J, Heald SM, Bareño J, Bloom I, Chen Z (2014) Formation of Li_2MnO_3 investigated by in situ synchrotron probes. J Power Sources 266:341–346
108. Zhang K, Zhao Z, Wu Z, Zhou Y (2015) Synthesis and detection the oxidization of Co cores of Co@SiO_2 core-shell nanoparticles by in situ XRD and EXAFS. Nanoscale Res Lett 10(1):37
109. Cormary B, Li T, Liakakos N, Peres L, Fazzini P-F, Blon T, Respaud M, Kropf AJ, Chaudret B, Miller JT, Mader EA, Soulantica K (2016) Concerted growth and ordering of

cobalt nanorod arrays as revealed by tandem in situ SAXS-XAS studies. J Am Chem Soc 138(27):8422–8431
110. Penfold TJ, Milne CJ, Chergui M (2013) Recent advances in ultrafast X-ray spectroscopy of solutions. In: Rice SA, Dinner AR (eds) Advances in chemical physics, 2nd edn. Wiley, Hoboken, pp 1–41
111. Borfecchia E, Garino C, Salassa L, Lamberti C (2013) Synchrotron ultrafast techniques for photoactive transition metal complexes. Phil Trans R Soc A 371:20120132. https://doi.org/10.1098/rsta.2012.0132
112. Ortega R (2012) X-ray absorption spectroscopy of biological samples. A tutorial. J Anal At Spectrom 27(12):2054–2065

In Situ X-Ray Absorption Spectroscopy to Study Growth of Nanoparticles

6

Chandrani Nayak, S. N. Jha, and Dibyendu Bhattacharyya

Contents

1 Definition of the Topic

In situ X-ray absorption spectroscopy (XAS) measurement during the growth of nanoparticles provides insight into the initial growth and nucleation process of nanoparticles. From XAS measurement and data analysis, information like changes in oxidation states and local structure of the cations during the formation of nanoparticles can be easily extracted. This chapter deals with experimental and analytical applications of synchrotron radiation based XAS technique for in situ measurement of growth of various metal and metal oxide nanoparticles.

C. Nayak · S. N. Jha · D. Bhattacharyya (✉)
Atomic and Molecular Physics Division, Bhabha Atomic Research Centre, Trombay, Mumbai, India

© Springer-Verlag GmbH Germany, part of Springer Nature 2018

C. S. S. R. Kumar (ed.), *In-situ Characterization Techniques for Nanomaterials*,
https://doi.org/10.1007/978-3-662-56322-9_6

2 Overview

The synthesis route of the nanoparticles determines the shape and size of the nanoparticles, which in turn decides the properties that the nanoparticles will exhibit. Therefore, the need to control the synthesis route to fabricate nanomaterials of desired properties demands in situ techniques like X-ray absorption spectroscopy (XAS) which can provide an insight into the nucleation and growth process.

Conventional XAS measurement is a slow technique and not at all suitable for in situ measurements. Therefore, conventional experimental setups or beamlines for XAS measurements were modified to implement this technique in situ with millisecond time resolution. Often this technique has also been complemented with other fast techniques to get a better overview of the systems to be studied. The available analytical tools have also been customized to handle large number of data generated from in situ XAS measurements and to identify different intermediate species formed.

In this chapter, we have provided a brief review on the various experimental and analytical techniques reported in the literature to carry out in situ XAS measurements for studying growth of nanoparticles from solution-based precursors. We have also discussed the results of some recent experiments and to show how these in situ measurements have given insight into the growth and nucleation process of the nanoparticle formation, which remained unexplored for a long time.

3 Introduction

Since its invention, nanoparticles find a wide variety of applications in the field of medicine, catalysis, biotechnology, fuel cells, solar cells, sensors, and environmental science [1–3]. Nanoparticles have fascinated the scientific community due to their interesting properties that is much different from their bulk counterpart. Also, the scope of tunability of properties with size of nanoparticles attracts material physicists to study these materials. With the essence that shape and size of nanoparticles determines their properties comes the need to understand the mechanism of nucleation and growth of these particles. The ex situ studies on nanoparticles gave us information about the properties once the particles are formed. However, to fabricate tailor made particles, a complete control of the formation process is inevitable. This envisages a new era of "in situ" studies. "In situ" is a Latin phrase, which translates to the English meaning "On-Site." Therefore, these measurements focus on characterizing the system when some process is going on. In situ studies are presently being carried out in various fields including nucleation and growth of nanoparticles [4], formation of thin films [5], catalytic reactions [6], photochemical processes [7], charging-discharging of batteries [8], etc.

In the field of growth of nanoparticles, the unavailability of fast techniques, which are one of the prerequisites of in situ studies, that can actually throw some light into the growth and nucleation process made these studies scarce for a long time. UV-Vis spectroscopy is one of the most popular and oldest techniques to study the kinetics of growth. Many studies have been done where depending on the intensity of the

surface plasma resonance (SPR) peak of nanoparticles, the growth kinetics has been predicted. For example, Mizutani et al. investigated the growth of gold nanoparticles synthesized by solution plasma sputtering method by in situ UV-Vis measurement [9]. However, this technique is limited to systems, which give absorption in this particular wavelength range. Also, this can only throw light on the kinetics of growth and is insufficient to reveal the structural changes during growth or the accurate changes in particle size. Though some researchers report the prediction of particle size from the SPR peak [10], these formulations were mostly applied to ex situ studies and were rarely applied to in situ studies as the system was very complicated when a process is going on due to presence of several intermediates. Transmission electron microscopy (TEM) [11, 12] is also another popular technique that can be used in situ to study the changes in particle size during nucleation and growth. Wu et al. studied the deposition of carbon on MgO supported Pt nanoparticles by in situ TEM measurement [13]. Their measurement reveals how carbon encapsulation occurs on Pt nanoparticles and the role of the Pt surface morphology. Growth of ZnO nanowires by hydrothermal synthesis was studied by in situ TEM measurement, which revealed a two step growth mechanism, where first ZnO nanoparticles were formed followed by anisotropic growth of ZnO nanoparticles into nanowires [14]. However, in situ TEM has the limitation that the electron beam can interfere with the reacting species, thus changing the whole redox reaction process to be studied. Also, it is very difficult to employ in situ TEM measurement in solution phase due to vacuum requirement. The conventional TEM has been modified to liquid phase TEM (LP-TEM) with special liquid cell designs that can be used to investigate the changes in particle size during growth in solutions [15]. However, creating different experimental conditions like variable temperature and pressure, irradiation, etc., is still a challenge for LP-TEM.

X-ray based techniques, on the other hand, generally are not system specific and in most of the cases, they do not alter the processes to be studied. With the advent of synchrotron-based techniques, many X-ray based experiments are being carried out in situ to investigate the growth of nanoparticles. Tay et al. [16] observed the growth and nucleation of electrodeposited ZnO nanostructures using a transmission X-ray microscope (TXM). TXM has the same advantages and requirements as TEM. The only relaxation is the dimension of the liquid cell in TXM can be of the order of millimeters, while for TEM it is of the order of hundred nanometers. Small angle X-ray scattering (SAXS) is another important X-ray based technique which can act as a substitute of TEM measurements revealing the changes in particle size during growth and nucleation [17, 18]. All the above techniques mostly yield information on real time changes in particle sizes only and cannot throw light on the evolution of the reduction process that is mainly responsible for the nucleation and growth of nanoparticles in such systems. Also these techniques cannot find out the coordination of atoms in clusters, which are formed in the initial phase of the growth and act as seeds for further growth of the nanoparticles. In this regard, X-ray absorption spectroscopy has played a crucial role in giving insight into the nucleation and formation process of nanoparticles from a very different aspect as compared to the other popular in situ techniques.

X-ray absorption spectroscopy (XAS), which includes both X-ray near edge structure (XANES) and extended X-ray absorption fine structure (EXAFS) techniques, is a powerful tool to determine the local structure of atoms in a material. It gives us information regarding bond distances, coordination number, and disorder of the neighboring atoms. It does not require any long-range order, therefore can be extensively used for a wide variety of materials. Also, by implementing specialized optical and mechanical design, it is possible to record an entire XAS spectrum with millisecond resolution. This establishes XAS as a fast technique and one of the most suitable candidates to see the structural changes during a reaction as well as changes in the oxidation states of the metal cations in situ. Recently, several in situ time-resolved XAS measurements have been carried out on nanoparticles synthesized by various routes, viz., Turkevich method by Polte et al. [19] and Lin et al. [20], Shiffrin-Brust method by Ohyama et al. [21], X-ray irradiation of ionic liquid by Ma et al. [22], photoreduction by Harada et al. [7, 23–25], polyol synthesis by Boita et al. [26], block copolymer assisted synthesis by Nayak et al. [27], etc. Through these experiments the understanding of these processes have been improved which has ultimately helped to obtain a better yield and size distribution of the nanoparticles.

Despite the several advantages that have popularized in situ XAS, some challenges are still there that need to be dealt with. One of the major disadvantages of all X-ray based techniques is that they give an ensemble average information. Therefore, if many species are present in the sample, which is the case for most reactions to be studied in situ, it is very difficult to identify them. Though analysis tools like PCA, MCR-ALS helps to identify reaction intermediates but they also have limitations. Therefore, several other techniques have also been complemented with time resolved XAS for simultaneous measurements to get a better insight into the reaction procedure. For example, Shannon et al. [28] complemented XAS with XRD to study solid-liquid catalytic reactions to get information on short-range and long-range structural changes. Tromp et al. [29] have carried out XAS and UV-Vis spectroscopy simultaneously. Raman, UV-Vis, and XANES have been used simultaneously by Briois et al. [30], while in situ XAFS, IR, and mass spectroscopy have been combined for heterogeneous catalysis studies by Newton et al. [31]. Complementary techniques give a broader view of the system and focus on different aspects of it, which in turn results in more consolidated conclusions.

In this chapter, we present a detailed account of the developments in experimental and analytical tools for the application of in situ EXAFS technique in probing the nucleation and growth of nanoparticles. It should be noted that few reviews are already available in the literature, which discuss the power of in situ EXAFS. For example, Newton et al. [6] had discussed the application of in situ EXAFS for investigating the process of catalysis. This above review published in 2001 deals with the different experimental setup for time resolved EXAFS, their advantages and disadvantages, and their application to study homogenous and heterogenous chemical systems. In 2016, Koziej [4] presented a review article to probe nanoparticle synthesis in solution using in situ hard X-ray spectroscopic techniques, which also includes XAS. The above review is mainly focused on growth of nanoparticles in

solution and briefly discussed several experimental techniques like EXAFS, XANES, and XES, which can be used as an in situ probe. In the present review, we have solely focused on in situ XAS and its application toward growth and nucleation of nanoparticles. We have discussed X-ray absorption spectroscopy as a technique and how it is modified as a fast technique (dispersive-EXAFS and quick EXAFS setup) for its implementation in in situ studies. The analytical tools for handling and analyzing the time resolved XAS (TR-XAS) data to predict different intermediate species have also been elaborately reviewed. Different in situ reaction cells used not only for TR-XAS experiments but also to complement other experimental techniques with TR-XAS have been introduced. At the end, the results of different in situ XAS experiments to study the growth of metal and metal oxide nanoparticles have been mentioned. These include some important experiments from 2010 till date with their key research findings. In nutshell, this chapter gives an elaborate overview of the success and popularity of in situ EXAFS as a technique to probe the growth and nucleation of nanoparticles.

4 X-Ray Absorption Spectroscopy

X-ray absorption spectroscopy (XAS) has been developed in the last few decades as one of the most powerful techniques in determining the local structure around elements in different sample environments. Due to its high resolution and element specificity, it has been used extensively as a structural probe in the world of material science. One of the main advantages of XAS is that no long-range order is required for structure determination. Therefore, this probe can be used to determine the structure of nanomaterials, amorphous and disordered solids, liquids, gels, molecular solutions, liquid crystals, macromolecules containing metallic or heavy atoms (polymers, biomolecules), etc.

X-ray interacts with matter in the form of X-ray absorption, elastic scattering, ineleastic scattering, and pair production. For the energy range involved in XAS measurements, the pair production phenomenon is negligible and X-ray absorption, elastic scattering, and inelastic scattering are the main interactions of X-rays with matter. In XAS, the X-ray absorption coefficient, μ of a sample is measured as a function of photon energy over a range of 1000 eV around the absorption edge of an element. A typical XAS spectrum can be divided into two regimes: X-ray absorption near edge apectroscopy (XANES) and extended X-ray absorption fine structure spectroscopy (EXAFS) as shown in Fig. 6.1. These two regimes involve the same physical process, i.e., photoelectric effect, but they differ in the energy range of the emitted photoelectron and hence provide different information regarding the system.

4.1 X-Ray Absorption Near Edge Spectroscopy (XANES)

XANES region extends upto 50 eV above the absorption edge and gives information about the external perturbations in the valence states to which electrons make

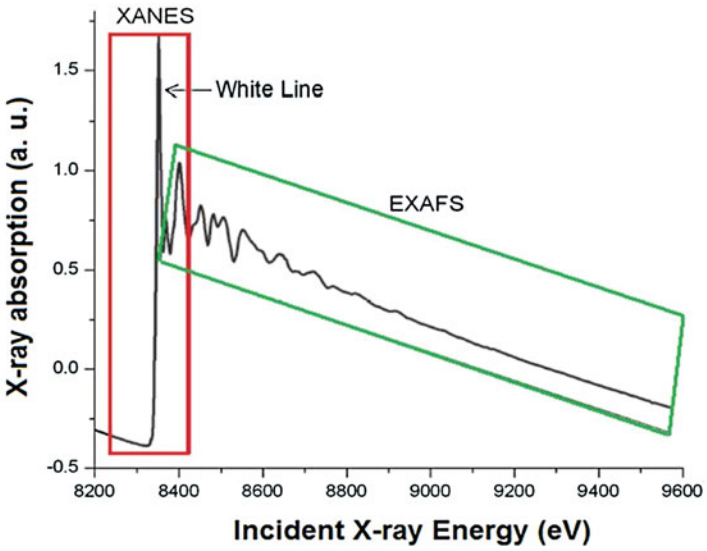

Fig. 6.1 A typical XAS spectrum

transitions from core levels upon absorption of X-ray photons. Hence, XANES can yield information regarding hybridization of orbitals in case of molecule or long-range order existing in a crystalline sample apart from the oxidation states of the absorbing atom in the material. Moreover, the shape of the absorption edge is related to the density of states available for the excitation of the photoelectrons. The absorption edges often show features like isolated peaks, shoulders, and strong peaks just above the absorption edge, popularly known as white line. These features are characteristic of the density of the unoccupied states to which excited photoelectrons may make transitions. Since the density of unoccupied states depends on the formal valence state, ligand type, and coordination geometry, therefore, XANES spectroscopy can be used as a fingerprint to identify phases.

An important and common application of XANES spectroscopy is to use the shift of the absorption edge position to determine the oxidation state of the particular atomic species. Figure 6.2 shows the XANES spectra of Cr metal foil, Cr_2O_3 and CrO_3 standards, which contain Cr cations in 0, +3, and +6 oxidation states, respectively. With increase in the oxidation state of the cation, the absorption edge shifts toward higher energy. Therefore, for an unknown sample, a comparison of the absorption edge position with that of standards gives the information about the oxidation state of the cation in the sample. In case of mixed oxidation state, a linear combination fitting of the absorption edge is used to predict the ratio of valence states present in the sample. In many cases, isolated peaks appear just before the absorption edge in the XANES spectra, which are known as pre-edge peaks. Appearance of the pre-edge peaks depends on the centrosymmetry of the coordination environment and hybridization of orbitals of the cations. For example, in

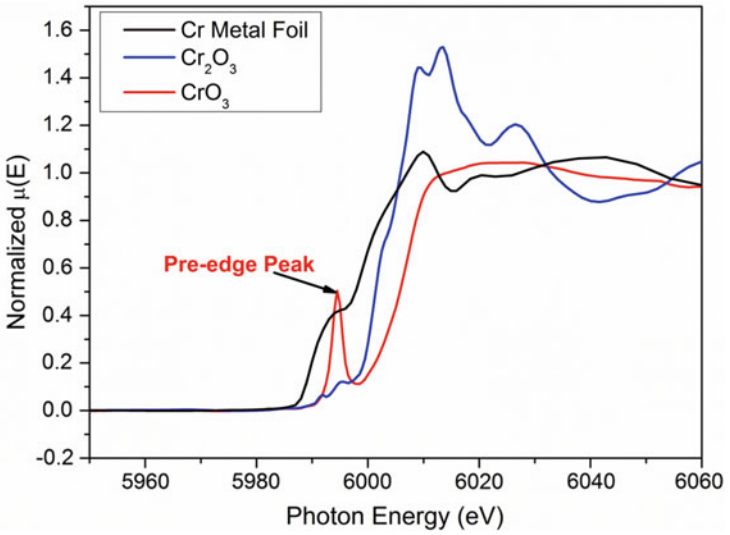

Fig. 6.2 Cr K edge XANES spectra of standard Cr metal and oxides

Fig. 6.2, CrO_3 which contains Cr(VI) cation shows a strong pre-edge peak. This peak corresponds to electron transition from 1 s to 3d orbital, which is not an allowed transition. However, the tetrahedral coordination of Cr(VI) facilitates the hybridization of the 3d and 4p orbitals, which makes the transition allowed. The octahedral Cr(III) cation in Cr_2O_3 having centrosymmetry does not allow the hybridization of the 3d orbitals, hence do not have the pre-edge peak. In case of Cr, the pre-edge peak can be used to determine the presence of Cr (VI) and Cr(III) species.

4.2 Extended X-Ray Absorption Fine Structure Spectroscopy (EXAFS)

The EXAFS region, which spans from 50 eV to 800 eV above the absorption edge, consists of fine structure oscillations arising due to back scattering of outgoing photoelectron by neighboring atoms and can give precise information regarding the short-range order and local structure around the particular atomic species in the material. Though the EXAFS oscillations were observed by scientists way back in 1930s, a robust theoretical formulation was established by Sayers et al. [32, 33] for this phenomenon in 1971, which also provides a way to derive meaningful parameters from the EXAFS oscillations. However, this technique becomes popular only with the advent of modern synchrotron sources. One of the prerequisite of EXAFS measurement is the availability of an intense and energy-tunable X-ray source. The background radiation from a laboratory based X-ray tube source offers a very weak tunable X-ray continuum, and this had been a serious limitation in obtaining EXAFS spectrum of reasonable quality till a long time. The availability of modern bright

synchrotron radiation sources since 1970s has removed this experimental difficulty and since then EXAFS has emerged out to be one of the most powerful tools for local structure determination. Presently, many synchrotron sources around the world are operational round the clock. Some examples are Spring 8 (8 GeV) in Japan, ESRF (6 Gev) in France, APS (7GeV) in USA, etc. Most of the synchrotron facilities have beamlines for EXAFS measurements which are being used extensively by researchers.

A quantum mechanical approach is needed to understand the origin of EXAFS oscillations. In photoelectric effect, an X-ray photon with sufficient energy is absorbed in the sample and an electron is emitted from the core shells of the atoms. The emitted electron, known as photoelectron, can be represented as an outgoing wave for an isolated atom. When the absorbing atom is surrounded by other atoms, the outgoing photoelectron wave is scattered by these surrounding atoms. The interference between the outgoing and scattered photoelectron wave causes an energy dependent variation in the X-ray absorption coefficient in accordance with the Fermi's golden rule, which are generally referred to as EXAFS oscillations. Since the EXAFS oscillations arise due to the presence of neighboring atoms, they can be analyzed to extract information like bond distances, coordination numbers, and disorder factor of neighboring atoms with respect to the absorbing atom [34, 35].

The EXAFS spectra can be theoretically represented by the EXAFS equation, which is written as a contribution of all scattering paths of the photoelectron.

$$\chi(k) = \sum_j \frac{S_0^2 N_j}{kR_j^2} \left| f_j(k) \right| e^{-2R_j/\lambda_e} e^{-2k^2\sigma_j^2} \sin\left(2kR_j + \delta_j(k)\right) \tag{6.1}$$

where N_j is the number of atoms in the jth coordination shell, and σ_j^2 is the mean square variation of distances about the average R_j of atoms in the jth shell. The terms $f_j(k)$, $\delta_j(k)$, and λ_e are the effective scattering amplitude, phase shift, and the mean free path of the photoelectron. k is the photoelectron wave vector, defined as $k = \sqrt{\frac{2m(E-E_0)}{\hbar^2}}$, where E is the incident photon energy and E_0 is the binding energy of the core shell electron. Equation 6.1 is the classic EXAFS equation proposed by Stern, Sayers, and Lytle [32, 33] for an unoriented sample with Gaussian disorder with corrections for many body effects incorporated.

5 Experimental and Instrumental Methodologies

XAS can be measured either in transmission or fluorescence geometries. Transmission mode simply involves measuring the X-ray flux before and after the beam is passed through a homogeneous sample. Under these conditions, the absorption coefficient is expressed in terms of the transmitted flux I and the incident flux I_0 by Beer Lambert Law:

$$\mu t = \ln\left(\frac{I_o}{I}\right) \tag{6.2}$$

Transmitted mode measurements are useful for uniformly thick bulk samples having optimum concentration of the absorbing species.

In X-ray fluorescence, a higher energy core-level electron fills the deeper core hole created by X-ray absorption, ejecting X-ray photons of well-defined energy. Since the fluorescence process is a secondary process of photoelectric absorption, all the features of the absorption spectra of a sample get reflected in its fluorescence spectra also and hence fluorescence spectra can also be used to study the EXAFS oscillations. In fluorescence mode, one measures the incident flux I_0 and the fluorescence X-rays I_f that are emitted following the X-ray absorption event and follows the relation:

$$\mu \propto I_f / I_o \tag{6.3}$$

The fluorescence mode is suitable for dilute samples, liquid samples, thin films on thick substrates, etc. In this measurement, usually the fluorescence detector is placed at 90° to the incident beam in the horizontal plane, with the sample at an angle (usually 45°) with respect to the beam. The fluorescence is emitted isotropically, and every effort is made to collect as much of the available signal as possible by increasing the solid angle of the detector. The scattered beam, on the other hand, is actually not emitted isotropically because X-rays from synchrotron are polarized in the plane of the synchrotron. It means that elastic scatter is greatly suppressed at 90 degrees to the incident beam, in the horizontal plane. Energy discrimination is also important because it can potentially allow us to completely suppress the scattered peak and other fluorescence lines, and collect only the intensity of the fluorescence lines of interest. This would greatly suppress the background intensity and increase the signal-to-noise level. Energy discrimination can be accomplished either physically, by filtering out unwanted emission before it gets to the detector by using a Z-1 filter, or electronically after it is detected. The two configurations (transmission and fluorescence) of EXAFS measurements are shown schematically in Fig. 6.3.

Subsequent to recording of the absorption spectra, the EXAFS oscillations need to be extracted from the absorption spectra. This involves the normalization of the absorption spectra to unit edge step, background subtraction, conversion from energy to k space, and Fourier transform to R space which gives the radial distribution function. The energy dependent EXAFS function $\chi(E)$ is defined as follows:

$$\chi(E) = \frac{\mu(E) - \mu_0(E)}{\Delta\mu_0(E_0)} \tag{6.4}$$

where E_0 is the absorption edge energy, $\mu_0(E_0)$ is the bare atom background, and $\Delta\mu_0(E_0)$ is the step in the $\mu(E)$ value at the absorption edge. After converting the energy scale to the photoelectron wave number scale (k) as defined by,

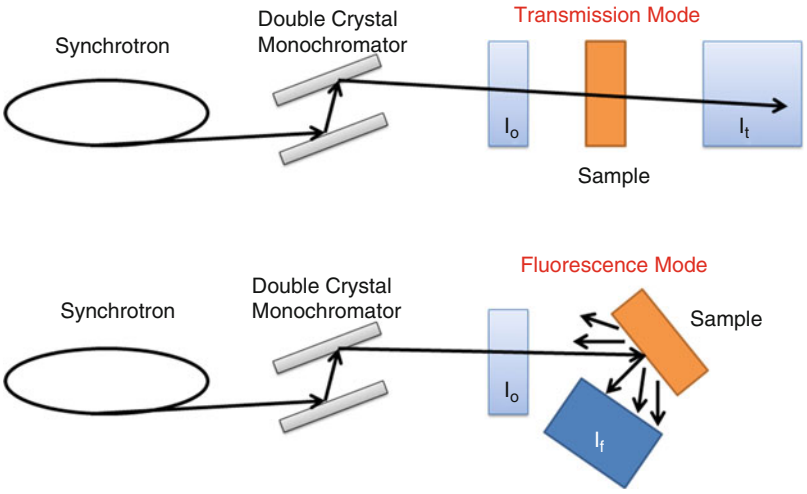

Fig. 6.3 Schematic setup of transmission and fluorescence mode EXAFS measurement

$$k = \sqrt{\frac{2m(E - E_0)}{\hbar^2}} \tag{6.5}$$

the energy dependent EXAFS $\chi(E)$ has been converted to the wave number dependent EXAFS $\chi(k)$, where m is the electron mass. Finally, $\chi(k)$ is weighted by k^n where n is chosen from 1 to 3, to amplify the oscillation at high k and the functions $\chi(k)k^n$ are Fourier transformed in r space to generate the $\chi(r)$ versus r (or FT-EXAFS spectra) plots in terms of the real distances from the center of the absorbing atom. The experimental $\chi(r)$ versus r plots are then fitted with theoretically simulated $\chi(r)$ versus r plots generated assuming a structure model, which provides the physical parameter values of the system as results of the fitting.

Various software packages are available for processing and analyzing EXAFS data, for example, IFEFFIT [36], EXAFSPAK [37], GNXAS [38], UWXAFS [39], etc. IFEFFIT is an open source program, which includes Athena subroutine for data processing and Artemis subroutine for data fitting. A simple flow chart depicting the data analysis methodology using IFEFFIT is given below (Fig. 6.4):

The raw experimental EXAFS data needs some preprocessing before a meaningful data analysis can be carried out to extract relevant information. The data processing includes several steps like conversion of raw data to $\mu(E)$ spectra, background subtraction, energy calibration of spectra, alignment of data, use of reference spectra, deglitching (i.e., the removal of spurious points from spectra), merging of data by calculating the average, and standard deviation at each point in a set of spectra and finally Fourier transformation and plotting. These operations were performed by the data processing software code "Athena." Once the raw data is processed appropriately, it is used in the software code "Artemis" for generating and fitting by a theoretical model.

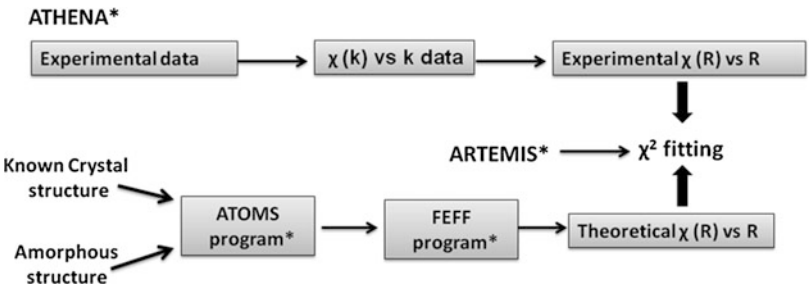

Fig. 6.4 Flow chart showing data reduction and fitting using IFEFFIT

The theoretical EXAFS data is the summation of EXAFS data simulated for different scattering paths. Each scattering path has a degeneracy N (the number of equivalent atoms in single scattering paths), an effective distance R (half path-length), and a mean square variation parameter σ^2, as mentioned in the EXAFS equation (Eq. 6.1). Once calculated, each of these paths can be easily modified during fitting of the experimental data to give different values of the parameters N, R, σ^2, and even E_0. Of the remaining parameters in Eq. 6.1, $f(k)$ and $\delta(k)$ (the scattering amplitude and phase shift due to the neighboring backscattering atom, respectively) and the photoelectron mean free path $\lambda(k)$ are calculated theoretically. The parameters that are often determined from a fit to the EXAFS spectrum affect either the amplitude of the EXAFS oscillations (N, S_0^2, σ^2) or the phase of the oscillations (ΔE_0 and ΔR, the energy shift, and the change in half path length, respectively). Since EXAFS data is limited by a finite k and r ranges, therefore, there is a limit to the number of parameters that can be extracted from the analysis of EXAFS data. Information theory is used to correlate the amount of information in the original EXAFS spectrum to the information in Fourier transform spectrum as determined from the Nyquist theorem [40]:

$$N_{\text{ind}} = \frac{2\Delta k \Delta r}{\pi} \tag{6.6}$$

where N_{ind} is the number of independent points, Δk is the Fourier transformed data range, and ΔR is the region used in EXAFS data analysis. Therefore, the number of fitting parameters of the EXAFS data should always be less than the number of independent points. The goodness of the fitting of EXAFS data is generally expressed by the R_{factor} which is defined as:

$$R_{\text{factor}} = \sum \frac{\left[\text{Im}\left(\chi_{\text{dat}}(r_i) - \chi_{\text{th}}(r_i)\right)\right]^2 + \left[\text{Re}\left(\chi_{\text{dat}}(r_i) - \chi_{\text{th}}(r_i)\right)\right]^2}{\left[\text{Im}\left(\chi_{\text{dat}}(r_i)\right)\right]^2 + \left[\text{Re}\left(\chi_{\text{dat}}(r_i)\right)\right]^2} \tag{6.7}$$

where, χ_{dat} and χ_{th} refer to the experimental and theoretical $\chi(r)$ values, respectively, and Im and Re refer to the imaginary and real parts of the respective quantities. In general, the value of R_{factor} factor less than 0.05 is considered as a reasonable fit.

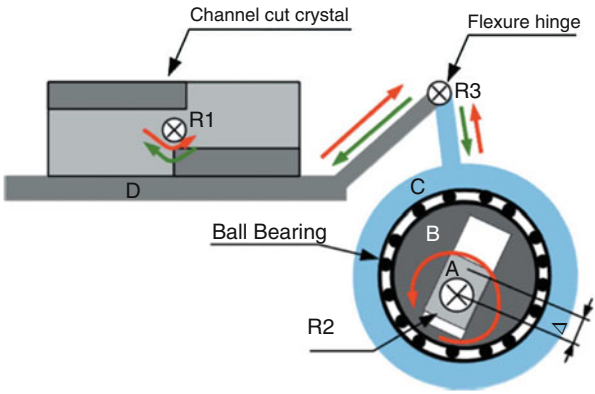

Fig. 6.5 Schematic of QEXAFS monochromator (Taken from Fonda et al. [43]. Reproduced with permission of the International Union of Crystallography)

5.1 Time Resolved X-Ray Absorption Spectroscopy (TR-XAS)

Conventional EXAFS measurement takes almost an hour to measure one complete spectrum with an acceptable S/N ratio of 10^3 or better and upto a reasonable k range of 12 $Å^{-1}$. This is done by step-wise scanning of the whole energy range of 1000 eV around the absorption edge. Therefore, the conventional step-wise scanning measurement is not at all suitable for time resolved studies, which needs second or millisecond resolution for data acquisition, and two alternative modes of measuring fast EXAFS spectra are: quick EXAFS(QEXAFS) and dispersive EXAFS (DEXAFS). Both of these modes have their own advantages and disadvantages [6].

5.1.1 Quick XAFS (QXAFS)

QEXAFS [41, 42] is a modified version of the conventional EXAFS measurement mode, which is optimized to reduce the measurement time of an EXAFS spectrum. In QEXAFS, XAFS spectrum is recorded during quick scanning of the monochromator. Therefore, this is limited by the speed of the monochromator movement achievable, the integration time required per point to achieve acceptable statistics, and the reproducibility of the monochromator movements in both forward and reverse direction. QEXAFS uses a specialized monochromator that allows fast and repetitive energy scans by oscillating the monochromator crystal. In this monochromator, channel cut crystals are mounted on a stage, which in turn is connected to a goniometer with fast movements that moves the crystal to the desired Bragg angle [43]. Figure 6.5 shows the schematics of the QEXAFS monochromator. The smooth oscillation of the monochromator crystal results in a continuous change of the Bragg angle and the reflected energy, which reduces the time of measurement to seconds. Recently, this technique has been improved to give millisecond time resolution [44, 45]. However, improved time resolution has led to new disadvantages such as loss of the fixed exit and a limited choice of energy range. One of the main advantages of QEXAFS technique is that it can measure very dilute sample or thin film samples using fluorescence mode of EXAFS measurement. Therefore, it can be extensively used for quick surface EXAFS measurements to study the in situ growth of thin

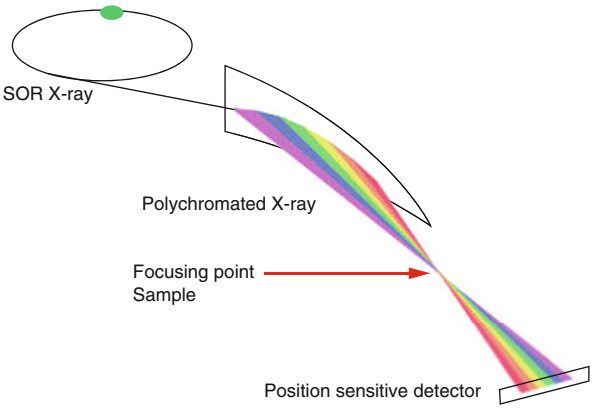

Fig. 6.6 Schematic optical layout of a typical dispersive EXAFS setup

films. Some examples of the QEXAFS measurement facilities are super XAS beamline at Swiss light source [44], BM29 at ESRF [45], ROCK beamline at Soleil synchrotron source [46], etc.

5.1.2 Dispersive XAFS (DXAFS)

In dispersive EXAFS, on the other hand, a band of X-ray energies are dispersed as well as focused on the sample using a long bent crystal (polychromator) and the transmitted and spatially dispersed defocused beam is detected on a position sensitive detector (PSD) as shown in Fig. 6.6 [47]. This mode of measurement demands high temporal and spatial beam stability. Since, the focused band of energies will always be associated with some defocussing aberrations, therefore, the uniformity of the sample is very crucial in this mode. The measurements are possible only in transmission mode; therefore, very dilute samples or surface studies using fluorescence mode is not possible in this technique. Since the whole spectrum is recorded in a single shot using a PSD, therefore, the time resolution of this mode is only limited by the integration time of the detector. Hence, using this mode it is possible to reach microseconds resolution. One of the major advantages of the DEXAFS technique is that the data is not affected by the noise generated from mechanical movements since there is no moving mechanism during the course of data acquisition. Another tempting advantage of this technique is since it focuses and measures a band simultaneously; therefore, for multi element system, different edges can be measured simultaneously at one shot. However, since the incident flux and the transmitted flux cannot be measured at the same instant of time and have to be measured with and without the sample separately, it is affected by the fluctuations in the synchrotron beam. Another major disadvantage of this technique is that for energies less than 5 KeV, the energy band available is not wide enough to record the full EXAFS spectrum and therefore only XANES information can be achieved for elements having edges at lower X-ray energies. Though DEXAFS gives a high time resolution, the measurable range energy and k range are intrinsically limited by the optics of the beamline, which ultimately affects resolution of the radial distribution function of the

FT-EXAFS spectrum. Therefore, data upto only two coordination shells can generally be extracted by DEXAFS, whereas upto three coordination shell can be extracted using QEXAFS technique. Due to the short analyzable range, the error in the reported values increases. Thus to summarize, though DEXAFS has lesser spatial resolution and more errors in the reported value, it offers much lower acquisition time scales to study fast processes [6]. Some examples of the DEXAFS measurement facilities are NW2A at photon factory, ID24 at ESRF, and BL-08 at Indus-2 [48].

5.2 Analytical Tools for TR-XAS

The popularity of in situ and *in-operando* XAS techniques increases with increase in instrumental performance, which results in sub-second time resolution measurements. In these experiments, XAS data were collected as a function of time while chemical or physical changes occur in the samples. Such an experiment generally results in accumulation of large number of XAS data sets and handling and analyzing such a large number of data sets became a challenge for TR-XAS measurements. Different approaches were used not only to analyze such a data set effectively, but also to differentiate different species formed during the time evolution of the sample. One of the methods is examination of isosbestic points [49]. Isosbestic points are the points where all spectra intersect. Presence of one or more isosbestic points implies the direct transformation of reactants to products without the formation of any intermediate species. However, their absence indicates the presence of intermediates in the reaction. This can give us an idea about the presence of intermediate species, but do not give any quantitative information regarding the number or structure of intermediates. For quantitative analysis, methods like linear combination fitting (LCF) are used to reproduce the data set as a linear combination of known standard spectra. This can be used to identify known species formed during the reaction. More sophisticated analytical tools based on linear algebra like principal component analysis (PCA) were used to determine the number of species formed during chemical reaction without using any standard. Chemometric method multivariate curve resolution-alternating least squares (MCR-ALS) is also applied to XAS data set to identify different species formed during a reaction. These analytical tools have made the analysis and handling of TR-EXAFS data very easy and efficient.

5.2.1 Linear Combination Fitting (LCF)

Linear combination fitting (LCF) is to reproduce a set of data as a linear combination of some standard data. The prerequisite for this fitting is the linear structure of the data, which is obeyed for the X-ray absorption coefficient. Therefore, the total absorption coefficient can be written as a sum of coefficients for all the species in the sample.

$$\mu_{\text{sample}} = \sum_i x_i \ \mu_i \tag{6.8}$$

where, x_i are the fractions of the species present in the sample, and μ_i are the standard XANES spectra. LCF involves modeling the spectrum for a sample of unknown

chemical speciation using spectra from representative standards. LCF subroutine available in XAS data analysis programs like Athena [50] and Sixpack has been extensively used in XAS analysis. The main limitation of LCF is the need of reference spectra of all the species having similar energy resolution and consistent normalization. Therefore, it can be used only for systems where the species in the sample are well known.

5.2.2 Principal Component Analysis (PCA)

Principal component analysis [51] (PCA) is a linear algebra based method to analyze a series of related data. Each data is represented as a vector in **n** dimensional space where **n** is the number of data point in a spectrum. If the measured data set contains **m** number of data, then it can be expressed in terms of **m** orthogonal basis vectors, referred as components. The basis vectors are the eigenvectors of the data matrix, **D(m,n)**. Ignoring the eigenvectors with small eigenvalues, minimum number of eigenvectors ($\mathbf{m_c}$) is chosen to represent the measured data set as a linear combination. These eigenvectors are known as principal components of the measured data set. To determine the least number of principal components a graphical method referred as "screen test" is generally used, where the eigenvalues are plotted in decreasing order and the number of principal components is chosen where the curve levels off to linear decline. The $\mathbf{m_c}$ number of principal components, which are required to reconstruct the data set within experimental noise, corresponds to the number of distinct species which contribute to the dataset. Thus, it gives us a way to determine the number of different species without any a priori knowledge about the identity of the species. However, the number of principal components is not necessarily equal to the number of different chemical species contained within the set of samples because the chemical species are not necessarily unique. The necessary condition for the success of PCA is the presence of distinctly different features in the spectra of each individual species. The next step in PCA is target transformation to relate the principle components to physical standards. Target transformations test the likelihood of a given standard spectrum to explain the variance in the set of spectra, and thereby identify the standards that most likely represent the data set. Because PCA relies on standard spectra, the same precautions used to interpret LCF apply.

Recently, PCA is used extensively for analyzing TR-XAS data [52, 53]. Wang et al. [53] has applied PCA analysis to in situ TR-XAFS data of reduction and re-oxidation reaction of Cu doped Ceria. They have used theoretical modeling to identify the intermediate phases. Fig. 6.7a shows the variation of the XANES spectra during the reaction and Fig. 6.7b shows the first five components sorted in descending order of their respective eigenvalues. The first three components appear to be sufficient to reproduce the spectra. However, the data were fitted with different number of principal components as shown in Fig. 6.7c, e and the fit residuals were plotted in Fig. 6.7d, f. From Fig. 6.7d, it is evident that when fitted with two components there is a misfit which is most prominent between $t = 660$–990 s. However, the fit quality greatly improves when three principal components are used to reproduce the spectra and the fit residuals are within noise limit. Therefore, this establishes the presence of intermediate and the time t^* when the intermediate

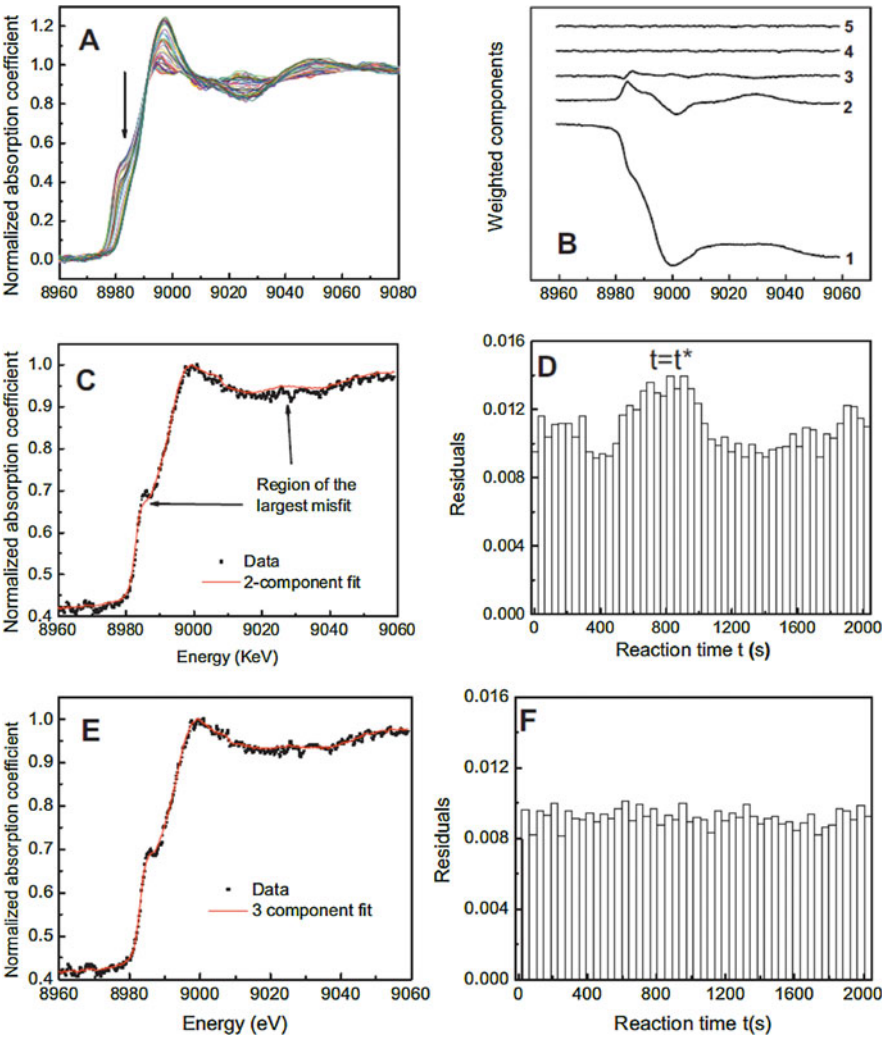

Fig. 6.7 PCA illustrating the method of trapping a reaction intermediate: (**a**) TR XANES of H_2 reduction of $Ce_{0.8}Cu_{0.2}O_2$ showing the structural evolution during the reaction (the *arrow* indicates reaction direction); (**b**) the first five components from PCA calculation weighted by eigenvalues; (**c**) representative spectrum (in *dots*) superimposed with the linear combination of two components (*solid line*); the *arrows* point to the largest misfits; (**d**) residual plots resulted from a two component fit (the *arrow* points to the time stamp (t*) of intermediate); (**e**) representative spectrum (*dots*) superimposed with the linear combination of three components (*solid*); (**f**) residual plot resulted from a three component fit (Taken from Wang et al. [53]. Reproduced with the permission of AIP Publishing)

dominates is the maxima of the residual plot when fitting is done with two components. The EXAFS spectra, μ_{int} recorded at t^* corresponds to the intermediate species. The EXAFS spectrum of the intermediate species is analyzed to identify the species.

5.2.3 Multivariate Curve Resolution with Alternating Least Squares (MCR-ALS)

MCR-ALS is a chemometric method for the resolution of spectroscopic data of time-evolving system with multiconstituents [54, 55]. The basic assumption of this method is the linear structure of the data set. The experimental data are first represented in a matrix form, called $\boldsymbol{D}$(m, n), in which the m is the number of XAS spectra recorded and n is the number of data points of XAS data in terms of energy. Matrix $\boldsymbol{D}$ can be expressed in terms of matrix containing the concentration profiles $\boldsymbol{C}$(m, k) and the matrix containing XAS spectra $\boldsymbol{S^T}$(k, n) of the k species in the unknown mixture.

$$\boldsymbol{D} = \boldsymbol{C}\boldsymbol{S^T} + \mathbf{E} \tag{6.9}$$

The matrix $\mathbf{E}$(m,n) is the residual variation of the data. The matrices C and S^T follow physically and chemically meaningful constraints. As a first step for applying MCR-ALS, we need a priori information about the number of species, which is the rank k of the matrices C and S^T. The PCA algorithm discussed in the earlier section helps us to find the rank k, which is the minimum number of orthogonal components required to reproduce the data set. Once the rank is determined using PCA, the MCR-ALS algorithm can be applied with initial estimates of C and S^T matrices. The alternating least square (ALS) optimization of the matrices C and S^T is done iteratively applying the following constraint.

$$\min \left\| D\text{-}CS^T \right\|^2 \tag{6.10}$$

Iterations are done alternatively on matrix C and S^T, while fixing the remaining parameters according to the following steps.

(a) Given D and the initial estimate of S^T, a minimization of C is carried out by the least square calculation considering relation (6.10) and the constraints for matrix C.
(b) Given D and the so-calculated C matrix, a minimization of S^T is carried out by the least square calculation considering relation (6.10) and the constraints for S^T.
(c) Then the reproduction of D using matrices C and S^T determined in steps (a) and (b) is done. If the convergence criterion is fulfilled, the process is finished. If not, the program goes back to step (a).

This iterative process gives the constituent species of the mixture and their concentration profiles with time. Recently, MCR-ALS has emerged out to be as a popular analytical method, which is effectively applied to the analysis of in situ XAS data.

5.3 Complementary Techniques

Understanding the kinetics and reaction mechanism of different processes remained a challenge for a long time. This is mainly because of the scarcity of suitable

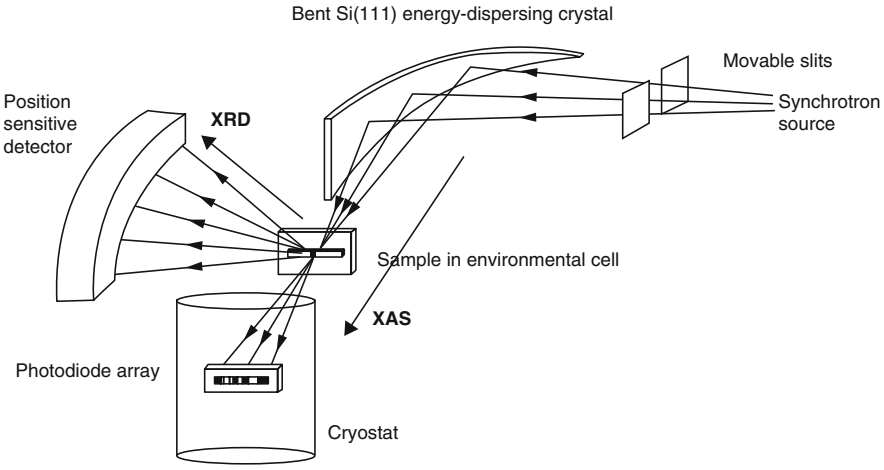

Fig. 6.8 Schematic of setup for simultaneous measurement of XRD and XAS (Taken from Couves et al. [58]. Adapted by permission from Macmillan Publishers Ltd: [Nature], copyright 1991)

technique that can probe the system during evolution and provide necessary information to understand the evolution process. However, no technique is self-sufficient and every technique helps us to understand only a part of the system. In case of complicated studies, where many species are involved, the analysis and conclusion become very challenging. Therefore, it is always better to rely on more than one technique to have a broad and better understanding of the processes. With this point of view, often several other techniques have been complemented with TR-XAS for simultaneous measurements to get a better insight into the reaction procedure. UV-Vis spectroscopy is often complemented with XAS measurement while studying the growth of nanoparticles. Growth of gold and platinum nanoparticle formation has been studied simultaneously by these techniques by several researchers. Stotzel et al. have used QEXAFS and UV-Vis techniques simultaneously to monitor the growth of TiO_2 nanoparticles [56]. This combination of techniques gives information not only about the local structure of different species in the solution but also about their optical properties. Polte et al. [19] have combined XANES and SAXS to study the growth of gold nanoparticles, which has helped to determine the changes in oxidation states of gold cations concurrently with shape, size, and polydispersity of the nanoparticles formed. In situ XRD and XAS are combined to observe the ZnO nanoparticle encapsulation into Zeolite-Y with heating upto 550 °C [57]. This combination gave insight into short-range and long-range structural changes in the samples. The experimental setup for combined XAFS-XRD measurement [58] has been shown in Fig. 6.8.

Many other techniques were also complemented to TR-XAS like IR spectroscopy [31], Raman spectroscopy [30], Mass spectrometry [31], etc. Briois et al. [30] studied oxidation of ethanol by cerium based catalysts using combined Quick-XANES, UV-Vis, and Raman spectroscopies. Newton et al. [31] complemented

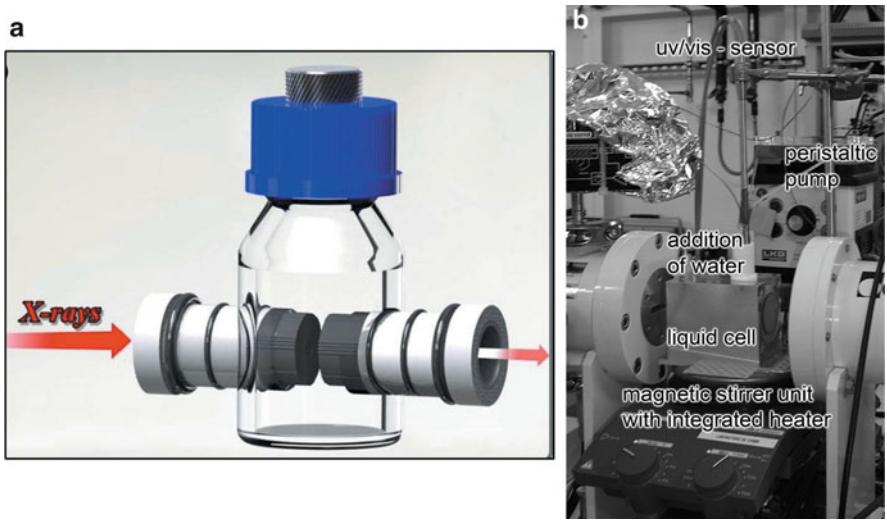

Fig. 6.9 Specially designed cell for in situ XAS measurement (**a**) (Taken from Boita et al. [59], Reproduced with permission of the International Union of Crystallography) (**b**) (Taken from Stötzel et al. [56]. Reprinted with permission from American Chemical Society, Copyright 2010)

FT-IR, dispersive EXAFS, and mass spectrometry techniques to investigate the structural changes in Rh-based catalysts during NO reduction of CO. These three techniques helped to correlate the surface speciation, local structure, and catalyst activity of the catalysts. Complementary techniques give a broader view of the system and focus on different aspects of it, which in turn results in more consolidated conclusions.

5.4 In Situ Cell Designs

Depending on the complicacies of the system to be studied, different in situ cells have been proposed. Most of the cells consist of two windows, which can be adjusted depending on the path length of X-ray required.

EXAFS measurement cell reported by Boita et al. [59] consists of a modified Schott Duran glass bottle that houses two hollow Teflon pistons. Each piston has a Kapton window attached at one end, and by moving the pistons in or out of the cell one may adjust the probed thickness of the liquid (i.e., the X-ray path) from 0.1 to 12 mm and thereby, optimize the edge jump. A magnetic stirrer can be placed under the reaction cell to rotate a magnetic bar placed in the solution and homogenizing it during the measurements. This setup, shown in Fig. 6.9a, also allows heating of the solution up to 423 K.

Many times the cells were modified to accommodated different complementary techniques along with EXAFS. For example, Stötzel et al. [56] have reported an in situ cell for simultaneous measurement of UV-Vis and QEXAFS data at low

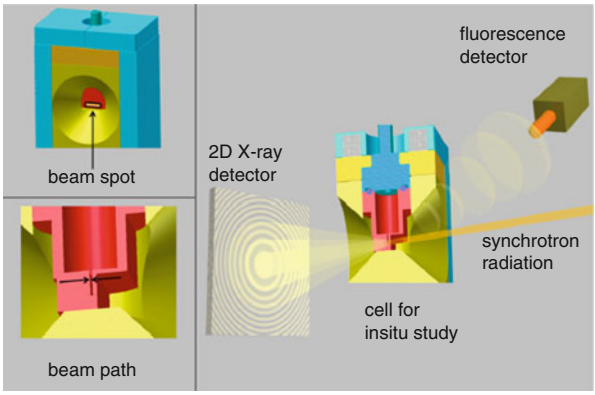

Fig. 6.10 In situ XAS/powder XRD measurement cell (Taken from Staniuk et al. [60]. Reprinted with permission from American Chemical Society, Copyright 2014)

energies. This cell provides a thin layer of solution in the path of the X-rays and enables the user to add water solution through a hole in the top of the cell. This hole is also used to insert the immersion probe of the UV-Vis spectrometer inside the solution without disturbing the X-ray experiments and vice versa. It is possible to heat and mix the solution in the cell using a magnetic stirrer with integrated heater, while the water solution could be added drop by drop with a peristaltic pump. The windows of the cell are polyethylene foils with a thickness of 10 μm, and the gap between them can be reduced by a thread to a few tenths of a micrometer. Fig. 6.9b shows the photograph of the experimental setup.

Staniuk et al. [60], on the other hand, have reported a cell for insitu XAS/powder XRD measurement which allows heating of the reaction solution with heating rate comparable to that of the CEM microwave. The measurement cell is assembled from three distinct parts (Fig. 6.10). The container for the reaction solution consists of PEEK, confining the sample at the bottom part and facing the fluorescence detector by a thin window (wall thickness of 0.5 mm). The PEEK container is fitted into a brass housing and sealed with a cap pressed against the top of the sample container by four screws. Tightly adapted alumina bricks surrounding the brass housing thermally isolate the measurement cell for better temperature control. A temperature sensor right at the bottom of the PEEK container controls the resistive heating of the reaction solution via a feedback loop and the sample was constantly irradiated during the time of reaction. PXRD and XAS data were recorded using a two-dimensional X-ray detector and fluorescence detector, respectively.

Nayak et al. [27] have designed a cell for simultaneous measurements of EXAFS and UV-Vis spectra during growth of nanoparticles. The reaction cell is made up of Teflon and has paths for both X-rays and UV–Vis radiation in mutually perpendicular directions. X-rays are transmitted through Kapton windows while the optical light is passed using optical fibers, which are capped with Teflon ferrules and are directly immersed into the solution. The cell has been designed and fabricated in such a way that the optical paths can vary from 5 mm to 20 mm for X-rays and from 2 mm to 20 mm for UV–Vis radiation. The volume of the cell varies according to the adjustment of the Kapton windows and optical fibers. The in situ reaction cell is

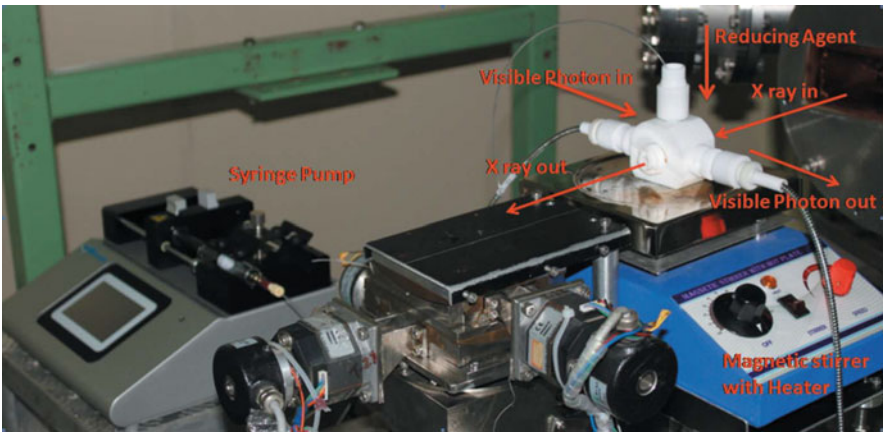

Fig. 6.11 In situ reaction cell for simultaneous measurements of EXAFS and UV-Vis spectra (Taken from Nayak et al. [27]. Reproduced with permission of the International Union of Crystallography)

placed on a magnetic stirrer-cum-heater for mixing and heating the reaction solution. The precursor is taken in the Teflon reaction cell and the respective reducer is injected into it through a Teflon tube using a computer controlled motor-driven syringe pump. Figure 6.11 shows the photograph of the experimental setup.

Flow setups have also been proposed where the reaction chamber and measurement chambers are separated as shown in the schematic shown in Fig. 6.12 [61]. In this setup, a reaction vessel is used for adding reactant, stirring and mixing, and the reaction solution is pumped to the measurement cell using a peristaltic or gear wheel pump where XAS and UV-Vis measurements were carried out. This setup is proposed to study slow homogeneous reactions where mixing of reactants are important. Yao et al. [62] have used a flow setup for in situ XAFS measurement to study growth of gold nanoparticles. The separation of the reaction chamber and measurement chamber facilitates the creation of different reaction conditions without disturbing the measurement setup.

6 Key Research Findings

6.1 Growth of Metal Nanoparticles

In 2010, Polte et al. [19] did in situ XANES measurements along with SAXS on levitated sample droplets to investigate the growth of gold nanoparticles by citrate synthesis. Though citrate synthesis was proposed by Turkevich in the year 1951, the mechanism of formation of nanoparticles through this route was not clear for a long time. In this experiment, liquid samples were extracted from the reaction solution at

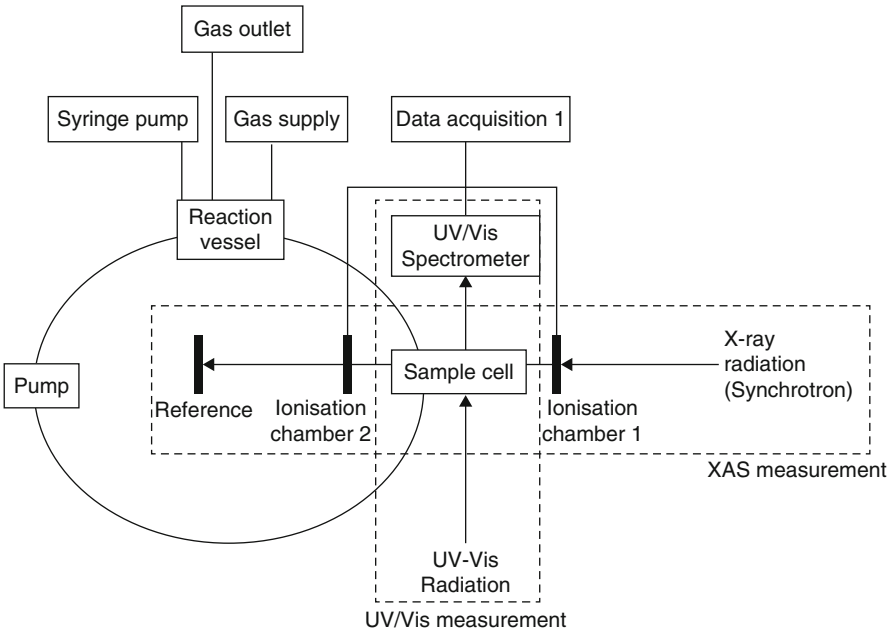

Fig. 6.12 Schematic diagram of the setup separating reaction and measurement cells (Taken from Bauer et al. [61]. Reproduced with permission of the International Union of Crystallography)

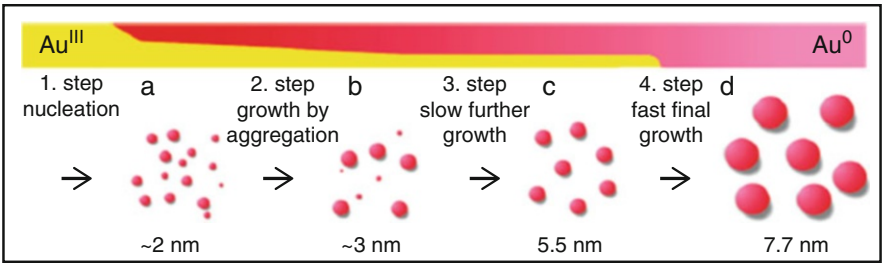

Fig. 6.13 Schematics of Au nanoparticles growth in citrate reduction (Taken from Polte et al. [19]. Reprinted with permission from American Chemical Society, Copyright 2010)

different times and placed as a droplet in the acoustic leviator for SAXS and XANES measurements. The XANES data were analyzed by fitting each spectrum as a linear combination of the initial state and the final state. From this study a four step mechanism of gold nanoparticles formation could be proposed, comprising of fast initial formation of small nuclei, coalescence of the nuclei into bigger particles, slow growth of particles sustained by ongoing reduction of gold precursor, and subsequent fast reduction ending with the complete consumption of the precursor species as shown in Fig. 6.13.

In 2011, Ohyama et al. [21] have carried out another experiment to understand the reduction of gold by sodium borohydraide ($NaBH_4$). Au nanoparticles were prepared by $NaBH_4$ reduction of $HAuCl_4$ in toluene, in the presence of dodecanethiol (DT). This synthesis is popularly known as Shiffrin–Brust method [62]. Au L_3 edge QEXAFS measurements were carried out in transmission mode with millisecond time resolution. A series of XANES spectra were analyzed to clarify the variation of the chemical state of Au atoms and the formation process of Au nanoparticles. The XANES spectral changes revealed that Au nanoparticles are formed by the reduction of the solution containing an equal quantity of Au^{3+} and Au^{+} ions. The signature for formation of Au was observed at 4.6 s. This is one of the first reports of observation of nuclei in formation process. From the EXAFS analysis, the structure of the Au nuclei is estimated to be an Au_4 cluster with an fcc crystal system.

In 2013, Ma et al. [22] reported the evolution of gold nanoparticles in ionic liquid by hard X-ray irradiation. Synchrotron hard X-ray not only acts as the radiation source, which causes the reduction of Au^{3+} ions, but also acts as a probe to study the whole process in realtime by QEXAFS. Figure 6.14 shows the in situ XANES spectra recorded during irradiation of the reaction solution. As the irradiation time increased, a decrease in intensity can easily be found at the white line peak (11922.6 eV), which is due to the electronic transition from the $2p_{3/2}$ core-level state to a vacant 5d state. There is no white line peak in the XANES spectrum of Au foil since the 5d state of Au^0 is fully occupied. Therefore, the intensity of this peak declined rapidly as Au was reduced from trivalent to zerovalent state. Another characteristic peak assigned to Au^0 in the energy region from 11,940 eV to 11,950 eV appeared and increased gradually. The features of the spectra gradually became close to that of Au foil. From EXAFS analysis, a new hypothesis and reaction mechanism has been proposed to explain the generation progress of gold nanoparticles. The initial breaking of the Au–Cl bond differentiates this irradiation method from traditional chemical methods. Intermediates like $AuCl_3$, $AuCl_2$, and $Cl_2Au\text{-}AuCl_2$ clusters have also been predicted.

Yao et al. [63] performed an in situ QEXAFS measurement using a continuous flow experimental setup for studying the nucleation and growth of gold nanoparticles in aqueous solution, reduced by citric acid and stabilized by PVP. The XANES and EXAFS data are shown in Fig. 6.15. The analysis of XAFS data indicates that the partially reduced $AuCl^{3-}$ ions are combined through the slightly elongated Au-Au bond to form the Au_nCl_{n+x} complex clusters rather than to form Au_n^0 clusters. These complex clusters play an important role in delaying the growth phenomenon and inducing the eventual coalescence.

The growth of Pt nanoparticles by polyol synthesis was studied by Boita et al. [26]. This method basically consists of mixing two ethylene glycol solutions, one containing polyvinylpyrrolidone, sodium citrate, and ascorbic acid, and the other containing the metallic precursor and potassium hexachloroplatinate. In situ DEXAFS measurements of the reaction solution were performed at the specially designed cell shown in Fig. 6.8a. A linear combination fitting of the XANES spectra using the initial (Pt^{+4}) and final (Pt^0) spectra were done to obtain the detailed time evolution of the zerovalent Pt fraction. The XAFS analysis could distinguish three

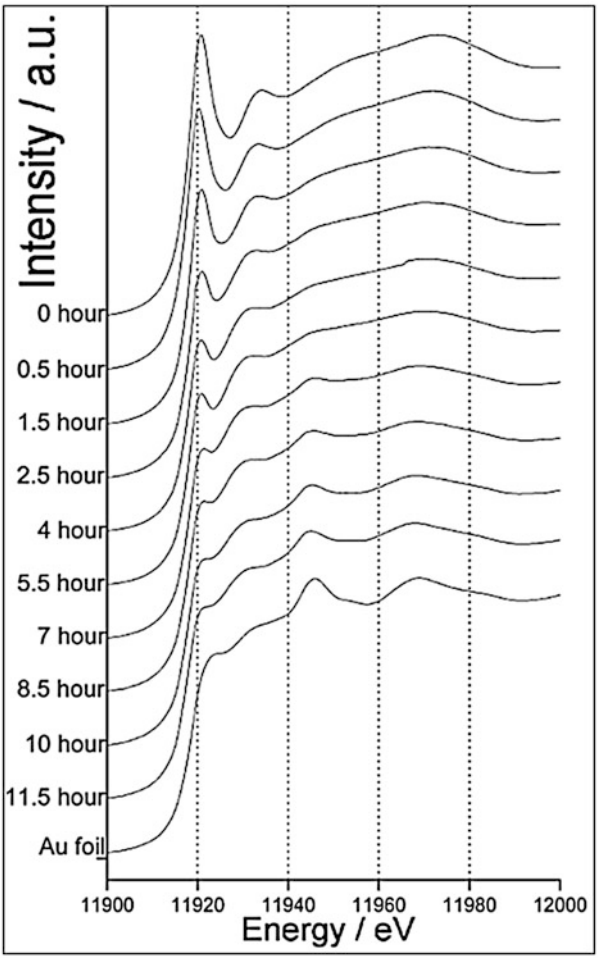

Fig. 6.14 In situ XANES spectra recorded during synthesis of Au nanoparticles by photoreduction method (Taken from Ma et al. [22]. Reproduced with permission from the PCCP Owner Societies)

different stages in the synthesis process: a fast nucleation event, followed by diffusion-limited Ostwald ripening growth ($R \propto t^{1/3}$), where R is the radius of the particles and t is the reaction time, and subsequent slow growth and stabilization of nanoparticles. The experiment also gave an evidence of Lamer nucleation burst scenario.

Nayak et al. [27] have studied the growth of gold and platinum nanoparticles stabilized by block copolymer. The nanoparticles were synthesized in a specially designed Teflon cell described in Sect. 5.4 (Fig. 6.11) and dispersive EXAFS and UV-Vis measurements were carried out simultaneously. LC fitting has been done to the XANES spectra which gave realtime information on the reduction process. The EXAFS spectra reveal the different stages of nucleation and growth and the structure

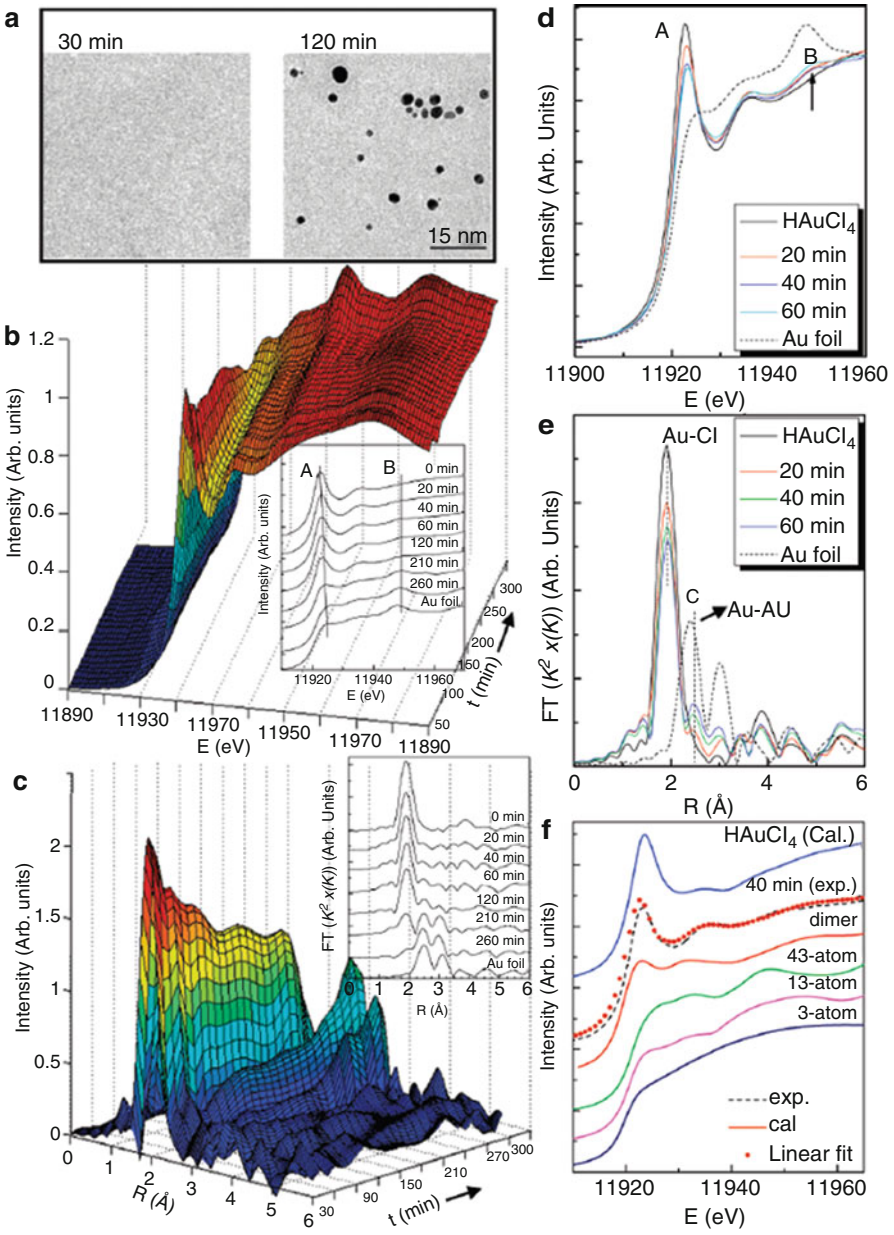

Fig. 6.15 Dynamic nucleation and growth of Au NCs studied by TEM and in situ XAFS. (**a**) TEM images of Au NCs obtained at different times for 30 and 120 min. (**b**) Time variations in normalized Au L_3-edge in situ XANES and (**c**) k^2-weighted EXAFS Fourier transforms (FTs) spectra. The *insets* show the typical Au L_3-edge XAFS spectra at different reaction time. (**d**) Some typical XANES spectra and (**e**) the corresponding FTs spectra for comparison. (**f**) XANES calculations for various Au clusters (Taken from Yao et al. [63]. Reprinted with permission from American Chemical Society, Copyright 2010)

of the clusters formed at the intermediate stages of growth. From the EXAFS analysis it has been found that the metal-metal bond coordination number shows abrupt discontinuities which corresponds to the formation of some stable clusters. The growth kinetics of both Au and Pt nanoparticles are found to be almost similar and are found to follow the three stages viz. (i) reduction of metal ions by block copolymer and formation of small cluster of typical five co-ordinations, (ii) absorption of block copolymer and reduction of metal ions on the surface of the cluster and increase in cluster size, and (iii) growth of metal nanoparticles stabilized by block copolymer. This was observed in the above study that the time scale involved in the 2nd and 3rd stages of the nanoparticle formation are similar for both gold and platinum nanoparticles since these stages are mainly governed by the block copolymer which is same in both the cases. However, the 1st stage of nucleation takes place earlier in case of Au than in case of Pt due to the difference in the reduction potential of the respective precursors. In both the cases, 12 atoms clusters are formed which act as seeds for further growth. However, for gold, these 12 atoms cluster first grows into the magic number 13 atoms cluster and then 147 atom clusters which further grows into gold nanoparticles. For platinum, the 12 atoms cluster grows into the magic number 55 atom cluster which further grows into platinum nanoparticles. The first two stages of the growth of Au and Pt nanoparticles as obtained by in situ XAS measurements are also corroborated by simultaneous in situ measurement of UV-Vis spectroscopy.

Harada et al., on the other hand, studied the growth of metal nanoparticles by photoreduction. The precursor solution in PVP is irradiated with a 500 W super-high-pressure mercury lamp. The growth of Au, Pt, Ag, Rh, and Pd nanoparticles are studied by in situ EXAFS. For Au nanoparticles [25], it has been found that the photochemical reduction results in the formation of Au^{2+} intermediates and Cl radicals. Formation mechanism comprising of three main steps has been proposed in the above paper: (1) The bond of Au-Cl rapidly dissociates due to the reduction from $AuCl_4^-$ to $AuCl_2^-$. (2) This is followed by reduction of $AuCl_2^-$ to Au^0 with the formation and growth of Au metal particles, the reduction from $AuCl_2^-$ to Au^0 being much slower than that from $AuCl_4^-$ to $AuCl_2^-$. (3) On the prolonged photoirradiation, $AuCl_2^-$ is completely consumed, and the growth process of Au metal particles is observed. From the Pt nanoparticles formation studies [23], it has been found that the formation in the photoreduction process is constituted of three elementary stages, reduction-nucleation, autocatalytic surface growth on nucleates, and Ostwald ripening based growth. The initial nucleation stage for the formation of Pt_4 nuclei is evidenced from the CN (around 3–4) of Pt − Pt bond pair, and the aggregative particle growth including the autocatalytic reduction of Pt ionic species on the surface of Pt_4 nuclei proceeds with irradiation time to produce particles with diameter of 1–2 nm (i.e., Pt_{13} or Pt_{55} nanoparticles expected from CN around 6–7). On the basis of either the solid-state reaction kinetics or the chemical mechanism-based kinetics, the aggregative particle growth exhibits a sigmoidal-like profile well described by the AE model or the two-step FW model. After the completion of aggregative growth in the later stage, the Ostwald ripening based growth becomes more pronounced, leading to the formation of larger Pt nanoparticles. The

comparison between Au and Pt nanoparticle formation leads to the fact that the dissociation of Cl from Au^{3+} proceeds more rapidly than that of Cl from Pt^{4+}. Also, the formation of Au nuclei is much faster than that of Pt nuclei, a result similar to that presented by Nayak et al. [27].

The growth of Ag nanoparticles synthesized by photoirradiation is also studied by in situ DEXAFS [24]. The study shows that the reduction rate of Ag^{+} ions could be quantitatively evaluated from the change of X-ray absorbance $\mu(E)$ assigned to the Ag–O contribution in the XANES region, whereas the temporal change of intermediate small Ag particles could be estimated by the Ag–Ag contribution. The rate constant of Ag^{+} reduction in the presence of photo-activator benzoin was found to be higher than that in the absence of benzoin. During the induction period, the first-order reaction of Ag^{+} ions occurred to produce Ag^{0} atoms, while the subsequent nucleation and growth process concurrently proceeded after the induction period. In the nucleation and growth process after the induction period, the intermediate small Ag particles (C.N. smaller than ca. 4) were generated and they were grown up to larger particles (C.N.s equal to 4.5 ± 1.5) in the longer photoreduction process.

Apart from the noble metal nanoparticles of Au, Pt, and Ag, reports are available in the literature on the growth of other metal nanoparticles also. For example, formation mechanism of Rh and Pd nanoparticles by photoreduction was studied by Harada and Inada using QEXAFS [7]. The reduction rate of Rh^{3+} and Pd^{2+} aqua chlorocomplexes were quantitatively evaluated from the change of X-ray absorbance $\mu(E)$ assigned to the contribution of metal-chloride bonds in these aqua chlorocomplexes in the XANES region, while the temporal change of intermediate small metal particles could be estimated by the metal-metal contribution in the EXAFS region. The reduction rate of Rh^{3+} aqua chlorocomplexes in PVP solutions was found to be slower than that of Pd^{2+}. This is probably because Rh^{3+} chlorocomplexes were more stable than Pd^{2+} chlorocomplexes at higher concentration of chlorine ions in the aqueous solutions. In addition, the reduction process of Rh^{3+} chlorocomplexes possessed an induction period before the onset of nucleation and growth of Rh particles, although Pd^{2+} chlorocomplexes displayed no induction period, since the reduction of Pd^{2+} complexes occurred immediately after the mixing of an ethanol solution of Pd^{2+} complexes with aqueous PVP solutions.

6.2 Growth of Metal Oxide Nanoparticles

Growth of TiO_2 nanoparticles has been studied by simultaneous QEXAFS and UV-Vis measurements using the setup shown in Fig. 6.9b [56]. TiO_2 nanoparticles have been synthesized by hydrolytic sol-gel route using titanium tetraisopropoxide (TTIP) as precursor. UV-Vis spectra were measured using an immersion probe in direct contact with the reactive solution with an optical path of 1 mm. LCF of the XANES spectra has been done using the spectra of expected components. Formation of TiO_2 nanoparticles from the reaction of TTIP with water involves the following

stepped temporal evolution: (i) At a very early stage, a polynuclear titanium species is produced from the polycondensation reaction of the hydrolyzed alkoxide precursor. This step is completed within the first few minutes, producing the oligomeric species identified as a dodecatitanate species with a $Ti_{11}O_{13}$ or $Ti_{12}O_{16}$ molecular framework. (ii) An intermediate stage is achieved when the total hydrolysis ratio is ranged between 1.00 and 1.35. This stage is characterized by the concomitant formation of dodecatitanate oligomeric species and titania nanoparticles. (iii) At the subsequent stage, oligomeric species are very slowly consumed in a polycondensation/aggregation process of growth of TiO_2 nanoparticles. The rate of this process is approximately proportional to the instantaneous amount of water addition and increases with higher temperatures. A pseudo first-order kinetic of formation of TiO_2 from dedecatitanate species is verified. (iv) At the advanced stage, a fast change of the scattering light properties of the system occurs, which is related to the sudden aggregation of freshly formed TiO_2 nanoparticles. With the combined techniques of UV-Vis spectroscopy and QEXAFS, it could be shown that the average particle size, determined via Mie scattering theory, is linked to the fraction of TiO_2 in the solution during the aggregation processes.

In situ X-ray absorption and diffraction studies were performed by Kränzlin et al. [64] to directly monitor the crystallization of different titania polymorphs in one and the same solution. The collected data revealed insights into a complex crystallization mechanism of titanium oxide in a macroscopically simple system. The time-dependent changes in the chemical environment directly trigger the activation energies (E_a) involved in the nucleation of either rutile or anatase TiO_2. Further, the results show that the thermodynamic equilibration does not determine the nucleation and growth of the TiO_2 crystals, as the rutile phase forms first, and, in the beginning, also with smaller sizes than anatase phase. Therefore, the crossover size d_{crit} of the size-induced phase transformation indeed is not an inherent material property of TiO_2 but strongly depends on environmental variables.

Growth of ZnO quantum dots was investigated by Caetano et al. [65] using in situ QXAFS/UV–Vis spectroscopy. UV–Vis data were recorded using a spectrometer fitted with an optic fiber coupler connected to an immersion probe in direct contact with the solution. QEXAFS spectra were recorded in transmission mode in every 10 s. LC fitting of the XAFS spectra were done to analyze the composition of the reaction solution at different times. From the results, it is evident that the kinetics of formation of colloidal ZnO nanoparticles is composed of two main periods: (i) the first one ($t < 40$ s) is characterized by a rapid decrease of the fraction Zn_4OAc_6 tetrameric precursor giving rise to an increasing quantity of ZnO in the medium and (ii) the period of time higher than 250 s corresponds to a quasi-steady-state chemical equilibrium zone, where only a few ZnO nuclei are formed and a considerable increase in quantum dot size and in the aggregation index is evidenced.

Hirsch et al. [66] explored the synthesis of MoO_2 nanoparticles doped with 2 at.% of Ni in a mixture of acetophenone and benzyl alcohol at 200 °C. In situ XANES measurements at Ni and Mo K edges were performed and the “doping” reaction, that is, incorporation of Ni in MoO_2, was discussed. The Mo K-edge spectra were

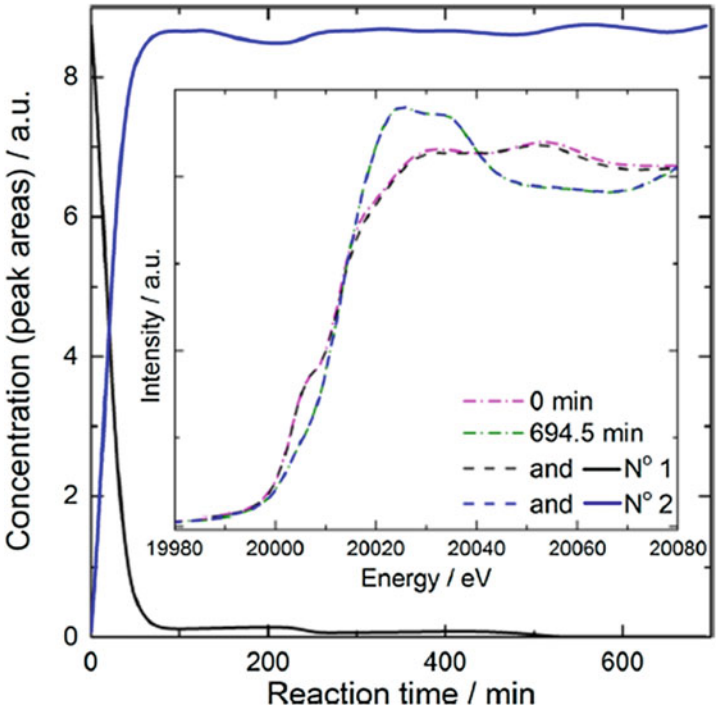

Fig. 6.16 Interdependence between two components recovered by MCR-ALS from XAS data recorded in situ at Mo K-edge. *Inset* shows XAS spectra taken at room temperature at the beginning (0 min, MoO_2Cl_2, *pink curve*) and at the end (694.5 min, MoO_2, *green curve*) of the reaction. Spectra of individual components recovered by MCR-ALS analysis (*black and blue curves*) are almost identical with MoO_2Cl_2 and MoO_2 (Taken from Hirsch et al. [66]. Reprinted with permission from American Chemical Society, Copyright 2014)

analyzed with MCR-ALS by fitting the XANES spectra with two components as shown in Fig. 6.16. Since two components are sufficient to fit the data it was concluded that Ni:MoO_2 directly nucleates in the final composition without formation of intermediates.

Staniuk et al. [60] studied the growth of cobalt oxide nanoparticles in an organic solvent. For in situ XAS/PXRD studies, the synthesis was performed in a specially designed cell that allows heating of the reaction solution as shown in Fig. 6.10. In situ X-ray absorption and diffraction measurements of the synthesis at 140 °C reveal that oxidation of Co^{2+} to $Co^{3+/2+}$ and reduction of Co^{2+} to Co^0 reactions take place simultaneously. It is followed by a rapid formation of Co_3O_4 nanoparticles and its consecutive solid-state reduction to CoO. In parallel, metallic Co nanoparticles also begin to grow. MCR-ALS analysis of X-ray absorption spectroscopy (XAS) data efficiently reveals the interdependence between four different reactions as shown in the schematics in Fig. 6.17.

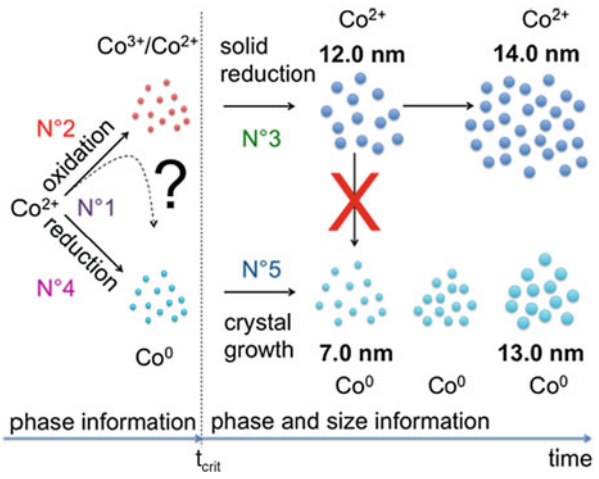

Fig. 6.17 Reactions mechanism behind the synthesis of Co-based nanoparticles, as revealed by in situ XAS studies (Taken from Staniuk et al. [60]. Reprinted with permission from American Chemical Society, Copyright 2014)

7 Conclusions and Future Perspective

This chapter provides an overview of the implementation of X-ray absorption spectroscopy technique for time resolved in situ studies on growth of nanoparticles. The two experimental arrangements generally used for time resolved XAS, namely, QXAFS and DXAFS, have been discussed elaborately with their respective advantages and disadvantages. DXAFS is faster technique, however has poor spatial resolution and has more noise in data compared to QXAFS. Various data analysis techniques like LCF, PCA, MCR-ALS, etc., which help in the identification of intermediate species, have also been reviewed in detail in this chapter.

Few examples are also mentioned to show the implementation of the experimental and analytical tools of TR-XAS and how they were used successfully to predict the mechanism of formation of nanoparticles. The examples were focused on the growth of metal nanoparticles mainly Au, Pt, Ag, Rh, and Pd and metal oxide nanoparticles like TiO_2, ZnO, Ni doped MoO_2, and CoO by different synthesis routes like chemical reduction route, photo irradiation, etc. XAS being a local probe with no constraint on sample environment was successfully used to probe the intial stages of nucleation and growth. It gives information regarding bond breaking of the precursor and formation of the nuclei, which act as seed for further growth. Different stages in which the reaction proceeds could easily be identified. With the aid of different analytical tools, the intermediates formed during the reaction and their effects on the reaction kinetics can easily be predicted. Very often, in situ XAS results were complemented with other measurement results also to get more consolidated picture of the process.

Through the examples, the trend to study different synthesis processes with high temporal resolution with the aid of TR-XAS in combination with other adjunct techniques can be appreciated. The availability of high brilliance synchrotron

sources across the world has facilitated these measurements. Special reaction cells were also designed to implement two or three simultaneous measurements by different techniques. This has opened up a new aspect of multidimensional spectroscopy, which results in more informative picture of the processes to be studied. In future, with the free electron lasers that has brilliance several orders higher than that of the present synchrotron sources, in situ TR-XAS can be improved to femto second time resolution, which will allow us to see systems and processes from an entirely new perspective. In the field of multidimentional in situ spectroscopy, lots of advances were also expected where we can probe a system or process under different experimental conditions, simultaneously with many different techniques.

References

1. Schmid G (ed) (2004) Nanoparticles: from theory to application. Wiley-VCH, Weinheim
2. Kohler M, Fritzsche W (2004) Nanotechnology: an introduction to nanostructuring techniques. Wiley-VCH, Weinheim
3. de Mello Donegá C (ed) (2014) Nanoparticles: workhorses of nanoscience. Springer, Berlin/Heidelberg
4. Koziej D (2016) Revealing complexity of nanoparticle synthesis in solution by in-situ hard X-ray spectroscopy-today and beyond. Chem Mater 28:2478–2490
5. Frahm R, Barbee TW Jr, Warburton W (1991) In situ structural study of thin-film growth by quick-scanning x-ray-absorption spectroscopy. Phys Rev B 44:2822–2825
6. Newton MA, Dent AJ, Evans J (2002) Bringing time resolution to EXAFS: recent developments and application to chemical systems. Chem Soc Rev 31:83–95
7. Harada M, Inada Y (2009) In situ time-resolved XAFS studies of metal particle formation by photoreduction in polymer solutions. Langmuir 25:6049–6061
8. Makimura Y, Sasaki T, Oka H, Okuda C, Nonaka T, Nishimura YF, Kawauchi S, Takeuchi Y (2016) Studying the charging process of a lithium-ion battery toward 10 V by in situ X-ray absorption and diffraction: lithium insertion/extraction with side reactions at positive and negative electrodes. J Electrochem Soc 163:A1450–A1456
9. Mizutania T, Ogawa S, Murai T, Nameki H, Yoshida T, Yagi S (2015) In situ UV–vis investigation of growth of gold nanoparticles prepared by solution plasma sputtering in NaCl solution. Appl Surf Sci 354:397–400
10. Amendola V, Meneghetti M (2009) Size evaluation of gold nanoparticles by UV-vis spectroscopy. J Phys Chem C 113:4277–4285
11. Zheng H, Smith RK, Jun YW, Kisielowski C, Dahmen U, Alivisatos AP (2009) Observation of single colloidal platinum nanocrystal growth trajectories. Science 324:1309–1312
12. Simonsen SB, Chorkendorff I, Dahl S, Skoglundh M, Sehested J, Helveg SJ (2010) Direct observations of oxygen-induced platinum nanoparticle ripening studied by in situ TEM. J Am Chem Soc 132:7968–7975
13. Jason W, Helveg S, Ullmann S, Peng Z, Bell AT (2016) Growth of encapsulating carbon on supported Pt nanoparticles studied by in situ TEM. J Catal 338:295–304
14. Hsieh T-H, Chen J-Y, Huang C-W, Wu W-W (2016) Observing growth of nanostructured ZnO in liquid. Chem Mater 28:4507–4511
15. DeYoreo JJ (2016) In-situ liquid phase TEM observations of nucleation and growth processes. Prog Cryst Growth Charact Mater 62:69–88
16. Tay SER, Goode AE, Nelson Weker J, Cruickshank AA, Heutz S, Porter AE, Ryan MP, Toney MF (2016) Direct in situ observation of ZnO nucleation and growth via transmission X-ray microscopy. Nanoscale 8:1849–1853

17. Abecassis B, Testard F, Spalla O, Barboux P (2007) Probing in situ the nucleation and growth of gold nanoparticles by small-angle X-ray scattering. Nano Lett 7:1723–1727
18. Caetano BL, Santilli CV, Meneau F, Briois V, Pulcinelli SH (2011) In situ and simultaneous Uv-vis/SAXS and Uv-vis/XAFS time-resolved monitoring of ZnO quantum dots formation and growth. J Phys Chem C 115:4404–4412
19. Polte J, Ahner TT, Delissen F, Sokolov S, Emmerling F, Thünemann AF, Kraehnert R (2010) Mechanism of gold nanoparticle formation in the classical citrate synthesis method derived from coupled in situ XANES and SAXS evaluation. J Am Chem Soc 132:1296–1301
20. Lin CS, Khan MR, Lin SD (2006) The preparation of Pt nanoparticles by methanol and citrate. J Colloid Interface Sci 299:678–685
21. Ohyama J, Teramura K, Higuchi Y, Shishido T, Hitomi Y, Kato K, Tanida H, Uruga T, Tanaka T (2011) In situ observation of nucleation and growth process of gold nanoparticles by quick XAFS spectroscopy. ChemPhysChem 12:127–131
22. Ma J, Zou Y, Jiang Z, Huang W, Li J, Wu G, Huang Y, Xu H (2013) An in situ XAFS study – the formation mechanism of gold nanoparticles from X-ray-irradiated ionic liquid. Phys Chem Chem Phys 15:11904–11908
23. Harada M, Kamigaito Y (2012) Nucleation and aggregative growth process of platinum nanoparticles studied by in situ quick XAFS spectroscopy. Langmuir 28:2415–2428
24. Harada M, Inada Y, Nomura M (2009) In situ time-resolved XAFS analysis of silver particle formation by photoreduction in polymer solutions. J Colloid Interface Sci 337:427–438
25. Harada M, Einaga H (2007) In situ XAFS studies of Au particle formation by photoreduction in polymer solutions. Langmuir 23:6536–6543
26. Boita J, Nicolao L, Alves MCM, Morais J (2014) Observing Pt nanoparticle formation at the atomic level during polyol synthesis. Phys Chem Chem Phys 16:17640–17647
27. Nayak C, Bhattacharyya D, Jha SN, Sahoo NK (2016) Growth of block copolymer stabilized metal nanoparticles probed simultaneously by in situ XAS and UV–Vis spectroscopy. J Synchrotron Radiat 23:293–303
28. Shannon IJ, Maschmeyer T, Sankar G, Thomas JM, Oldroyd RD, Sheehy M, Madill D, Waller AM, Townsend RP (1997) A new cell for the collection of combined EXAFS/XRD data in situ during solid/liquid catalytic reactions. Catal Lett 44:23–27
29. Tromp M, Sietsma JRA, van Bokhoven JA, van Strijdonck GPF, van Haaren RJ, van der Eerden AMJ, van Leeuwen PWNM, Koningsberger DC (2003) Deactivation processes of homogeneous Pd catalysts using in situ time resolved spectroscopic techniques. Chem Commun 1:128–129
30. Briois V, Lützenkirchen-Hecht D, Villain F, Fonda E, Belin S, Griesebock B, Frahm R (2005) Time-resolved study of the oxidation of ethanol by cerium(IV) using combined quick-XANES, UV−Vis, and Raman spectroscopies. J Phys Chem A 109:320–329
31. Newton MA, Jyoti B, Dent AJ, Fiddy SG, Evans J (2004) Synchronous, time resolved, diffuse reflectance FT-IR, energy dispersive EXAFS (EDE) and mass spectrometric investigation of the behaviour of Rh catalysts during NO reduction by CO. Chem Commun 21:2382–2383
32. Sayers DE, Stern EA, Lytle FW (1971) New technique for investigating noncrystalline structures: Fourier analysis of the extended x-ray absorption fine structure. Phys Rev Lett 27:1204–1207
33. Stern EA (1974) Theory of the extended x-ray-absorption fine structure. Phys Rev B 10:3027–3037
34. Konigsberger DC, Prins R (1988) X ray absorption: principles, applications, techniques of EXAFS, SEXAFS and XANES. Wiley, New York
35. Bunker G (2010) Introduction to XAFS: a practical guide to X ray absorption fine structure spectroscopy. Cambridge University Press, Cambridge
36. Newville M (2001) IFEFFIT: interactive XAFS analysis and FEFF fitting. J Synchrotron Radiat 8:322–324
37. George GN, Pickering IJ (2000) EXAFSPAK: a suite of computer programs for analysis of X ray absorption spectra. Stanford Synchrotron Radiation Laboratory, Stanford. EXAFSPAK Manual

38. Filipponi A, Di Cicco A (1995) X-ray-absorption spectroscopy and n-body distribution functions in condensed matter. II. Data analysis and applications. Phys Rev B 52:15135–15149
39. Stern EA, Newville M, Ravel B, Yacoby Y, Haskel D (1995) The UWXAFS analysis package: philosophy and details. Physica B 208–209:117–120
40. Kelly SD, Hesterberg D, Ravel B (2008) Analysis of soils and minerals using X-ray absorption spectroscopy. In Ulery AL, Drees R (eds) Methods of soil analysis – part 5. Mineralogical methods. Soil Science Society America, Madison, pp 387–464. ISBN 13: 978-0891188469
41. Frahm R (1988) Quick scanning exafs: first experiments. Nucl Inst Methods Phys Res A 270:578–581
42. Frahm R, Richwin M, Lützenkirchen-Hecht D (2005) Recent advances and new applications of time-resolved X-ray absorption spectroscopy. Phys Scr T115:974–976
43. Fonda E, Rochet A, Ribbens M, Barthe L, Belina S, Briois V (2012) The SAMBA quick-EXAFS monochromator: XAS with edge jumping. J Synchrotron Radiat 19:417–424
44. Müller O, Nachtegaal M, Just J, Lützenkirchen-Hecht D, Frahm R (2016) Quick-EXAFS setup at the SuperXAS beamline for in situ X-ray absorption spectroscopy with 10 ms time resolution. J Synchrotron Radiat 23:260–266
45. Prestipino C, Mathon O, Hino R, Beteva A, Pascarelli S (2011) Quick-EXAFS implementation on the general purpose EXAFS beamline at ESRF. J Synchrotron Radiat 18:176–182
46. Briois V, La Fontaine C, Belin S, Barthe L, Moreno T, Pinty V, Carcy A, Girardot R, Fonda E (2016) ROCK: the new quick-EXAFS beamline at SOLEIL. J Phys Conf Ser 712:012149
47. Lee PL, Beno MA, Jennings G, Ramanathan M, Knapp GS, Huang K, Bai J, Montano PA (1994) An energy dispersive x-ray absorption spectroscopy beamline, X6A, at NSLS. Rev Sci Instrum 65:1–6
48. Bhattacharyya D, Poswal AK, Jha SN, Sabharwal SC (2009) First results from a dispersive EXAFS beamline developed at INDUS-2 synchrotron source at RRCAT, Indore, India. Nucl Inst Methods Phys Res A 609:286–293
49. Wang X, Hanson JC, Frenkel AI, Kim J-Y, Rodriguez J'A (2004) Time-resolved studies for the mechanism of reduction of copper oxides with carbon monoxide: complex behavior of lattice oxygen and the formation of suboxides. J Phys Chem B 108:13667–13673
50. Ravel B, Newville M (2005) ATHENA, ARTEMIS, HEPHAESTUS: data analysis for X-ray absorption spectroscopy using IFEFFIT. J Synchrotron Radiat 12:537–541
51. Wasserman SR, Allen PG, Shuh DK, Bucher JJ, Edelstein NM (1999) EXAFS and principal component analysis: a new shell game. J Synchrotron Radiat 6:284–286
52. Frenkel AI, Kleifeld O, Wasserman SR, Sagi I (2002) Phase speciation by extended x-ray absorption fine structure spectroscopy. J Chem Phys 116:9449–9455
53. Wang Q, Hanson JC, Frenkel AI (2008) Solving the structure of reaction intermediates by time-resolved synchrotron x-ray absorption spectroscopy. J Chem Phys 129:234502-1–234502-7
54. Cassinelli WH, Martins L, Passos AR, Pulcinelli SH, Santilli CV, Rochet A, Briois V (2014) Multivariate curve resolution analysis applied to time-resolved synchrotron X-ray absorption spectroscopy monitoring of the activation of copper alumina catalyst. Catal Today 229:114–122
55. Voronov A, Urakawa A, van Beek W, Tsakoumis NE, Emerich H, Rønning M (2014) Multivariate curve resolution applied to in situ X-ray absorption spectroscopy data: an efficient tool for data processing and analysis. Anal Chim Acta 840:20–27
56. Stötzel J, Lutzenkirchen-Hecht D, Frahm R, Santilli CV, Pulcinelli SH, Kaminski R, Fonda E, Villain F, Briois V (2010) QEXAFS and UV/Vis simultaneous monitoring of the TiO_2-nanoparticles formation by hydrolytic sol-gel route. J Phys Chem C 114:6228–6236
57. Meneau F, Sankar G, Morgante N, Cristol S, Catlow CRA, Thomas JM, Greaves GN (2003) Characterization of zinc oxide nanoparticles encapsulated into zeolite-Y: an in-situ combined X-ray diffraction, XAFS, and SAXS study. Nucl Inst Methods Phys Res B 199:499–503
58. Couves JW, Thomas JM, Waller D, Jones RH, Dent AJ, Derbyshire GE, Greaves GN (1991) Tracing the conversion of aurichalcite to a copper catalyst by combined X ray absorption and diffraction. Nature 354:465–468

59. Boita J, Alves M d CM, Morais J (2014) A reaction cell for time-resolved in situ XAS studies during wet chemical synthesis: the $Cu_2(OH)_3Cl$ case. J Synchrotron Radiat 21:254–258
60. Staniuk M, Hirsch O, Kranzlin N, Bohlen R, van Beek W, Abdala PM, Koziej D (2014) Puzzling mechanism behind a simple synthesis of cobalt and cobalt oxide nanoparticles: in situ synchrotron X-ray absorption and diffraction studies. Chem Mater 26:2086–2094
61. Bauer M, Heusel G, Mangold S, Bertagnolli H (2010) Spectroscopic set-up for simultaneous UV-Vis/(Q)EXAFS in situ and in operando studies of homogeneous reactions under laboratory conditions. J Synchrotron Radiat 17:273–279
62. Brust M, Walker M, Bethell D, Schiffrin DJ, Whyman R (1994) Synthesis of thiol-derivatised gold nanoparticles in a two-phase liquid–liquid system. J Chem Soc Chem Commun:801–802
63. Yao T, Sun Z, Li Y, Pan Z, He W, Yi X, Nomura M, Niwa Y, Yan W, Ziyu W, Jiang Y, Liu Q, Wei S (2010) Insights into initial kinetic nucleation of gold nanocrystals. J Am Chem Soc 132:7696–7701
64. Kränzlin N, Staniuk M, Heiligtag FJ, Luo L, Emerich H, van Beek W, Niederberger M, Koziej D (2014) Rationale for the crystallization of titania polymorphs in solution. Nanoscale 6:14716–14723
65. Caetano BL, Santilli CV, Pulcinelli SH, Briois V (2011) SAXS and UV–Vis combined to quick-XAFS monitoring of ZnO nanoparticles formation and growth. Phase Transit 84:714–725
66. Hirsch O, Zeng G, Luo L, Staniuk M, Abdala PM, van Beek W, Rechberger F, Suess MJ, Niederberger M, Koziej D (2014) Aliovalent Ni in MoO_2 lattice – probing the structure and valence of Ni and its implication on the electrochemical performance. Chem Mater 26:4505–4513

In Situ Characterization Tools for Bi_2Te_3 Topological Insulator Nanomaterials

7

P. Ngabonziza, M. P. Stehno, G. Koster, and A. Brinkman

Contents

1 Definition of the Topic

In situ characterization of topological insulator nanomaterials using several, complementary surface analysis techniques enables to investigate topological surface states without exposing the samples to ambient conditions. Adsorbants from exposure to air and other ex situ contaminations result in notable changes in the bulk and

P. Ngabonziza (✉)
Faculty of Science and Technology and MESA+, Institute for Nanotechnology, University of Twente, Enschede, The Netherlands

Department of Physics, University of Johannesburg, Johannesburg, South Africa
e-mail: p.ngabonziza@fkf.mpg.de

M. P. Stehno · G. Koster · A. Brinkman
Faculty of Science and Technology and MESA+, Institute for Nanotechnology, University of Twente, Enschede, The Netherlands

© Springer-Verlag GmbH Germany, part of Springer Nature 2018

C. S. S. R. Kumar (ed.), *In-situ Characterization Techniques for Nanomaterials*,
https://doi.org/10.1007/978-3-662-56322-9_7

surface state properties of topological insulators. In this chapter, we describe recent developments in the in situ characterization of topological insulator nanomaterials. Extensive studies on individual samples are made possible by connecting the deposition chamber to a large number of surface analysis tools and by using a vacuum suitcase technology which allows sample transfer in ultra-high vacuum conditions between vacuum systems worldwide.

2 Overview

Topological insulators (TIs) are novel class of materials that feature unique topological properties in their band structure, which allow them to behave as insulators in the bulk while their boundaries are conducting. One of the current challenges in the field of TIs, in particular for three-dimensional TIs, is to prepare high-quality, bulk-insulating samples with a low number of intrinsic defects. Molecular beam epitaxy (MBE) is an established technique for preparing high-quality TI samples with few intrinsic defects and high surface mobilities. However, the surface states of the MBE grown thin films suffer from degradation and unintentional doping once the samples are exposed to air or other contaminations, thus obscuring the topological properties of the material. To study the topological surface states, it is desirable to carry out the entire sample characterization procedure in situ. In practice, this means that the TI thin film is kept in ultra-high vacuum (UHV) conditions for the duration of the study. Analysis tools must be attached to the deposition chamber or a portable UHV chamber must be used for transport to different locations.

Here, we present recent advances in the in situ characterization of MBE grown TI nanomaterials. After a brief introduction to the material bismuth-telluride (Bi_2Te_3) and the MBE technique, we present a detailed study of the surface properties of Bi_2Te_3 thin films using complementary in situ characterization techniques: reflection high energy electron diffraction (RHEED), X-ray photoemission spectroscopy (XPS), angle resolved photoemission spectroscopy (ARPES), scanning tunneling microscope (STM), and the scanning tunneling spectroscopy (STS) are used to characterize the surface morphology, structure, stoichiometry, and the electronic band structure of the material. We conclude that MBE grown Bi_2Te_3 thin films are high-quality, bulk-insulating TIs.

3 Introduction

Three-dimensional (3D) TIs are materials that are characterized by a band gap in the electronic band structure while their surfaces host nongapped spin-momentum locked states [1, 2]. The topological surface states (TSS) arise due to strong spin-orbit interactions, which lead to a band inversion in the bulk of the material. Breaking of the translational symmetry at the surface forces the band gap to close.

The resulting TSS features a linear, Dirac-type dispersion with a helical spin structure [3]. Shortly after the theoretical prediction of topological insulators [1], the alloy Bi_xSb_{1-x} was confirmed experimentally to be a 3D TI [4]. However, the Dirac surface band of this material coexists with other electron and hole pockets [4, 5], which makes it unsuitable for detailed studies of the topological surface state. Soon afterwards, the materials Sb_2Te_3, Bi_2Te_3, and Bi_2Se_3 were predicted and experimentally confirmed to be 3D TIs. These compounds have a bulk band gap of several 100 meV with surface states that form a single Dirac cone [2, 6–9], which makes them candidate materials for future research of exotic topological states, such as Majorana fermions and magnetic monopoles [10, 11]. Since then, many more materials have been added to the list of 3D TIs [12].

Modern in situ characterization tools play an essential role in the experimental verification of TI properties. To this day, ARPES and spin-resolved ARPES are the only experimental methods that provide direct evidence for band inversion and the presence of topological surface states in a material [5, 8]. Other in situ surface characterization methods, such as XPS and RHEED, prove invaluable for the optimization of thin film deposition techniques, an important step towards the integration of TI materials in electronic devices. We show the importance of characterizing individual films by a large number of complimentary in situ tools when optimizing growth conditions. The analysis is made possible by attaching the growth chamber to several analysis tools and accessing others by transporting the sample in a portable UHV chamber, a vacuum suitcase. Applying this technology to the second generation TI compound Bi_2Te_3, we demonstrate a new route to achieving intrinsic conduction through topological surface states of Bi_2Te_3 topological insulator thin films.

The material Bi_2Te_3 has a rhombohedral crystal structure. It consists of quintuple layers (QLs) of bismuth and tellurium atoms with a stacking sequence: Te[1]-Bi-Te [2]-Bi-Te [1]. Weak Van der Waals forces bind the individual QLs together, which gives easy access to the (111) surface by cleaving [2]. To detect topological surface states and subsequently employ their properties in electronics devices, the Fermi level must be placed in the bulk band gap. Great care must be taken to minimize the amount of charged defects in the crystal and to avoid surface contamination that causes band bending, which can be strong enough to populate states in the bulk valence or conduction bands. One approach to overcome this bulk conduction issue is to prepare high quality thin films that are bulk insulating.

Molecular beam epitaxy (MBE) is an established method for growing high-quality crystalline thin films of TIs with surface-dominated conduction [13–15]. Using this technique, progress has been made recently in synthesizing a new generation of high-quality, bulk-insulating Bi_2Te_3 thin films [16, 17]. Unfortunately, when the as-grown, pristine films are exposed to air, a moderate increase in the doping level of the Bi_2Te_3 films has been observed which is due to ex situ contaminations. The conductivity of the film is no longer determined by the surface states alone [16–18]. Thus, we need to prepare the thin films and carry out all subsequent characterization steps under UHV conditions.

4 Experimental Methodology

4.1 Combined System for In Situ Thin Film Deposition and Characterization

MBE has been extensively employed for the growth of TI nanomaterials, and bulk insulating TI thin films have been reported [16, 19–22]. The growth conditions can be controlled precisely, which results in TI thin films with low defect density and surface-dominated conduction [13–15]. In addition, MBE makes it easy to combine different TI compounds to form, e.g., p-n junctions [23, 24], or TIs with other materials such as TI-ferromagnetic insulator heterostructures [25]. The high flexibility in combining different elements, the good control over the film thickness, the possibility of in situ capping right after growth to avoid extrinsic defects in subsequent device fabrication steps, and the possibility of uniform deposition over a large area make MBE the most versatile method for the synthesis of functional TI nanomaterials.

In this chapter, we confine our discussion to MBE grown high-purity Bi_2Te_3 TI thin films and their subsequent in situ analysis. We describe how surface characterization tools can be used to optimize the process of TI thin film growth and to prove the existence of topological surface states in the samples. The large number of complementary methods, we want to employ, requires an extension of the concept of in situ analysis: We use a modern multicluster vacuum system architecture with multiple deposition and analysis chambers for in situ synthesis and surface characterization of thin film samples. Additionally, the system can be interfaced with a *vacuum suitcase*, a technology for long distance transport in UHV. The multicluster tool at University of Twente is shown in Fig. 7.1. It comprises of UHV chambers for MBE and pulsed-laser deposition (PLD) of thin films and various surface characterization tools: reflection high energy electron diffraction (RHEED), X-ray photoelectron spectroscopy (XPS), and low-temperature scanning four-probe microscope (SPM). The individual UHV growth and analysis chambers are connected via a distribution chamber (DC). The distribution chamber is also used to store various thin film samples in vacuo. This flexible setup allows to prepare, store, and characterize thin film samples without breaking vacuum over an extended period of time. Many more analysis tools can be accessed by vacuum transferring the samples to other facilities at the University of Twente and other collaborating institutions in the Netherlands and worldwide. The vacuum suitcase technology, we use for long distance transport, is described in the next section.

4.2 Vacuum Suitcase

ARPES and low-temperature STM play an important role in identifying topological surface states in the electronic dispersion of TI materials [16]. These analyses were carried out by collaborators in specialized facilities. To transport thin films to the STM and ARPES systems, we used a UHV vacuum suitcase.

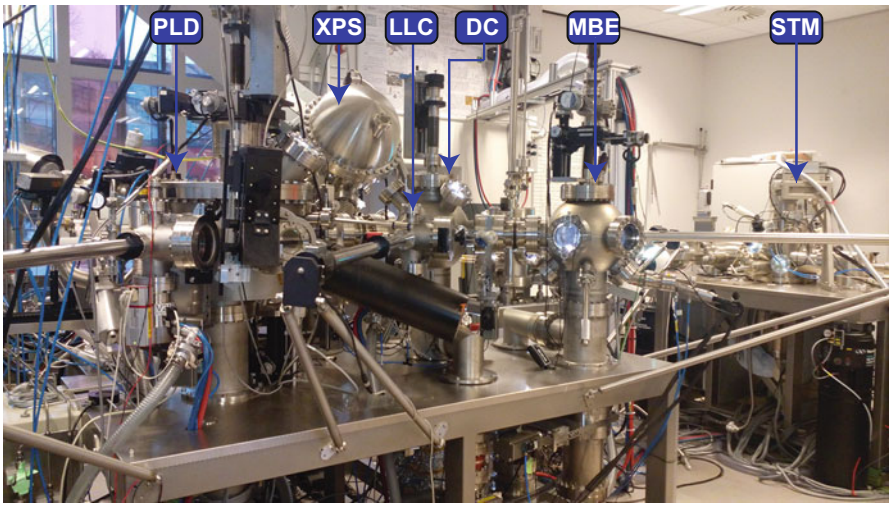

Fig. 7.1 The COMAT system. Photograph of the combined vacuum system where different vacuum chambers are indicated. The base pressure of each system is: MBE ($<5 \times 10^{-10}$ mbar), PLD (5×10^{-8} mbar), XPS ($<5 \times 10^{-11}$ mbar), STM ($<1.2 \times 10^{-11}$ mbar) and the DC (5×10^{-10} mbar). A RHEED electron gun and RHEED camera are connected to the PLD chamber for thin film surface analysis during and after growth

In the multicluster system (see Fig. 7.1), samples are transferred to the UHV suitcase via the DC chamber using a magnetic transfer stick together with a vertical transfer arm as shown in Fig. 7.2a. Figure 7.2b displays the vacuum case layout, consisting of a 6-ways cross with pumps installed onto one single flange. This vacuum suitcase is a compact system with the capability to keep UHV conditions for weeks with no power during transportation [26]. The combination of a non-evaporable getter (NEG) pump[1] with an ion pump allows to pump the entire spectrum of gases [27]. Hydrogen is pumped very efficiently by the NEG element (100 l/s pumping speed for H_2 and H_2O), as well as all other chemically active gases. Argon and methane are not pumped well by the NEG pump; therefore, it must be backed up by an ion pump element [28]. This dual pumping capability helps in keeping the pressure lower than 2×10^{-10} mbar throughout sample transfer and transportation. Inside the suitcase, samples are stored on a carousel which can hold up to 10 samples (see Fig. 7.2c). A detailed description of the vacuum suitcase technology and a review of the working principle of compact nonevaporable getter pumps and small ion pumps are given in references [27–30].

[1]The pumping principle is based on sorbing chemically active gases with the NEG material. The getter material contained in the pump cartridge does not need to be evaporated, it only needs to be reactivated, under dynamic vacuum, to diffuse the passivation layer covering the surface of getter particle in the bulk of the material.

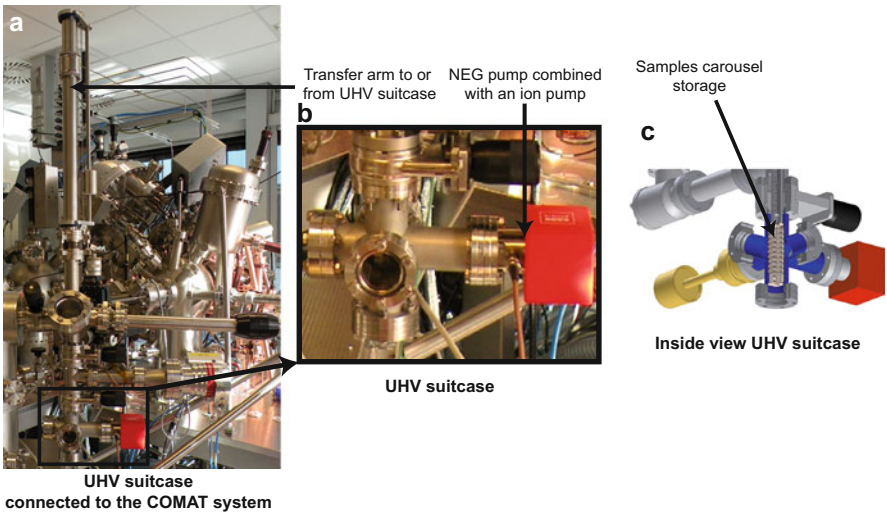

Fig. 7.2 Transport of samples under in situ conditions. (**a**) The UHV suitcase connected to the multi-cluster tool. (**b**) Picture of the vacuum suitcase. (**c**) Schematic illustration of the inside view of the UHV suitcase

5 Key Research Findings

5.1 In Situ Reflection High Energy Electron Diffraction

5.1.1 Basic Principles of RHEED

In situ reflection high-energy electron diffraction (RHEED) is frequently used to study the growth mechanism and the surface structure of thin films [31–33]. The RHEED technique is exceptionally sensitive to variations in surface roughness and morphology during thin film growth, which makes it an ideal tool for monitoring layer-by-layer growth in molecular-beam epitaxy. The standard RHEED method requires UHV conditions, which are met easily in MBE systems. RHEED can also be performed in low vacuum (e.g., during pulsed-laser deposition); however, the contrast is limited by electron scattering with the background gas.

Figure 7.3 depicts a schematic illustration of the working principle of a typical RHEED system. For RHEED measurements, a beam of high-energy electrons (10–50 keV) is directed on the surface of the sample at a grazing angle of a few degrees ($0.1 - 5^{\circ}$). Due to the low grazing angle of incidence, the high-energy electrons interact with only few atomic layers, close to the sample surface [32, 33]. A photo-luminescent screen in combination with a CCD camera is used to measure the intensity of reflected electrons. The specular spot is the mirror-like reflection of the electrons from the sample surface. The surface crystal structure can be determined from the position of the diffraction spots, which form circular patterns on the screen. The radii of the circles depend on the crystal plane spacing. The scattering wave

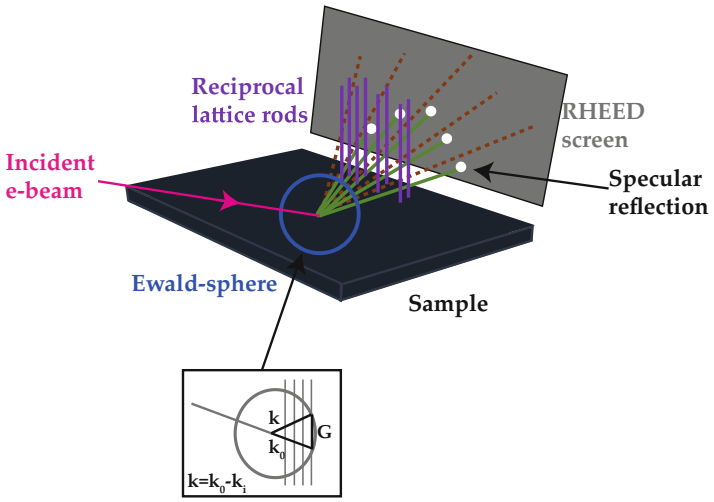

Fig. 7.3 A schematic illustration of the working principle of a RHEED system. When there is intersection of the reciprocal rods with the Ewald sphere and the diffraction conditions are met, specular RHEED spots are observed on the phosphor screen

vectors $\vec{k}$ obey the reciprocal space relation $\vec{k} = \vec{k}_0 - \vec{k}_i$ where $\vec{k}_0$ is the wave vector of the incident beam ($\left|\vec{k}_0\right| = 2\pi/\lambda$) and $\vec{k}_i$ is a lattice vector that connects two intersection points of the Ewald sphere with the lattice places. The radius of the Ewald sphere is determined by the wave length λ of the incident electrons (see Fig. 7.3).

RHEED is an essential tool for studying the growth dynamics of layer-by-layer deposited films. By monitoring the intensity variations of various features in the RHEED pattern, surface roughness and changes in the crystalline structure can be tracked in real time [34]. The progress in film growth can be controlled by measuring the intensity of the specular reflection. It is largest for an atomically flat surface. As soon as material is deposited, the surface roughness increases causing the intensity to drop. In layer-by-layer growth mode, the gaps in the monolayer coverage fill as more material arrives on the surface, which reduces the surface roughness and increases the reflectivity again. Upon completion of a full crystal layer, the intensity becomes a maximum again. By counting the maxima, the film thickness can be determined with monolayer precision [32]. Below, we discuss RHEED data on Bi_2Te_3 thin films.

5.1.2 In Situ RHEED Measurements of Bi_2Te_3 Topological Insulator Nanomaterials

RHEED has been used extensively to monitor the growth dynamics of Bi_2Te_3 thin films [15, 19, 35, 37–39] and other TI materials in general [40–43]. Liang He et al. employed in situ RHEED to investigate the layer-by-layer growth mode of Bi_2Te_3 thin films [15]. Figure 7.4a (left) depicts an in situ RHEED image of an as-grown Bi_2Te_3 thin film. The sharp, streaky RHEED pattern indicates that the film has an

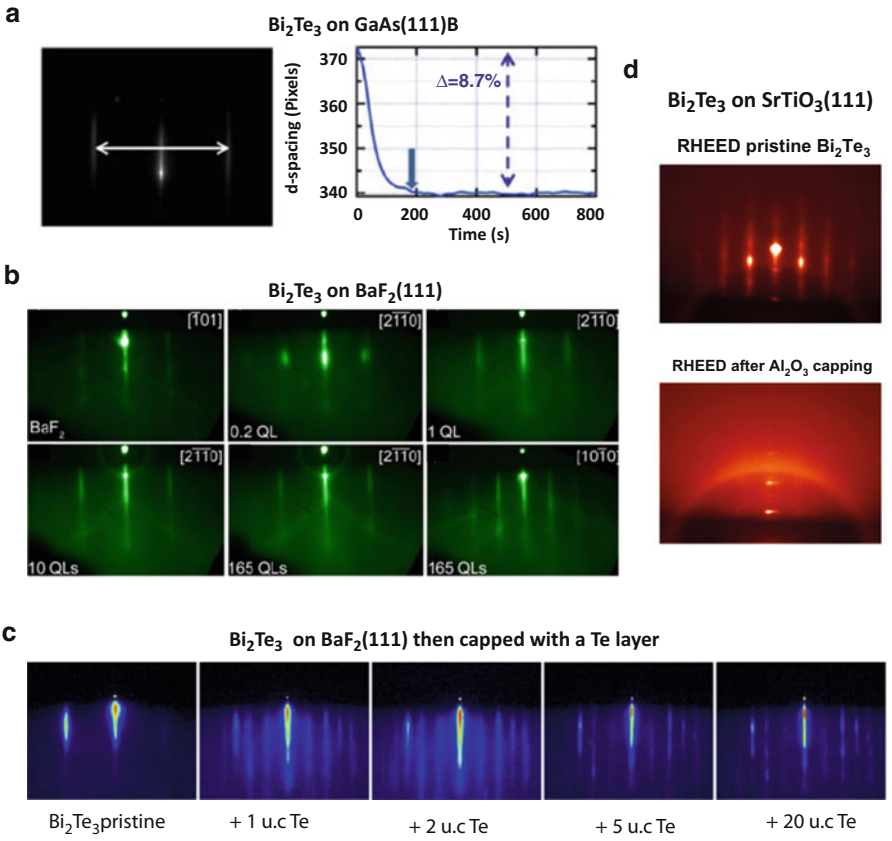

Fig. 7.4 RHEED pattern of a Bi_2Te_3 thin film grown on different substrates. (**a**) A typical RHEED image of an as-grown Bi_2Te_3 film on GaAs[111]B. The left graph shows the evolution of the d-spacing as a function of growth time. The solid blue arrows indicate the growth time of the first quintuple layer (Figure from Ref. [15], copyright John Wiley and Sons). (**b**) RHEED patterns acquired at different growth stages of Bi_2Te_3 grown on BaF_2 [111] substrate: just before the growth starts and for increasing Bi_2Te_3 film coverage after 0.2 QL, 1 QL, 10 QLs and at the end of growth at 165 QLs (Figure reproduced from [35], with the permission of American Institute of Physics (AIP) Publishing). (**c**) RHEED patterns of a pristine 20 QL Bi_2Te_3 film and the same film at different stages of in-situ Te capping (Figure from Ref. [36], with the permission of AIP Publishing). (**d**) RHEED patterns of a Bi_2Te_3 grown on $SrTiO_3$ [111] substrate before (top) and after (bottom) in-situ capping the sample with an insulating layer of Al_2O_3 grown by pulsed laser deposition (Figure from Ref. [18], copyright John Wiley and Sons)

atomically flat surface morphology. The d-spacing, which is inversely proportional to the lattice constant, is indicated in the image by the white double arrow between the two first-order stripes. The evolution of the d-spacing during growth is shown in Fig. 7.4a (right). The solid blue arrow indicates the finishing time of the first quintuple layer (QL). After the growth of the first QL, the d-spacing becomes

constant, which demonstrates that the lattice is almost fully relaxed to that of the TI thin film. This growth characteristics confirm the Van der Waals epitaxy growth mode, meaning that the substrate and film are weakly bonded and no strain will be transferred into the sample [15].

Fornari et al. employed in situ RHEED for the systematic investigation of the initial growth stages, from the deposition of the first few QL of Bi_2Te_3 thin films, all the way up to 165 QLs [35]. Figure 7.4b depicts in situ RHEED patterns acquired during the epitaxial growth of Bi_2Te_3 thin films on BaF_2 [111] substrate. The RHEED images show the substrate surface just before growth and for increasing Bi_2Te_3 film coverage from 0.2 QL, 1 QL, 10 QLs until the end of the deposition at the sample thickness of 165 QLs. The RHEED streaks along $\left[2\ \bar{1}\ \bar{1}\ 0\right]$ azimuth of the (0001) Bi_2Te_3 layer are observed already after the deposition of only 0.2 QL, and they become clear at the sample thickness of 1 QL. As the thickness of the Bi_2Te_3 layer is increased to 10 QLs, the sharp RHEED streaks are fully developed. These RHEED data, with well-defined streaks, confirm the layer-by-layer growth mode from the start of the deposition, and they are indicative of a high-quality film with smooth single crystalline domains. At the end of the deposition, the RHEED pattern (measured along the azimuth) for the film with 165 QLs is identical to the one measured for 10 QLs. This confirms that the film surface retains the same characteristics throughout the entire deposition process [35].

In addition to monitoring the growth dynamics in the early growth stages, recently, Ngabonziza et al. [18] and Hoefer et al. [36] have independently employed RHEED for the in situ characterization of Bi_2Te_3 thin film before and after capping the films in situ with an Al_2O_3 layer or a Te layer (see Fig. 7.4c, d). Sharp RHEED streaks with clearly defined Kikuchi lines are observed for the pristine Bi_2Te_3 film, which is indicative of a high-quality film with smooth single crystalline domains. Upon capping with a Te layer (1 u.c ~ 0.6 Å), additional sharp RHEED streaks appear, which demonstrate that the MBE-evaporated Te overlayer grows epitaxially on the Bi_2Te_3 films (see Fig. 7.4c) [36]. On the other hand, we used PLD for depositing an amorphous capping layer of Al_2O_3 on our sample. Figure 7.4d depicts a RHEED pattern of the pristine Bi_2Te_3 film before capping with the Al_2O_3 layer. Again, sharp RHEED streaks are indicative of a high-quality film with smooth, single, crystalline domains. The featureless control image in Fig. 7.4d, taken after the Al_2O_3 deposition, indicates that an amorphous layer has formed. For the Al_2O_3 deposition, the sample was transferred to the attached PLD chamber without breaking vacuum.

5.2 In Situ X-Ray Photoemission Spectroscopy

5.2.1 XPS Basics

Surface elemental composition, stoichiometry, and contamination effects can be investigated right after growth using in situ X-ray photoemission spectroscopy (XPS). The XPS technique is based on the detection of the photoelectrons of core

states that are emitted when a beam of high-energy photons (0.1–2 keV) is directed onto the surface of the sample.

The XPS technique is a surface-sensitive technique because of the small escape depth of the electrons. The mean free path of the electrons is very small (5 nm for kinetic energies in the keV range) [44]. This implies that a large fraction of the photoemission intensity is originating from the topmost layers of the sample. The escape depth is limited by inelastic scattering and the emission of secondary electrons [45, 46]. This is mainly due to electron-electron and electron-phonon interactions. The secondary electrons give rise to an inelastic background that is present in almost all photoemission experiments, which typically decreases as kinetic energy increases. The background contains also information about the sample. Below, we demonstrate the use of XPS for the analysis of the surface stoichiometry of TI nanomaterials.

5.2.2 In Situ XPS Measurements of Bi_2Te_3 Topological Insulator Nanomaterials

Different studies employed XPS for in situ surface characterization, in particular, for the investigation of the surface elemental composition and determination of surface stoichiometry of TIs [16–18, 22, 36, 37, 43, 47–52]. We performed systematic in situ XPS measurements of MBE grown Bi_2Te_3 samples. The thin films were transferred from the deposition chamber to the XPS chamber via a distribution chamber (see Fig. 7.1) without breaking UHV conditions [16, 18]. Figure 7.5a depicts an XPS survey scan of a 30 nm Bi_2Te_3 film grown on Al_2O_3 (0001). The elements Bi and Te are resolved with no noticeable extra peaks of carbon or oxygen as often seen in films exposed to atmosphere [47, 49, 50, 53]. This confirms that the film has a clean surface without contaminations. Figure 7.5b, c depicts high-resolution scans of Te 3*d* and Bi 4*f* peaks, respectively. The binding energies of the Te $3d_{5/2}$ and Te $3d_{3/2}$ peaks and those of Bi $4f_{7/2}$ and Bi $4f_{5/2}$ are consistent with the expected values [54]. There are no detectable oxidation effects.

For the analysis of the photoemission spectra (e.g., determination of the surface stoichiometry), it is necessary to select the background type and peak lineshape functions carefully in order to obtain quantitative information. There exist numerous background models that can be used in the peak fitting of XPS data. For the analysis of XPS lineshapes, the most commonly used background is the Shirley background [55]. It was introduced in lineshape fittings to take the asymmetry on the low kinetic energy side of the photoemission peaks into account. This asymmetry is due to the inelastic scattering that the photoelectrons experience before leaving the sample [55]. To fit the Bi_2Te_3 XPS spectra in Fig. 7.5b, c, a Voigt function was used [56, 57]. This function is a combination of Gaussian and Lorentzian lineshapes. In the Voigt function, the Gaussian contribution takes into account the line broadening due to the experimental resolution, while the Lorentzian contribution models the lifetime of the core excited hole. The Voigt profile is given by [56, 57]:

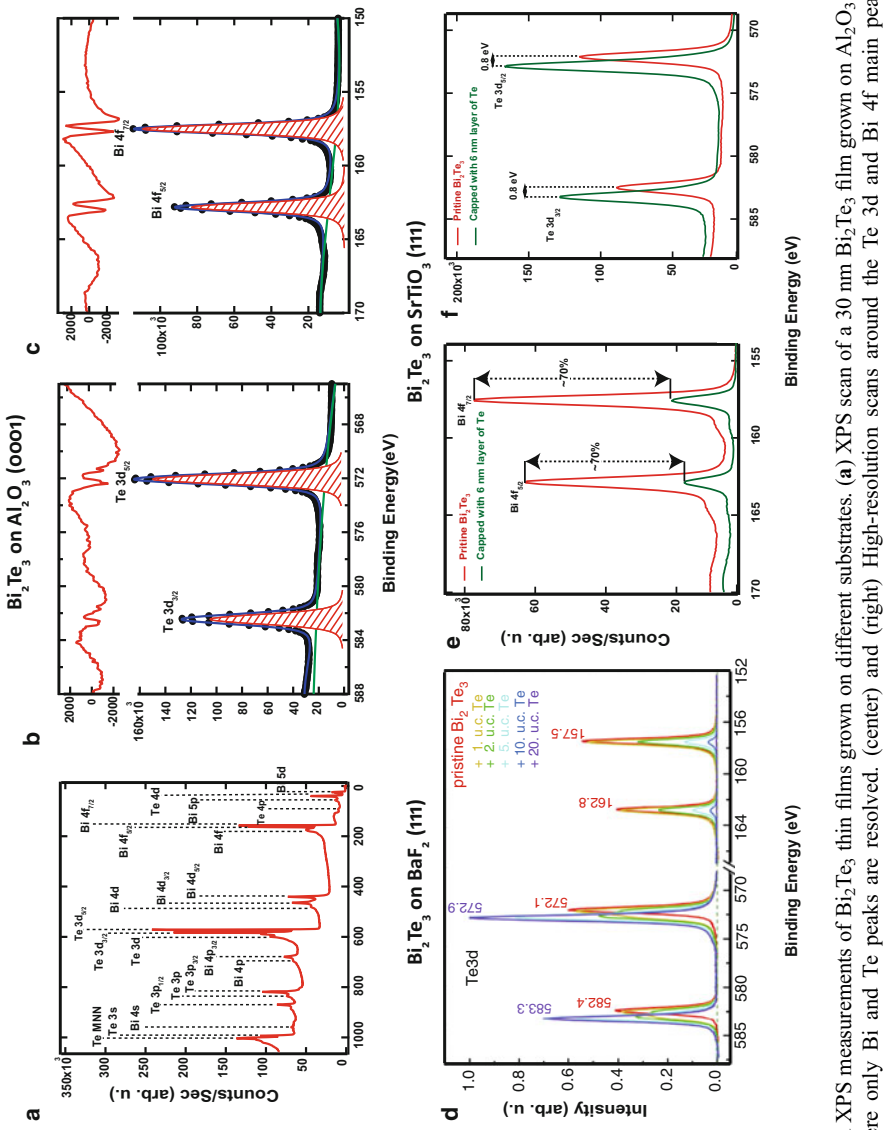

Fig. 7.5 In situ XPS measurements of Bi_2Te_3 thin films grown on different substrates. (**a**) XPS scan of a 30 nm Bi_2Te_3 film grown on Al_2O_3 (0001). General scan (left), where only Bi and Te peaks are resolved. (center) and (right) High-resolution scans around the Te 3d and Bi 4f main peaks, respectively

$$V(x;\sigma,\gamma) = \int_{-\infty}^{\infty} G(x';\sigma)L(x-x';\gamma)\,\mathrm{d}x' \tag{7.1}$$

where x is the energy difference from the line center, $G(x';\sigma)$ the centred Gaussian profile

$$G(x';\sigma) = \frac{\mathrm{e}^{-x'^2/(2\sigma^2)}}{\sigma\sqrt{2\pi}}$$

and $L(x-x';\gamma)$ the centred Lorentzian profile given by:

$$L(x;\gamma) = \frac{\gamma}{\pi(x^2+\gamma^2)}.$$

The surface stoichiometry is then obtained by subtracting a Shirley background from the signal and fitting each peak with a Voigt function, see Fig. 7.5b, c. Thereafter, the atomic ratio of Bi and Te can be calculated using the expression [54, 58]:

$$\frac{n_{\mathrm{Te}}}{n_{\mathrm{Bi}}} = \frac{I_{\mathrm{Te}}/I_{\mathrm{Bi}}}{S_{\mathrm{Te}}/S_{\mathrm{Bi}}}; \tag{7.2}$$

where n_{Te} and n_{Bi} are the density of Te and Bi atoms, respectively. I_{Te} and I_{Bi} are the integrated Te and Bi peak intensities, whereas S_{i} are the atomic sensitivity factors, which depend on the X-ray source and the element of interest [58]. Fitting the area under the Te $3d_{5/2}$, Te $3d_{3/2}$ and Bi $4f_{7/2}$, Bi$4f_{5/2}$ peaks, the surface chemical stoichiometry was determined to be 1.49 ± 0.05, which shows that the ratio of Bi to Te is very close to the expected 2:3 ratio in the Bi_2Te_3 system.

Hoefer et al. prepared bulk insulating Bi_2Te_3 thin films under UHV conditions and investigated the surface state properties of their samples using in situ XPS measurements, before and after capping the Bi_2Te_3 films with an epitaxially grown capping layer of Te [36]. Figure 7.5d depicts an in situ XPS scan of the Te 3*d* and Bi 4*f* core levels of a 20 QL Bi_2Te_3 film with Te capping of different thicknesses. For the pristine film, very narrow, symmetric Te 3*d* and Bi 4*f* core level lines were measured (see red curve in Fig. 7.5d). Upon capping the sample with Te layers of different thicknesses, it was noticed that the intensity of the Bi 4*f* core level decreased, without any changes in the line shape or energy position. This indicates that the Bi in Bi_2Te_3 is not altered chemically by the deposited capping layer of Te.

Fig. 7.5 (continued) (Figure reproduced from Ref. [16], copyright American Physical Society). (**b**) XPS scan of a pristine 20 nm Bi_2Te_3 film grown on BaF_2 (111) before and after the sample is capped with Te layers of different thicknesses (Figure from Ref. [36]). (**c**) XPS spectra of pristine Bi_2Te_3 grown on $SrTiO_3$. High-resolution scans of Bi 4f (left) and Te 3d (right) core levels measured before and after capping with a 6 nm layer of Te (Figure reproduced from Ref. [18], with permission of John Wiley and Sons Publishing)

On the other hand, the Te $3d_{5/2}$ and Te $3d_{3/2}$ lineshapes were observed to be slightly influenced by this capping procedure. The peak shapes had developed a shoulder with ≈0.8 eV higher binding energies after the deposition of the Te overlayer, which was attributed to the presence elemental Te [54]. These XPS data are in agreement with recent in situ XPS measurements on 15 nm thick Bi_2Te_3 films that were capped with a 6 nm thick Te layer (see Fig. 7.5e) [18] and suggest that the surface states of the pristine Bi_2Te_3 samples are not affected by the Te capping. This observation corroborated with subsequent in situ four-point probe conductivity and angle resolved photoemission spectroscopy on Bi_2Te_3 films that are discussed below [16, 17, 36].

5.3 In Situ Angle Resolved Photoemission Spectroscopy

5.3.1 Basic Principles of ARPES

Angle resolved photoemission spectroscopy (ARPES) is a refinement of the photoemission spectroscopy technique. It is the most direct method to measure the electronic dispersion on the sample surface. It analyzes both the kinetic energy and the angular distribution (or momentum) of the emitted electrons [59–61]. Figure 7.6 sketches the geometry of an ARPES experiment. From the measured kinetic energies E_{kin} and momenta **K** of the photoelectrons in vacuum, one determines the binding energy E_B and the momentum **k** of the electrons inside the crystal, i.e., the band

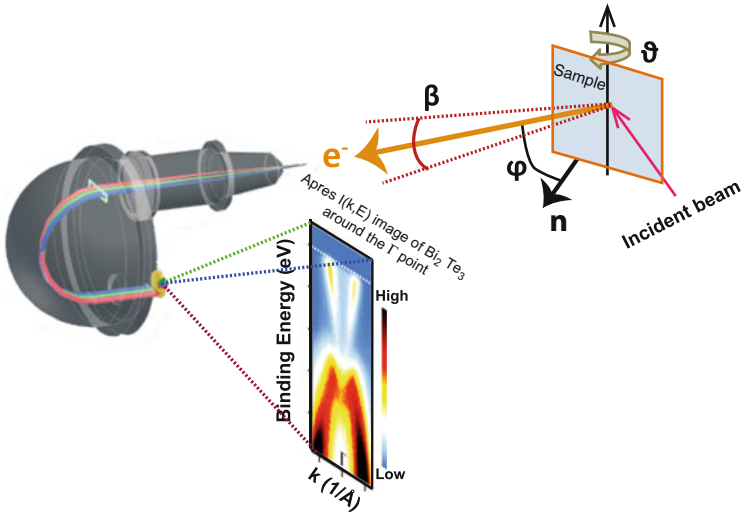

Fig. 7.6 A schematic layout of the experimental geometry for ARPES. Upon shining photons ($h\nu$) on the sample, the emission direction of the photoelectrons is specified by the polar φ angle (emission angle) and azimuthal ϑ (manipulator angle). The vector n is the sample surface normal and the angle β is the analyzer acceptance angle of the outgoing photoelectrons in momentum space

dispersion relations $E\left(\vec{k}\right)$ of the electrons in the solid [59, 61]. The modulus of the momentum **K** in vacuum is given by:

$$\mathbf{K} = \frac{\mathbf{P}}{\hbar} = \frac{\sqrt{2mE_{\text{kin}}}}{\hbar}; \tag{7.3}$$

where $\mathbf{P} = \sqrt{2mE_{\text{kin}}}$ and m are the momentum and mass of photoelectrons, respectively. In terms of the polar φ and azimuthal ϑ angles in Fig. 7.6, $\mathbf{K}_{\parallel}$ and $\mathbf{K}_{\perp}$ can be expressed into components as follows:

$$K_{\parallel} = \begin{cases} K_x = \frac{1}{\hbar}\sqrt{2mE_{\text{kin}}}\sin\varphi\cos\vartheta; \\ K_y = \frac{1}{\hbar}\sqrt{2mE_{\text{kin}}}\sin\varphi\sin\vartheta; \end{cases} \tag{7.4}$$

$$K_{\perp} = K_z = \frac{1}{\hbar}\sqrt{2mE_{\text{kin}}}\cos\vartheta. \tag{7.5}$$

From Eq. 7.4, and using the fact that only $\mathbf{K}_{\parallel}$ is conserved (the surface does not break translational symmetry while moving across the surface normal direction of the crystal), the component parallel to the surface of the electron crystal momentum is given by [59].

$$\mathrm{k}_{\parallel} = \sqrt{K_x^2 + K_y^2} = \frac{1}{\hbar}\sqrt{2mE_{\text{kin}}}\sin\varphi. \tag{7.6}$$

Therefore, the parallel component of the momentum inside the solid $\mathbf{k}_{\parallel}$ is fully determined by measurement of the emission angle φ and kinetic energy of the photoelectrons in vacuum.

Often in an ARPES experiment, 2D color maps are used because they present data more conveniently. The acquired 2D color map shows the ARPES intensity $I(k, E_{\text{B}})$ as function of momentum k and binding energy E_{B} (see Fig. 7.6).

5.3.2 In Situ ARPES Measurements of Bi_2Te_3 Topological Insulator Nanomaterials

ARPES is perhaps the most important tool for the investigation of topological insulator materials [62–65] and one of the key techniques to determine the electronic dispersion of quantum materials [59–61, 66]. It played a major role in the discovery of 3D TIs [4, 8, 9] and the exploration of the novel properties of their surface states [5, 67–69]. Here, we review and discuss recent in situ ARPES results on Bi_2Te_3 TI thin films.

In situ ARPES is an essential tool for the optimization of TI thin film growth. The concentration of bulk dopants, and thus the position of the Fermi level in the band structure, depends sensitively on the growth conditions, e.g., the deposition rate and

the substrate temperature. A low bulk dopant concentration is required to pin the Fermi level in the band gap and harness the properties of the topological surface states for applications. Only few reports of as-grown bulk-insulating Bi_2Te_3 thin films exist that were grown without counterdoping [16, 17, 19, 20, 36]. Using in situ ARPES, Wang et al. [20] demonstrated that Bi_2Te_3 thin films can be grown without extrinsic defects on Si substrates. They showed that the Fermi level in the samples is tuned by adjusting the substrate temperature during growth. Figure 7.7a depicts a series of ARPES images taken around the Γ point of 60 nm thick Bi_2Te_3 films grown on Si(111) substrates: Whereas the Fermi level is in the bulk conduction band, 340 meV above the Dirac point, for in the n-doped film grown at 560 K (Fig. 7.7a, leftmost image), it drops as the substrate temperature is increased. For the p-doped film grown at 620 K, the Fermi level lies in the bulk valence band (Fig. 7.7a, rightmost image). This was achieved without any counterdoping which is important as doping tends to decrease the carrier mobility.

Lattice matching is another important parameter that influences the film morphology. To test the electronic properties of films grown on atomically flat, lattice-mismatched surfaces, we performed systematic in situ ARPES measurements of Bi_2Te_3 thin films grown on sapphire (Al_2O_3 [0001]) and strontium titanate ($SrTiO_3$ [111]) substrates [16]. The Bi_2Te_3 thin films were grown by MBE and transferred to a stand-alone ARPES system using the vacuum suitcase described in Sect. 4.2. The transfer took a total of 3 days for which the samples were stored in the suitcase at a pressure lower than 2×10^{-9} mbar. Figure 7.7b depicts a set of ARPES images of a 15 nm thick Bi_2Te_3 film grown on $SrTiO_3$ (111). All the spectra were taken around the Γ point in the vicinity of the Fermi level, at a temperature of ~17 K, over different time intervals in UHV conditions. Clearly, at the beginning of the measurements, the Fermi level (white dashed line) lies well within the bulk band gap and intersects only the topological surface states without observable contribution of the bulk conduction band at E_F. This result confirms that despite a large lattice mismatch between the film and the substrate [70], high quality intrinsic Bi_2Te_3 films are grown. In addition, the fact that the samples were measured after being stored into the UHV suitcase for 3 days and no bulk conduction bands were observed further indicates that the surface states of these films are stable as long as the films are kept in situ or under UHV conditions. This conclusion is consistent with other in-situ ARPES studies on Bi_2Te_3 thin films [17, 36, 71]. On the other hand, when samples were exposed continuously to the photon beam for about 1 h, bulk conduction bands started to appear, and the Fermi level was touching the bottom of the bulk conduction band. Prolonged exposure to the beam of electrons during spectroscopy experiments can produce changes in the surface band structure of the materials, as the authors of recent ARPES studies on Bi_2Te_3 and $Bi_{1.46}Sb_{0.54}Te_{1.7}Se_{1.3}$ TI compounds [65, 72] and terahertz spectroscopy on HgTe/HgCdTe quantum wells [73] pointed out. Raising the temperature back to room temperature and allowing the sample to recover for sometime in UHV conditions resets the sample to the initial, bulk insulating condition (see Fig. 7.7b).

We also investigated the effect of an exposure of the films to ambient conditions on the band structure of TI materials using in situ ARPES experiments [16]. This is

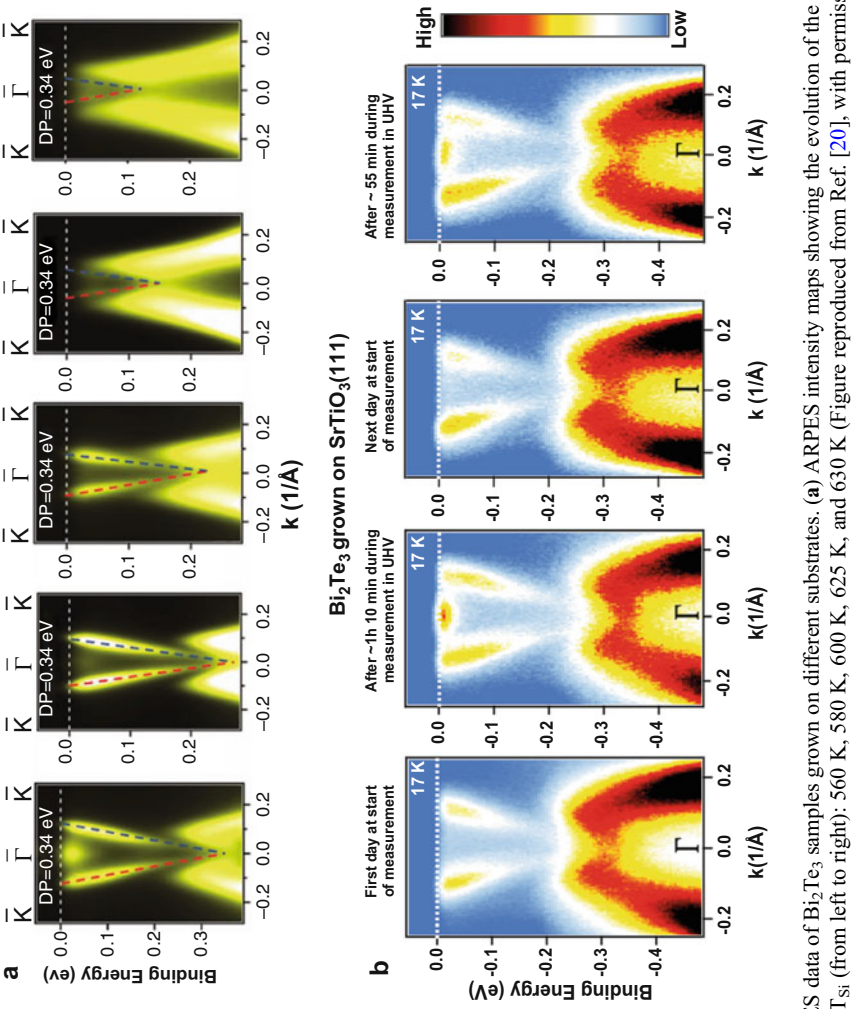

Fig. 7.7 In situ ARPES data of Bi_2Te_3 samples grown on different substrates. (**a**) ARPES intensity maps showing the evolution of the band structure with the substrate temperature, T_{Si} (from left to right): 560 K, 580 K, 600 K, 625 K, and 630 K (Figure reproduced from Ref. [20], with permission of John Wiley and

relevant since it helps to understand how extrinsic defects affect surface and bulk states of TI materials. Figure 7.8a shows ARPES spectra around the Γ point of a 20 nm Bi_2Te_3 film, grown on sapphire. The samples were measured (leftmost) at 17 K, (center) at room temperature before exposure and (rightmost) after 10 min exposure to ambient conditions. For the pristine film measured at 17 K, the characteristic V-shaped Dirac surface state is observed clearly, and only the surface states intersect the Fermi level (white, dashed line). Measuring the same film at room temperature, the Fermi level is still well within the bulk band gap, below the bottom of the bulk conduction band (middle image in Fig. 7.8a). Due to the thermal population, states up to ~50 meV above the Fermi level are also resolved in the room temperature image. After in situ measurements, this 20 nm Bi_2Te_3 was taken out of the ARPES chamber and exposed to air for 10 min. After this short exposure, the sample was introduced again into the ARPES chamber, without any further treatments such as annealing. There are noticeable changes in the measured band structure of the film. Compared to the pristine sample, bulk valence bands have moved downward, and the linearly dispersing Dirac surface states are not resolved in the ARPES spectrum after the exposure to air. This observation was interpreted to be an indication that the sample degradation is deeper than the probing depth of the ARPES experiment (~1 nm) [16]. Therefore, for films exposed to air, the conductance of the films will be affected by these changes (e.g., upward shift of Fermi level) in the band structure. The degradation effect of the TI surface states, as observed in ARPES spectra after exposure to air, underlines the need to carry these experiments out under ultra-high-vacuum conditions. Alternatively, one can protect films before taking them ex situ for further studies, to avoid deterioration of the surface properties [49] such as the reduction of the spin polarization [74], and the change of sign of the carriers in the surface conductivity of TI materials [75].

Recently, in situ ARPES experiments were also used to identify a suitable capping material for the protection of the topological surface states of bulk insulating Bi_2Te_3 TI films [36]. Figure 7.8b depicts ARPES spectra of a 20 nm Bi_2Te_3 thin film before and after being capped in situ with 6 Å (1 u.c.) and 12 Å (2 u.c.) Te layers, respectively, and two other 20 QL Bi_2Te_3 films after removal of a 20 u.c Te capping layer (one was kept in UHV and the other was exposed to air for 5 min). For all five measurements, the Dirac cone and the topological surface states of Bi_2Te_3 are observed. Most notably, for all the Te capping layers up to 20 u.c, the Fermi level intersects only with the topological surface states without any observable contribution from bulk bands, which indicates that the surface states of the pristine samples

Fig. 7.7 (continued) Sons Publishing). (**b**) ARPES spectra of a 15 nm thick Bi_2Te_3 film grown on $SrTiO_3$ (111). Measurements were taken over different time intervals in UHV conditions during ARPES measurements. Only topological surface states at the Fermi level are observed at the beginning of the experiment, but after prolonged exposure of the film to the photon beam, bulk conduction bands start to appear. The spectra were measured at 17 K. These observations further support the fact that these films do not degrade in UHV conditions (Figure reproduced from Ref. [16], copyright American Physical Society)

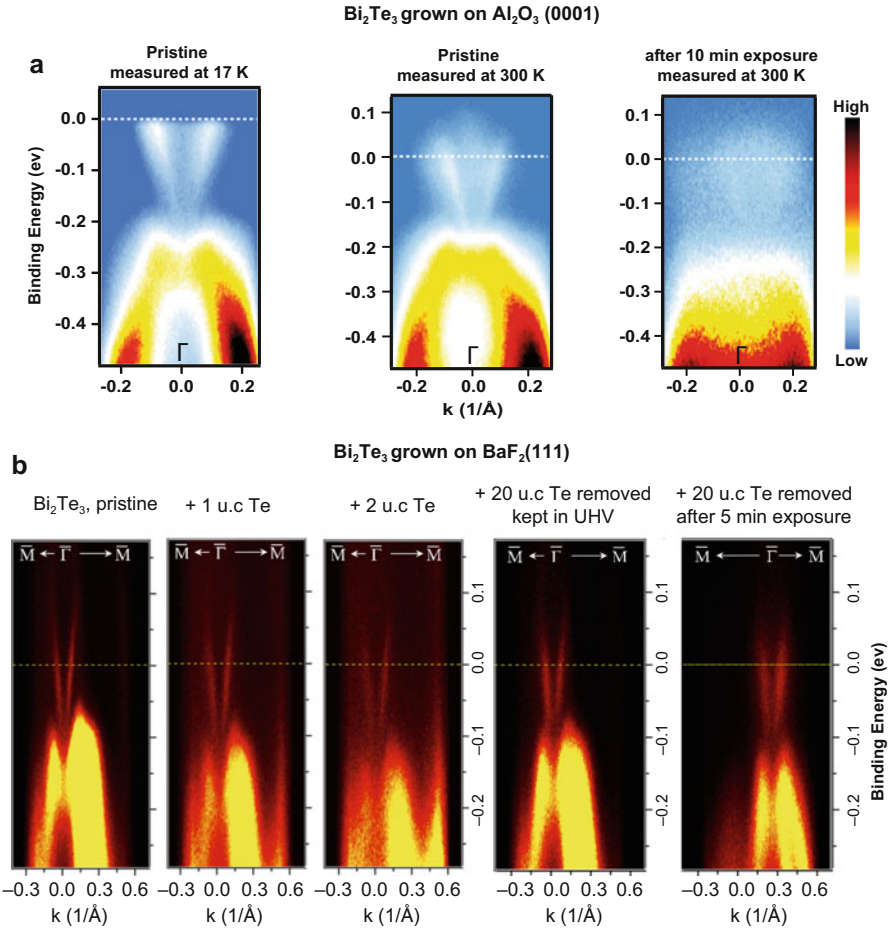

Fig. 7.8 Impact of exposing Bi_2Te_3 films to ambient conditions and importance of capping films in-situ before exposure. (**a**) ARPES I(k,E) images a 20 QL film around the Γ point at 17 K and 300 K, before (leftmost and middle) and after exposure to air (rightmost). The white dashed line indicates the position of the Fermi level (Figure from Ref. [16], copyright American Physical Society). (**b**) ARPES images of a pristine 20 nm Bi_2Te_3 film, and the same sample later after being capped with a Te layer of 6 Å (1 u.c) and 12 Å (2 u.c), respectively. The sample was measured at room temperature. (Rightmost two images) ARPES spectra of two different films after removal of a 12 nm Te capping layer (Figure from Ref. [36])

were not affected by this Te capping layer. Moreover, the fact that after annealing the Te capped samples in UHV at 220 °C, all the band structure features of the pristine film were recovered convincingly shows that the Te capping layer can be removed by thermal annealing in vacuum without destroying the surface of the Bi_2Te_3 films. To investigate if the Te capping layer actually protects the TI surface states against degradation when samples are exposed to ambient conditions, a Bi_2Te_3 film capped

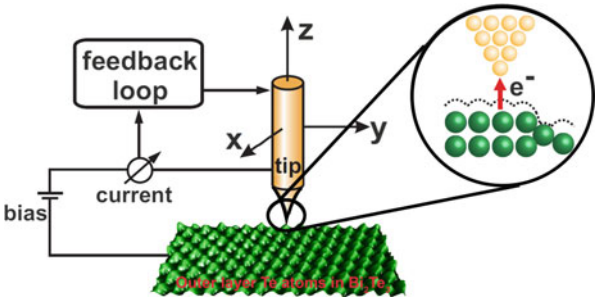

Fig. 7.9 Schematic illustration of the working principle of an STM system

with a 20 u.c Te was exposed to air for 5 min at room temperature. The ARPES spectrum after 5 min exposure and removal of the Te layer in situ (by thermal annealing) is clearly the same as that of the pristine Bi_2Te_3 film kept in UHV. This observation demonstrates the efficacy of the Te overlayer in protecting the Bi_2Te_3 surface against extrinsic defects for films exposed to air.

5.4 In Situ Scanning Tunneling Microscopy

5.4.1 Basic Principles of STM

Scanning tunneling microscopy (STM) played a key role in the discovery of TI materials. It was used, for example, to visualize the 2D Dirac surface states and to demonstrate some of the novel properties of TI materials, such as the absence of backscattering from nonmagnetic impurities and the high transmission of TI surface states at step edges and barriers that reflect or absorb conventional surface states [76, 77].

Figure 7.9 illustrates the working principle of the scanning tunneling microscope. The STM images the surface of a conducting sample at the atomic scale based of the principle of electronic tunneling. An atomically sharp tip (mostly chemically etched tungsten) is scanned over the surface of the sample at a distance of approximately 1 nm. The tunneling current I depends on several parameters, but the most commonly used expression is the Simmons equation [78]:

$$I \propto \frac{V}{Z}\exp(-2\kappa Z);$$

where V is the applied voltage between the STM tip and the sample surface, ρ the density of states, κ the decay length, and Z the STM tip-sample separation distance. By applying a constant voltage between the STM tip and the sample surface, a tunneling current will start to flow. The size of this current depends on the bias voltage, the tip-sample separation, the lateral position of the tip with respect to the sample, and the local density of states (LDOS). The atomic corrugation of the surface gives rise to variations in the tunneling current with distance Z between the sample and the tip. Thus, scanning the tip across the surface while using a

feedback loop (in the z-direction) to keep the tunneling current constant, the surface topography of the sample is recorded.

Besides topographic imaging, STM is widely used for spectroscopy. For the scanning tunneling spectroscopy (STS) measurement method, the STM tip is first moved into position above the sample surface. Then, the tunneling current is measured either in current-distance spectroscopy mode, as function of the tip-sample separation I(Z), in current-time spectroscopy mode (I(t)) or as function of the bias voltage: current-voltage mode I(V). While the I(Z) spectroscopy is useful for the determination of the work function of the material, the I(t) spectroscopy mode is advantageous for the investigation of dynamics events on the samples surface, and the current-voltage I(V) spectroscopy provides information about the electronic properties of the measured sample [79–81].

5.4.2 In Situ STM and STS Measurements of Bi_2Te_3 Topological Insulator Nanomaterials

Due to its extremely high spatial resolution and surface sensitivity, STM has been used extensively to study the surface states of materials. In particular, STM played an essential role for the investigation of TIs characteristic properties, such as topological protection of the surface states [76, 82], quantization of massless Dirac fermions in a magnetic field [83–85], and interaction of the topological surface state with various types of defects and adatoms [86–89]. Here, we review and analyze recent in situ spectroscopy and topography measurements on Bi_2Te_3 TI thin films.

We have carried out a systematic study of the effect of in situ storage, of the exposure to pure oxygen at atmospheric pressure, and of ex situ contamination of high quality intrinsic Bi_2Te_3 films [16]. Our samples were grown on insulating substrates, Al_2O_3 (0001) and $SrTiO_3$ (111). To transfer the Bi_2Te_3 films to the low temperature STM chamber, which was not connected to the growth chamber (see Fig. 7.1), a vacuum suitcase (described in Sect. 4.2) was used. During the transfer process, the pressure stayed in the lower 1×10^{-9} mbar range. The in situ STM/STS data were acquired at 77 K.

Figure 7.10a depicts a typical STM topography image of a 30 nm thick Bi_2Te_3 film grown on sapphire. The atomically flat morphology is evident, and the corresponding height profile across the surface is plotted in Fig. 7.10b. As expected, step height of adjacent terraces is 10.3 Å, equivalent to the size of a quintuple layer (QL) unit cell of Bi_2Te_3 [2]. Figure 7.10c shows the atomic resolution image of the surface for the pristine Bi_2Te_3 film. The surface tellurium atoms are clearly observed, exhibiting a hexagonal unit cell (see right bottom inset in Fig. 7.10c) with a lattice constant of about 4.3 Å. We did not resolve surface adatoms, thus indicating that our samples have clean surface, free from contaminations. To investigate the effect of exposure to ambient conditions, we took the film out of the STM system and exposed it to air for 10 min. Figure 7.10d depicts an atomically resolved STM topography image of this sample after exposure to air. There are notable changes in

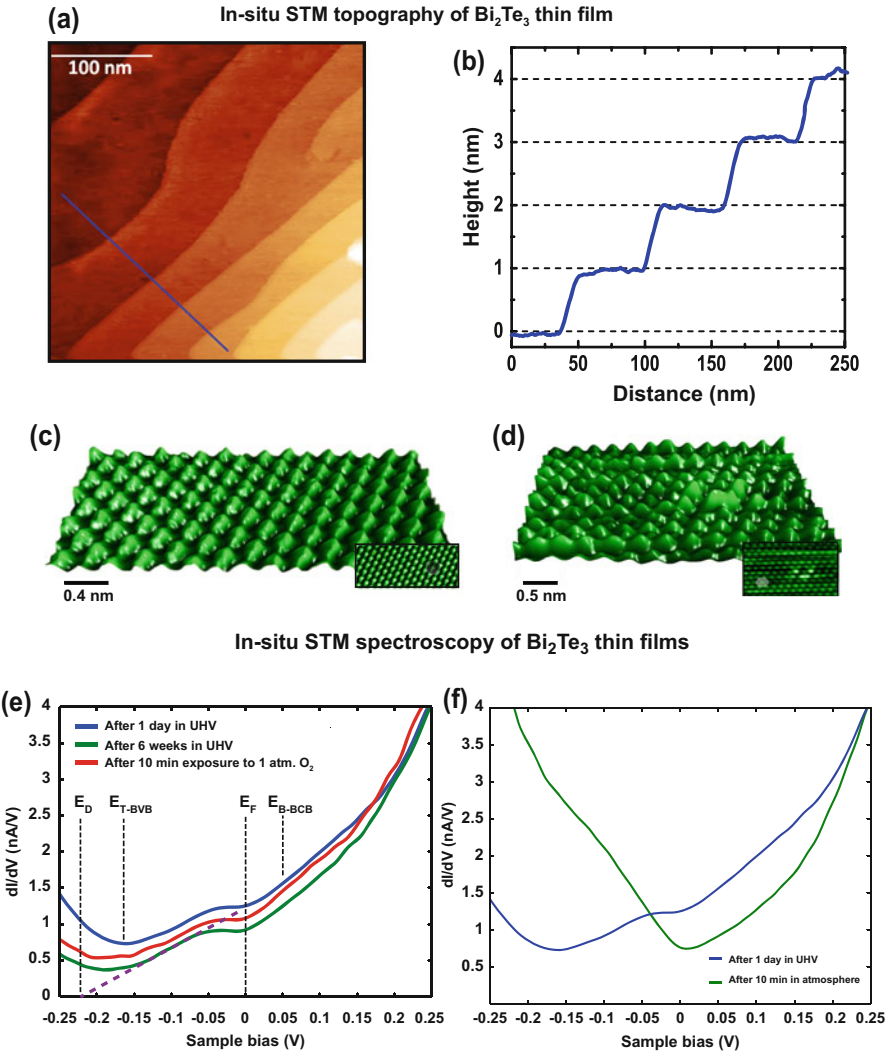

Fig. 7.10 (**a**) In situ STM topography image (250 × 250 nm^2 area) of Bi_2Te_3 film. (**b**) Line profile across a series of wide steps (blue line). (**c**) Atomic resolution topography image (6 × 6 nm^2 area). (**d**) Topography image (6 × 6 nm^2 area) of the same sample after exposure to ambient conditions. The surface tellurium atoms (right bottom inset) are still resolved together with noticeable defects as compared to before exposure. (**e**) Spectroscopy spectra of the same film (blue curve). Effect of storing films in situ under UHV conditions for weeks (green curve) and exposing them to pure oxygen (red curve). (**f**) dI/dV spectra of the same films after a 10-min exposure to ambient conditions (green); for comparison, plotted together with the spectra before exposure (blue) (Figures are from Ref. [16], copyright American Physical Society)

the surface topography of the film. We can readily identify additional defects due to ex situ contamination. This observation shows clearly that exposure to ambient pressures changes the surface topography of our Bi_2Te_3 thin films notably, thus emphasizing the need to protect the surface states from degradation and avoid unintentional doping induced by extrinsic defects.

Figure 7.10e depicts low temperature differential conductance curves of a 30 nm thick Bi_2Te_3 film grown on sapphire. Data were measured after 1 day in the STM chamber (blue line), after 6 weeks in situ storage (green), and later, after being oxidized for 10 min in 1 atm. of pure O_2 (red). In order to acquire differential conductivity spectra, we did numerical differentiation of more than 3600 I-V curves with setpoint parameters of $V_b = +350$ mV at $I = 1$ nA. The I-V spectra were also recorded by means of a standard lock-in technique with a time constant of 10 ms. The lock-in data were consistent with the results obtained by numerical differentiation. In Fig. 7.10e, E_{B-BCB} is the bottom of the bulk conduction band and E_{T-BVB} is the top of the bulk valence band. E_F and E_D indicate Fermi level and Dirac point, respectively. To determine the position of E_{B-BCB} and E_{T-BVB}, we identified the points at which the conductance increases sharply due to tunneling into bulk bands, and we used the reported value of the bulk conduction band (210 meV) of Bi_2Te_3 [8, 90] to calibrate the energy axis against the measured bias voltage. In all 3 conductance spectra, we observed a region where the conductance increases linearly with bias as expected when tunneling into TI surface states with linear dispersion relation. From ARPES data, it is known that the Dirac point of Bi_2Te_3 is buried inside the BVB [8, 16]; thus, by extrapolating this region with linear DOS, we estimate the Dirac point to be at ~0.23 eV below the Fermi level. Furthermore, the linear part of all the three STS spectra has a plateau at ~ -50 mV. The presence of a plateau has been reported previously in STS spectra of Bi_2Te_3 thin films and single crystals [76, 91, 92]. It is often attributed to the hexagonal warping effect of the surface state band in Bi_2Te_3 samples [76, 93, 94].

Remarkably, in a long-term study encompassing 3 STS spectroscopy measurements (Fig. 7.10e) over a period of several weeks and exposure to an atmosphere of pure oxygen, we found no shifts in the spectra nor surface degradation of our Bi_2Te_3 thin film. The overall key features, the linear surface band, the plateau due to "warping," and the position of the Fermi energy relative to the bulk bands, remain unchanged. This finding is in agreement with the ARPES data presented above (see Sect. 5.3) since these thin films were also measured after storage for 3 days in the portable vacuum suitcase, and we did not detect any sign of bulk conduction bands at the start of the ARPES measurements. These data further confirm that in situ storage in ultra-high vacuum and exposure to pure oxygen at atmospheric pressures leave the band structure of Bi_2Te_3 thin films at the surface unaffected.

Next we studied the impact of exposure to air in STS data. The sample was taken out of the STM system and exposed to ambient conditions for 10 min. After this procedure, several spectroscopy maps were acquired for different positions on the exposed surface of the film, using the same setpoint parameters as for the spectra presented in Fig. 7.10e. In Fig. 7.10f, we show dI/dV spectra of a Bi_2Te_3 film grown on sapphire before (blue) and after (green) the exposure to air. For comparison, we

plot together the conductance curves before (blue) and after ex situ exposure (green). We observe clear changes in the shape of the STS spectra, as was also the case for the ARPES spectra of the film exposed to air (see Fig. 7.8a). The region previously associated with the linearly dispersing surface bands is absent in the exposed film, indicating the deterioration of surface states after exposure to the environment. Here, we note that whether bands shift upward or downward depends sensitively on the exact exposure conditions as well as the position where spectra are taken (e.g., close to a defect). Based on a comparison of measured STM topography data before and after exposure (see Fig. 7.10c, d), we believe that extrinsic defects due to the contamination are responsible for the observed changes in the Dirac surface states spectra of our Bi_2Te_3 STS spectra. Extrinsic defects are often responsible for the change of sign of the carriers in the surface conductivity of TIs [74]. This finding also emphasizes that for further ex situ investigations, films should first be capped in-situ to avoid any possible contamination. Recently, we developed a method for growing capping layers with minimal damage to the surface states of intrinsically insulating Bi_2Te_3 thin films [18]. Using two different capping materials, an Al_2O_3 layer grown by pulsed laser deposition and an epitaxially grown Te layer, we demonstrated the effectiveness of in situ capping for protecting the TI surfaces from adsorbates and other contaminations.

6 Conclusions and Future Perspective

In summary, we presented different in situ surface characterization tools of topological insulator nanomaterials. We confined our discussion to MBE grown Bi_2Te_3 TI thin films, and their subsequent in situ characterizations. We showed that RHEED during thin film deposition is an excellent technique for monitoring the growth dynamics and for structural analysis of the surface of Bi_2Te_3 samples. XPS is a complementary tool for the in situ investigation of the surface elemental composition as well as the study of surface chemical stoichiometry of as-grown films. Combining in situ spectroscopy and topography techniques (ARPES, STS and STM), we demonstrate that the electronic band structure and surface morphology of Bi_2Te_3 are not affected by in vacuo storage and exposure to oxygen. Breaking vacuum and exposing the sample surface to air results in notable changes in the surface band structure spectra and topography of Bi_2Te_3 samples. The prospect for future in situ characterization of TI nanomaterials includes the possibility of performing magnetotransport experiments without exposing the sample surface to ambient conditions. A possible route is to make minor modification of the vacuum suitcase so that it can be fit to almost any vacuum system, e.g., quantum transport measurement systems, thus redefining the concept of in situ characterization; of course, sample contacting issues should be first envisaged. Alternatively, thin films should first be capped in situ to avoid any possible contamination as has already been demonstrated [18]. The portable vacuum suitcase can also be used for further in situ analysis at different locations like synchrotron radiation facilities.

Acknowledgments We thank Dominic Post and Mark Golden for their support in the development of the vacuum suitcase. This work was financially supported by the Dutch Foundation for Fundamental Research on Matter (FOM), the Netherlands Organization for Scientific Research (NWO), and by the European Research Council (ERC).

References

1. Kane CL, Mele EJ (2005) Z_2 topological order and the quantum spin hall effect. Phys Rev Lett 95:146802
2. Zhang H, Liu C-X, Qi X-L, Dai X, Fang Z, Zhang S-C (2009) Topological insulators in Bi_2Te_3, Bi_2Te_3 and Sb_2Te_3 with a single Dirac cone on the surface. Nat Phys 5:438–442
3. Fu L, Kane CL (2007) Topological insulators with inversion symmetry. Phys Rev B 76:045302
4. Hsieh D, Qian D, Wray L, Xia Y, Hor YS, Cava RJ, Hasan MZ (2008) A topological Dirac insulator in a quantum spin hall phase. Nature (London) 452:970–974
5. Hsieh D, Xia Y, Wray L, Qian D, Pal A, Dil JH, Meier F, Osterwalder J, Bihlmayer G, Kane CL, Hor YS, Cava RJ, Hasan MZ (2009) Observation of unconventional quantum spin textures in topological insulators. Science 323(5916):919–922
6. Liu C-X, Qi X-L, Zhang H, Dai X, Fang Z, Zhang S-C (2010) Model Hamiltonian for topological insulators. Phys Rev B 82:045122
7. Xi Y, Qian D, Hsieh D, Wray L, Pal A, Lin H, Bansil A, Grauer D, Hor YS, Cava RJ, Hasan MZ (2009) Nat Phys 5:398–402
8. Chen YL, Analytis JG, Chu J-H, Liu ZK, Mo S-K, Qi XL, Zhang HJ, Lu DH, Dai X, Fang Z, Zhang SC, Fisher IR, Hussain Z, Shen Z-X (2009) Experimental realization of a three-dimensional topological insulator, Bi_2Te_3. Science 325(5937):178–181
9. Hsieh D, Qian D, Wray L, Xia Y, Hor YS, Cava RJ, Hasan MZ (2009) A tunable topological insulator in the spin helical Dirac transport regime. Nature (London) 460:1101–1105
10. Fu L, Kane CL (2008) Superconducting proximity effect and Majorana fermions at the surface of a topological insulator. Phys Rev Lett 100:096407
11. Qi X-L, Li R, Zang J, Zhang S-C (2009) Inducing a magnetic monopole with topological surface states. Science 323(5918):1184–1187
12. Ando Y (2013) Topological insulator materials. J Phys Soc Jpn 82(10):102001, and references therein
13. He L, Xiu F, Yu X, Teague M, Jiang W, Fan Y, Kou X, Lang M, Wang Y, Huang G, Yeh N-C, Wang KL (2012) Surface-dominated conduction in a 6 nm thick Bi_2Se_3 thin film. Nano Lett 12(3):1486–1490
14. Taskin AA, Sasaki S, Segawa K, Ando Y (2012) Manifestation of topological protection in transport properties of epitaxial Bi_2Se_3 thin films. Phys Rev Lett 109(6):066803
15. He L, Kou X, Wang KL (2013) Review of 3D topological insulator thin-film growth by molecular beam epitaxy and potential applications. Phys Status Solidi Rapid Res Lett 7(1–2):50–63, and reference therein
16. Ngabonziza P, Heimbuch R, de Jong N, Klaassen RA, Stehno MP, Snelder M, Solmaz A, Ramankutty SV, Frantzeskakis E, van Heumen E, Koster G, Golden MS, Zandvliet HJW, Brinkman A (2015) In-situ spectroscopy of intrinsic Bi_2Te_3 topological insulator thin films and impact of extrinsic defects. Phys Rev B 92(3):035405
17. Hoefer K, Becker C, Rata D, Swanson J, Thalmeier P, Tjeng LH (2014) Intrinsic conduction through topological surface states of insulating Bi_2Te_3. Proc Natl Acad Sci USA 111(42):14979–14984
18. Ngabonziza P, Stehno MP, Myoren H, Neumann VA, Koster G, Brinkman A (2016) Gate-tunable transport properties of in-situ capped Bi_2Te_3 topological insulator thin films. Adv Electron Mater 2:1600157

19. Li Y, Wang G, Zhu X, Liu M, Ye C, Chen X, Wang Y, He K, Wang L, Ma X, Zhang H, Dai X, Fang Z, Xie X, Liu Y, Qi X, Jia J, Zhang S, Xue Q (2010) Intrinsic topological insulator Bi_2Te_3 thin films on Si and their thickness limit. Adv Mater 22(36):4002–4007
20. Wang G, Zhu X, Sun Y, Li Y, Zhang T, Wen J, Chen X, He K, Wang L, Ma X, Jia J, Zhang SB, Xue Q (2011) Topological insulator thin films of Bi_2Te_3 with controlled electronic structure. Adv Mater 23(26):2929–2932
21. Brüne C, Liu CX, Novik EG, Hankiewicz EM, Buhmann H, Chen YL, Qi XL, Shen ZX, Zhang SC, Molenkamp LW (2011) Quantum hall effect from the topological surface states of strained bulk HgTe. Phys Rev Lett 106(12):126803
22. Zhang G, Qin H, Chen J, He X, Lu L, Li Y, Wu K (2011) Growth of topological insulator Bi_2Se_3 thin films on $SrTiO_3$ with large tunability in chemical potential. Adv Funct Mater 21:2351–2355
23. Lanius M, Kampmeier J, Weyrich C, Koölling S, Schall M, Schüffelgen P, Neumann E, Luysberg M, Mussler G, Koenraad PM, Schäpers T, Grützmacher D (2016) P–N junctions in ultrathin topological insulator Sb_2Te_3/Bi_2Te_3 heterostructures grown by molecular beam epitaxy. Cryst Growth Des 16:2057–2061
24. Eschbach M, Młyńczak E, Kellner J, Kampmeier J, Lanius M, Neumann E, Weyrich C, Gehlmann M, Gospodaric P, Döring S, Mussler G, Demarina N, Luysberg M, Bihlmayer G, Schäpers T, Plucinski L, Blügel S, Morgenstern M, Schneider CM, Grützmacher D (2015) Realization of a vertical topological p–n junction in epitaxial Sb_2Te_3/Bi_2Te_3 heterostructures. Nat Commun 6:8816
25. Jiang Z, Chang C-Z, Tang C, Zheng J-G, Moodera JS, Shi J (2016) Structural and proximity-induced ferromagnetic properties of topological insulator-magnetic insulator heterostructures. AIP Adv 6:055809
26. Sertore D, Michelato P, Monaco L, Manini P, Siviero F (2011) Use of NEG pums to ensure long term performance of high quantum efficiency photocatodes. In: Proceedings of IPAC, San Sebastián
27. Firpo G, Pozzo A (2004) New getter pump for ultrahigh vacuum systems and transportable enclosure. Rev Sci Instrum 75:4828
28. Saes group, https://www.saesgetters.com/products/nextorr-pumpsNEXTorr: The ideal pump for your portable vacuum case, 2016
29. Park CD, Chung SM, Manini P (2011) Combination of compact nonevaporable getter and small ion pumps for ultrahigh vacuum systems. J Vac Sci Technol A 29:011012
30. Scherer DR, Fenner DB, Hensley JM (2012) Characterization of alkali metal dispensers and non-evaporable getter pumps in ultrahigh vacuum systems for cold atomic sensors. J Vac Sci Technol A 30:061602
31. Larsen PK, Dobson PJ (eds) (1988) Reflection high-energy electron diffraction and reflection electron imaging of surfaces. Plenum Press, New York
32. Braun W (1999) Applied RHEED: reflection high-energy electron diffraction during crystal growth. Springer, Berlin
33. Peng LM, Dudarev SL, Whelan MJ (2004) High-energy electron diffraction and microscopy. Oxford University Press, Oxford, UK
34. Neave JH, Joyce BA, Dobson PJ, Norton N (1983) Dynamics of film growth GaAs by MBE from RHEED observations. Appl Phys A 31:1–2
35. Fornari CI, Rappl PHO, Morelhão SL, Abramof E (2016) Structural properties of Bi_2Te_3 topological insulator thin films grown by molecular beam epitaxy on (111) BaF_2 substrates. J Appl Phys 119:165303
36. Hoefer K, Becker C, Wirth S, Tjeng LH (2015) Protective capping of topological surface states of intrinsically insulating Bi_2Te_3. AIP Adv 5:097139
37. Roy A, Guchhait S, Sonde S, Dey R, Pramanik T, Rai A, Movva HCP, Colombo L, Banerjee SK (2013) Two-dimensional weak anti-localization in Bi_2Te_3 thin film grown on Si(111)-(7×7) surface by molecular beam epitaxy. Appl Phys Lett 102:163118
38. Rapacz R, Balin K, Wojtyniak M, Szade J (2015) Morphology and local conductance of single crystalline Bi_2Te_3 thin films on mica. Nanoscale 7:16034

39. Wang K, Liu Y, Wang W, Meyer N, Bao LH, He L, Lang MR, Chen ZG, Che XY, Post K, Zou J, Basov DN, Wang KL, Xiu F (2013) High-quality Bi_2Te_3 thin films grown on mica substrates for potential optoelectronic applications. Appl Phys Lett 103:031605
40. Xie M-H, Guo X, Xu Z-J, Ho W-K (2013) Molecular-beam epitaxy of topological insulator Bi_2Se_3 (111) and (221) thin film. Chin Phys B 22(6):068101, and references therein
41. He L, Xiu F, Wang Y, Fedorov AV, Huang G, Kou X, Lang M, Beyermann WP, Zou J, Wang KL (2011) Epitaxial growth of Bi_2Se_3 topological insulator thin films on Si (111). J Appl Phys 109:103702
42. Kou XF, He L, Xiu FX, Lang MR, Liao ZM, Wang Y, Fedorov AV, Yu XX, Tang JS, Huang G, Jiang XW, Zhu JF, Zou J, Wang KL (2011) Epitaxial growth of high mobility Bi_2Se_3 thin films on CdS. Appl Phys Lett 98:242102
43. He X, Guan T, Wang X, Feng B, Cheng P, Chen L, Li Y, Wu K (2012) Highly tunable electron transport in epitaxial topological insulator $(Bi_{1-x}Sb_x)_2Te_3$ thin films. Appl Phys Lett 101:123111
44. Seah MP, Dench WA (1979) Quantitative electron spectroscopy of surfaces: a standard data base for electron inelastic mean free paths in solids. Surf Interface Anal 1(1):2–11
45. van der Heide P (2012) X-ray photoelectron spectroscopy: an introduction to principles and practices. Wiley, Hoboken
46. Carlson T (1975) Photoelectron spectroscopy. Annu Rev Phys Chem 26:211–234
47. Yashina LV, Sánchez-Barriga J, Scholz MR, Volykhov AA, Sirotina AP, Neudachina VS, Tamm ME, Varykhalov A, Marchenko D, Springholz G, Bauer G, Knop-Gericke A, Rader O (2013) Negligible surface reactivity of topological insulators Bi_2Se_3 and Bi_2Te_3 towards oxygen and water. ACS Nano 7(6):5181–5191
48. Thomas CR, Vallon MK, Frith MG, Sezen H, Kushwaha SK, Cava RJ, Schwartz J, Bernasek SL (2016) Surface oxidation of $Bi_2(Te,Se)_3$ topological insulators depends on cleavage accuracy. Chem Mater 28:35–39
49. Kong D, Cha JJ, Lai K, Peng H, Analytis JG, Meister S, Chen Y, Zhang H, Fisher IR, Shen Z, Cui Y (2011) Rapid surface oxidation as a source of surface degradation factor for Bi_2Se_3. ACS Nano 5(6):4698–4703
50. Guo J, Qiu F, Zhang Y, Deng H, Hu G, Li X, Yu G, Dai N (2013) Surface oxidation properties in a topological insulator Bi_2Te_3 film. Chin Phys Lett 30(10):106801
51. Meng L, Meng H, Gong W, Liu W, Zhang Z (2011) Growth and characterization of Bi_2Se_3 thin films by pulsed laser deposition using alloy target. Thin Solid Films 519:7627–7631
52. Golyashov VA, Kokh KA, Makarenko SV, Romanyuk KN, Prosvirin IP, Kalinkin AV, Tereshchenko OE, Kozhukhov AS, Sheglov DV, Eremeev SV, Borisova SD, Chulkov EV (2012) Inertness and degradation of (0001) surface of Bi_2Se_3 topological insulator. J Appl Phys 112:113702
53. Bando H, Koizumi K, Oikawa Y, Daikohara K, Kulbachinskii VA, Ozaki H (2000) The time-dependent process of oxidation of the surface of Bi_2Te_3 studied by x-ray photoelectron spectroscopy. J Phys Condens Matter 12:5607–5616
54. Moulder JF, Stickle WF, Sobol PE, Bomben KD (1995) Handbook of X-ray photoelectron spectroscopy. Physical Electronics, Inc., Eden Prairie
55. Shirley DA (1972) High-resolution X-ray photoemission spectrum of the valence bands of gold. Phys Rev B 5:4709
56. He J, Zhang Q (2007) An exact calculation of the Voigt spectral line profile in spectroscopy. J Opt A Pure Appl Opt 9:565–568
57. Luque JM, Calzada MD, Saez M (2005) A new procedure for obtaining the Voigt function dependent upon the complex error function. J Quant Spectrosc Radiat Transf 94:151–161
58. Seah MP, Gilmore IS, Spencer SJ, Quantitative XPS (2001) Analysis of X-ray photoelectron intensities from elemental data in a digital photoelectron database. J Electron Spectrosc Relat Phenom 120(1–3):93–111
59. Damascelli A (2003) Angle-resolved photoemission studies of the cuprate superconductors. Rev Modern Phys 75(2):473–541

60. Lee WS, Vishik IM, Lu DH, Shen Z-X (2009) A brief update of angle-resolved photoemission spectroscopy on a correlated electron system. J Phys Condens Matter 21(16):164217
61. Damascelli A (2004) Probing the electronic structure of complex systems by ARPES. Phys Scr T109:61–74
62. Xie Z, He S, Chen C, Feng Y, Yi H, Liang A, Zhao L, Mou D, He J, Peng Y, Liu X, Liu Y, Liu G, Dong X, Yu L, Zhang J, Zhang S, Wang Z, Zhang F, Yang F, Peng Q, Wang X, Chen C, Xu Z, Zhou XJ (2014) Orbital-selective spin texture and its manipulation in a topological insulator. Nat Commun 5:3382
63. Zhang J, Chang CZ, Zhang Z, Wen J, Feng X, Li K, Liu M, He K, Wang L, Chen X, Xue QK, Ma X, Wang Y (2011) Band structure engineering in $(Bi_{1-x}Sb_x)_2Te_3$ ternary topological insulators. Nat Commun 2:574
64. Souma S, Kosaka K, Sato T, Komatsu M, Takayama A, Takahashi T, Kriener M, Segawa K, Ando Y (2009) Direct measurement of the out-of-plane spin texture in the Dirac-cone surface state of a topological insulator. Phys Rev Lett 106:216803
65. Frantzeskakis E, de Jong N, Zwartsenberg B, Bay TV, Huang YK, Ramankutty SV, Tytarenko A, Wu D, Pan Y, Hollanders S, Radovic M, Plumb NC, Xu N, Shi M, Lupulescu C, Arion T, Ovsyannikov R, Varykhalov A, Eberhardt W, de Visser A, van Heumen E, Golden MS (2015) Dirac states with knobs on: interplay of external parameters and the surface electronic properties of three-dimensional topological insulators. Phys Rev B 91:205134
66. Lu D, Vishik IM, Yi M, Chen Y, Moore RG, Shen Z-X (2012) Angle-resolved photoemission studies of quantum materials. Ann Rev Condens Matter Phys 3:129–167
67. Hsieh D, Xia Y, Qian D, Wray L, Meier F, Dil JH, Osterwalder J, Patthey L, Fedorov AV, Lin H, Bansil A, Grauer D, Hor YS, Cava RJ, Hasan MZ (2009) Observation of time-reversal-protected single-Dirac-cone topological-insulator states in Bi_2Te_3 and Sb_2Te_3. Phys Rev Lett 103:146401
68. Nishide A, Taskin AA, Takeichi Y, Okuda T, Kakizaki A, Hirahara T, Nakatsuji K, Komori F, Ando Y, Matsuda I (2010) Direct mapping of the spin-filtered surface bands of a three-dimensional quantum spin Hall insulator. Phys Rev B 81:041309(R)
69. Zhang Y, He K, Chang CZ, Song CL, Wang LL, Chen X, Jia JF, Fan Z, Dai X, Shan WY, Shen SQ, Niu Q, Qi XL, Zhang SC, Ma XC, Xue QK (2010) Crossover of the three-dimensional topological insulator Bi_2Se_3 to the two-dimensional limit. Nat Phys 6:584–588
70. Eibl O, Nielsch K, Peranio N, Völklein F (2015) Thermoelectric Bi_2Te_3 nanomaterials. Wiley-VCH Verlag GmBh & Co. KGaA, Weinheim
71. Lee JJ, Schmitt FT, Moore RG, Vishik IM, Ma Y, Shen ZX (2012) Appl Phys Lett 101:013118
72. Kordyuk AA, Kim TK, Zabolotnyy VB, Evtushinsky DV, Bauch M, Hess C, Büchner B, Berger H, Borisenko SV (2011) Photoemission-induced gating of topological insulators. Phys Rev B 83:081303
73. Olbrich P, Zoth C, Vierling P, Dantscher K-M, Budkin GV, Tarasenko SA, Bel'kov VV, Kozlov DA, Kvon ZD, Mikhailov NN, Dvoretsky S, Ganichev SD (2013) Giant photocurrents in a Dirac fermion system at cyclotron resonance. Phys Rev B 87:235439
74. Wang X, Bian G, Miller T, Chiang T-C (2012) Fragility of surface states and robustness of topological order in Bi_2Te_3 against oxidation. Phys Rev Lett 108:096404
75. Taskin AA, Ren Z, Sasaki S, Segawa K, Ando Y (2011) Observation of Dirac holes and electrons in a topological insulator. Phys Rev Lett 107:016801
76. Alpichshev Z, Analytis JG, Chu J-H, Fisher IR, Chen YL, Shen ZX, Fang A, Kapitulnik A (2010) STM imaging of electronic waves on the surface of Bi_2Te_3: topologically protected surface states and hexagonal warping effects. Phys Rev Lett 104:016401
77. Seo J, Roushan P, Beidenkopf H, Hor YS, Cava RJ, Yazdani A (2010) Transmission of topological surface states through surface barriers. Nature 466:343–346
78. Simmons JG (1963) Generalized formula for the electric tunnel effect between similar electrodes separated by a thin insulating film. J Appl Phys 34:1793
79. Julian Chen C (2007) Introduction to scanning tunneling microscopy, 2nd edn. Oxford University Press, Oxford, UK

80. Binnig G, Rohrer H (1987) Scanning tunneling microscopy: from birth to adolescence. Rev Modern Phys 59(3):615
81. Wiesendanger R (1994) Scanning probe microscopy and spectroscopy: methods and applications. Cambridge University Press, Cambridge, UK
82. Roushan P, Seo J, Parker CV, Hor YS, Hsieh D, Qian D, Richardella A, Hasan MZ, Cava RJ, Yazdan A (2009) Topological surface states protected from backscattering by chiral spin texture. Nature 460:1106–1110
83. Cheng P, Song C, Zhang T, Zhang Y, Wang Y, Jia J-F, Wang J, Wang Y, Zhu B-F, Chen X, Ma X, He K, Wang L, Dai X, Fang Z, Xie X, Qi X-L, Liu C-X, Zhang S-C, Xue Q-K (2010) Landau quantization of topological surface states in Bi_2Se_3. Phys Rev Lett 105:076801
84. Hanaguri T, Igarashi K, Kawamura M, Takagi H, Sasagawa T (2010) Momentum resolved Landau-level spectroscopy of Dirac surface state in Bi_2Se_3. Phys Rev B 82:081305(R)
85. Jiang Y, Wang Y, Chen M, Li Z, Song C, He K, Wang L, Chen X, Ma X, Xue Q-K (2010) Landau quantization and the thickness limit of topological insulator thin films of Sb_2Te_3. Phys Rev Lett 108:016401
86. Alpichshev Z, Biswas RR, Balatsky AV, Analytis JG, Chu J-H, Fisher IR, Kapitulnik A (2012) STM imaging of impurity resonances on Bi_2Se_3. Phys Rev Lett 108:206402
87. Honolka J, Khajetoorians AA, Sessi V, Wehling TO, Stepanow S, Mi J-L, Iversen BB, Schlenk T, Wiebe J, Brookes NB, Lichtenstein AI, Hofmann P, Kern K, Wiesendanger R (2012) In-plane magnetic anisotropy of Fe atoms on Bi_2Se_3 (111). Phys Rev Lett 108:256811
88. Beidenkopf H, Roushan P, Seo J, Gorman L, Drozdov I, San Hor Y, Cava RJ, Yazdani A (2011) Spatial fluctuations of helical Dirac fermions on the surface of topological insulators. Nat Phys 7:939–943
89. Hor YS, Roushan P, Beidenkopf H, Seo J, Qu D, Checkelsky JG, Wray LA, Hsieh D, Xia Y, Xu S-Y, Qian D, Hasan MZ, Ong NP, Yazdani A, Cava RJ (2010) Phys Rev Lett 81:195203
90. Zahid F, Lake R (2010) Thermoelectric properties of Bi_2Te_3 atomic quintuple thin films. Appl Phys Lett 97:212102
91. Chen M, Peng J-P, Zhang H-M, Wang L-L, He K, Ma X-C, Xue Q-K (2012) Molecular beam epitaxy of bilayer Bi(111) films on topological insulator Bi_2Te_3: a scanning tunneling microscopy study. Appl Phys Lett 101:081603
92. Zhang T, Cheng P, Chen X, Jia JF, Ma X, He K, Wang L, Zhang H, Dai X, Fang Z, Xie X, Xue Q-K (2009) Experimental demonstration of topological surface states protected by time-reversal symmetry. Phys Rev Lett 103:266803
93. Liang F (2009) Hexagonal warping effects in the surface states of the topological insulator Bi_2Te_3. Phys Rev Lett 103:266801
94. Adroguer P, Carpentier D, Cayssol J, Orignac E (2012) Diffusion at the surface of topological insulators. New J Phys 14:103027

8 In Situ Characterization of Size, Spatial Distribution, Chemical Composition, and Electroanalytical Response of Hybrid Nanocomposite Materials

Julio Bastos-Arrieta, Raquel Montes, Cristina Ocaña, Marisol Espinoza, Maria Muñoz, and Mireia Baeza

Contents

J. Bastos-Arrieta (✉)
Department of Chemical Engineering, Universitat Politècnica de Catalunya, Barcelona, Spain

Barcelona Research Center in Multiscale Science and Engineering, Barcelona, Spain

Physical Chemistry, Technische Universität Dresden, Dresden, Germany
e-mail: julio.bastos@upc.edu; julio.bastos@tu-dresden.de

R. Montes
Departament d'Enginyeria Química, Biològica i Ambiental, Escola d'Enginyeria, Universitat Autònoma de Barcelona, Barcelona, Spain

Departament d'Enginyeria Química, Biològica i Ambiental, Carrer de les Sitges S/N, Edifici Q, Escola d'Enginyeria Bellaterra, Barcelona, Spain

C. Ocaña
Departament Micronano Sistemes, CSIC, Institute of Microelectronics of Barcelona IMB CNM, Bellaterra, Spain

Johan Gadolin Process Chemistry Centre, c/o Laboratory of Analytical Chemistry, Abo Akademi University, Turku, Finland

M. Espinoza
Department of Chemistry, Universidad Autónoma Metropolitana, México, D. F., México

M. Muñoz · M. Baeza
Departament de Química, Facultat de Ciències, Carrer dels Til·lers, Edifici C-Entrada Nord, Bellaterra, Barcelona, Spain

© Springer-Verlag GmbH Germany, part of Springer Nature 2018

C. S. S. R. Kumar (ed.), *In-situ Characterization Techniques for Nanomaterials*,
https://doi.org/10.1007/978-3-662-56322-9_8

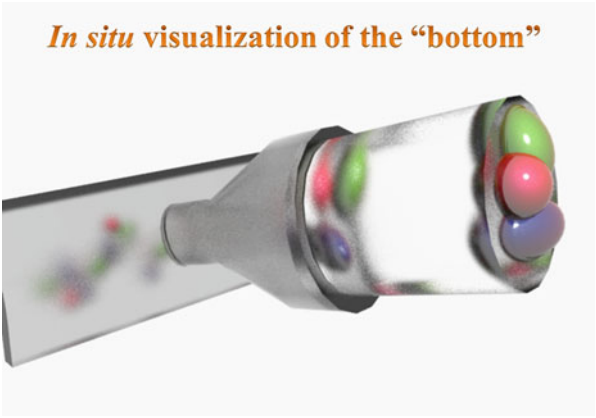

1 Definition of the Topic

Life in the twenty-first century is dependent on an unlimited variety of advanced hybrid materials – among them, nanomaterials (NMs). The design of these NMs mostly depends on the current necessities of the society, the availability of resources, and the investment required for an appropriate scale-up production. Thus, regarding the preparation of novel NMs, it is mandatory for the evaluation of their properties in order to satisfy the desired applications with high performance. In this chapter, we discuss different techniques that offer the possibility of the in situ characterization of NMs and nanocomposite materials (NCs), in terms of their chemical composition, spatial distribution, and optical and electrochemical features, without modifying the material itself.

2 Overview

The advances of materials science have involved the improvement of characterization techniques. For instance, initial scientific observations were realized only by optical microscopy. Later on the resolution and the scope of interest led to the apparition of electron microscopy. Currently, the need to arrive to atomic resolution (or beyond) allows the use of the term nanoscopy. This evolution joins the necessity of a better understanding of the structure–properties relation in the novel materials. An important case is the development of ultrafast microscopy in which images can be taken in nanoseconds time interval, which opens new ways to study the dynamics of different processes.

After the design and synthesis of a nanocomposite material, the next step is the full characterization of its principal features, such as nanoparticle size and distribution, chemical composition, morphology, and special properties. A complete and appropriate characterization is must for the deeper understanding of the behavior of the nanocomposite material and, therefore, its further synthesis optimization or possible commercialization of the final added value materials. The importance of the characterization is related as well with the concerns on the possible effects of nano-sized materials on the human body and the environment are increasing recently, added to the lack of specific legislation for the nano-sized structured materials.

Here we describe the application of different electron microscopy, optical and electrochemical techniques (e.g., field emission scanning electron microscopy, laser confocal microscopy, cyclic voltammetry) that have showed to be suitable for the detailed description of novel NMs and NCs, by describing the morphology, surface interactions, chemical composition, electrochemical performance, and even quantification assays of the NMs or the NCs hybrid materials.

3 Introduction

Life in the twenty-first century is ever dependent on an unlimited variety of advanced materials. The term material may be broadly defined as any solid-state component or device that may be used to address a current or future societal need. For instance, simple building materials such as nails, wood, coatings, etc., address our need of shelter.

The main aim of material scientist is to overcome with new efficient and low cost methodologies for the preparation of novel materials. Taking that into account, the incorporation of nanomaterials (NMs) into bulk components has become a priority [1–4].

Nanostructured materials including nanoparticles, nanowires, nanobands, and carbon nanotubes (CNTs) have been intensively investigated due to their size-related features and special chemical and physical properties [5]. The size dependence of their properties has been focus of many studies like the one of Plieth *et al*., who studied the variation of the reduction potential [6].

Due to surface to volume ratio of nanoparticles (NPs), the high percentage of surface atoms introduces size-dependent properties. The finite size of the particle confines the spatial distribution of electrons, leading to quantized energy levels product to size scale. This fact is very important for semiconductor materials and optics. This effect is specially seen in nanocrystal, leading to major discoveries in solid-state physics. The relevance of nanotechnology is because of the special properties caused by the nanoscale, in which materials have new phenomena and properties (physical and chemical), different from the analogous at the macroscopic scale [7].

It is noteworthy that NPs can aggregate not only as a result of a further manipulation but also during their growth. A typical mechanism of aggregation is the Ostwald ripening which is a growth mechanism where small particles dissolve and are consumed by larger particles [8–11]. Thus, the average NP size increases with time, the particle concentration decreases, and their solubility diminishes.

The use of engineered NPs as a consequence of the emerging field of materials science and mainly of nanotechnology is a concern of environmental scientists worldwide. However, a few studies have already demonstrated the toxic effects of NPs on various organisms. Despite the extensive publications and studies involving nanotechnology, it is still in discovery phase in which novel materials are first synthesized in small scale in order to identify new properties and further applications [12–14].

NMs are now being manufactured and used in many products of different chemistry fields. However, our knowledge of the human health effects and environmental engineered nanomaterials or nanoparticles is incomplete [15]. Current legislation does not specifically address NMs or NPs, and there are concerns about nomenclature, defining nanomaterials as new substance under chemical regulations such as REACH, and the appropriateness of current test methods.

Generally, beneficial effects of NMs are well recognized, but the potential eco-toxicological effects and impacts on human health of NPs have so far received little attention. The high speed of penetration of NMs-based consumer products bring about the need for a better understanding about the potential impacts that nanoparticles may have on biological systems [16]. Some recent studies have shown that there are reasons to suspect that nanoparticles may display toxicological effects on biological systems [17]. Concerns on the effects of nano-sized particles on the human body and the environment are increasing recently. The high surface-to-volume ratio of nanomaterials makes them more reactive and potentially more toxic. Because they are more reactive, they may interact with other materials during disposal and recycling of nanoparticle-bearing composite materials. Others fear that NMs may cause new allergens, new toxic strains, and increased rates of nanoparticles absorption by the environment. So, an important feature regarding this is the performance of an appropriate characterization of these kinds of NMs after their application in nanotechnology.

Some aspects can be taken into account referring to NPs release and effects:

- NPs effects are scale dependent and not the same in larger scale or agglomerates. This means that effects may be quiet different to adopt specific and more appropriate regulations.
- These differences are based on size, surface chemistry, and other specific interactions depending on the scale. Thus, the same material may have different regulations through the different sizes presented.
- Effects must be conclusive to those products for which commercialization is imminent. So, the NPs presented in the final product may be the ones that the studies should focus on.

Therefore, the stabilization of NPs is specifically required to prevent their agglomeration and noncontrollable shape or size changes, and possible release to the environment. Regarding this fact, the use of supports (e.g., polymeric) for the preparation of hybrid nanocomposite materials (NCs) is one of the most common and efficient way to avoid the issue of the NPs stability [18–23]. Therefore, the appropriate preparation methodology of NCs can be established depending on how are the NPs incorporated to the supporting matrix [10, 24] (a) in situ synthesis or (b) ex situ synthesis with posterior incorporation of NPs.

In this regard, the increase of the safety of NMs is of particular importance. One way to prevent risk is the development of the environmentally safe NCs, for instance, the ones that consist in a functional polymer with immobilized functional NPs with tuned distribution in the supporting matrix, depending on the final application of the hybrid novel material, such as electrochemical assays, heterogeneous catalysis, or novel water treatment procedures [25].

In the last years, different types of nanomaterials have been developed, with different composition and morphology, which are in function of the application of interest, so their characterization by means of several techniques is of great importance. Due to these, this chapter describes the main characterization techniques used to determine the specific properties of materials within the nanoscale such as the determination of the molecular surface and electronic properties of the materials as well as their electrochemical behavior.

The best characterization tools provide valuable information about morphology, chemical composition, size, spatial distribution, electrochemical features, among others, with the less alteration of modification of the sample itself. Consequently, the application of in situ characterization techniques for the description of novel materials is needed. In this chapter, we describe the characterization techniques that have proved their suitability providing detailed information of NMs and NCs, such as field emission scanning electron microscopy, laser confocal microscopy, and cyclic voltammetry.

Moreover, the chapter is a powerful tool in the knowledge of nanomaterials and nanocomposite materials due to the incredible contribution of many authors who are experts in different disciplines. In addition, it could be used as a handbook to check and employ several characterization and visualization techniques, making the chapter of great interest to both research and academic fields.

4 Experimental and Instrumental Methodology

4.1 Scanning Electron Microscopy and Transmission Electron Microscopy

Scanning electron microscopes (SEM) coupled with an energy-dispersive spectrometer (EDS) Zeiss EVO MA 10 and Zeiss MERLIN FE-SEM and transmission electron microscope (TEM) studies were carried out using JEOL 2011 and JEOL 1400. SEM and TEM techniques were used to obtain the metal concentration profiles across the cross-section of the FMNPs containing materials, to characterize the morphology of the polymer surface and for determination of FMNPs diameters. Samples were prepared by embedding several granules in the epoxy resin followed by cutting with a ultramicrotome (Leica EM UC6) using a 35° diamond knife (Diatome) at liquid nitrogen temperature (−160 °C).

4.2 Scanning Transmission Microscopy

(S)-TEM images were obtained using FEI Tecnai F20 S/TEM from the electron microscopy facilities of Institut Català de Nanociència i Nanotecnologia (ICN2). This device offers high-resolution imaging, down to atomic scale, of the structure and morphology of samples in TEM and STEM modes up to 200 kV operating voltage. Moreover, the chemical analysis at nanometer level and chemical mapping via energy dispersive X-ray spectroscopy (EDS) can be achieved.

4.3 Confocal Microscopy

Samples were mounted on bottom-glass culture dishes (Mat-Tek Corp., Ashland) and were examined using a TCS-SP5 (Leica Microsystems, Heidelberg, Germany) confocal laser scanning microscope located in microscopy facilities of Universitat Autònoma de Barcelona. Fluorescence emission spectra were obtained using a 63 objective with an excitation wavelength of 405 nm for all spectra. Recording data has a wavelength range from 425 nm to 775 nm with a band width of 10 nm and a spectral resolution of 7 nm.

4.4 Electrochemical Characterization of Nanocomposite Sensor Materials

Electrochemical impedance spectroscopy (EIS) measurements are performed in a 0.1 M KCl solution containing 0.01 M $[Fe(CN)_6]^{3-}/[Fe(CN)_6]^{4-}$ under quiescent condition. The impedance spectra were recorded in the frequency range 0.1 Hz to 100 kHz at the redox equilibrium potential. The equilibrium potential of each electrode evaluated has been obtained by cyclic voltammetry measurements.

The signal amplitude to perturb the system is 10 mV. The electrochemical parameters (ohmic resistance, R_Ω; charge-transfer resistance, R_{ct} and double-layer capacitance, C_{dl}) are obtained by fitting the data obtained to an equivalent circuit, which is sufficiently suitable to interpret the RΩ, Rct, and Cdl values in terms of interfacial phenomena that occur at the electrochemical cell.

Cyclic voltammetry (CV) was performed in a 0.1 M KCl solution containing 0.01 M of the benchmark $[Fe(CN)_6]^{3-}/[Fe(CN)_6]^{4-}$ redox couple under quiescent condition. Measurements are carried out at 10 mV/s of scan, using a potential range from −1.5 V to 1.5 V.

5 Key Research Findings

5.1 In Situ Characterization of Metal–Polymer NCs with Feasible Bactericide and Catalytic Applications

The system NP-polymeric support shows a series of interactions that lead to the increase of their stability, reducing the possibility of release and consequently decreasing the environmental impact of NMs when present in hybrid NCs materials. This can be explained by the increase of viscosity of the immobilizing support matrix and the decrease of the energy of particle-particle interaction in NPs systems regarding the NMs prepared in solution. Figure 8.1 presents the schematic stability offered by the host polymer matrix to the NPs to reduce the risk of release [26].

The modification polymeric matrices such as ion exchangers with NMs can be carried out by using the intermatrix synthesis (IMS) technique coupled with the Donnan exclusion effect (DEE). Such combination allows for production of polymer-metal NCs with the tuned distribution of NPs, for example, near the surface of the polymer what appears to be the most favorable in their practical applications [25, 27–31].

IMS technique is an efficient and simple methodology for the in situ preparation of metal-polymer bifunctional nanocomposites. The general principles of IMS apply to all types of matrices (polymeric or not) with ion exchange functionality and for different types of FMNPs.

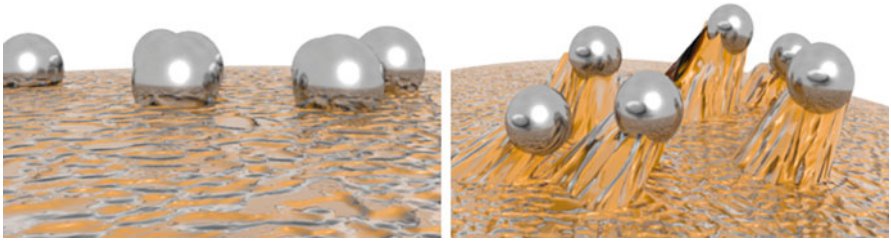

Fig. 8.1 NPs stabilized by a polymeric support within a NC (left) that offers mechanical resistance (right) to reduce the risk of NMs release

The main requirements for an ion exchange matrix to be used as a support for the IMS technique include: [22, 25]

- The matrix must be chemically compatible with the FMNPs surface.
- It bears a charge due to the presence of well-dissociated functional ion exchange groups. This requires a preconditioning acid–base and NaCl treatment of the supporting matrix before IMS technique that usually results in the Na^+-form for cationic exchangers and the Cl^--form for anionic exchangers.
- The functional groups act as nanoreactors.
- Appropriate distances between the functional groups, in order to avoid agglomeration of FMNPs due to steric effects on the surface.
- Sufficient flexibility of the polymer chain segments to facilitate movements of ionic carriers.
- Appropriate swelling ratio of the matrix.
- Adequate hydrophilicity: as IMS is an environmentally friendly methodology that is carried out in aqueous media.

Regarding these points, the matrix acts as nanoreactors for the NPs and provide a confined medium for the synthesis controlling particle size and distribution. Moreover, stabilizes and isolates the generated NPs, preventing their aggregation.

5.1.1 Characterization of the Enhanced Spatial Distribution of Pd and ag NPs in NCs

DEE refers to the impossibility to penetrate deeply in a matrix when there is a coincidence between the charge of the outside ions (e.g., from the reducing agent) and the ones of the functional groups on the polymer surface. Thus, an equilibrium between ion concentration (either functional groups or from metal or reducing agent solution) and electrostatic repulsion takes place.

Coupling IMS with DEE [11, 32, 33] predicts that the use of negatively charged reducing agents such as $NaBH_4$, leads to the location of the NPs mainly on the surface of the supporting matrix due to the electrostatic repulsion between the BH_4^- and the functional groups of the matrix (negatively charged as well).

Anion Exchange Matrices as Support for NCs Prepared by Intermatrix Synthesis

Considering the case of anion exchange matrices and the IMS of Pd-NPs, the first stage of IMS coupled with DEE is the sorption of the reducer anions on the positively charged functional groups [18, 34, 35] of the matrix (Eq. 8.1). The second stage (Eq. 8.2) is the treatment of the polymer with solution of positively charged metal ions. Their rejection by the matrix bearing the charge of the same sign does not allow them to deeply penetrate into the polymer, and their interaction with reducing agent proceeds (as in the previous case) near the surface of the support.

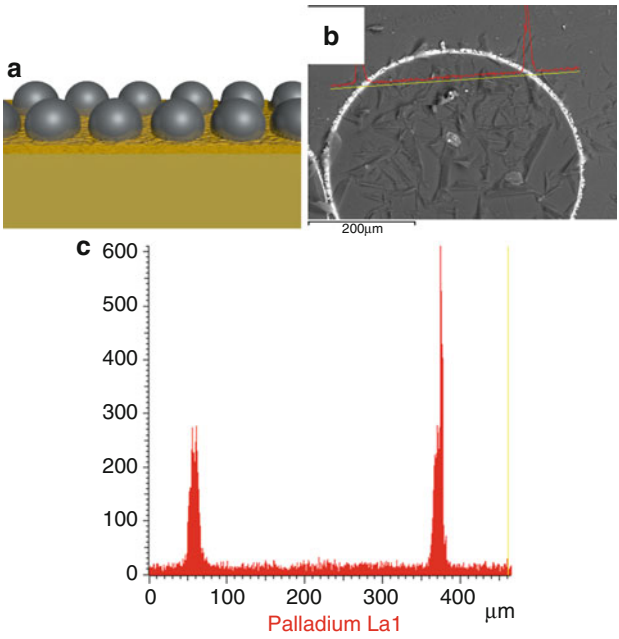

Fig. 8.2 (**a**) Schematic representation of NPs distribution on NC materials due to DEE and IMS technique. (**b**) SEM image of cross section of Pd-NPs on an anion exchange resin and (**c**) EDS line-scan of indicated zone in B, showing that Pd-NPs are mainly located on the surface of the granulated polymer

$$R-(R_4-N)^{+}Cl^{-}+NaBH_4 \rightarrow R-(R_4-N)^{+}BH_4^{-}+NaCl \tag{8.1}$$

$$R-\left(R^{'}{}_4-N\right)^{+}BH_4^{-}+\left[Pd(NH_3)_4\right]Cl_2+6H_2O \rightarrow (R_4-N)^{+}Cl^{-}\,Pd^0+7H_2+2B(OH)_3+4NH_3 \tag{8.2}$$

Figure 8.2 shows the feasible customized distribution of Pd-NPs on an anionic exchange resin, prepared by IMS [35]. This tuned distribution is particularly important in practical application of such materials for complex water treatment. Note that similar procedure has been also applied for the synthesis of metal oxide nanoparticles inside ion exchange resins for removal of arsenic from water [36] and for the preparation of heterogeneous catalysts [35].

As shown in Fig. 8.2, **chemical mapping** by energy sispersive X-ray spectroscopy (EDS) can be achieved in order to obtain the spatial distribution of the Pd-NPs by the differentiation of chemical composition within the NC material. In this case, it is clearly observed how the Pd-NP content is mainly located on the surface of the nanocomposite material, as the synthetic route intended to.

EDS analysis requires high voltage (in the case of Fig. 8.2, from SEM). But when the study of this kind of NC materials is carried out in field emission SEM (FE-SEM)

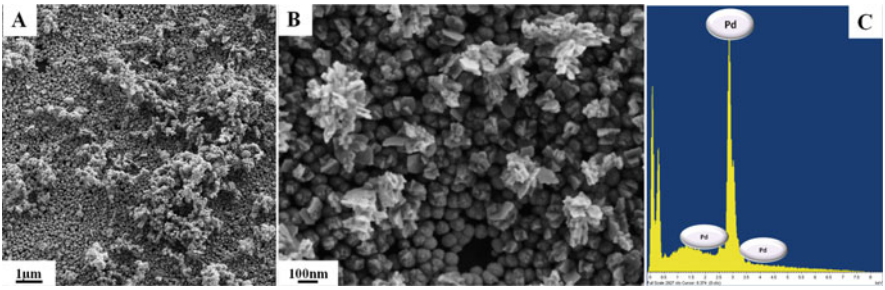

Fig. 8.3 (**a** and **b**) present FE-SEM of Pd-NPs on anion exchange polymer, obtained at 4 kV voltage. (**c**) presents the corresponding EDS spectra of (**b**), showing that the chemical identity of the NPs corresponds to Pd. Magnification of (**b** ⋙ **a**)

instrumentation, as Zeiss® Merlin, it can be combined with a fast change of voltage in order to obtain high resolution images of the NPs and then proceed with the composition analysis, as shown in Fig. 8.3.

SEM images of the surface of NCs granules present the morphology change of the polymer surface due to the formation of fractal-like structures (Fig. 8.3b). In this case, the formation of Pd-NP fractals on the surface of polymer can be explained by the action of diffusion limited aggregation (DLA) mechanism [37]. Moreover, it can be observed the presence of spherical Pd-NPs dispersed over the surface of the polymeric support, which allows enhanced performance for catalytic assays.

The efficiency of these Pd-NPs on anion exchange materials as heterogeneous catalysts were successfully tested for Suzuki cross coupling reaction (SCCR), for which Pd catalysts are known to be suitable catalysts for this reaction, with applicability to the synthesis of fine chemicals [10, 19, 29, 38, 39].

Cation Exchange Matrices as Support for NCs Prepared by Intermatrix Synthesis

Intermatrix synthesis of Ag-NPs on cation exchange polymer resin can be tuned in order to obtain different NPs concentration profiles over the final added value NC material. This can be achieved by the selection of different reducing agents during the NPs formation stage of IMS.

Characterization of Ag-NPs on Gel-Type Cationic Polymeric Matrix with Formaldehyde as Neutral Reducing Agent

The preparation of Ag-NPs on a gel-type cationic polymeric resin using formaldehyde as neutral reducing agent is presented in Eqs. 8.3 and 8.4:

$$R - SO_3^- \, Na^+ + Ag^+ \rightarrow R - SO_3^- \, Ag^+ + Na^+ \tag{8.3}$$

$$\begin{aligned} 2R - SO_3^- \, Ag^+ + CH_2O + H_2O \rightarrow 2R \\ - SO_3^- \, Na^+ \, HCOO^- + 3\,H^+ + 2Ag^0 \end{aligned} \tag{8.4}$$

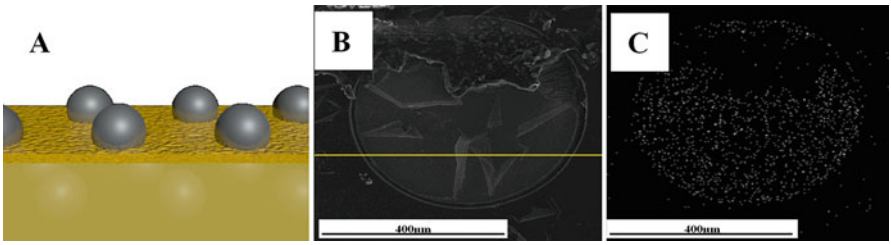

Fig. 8.4 (**a**) Schematic representation of NPs distribution on NC materials due to DEE and IMS technique when using a neutral reducing agent. (**b**) Cross section of Ag-NPs containing nanocomposite with the corresponding EDS element mapping on C. (**c**) Shows the interior distribution of Ag-FMNPs due to IMS with formaldehyde as reducing agent

Equation 8.3 shows the typical NPs–precursor loading stage, in this case of silver ions due to the exchange of Na^+ to Ag^+. Consequently, Eq. 8.4 presents the formation of Ag-FMNPs. The silver content in the final NCs was found to be 159 mg Ag × g^{-1} NC, which corresponds to 70% efficiency of silver loading during stage 1.

In order to confirm the Ag-NPs intern distribution in the gel-type polymer, SEM characterization and EDS analysis were performed to the samples. As it can be seen in Fig. 8.4, the element mapping and the LineScan EDS analysis verify this. Moreover, distribution is consistent and conclusive of DEE influence during the appearance of the NPs in the second stage of IMS.

The control of the NPs distribution (size and interparticle distance) makes valid the idea of incorporating these NPs in the interior of a stabilizer matrix. In order to achieve this, some researchers have used a methodology very similar to IMS. For example, the preparation of NC microspheres containing Ni-NPs can be accomplished via chemical surface modification [40, 41].

Characterization of Ag-NPs on Gel-Type Cationic Polymeric Matrix with $NaBH_4$ As Negatively Charged Reducing Agent

Equations 8.5 and 8.6 show the example of IMS stages for the synthesis of Ag-NPs on a sulfonic cationic exchanger.

Metal loading stage:

$$R - SO_3^- Na^+ + Ag^+ \rightarrow R - SO_3^- Ag^+ + Na^+ \tag{8.5}$$

Metal reduction stage:

$$\begin{aligned} R - SO_3^- Ag^+ + NaBH_4 + 3H_2O \rightarrow R \\ - SO_3^- Na^+ + 7/2H_2 + B(OH)_3 + Ag^0 \end{aligned} \tag{8.6}$$

After finishing the metal reduction the functional groups of the supporting matrix appear to be converted back into the initial ionic form (Na-form). This means that complete IMS cycles can be repeated without any additional pretreatment of the ion

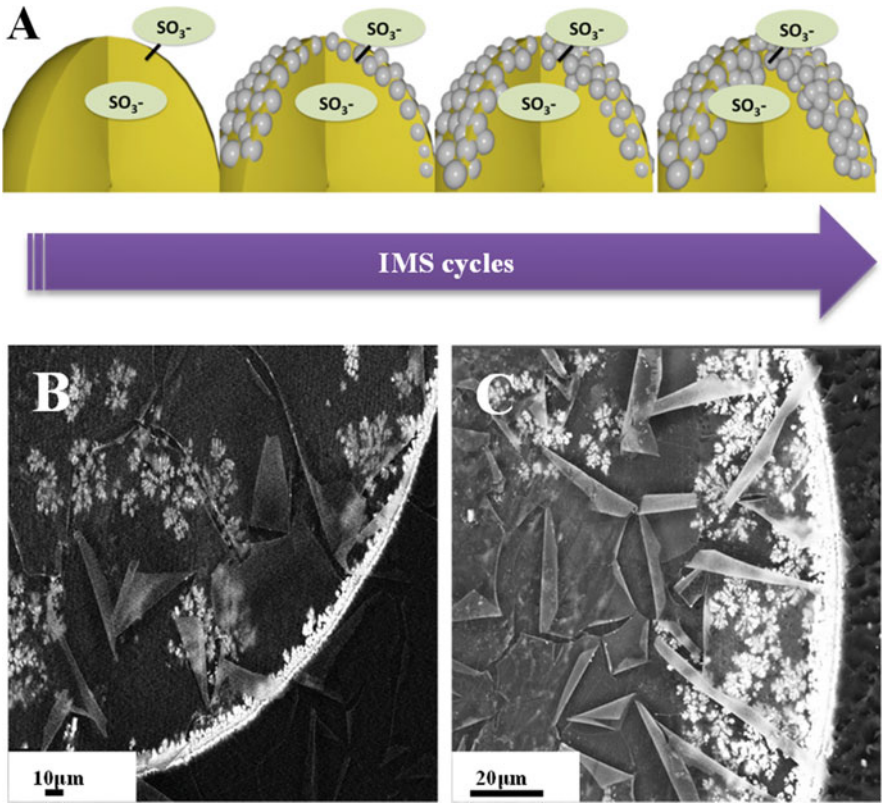

Fig. 8.5 (**a**) Schematic representation of the increase of Ag-NPs layer consecutive IMS cycles, (**b** and **c**) present actual SEM images of cross section samples of Ag-NPs containing composites, where the white zones verify the location of the NPs mainly on the surface and the thickness increase

exchanger [35, 42, 43]. This could result in the accumulation of a higher amount or increase of the thickness of the NPs when the same metal precursor is used, as presented in Fig. 8.5.

As it is seen from Eq. 8.6, the negatively charged borohydride anions cannot deeply penetrate into the polymeric matrix bearing the charge of the same sign due to the action of DEE. As a result, the reduction of Ag ions leading to the formation of Ag-NPs proceeds near the surface of the polymer. Finally, the increase of Ag-NPs layer thickness in the NC showed in Fig. 8.5 can be also tuned by changing the time of the metal loading stage, and consequently customize the NP content in the final hybrid material [25, 43]. Consequently, this fact could lead to the preparation of efficient bactericide layer with the minimum quantity of NPs and with the most favorable distribution for novel bactericide materials, with lower production cost and time [42].

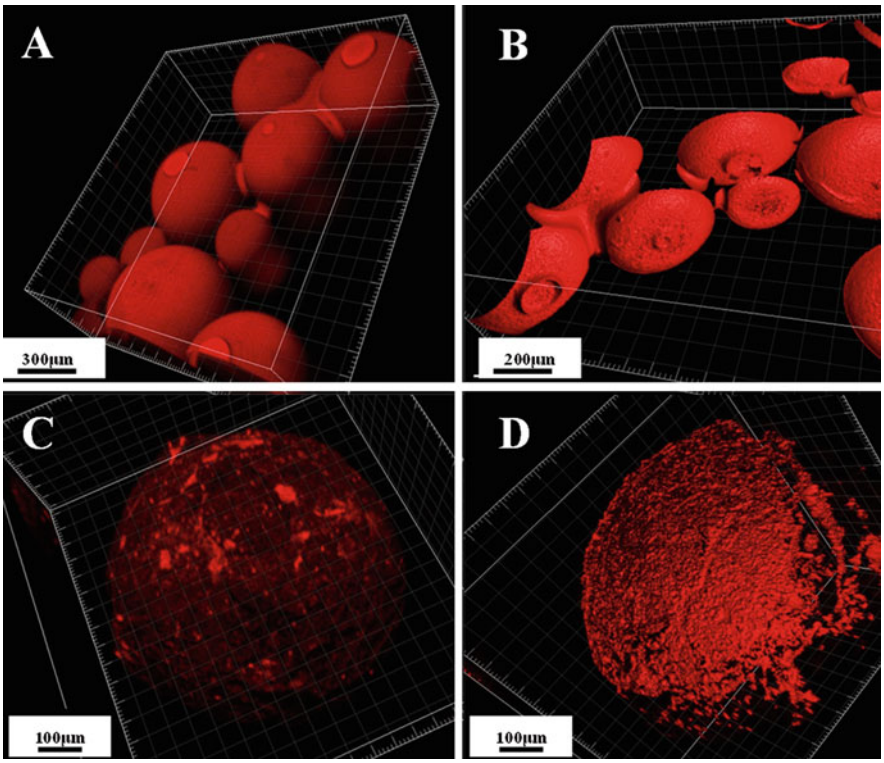

Fig. 8.6 Laser confocal microscopy 3D images from (**a** and **b**) raw polymer material with smooth surface and (**c** and **d**) Ag-NPs nanocomposite after IMS, showing the increase of roughness on the surface due to the presence of nanoparticles

5.1.2 Surface Characterization and Morphology of NCs Modified with Silver Nanoparticles

The incorporation of NPs in a nanocomposite material can greatly influence in the final properties of the hybrid materials. Moreover, the interaction of these NPs can promote surface morphological changes in polymeric supports [44 and 45]. Thus, considering the abovementioned case of Ag-NPs on cationic exchangers, Fig. 8.6 presents the surface change of a gel-type polymer due to NPs, obtained by laser confocal microscopy.

FE-SEM analysis of these Ag-NPs containing NCs showed clearer morphological changes (Fig. 8.7). These morphological changes are associated with the inter-polymer mechanical stress, resulting from a strong interaction between Ag-NPs and the gel-type polymer chains [27]. These NPs present an average diameter of 17 ± 1 nm. The appearance of nanoporosity results, in turn, in increase of the internal surface area, which can be one of the factors explaining the excellent performance of these NCs in bactericide assays [42, 43].

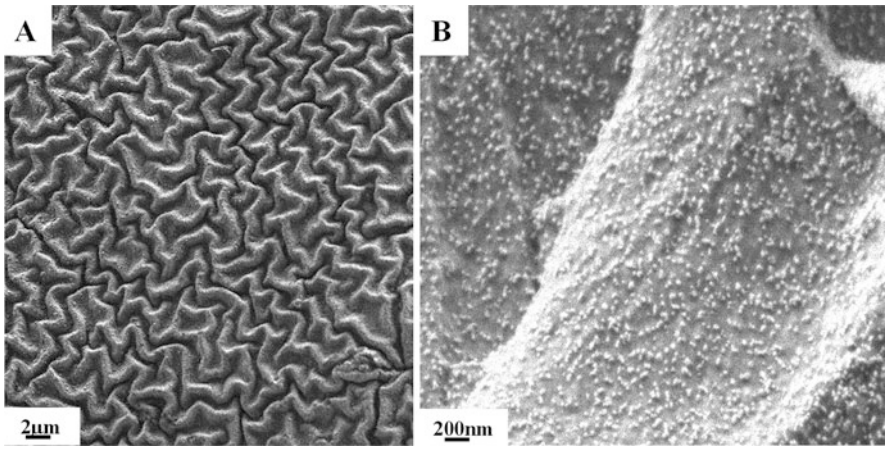

Fig. 8.7 FE-SEM images of (**a**) increase of roughness on polymer surface due to the appearance of Ag-NPs with no evident agglomerates, as (**b**) shows well spatial distribution of NPs over the surface with increased magnification

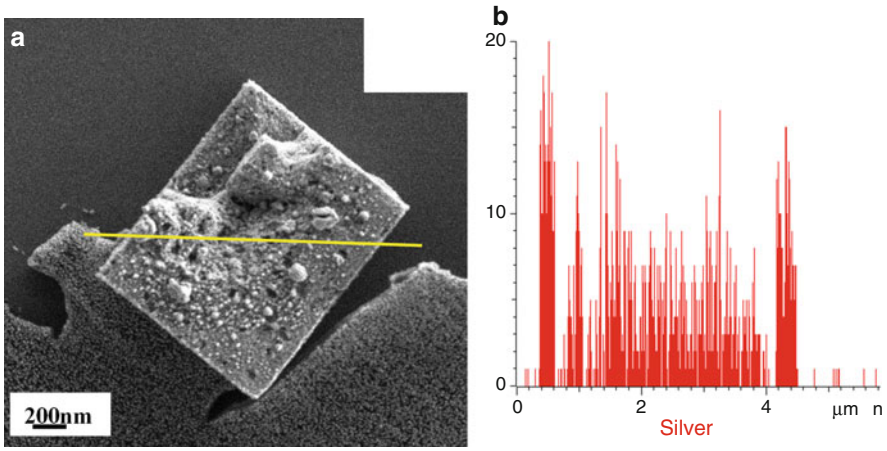

Fig. 8.8 FE-SEM images of Ag microstructures (**a**) and corresponding EDS LineScan, (**b**) showing chemical composition

IMS on this cation exchanger gel–type polymer produces well-distributed Ag-NPs with no evident agglomerates. In addition to the appearance of nanoporosity on the surface of this gel-type polymers, some regular shape define silver nano- and microstructures were found with further FE-SEM characterization. This fact summed to the morphological surface changes, and the stabilization offered by the matrix itself may explain the feasibility of this technique to obtain well-defined silver structures shown in Fig. 8.8.

5.2 In Situ Characterization of Nanomaterials: Multiwalled Carbon Nanotubes, CdS Quantum Dots, and Au Nanoparticles

5.2.1 Carbon Nanotubes Modified with CdS Quantum Dots

The modification of carbon nanotubes (CNTs) with quantum dots can be achieved by activating their surface with an appropriate acidic treatment. This treatment enhances the ion exchange suitability of CNTs. Consequently, IMS of QDs can be carried out by firstly carrying out the loading of the functional groups with QDs precursor, while the second one includes the formation of QDs by precipitation reaction (instead of reduction). IMS can be described for the case of multiwalled CNTs (MWCNTs) as follows: [25, 30]

$$2[\mathrm{MWCNTs} - \mathrm{COO}^{-}\ \mathrm{Na}^{+}] + \mathrm{Cd}^{2+} \rightarrow [\mathrm{MWCNTs} - \mathrm{COO}^{-}]_2\ \mathrm{Cd}^{2+} + 2\mathrm{Na}^{+} \tag{8.7}$$

$$[\mathrm{MWCNTs} - \mathrm{COO}^{-}]_2\ \mathrm{Cd}^{2+} + \mathrm{Na}_2\mathrm{S} \rightarrow 2\ [\mathrm{MWCNTs} - \mathrm{COO}^{-}\ \mathrm{Na}^{+}] + \mathrm{CdS}\downarrow \tag{8.8}$$

After the QDs formation reaction on the MWCNTs surface, the functional groups appear to be regenerated, as they are converted back into the Na^+ form. This means that the QDs formation cycle can be repeated again by using both equations without any additional pretreatment of CNTs. This allows for accumulation of the desired amount of QDs on the surface of MWCNTs as seen in Fig. 8.9.

In this case, for the characterization of QD-MWCNTs, it was needed to carry it out by the combination of scanning and transmission microscopy in the STEM device. In this sense, the resolution of the techniques arrives to the nanoscale order. Moreover, chemical composition if realizable from the image (Fig. 8.9b), as the white zones reveal higher atomic weight composition in contrast to darker zones. Thus, what it seemed to be a nonloaded CNT (Fig. 8.9a), the implementation of

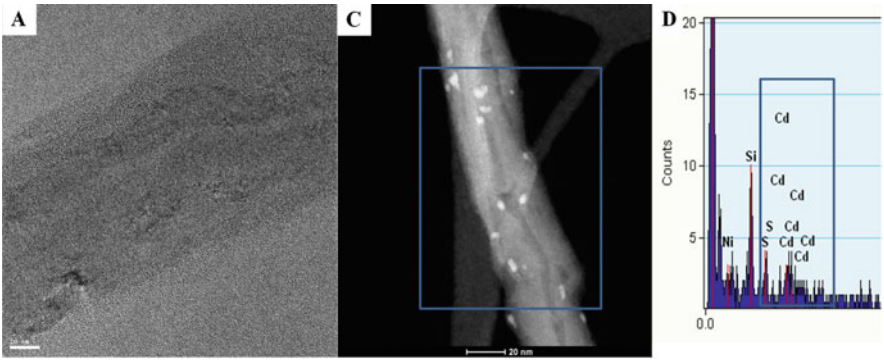

Fig. 8.9 TEM (**a**) and S-TEM (**b**) characterization of MWCNTs with CdS-QDs, with the corresponding EDS chemical mapping, showing the presence of Cd

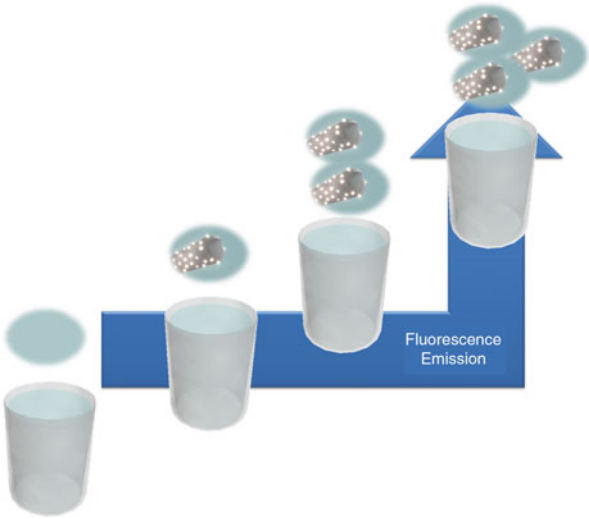

Fig. 8.10 Schematic representation of proportional fluorescent response of QDs for the calculation of CNT concentrations in water [50]

STEM characterization evidence the presence of CdS-QDs is 2.3 ± 0.4 nm well distributed over the surface of the support.

QDs are known to present quantum confinement effects during light excitation, which gives them interesting optical and semiconducting properties. Tuning these features and coupled them with its surface modification or using them for the surface modification of these reactive surfaces led to explore the application of these hybrid material to the field of sensors (fluorescent and biosensors) and to bioassays [46–49]. Due to these interesting features, the incorporation of fluorescent QDs into nanocomposite materials could lead to the design of in situ determination protocols for nanomaterials. For instance, the fluorescence emission of CdS–QDs on MWCNTs showed to be proportional to the amount of CNTs loaded with them [50], as schematically presented in Fig. 8.10. These results open the way for novel analytic procedures for using optic response of different nanomaterials for the autodetection in different environments as, for example, the use of auto fluorescent Ag and Au–NPs or even fluorescent nanodiamonds for biosensing purposes [51–55].

5.2.2 Characterization of Au-NPs Nanoparticle Based Biosensors for Theranostic Applications

Nanoparticles play an important role in current sensing and biosensing technologies. These materials are showing improvement of the performance of biosensing systems in general (i.e., proteins, cells, heavy metals) and that of electrochemical sensing devices particularly. In addition to the biosensing applications, the use of these, as carriers of biomolecules and their application in biomedical and nutritional technologies, between others, is an emerging research field in the last years. It is well known that NPs exhibit physical properties that are truly different from both small molecules and bulk material [56–60]. Au-NPs have been extensively proposed for applications

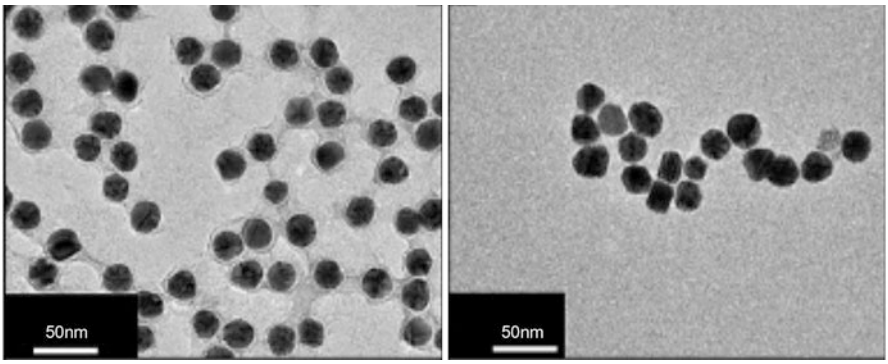

Fig. 8.11 (**a**) TEM image (after negative staining pretreatment) obtained for a CGP/Au-NPs suspension prepared following the experimental procedure detailed at methods section (left) and (**b**) An unmodified Au-NPs suspension (right)

in several fields such as the environmental and the food/agriculture one, being especially relevant their application for biomedical and therapeutic purposes [61].

Merkoçi et al. [62] worked on the design of Au-NPs, as both carriers/electrocatalytic labels, with the properties of k-casein derived peptides to bind specific bacterial fimbriae adhesions. These peptides-modified nanoparticles are used for the evaluation of the interaction between the peptides and the K88 fimbriae bacteria (K88) and found with interest for future potential applications not only for biosensing purposes but also for therapeutic applications. Such theranostic platform can also be extended to other biotechnological applications, including food, health, and pharmaceutical fields.

In order to check the Au-NPs surface modification after the conjugation, these suspensions were evaluated followed by TEM analysis using a negative staining pretreatment. Negative staining is an established method, often used in diagnostic microscopy, for contrasting a thin specimen with an optically opaque fluid. Typical stainers are ammonium molybdate, uranyl acetate, uranyl formate, phosphotungstic acid, osmium tetroxide, osmium ferricyanide, or auroglucothionate because they scatter electrons well and easily adsorb onto biological matter. Due to these properties, this method is used to view viruses, bacteria, bacterial flagella, biological membrane structures, and proteins or protein aggregates, which all have a low electron-scattering power. For this reason, this sample pretreatment was chosen in order to observe the presence of the peptides around the Au-NPs in the prepared conjugates. Under these optimum conditions, a good Au-NPs dispersion along with a "dark shadow" around them is noticed, as can be observed in Fig. 8.11 left; this shadow is not observed for the unmodified Au-NPs (Fig. 8.11, right).

As detailed in methods section, first of all different CGP peptide concentrations and different CGP/Au-NPs conjugation ratios were assayed. A summary of the TEM images obtained under these different conditions and the proposed conjugate configurations are shown in Fig. 8.12 finding that the optimum conditions corresponded to a CGP concentration of 0.01 mg/mL and a CGP:Au-NPs concentration ratio of 3:1.

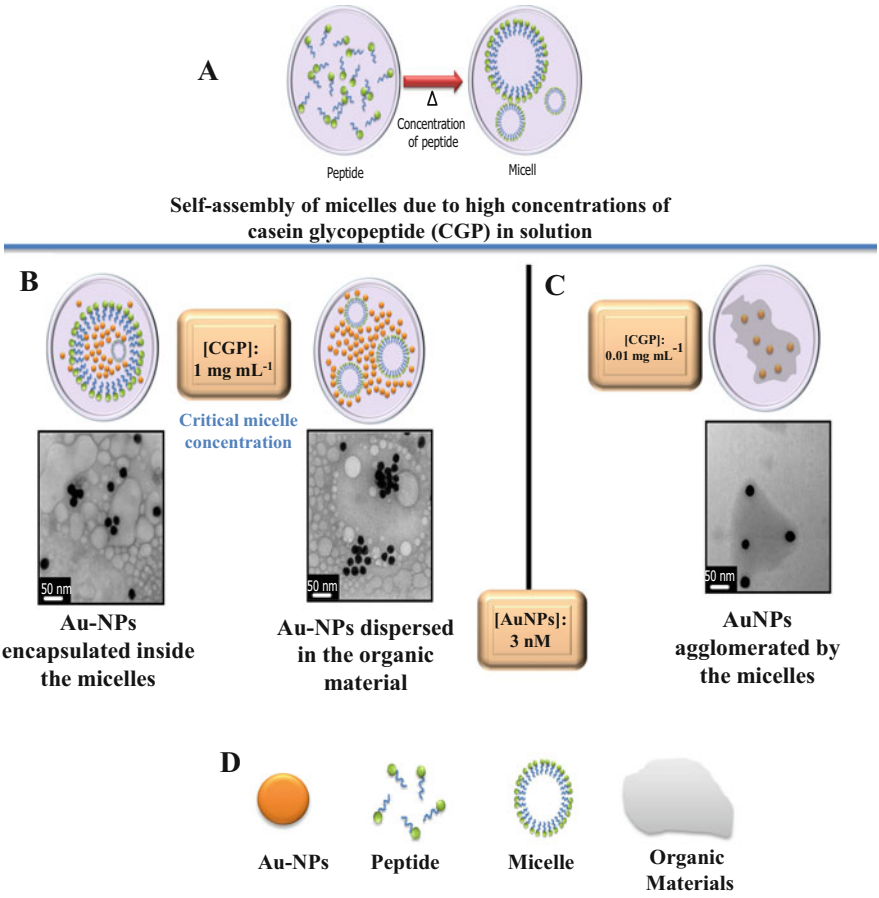

Fig. 8.12 Schematic representation of the proposed CGP/Au-NPs configurations and the corresponding TEM images (obtained after negative staining pretreatment). (**a**) Scheme of the self-assembly of micelles due to high concentrations of CGP in solution (1 mg/mL). At this high concentration in solution, the Au-NPs can be either agglomerated by the presence of the micelles (**b**-left) or encapsulated inside the micelles (**b**-right). However, for lower CGP concentrations (0.01 mg/mL) the Au-NPs are well dispersed and the organic material (the "dark shadow") seems to cover the Au-NPs (**c**). Definitions of the images symbol in (**d**)

Under these conditions, the agglomeration induced by micelles as well as the encapsulation of the Au-NPs inside the micelles are avoided (both phenomena are observed for higher peptide concentrations).

Once the peptide/Au-NPs conjugates were formed, their interaction with a fimbriated *E. coli* (K88) was evaluated. As explained before, it is known that some peptides such as k-casein derived ones (this is the case of CGP and CGMP-10) are potential inhibitors of bacterial adhesion to intestinal mucous, being this of potential application in nutritional treatments in order to avoid serious digestive affections, mainly thanks to their ability to bind cholera and *E. coli* enterotoxins. The study

finally showed that the Au-NPs can be easily loaded with k-casein derived, driven toward fimbria bacteria and electrochemically detected distinguishing the fimbriae (K88) from nonfimbriae (NF) bacteria [62].

5.3 Electrochemical Characterization of Graphite–Epoxy–Enzyme and Graphite-Epoxy-Metal Nanoparticles (Bio) Nanocomposite Sensors

5.3.1 Characterization and Optimization: An Important Feature for the Development of Nanocomposites Sensors for Glucose Determination

Electrodes based on nanocomposites can be defined as the result of combining two or more different materials in solid phase where, at least, one of the constituent parts has a nanometer scale dimension [63]. In addition, these (nano)materials do not lose their individual identities but still impart their properties to the product resulting from their combination. Building blocks with dimensions in the nanosize range enable us the possibility to design and develop new materials with unprecedented versatility and improvement in their physical and chemical properties.

Among the wide range of nanocomposites, the development of nanocomposites based on conductive phases dispersed in polymeric matrices has led to important advances in electronics and electrochemistry. In general, nanocomposite materials based on different forms of carbon nanostructures as conductive phase (such as graphite, carbon nanotubes, and graphene) have played a leading role in the analytical electrochemistry field, particularly in sensor devices due to their interesting advantages as easy surface renewal or low background current, among others. Regarding electrodes based on these conductive materials, the exposed carbon area is lower than the electrode geometric area, where a part of the space is occupied by the insulating matrix (polymer), producing conducting and non-conducting areas on the surface. Since the capacity of the electrode or electrical conductivity is measured almost exclusively by the amount of exposed carbon on the surface, the background current resulting from this capacity is less than what would be expected by the geometric area of the electrode, usually in one or more orders of magnitude.

On the other hand, conductive properties of the nanocomposites depend on the nature of each component, amount of conducting material, or conductive particle loading and their distribution. Moreover, there is a direct relationship between the nanocomposite electric conductivity and the amount of conductive material. So, an important feature is performing a previous characterization of these kinds of materials in order to obtain the optimal composition which provides the best electrochemical properties for their analytical application as an electrochemical transducer. Consequently, the electroanalytical properties of these electrodes based on nanocomposites are improved such as detection limit, sensitivity, stability, and reproducibility.

Up to now the principle applied to the optimization of the composite proportions has been done using the percolation theory, under the criteria of maximizing the

conductive particle loading, without losing its physical and mechanical stability, but without taking care if the composite provides the best electroanalytical characteristics of response [64]. Recently, it has established new alternative strategies of characterization which demonstrates that if the composite proportions are optimized the response of the electrode is improved [65] in terms of the signal-to-noise ratio which has a direct relationship with the limit of detection. The characterization and optimization of the electrochemical properties as function of the conducting particle loading of these nanomaterials can be evaluated using powerful electrochemical techniques such as electrochemical impedance spectroscopy (EIS) and cyclic voltammetry (CV). EIS measurements provide, in an easy way, information about the electron-transfer rate, double-layer capacitance, contact resistance, and resistance of the solution. The electrochemical properties required by a transducer are high electron-transfer rate, the lowest double-layer capacitance, and ohmic resistance in order to guarantee the optimal electroanalytical characteristics of the electrode response as high sensitivity, a high signal/noise ratio, and low detection limits. Consequently, by EIS technique it is possible to determine the optimal composite composition that exhibits these improved electroanalytical properties. These results can also be complemented with voltammetric measurements, which provide information about the charge-transfer resistance and electrode active area. Moreover, by CV measurements it is possible to evaluate the reversibility of the process.

Recently, the electrochemical properties of the bio-nanocomposites as a function of the conductive particle and biological charge material present on the transducer matrix have been studied [66]. In this work, two series of eight different graphite-epoxy compositions have been constructed by varying the graphite loading from 13% to 20% (w/w) and the amount of glucose oxidase (GOD) was 1% and 2% (w/w), respectively. The optimization of the conductive particle distribution and the amount of the biological material inside the biomaterial has allowed an improvement of the electrochemical properties, regarding the electroanalytical properties such as signal stability and limit of detection. The high signal-to-noise ratio obtained in the electrochemical transduction has allowed enhancing the limit of detection of the biosensor. In the present study, it has been demonstrated the feasibility of EIS and CV for the characterization and optimization of biosensors based on graphite–epoxy–enzyme, using an enzyme model.

Figure 8.13a, b show the cyclic voltammograms obtained for the different graphite compositions and amount of GOD (1% and 2% (w/w)). As it can be observed, an increase on the graphite loading in the bio-nanocomposite electrodes allow obtaining well-defined peaks, and an increase on the current intensity value is achieved. This behavior is obtained for both GOD compositions. It can be observed that electrodes from 13% to 17% of graphite, the oxidation and reduction peaks are more separated. The obtained voltamperograms present behavior more similar to a microelectrode array where the radial diffusion is the predominant [67]. Compositions with higher graphite loading (20%), the voltamperograms showed oxidation and reduction peaks closer and the curves obtained present similar shape to a macroelectrode, where the mass transport is controlled by the lineal diffusion.

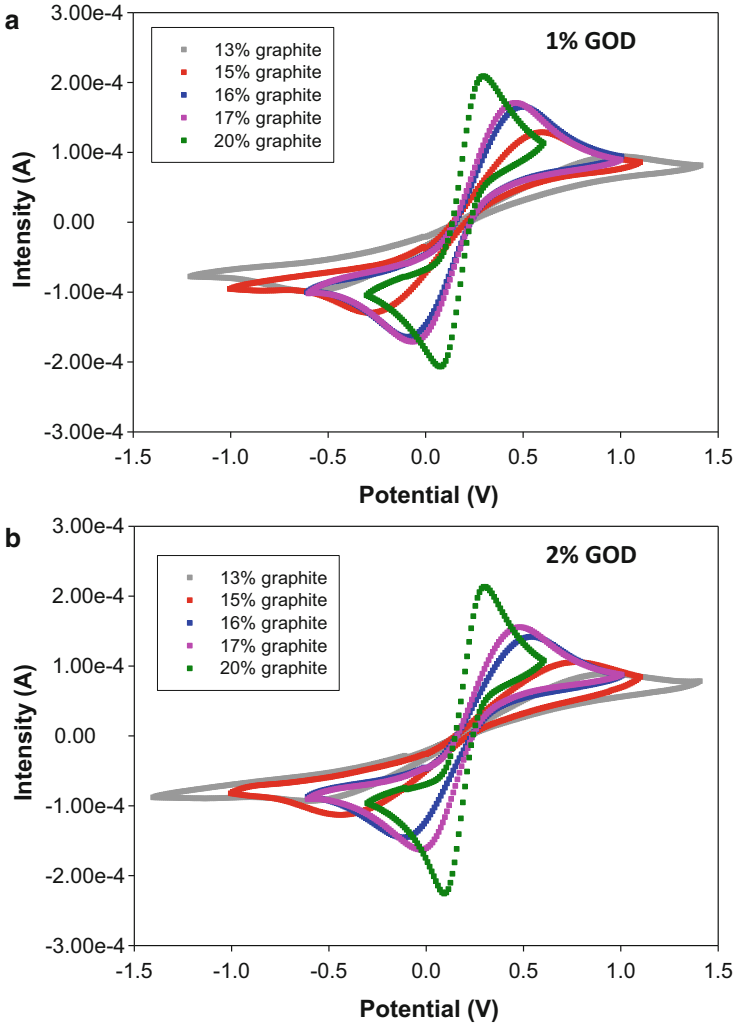

Fig. 8.13 Cyclic voltammograms for Bio-nanocomposites electrodes with different amount of graphite loading and both GOD compositions evaluated: (**a**) 1% of GOD and (**b**) 2% of GOD. Measureaments were carried out using 0.01 M ferricyanide/ferrocyanide and 0.1 M KCl. Scan rate 10 mV/s

According to the results obtained on the electrochemical characterization, the optimum bio-nanocomposite proportion based on graphite–epoxy which incorporates the enzyme glucose oxidase (GOD) on the matrix ranges between 16% and 17% of graphite for both enzyme compositions, 1% and 2% of GOD. The optimized bio-nanocomposites presented enhanced electroanalytical properties of response compared to the nonoptimized electrodes, both limit of detection and

Table 8.1 Analytical performance comparison of nanobiocomposites sensors for glucose determination

% Graphite (2% GOD)	Sensitivity ($\mu A \cdot L \cdot mmol^{-1}$)	Detection limit (mM)	Ref.
16% graphite loading	0.210	0.046	[66]
17% graphite loading	0.231	0.035	[66]
Nonoptimized composition (18% graphite loading)	0.100	0.100	[68]

sensitivity (see Table 8.1), with the same enzyme proportion. So, it is important to highlight that these results showed that in order to obtain low limit of detection the amount of graphite loading is more critical than the enzyme loading in bio-nanocomposites.

Moreover, these strategies of characterization and optimization have been recently applied for bio-nanocomposites based on graphite-epoxy which incorporates on the matrix IgG [69]. The electrochemical characterization has allowed the improvement of the electroanalytical properties of response of the bio-nanocomposites and, therefore, it has been possible to reduce the antigen-antibody ratio used on the competitive assay. Compositions between 16% and 17% of graphite loading present lower ohmic resistance, charge-transfer resistance, and double-layer capacitance values. In this case, with optimized bio-nanocomposites it is possible to reduce the GaRIgG concentration from 0.33% (w/w) (conventional composition used in this assay with non-optimized electrodes [70]) to 0.017% (w/w). Under these experimental conditions, optimized bio-nanocomposites (16% and 17% of graphite loading) sensors allow detecting IgG concentrations of 6.9 ng/mL and 1.4 ng/mL, respectively. Nonoptimized electrodes (20%) cannot achieve these concentrations of IgG detection under these experimental conditions.

On the other hand, EIS has been used in other electrochemical application for the characterization of (bio)nanocomposites. For example, on the literature it has been reported by Li et al. [71]. In this work, a novel label-free electrochemical impedance immunosensor was fabricated based on bovine serum albumin-nitidine chloride-reduced graphene oxide (BSA-NC-rGO) nanocomposite for carcino-embryonic antigen (CEA) quantitative determination. The fabrication steps were monitored by EIS. Moreover, trace detection of CEA can be achieved by monitoring the change of EIS signal before and after antibody-antigen recognition reaction. The charge-transfer resistance (R_{et}) value of BSA-NC-rGO/GCE increases compared with that of bare GCE, suggesting that BSA-NC-rGO nanocomposite has been successfully fixed on the GCE surface. After electrochemical deposition of AuNPs on BSA-NC-rGO/GCE, R_{et} value of AuNPs/BSA-NC-rGO/GCE decreases significantly. Compared with that of AuNPs/BSA-NC-rGO/GCE, an obvious enhancement is observed in R_{et} value of anti-CEA/AuNPs/BSA-NC-rGO/GCE. After BSA is adsorbed on the anti-CEA/AuNPs/BSA-NC-rGO/GCE, further increase of R_{et} value is observed at

BSA/anti-CEA/AuNPs/BSA-NC-rGO/GCE. When CEA reacts with anti-CEA specifically, R_{et} value of CEA/BSA/anti-CEA/AuNPs/BSA-NC-rGO/GCE increases significantly which is due to that high steric hindrance of antigen-antibody complex blocks the electron transfer of $[Fe(CN)_6]^{3-/4-}$ to electrode surface. The proposed immunosensor exhibits high sensitivity and good selectivity for the determination of CEA in the blood samples. Under optimum conditions, CEA could be quantified in a wide range of 0.1–200 ng·mL^{-1} (R = 0.9948) with low detection limit of 0.067 ng·mL^{-1}.

A label-free and amplified electrochemical impedimetric aptasensor based on functionalized graphene nanocomposites (rGO–AuNPs) was developed for the detection of thrombin, which played a vital role in thrombosis and hemostasis by Wang et al. [72]. In this work, EIS measurements were used on the detection of thrombin. With increasing concentration of thrombin, the EIS signals were increased obviously indicating that the aptasensor possessed high sensitivity to thrombin. The R_{ct} increase was linearly proportional to the thrombin concentration from 0.3 to 50 nM and a detection limit of 0.01 nM thrombin was achieved.

Chen et al. [73] have developed an impedimetric immunosensor for the determination of bovine interleukin-4, a cytokine involved in the immune response to certain parasites and the development of some bovine diseases. For these purpose, EIS measurements were used on the characterization of the immunosensor. EIS was used to examine the interface property of the surface-modified electrode. The electron-transfer resistance (R_{ct}) can be quantified using the semicircle diameter in the Nyquist plot of impedance spectra. The bare GCE showed very small semicircle, indicating a low electron-transfer resistance. The R_{ct} value of the chitosan/GCE was larger than that of the bare GCE, suggesting that the formation of a layer of chitosan film on the GCE surface hinders the electrode transfer between the redox probe and the electrode surface. After rGO/chitosan composite was modified on the GCE surface, the R_{ct} value decreased due to the facilitated electron transfer by rGO nanosheets. When bov-IL-4 antibody was trapped in rGO/chitosan composite, the R_{ct} value increased greatly, suggesting successful loading of the antibody on rGO/chitosan modified electrode. After bov-IL-4 antibody/rGO/chitosan/GCE was blocked with BSA, the R_{ct} value further increased. The further increase of the R_{ct} also could be seen when the bov-IL-4 antigen was captured by the immunosensor. The possible reason is that the formed protein layer on the electrode surface blocked significantly the diffusion of ferricyanide probe toward the electrode surface. The bov-IL-4 detection was carried out by measuring the relative increase of impedance values in corresponding specific reaction of bov-IL-4 antigen and bov-IL-4 antibody. The relative increase in impedance on exposure of the sensor to solutions containing bovine interleukin-4 is linearly proportional to its logarithmic concentration in the 0.1 to 50 ng·mL^{-1} and the detection limit is 80 pg·mL^{-1}. So, the immunosensor is selective, well reproducible, and acceptably stable. It presents a useful tool for further studies on the role of this cytokine in the immunology and pathogenesis of bovine diseases.

Regarding the CV technique as a characterization tool, on the literature it has been reported an electrochemical study and characterization of an amperometric biosensor based on the immobilization of laccase enzyme in a nanostructure of TiO_2 synthesized by the sol-gel method by Romero et al. [74]. In this work, CV measurements have been used in order to evaluate the electrochemical behavior of the nanobiosensors. In this work, a laccase amperometric nanobiosensors were developed to detect the catechol compound. The laccase enzyme (LAC) immobilization was performed on nanostructures of (a) titania (TiO_2); (b) titania/Nafion (TiO_2/NAF) (both immobilized by the sol-gel method) and a third nanostructure, which consisted of a single biosensor composite of Nafion and laccase enzyme denoted as NAF/LAC. The Nafion was deposited on a graphite electrode and used to avoid "cracking" on the matrix. In this study, CV was applied to illustrate electron transfer with reference to this multicopper enzyme, the graphite surface, and the various modified electrodes, without changing the accepted technique. For the transducer of graphite and nanobiosensors of TiO_2/NAF/LAC and TiO_2/LAC well-defined peaks are obtained which can be attributed to graphite and the semiconducting properties of TiO_2, respectively. However, NAF/LAC nanobiosensor presented small current peaks in the cyclic voltammogram (less well-defined peaks) due to the Nafion being partially surrounded by hydrophobic regions of sulfonate perfluorinated ionomer, which hinders the ion transfer and nonconductive properties of the enzyme. Moreover, the TiO_2/NAF/LAC and TiO_2/LAC nanobiosensors exhibit less reversibility and better response in the peak current than the electrode NAF/LAC.

5.3.2 Nanocomposite Electrodes Modified with Ag and Au Nanoparticles

Conducting composites, such as carbon–epoxy composites, are an interesting alternative for the construction of electrochemical sensor. The capability of integrating various materials is one of their main advantages since it can provide added values in the increase of the sensitivity and selectivity if compared to more traditional electrodes [75]. These materials can be, on one hand, biological materials and, on the other hand, can be nanomaterials such as metallic nanoparticles. In this sense, nanoparticles have been led to important advances on electrochemical electrodes development due to their catalytic properties [76]. Moreover, the immobilization of these nanomaterials can be done directly on the electrode surface.

Recently, in a preliminary study, it has been evaluated the effect on the electrode surface of optimized graphite-epoxy electrodes modified with gold and silver nanoparticles using different dilution ratios. The graphite-epoxy composition was previously optimized by means of systematic strategies of characterization such as EIS and CV measurements [65]. In that study, it has been concluded that the optimal proportions of graphite loading ranges between 15% and 16% of graphite loading. So in this preliminary study, it has been chosen 15% of graphite loading, as a bare

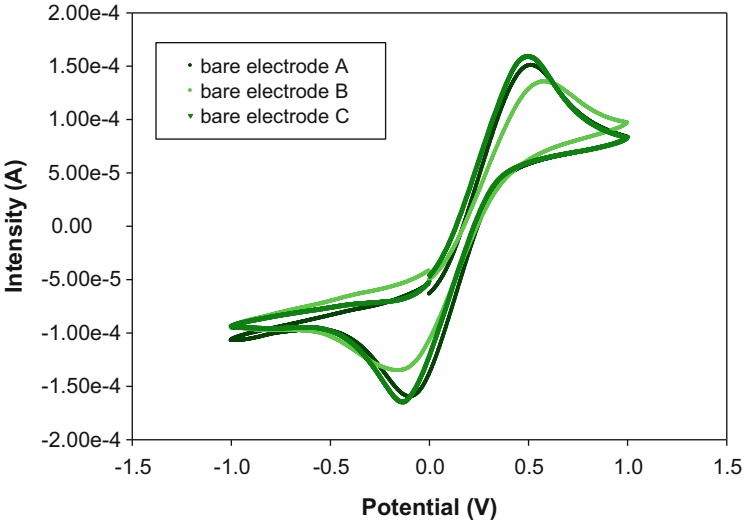

Fig. 8.14 Cyclic voltammograms for the optimized graphite bare electrodes. Measurements were carried out using 0.01 M ferricyanide/ferrocyanide and 0.1 M KCl. Scan rate 10 mV/s

electrode due to small variations in compositions around this optimal range do not produce high changes in the electrochemical behavior. In the present study, three different nanoparticles proportion has been evaluated: 1 to 2, 1 to 3, and 1 to 5. Firstly, by cyclic voltammetry measurements it has been evaluated the reproducibility of the graphite bare electrodes. The cyclic voltammograms obtained are depicted on Fig. 8.14. As it can be observed, good reproducibility has been obtained on the cathodic and anodic peaks. The active area calculated for the bare electrodes is 0.29 ± 0.03 cm^2 (Annex, Eq. 8.18).

After the surface modification with the nanoparticles, electrochemical impedance spectroscopy measurements have been used for the evaluation of the electrochemical parameters such as ohmic resistance, charge-transfer resistance, and double layer capacitance. The modification of the bare electrode surface with the nanoparticles produced an increase on the ohmic resistance and charge-transfer resistance due to the presence of the nanoparticles attached (see Fig. 8.15a, b). This increase is more significant when the dilution ratio decreases. However, it is observed a decrease on the double-layer capacitance value, parameter which is directly related to the charge or background current, compared to the bare electrode (Fig. 8.15c). So, an improvement on the signal-to-noise ratio is achieved for the nanoparticles presence due to the catalytic effect of them. This behavior is observed for both nanoparticles (gold and silver). After the results obtained on the electrochemical characterization it can be conclude that the optimal dilution ratio is 1–3.

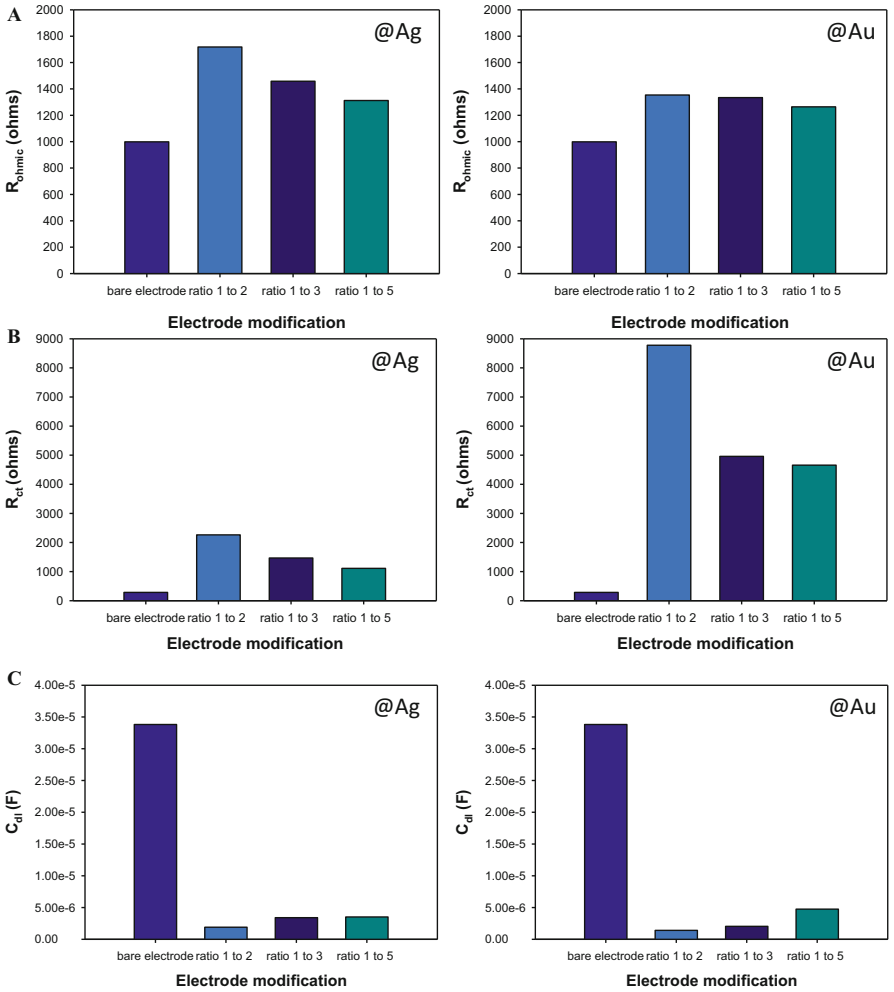

Fig. 8.15 Values of (A) ohmic resistance, (B) charge-transfer resistance, and (C) double-layer capacitance for the bare electrode and modified bare electrodes with different @Ag and @Au ratios, using the redox probe $Fe(CN)_6^{3-}/Fe(CN)_6^{4-}$ under quiescent condition in 0.1 M KCl and redox equilibrium potential

6 Conclusions and Future Perspectives

Nanoparticle and nanocomposite technologies have particular emphasis devoted to modifying surface chemistry at nanoscale, size, and shape to tailor the thermodynamic driving forces in material assembly processes. Fundamental understanding of the role of these hybrid materials requires the development of sensitive

characterization techniques, in order to describe precisely and in detail the properties desired for novel applications.

Nanocomposites appear to be a green solution to the risk of the release of nanomaterials to the environment. Thus, the characterization stage of these materials is essential to test the suitability of this argument. Moreover, more consisting results of the feasibility of materials for a desired purpose, can be obtained if the materials are *in situ* characterized without modifying their properties.

Consequently, different electron (SEM, FE-SEM, TEM, STEM) and laser (confocal) microscopy techniques coupled with analytical techniques (EDS) have shown to be more than appropriate methodologies for the detailed studies of hybrid nanocomposite materials with different compositions, polymeric supports, NP distribution, and for different further applications.

EIS technique has been demonstrated as a powerful characterization tool for the development of more efficient bio-nanocomposite sensors. EIS provides useful information about the electrochemical parameters as function of the carbon loading present on the bio-nanocomposites electrode. On one side, it is possible to extract the ohmic resistance, which can be related to the electric properties of the bio-nanocomposite. On the other side, other very useful parameters can be extracted which affect directly to the electroanalytical response. One of them is the charge-transfer resistance, which is related with the heterogeneous electron-transfer rate and which depends on the surface electrochemical reactivity. Moreover, EIS also allows the extraction of the electrode capacitance which can be correlated to the background current, an important parameter to minimize in order to enhance the signal/noise ratio. Consequently, all these parameters are relevant for the composite response and by a proper evaluation of them one can choose the proportion which fulfills the electroanalytical requirements of high sensitivity, fast response, and low limits of detection. Moreover, the feasibility of this technique on the determination of different analytes allowed obtaining limits of detection lower than the ones achieved with other techniques. On the other hand, CV is an appropriate technique for the evaluation of electron-transfer rate and reversibility of the process that are taking place on the electrode surface.

The advances in electron microscopy techniques, which in near future may be called nanoscopic, allow to obtain extremely fine data of surface parameters, nanoparticle distribution, chemical composition, and distribution in hybrid nanocomposite materials; these enhancements in characterization tools must come with the corresponding modification of the way nanomaterials and nanocomposites are prepared. Thus, intermatrix synthesis technique represents one environmentally friendly procedure for the tuned preparation of nanoparticles and nanocomposites materials. This and similar methodologies will focus in new optical and electrochemically active nanomaterials (e.g., bioinspired) that may be used for the quick analytical quantification of nanostructured materials in different media, as a mid-long term scientific challenge. Moreover, the coupling of the existing techniques with new sensitive ones (e.g., Nanochemical imaging, atomic force microscopy, X-ray nanotomography) will offer valuable information at atomic resolution (or below) in manner of nanoseconds.

Acknowledgments JB and RM thank UAB for the Ph.D. fellowships and mobility grants during Ph.D. studies. CO acknowledges funding from the People Programme (Marie Curie Actions) of the 7th Framework Programme of the European Union (FP7/2007-2013) under REA grant agreement no. 600388 (TECNIOSpring programme), and from the Agency for Business Competitiveness of the Government of Catalonia (ACCIÓ).

Annexe

Basics of Electrochemical Techniques for the Characterization and Optimization of Nanocomposite Sensing Materials

Electrochemical methods are interesting tools, which provide very useful information in order to characterize (bio)nanocomposites [66]. Electrochemical impedance spectroscopy (EIS) and cyclic voltammetry (CV) are the most common.

Electrochemical Impedance Spectroscopy

EIS is one of the most powerful and reliable methods to extract information about electrochemical characteristics of electrochemical systems [77, 78], thus it is extensively applied in several fields, e.g., corrosion [79, 80], electrode kinetics [81, 82], coatings, membranes [83], batteries [84, 85] and fuel cells [86, 87], interfaces, biochemistry, and solid-state electrochemistry [88].

Basically, it is based on applying an AC potential to an electrochemical cell and measuring the current through the cell. When a process occurs in an electrochemical cell, it can be modeled using combination of electrical components using the principle of the equivalent circuits. This principle consists on obtaining values of electrical parameters such as resistance, capacitance, etc., when an experimental spectrum is fitted with a theoretical curve corresponding to the selected circuit model.

Two different types of impedance measurements can be performed: Faradaic and non-Faradaic measurements. In the first case, redox species are added to the bulk solution in order to test the electrical properties at the interface solution-electrode. In the second one, no additional reagents are required and the measured current is due to the charging of the double layer at the interface electrolyte-electrode [95]. Faradaic or non-Faradaic measurements are used depending on the application. This part of the chapter is focused on the first method.

If it is applied a sinusoidal potential excitation E_t:

$$E_t = E_o \cdot \sin(\omega \cdot t) \tag{8.9}$$

Where E_t is the potential at time t, E_o is the amplitude of the signal, and $\omega = 2\pi f$ is the angular frequency (f is the frequency expressed in Hertz (Hz)).

An AC current signal with a current intensity I_t is obtained in response to this potential applied. I_t also depending on t with the same frequency but with an amplitude I_o and a phase angle φ depending on the impedance of the system.

$$I_t = I_o \cdot \sin(\omega \cdot t + \varphi) \tag{8.10}$$

To calculate the impedance of the system, an expression analogous to Ohm's law is used:

$$Z = \frac{E_t}{I_t} = \frac{E_o \cdot \sin(\omega \cdot t)}{I_o \cdot \sin(\omega \cdot t + \varphi)} = Z_o \cdot \frac{\sin(\omega \cdot t)}{\sin(\omega \cdot t + \varphi)} \tag{8.11}$$

According to Euler's expression:

$$\exp(j\varphi) = \cos\varphi + j\sin\varphi \tag{8.12}$$

A common way to represent the impedance vector model is to use complex notation:

$$E(t) = E_o \cdot \exp(j\omega \cdot t) \tag{8.13}$$

$$I(t) = I_o \cdot \exp(j\omega \cdot t - j\varphi) \tag{8.14}$$

Therefore, impedance is represented as:

$$Z = \frac{E}{I} = Z_o \exp(j\varphi) = Z_o(\cos\varphi + j\sin\varphi) = Z_r + jZ_i \tag{8.15}$$

where Z_r is the real part of the impedance and Z_i the imaginary part.

In order to acquire an impedimetric spectrum, an AC excitation signal is setting to the system within a selected frequency range, reaching to obtain an AC current response for each analyzed frequency value.

The most common graphical representation of impedimetric data is the Nyquist diagram, in which the imaginary part of the impedance $-Z_i$ is plotted versus the real part Z_r. In this plot, each point corresponds to a different frequency of the selected frequency range. In Figure 8.16 is represented a Nyquist diagram, where the impedance vector with magnitude $|Z|$ ($|Z|$ correspond to Z_o) forms with the X-axis an angle corresponding to the phase angle φ. The high frequency data are represented on the left part of the diagram while the low frequency data are on the right one.

Another way of representation data is bode diagram where the modulus of the impedance (Log$|Z|$) and the phase angle (φ) between the AC potential and the AC current are plotted as a function of the frequency (log ω). The impedance data, which are frequency independent, represent the behavior of the resistive processes (phase angles close to 0), whereas the ones that are dependent on the frequency are more related to capacitive or diffusive processes (phase angles between $-90°$ or $-45°$).

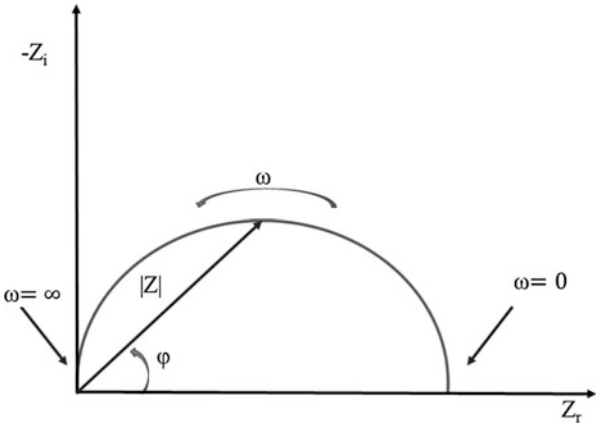

Fig. 8.16 Schematic representation of Nyquist diagram

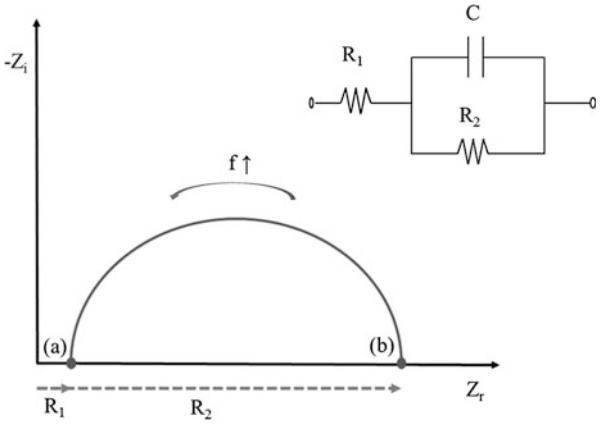

Fig. 8.17 Nyquist diagram and its corresponding equivalent circuit

The processing of data is performed by setting the data to an equivalent circuit that reproduces the spectrum of impedances during the experiment. These circuits are formed by electrical elements (such as resistors, capacitors, inductors, etc.) that combine to reproduce the behavior of real processes such as electrolyte resistance between the reference electrode and the charge of the double layer or charge transfer that takes place over a faradaic process.

Figure 8.17 shows an example of Nyquist diagram to a simple equivalent circuit formed by resistance R_1 in series with the parallel combination of a capacitance C and another R_2 ($R_1(R_2C)$). The impedance spectra is represented by a semicircle. Beginning in The point (a) corresponds to R_1 value and the point (b) to the equal $R_1 + R_2$. The value of capacitance of the capacitor C is obtained by the maximum value of imaginary impedance in the spectrum. The majority of impedance spectra corresponding to electrochemical systems can be fitted to this type of equivalent circuit. In those cases, the parameter R_1 represents the resistance of the solution (R_s), R_2 corresponds to the resistance (R_{ct}) to the charge transfer between the solution and

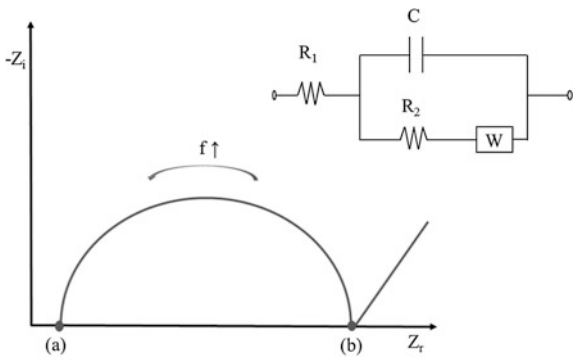

Fig. 8.18 Nyquist diagram and its corresponding equivalent circuit called Randles circuit

the electrode surface, and C represents the capacitance of the double layer due to the interface between the electrode and the electrolytic solution.

A Warburg impedance parameter must be considered when it is recorded at low frequencies. This parameter is related to the mass transfer between the solution and the electrode surface and can be modeled as a frequency dependent reactance with equal real and imaginary components.

$$Z_w = \sigma \cdot (\omega)^{-\frac{1}{2}} \cdot (1 - j) \tag{8.16}$$

Where ω is the angular frequency and σ is the Warburg coefficient (constant for a defined system).

The Warburg impedance appears on a Nyquist diagram as a diagonal line with a slope of 45°. In an electrochemical system or process, it represents the diffusion of electrochemical species in the solution. Figure 8.18 shows the impedimetric spectra and the most favorite model of equivalent circuit for a simple electrochemical reaction called Randles equivalent circuit.

In some cases, the semicircles of Nyquist diagrams present a depressed and not completely symmetric shape; this is due to the nonideal behavior of most capacitors in electrochemical systems. In order to fit better the experimental data to the theoretical curves, a constant phase element (CPE) is used instead of a capacitor [96]. The impedance of a CPE is represented by:

$$Z_{\text{CPE}} = (j \cdot \omega)^{-\alpha} / \text{C} \tag{8.17}$$

Where ω is angular frequency, C is capacitance, and α is an exponent, $\alpha(0 - 1)$. In a constant phase element, the exponent α is lower than 1, even though $\alpha = 1$ corresponds to the ideal capacitor.

It is also important to highlight that impedimetric measurements should be interpreted according to the electrochemical system under study in order to understand and attribute the electrical elements corresponding to the electrochemical phenomena.

Cyclic Voltammetry

CV is a technique widely used within the field of electrochemistry. From a simple measurement, it is possible to extract useful information in different technical fields. It is also used in non-analytical purposes including basic studies of electrocatalytic properties [89, 90], redox processes [91, 92], reaction mechanisms, or the study of a reaction intermediate species. Concerning biocomposites, CV is also employed as a characterization technique, sometimes together with EIS in order to complement both techniques [66, 93].

This technique is based on the current intensity measurement when it is applied a triangular excitation signal, varying the applied potential using constant scan rate, inside a prefixed working potential, both direct or indirect direction. In case of positive potentials (anodic direction), the electrode becomes an oxidant agent. However, when the potential lies to negative values (cathodic direction) it becomes a reduction agent. So, it is possible to achieve a value where the electroactive species oxidation is favorable and the anodic current intensity increases remarkably. It is achieved a maximum value which corresponds to the condition of electrode maximum polarization, and it is generated in a characteristic oxidation peak. Since the measurements are carried out without agitation conditions, when the scan direction is reversed, the electroactive oxidized species that are present on the electrode surface starts to be reduced generating a cathodic current until a maximum value. In this point, a reduction peak is generated.

The most important parameters that could be extracted from a cyclic voltagramm are cathodic current peak (i_{pc}) and anodic current peak (i_{pa}), as well as their potential values in those points (cathodic peak potential, E_{pc} and anodic peak potential, E_{pa}). These parameters are defined as it is shown in Fig. 8.19. Under ideal reversible conditions the following conditions are met:

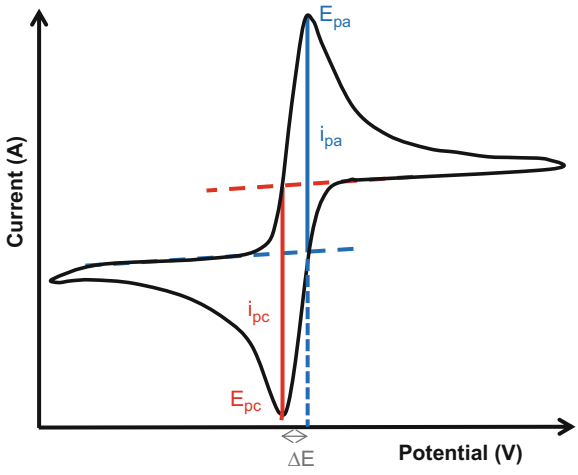

Fig. 8.19 Schematic representation of a cyclic voltagramm for an ideal reversible redox system

(i) Separation between potential peaks is $0.059/n$, where n corresponds to the number of electrons that are taking part on the reaction ($\Delta E = E_{pa} - E_{pc} = 0.059/n$).
(ii) Cathodic current peak value is the same that anodic current peak, in absolute value ($|i_{pa}| = |i_{pc}|$).
(iii) Peak potentials are independent of the scan rate (v).
(iv) Peak current is proportional to the square root of the scan rate ($v^{1/2}$).

Commonly, it is used a redox system which is totally reversible (Fe^{2+}/Fe^{3+}, $[Fe(CN)6]^{3-}/[Fe(CN)_6]^{4-}$, $[Ru(NH_3)_6]^{2+}/[Ru(NH_3)_6]^{3+}$, etc.) in order to perform the viability studies of an electroanalytical device, or in order to compare the behavior of the different electrodes or electrochemical devices developed.

Another important relationship which allows evaluating the reversibility of the system is the modified Randles– Sevčik equation. This equation connects the current peak (I_p), the concentration of the electroanalytical species that is reacting, and the scan rate (Eq. 8.18) [97].

$$I_p = 3.01 \cdot 10^5 n^{3/2} (\alpha D_a v)^{1/2} A C_a \tag{8.18}$$

Where n is the number of electrons that are participating on the redox reaction, α corresponds to the transfer coefficient, D_a corresponds to the diffusion coefficient of the reduced or oxidized species, v represents the scan rate, A is the electroactive area, and C_a is the bulk concentration of the electroactive species. This equation is adequate for electron transfer-controlled processes. For a reversible system where the process is controlled by the diffusion it is obtained a linear relationship between I_p and $v^{1/2}$.

On the other hand, the relationship between log(I) and the potential is the Tafel diagram (Fig. 8.20). In order to obtain this diagram it is necessary that the

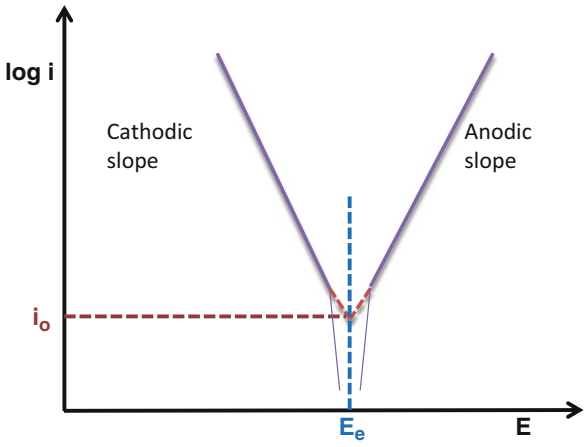

Fig. 8.20 Tafel diagram for a reversible electrochemical species: i_o corresponds to exchange current and E_e corresponds to equilibrium potential

electrochemical process is not controlled by the electron-transfer. This diagram provides information about the exchange current (i_o), which is related to the reversibility of the process. At the same time, this constant provides information about the charge-transfer resistance (R_{ct}) of the process by means of the following equation:

$$i_o = \mathrm{RT}/n\mathrm{FR}_{ct} \tag{8.19}$$

An estimation of the electrode reproducibility based on nanocomposites due to the handmade electrode fabrication process is necessary before its analytical applications. Cyclic voltammetry measurements, as it has been described above, allow obtaining useful electrochemical parameters such as electroactive area and charge-transfer resistance. Knowledge of the real surface area of electrodes is, therefore, needed since normally the geometric area does not correspond to the electroactive surface of the electrode [94]. Moreover, charge-transfer resistance value is inversely proportional to the electron-transfer rate. Both parameters affect the overall analytical performance of the nanocomposite sensors.

References

1. Van Hove MA (2006) From surface science to nanotechnology. Catal Today 113:133–140
2. Serrano E, Rus G, García-Martínez J (2009) Nanotechnology for sustainable energy. Renew Sust Energ Rev 13:2373–2384
3. Sanchez F, Sobolev K (2010) Nanotechnology in concrete – a review. Constr Build Mater 24:2060–2071
4. Misra P (2009) Introduction. In: Blackman JA (ed) Metallic nanoparticles, 1st edn. Elsevier, Amsterdam
5. Xiao Y, Li CM (2008) Nanocomposites: from fabrications to electrochemical bioapplications. Electroanalysis 20:648–662
6. Role T, Scattering ER (1982) Electrochemical properties of small clusters of metal atoms and their role in surface enhanced raman scattering. J Phys Chem 460:3166–3170
7. Wang ZL. (Ed.) (1999) Characterization of Nanophase Materials. Nanomaterials for Nanoscience and Nanotechnology. Weinheim, FRG: Wiley-VCH Verlag GmbH. https://doi.org/10.1002/3527600094.
8. Tiano AL, Koenigsmann C, Santulli AC, Wong SS (2010) Solution-based synthetic strategies for one-dimensional metal-containing nanostructures. Chem Commun (Camb) 46:8093–8130
9. Muñoz-Rojas D, Oró-Solé J, Ayyad O, Gómez-Romero P (2008) Facile one-pot synthesis of self-assembled silver@Polypyrrole Core/Shell Nanosnakes. Small 4:1301–1306
10. Domènech B, Bastos-Arrieta J, Alonso A (2012) Bifunctional polymer-metal nanocomposite ion exchange materials. In: Kilislioglu A (ed) Ion exchange technologies. InTech, Barcelona, pp 35–72
11. Donnan FG (1995) Theory of membrane equilibria and membrane potentials in the presence of non-dialysing electrolytes. A contribution to physical-chemical physiology. J Membr Sci 100:45–55
12. Sharifi S, Behzadi S, Laurent S, Forrest ML, Stroeve P, Mahmoudi M (2012) Toxicity of nanomaterials. Chem Soc Rev 41:2323–2343

13. Chan VSW (2006) Nanomedicine: an unresolved regulatory issue. Regul Toxicol Pharmacol 46:218–224
14. Franco A, Hansen SF, Olsen SI, Butti L (2007) Limits and prospects of the "incremental approach" and the European legislation on the management of risks related to nanomaterials. Regul Toxicol Pharmacol 48:171–183
15. Handy RD, Shaw BJ (2007) Toxic effects of nanoparticles and nanomaterials: implications for public health, risk assessment and the public perception of nanotechnology. Health Risk Soc 9:125–144
16. Bouwmeester H, Dekkers S, Noordam MY, Hagens WI, Bulder AS, de Heer C, ten Voorde SECG, Wijnhoven SWP, Marvin HJP, Sips AJAM (2009) Review of health safety aspects of nanotechnologies in food production. Regul Toxicol Pharmacol 53:52–62
17. Oberdörster G, Stone V, Donaldson K (2007) Toxicology of nanoparticles: a historical perspective. Nanotoxicology 1:2–25
18. Cumbal L, Sengupta AK (2005) Arsenic removal using polymer-supported hydrated iron(III) oxide nanoparticles: role of donnan membrane effect. Environ Sci Technol 39:6508–6515
19. Campelo JM, Luna D, Luque R, Marinas JM, Romero A a (2009) Sustainable preparation of supported metal nanoparticles and their applications in catalysis. ChemSusChem 2:18–45
20. Ramesh GV, Porel S, Radhakrishnan TP (2009) Polymer thin films embedded with in situ grown metal nanoparticles. Chem Soc Rev 38:2646–2656
21. Burato C, Centomo P, Pace G, Favaro M, Prati L, Corain B (2005) Generation of size-controlled palladium(0) and gold(0) nanoclusters inside the Nanoporous domains of gel-type functional resins: Part II: prospects for oxidation catalysis in the liquid phase. J Mol Catal A Chem 238:26–34
22. Ruiz P, Muñoz M, Macanás J, Muraviev DN (2010) Intermatrix synthesis of polymer−copper nanocomposites with tunable parameters by using copper Comproportionation reaction. Chem Mater 22:6616–6623
23. Ruckenstein E, Park JS (1989) Preparation of polymer composites. A colloidal pathway. Chem Mater 1:343–348
24. Sarkar S, Guibal E, Quignard F, SenGupta a K (2012) Polymer-supported metals and metal oxide nanoparticles: synthesis, characterization, and applications. J Nanopart Res 14:715
25. Muraviev DN (2005) Inter-matrix synthesis of polymer stabilised metal nanoparticles for sensor applications. Contrib Sci 3:19–32
26. Domènech B, Muñoz M, Muraviev DN, Macanás J (2014) Uncommon patterns in Nafion films loaded with silver nanoparticles. Chem Commun (Camb) 50:4693–4695
27. Bastos-Arrieta J, Muñoz M, Ruiz P, Muraviev DN (2013) Morphological changes of gel-type functional polymers after Intermatrix synthesis of polymer stabilized silver nanoparticles. Nanoscale Res Lett 8:255
28. Ruiz P, Muñoz M, Macanás J, Turta C, Prodius D, Muraviev DN (2010) Intermatrix synthesis of polymer stabilized inorganic nanocatalyst with maximum accessibility for reactants. Dalton Trans 39:1751–1757
29. Alonso A, Macanás J, Shafir A, Muñoz M, Vallribera A, Prodius D, Melnic S, Turta C, Muraviev DN (2010) Donnan-exclusion-driven distribution of catalytic ferromagnetic nanoparticles synthesized in polymeric fibers. Dalton Trans 39:2579–2586
30. Ruiz P, Macanás J, Muñoz M, Muraviev DN (2011) Intermatrix synthesis: easy technique permitting preparation of polymer-stabilized nanoparticles with desired composition and structure. Nanoscale Res Lett 6:343
31. Konev DV, Fertikov VV, Kravchenko T a, Kalinichev a I (2008) The inverse problem of the kinetics of redox sorption taking into account the size of ultradisperse metal particles in an electron-ion exchanger. Russ J Phys Chem A 82:1363–1367
32. Levenstein R, Hasson D, Semiat R (1996) Utilization of the donnan effect for improving electrolyte separation with nanofiltration membranes. J Membr Sci 116:77–92
33. Mijangos F, Tikhonov N, Ortueta M, Dautov A (2002) Modeling ion-exchange kinetics in bimetallic systems. Ind Eng Chem Res 41:1357–1363

34. Alonso A, Muñoz-Berbel X, Vigués N, Rodríguez-Rodríguez R, Macanás J, Mas J, Muñoz M, Muraviev DN (2012) Intermatrix synthesis of monometallic and magnetic metal/metal oxide nanoparticles with bactericidal activity on anionic exchange polymers. RSC Adv 2:4596–4599
35. Bastos-Arrieta J, Shafir A, Alonso A, Muñoz M, Macanás J, Muraviev DN (2012) Donnan exclusion driven Intermatrix synthesis of reusable polymer stabilized palladium nanocatalysts. Catal Today 193:207–212
36. Greenleaf JE, Lin J, Sengupta AK (2006) Two novel applications of ion exchange fibers: arsenic removal and chemical-free softening of hard water. Environ Prog 25:300–311
37. Witten TA, Sander LM (1983) Diffussion-limited aggregation. Phys Rev B 27:5686–5697
38. Zhang Y, Cui X, Shi F, Deng Y (2012) Nano-gold catalysis in fine chemical synthesis. Chem Rev 112:2467–2505
39. Wu Y, Wang D, Li Y (2014) Nanocrystals from solutions: catalysts. Chem. Soc. Rev 43(7), 2112–2124. https://doi.org/10.1039/C3CS60221D
40. Akamatsu K, Adachi S, Tsuruoka T, Ikeda S, Tomita S, Nawafune H (2008) Nanoparticles with Controlled Microstructures. Chem Mater 20:3042–3047
41. Akamatsu K, Fujii M, Tsuruoka T, Nakano S, Murashima T, Nawafune H (2012) Mechanistic study on microstructural tuning of metal nanoparticle/polymer composite thin layers: hydrogenation and decomposition of polyimide matrices catalyzed by embedded nickel nanoparticles. J Phys Chem C 116:17947–17954
42. Alonso A, Muñoz-Berbel X, Vigués N, Macanás J, Muñoz M, Mas J, Muraviev DN (2012) Characterization of fibrous polymer silver/cobalt nanocomposite with enhanced bactericide activity. Langmuir 28:783–790
43. Alonso A, Vigués N, Muñoz-Berbel X, Macanás J, Muñoz M, Mas J, Muraviev DN (2011) Environmentally-safe bimetallic Ag@Co magnetic nanocomposites with antimicrobial activity. Chem Commun (Camb) 47:10464–10466
44. Muraviev DN, Macanás J, Ruiz P, Munoz M, Muñoz M (2008) Synthesis, stability and Electrocatalytic activity of polymer-stabilized monometallic Pt and bimetallic Pt/Cu Core-Shell nanoparticles. Phys Status Solidi Appl Mater Sci 205:1460–1464
45. Muraviev D, Macanas J, Farre M, Munoz M, Alegret S (2006) Novel routes for inter-matrix synthesis and characterization of polymer stabilized metal nanoparticles for molecular recognition devices. Sensors Actuators B Chem 118:408–417
46. Elliott SD, Moloney MP, Gun'ko YK (2008) Chiral shells and achiral cores in CdS quantum dots. Nano Lett 8:2452–2457
47. Petryayeva E, Algar WR, Medintz IL (2013) Quantum dots in bioanalysis: a review of applications across various platforms for fluorescence spectroscopy and imaging. Appl Spectrosc 67:215–252
48. Moloney MP, Gun'ko YK, Kelly JM (2007) Chiral highly luminescent CdS quantum dots. Chem Commun (Camb) 7345:3900–3902
49. Bera D, Qian L, Tseng T-K, Holloway PH (2010) Quantum dots and their multimodal applications: a review. Materials (Basel) 3:2260–2345
50. Bastos-Arrieta J, Muñoz J, Stenbock-Fermor A, Muñoz M, Muraviev DN, Céspedes F, Tsarkova LA, Baeza M (2016) Intermatrix synthesis as a rapid, inexpensive and reproducible methodology for the in situ functionalization of nanostructured surfaces with quantum dots. Appl Surf Sci 368:417–426
51. Sokolova V, Epple M (2011) Synthetic pathways to make nanoparticles fluorescent. Nanoscale 3:1957–1962
52. Kozlova D, Chernousova S, Knuschke T, Buer J, Westendorf AM, Epple M (2012) Cell targeting by antibody-functionalized calcium phosphate nanoparticles. J Mater Chem 22:396
53. Jun Han Z, Rider AE, Ishaq M, Kumar S, Kondyurin A, Bilek MMM, Levchenko I, Ostrikov (Ken) K (2013) Carbon nanostructures for hard tissue engineering. RSC Adv 3:11058
54. Chernousova S, Klesing J, Soklakova N, Epple M (2013) A genetically active Nano-calcium phosphate paste for bone substitution, encoding the formation of BMP-7 and VEGF-A. RSC Adv 3:11155

55. Mahl D, Diendorf J, Ristig S, Greulich C, Li ZA, Farle M, Köller M, Epple M (2012) Silver, gold, and alloyed silver-gold nanoparticles: characterization and comparative cell-biologic action. J Nanopart Res 14(10):1153
56. de la Escosura-Muñiz A, Merkoçi A (2010) Electrochemical detection of proteins using nanoparticles: applications to diagnostics. Expert Opin Med Diagn 4:21–37
57. Perfézou M, Turner A, Merkoçi A (2012) Cancer detection using nanoparticle-based sensors. Chem Soc Rev 41:2606
58. Aragay G, Pons J, Merkoçi A (2011) Enhanced electrochemical detection of heavy metals at heated graphite nanoparticle-based screen-printed electrodes. J Mater Chem 21:4326
59. Merkoçi A (2010) Nanoparticles-based strategies for DNA, protein and cell sensors. Biosens Bioelectron 26:1164–1177
60. Mohanraj V, Chen Y, Chen M (2006) Nanoparticles – a review. Trop J Pharm Res 5:561–573
61. Saha K, Agasti SS, Kim C, Li X, Rotello VM (2012) Gold nanoparticles in chemical and biological sensing. Chem Rev 112:2739–2779
62. Espinoza-Castañeda M, de la Escosura-Muñiz A, González-Ortiz G, Martín-Orúe SM, Pérez JF, Merkoçi A (2013) Casein modified gold nanoparticles for future theranostic applications. Biosens Bioelectron 40:271–276
63. Mamalis AG, Vogtländer LOG, Markopoulos A (2004) Nanotechnology and nanostructured materials: trends in carbon nanotubes. Precis Eng 28:16–30
64. Ramírez-García S, Alegret S, Céspedes F, Forster RJ (2004) Carbon composite microelectrodes: charge percolation and electroanalytical performance. Anal Chem 76:503–512
65. Montes R, Bartrolí J, Céspedes F, Baeza M (2014) Towards to the improvement of the analytical response in voltammetric sensors based on rigid composites. J Electroanal Chem 733:69–76
66. Montes R, Bartrolí J, Baeza M, Céspedes F (2015) Improvement of the detection limit for biosensors: advances on the optimization of biocomposite composition. Microchem J 119:66–74
67. Wang J (2000) Practical considerations. In: Analytical electrochemistry. Wiley-VCH, New York, pp 100–139
68. Perez B, Pumera M, del Valle M, Merkoci A, Alegret S (2005) Glucose biosensor based on carbon nanotube epoxy composites. J Nanosci Nanotechnol 5:1694–1698
69. Montes R, Céspedes F, Baeza M (2016) Highly sensitive electrochemical immunosensor for IgG detection based on optimized rigid biocomposites. Biosens Bioelectron 78:505–512
70. Santandreu M, Solé S, Fàbregas E, Alegret S (1998) Development of electrochemical immunosensing systems with renewable surfaces. Biosens Bioelectron 13:7–17
71. Li Y, Zhang Z, Zhang Y, Deng D, Luo L, Han B, Fan C (2016) Nitidine chloride-assisted bio-functionalization of reduced graphene oxide by bovine serum albumin for impedimetric immunosensing. Biosens Bioelectron 79:536–542
72. Wang Q, Zhou Z, Zhai Y, Zhang L, Hong W, Zhang Z, Dong S (2015) Label-free aptamer biosensor for thrombin detection based on functionalized graphene nanocomposites. Talanta 141:247–252
73. Chen X, Qin P, Li J, Yang Z, Wen Z, Jian Z, Zhao J, Hu X, Jiao X (2015) Impedance immunosensor for bovine interleukin-4 using an electrode modified with reduced graphene oxide and chitosan. Microchim Acta 182:369–376
74. Romero-Arcos M, Garnica-Romo M, Martínez-Flores H (2016) Electrochemical study and characterization of an amperometric biosensor based on the immobilization of laccase in a nanostructure of TiO2 synthesized by the sol-gel method. Materials (Basel) 9:543
75. Fenga PG, Stradiotto NR, Pividori MI (2010) Preparation and characterization of graphite-epoxy composite modified with zinc hexacyanoferrate and their electrochemical behaviour in presence of substituted anilines. Electroanalysis 22:2979–2984
76. Muñoz J, Bastos-Arrieta J, Muñoz M, Muraviev DN, Céspedes F, Baeza M (2014) Simple green routes for the customized preparation of sensitive carbon nanotubes/epoxy nanocomposite electrodes with functional metal nanoparticles. RSC Adv 4:44517–44524
77. McDonald JR (1987) Impedance spectroscopy. Wiley, New York
78. Ashe D, Alleyne T, Iwuoha E (2007) Serum cytochrome c detection using a cytochrome c oxidase biosensor. Biotechnol Appl Biochem 46:185–189

79. YH G, Ma HJ, Yue W, Tian B, Chen LL, Mao DL (2016) Microstructure and corrosion model of MAO coating on nano grained AA2024 pretreated by ultrasonic cold forging technology. J Alloy Compd 681:120–127
80. Fonseca-Garcia A, Perez-Alvarez J, Barrera CC, Medina JC, Almaguer-Flores A, Sanchez RB et al (2016) The effect of simulated inflammatory conditions on the surface properties of titanium and stainless steel and their importance as biomaterials. Mater Sci Eng C Mater Biol Appl 66:119–129
81. Hernandez S, Gerardi G, Bejtka K, Fina A, Russo N (2016) Evaluation of the charge transfer kinetics of spin-coated BiVO4 thin films for sun-driven water photoelectrolysis. Appl Catal B Environ 190:66–74
82. Wang LZ, Yang SX, Wu B, Li P, Li ZN, Zhao YM (2016) The influence of anode materials on the kinetics toward electrochemical oxidation of phenol. Electrochim Acta 206:270–277
83. Jing Y, Guo L, Chaplin BP (2016) Electrochemical impedance spectroscopy study of membrane fouling and electrochemical regeneration at a sub-stoichiometric TiO2 reactive electrochemical membrane. J Membr Sci 510:510–523
84. Hwang T, Lee JK, Mun J, Choi W (2016) Surface-modified carbon nanotube coating on high-voltage LiNi0.5Mn1.5O4 cathodes for lithium ion batteries. J Power Sources 322:40–48
85. Lan CK, Bao Q, Huang YH, Duh JG (2016) Embedding nano-Li4Ti5O12 in hierarchical porous carbon matrixes derived from water soluble polymers for ultra-fast lithium ion batteries anodic materials. J Alloy Compd 673:336–348
86. Zhang CY, Liang P, Yang XF, Jiang Y, Bian YH, Chen CM et al (2016) Binder-free graphene and manganese oxide coated carbon felt anode for high-performance microbial fuel cell. Biosens Bioelectron 81:32–38
87. Li WY, Guan B, Yan JH, Zhang N, Zhang XX, Liu XB (2016) Enhanced surface exchange activity and electrode performance of (La2-2xSr2x)(Ni1-xMnx)O4+delta cathode for intermediate temperature solid oxide fuel cells. J Power Sources 318:178–183
88. Dhaiveegan P, Elangovan N, Nishimura T, Rajendran N (2014) Electrochemical characterization of carbon and weathering steels corrosion products to determine the protective ability using carbon paste electrode (CPE). Electroanalysis 26:2419–2428
89. Cheng CK, Lin CH, HC W, Ma CCM, Yeh TK, Chou HY et al (2016) The two-dimensional nanocomposite of molybdenum disulfide and nitrogen-doped graphene oxide for efficient counter electrode of dye-sensitized solar cells. Nanoscale Res Lett 11(9):117
90. Ning HL, Xin YL, Xu LK, Du AL (2016) Properties of IrO2-Ta2O5 coated titanium anodes modified with graphene. Rare Metal Mater Eng 45:945–950
91. Wiesing M, Baben MT, Schneider JM, de los Arcos T, Grundmeier G (2016) Combined electrochemical and electron spectroscopic investigations of the surface oxidation of TiAlN HPPMS hard coatings. Electrochim Acta 208:120–128
92. Jovanovi IN, Cizmek L, Komorsky-Lovric S (2016) Electrochemistry-based determination of pungency level of hot peppers using the voltammetry of microparticles. Electrochim Acta 208:273–281
93. Lupu S, Lete C, Balaure PC, del Campo FJ, Munoz FX, Lakard B et al (2013) In situ electrodeposition of biocomposite materials by sinusoidal voltages on microelectrodes array for tyrosinase based amperometric biosensor development. Sens Actuators B Chem 181:136–143
94. Fotouhi L, Fatollahzadeh M, Heravi MM (2012) Electrochemical behavior and Voltammetric determination of sulfaguanidine at a glassy carbon electrode modified with a multi-walled carbon nanotube. Int J Electrochem Soc 7:3919–3928
95. Daniels JS, Pourmand N (2007) Label-Free Impedance Biosensors: Opportunities and Challenges, Electroanalysis 19:1239–1257
96. Katz E, Willner I (2003) Electroanalysis 15:913–947
97. Pacios M, del Valle M, Bartrolí J, Esplandiu MJ (2008) Journal of Electroanalytical Chemistry 619–620

Quartz Crystal Resonator for Real-Time Characterization of Nanoscale Phenomena Relevant for Biomedical Applications

9

Luis Armando Carvajal Ahumada, Oscar Leonardo Herrera Sandoval, Nuria Peña Perez, Felipe Andrés Silva Gómez, Mariano Alberto García-Vellisca, and José Javier Serrano Olmedo

Contents

L. A. Carvajal Ahumada (✉)
Centro de tecnología Biomédica (CTB), Universidad Politécnica de Madrid (UPM), Madrid, Spain

Facultad de Ingeniería y Ciencias Básicas, Universidad Central, Bogotá, Colombia

Centro de investigación y desarrollo tecnológico de la industria electro electrónica y TIC, Bogotá, Colombia
e-mail: lcarvajala1@ucentral.edu.co

O. L. Herrera Sandoval
Facultad de Ingeniería y Ciencias Básicas, Universidad Central, Bogotá, Colombia

Centro de investigación y desarrollo tecnológico de la industria electro electrónica y TIC, Bogotá, Colombia

N. Peña Perez · M. A. García-Vellisca · J. J. Serrano Olmedo
Centro de tecnología Biomédica (CTB), Universidad Politécnica de Madrid (UPM), Madrid, Spain

F. A. Silva Gómez
Corporación de Alta Tecnología para la Defensa (CODALTEC), Villavicencio, Colombia

© Springer-Verlag GmbH Germany, part of Springer Nature 2018

C. S. S. R. Kumar (ed.), *In-situ Characterization Techniques for Nanomaterials*,
https://doi.org/10.1007/978-3-662-56322-9_9

1 Definition of the Topic

Thickness shear mode (TSM) sensors and, more in particular, Quartz Crystal Resonator (QCR) sensors are very efficient systems because of their elevated accuracy, sensitivity, and biofunctionalization capacity. They are highly reliable when measuring the deposited sample, both for gaseous and liquid media. Moreover, they have the capacity of monitoring in real-time and their manufacturing cost is relatively low. These characteristics explain the many possible applications of QCR sensors. In this chapter, we describe recent remarkable applications of QCR's in different contexts as medical and environmental monitoring applications or mixed applications with other techniques as Atomic Force Microscopy (AFM), Surface Plasmon Resonance (SPR) or electrochemical techniques in order to improve the QCR sensor response.

2 Overview

Development of chemical sensors based on nanotechnology, particularly for applications in life science, has significantly increased the demand for in situ surface analysis tools. Real-time, noninvasive techniques are required to study surface reactions and nanoscale effects to understand the processes that take place at the solid-gas and solid-liquid interface. Detecting and quantifying minute changes in mechanical properties, adsorption of biomolecules, and forces at the interface caused by molecular contacts contribute to solve problems related to biology, physics, and chemistry.

Acoustic resonators are an important type of interfacial sensors. Quartz crystal resonators (QCR) are very famous acoustic resonators because their versatility converts them in indispensable tools for different applications from studying viscoelastic properties of soft matter to analyzing the motility of living cells among others.

Quartz crystal microbalance (QCM) based sensing has considerably developed over the last two decades. Fields such as material science, electrochemistry, and medical and environmental monitoring have taken advantage of this improvement in QCM-based sensing. This review considers the latest advances produced in QCM-based sensors and provides with an overview of the current state of the field, describing some of the most promising applications.

3 Introduction

Although the QCR technology is considered mature and many documents have been written in relation to its use in a wide range of sensing applications. This chapter emphasizes the use of the QCR's in biomedical applications. Nowadays, sensors for

biological and biomedical applications are taking special importance because there is a necessity of decreasing the price of the medical treatments for chronical diseases and improving the diagnostic. Moreover, there is an intention of expanding good medical services at the global level, especially in developing countries. Biosensors as QCR's have a very important role in this goal because their simplicity, high sensitivity, and reliable performance at a low cost make them exceptional tools for achieving this purpose.

The quartz crystal resonator (QCR) is a surface acoustic wave transducer used as an analytical instrument in complex media. There are different applications for the QCR; the most traditional one is the gravimetric application, called quartz crystal microbalance (QCM). The bases of the gravimetric applications were published by Günter Sauerbrey in 1959 [1]. Sauerbrey observed that an oscillating quartz crystal changes its resonance frequency in a linear manner depending on the mass adsorbed on its surface.

This linear dependency of the frequency changes on the mass adsorbed can be described by:

$$\Delta f = -\frac{2{f_0}^2}{A\sqrt{\rho_q \mu_q}}\Delta m \tag{9.1}$$

$$f_0 = \frac{n}{2h_q}\left(\sqrt{\mu_q / \rho_q}\right) \tag{9.2}$$

where ρ_q and μ_q are the specific density and the shear modulus of quartz, respectively; f_0 is the fundamental resonant frequency of quartz, related to its thickness h_q (10 MHz ~ 167 μm); Δm is the thin film mass deposited; A is the piezoelectrically active crystal area; and n is the overtone number [2].

The Sauerbrey model has three conditions: the deposited mass must be relatively small in comparison with the mass of the crystal plate. The deposited mass must be rigid and its distribution over the electrode area must be uniform.

During the eighties, the use of QCRs was further extended due to Kanazawa, Gordon, and coworkers [3, 4]. Their work on liquid applications of QCR technology has expanded the number of potential applications intensely, specifically in biotechnology and biosensor applications [5–12].

In contact with liquids, the crystal is capable of giving information about the density-viscosity product $(\rho\eta)^{1/2}$ [13, 14] of the fluid by changing its resonant frequency and quality Q-factor according to Kanazawa equations [3]:

$$\Delta f = -\sqrt{n}{f_0}^{3/2}\sqrt{\frac{\rho_L \eta_L}{\pi \rho_q \mu_q}} \tag{9.3}$$

$$\delta = \sqrt{\frac{2\eta_L}{\omega \rho_L}} \tag{9.4}$$

where ρ_L and η_L are the density and viscosity of the fluid respectively. Equation 9.4 shows the decay characteristic length (δ) as proportional to the viscosity to density

ratio of the liquid and as inversely proportional to the angular frequency (ω) [2, 15]. For a 10 MHz AT-cut quartz crystal in contact with water this length is: $\delta = 178$ nm. That is the acoustic wave generating for the crystal propagated into the fluid is completely attenuated at 178 nm measured from crystal surface. In consequence, quartz crystal resonators respond to the fluid that is present in regions very near to its surface [15].

The use of QCR with liquids opened new investigation lines and made these transducers more attractive for biomedical applications. Due to this, biological samples need a liquid media to conserve its properties. Currently, there are applications to detect mass changes in polymer brushes, absorbed proteins, cell cultures, and polyelectrolyte multilayers [5, 16–19]. There are also applications that use QCRs to determine the properties of a liquid in contact with its electrode (non-gravimetric applications) [2, 20, 21]. Moreover, QCR technology has contributed significantly in the development of sensitive devices with the aim of detecting and quantifying the concentration of specific molecules (DNA, proteins, etc.) in gaseous and liquid media [22].

From 1990, the use of QCMs in liquid samples spread mainly driven by a novel instrumentation that permitted lower costs, more integration with other techniques, and more facilities for using the sensors outside of laboratories (in situ applications). In addition, there was a growing interest in QCR's applications on the soft matter at interfaces. For instance, typical samples considered were polymer brushes, supported lipid bilayers, polyelectrolyte multilayers, adsorbed proteins, cell cultures, and functional polymer films in a wider sense [8, 10, 23, 24].

Due to the fact that the behavior of QCR sensors in gases is similar to the response of quartz crystals used as frequency references in electronic circuits, there are many circuit configurations commonly used in electronic circuits that can be used to obtain the desired crystal response for biosensing applications [7, 8, 25, 26].

Moreover, the crystals used commonly as reference frequency in electronic circuits (crystals low-cost) can be used as sensors because the characteristics of the quartz substrate are the same to the crystals with gold electrode (commonly used in biosensing). However, for applications of sensing using these low-cost crystals, the case must be removed and commonly the crystal surface is functionalized with a chemically sensitive coating. The procedure of case opening reduces the quality factor (Q) by 1/3, and the aging is 100–1000 times larger [26]. In addition, the surface of the low-cost crystals is not the most appropriate for biosensing applications because it is not inert to biochemical reactions. In consequence, the gold electrodes are more used for biosensing applications due to the gold metal is chemically inert.

In addition, for any crystal, the viscoelastic properties of macromolecular coating materials have a strong impact on its vibration and further diminish Q. When the QCR sensor is in contact with liquid media, the oscillation is significantly damped too and again the quality factor is significantly decreased.

With the aim of explaining QCR behavior, many theoretical models have been developed, especially at their resonance frequency and near frequency ranges. In particular, the equivalent electrical model BVD has been tested as a useful tool.

3.1 Equivalent Circuit of the Quartz Crystal Resonator

The equivalent electric model of quartz crystal resonator (QCR) can be derived from the one-dimensional transmission line model, which is used to study electrical conductors. This analysis was done by Granstaff et al. [27], using the Mason model as described in Rosenbaum [28, 29].

Mason model uses the theory of transmission lines to represent the physical behavior of the crystal and the sample layers in one dimension. The model distinguishes between piezoelectric and nonpiezoelectric materials. The nonpiezoelectric film is mathematically represented by a 2×2 matrix and physically represented by a two-port circuit [27, 28]. The piezoelectric material is also represented by transmission lines. Granstaff et al. used a circuit with two acoustic ports and one electrical port [27, 28].

As result of this mathematical analysis, the BVD (Butterworth-Van Dyke) model was obtained. This model is shown in Fig. 9.1 [2, 27, 30, 31].

In electrical notation, L_q is the dynamic inductance and represents the oscillating mass of the quartz crystal. The dynamic capacitance (C_q) represents the elasticity of the oscillating crystal body. The dynamic resistance (R_q) denotes the friction of the quartz slice as well as all kinds of acoustic damping. The static capacitance C_0 models losses caused by external electrical components to the sensor and the parasitic capacitance generated by the electrodes on the crystal [32, 33].

$$C_q = \frac{8{e_{26}}^2 A}{(N\pi)^2 \overline{C_{66}} h_q} \tag{9.5}$$

$$L_q = \frac{1}{{\omega_s}^2 C_q} \tag{9.6}$$

$$R_q = \frac{\eta_q}{\overline{C_{66}} C_q} \tag{9.7}$$

$$C_0 = \frac{\varepsilon_{22} A_e}{h_q} \tag{9.8}$$

Where $\overline{C}_{66}$ is the piezoelectrically stiffened elastic constant for loss-less quartz ($2{,}947 \times 10^{10}$ N/m^2), e_{26} is the piezoelectric stress constant for quartz

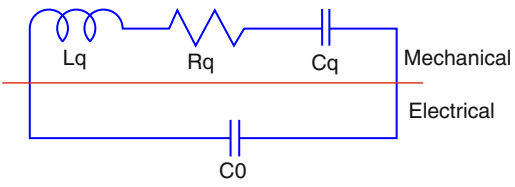

Fig. 9.1 Schematic of BVD model for Quartz crystal resonator (Undamped) (Adapted from [2], https://doi.org/10.1016/j.sna.2016.01.021. Creative Commons license)

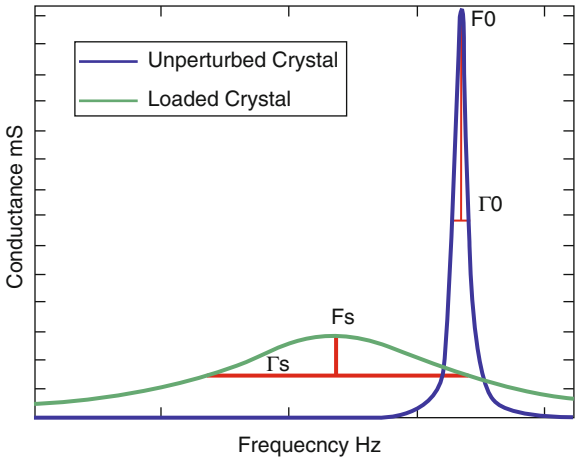

Fig. 9.2 Change in morphology of the conductance curve (G) for bare crystal and in contact with a liquid (Reproduced from [35], https://doi.org/10.3390/s16111959, under the Creative Commons Attribution License)

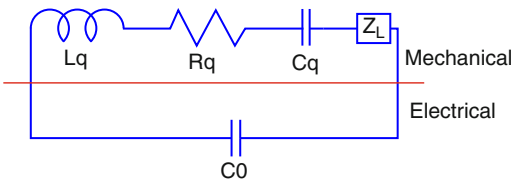

Fig. 9.3 Schematic of BVD model for Quartz crystal resonator (Damped) (Adapted from [2], https://doi.org/10.1016/j.sna.2016.01.021. Creative Commons license)

(9,53 $\times$ 10^3 A·s/m^2), ε_{22} is the quartz permittivity (3.982 $\times$ 10^{-11} A^2·s^4/kg·m^{-3}), A is the active electrode area (m^2), h_q is the quartz crystal thickness (m), η_q effective viscosity of quartz (3.5 $\times$ 10^{-4} kg/m·s), and ω_s is the series resonance frequency ($2\pi F_s$) [34].

According to theoretical models, when the QCR electrode is in contact with a sample, morphology of the conductance curve changes as it is shown in Fig. 9.2. In particular, the curve moves to the left on the frequency axis, increasing its bandwidth, and decreasing its magnitude. Figure 9.2 shows changes in series resonant frequency (F_s) and in half band half width (Γ). The electrical model BVD explains this phenomenon by adding an impedance (Z_L) that represents the characteristics of the sample [2, 7, 8, 34].

The model BVD for a crystal with material deposited on its electrode surface (mass or liquid) is shown in Fig. 9.3:

For a crystal in contact with a mass layer, Z_L has an inductance behavior (L_{mass}). This inductance models the mass effect on the crystal:

$$L_{mass} = \frac{2\omega L_q \rho_s}{N\pi} * \sqrt{\left(\frac{1}{\rho_q G_q}\right)} \tag{9.9}$$

where ρ_s is the density per unit area of the mass layer.

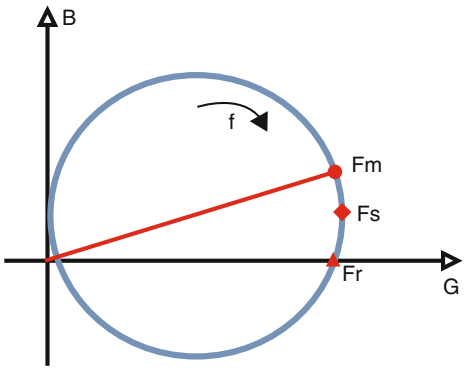

Fig. 9.4 Locus diagram of the crystal admittance (Adapted from [36] with permission from The Royal Society of Chemistry)

In case of the crystal in contact with a liquid layer, L_{liquid} and R_{liquid} are used to model the liquid effect in the crystal:

$$L_{\text{liquid}} = \frac{\omega L_q}{N\pi} * \sqrt{\left(\frac{2\rho_l \eta_l}{\omega \rho_q G_q}\right)} \tag{9.10}$$

$$R_{\text{liquid}} = \frac{\omega L_q}{N\pi} * \sqrt{\left(\frac{2\omega\rho_l \eta_l}{\rho_q G_q}\right)} \tag{9.11}$$

where ρ_l and η_l are the density and the viscosity of the liquid, respectively.

In liquid applications (quartz crystal with single side contact with a liquid), the quality factor Q is given by:

$$Q = \frac{\omega\left(L_q + L_{\text{liq}}\right)}{R_q + R_{\text{liq}}} \tag{9.12}$$

The additive contributions to L_q and R_q are similar because the real and imaginary parts of Z_L are similar too. As $L_q \gg L_{\text{liq}}$ and $R_q \ll R_{\text{liq}}$, the quality factor Q changes inversely with $\sqrt{F_0}$ [26]. This phenomenon can be observed in the plot of the conductance (G).

Using the typical nomenclature, ($R_q + R_{\text{sample}}$) is called R_s and ($L_q + L_{\text{sample}}$) is called L_s. R_s can be obtained with the inverse of the maximum value of the conductance curve. For undamped crystal (without sample) $R_q = R_s$ and $L_q = L_s$.

The equivalent circuit BVD also permits to identify the real and imaginary components of the crystal admittance. Using these components is possible to obtain the locus diagram of admittance $Y = G + jB$.

According to Fig. 9.4, there are three representative resonant frequencies (Fm, Fs and Fr). The first one (Fm) is obtained when the admittance value (Y) of the resonator is maximum. The second one (Fs) is obtained when the conductance value (G) of the

resonator is maximum. This frequency is denominated "series resonant frequency." The last one (Fr) is obtained when the susceptance value (B) is zero. This frequency is called "frequency at minimum impedance with zero phase" [2, 26, 37].

For a bare crystal (without sample), the real part of the crystal impedance Rs is very small; in consequence, the difference between the representative frequencies is not evident. However, when the sample is deposited, the damped generated on the crystal is related to the increase of the Rs and the difference between the frequencies is more obvious [7, 8, 26].

According to circuit theory, the resonant frequency for an ideal resonator is:

$$F_s = \frac{1}{2\pi\sqrt{L_s C_s}} \tag{9.13}$$

According to Wolfbeis [26], for small Rs, the characteristic frequency (Fr) may be calculated as:

$$F_r \approx \frac{1}{2\pi\sqrt{L_s C_s}} + \frac{{R_s}^2 C_0}{{L_s}^2 C_s} \tag{9.14}$$

It is important to note that Fr depends on the equivalent resistance Rs.

The only frequency independent of the influence of the capacitance C_0 is Fs. Fm and Fr depend on the C_0 value. In addition, external capacitances due to the external circuits connected to the crystal amplify the deviation between Fm and Fr with Fs [7, 26].

4 Experimental and Instrumental Methodology

4.1 Functionalization Electrode Surface

Interactions among active components inside an analyte and biocompatible components immobilized on an active surface are the basis of a biosensor operation. This interplay generates a biochemical signal related to physical or chemical features of the analyte in the sample. In this way, biosensors constitute a useful tool for understanding and evaluating biological processes. There are many techniques to coat and functionalize the electrode surface. For instance: (1) Self-assembled monolayers (SAMs) immobilize ligands in a high density, and often use poly(ethylene glycol) spacers. (2) A polyelectrolyte provides a thin layer of charge (positive or negative) for ionic interactions. (3) Viologen functionalized electroactive nanoclusters can be electrochemically deposited on the QCM surface. (4) X-ray crystal structure of a protein A fragment commonly used in the immobilization of antibody [38].

However, self-assembled monolayers (SAMs) are more typically used in QCM electrodes for biosensing applications due to its easy elaboration and strong covalent bond. SAMs are molecular assemblies that can be used to attach the capture

molecules to a surface such as gold. One advantage of the use of SAMs is avoiding the problem of lack of control over the orientation of the molecules; this problem arises when working with direct immobilization of solid materials. SAMs can be modified with chemical activators that bring it efficient properties to achieve an optimum immobilization of the analyte. The use of SAMs in QCM has shown to provide high sensitivity and the improvement in control over molecule orientation generates a better repeatability of experiments [39].

In Sect. 5.5, there are some novel techniques and materials for coating the crystal surface for instance: graphene oxide thin films, polyelectrolytes layers, and carbon nanotubes.

4.2 Impulse and Decay Method

This method consists of exciting the quartz crystal with an electric impulse signal between its electrodes. If the excitation is an ideal impulse, the quartz resonator will oscillate influenced only by its acoustic properties (mechanical damping). These oscillations will damp the amplitude due to the resistance component in the crystal. The effects of the external electronic circuit are negligible [26]. This is the principal advantage of this method because the oscillation frequency depends only on the motional elements.

The company Q-Sense has patented this method as "the QCM with dissipation monitoring (QCM-D)" [40]. The QCM-D method consists in obtaining the dissipation factor (D) by sensing the decay of the crystal oscillations after a short excitation pulse close to the resonant frequency (F_0). The decay rate is proportional to the energy dissipation of the oscillator [5, 41].

With the aim to sense the decay time of the oscillation, the oscillatory voltage between the electrodes is obtained and adjusted after the driving power is switched off. In this way, the signal in the quartz decays close to the series resonant mode [41, 42].

The amplitude decay rate depends on the properties of the oscillator and the sample under study [5, 41, 43, 44]. To obtain the output frequency (F), the signal sensed with a frequency given by the resonant frequency of the quartz crystal (F_0) is mixed with a reference frequency (F_{ref}) and filtered with a low-pass band filter. This procedure gives an output frequency (F) related to the difference between F_0 and F_{ref} ($F = F_0 - F_{\text{ref}}$) [5, 41, 42].

The frequency (F) is adjusted using the following exponentially damped sinusoidal:

$$A(t) = A_0 e^{t/\tau} \sin(2\pi F t + \alpha) \tag{9.15}$$

where A_0 is the amplitude at $t = 0$, τ is the decay time constant, and α is the phase angle.

Additionally, the dissipation parameter is inversely proportional to τ:

$$D = \frac{1}{Q} = \frac{1}{\pi \text{Ft}} = \frac{E_{\text{dis}}}{2\pi E_{\text{sto}}} \tag{9.16}$$

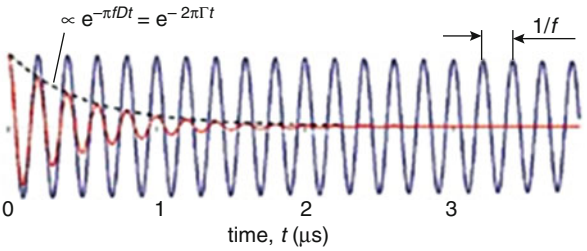

Fig. 9.5 Impulse excitation QCM-D method (Adapted with permission from [45]. Copyright (2011) American Chemical Society)

where Q is the quality factor. The parameter D can be also expressed as the Energy dissipated (E_{dis}) during one oscillation period over the Energy stored (E_{sto}) in the oscillating system [5, 41]. The parameter D is dimensionless. The following figure explains the technique QCM-D behavior:

In QCM-D method, the voltage between the electrodes is intermittently switched off and the decay time of the oscillation is observed. According to Fig. 9.5, the resonant frequency $f = F$s and the energy dissipation $D = 2\Gamma/F$s are extracted from the decay curve. The blue curve corresponds to a crystal oscillating in the air. The red curve corresponds to a crystal in contact with sample generating dissipation [45].

The resolution reached with this technique is around ± 0.1 Hz for the frequency and 1×10^{-7} for the dissipation factor [5].

Furthermore, the QCM-D technique permits to find Fs and D parameters at different overtones ($n = 1,3,5,\ldots$) of a fundamental resonant frequency [5].

QCM-D technique has been used widely in different studies, i.e.: cellular characterization [24, 46–49], protein detection [10, 50–54], DNA detection [12, 55–59], and viscosity analysis of different substances [2, 6, 56, 60–64].

Immobilization of DNA and proteins can be accurately measured by tracking changes in frequency and fitting these data to the Sauerbrey equation. However, in the case of samples containing water, as in protein, cellular studies or viscosity analysis, the factor D is a fundamental value to obtain a full characterization of the viscoelastic layer structure absorbed [5, 24, 49].

According to Dixon [5], the size and flexibility of the layer deposited on the crystal electrode is directly proportional to the factor D. Furthermore, plotting ΔF versus ΔD permits to obtain information about the conformation of the absorbed material and quantify variables related to viscoelastic properties (shear viscosity and storage modulus) [5].

QCM-D technology was commercialized by Q-Sense in 1996. Nowadays, there are many different versions of QCM-D instruments available from Q-Sense; a single channel version, four channel version, combined technique with microscopy, electrochemistry, or ellipsometry [40].

4.3 Oscillators Method

Considering that the quartz crystal behaves like a simple resonator with a high-quality factor; a typical method to reach its vibration is through oscillator circuits.

With the aim of generating stable oscillations, the oscillator circuit must excite the quartz crystal with a frequency where a sharp phase slope occurs [26]. This condition is fulfilled at the characteristic frequency (F_r). In consequence, when using the oscillators method, the quartz crystal does not oscillate at series resonance frequency because $F_r \neq F_s$. For crystals in contact with samples, this problem increases. In order to correct this phenomenon, the stray capacitance C_0 must be externally compensated [7, 14, 26, 33, 37, 65].

According to the equivalent circuit model BVD, the phase for a quartz crystal is defined as:

$$\varphi = \frac{\mathrm{Im}(Z)}{\mathrm{Re}(Z)} \tag{9.17}$$

where Z is the equivalent impedance of the crystal. When the capacitance C_0 is compensated, $Z = Z_m$. Here Z_m is the equivalent impedance for the series arm in the model (mechanical impedance- Fig. 9.1) [15, 26, 27, 32, 34, 37, 66–69]. In this case, the phase can be defined as:

$$\varphi = \frac{\mathrm{Im}(Z_m)}{\mathrm{Re}(Z_m)} = \frac{{}^{\omega}L_s - 1/_{\omega C_s}}{R_s} \tag{9.18}$$

After C_0 compensation, the conductance value G is maximum ($\mathrm{Re}|Z_m| \rightarrow \max$), the susceptance value B is zero ($\mathrm{Im}|Z_m| \rightarrow 0$) and the phase $\varphi = 0$ at series resonant frequency F_s. In other words, making the C_0 compensation, the crystal vibrates at F_s. According to Wolfbeis [26], the difference in the phase φ before the C_0 compensation and after the C_0 compensation for a crystal in contact with water is around 144 Hz.

In the oscillator methods, there are other variables called A and k, related to the open loop gain and feedback factor respectively. Using these variables, the electronic circuit must guarantee a stable oscillation compensating the sample damping. Some studies propose an automatic control for these variables [14, 70–72].

There are several designs of oscillator to work with liquid samples; for instance: emitter coupled oscillators [73–76], ACC oscillator [37, 77], lever oscillator [70], active bridge oscillator [71], and Bridge symmetric crystal oscillator [72].

4.4 Lock-In Method

The circuit proposed by Nakamoto [66] is a good example for the lock-in method. This circuit is composed of a voltage controller crystal oscillator (VCXO), and the RF voltage supply is a system of amplitude gain. Both systems create the variable input RF signal to the crystal.

As RF current detector, Nakamoto has used a toroidal-core transformer (I-U converter) [66]. Both signals, the RF voltage supply, and the current signal obtained are multiplied using a double balanced mixer (DBM) whose output is the product of these signals.

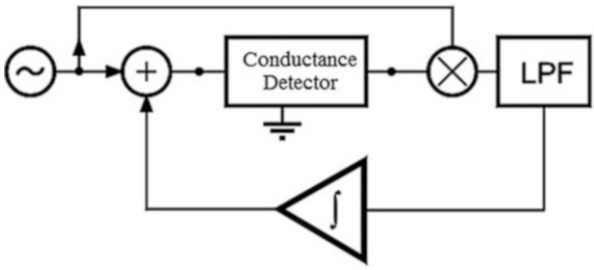

Fig. 9.6 Sensor schematic for Jakoby technique (Reproduced from [7], https://doi.org/10.3390/s8010370)

According to Nakamoto, the output signal has two components: DC and 2ω component. The 2ω component is eliminated by a low-pass filter (LPF). The DC signal is proportional to the real part of the crystal admittance [66]. The peak value of the DC signal is detected by a peak detector circuit during the frequency sweep.

The same method has been used by other such as Jakoby [7, 14]. Jakoby et al. include a similar scheme proposed by Nakamoto (named conductance detector) inside another loop indicated in Fig. 9.6.

According to Fig. 9.6, the second loop (integrator loop) permits to modulate the frequency of the feedback signal and to add it to the input sinusoidal signal. The output signal from the integrator determines the central frequency of the sweep. The amplitude of the input signal controls the sweep range. As result, the circuit detects the peak of conductance curve automatically [14].

4.5 Impedance Analysis

Impedance analyzer equipment measures the impedance or admittance of the quartz crystal in a wide range of frequencies for a complete characterization in the frequency domain. The sweep must be done close to resonance frequency to obtain values of interest. Currently, there is a lot of equipment capable of obtaining a complete impedance characterization in a wide frequency spectrum.

The use of an impedance analyzer is the easiest way to obtain the frequency response of the crystal because it is not necessary any other external circuit connected to the crystal. Additionally, the impedance analyzer can obtain the resistance and the reactance or the conductance and the susceptance with a good precision. In turn, using the conductance curve is possible to obtain the series resonance frequency F_s, R_q, and the quality factor Q. Also, it is possible to compensate the external influences over the crystal by means of instrument calibration.

However, for low-cost sensor applications, an impedance analyzer has two important disadvantages: high price and nonportability. In any case, the impedance analyzer is very useful as a first approximation to understand the behavior of the crystal.

Using a similar principle to the impedance analyzer, several electronic circuits have been designed to obtain the spectrum of impedance or admittance of the crystal

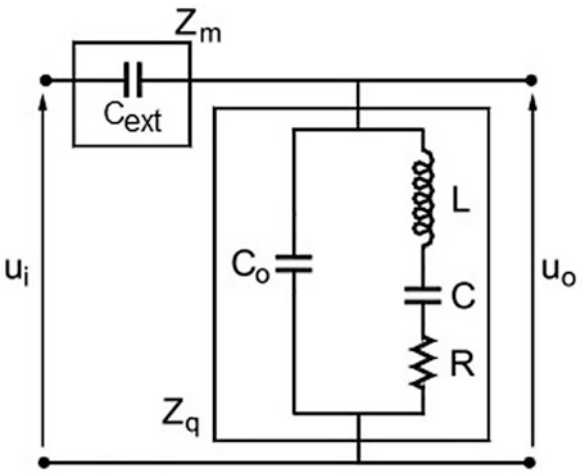

Fig. 9.7 Sensor schematic by Calvo technique (Adapted from [30] with permission from The Royal Society of Chemistry)

in a range of frequencies close to resonance [2, 30, 78, 79]. These electronic circuits are capable of obtaining the series resonance frequency (f_s) and the half band half width (Γ) for each measure cycle in a few seconds. Typically, the electronic circuit is configured for a specific range of frequencies, depending on the fundamental frequency of crystal; for example: if the fundamental frequency of resonance of crystal is 10 MHz, the electronic circuit is designed to perform a frequency sweep close to 10 MHz.

In the circuit proposed by Calvo et al. (Fig. 9.7), a capacitor is connected in series to the crystal. A sinusoidal signal is applied between the external capacitor and the grounded crystal electrode [30]. In this study, the authors perform several frequency sweeps close to the resonant frequency of the crystal, and they obtain the average values of the input and output voltages using an analog/digital converter and a computer.

The resultant equation for the transfer function according to Calvo's circuit is:

$$\frac{V_{\text{out}}}{V_{\text{in}}} = \frac{\sqrt{\left(\omega L - 1/\omega C\right)^2 + R^2}}{\sqrt{\left(\omega L - 1/\omega C + \omega L C_0/C_{\text{ext}} - C_0/\omega C C_{\text{ext}} - 1/\omega C_{\text{ext}}\right)^2 + \left(R + RC_0/C_{\text{ext}}\right)^2}} \tag{9.19}$$

The transfer function spectrum: $|Vo/Vi|(\omega)$, for the quartz crystal in contact with a viscoelastic fluid layer is obtained by nonlinear fitting of the experimental data using the analytical transfer function (Eq. 9.20) [30]. Figure 9.8 shows the resultant spectrum.

The transfer function spectrum is composed of 100 frequencies points around the natural resonant frequency of the crystal. The spectrum is built in 0.25 s (real-time evaluation) [30].

Using this method, the authors have also obtained the electrical equivalent circuit elements shown in Fig. 9.7. The results are shown in Table 9.1.

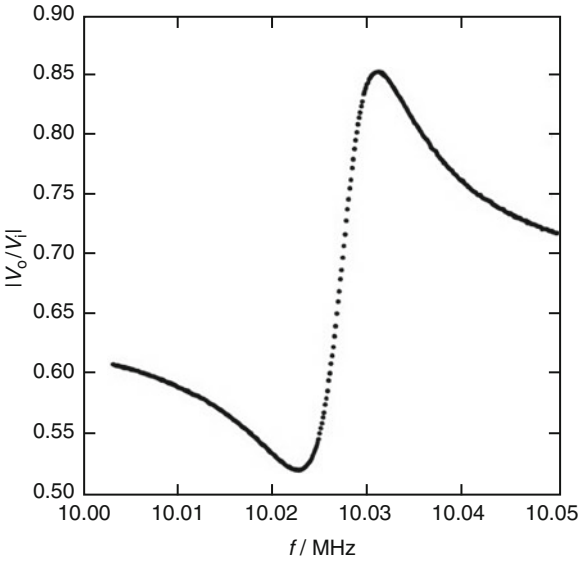

Fig. 9.8 Absolute values of the transfer function |Vo/Vi| (Reproduced from [30] with permission from The Royal Society of Chemistry)

Table 9.1 Typical values of the quartz crystal equivalent circuit components (Adapted from [30] with permission from The Royal Society of Chemistry)

	QUARTZ	Water	Hydrogel in air
X_{Lf}/Ω	ca. 4.7×10^5	214	364
L/mH	ca. 7.5	3.5×10^{-3}	7.45×10^{-3}
R/Ω	ca. 90	214	0

In a more recent work [2, 35], the acquisition of the current through the crystal (I), the voltage between its electrodes (V), and a signal related to the susceptance of the crystal (B) is proposed. In this method, a frequency sweep is done using a configurable sinusoidal generator. For each frequency value, a voltage, current, and susceptance values are acquired. Current is detected using the toroidal transformer (Fig. 9.9). Voltage and current signals are mixed in order to obtain the signal related to crystal susceptance. Signals (I) and (V) are filtered and rectified with the aim of obtaining their peak values (I_p and V_p). The three signals are acquired using an arduino DUE card. Admittance signal is obtained as: I_p/V_p. Conductance signal is obtained using admittance and susceptance data according to the following equation:

$$|\mathbf{G}| = \sqrt{\left(|\mathbf{Y}|^2 - |\mathbf{B}|^2\right)} \tag{9.20}$$

Conductance (G) and susceptance (B) are plotted versus data frequencies of the signal generator.

In a similar way to Calvo's method, the absolute value of the admittance spectrum is obtained (Fig. 9.10).

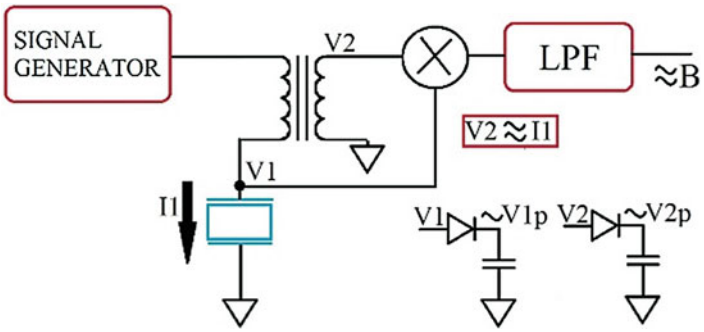

Fig. 9.9 Sensor schematic by Carvajal technique (Reproduced from [36], https://doi.org/10.3390/s16111959, under the Creative Commons Attribution License)

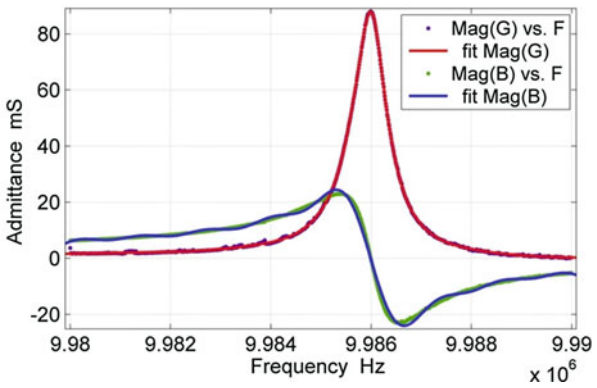

Fig. 9.10 Admittance spectrum (Reproduced from [2], https://doi.org/10.1016/j.sna.2016.01.021. Creative Commons license)

Table 9.2 Results for unloaded crystal and crystal in contact with water (Adapted from [2]. https://doi.org/10.1016/j.sna.2016.01.021. Creative Commons license)

		RQ (Ω)	F_s (Hz)	Γ (Hz)
Air	Mean	14.15	9985755.9	365.5
	SD	0.4	7.4	3.9
Water	Mean	202.2	9,983,738	2904.8
	SD	1.9	14.2	97.1

The experimental admittance and susceptance spectrums obtained are fitted using a summation of Gaussian functions and a summation of sine functions, respectively [2].

Carvajal and coworkers have calculated the series resonant frequency, the R_q value as the inverse of the maximum value of the admittance spectrum, and the half band half width (Γ) [2]. The measures were done for the unloaded crystal (air) and the crystal in contact with water (Table 9.2).

5 Key Research Findings

5.1 Monitoring Cellular Responses

Cell health can be characterized by analyzing intrinsic properties such as growth, repair, protein degradation, and gene expression. As cells respond to different types of perturbations, it is important to determine which molecules are interfering with a cell activity [24]. Cells respond to stressful agents by complex pathways that often lead to cytoskeletal changes in the cells. These changes can be detected using different techniques, such as microscopy or flow cytometry. However, the use of these techniques requires fixing or lysing cells, so they cannot be used for real-time characterization of cell health [24].

Quartz crystal microbalance with dissipation monitoring (QCM-D) may be used for real-time in situ detection of cytoskeletal changes in live primary endothelial cells in response to different cytomorphic agents. However, from a single measurement of frequency (F), it is not simple to relate with structural or conformational changes occurring at the sensor surface. Energy dissipation (D) is a useful indicator of the viscoelastic properties of deposited material. It should also be monitored by detecting cytoskeletal changes as cell responses. In that case, energy dissipation can be modeled as a purely liquid effect as well as a purely elastic mass effect [24]. Fatisson and coworkers show that the interaction between cells and surface produce a unique and reproducible dissipation against frequency. In the same research [24], it is shown that the early stages of cytoskeletal changes can be detected providing reproducible and characteristic QCM-D signals.

The results show that a fast (few minutes) sensing response can be obtained in situ and in real time. Fatisson et al. have used two different surfactants (TX-100 and LPS) in order to generate the cytoskeletal changes in bovine aortic endothelial cells (BAEC) and can characterize them with the QCM-D [24].

According to Figs. 9.11 and 9.12, using TX-100, there were two phases in QCM-D signal whereas using LPS there was only one phase. In addition, in the presence of LPS, the ΔF signal has a more stable incremental behavior while ΔD decreased, indicating less mass in contact with the sensing region. In the case of TX-100, the ΔF signal decreased indicating more mass detected. Since the D factor increases with material viscoelasticity, a low D factor generally indicates that the material is rigid. For TX-100, ΔD decreases in phase I, suggesting rigid mass on the surface. For TX-100, phase II indicates mass loss on the surface related to lysis in the cell. Authors have compared the QCM-D results with microscopy confirming the hypothesis related to cytoskeletal changes.

5.2 Medical Applications

QCM has been found to be a very important tool in the diagnosis of medical diseases. Some relevant research topics are blood coagulation analysis [80–84], Alzheimer disease [85, 86], cancer [87–90], and pathogen detection [46, 48, 54, 91].

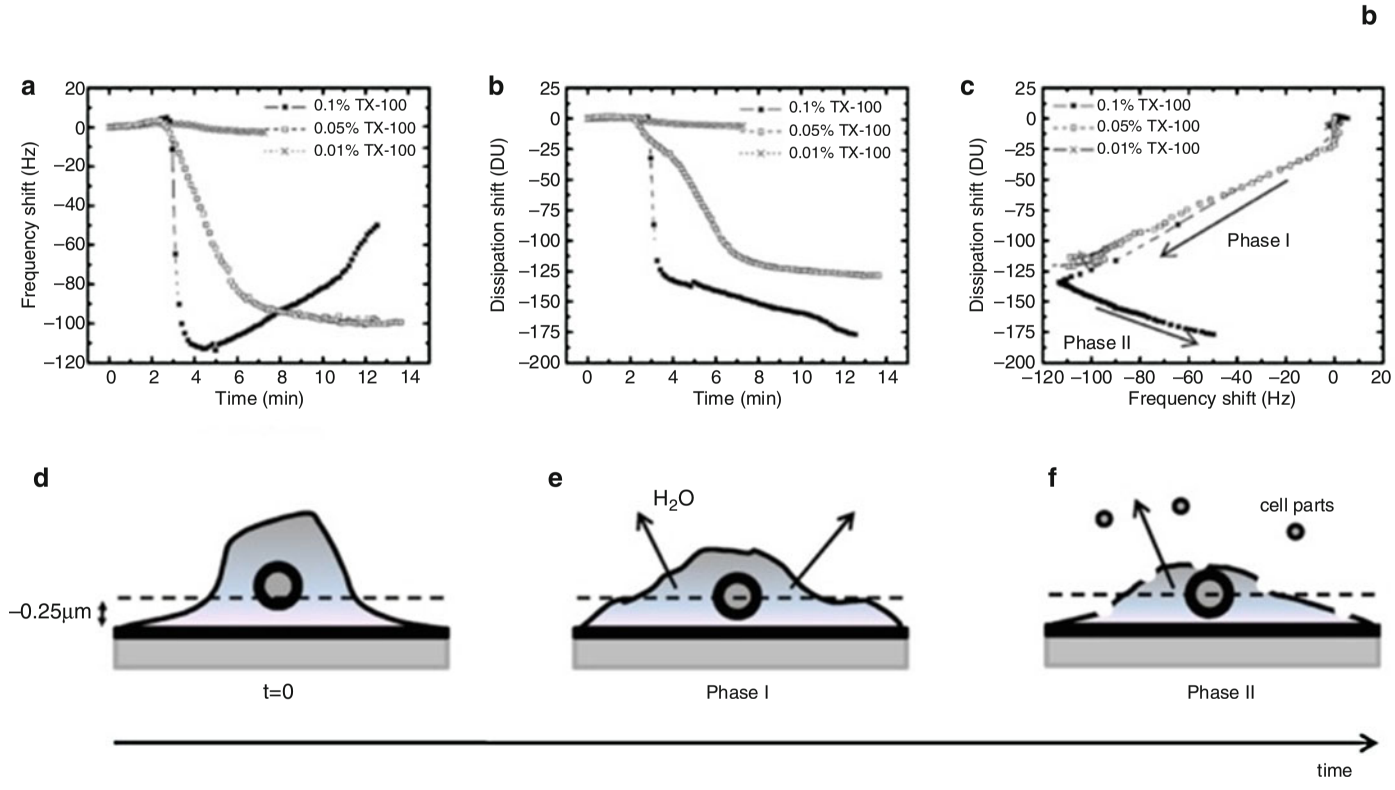

Fig. 9.11 Results obtained for TX-100: (**a**) frequency and (**b**) dissipation shifts (1st overtone) for BAEC response. (**c**) Δf plot resulting from (**a**) and (**b**) curves. Phase I: hyperosmoticmedium effect, and Phase II: cell lysis is occurring. (**d**) a nontreated resting cell compared to the likely theory for the effects of TX-100: (**e**) hyperosmotic effect, Phase I, and (**f**) cell lytic effect, Phase II. (Reprinted from [24], copyright (2010), with permission from Elsevier)

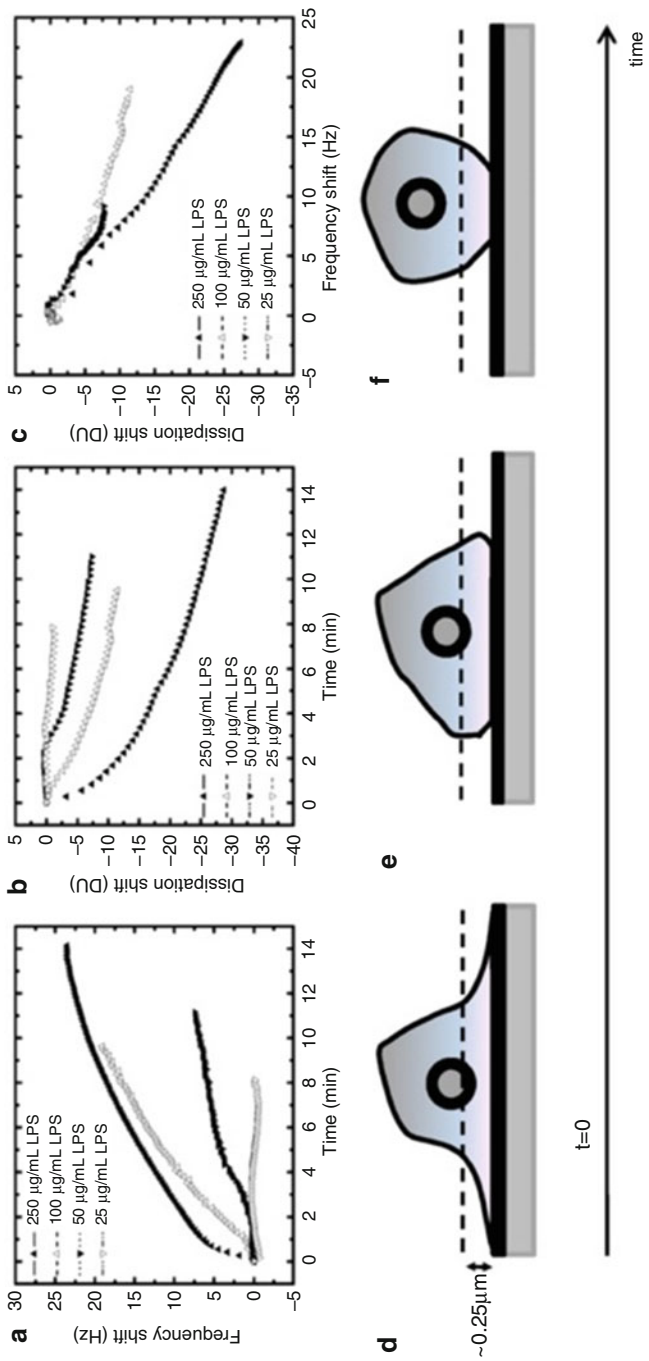

Fig. 9.12 Results obtained for LPS. (**a**) frequency and (**b**) dissipation shifts (1st overtone) for BAEC response. (**c**) Δf plot resulting from (**a**) and (**b**) curves. (**d**–**f**) Schematic diagrams representing the effect of LPS on BAEC with time, starting with a nontreated cell ($t = 0$, d). (Reprinted from [24], copyright (2010), with permission from Elsevier)

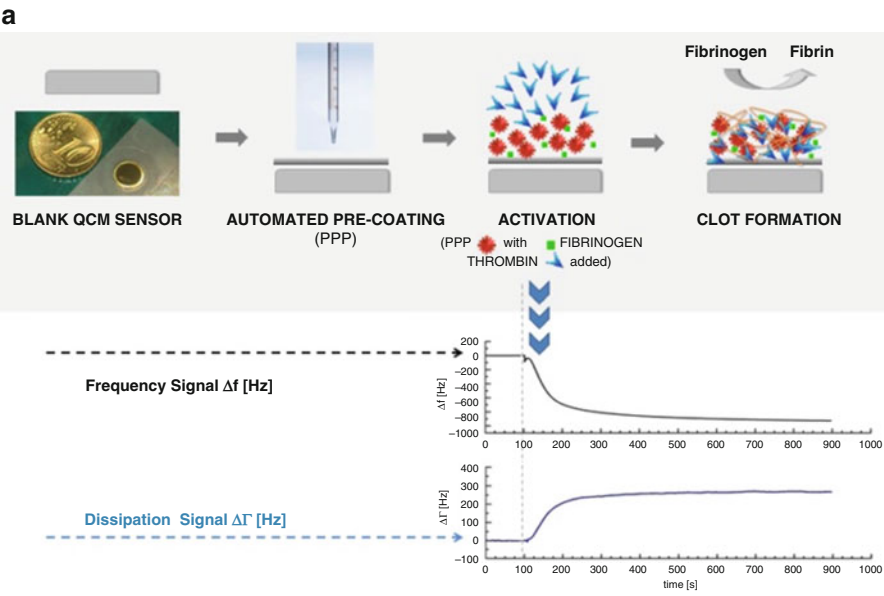

Fig. 9.13 (**a**) Illustration of the general idea of a QCM-based coagulation measurement based on Clauss assay on a precoated quartz (PPP) (Reproduced from [80], https://doi.org/10.3390/s16030282, under the Creative Commons Attribution License)

5.2.1 Blood Coagulation Analysis

In particular, the QCM-D method has been applied for measurement of parameters associated with hemostasis such as assessment of fibrinogen levels and thromboplastine time [80–84]. Hemostasis includes the different processes required to avoid blood loss during an injury. The organism needs to make sure that the flow of blood is not altered in other regions of the body. Two main steps occur after an injury. Firstly, platelets aggregate forming a plug. Secondly, a fibrin mesh is formed from its precursor: fibrinogen [92]. Hemostasis monitoring is relevant during surgical operations, especially in cardiac surgery when working with circulation devices that operate outside the body of the patient [92].

Gehring and coworkers have prepared a series of dilutions (1:5–1:40) using reference plasma to give a range of fibrinogen concentrations. The clotting times of these dilutions are measured [80]. The crystal used was a piezoelectric 10 MHz AT-cut quartz, and the parameters taken into account in the study were three: fQCM, frequency signal shift; dQCM, dissipation signal shift; and tfQCM, mathematically calculated turning point of fQCM. Gehring et al. [80] induced the coagulation on the sample, and QCM signal changes were monitored in real time during clot formation. In consequence, it was possible to use the frequency and dissipation signal shift for interpretation and evaluation (Fig. 9.13).

QCM results were compared to Clauss fibrinogen assay (CFA) technique for internal and external reference methods (immunological assessment of fibrinogen,

optical coagulometry, mechanical coagulometry). QCM-D sensor device for coagulation measurements has a high degree of correlation to reference techniques like activated partial thromboplastin time (aPTT) [80–84]. As future quantitative fibrinogen measurements, the new important question is related to find out whether the observed signal changes were caused by mass adsorption only, by changes in viscosity, or by a combination of both [80].

In a similar study, Yao et al. [84] have used a QCM with a 10 MHz quartz crystal AT-cut in order to determine the activated partial thromboplastin time (APTT) for 120 anticoagulated plasma specimens. They spin-coated the crystal surface with polystyrene (0.5 wt% in chloroform) at 2500 rpm for 5 min to make a hydrophobic surface which is favorable to fibrinogen absorption. They compared the results obtained about the concentration of fibrinogen and FVIII in the plasma specimens with an optical coagulometer (STAGO-ST4). The correlation coefficient was 0.949 for fibrinogen and 0.948 for factor VIII [84].

Additional to the mass deposition study, an analysis of viscosity was performed. During blood coagulation, the coagulation reaction changes the viscosity of the plasma, and then changes the frequency of the QCM. The frequency changes of the QCM biosensor reflect not only the quality change but also variations in the density and viscosity of the system. The viscosity change shifts the resonance frequency of the QCM biosensor enabling real-time continuous monitoring of this biological event. The viscosity of the reaction system changes instantaneously during the coagulation formation, and the mass deposition on the surface of crystal also changes. Both of them caused the sudden frequency change of the crystal [84]. In order to differentiate the effect caused by mass deposition and by a change of the viscosity, Yao and coworkers monitored the fibrin clot formation. When the fibrin clot finally formed, there was a significant change of viscosity which resulted in a significant frequency change. The significant changes of frequency indicate the endpoint of the coagulation reaction, as there are no subsequent changes in viscosity that would result in a change in frequency signal [84].

Yao et al. have obtained a good linear relationship in a double-logarithmic plot of APTT versus fibrinogen concentration in the range of 1.58–6.30 g/L. Additionally, for factor VIII, the detection range of the QCM biosensor is 0.0185–0.111 mg/L. The time required to complete the analysis was just 10 min [84].

5.2.2 Alzheimer Disease

Regarding the use of QCM in diagnosing diseases, other remarkable works are related to Alzheimer [85, 86]. A clear indicator of Alzheimer's disease (AD) is the deposition of β amyloid (Aβ) in the form of senile plaques (SP) in the walls of cerebral and meningeal blood vessels. Aβ is derived from a larger transmembrane spanning protein known as the amyloid precursor protein (APP). Aβ region of APP are amino acids 11–15 of the transmembrane domain and 28 amino acids of the extracellular domain.

Nowadays the clinic diagnosis of AD is done via detection of $A\beta_{1-42}$ in ELISA sandwich immunoassay. This method is reliable but expensive and cannot be used

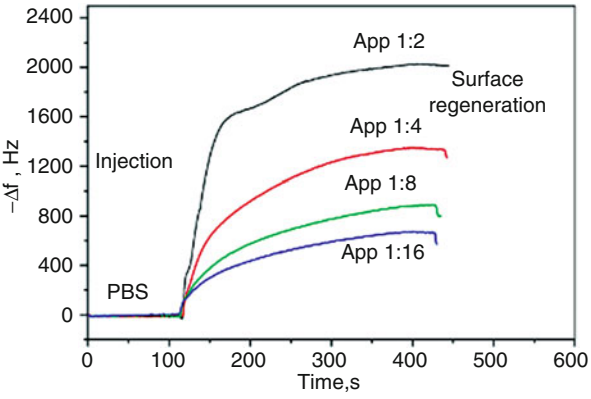

Fig. 9.14 Sensor responses to binding of APP_{770} of different concentrations in CM to DE2 antibodies immobilized on the surface (Reprinted from [85]. copyright (2010), with permission from Elsevier)

for early diagnosis of the disease. A promising technology for early diagnosis is surface plasmon resonance (SPR), which offers high sensitivity. A recent method related to SPR is called total internal reflection ellipsometry (TIRE); this technology has been used as an analytical tool in different biosensing projects. Unlike SPR, which is based on the monitoring of light intensity, TIRE detects simultaneously the amplitude ratio and the phase shift of polarized light.

The project by Mustafa et al. [85] uses TIRE for the detection of $A\beta_{1-16}$ which is not the actual marker for AD, but it is a smaller water-soluble peptide and will serve as a step forward in the big objective of developing a rapid diagnostic tool for AD [85]. QCM was used to monitor in situ the immune reaction between AP_{770} and DE2 antibodies in complete medium (CM), a mixture of salts, amino acids, and different proteins. DE2 are specific monoclonal antibodies raised against $A\beta_{1-16}$. The objective of QCM measurements was to verify if this method works for the detection of APP_{770} in a CM solution with the help of monoclonal antibodies DE2. For this reason, the experimental setup also used a QCM without DE2 as a control test.

As result, the spectrum of TIRE shows differences in the parameters after each step in the sequence: PAH, Protein F, DE2 antibodies, and $A\beta_{1-16}$. $A\beta_{1-16}$ was also tested in different concentrations (0.05, 0.5, 5.0, 50, 500, and 5000 ng/ml). After the spectrum analysis, it was found that the obtained values of thickness correlate with the size of adsorbed molecules as well as their concentrations on the surface. The observed calibration curve was a sigmoid which is typical for immune reactions, with an approximate linear range between 2 ng/ml and 500 ng/ml. The minimal detected concentration was 0.05 ng/ml, which is considered as a very high sensitivity making this a promising method for AD diagnostic.

In the QCM experiment, the comparison between the channel coated with DE2 and the control channel (without DE2), it was found that the responses were almost identical, which proves the insignificance of nonspecific binding of other proteins present in CM.

Figure 9.14 shows the response of the QCM sensor of APP_{770} diluted in CM. Overall results can be seen as progress in the detection of larger molecules such as the actual marker of Alzheimer's disease in real biological samples.

In a similar way, Wang et al. [86] have studied the relation between resveratrol and its derivatives (abundant natural polyphenols in red wine) with the reduced incidence of Alzheimer's disease (AD). A QCM has been used to measure the mass deposition rate and to evaluate the binding of Aβ aggregates to the lipid membranes: 1-Palmitoyl-2-oleoylphosphatidylcholine (POPC), dipalmitoylphosphatidylcholine (DPPC), and dipalmitoylphosphatidylglycerol (DPPG). These membranes were formed on the surface of a SiO_2-coated QCR. The binding of Aβ aggregates to membranes is believed to cause defects within the membrane and results in functional disorders. Thus, polyphenols in red wine can reduce this binding and protect the membranes [86]. Based on these results, new treatments against AD could be developed.

5.2.3 Cancer

Cancer is one of the most concerning diseases nowadays. Point of care detecting devices, using biosensors that detect cancer biomarkers, may be an effective tool for diagnosing this disease. Providing with an early and accurate diagnosis is fundamental as receiving an early and effective treatment may prevent cancer from becoming metastatic.

According to Uludağ et al. [87], prostate cancer is the most common in Europe and can be detected by identifying an increase in the prostate-specific antigen (PSA) or alpha 1-antichymotrypsin (ACT) PSA levels in serum. In this way, PSA may be used as a biomarker. Detection methods such as electrochemical, optical, microcantilever, fluorescence, and QCM biosensors have been used. PSA detection limit using these methods varies between 0.2 pg/mL and 10 ng/mL. Traditionally, Au nanoparticles have been used to amplify the detection signal, and the test has been performed in buffered solutions. To obtain clinically relevant results, it is essential to perform the test in serum but in this medium nonspecific binding occurs between the sensor surface and serum proteins.

Uludağ and coworkers have proposed a cancer biomarker analysis using an antibody-coated QCM together with Au nanoparticles to increase the mass due to antigen binding and therefore the sensitivity of the assay. A QCMA-1 biosensor was used. Gold-coated QCMA-1 sensor chips (20 MHz) have two sensing arrays each, which allows measuring active and control sensor surfaces simultaneously. The surface of the sensor was modified adding a self-assembled monolayer (SAM). Monoclonal anti-PSA antibodies (capture antibody) and mouse IgG antibody (control antibody) were immobilized on the sample and control sensing arrays. Besides, Au nanoparticles were modified with anti-PSA-detection antibody and reserved [87].

BSA nonspecific binding (using PBS/T buffer with BSA) to the control sensor was studied through binding test, and it was observed that the control sensor did not give any frequency shift even for the highest PSA concentration. Nonspecific BSA binding to the capture surface was observed injecting BSA for 3 min and it was detected to be of 4 ± 1 Hz. For the sandwich assay, anti-PSA detection antibody was injected to the capture surface in the absence of the antigen (PSA), and the nonspecific binding was detected as 5 ± 2 Hz. The nonspecific responses were subtracted from the PSA or PSA detection antibody data [87].

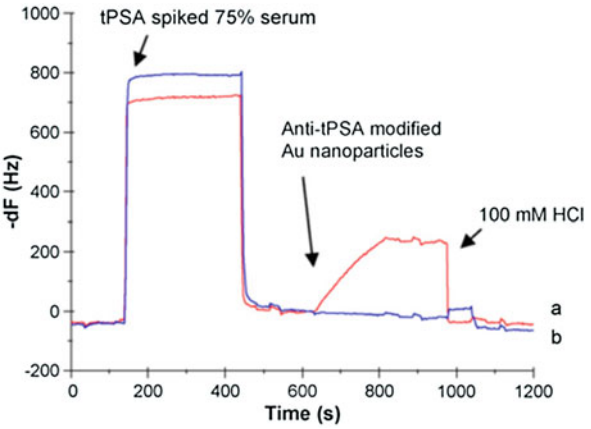

Fig. 9.15 Results obtained for Anti-tPSA modified with AU nanoparticles on active (**a**) and control (**b**) surfaces (Reprinted from [87], https://doi.org/10.1016/j.talanta.2010.04.034, copyright (2010), with permission from Elsevier)

Uludağ and coworkers obtained the PSA-binding calibration curve in a concentration range 4.7–5000 ng/mL. Binding association and dissociation rates were calculated fitting the binding response curves to a 1:1 Langmuir binding model. A calibration curve was obtained also for the sandwich assay in a concentration range between 150 and 2.3 ng/mL. PSA detection limit turned out to be 4.7 ng/mL (four folds more sensible than the direct assay). The success of these results encouraged the assay to be performed using human serum (which usually increases the detection limit).

PSA direct and sandwich assays were analyzed using buffer, 10% serum and 40% serum. No response was obtained when performing the direct assay in 40% serum concentration but still a response was obtained with the sandwich assay. So, the sandwich assay was performed in 75% serum, and a calibration curve was obtained in a concentration range between 2.3 and 150 ng/mL tPSA. The initial detection limit obtained by the authors was 9.4 ng/mL, which is not sensitive enough for PSA detection. To enhance the sensitivity, Uludağ, et al. [87] used modified Au nanoparticles to perform a sandwich assay. With this method, the detection limit lowered to 0.29 ng/mL.

Figure 9.15 shows that the assay performed using the developed matrix buffer together with the modified Au nanoparticles has potential for a fast and sensitive detection of cancer biomarkers in serum. Additional advantages of the method are short assay time, label-free method, reusable sensor chip, and detection of PSA in high serum concentrations.

In another notable study, M. Bianco and coworkers have proposed the use of QCM in order to detect pancreatic cancer [89]. Pancreatic ductal adenocarcinoma (PDAC) is cataloged as the most aggressive of all cancer types. In particular, this cancer is characterized by a rapid progression and resistance to conventional treatments. The authors have validated three different methods of functionalization: 1. β-mercaptoethanol (MCE) ex situ quartz crystal, 2. Mercaptoundecanoic acid (MUA)/*N*-hydroxysuccinimide (NHS)/*N*-(3-dimethylaminopropyl)-*N*- ethylcarbodiimide hydro-chloride

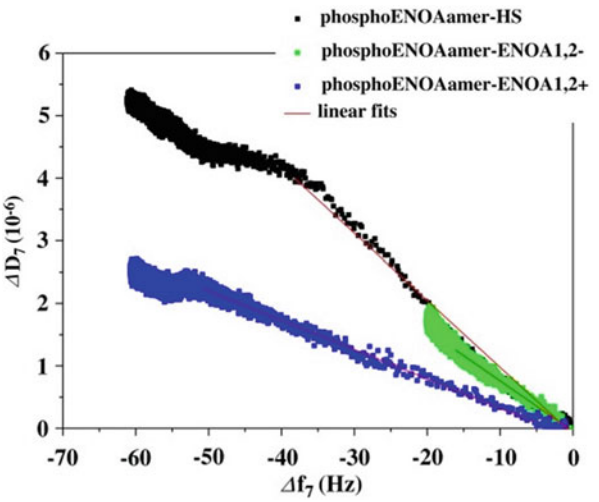

Fig. 9.16 ΔD7 versus ΔF7 plots for phosphoENOAmer-HS sera (black dots), phosphoENOAmer-ENOA1,2$^-$ sera (green dots), phosphoENOAmer-ENOA1,2$^+$ sera (blue dots) and related linear fits (red lines) (Reprinted from [89], https://doi.org/10.1016/j.bios.2012.10.012, copyright (2012), with permission from Elsevier)

(EDC) ex-situ quartz crystal, and 3. α-Meth- oxy-ω-mercapto (PEG) ex situ quartz crystal. In every case, a final washing of ultra-pure water was used to remove the unadsorbed thiol compounds [89]. In the case of MUA/NHS/EDC, the authors have added 1 M EA solution with the aim of passivating the reactive surface. The SAM formed on the QCM sensor surface was named by the authors as MUA/EA [89]. According to Bianco results, the best functionalization method was a thiol self-assembled monolayer (SAM) based on an MUA (MUA/EA) because the background signal achieved was the smallest in comparison with the other functionalization strategies. The authors have used AFM images to confirm this result [89].

Using the functionalization strategy selected, the peptide antigen is immobilized. The procedure consists in incubating the surface with 50 mL of 200 nM phosphoENOAmer or ENOAmer for 2 h to temperature controlled. (ENOAmer and phosphoENOAmer peptides differ only in the phosphorylation of Serine 419) [89].

QCM measurements of autoantibody response to ENOA-derived peptides were performed. The presence of autoantibodies against ENOA1,2 is associated with pancreatic cancer disease [89]. Three different samples (ENOA1,2$^+$, ENOA1,2$^-$, and HS sera) have been proposed in order to evaluate the sensor performance. Human serum (HS) has been obtained from healthy patients, ENOA1,2$^-$ have been obtained from PDAC patients without the presence of antibodies, and ENOA1,2$^+$ have been obtained from PDAC patients that contain antibodies.

According to Bianco results, HS and ENOA 1,2$^+$ sera interact with phosphoENOAmer peptide more than with ENOAmer. Moreover, ENOA 1,2$^-$ sera interact strongly with ENOAmer peptide, while showing a weaker interaction with phosphoENOAmer [89]. In addition, the dissipation signal ΔD has been compared with ΔF in the seventh overtone with the aim of obtaining information about viscoelastic properties of the layer (Fig. 9.16).

The slope was calculated using the results from Fig. 9.16. According to Bianco interpretation, the small value of the slope for the phosphoENOAmer-ENOA1,2^{+} serum indicates a strong and compact film. In addition, the result indicates that specific interactions produce more well-ordered antibody films than un-specific ones [89]. In this way, the combined analysis between ΔF and $\Delta \Gamma$ has permitted to discriminate specific interactions with ENOA1,2^{+} antibodies in patients with PDAC.

5.2.4 Pathogen Detection

QCM-D method also has been used in the detection of bacterial or viruses. There are many studies to detect different infections and pathogens. For instance, salmonella, tuberculosis, and avian influenza virus. In relation to Salmonella, its accidental contamination in foods is a major problem for the food industry worldwide [46]. Salmonella serotypes are among the most common bacteria responsible for foodborne gastroenteritis. In Salam's work [46], the use of QCM biosensor with a microfluidic system for the rapid and real-time detection of Salmonella typhimurium is proposed. The binding of the Salmonella cells onto the immobilized anti-Salmonella antibody generates a shift in the sensor frequency, which was correlated to cells concentration in the sample. Salmonella cells were detected using direct, sandwich, and sandwich assay with antibody-conjugated gold nanoparticles. These results are shown in the Figs. 9.17 and 9.18. The performance of the QCM biosensor developed with gold nanoparticles gave the highest sensitivity with a limit of detection (LOD) ~10–20 colony forming unit (CFU) mL^{-1} [46].

In relation to tuberculosis, the Mycobacterium Tuberculosis (Mtb) epidemic is larger than previously estimated, reflecting new surveillance and survey data from India. However, the number of TB deaths and the TB incidence rate continue to fall globally and in India. In 2015, there were 10.4 million new (incident) estimated TB cases worldwide, of which 5.9 million (56%) were among men, 3.5 million (34%) among women, and 1.0 million (10%) among children. People living with HIV accounted for 1.2 million (11%) of all new TB cases [93].

With the aim to detect Mtb, an immunosensor based on QCM has been successfully designed and employed to screen for both whole Mtb bacilli and an Mtb surface antigen, lipoarabinomannan (LAM) [48]. Additionally, the assays can be adapted for use with antibodies to multidrug resistant tuberculosis, reducing the time it takes to develop diagnostics for new strains of tuberculosis [48]. As results, Hiatt et al. report the QCM successfully measured the adsorption of Mtb and LAM in less than 20 min. The Mtb mass detected was around 23 $\pm$ 1 ng for the interaction with antibody LAM (α-LAM) and 14 $\pm$ 1 ng for the interaction with anti-H37Rv. Figure 9.19 shows a total detection experiment for LAM. The α-LAM antigen has a strong affinity for LAM. According to [48], the α-LAM immunosensor has the most potential application in point of care detection.

Regarding influenza virus, avian influenza viruses (AIV) are a significant concern globally due to its high mortality rate both in poultry and humans, constituting a major threat for public health and causing enormous economic loses. In [54], an apta-sensor based on ssDNA crosslinked polymeric hydrogel and QCM for rapid,

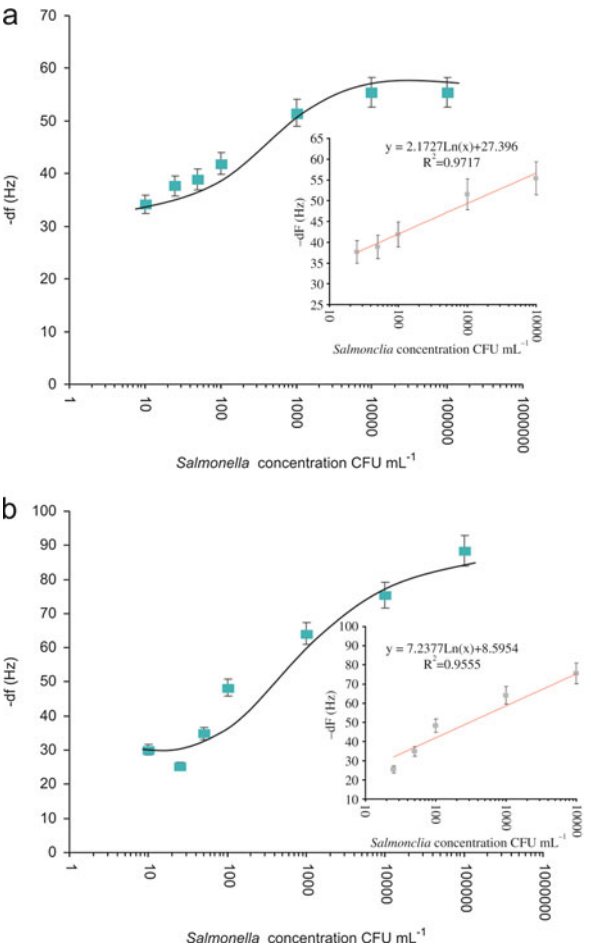

Fig. 9.17 Results for Salmonella. Salmonella standard plot with –dF (Hz) versus Salmonella concentration on the QCMA-1 sensor for (**a**) direct binding assay (LOD = 1.83×10^2 CFU ml^{-1}) and (**b**) sandwich assay (LOD = 1.01×10^2 CFU ml^{-1}). Linear slope taken from Salmonella standard plot, error bar = 3 data points, all control subtracted data (Reprinted from [46], https://doi.org/10.1016/j.talanta.2013.06.034, copyright (2013), with permission from Elsevier)

sensitive, and specific detection of AIV H5N1 is described. The aptamers (artificial nucleic acid ligands, specifically generated against certain targets) are used for recognizing the antigen due to their advantages over antibodies: overcoming the use of animals for their production can be chemically modified and easily labeled and have good thermal stability.

Wang et al. [54] used three hydrogels with different acrylamide ratios, and the aptamer monomers were synthesized (hydrogel I (100:1), hydrogel II (10:1), and hydrogel III (1:1)). Hybridization between an aptamer with high affinity and specificity against (AIV) H5N1 and ssDNA formed the crosslinker in the polymer hydrogel. It was immobilized on the gold surface of a QCM sensor using a self-assembled monolayer (SAM). The immobilization of aptamer hydrogel I, II, and III on gold-coated quartz crystals resulted in frequency shifts (ΔF) of -78 ± 14, -81 ± 17, and 83 ± 19, respectively [54]. Tests were performed to prove the

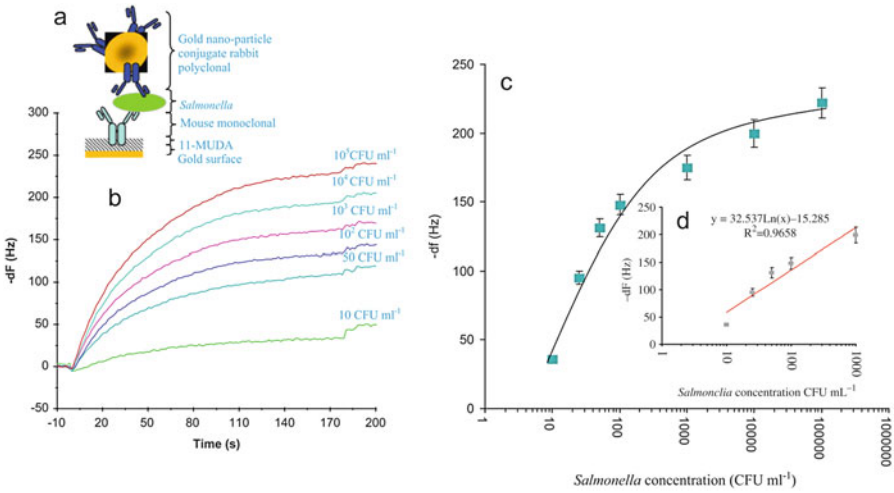

Fig. 9.18 Results for Salmonella. (**a**) Schematics of the sandwich assay with nanoparticles, (**b**) frequency response profiles for Salmonella assay with different cell concentrations, (**c**) Salmonella standard plot with −dF (Hz) versus Salmonella concentration (LOD =?10–20 CFU ml^{-1}), (**d**) linear slope taken from Salmonella standard plot, error bar = 3 data points, all control subtracted data (Reprinted from [46], https://doi.org/10.1016/j.talanta.2013.06.034, copyright (2013), with permission from Elsevier)

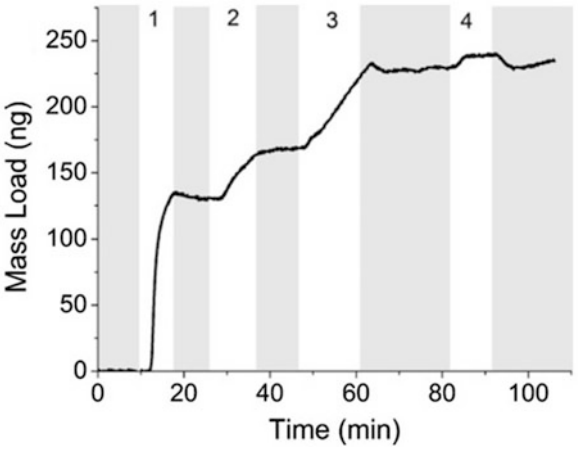

Fig. 9.19 Real-detection of LAM (8 μg/mL). The total mass detected in each step is as follows: (1) 131 ng protein A, (2) 39 ng BSA, (3) 61 ng α-LAM, and (4) 12 ng LAM (Reprinted from [48], https://doi.org/10.1016/j.snb.2012.06.095, copyright (2012), with permission from Elsevier)

feasibility for AIV H5N1 detection. When the hydrogels were exposed to the target virus, an abrupt swelling was produced due to the binding reactions with the aptamer that caused the dissolution of the linkage between the aptamer and ssDNA [54]. Figure 9.20 shows the results obtained using the aptamer hydrogel I. The total detection lasted 30 min.

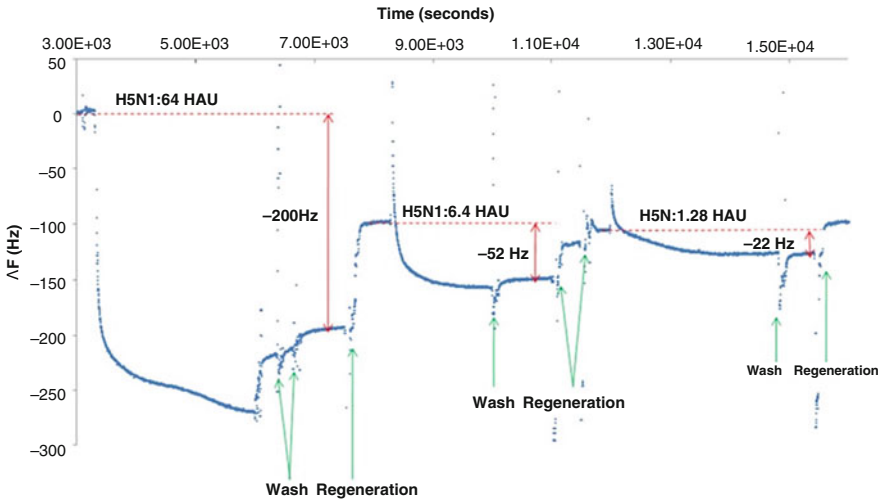

Fig. 9.20 ΔF obtained for aptamer hydrogel I with different titers of AIV H5N1 (64, 6.4, and 1.28 HAU, respectively) (Reprinted from [54], https://doi.org/10.1016/j.bios.2012.10.038, copyright (2012), with permission from Elsevier)

5.3 Environmental Monitoring

Monitoring the environment is a fundamental activity in many fields because many daily processes involve chemicals potentially destructive to the environment and also to the human health [94–96]. About the QCM studies, humidity monitoring and detection of organic compounds are relevant research fields.

5.3.1 Humidity Monitoring

Studies associated with humidity sensors have special attractive because of their wide and essential applications in both industrial and domestic environments [67, 95, 97, 98]. Humidity measures are associated with indoor air quality monitoring, heating ventilating air conditioning, manufacturing process control, and agriculture and electric devices [50, 94, 95, 99]. Humidity can also affect the own measures in the QCR sensors, for example, used in gas monitoring [98].

Different materials have been developed as the coating films to detect various kinds of vapors and humidity. Recently, Yao et al. [67] have used graphene oxide (GO) as a sensitive material for coating the quartz crystal microbalance in order to measure the relative humidity. In addition, Tai et al. have proposed the use of protonated polyethylenimine-graphene oxide nanocomposite thin film with the aim of measuring humidity [99] (Sect. 5.5.1).

Xie and coworkers have also proposed a humidity sensor using ZnO colloid particles as a coating material on a QCR surface [95]. ZnO particles can be grown in different morphologies and can give high sensitivity regardless of the chemical environment in which they are employed.

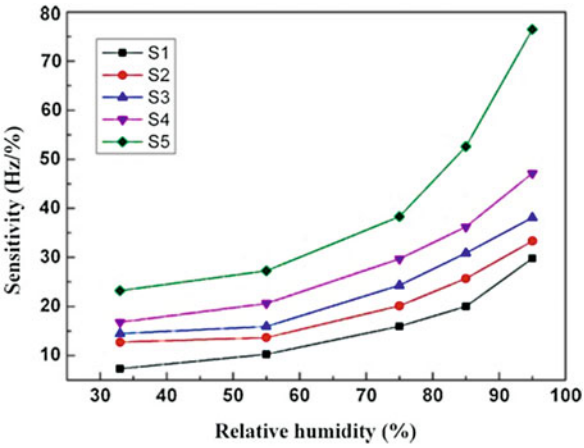

Fig. 9.21 Sensitivity curves in RH range from 33% to 95%. ZnO average diameter: S1 = 100 nm, S2 = 370 nm, S3 = 500 nm, S4 = 560 nm, S5 = 680 nm (Reproduced from [95], https://doi.org/10.1016/j.snb.2012.12.033, copyright (2012), with permission from Elsevier)

These particles were synthesized by the self-assembly method on QCM wafers as humidity sensors. The fabrication process consisted in preparing a suspension of zinc acetate dihydrate and diethylene glycol, which created precipitation of ZnO spheres. Once this process was completed, a secondary reaction was needed to produce the ZnO colloid spheres. To have the final particles, the reactant had been kept stirring at 180 °C for 6 h. After the final suspension, the QCM wafers were covered with it to obtain a coating which had to be dried in a furnace at 80 °C for 1 h [95].

The sensor was tested at room temperature with a variation of the relative humidity (RH) from 11% to 95%. The used controlled humidity environments with different aqueous solutions: LiCl, MgCl2, Mg(NO3)2, NaCl, KCl, and KNO3, all of the measurements were done in a closed glass vessel and kept in the glass chamber for 24 h before performing the measurement. The frequency signals were measured during the adsorption process and desorption process [95].

The measurements show that the resonance frequency shift increased with increasing relative humidity for all the samples, and it was also observed that with the increase of the diameter of the ZnO colloid spheres. The frequency shift tended to increase under the same humidity condition, indicating an increase in humidity sensitivity (Fig. 9.21) [95]. Compared with the previous work [100, 101], these sensors have extremely high humidity sensitivity. According to Xie and coworkers, a possible explanation is that the water molecules could be adsorbed easily on the big colloid spheres due to steric effect of the secondary particles [95]. The results indicate that the humidity changes are closely related to the particle diameters.

Another important factor for this kind of sensors is the response time in absorption process and recovery time in desorption process which correspond to the adsorption and desorption of water molecules on the surface of the studied material. The two parameters are measured by putting the film in contact with the suspensions of the lowest and the highest relative humidity values [95]. Comparing the measurements, Xie and coworkers have observed that at low relative humidity (33% and 55%) the recovery time was longer than the response time, in comparison with high

relative humidity (75%, 85%, and 95%). This occurs because for low RH chemisorption takes place, in consequence, the equilibrium time is short as well as the response time. But, when humidity rises, physisorption takes place and the equilibrium time is longer and therefore the response time will also increase. But for the desorption process, the chemisorption desorption equilibrium time is longer than the physisorption one [95].

In relation to gas sensors based on quartz crystal microbalance (QCM), the presence of humidity can affect the performance. In addition, it is very difficult to remove this effect completely from the environment [98]. Mumyakmaz and coworkers propose a solution using compensation methods, which allow doing measurements at variable humidity conditions and obtaining more accurate values. They use a principal component analysis (PCA) algorithm combined with the ANN method to implement a nonlinear principal component regression (PCR) method [98].

For the correct use of the ANN method, it has first to be trained to be able to do predictions, it consists on obtaining gradients that are added together and used to determine the changes in the weights and biases. For this purpose, Mumyakmaz et al. have used the Levenberg–Marquardt training algorithm that seems the fastest method for training moderate-sized feed-forward neural networks.

The technique was validated using different toluene concentrations. The method implemented works with predictions of concentration recorded from six different sensors coated with different phthalocyanines connected to the experimental data [98].

It works in subblocks, normalization and denormalization, to obtain better accuracy in each prediction. This occurs because the neural network training becomes more precise when working with preprocessing steps and the redundant data is removed, therefore the amount of normalized data is reduced, simplifying the problem for the ANN method but maintaining a good accuracy for the predictions. The accuracy is also due to the multilayer architecture for the data processing. This artificial neural model can simulate a real human nervous system.

After eliminating values with big errors due to the lack of validation and testing data during the ANN training, the authors reported that the system error rates are around 1.15% when working with a specific range of humidity between 0–67.5% and 0–4550 ppm of toluene. For input values outside of the mentioned range, the system also produces an output but the error rates will probably be bigger than the specified data space [98].

5.3.2 Organic Compound Detection

Monitoring and controlling pollution is one of the domains that have attracted the attention of many researchers, due to the importance of sustaining a high-quality environment. As remarkable works, there are studies in liquid quality [94, 96, 102] and gas detection [103, 104].

In relation to the liquid quality, Harbeck and coworkers have proposed the use of QCM coated with phthalocyanines (Pcs) to monitor different classes of organic pollutants in aqueous media (especially chlorinated aliphatic compounds and aromatic hydrocarbons) [94, 96, 102]. The Pcs are recognized due to their excellent

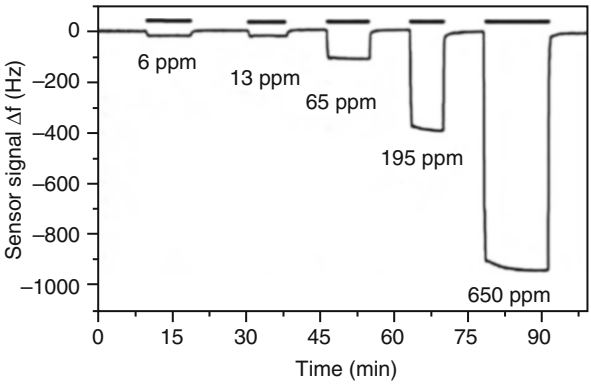

Fig. 9.22 Sensor signal of the QCM sensor during subsequent exposure to samples containing chloroform (concentration 6–650 ppm in water) (Reprinted from [94], https://doi.org/10.1016/j.snb.2010.06.062, copyright (2010), with permission from Elsevier)

sensing capabilities, chemical stability, wide-ranging modification of the sorption properties, and strong and reversible interactions with different analytes [94].

In the work done by Harbeck, four Pcs have polyoxy and three others have alkyloxy as sensitive materials for the detection of organic pollutants in aqueous media.

The natural frequency of the crystals used was 4.95 MHz AT-cut but the different analytes were tested at 3rd overtone (14.86 MHz) instead of the fundamental because the overtone gives higher stability and better signal-to-noise relation [94].

The coating process was monitored and the homogeneity of the coating layers was verified using an optical microscope. Using the Sauerbrey equation, the thickness of the coating layers were defined at 150 nm [94]. The analytes used in the tests were the following organic solvents: dichloromethane, chloroform, toluene, o-xylene, p-xylene, trichloroethylene, tetrachloroethylene, and chlorobenzene. Harbeck and coworkers have chosen these solvents due to represent different chemicals classes and to span a wide range of solubility in water. Approximately 100 μl of the analytes were added to 500 ml of ultra-pure water in order to prepare the solutions. The range of concentrations obtained was from 0.15 to 650 ppm (mg/kg) [94]. In relation to the tests done, the sensor signal increases with increasing concentration of the analyte. In addition, the crystal response is a very strong signal related to the concentration of the sample deposited (Fig. 9.22).

As a result, Pc with polyoxy moieties exhibit good adhesive properties to the sensor surface allowing detailed testing without changes in sensing properties. However, Pc with the alkyloxy ligands does not have good adhesive properties and apparently detached from the sensor during the tests. In relation to the coating layer amount, the tests indicated that a higher amount of sensitive layer permits a higher sensor response. But, the increase of sensitive material deposited is related to more surface roughness. As consequence, the noise level increase too. Regarding sensitivities obtained, the lowest sensitivity was observed for dichloromethane (0.2, 0.6, 0.4, 0.8) and the highest for the p-xylene (1.7, 7.4, 5.8, 8.4), o-xylene (3.4, 7.0, 6.6, 8.3), and tetrachloroethylene (1.5, 4.1, 3.1, 8.0) for each Pcs with polyoxy moieties respectively. The limit of detection was calculated with the sensor

sensitivities using three standard deviations of baseline noise. All analytes showed detection limits better than 1 ppm with the exception of dichloromethane [94].

Regarding gas detection, formaldehyde has a special importance due to its extended use in a broad field of day-to-day products that are in contact with humans. This compound is dangerous for human health when having over 0.5 ppm and constitutes a severe danger to life and health when reaching 100 ppm.

With the aim of creating a selective sensor to detect formaldehyde gas with high sensitivity but at the same time as simple as possible and that works rapidly, Hu et al. [103] have investigated coated surfaces with nanostructures of polymer and bacterial cellulose (BC).

The authors propose a BC membrane as crystal coating because it has a big surface area (103 m^2/g) and high porosity. However, this nanostructure needs to strengthen the interactions with formaldehyde vapor, so it has to be combined with another material (polyethyleneimine – PEI). This interaction is shown in Fig. 9.23 [103].

The coating was done by dripping coating technique obtaining a nanoporous three-dimensional PEI/BC membrane of nanofibers with a diameter of 30–60 nm. A membrane coated only with BC, another only with PEI, and one with PEI/BC were created to compare sensitivities. The experiments where held at a constant temperature of 22 °C with relative humidity at 50%, 60%, and 70%, and with formaldehyde concentrations of 1, 10, 30, 50, and 100 ppm with 15 min as adsorption time. During this time, the shift of the resonance frequency was monitored [103].

The results obtained to verify that the combination of PEI and BC for the membrane coating makes the QCM sensor very sensitive to the formaldehyde vapors. In addition, for only BC coating, the sensor was not sensitive to formaldehyde. In consequence, only a BC layer cannot be used as sensing material. On the other hand, for membranes only with PEI, the sensor did not detect formaldehyde when the concentration was 1 ppm. For higher quantities, the response of the sensor was slow in comparison with measurements using both coatings forming a nanofibrous membrane. This can be explained because of the morphology of the PEI/BC membrane, which gives a bigger surface area than a continuous one and, therefore, makes the sensor more sensitive [103]. As an additional result, Hu and coworkers related high levels of relative humidity with an increase of sensor sensitivity. This phenomenon is due to the high absorbance of H_2O molecules from the hydrophilic amine groups of PEI and the hydroxyl groups of BC, which make easier the absorption of formaldehyde molecules by forming hydrogen bonds.

5.3.3 Applications in Analysis of Food Quality

There are many applications in which quartz crystal resonators are used to detect adulteration [105], bad practices in the food elaboration causing low quality in foods, and agricultural diseases [46, 50].

In relation to milk products, Sakti et al. [105] have proposed an immunosensor based on quartz crystal microbalance to differentiate goat milk to cow milk. Adulteration of goat milk is usually done using cow milk. Specifically, they developed the immunosensor using a commercial crystal resonator and polyclonal

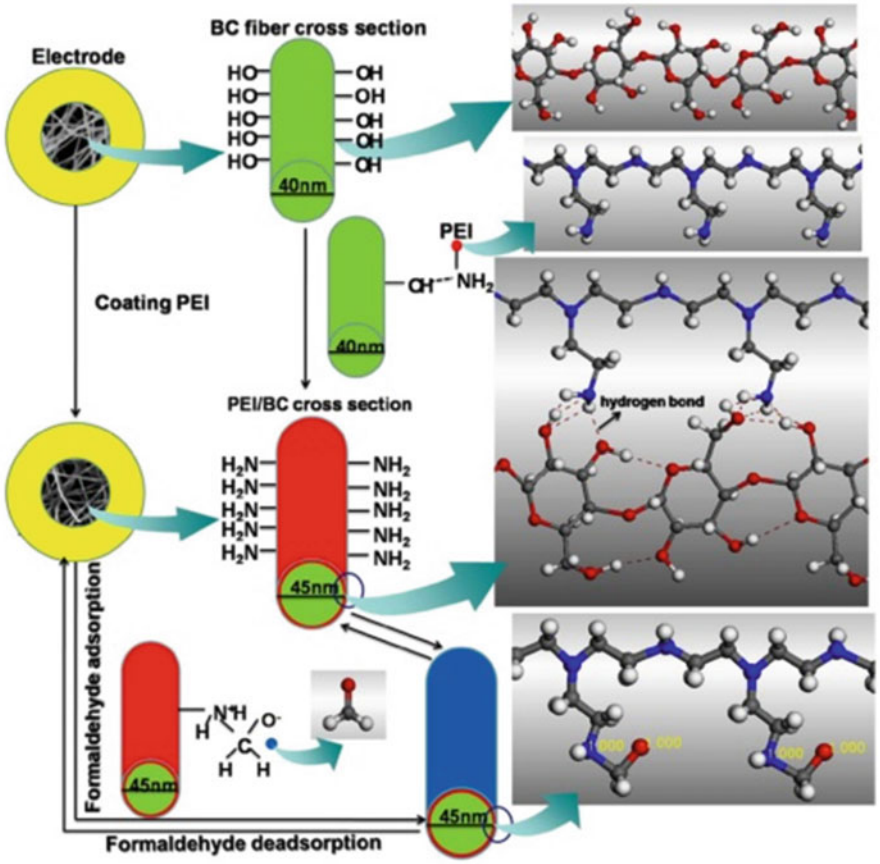

Fig. 9.23 Schematic diagram of the interaction of BC and PEI, and formaldehyde and PEI. (Reprinted from [103], https://doi.org/10.1016/j.snb.2011.05.021, copyright (2011), with permission from Elsevier)

antibody specific to cow milk protein. A specific protein at 208 KDa is found only in cow milk and does not exist in goat milk. To detect the PSS 208 kDa protein, antibody specific to the PSS 208 was developed. The purified antibody was immobilized on top of the sensor surface on a polystyrene layer [105]. As a result, the optimum concentration of the polyclonal antibody for specific cow milk protein (PSS 208) was found at a concentration of 1000 ppm. The developed QCM immunosensor for detecting cow milk existence has a detection limit of 1 ppm. These limits of detection were adequate to be used as a candidate for goat milk adulteration using cow milk detection apparatus.

Other interesting work related to quality food products have been done by Afonso and coworkers [50]. They have reported studies related to piezoelectric immunoassays for cysteine peptidase (CPXaC) using a polyclonal antibody against CPXaC

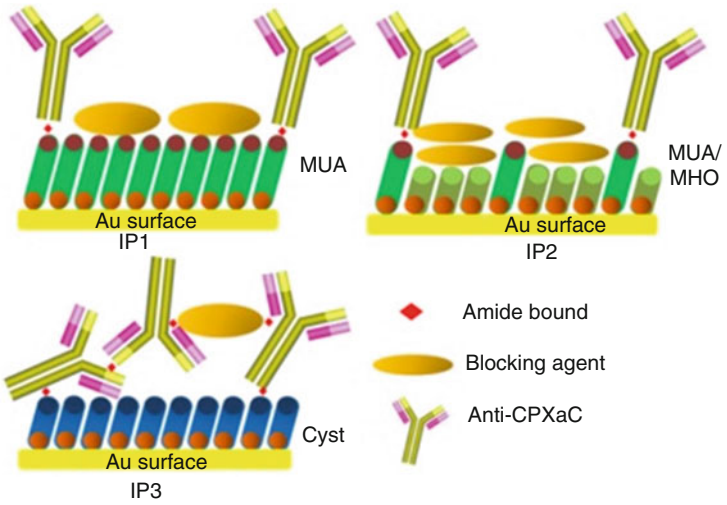

Fig. 9.24 Schematic showing the procedures proposed (IP1, IP2, IP3) (Reprinted from [50], https://doi.org/10.1016/j.talanta.2012.11.003, copyright (2012), with permission from Elsevier)

(anti-CPXaC). CPXaC is produced by citrus fruits infected with Xanthomonas citri (Xcc) bacterium. The authors propose to use this potential target in conjunction with QCR technique to develop an effective and rapid detection system for the citrus canker caused by the Xanthomonas. According to the authors, citrus canker does not have treatment, so once the infected tree is detected, the surrounding trees must be eliminated to prevent more infections and high economic losses [50].

In Afonso study, three anti-CPXaC immobilization procedures have been evaluated according to the following immobilization procedures (Fig. 9.24): IP1: The polyclonal anti-CPXaC was immobilized in 11-mercaptoundecanoic acid (MUA); IP2: The polyclonal anti-CPXaC was immobilized in a mixture (1:10) of MUA and 6-mercapto-1-hexanol (MHO); IP3: anti-CPXaC was immobilized using cystamine (Cyst).

All samples were analyzed using a quartz crystal microbalance with dissipation QCM-D. The variation in the signals ΔF and ΔD was monitored in real time [50]. A buffer phosphate saline (PBS) with pH 7.2 (0.01 mol/L phosphate, 0.15 mol/L NaCl) was used.

The results reported by Afonso et al. show that the largest changes in ΔF have been achieved with immobilization procedure IP2 and IP1; the lowest with IP3. Comparing IP2 with IP1, the authors observed that the presence of MHO increases the change of ΔF around 70%. About to ΔD, IP3 presented a change of 0.1×10^{-6}, followed by 0.93×10^{-6} for MUA, and 3.8×10^{-6} for MUA/MHO [50]. This result indicates that the variation in frequency can be attributed not only to the antigen mass but also to conformational changes and/or water trapped in the film. However, the immobilization procedure selected was IP1 because the sensor constructed using MUA presents the smallest variation in $\Delta D/\Delta F$. In consequence, IP1 generates a

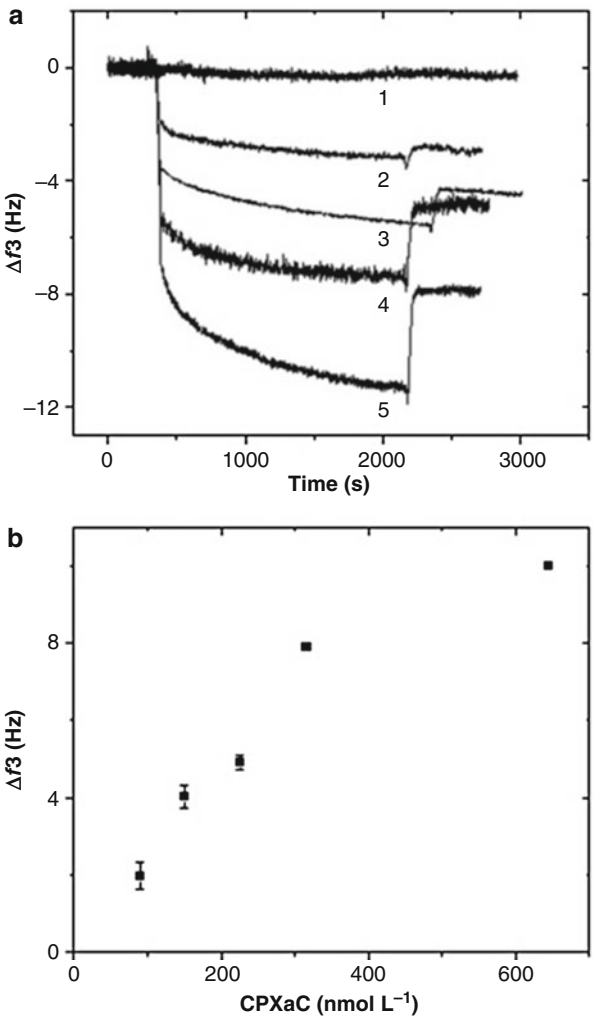

Fig. 9.25 (**a**) Curves of ΔF using IP1 for different CPXaC concentrations from 0 to 64.5×10^{-8} mol L^{-1}. (**b**) Analytical curve for CPXaC immunosensor (Reprinted from [50], https://doi.org/10.1016/j.talanta.2012.11.003, copyright (2012), with permission from Elsevier)

more rigid layer and the authors have used the Sauerbrey equation to analyze the immunosensor experiments (Fig. 9.25).

The specificity study was done comparing two crystals, both altered with IP1 but the second without the addition of the antibody. In the crystal without the antibody, the authors observed a frequency shift when the antigen CPXaC was added; but after they washed the crystal with PBS buffer, the frequency returned to the initial values, indicating nonspecific binding Fig. 9.26a. According to Fig. 9.26b, the specificity was also validated with different proteins: canecystatin, BSA, and cysteine peptidase.

However, no detectable signal was observed for the nontarget proteins. This result indicates the good selectivity and specificity of the sensor for CPXaC from Xcc [50]. The limit of detection obtained by the authors was of 13.0 nmol/L.

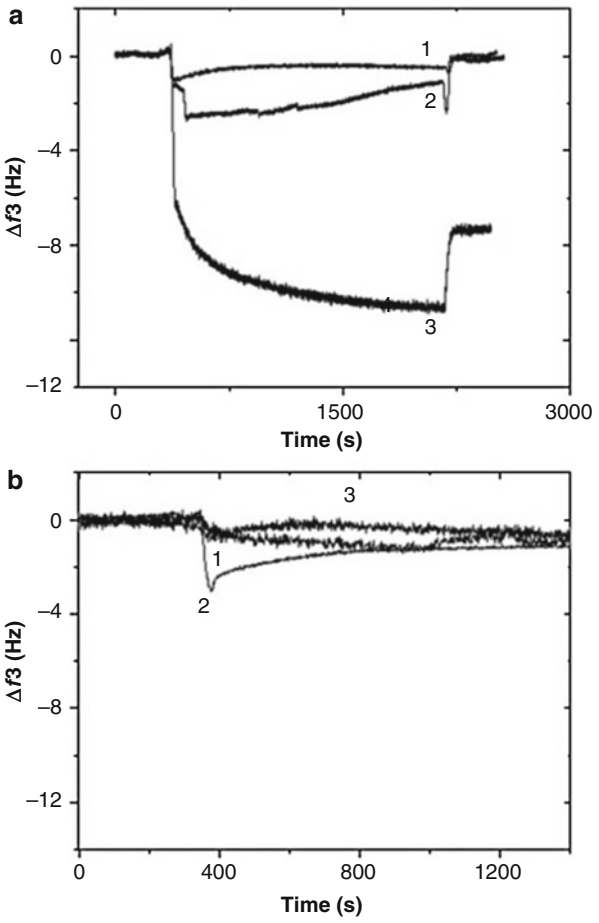

Fig. 9.26 Results for specificity tests. (**a**) Frequency variation for (curves 1 and 2) 32 and 64.5×10^{-8} mol L^{-1} CPXaC were injected into the cell with crystal modified without antibody, and (curve 3) 32×10^{-8} mol L^{-1} CPXaC added into the cell with piezoelectric crystal modified with attached antibody. (**b**) Addition of 4.15×10^{-6} mol L^{-1} canecystatin (curve 1), 3.03×10^{-6} mol L^{-1} BSA (curve 2) and 32.0×10^{-8} mol L^{-1} cysteine peptidase (curve 3) (Reprinted from [50], https://doi.org/10.1016/j.talanta.2012.11.003, copyright (2012), with permission from Elsevier)

5.4 High-Frequency Crystals

During the conventional manufacturing process, the minimum thickness of the quartz crystal is controlled due to mechanical stability issues. Resonance frequencies used by typical crystals are 5 MHz and 10 MHz, with corresponding plate thicknesses of 0.33 mm and 0.17 mm, which provide an appropriate mechanical stability [106]. An increase in the sensor sensitivity can be achieved when decreasing the thickness of quartz crystal plate (hq). A minimal thickness reached is around 55 μm due to limit mechanical fragility with a fundamental frequency of 30 MHz. These crystals have a smaller diameter (8 mm) and they are more thin and fragile [106].

The photolithography and wet etching processes can permit to manufacture smaller thicknesses and to fabricate mechanically stable quartz plates with higher resonance frequencies and smaller diameters in a supporting quartz frame [11, 31, 106–108].

For instance, Hung and coworkers used the deep reactive ion etching (RIE) to fabricate quartz resonators in a single chip. The diameter reached is in range 0.05–1.0 mm and the thickness in range 18–82 μm [109].

5.4.1 Multichannel Quartz Crystal Resonators

A multichannel quartz crystal resonator (MQCR) is a set of several resonators in the same sensor system. This system works as a full sensor platform to analyze the same sample with different characteristics [107, 108]. For example, the platform permits to analyze the same sample to different overtones simultaneously or to functionalize each individual electrode with a specific detection layer to identify different compounds in the same sample. Monolithic multichannel quartz crystal microbalances (MQCMs) are a type or multichannel QCR. An MQCM is a set of several microbalances on a single quartz substrate [11, 31, 107]. Miniaturizing QCMs is necessary for developing MQCMs, as large arrays must be constructed. QCM miniaturization leads to additional benefits including lower cost, less sample/reagent consumption, faster sensing response, and shorter diagnostic time. However, MQCMs still have to overcome the challenge of avoiding interferences.

Conventional MQCM consist of an array of electrode pairs deposited on both sides of an AT-cut quartz crystal usually of a thickness of few hundreds of microns. Acoustic wave induced by one QCM will propagate laterally and may interfere with QCM in the vicinity causing acoustic interference.

In large arrays space between electrodes must be small, which contributes to increasing the interferences, mainly if the QCMs are identical and operate at the same resonance frequency. Also, frequency interference decreases in MQCMs with unequal electrode pairs [110]. Besides of spaces between electrodes, acoustic interference depends on MQCM device parameters such as geometry, dimensions and thickness of each electrode, and mechanical and piezoelectric properties of the quartz substrate and electrode materials.

Usually, impedance measurements of the two QCMs under exchanged external load may be used to experimentally study interference between two contiguous QCMs and an electrical equivalent circuit, such as Butterworth–Van Dyke (BVD) model and transmission line representation, is used to model and describe the response. These models show a simplified, one-dimensional, MQCM configuration as the vibration profile is assumed to be uniform throughout the electrode surface. Modeling results are generally valid near to the resonance frequency. However, it neglects important features such as coupling modes and energy trapping of the electrode layer. Sensitivity and electrode size are also relevant MQCM problems as they are both related to the thickness of the crystal, which is limited as thin quartz plates are too fragile.

In addition to acoustic interference, other problems of conventional MQCM include spurious vibration, limited sensitivity, and limited size of electrodes. Spurious vibration occurs because of coupling between thickness shear (TS) and other modes including thickness flexural (TF), face shear (FS), thickness twist (TT), and higher order modes [107].

In order to improve the MQCM behavior, several design strategies could be implemented: to use different electrode sizes to avoid strong interferences, to

increase the electro size for improving electrode trapping (although this could bring higher order modes and introduce higher order frequency interference), and to increase the electrode separation. Other strategy consists in modifying the structure of the quartz crystal in order to obtain higher frequency. The following modifications are the more typical:

- *Mesa shape*: Achieved by varying quartz thickness between electrode and interelectrode regions to increase the resonance frequency difference. There are four configurations related to mesa shape: Plano-Mesa, Plano-inverted-mesa, Bi-mesa, and Bi-inverted-mesa [107].
  Mesa shape has several advantages: low interference, large array size, and density and mass sensibility. As disadvantages: it requires a difficult deep etching process, limited resonance frequency, mass sensitivity, electrode size, and some remaining frequency mode coupling, particularly TS-TF and TS-extension.
  Plano inverted-mesa has been the most frequently reported because it simultaneously offers low interference, high resonance frequency, high mass sensitivity and compatibility with flow injection, and multi-frequency system [107].
- *Convex shape*: Achieve by using a spherical convex-shaped structure aiming to avoid coupling between TS and TF modes. This would prevent energy to be taken from the usable frequency vibration, which lowers the Q-factor that is relevant for ultrasensible liquid detection. There are two configurations: planoconvex and biconvex. The advantages are: low interference, very low mode couplings except for Ts-extension, and large size array and density. The disadvantages are: sophisticated patterning, difficult deep etching process, limited resonance frequency, mass sensitivity and electrode size, and TS-extension mode coupling.
- *X-axis inversion*: Aiming to increase the difference between the electrode and interelectrode regions of the structure without requiring physically removing the quartz. Instead, a thermal treatment is used. The advantages are low interference, the large size array and density, and no mechanical etching process. The disadvantages are limited resonance frequency, mass sensitivity, and electrode size, and sophisticated thermal treatment process (Figs. 9.27 and 9.28).

5.5 Coated QCM Sensors

Technically, in all QCR applications related to real-time sensing, any coating technique is used with the aim of functionalizing the crystal surface. This functionalization provides the quality of the selectivity to the crystal. In this way, the crystal is capable to identify the analyte of interest in the sample [54, 67, 80, 94, 111–113]. For instance, coating is essential in biological processes like blood contact applications where biocompatibility is determined by specific interactions with blood and its components. In addition, the objective of biomaterials coatings is also to eliminate or reduce the nonspecific adsorption of proteins in order to improve the biocompatibility.

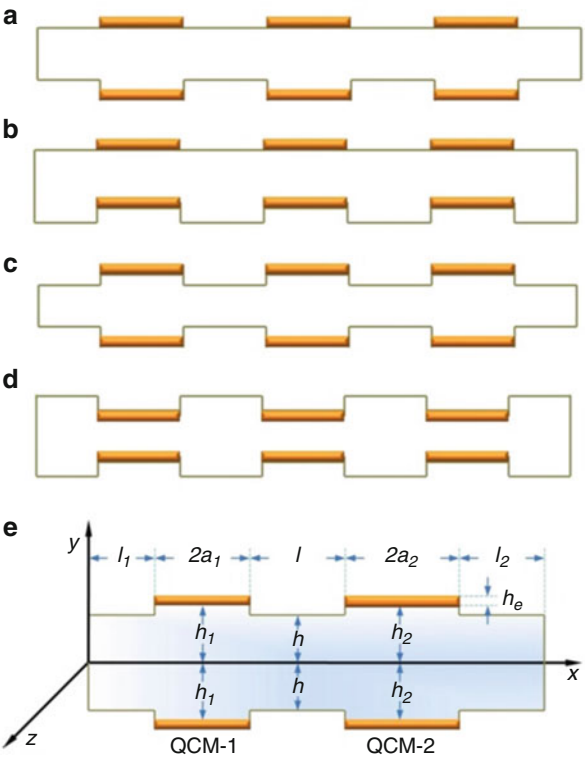

Fig. 9.27 Mesa-shaped structures: (**a**) plano-mesa, (**b**) plano-inverted-mesa, (**c**) bi-mesa and (**d**) bi-inverted-mesa (Reprinted from [107], https://doi.org/10.1016/j.aca.2010.12.022, copyright (2010), with permission from Elsevier)

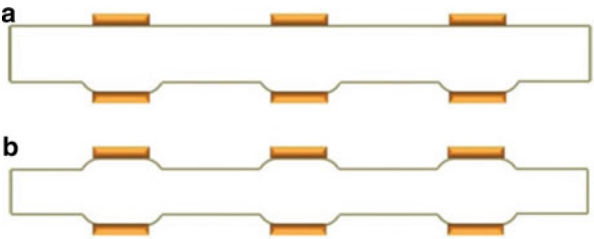

Fig. 9.28 Convex-shaped structures: (**a**) planoconvex and (**b**) biconvex (Reprinted from [107], https://doi.org/10.1016/j.aca.2010.12.022, copyright (2010), with permission from Elsevier)

5.5.1 Graphene Oxide Thin Film

Recently, Yao et al. [67] propose a graphene oxide (GO) thin film coated quartz crystal microbalance as a humidity sensor. Furthermore, Tai et al. [99] also proposed the use of protonated polyethylenimine-graphene oxide nanocomposite thin film in a similar way to Yao with the aim of measuring humidity.

Adsorption and desorption of water molecules produce a change in the mass or electrical properties of a thin sensitive film. Nanocarbonaceous materials were known to have excellent gas adsorption properties. Graphene, as 2D nano-carbonaceous materials, has outstanding electrical, thermal, and mechanical properties. By functionalizing graphene with = O and –OH groups, a more hydrophilic material is achieved [67].

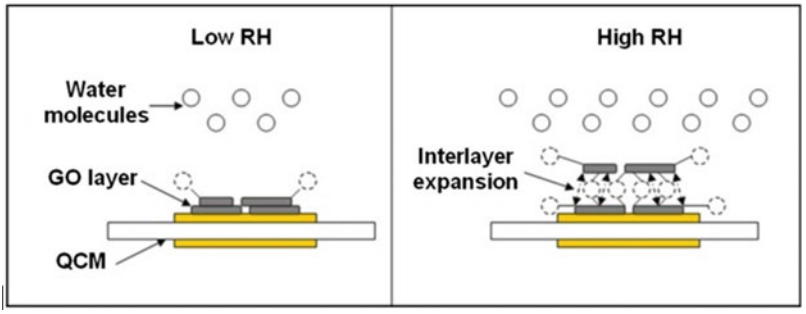

Fig. 9.29 An illustration of the humidity sensing mechanism of GO thin film coated QCM. (Reprinted from [67], https://doi.org/10.1016/j.apsusc.2011.04.028, copyright (2011), with permission from Elsevier)

Yao et al. obtained the graphene oxide GO from synthesizing graphite by a modified Hummers method and a successive exfoliation of the graphite oxide. AT-cut 10 MHz QCMs with 5 mm diameter gold electrodes on both sides were used (~9.99 MHz fundamental frequency). GO was deposited on QCM by spin-coating and three QCMs with different coating loads (sample 1, sample 2, and sample 3), therefore different frequency shifts (2620 Hz, 4953 Hz, 7184 Hz) were prepared [67]. Figure 9.29 shows how the sensor responds to RH levels.

By connecting the QCMs to a phase-locked oscillator (which provided the resonant frequency and an output DC voltage), the resonant frequency and the crystal resistance were measured. RH sensing characteristics were tested by exposing the sensors to different saturated salt solutions (LiBr, LiCl, CH3COOK, MgCl2, K2CO3, Mg(NO3)2, NH4NO3, NaCl, KCl, KNO3, and K2SO4 solutions that provided 6.4%, 11.3%, 22.5%, 32.8%, 43.2%, 54.3%, 62.1%, 75.3%, 84.3%, 93.5%, and 97.3% RH levels, respectively).

The curves obtained behaved linearly for most of the relative humidity (RH) range. Thicker GO coating loads were observed to give place to larger frequency shifts, so sensitivity may be improved by increasing the coating load. The frequency shifts barely varied along time for the three used sensors, proving their long-term stability. The maximum humidity hysteresis occurred at high RH for the three sensors, and the curve also tends to increase with thicker GO coating loads (Fig. 9.30).

The physical changes of material properties were characterized using the crystal's motional resistance, which was observed to change slightly in the low RH range (<54.3% RH). This would mean that the change of crystal energy loss was insignificant. However, in the high RH range (>54.3% RH), a larger change in the motional resistance was observed. This is explained by the change of crystal energy loss due to water molecules entering into carbon interlayer and producing an expansion of the GO layers.

In this way, QCM frequency response was found to be dependent on water molecules adsorbed/desorbed masses on GO both in the low and high RH range but also to be dependent on variations of the interlayer expansion stress of GO in the high RH range [67].

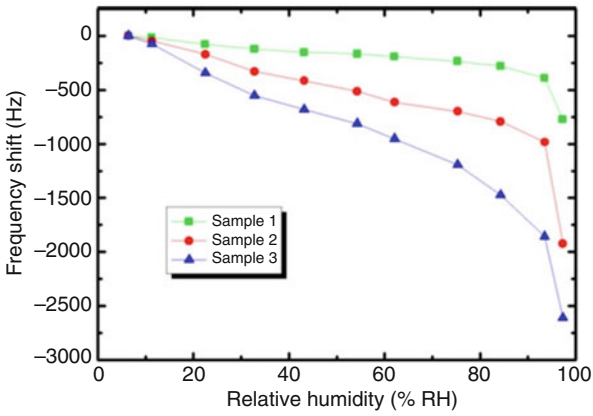

Fig. 9.30 Frequency shift of GO thin film coated QCMs as a function of RH (Reprinted from [67], https://doi.org/10.1016/j.apsusc.2011.04.028, copyright (2011), with permission from Elsevier)

The results obtained by the authors are satisfactory because an excellent humidity sensitivity (22.1 Hz/%RH mas) and a linear frequency response versus RH in the wide detection range 6.4–93.5% RH were observed. GO thin film coated QCM is therefore a promising application in humidity detection [67].

5.5.2 Polyelectrolyte Layers

Assembly by polyelectrolyte layers is another traditional technique that uses polymers for coating sensor surfaces [17, 18, 23, 63, 97, 114–117]. In the case of polyelectrolytes layer by layer (LbL) thin film assembly, the construction of films by alternately adsorbing positively and negatively charged polyelectrolytes has been investigated [18, 63, 114].

Recently, Dunér and coworkers have done studies of viscoelasticity response from a continuously growing grafted polyelectrolyte layer using a QCM-D [63]. In these studies, the in situ monitoring of quartz crystal microbalance with dissipation of the growth response of a film of a viscoelastic polymer through the surface sensor is done when it is within the region of thick film. Their results have been compared with the Voigt model.

The Voigt model is applied to analyze changes in frequency and dissipation to extract information from the layers with viscoelastic behavior [21, 60, 63, 115, 118, 119]. Such models use the frequency change (ΔF) and dissipation change (ΔD) as input and return shear elasticity, shear viscosity, thickness, and density (Fig. 9.31).

They monitored the growth of a viscoelastic layer with a certain thickness in real time verifying soft signal change depending on the film thickness using both the frequency difference ΔF as the dissipation difference ΔD. According to the experiments, the authors propose the use one of the two parameters (ΔF or ΔD) to evaluate changes in the film when the other parameter is no longer sensitive to these changes [63].

In particular, the authors note that for longer times than 150 s, a growth rate of thickness was observed almost linear [63]. Theory and experiments are consistent and confirm that a variation in viscoelastic mass at certain intervals of thickness may

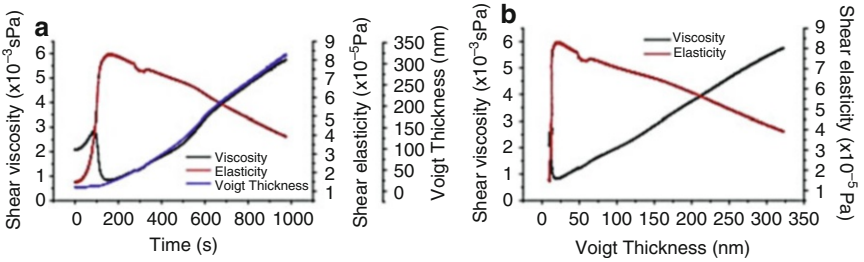

Fig. 9.31 Shear viscosity, shear elasticity, and thickness plotted as a function of time (**a**). Shear viscosity and shear elasticity as a function of Voigt thickness (**b**). A thickness of about 21 nm is obtained at the peak elasticity (Reprinted from [63], https://doi.org/10.1016/j.jcis.2013.07.008, copyright (2013), with permission from Elsevier)

generate more significant changes in ΔD signal than in ΔF signal [63]. This result can be interesting to monitor in qualitative way changes related to swelling phenomena in relatively thick films. However, to obtain quantitative information of the deposited material is not enough to use only one of these variables, ΔF or ΔD [63].

As a sensitivity measure, Dúner and coworkers propose to obtain the derivative of ΔF or ΔD with respect to the thickness and draw it depending on the thickness [63]. In this way, intervals of higher sensitivity conditions may be detected. This method can be useful in any application involving viscoelastic phenomena.

5.5.3 Carbon Nanotubes (CNTs)

Carbon nanotubes (CNTs) are other useful and very attractive material for coating different surfaces as QCR's electrodes. Pejcic et al. proposed the use of functionalized carbon nanotubes for coating QCR electrodes with the purpose of developing a real-time hydrocarbon sensor [120].

Even though nongravimetric measurements for environmental monitoring are problematic, quartz crystal microbalances (QCMs) may be a useful tool to detect these compounds. Several groups have been able to use QCM to detect hydrocarbons with improved sensitivity when certain conditions are met [120].

Low-density hydrophobic polymers with low glass-transition temperature (GTT) are more sensitive toward nonpolar hydrocarbons. Analyte selectivity is a major challenge in QCM sensor acceptance. Carbon nanotubes (CNT) have large adsorption capacities that can be chemically tuned and a large surface area. Studies have proved hydrocarbon in gas phase detection using QCM with CNT but it is not known how the materials would perform in the aqueous phase. Other recent study [121] proposed the design of surface acoustic wave gas sensors based on polyisobutylene and carbon nanotube composites.

Pejcic and coworkers [120] investigate a QCM sensor incorporating different carbon nanotube–polymer composite coatings for the detection of aromatic

hydrocarbons in water in order to evaluate the possible impact of adding CNT on the sensitivity and selectivity of a polymer-coated QCM sensor.

Different types of CNT were used (short multiwall carbon nanotube, long multiwall carbon nanotube, and single-wall carbon nanotube) and were functionalized by adding octadecylamine (ODA) to their sidewalls. AT-cut gold-coated quartz crystal (5 MHz) was used, and a thin film of either a polymer or a CNT polymer solution was placed by spin coating [120]. An automated flow cell system which contained an array of four QCRs was used to perform parallel experiments (at a flow rate of 150 microliters per minute). Deionized water was used for obtaining a baseline and calibration curves were built using a concentration range between 0 and 100 ppm. All measurements were performed in less than 4 h to avoid long contact with water, which affects to sensitivity and reproducibility.

QCM sensor measurements using different polymer films for coating (approximately 200 $\pm$ 70 nm thick) were performed to assess their response to benzene, toluene, ethylbenzene, p-xylene (BTEX), and naphthalene (Fig. 9.32).

It was observed that the frequency shifted more negative with increasing p-xylene levels, which are consistent with the hydrocarbon partitioning into the polymer films. Polybutadiene (PB) and polyisobutylene (PIB) responses were faster than polystyrene (PS) and polystyrene-co-butadiene (PSB) responses, which were expected since polymers with high GTT (such as PS and PSB) have been showed to respond much slower [120]. PB and PIB responded linearly to BTEX and naphthalene dissolved in deionized water over the 0–80 ppm range while PS and PSB behaved less linearly due to plasticization processes (hydrocarbon sorption/diffusion varies significantly with hydrocarbon concentration and water aging). From the slope of the calibration curves, hydrocarbon sensitivity was obtained. According to Fig. 9.32, PB was the most sensitive for all analytes. PS was the least sensitive for toluene, ethylbenzene, p-xylene, and naphthalene [120].

According to Fig. 9.33, the sensitivity of QCMs slightly varies when a polymer is doped with low CNT levels but significantly decreases at higher CNT levels for compounds such as p-xylene. Taking into account that the sensibility decreases adding CNT's for some polymers and increases for other ones (decrease for PSB and increase for PS and PIB), the addition of CNT may play an important role in improving the polymer selectivity for certain hydrocarbon compounds. Hydrocarbon sensitivity seems to be independent of the CNT type.

Figure 9.34 shows that increasing the film thickness increases the QCM sensitivity of both the polymer and the CNT polymer-composite. Attenuated total reflectance (ATR)-FTIR shows that CNT preferentially interacts with specific hydrocarbon types. Pejcic and coworkers obtained a reasonable correlation for PB, PSB, and PIB when comparing the sensitivity of several hydrocarbons to the octanol-water partitioning coefficients.

A final analysis was done using total petroleum hydrocarbons (TPH) with the four different coatings with and without CNTs. The highest response was obtained with the PB and PB-CNT coatings. However, the response of PIB significantly increased with the use of CNT's (PIB-CNT) [120].

5.5.4 Poly(Ethylene Terephthalate) (PET) Films

Polyethylene terephthalate (PET) is a common thermoplastic polymer belonging to the family of the polyesters and is typically used in clothes fibers, containers for liquids and foods, biomaterials applications, etc. Recently, Indest and coworkers have done a study focusing on understanding the adsorption behavior of human

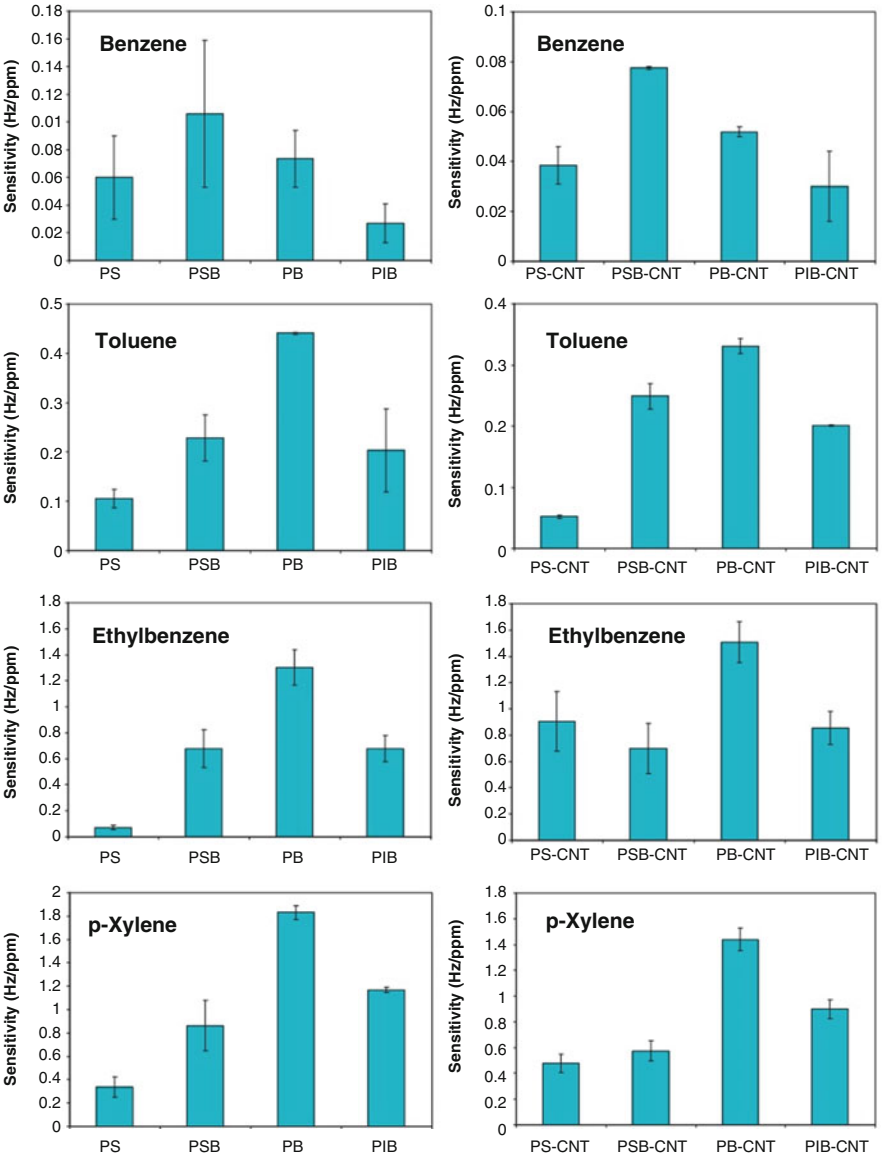

Fig. 9.32 (continued)

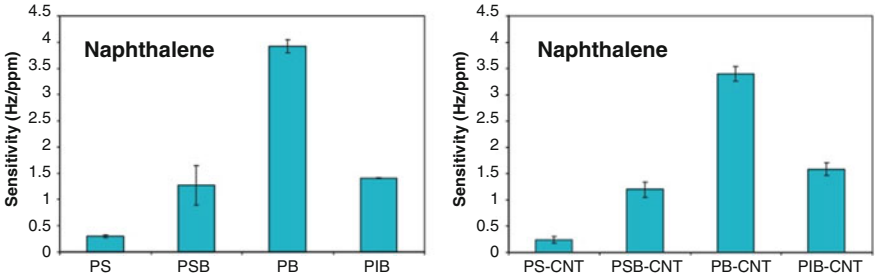

Fig. 9.32 QCM sensitivity of various polymeric-based films exposed to different aromatic hydrocarbon compounds (Reprinted from [120], https://doi.org/10.1016/j.talanta.2011.06.062, copyright (2011), with permission from Elsevier)

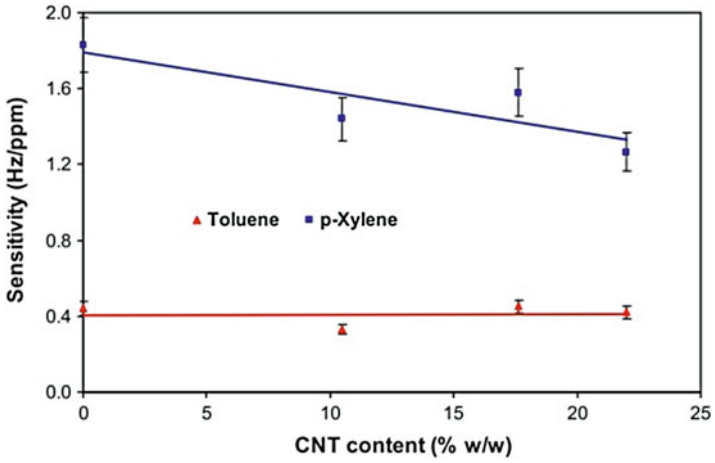

Fig. 9.33 Effect of CNT (short MWCNT) content on the sensitivity of PB coated QCM for toluene and p-xylene (Reprinted from [120], https://doi.org/10.1016/j.talanta.2011.06.062, copyright (2011), with permission from Elsevier)

serum albumin (HSA) of different PET surfaces [122]. PET surface can be modified by adding different polysaccharides with specific biological activities in an attempt to improve biocompatibility [122]. The test procedure consisted in monitoring HSA adsorption with quartz crystal microbalance with dissipation unit (QCM-D) on the following surfaces: (a) PET, (b) PET-H/chitosan, (c) PET-H/chitosan/fucoidan, and (d)PET-H/chitosan/chitosan sulfate. Before the adsorption, the layers on the QCM were immersed in phosphate buffer saline (PBS). Then a solution of HSA in PBS was introduced in the cell waiting until equilibrium in frequency measures, finally the surface was rinsed again with PBS solution to verify stability.

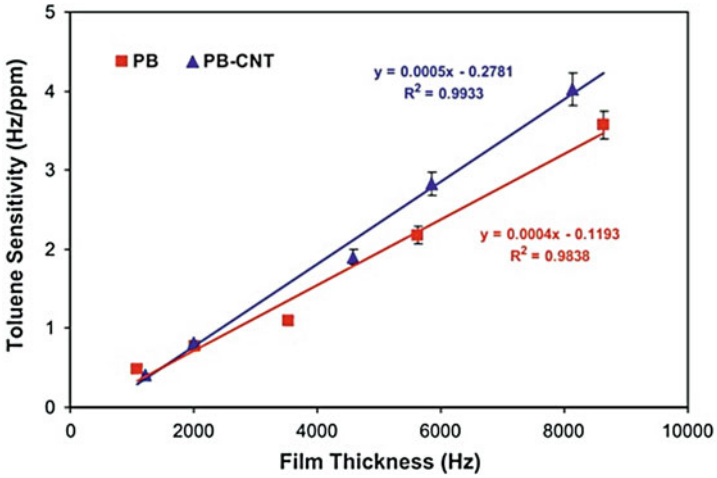

Fig. 9.34 Effect of film thickness on the toluene sensitivity of (PB) and (PB-CNT) coated QCM sensor (Reprinted from [120], https://doi.org/10.1016/j.talanta.2011.06.062, copyright (2011), with permission from Elsevier)

Figure 9.35a shows the results of frequency change as a function of time for adsorption of HSA in all different surfaces; it can be observed that PET surface had the largest frequency shift, hence more protein was adsorbed on the hydrophobic PET surface than on the hydrolyzed ones. Energy dissipation is shown in Fig. 9.35b, from these results it can be concluded that larger energy dissipation on PET-H layer indicates that the adsorbed layer of HSA was thicker and less compact than for the rest of surfaces [122]. Energy dissipation together with frequency shift can give insights of mass distribution on the surface. The slightly lower frequency shift of PET-HC compared to PET-H was explained using images from an Atomic Force Microscope, identifying that chitosan does not cover the whole PET-H surface, but rather forms some kind of blobs on the surface. The most extreme case is for chitosan sulfate where protein adsorption does not occur [122].

5.6 Multicomponent Sensing Platforms

The multicomponent sensing has been effective in the identification of different compounds. Multicomponent sensing consists in the detection of independent parameters that are processed simultaneously using different technologies. The main goal of this practice is to increase the sensitivity and the selectivity of the sensor system. The applications for multi-component sensing platforms using quartz crystals resonators as complementary technique are widely diverse [123]. QCR is an adaptable technology easily used in conjunction with fluorescence

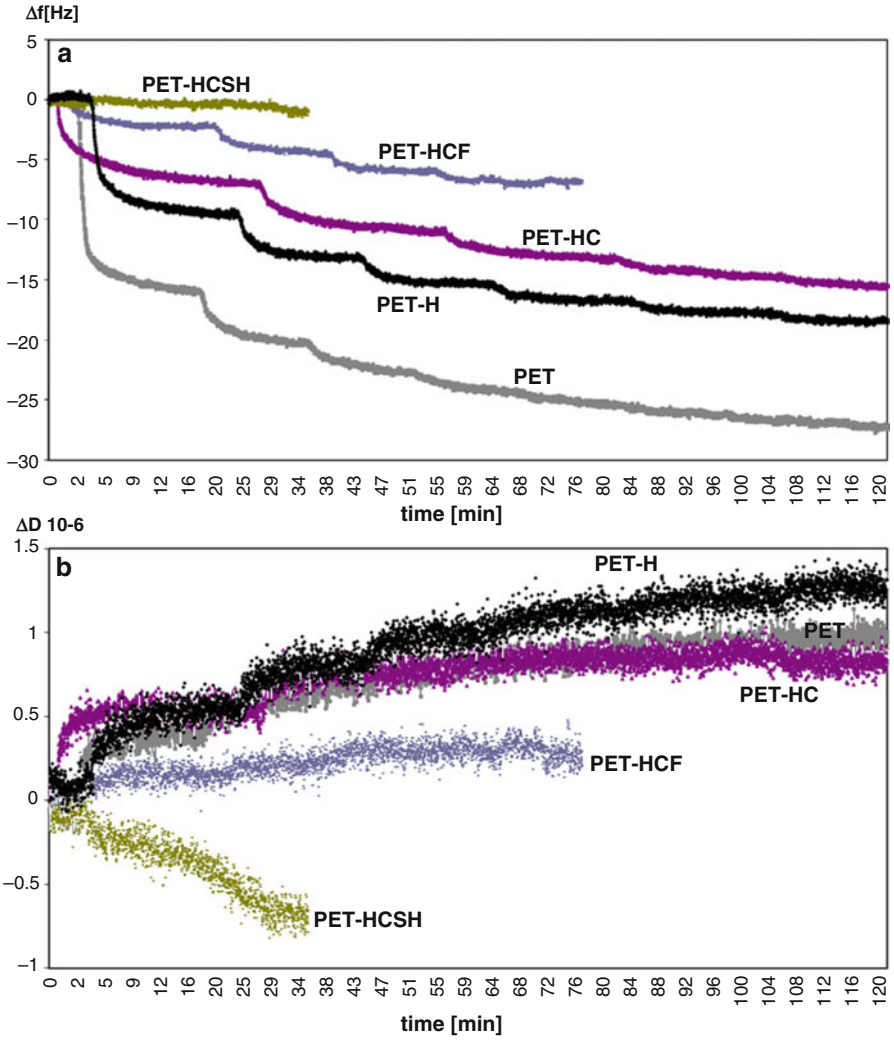

Fig. 9.35 Change in frequency (Δf_3, third overtone) (**a**) and change in dissipation (ΔD_3) (**b**) as a function of time for HSA adsorption (0.05 g/L HSA, PBS solution) on nonhydrolyzed (PET) – grey line, hydrolyzed PET film (PET-H) – black line, and modified films with chitosan (PET-HC, 0.2 g/L) – violet line, fucoidan (PET-HCF, 0.03 g/L) – blue line, and chitosan sulfate (PET-HCSH, 0.03 g/L) – green line (Reprinted from [122], https://doi.org/10.1016/j.colsurfa.2010.03.003, copyright (2010), with permission from Elsevier)

technique [24, 81, 124], surface plasmon resonance (SPR) technique [39, 125], spectroscopic ellipsometry [85], cyclic voltammetry, differential pulse voltammetry [126], spectrophotometry, [127] Electrochemical techniques (EQCM) [18, 127–129], electrokinetic-QCM (EKQCM) [130].

5.6.1 Fluorescence Technique

QCM sensing can be combined with fluorescence quenching for explosive identification applications. The current main method for the detection of nitroaromatics compounds (NAC) is fluorescence quenching which has a high sensitivity. A drawback of this method is that NACs are usually present with other substances (interferents) that can affect the response. QCM technique can help in the discrimination of interferents in order to improve the overall response of the sensors [124].

With the aim of demonstrating the improvement of multisensing platform, Clavaguera and coworkers have validated the techniques together and separately [124].

The authors used a crystal with gold-plated metal electrodes on both sides. One of the sides of the crystal was coated with the sensing compound. The electric circuit designed was a Colpitts oscillator loop with a transistor as common emitter. The measure of the frequency was taken with a frequency counter with an accuracy of ± 1 Hz [124]. The sensitive layer was prepared by applying spray with the compound diluted in Tetrahydrofuran (THF).

First, the detection of dinitrotoluene (DNT) with QCM sensor was tested using different interferents: chloroform, dichloromethane, ethanol, methylethylketone, and toluene. The experiment was performed first by exposing the QCM to ambient air, the organic vapors for 10 min, and ambient air again. The response for each vapor was assessed dividing the frequency shift by the vapor pressure of the analyte. The sensitive layer mass changed by the exposure to the vapor, generating a change in the fundamental oscillation frequency. The tendency of the frequency was to decrease while exposed to organic vapors. Once the organic vapors were removed, the original vibration frequency was recovered within few seconds. The exposure of DNT produced a significant frequency shift (70 Hz approx.), so the material can be considered as a sensitive coating. This frequency shift was at least four orders of magnitude larger than the observed for the solvents. The adsorption process when exposed to DNT appears to be slow, which might indicate that the process involves not only a surface process but also bulk diffusion [124].

After, the fluorescence sensor was tested using as target DNT, dichloromethane, ethanol, methylethylketone, and toluene. For the experiment, a spectrofluometer was used, first with air, then the solvent or DNT, and then air again. The fluorescence emission under solvent showed that this coating is not sensitive to those vapors since there is not possible to differentiate the emission response as it remains constant. As opposite, there was a significant intensity decrease of 15% within 10 min, when exposed to 120 ppb of DNT.

Finally, the simultaneous detection with QCM and fluorescence sensor was validated. The sensitive material was positioned in the center of the chamber with the proper orientation to maximize the emission intensity. During the experiment, both responses were monitored simultaneously from the coated QCM. When tested with DNT, the frequency shift of QCM was 5 Hz, and a 13% of fluorescence quenching was observed after 15 min of exposure. This approach can be helpful to discriminate interferents from nitroaromatics and to investigate the fluorescence response of sensor in a complex mixture of vapors [124].

According to the results obtained by the authors, the methods applied separately present drawbacks and advantages, but simultaneous use of methods presents an opportunity to enhance selectivity and sensitivity.

5.6.2 Surface Plasmon Resonance

The techniques of quartz crystal microbalance (QCM) and surface plasmon resonance (SPR) have been used to characterize SAM structures and to analyze in real time the response of adsorbed analyte mass [39]. SPR is a sensitive optical technique for the detection of several biomolecular interactions on a transducer surface. This technique works by making a light beam to radiate over a thin metal film at a particular angle; when an interaction happens, a shift in the SPR resonance angle is induced that is directly related to the amount of molecule interacting in the sensor surface.

Ansorena and coworkers have done a comparative study using QCR and SPR. The authors have also evaluated two different SAMs (SAM-MPA and SAM-MUA) for sensing lipopolysaccharide (LPS) using polymyxin B salt sulfate (PmB) as ligand. The polycationic drug PmB interacts with high specificity and efficiency with LPS. The difference between the two types of SAMs is the thiolated acid used: MPA and MUA [39].

The experiment consisted of the following tests:

- Using QCM for monitoring the detection of LPS. First without SAM as a control measurement, then with SAM-MPA and finally with SAM-MUA. Each case was analyzed using ligand PmB and without ligand.
- Using SPR for monitoring the detection of LPS. The same procedure as above: first without SAM, then with SAM-MPA, and finally with SAM-MUA. Each case with and without PmB.

The main idea in the Ansorena study was to determine which SAM (MPA or MUA) provides higher sensitivity for the compound detection. The results showed that SAM-MPA allows a more effective LPS detection.

The work also served to compare the performance of QCM and SPR techniques. The use of PmB ligand proved to be more effective in the case of QCM than in SPR as can be observed in Fig. 9.36. Ansorena and coworkers also found that in QCM assays the variability of measures was very similar (10% approximately) in contrast with SPR technique with variability between 10% and 50%. Thus, they concluded that QCM experiments show higher repeatability than SPR [39].

5.6.3 Electrochemical Techniques and EQCM

Voltammetry can be defined as an electrochemical technique that studies the current flux as a function of an applied potential in a specific sample with the aim of investigating the reactivity of an analyte.

In particular, in cyclic voltammetry (CV), the voltage applied in the working electrode is increased linearly versus time. After a set potential is reached in a CV experiment, the working electrode's potential is ramped in the opposite direction to

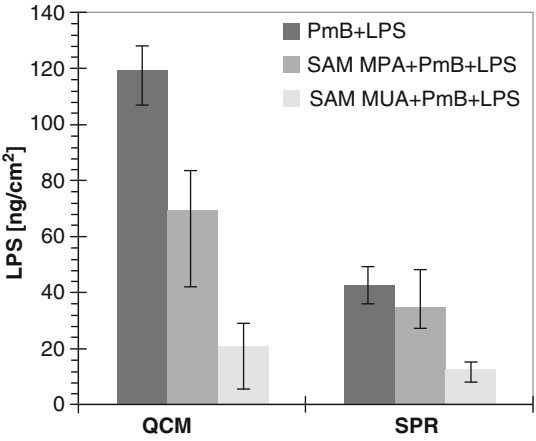

Fig. 9.36 LPS mass detection (ng/cm^2) with the use of PmB. QCM results (left) and SPR results (right) Reprinted from [39], https://doi.org/10.1016/j.snb.2011.01.027, copyright (2011), with permission from Elsevier)

return to the initial potential. The corresponding current that flows is monitored and plotted versus the voltage applied. This plot is called cyclic voltammogram trace. Cyclic voltammetry is commonly used to study the electrochemical properties of an analyte in solution.

EQCM is a variant of the technique in which the active electrode is employed as the working electrochemical electrode. Several applications in the field of electroanalytical chemistry of EQCM have been reported [18, 127–129]. These include studies of formation of films, viscoelastic behavior, transport of ions, etc. In particular, Mech and coworkers have used the electrochemical quartz crystal microbalance (EQCM) technique in combination with cyclic voltammetry to realize studies related to stability measures in the process of generating cobalt layers [127].

Cobalt and its alloys are materials of great interest due to their magnetic properties; they can be used in the construction of spin valve devices, magnetic data carriers, and heterogeneous catalyzers, among others. However, one problem is that Co^{2+} ions in ammonium chloride solutions are not stable, and they are oxidized when the electrolyte is in contact with oxygen. Stability is essential in electrodeposition process and may also affect the reproducibility of electrochemical measurements. The voltammetry voltages were within the range from 0.1 V to −1.1 V. The voltammogram registered for the Au electrode in the electrolyte containing 50 mM $[Co(NH_3)_6]^{3+}$ permitted the measure of the flow of charge together with the reaction of reduction of cobalt complexes and water molecules [127].

Voltammetry combined with EQCM allows to determine the regions where working electrode polarization is accompanied by a change in the electrode mass. Figure 9.37 shows the changes in current and frequency during hexaminecobalt(III) electro reduction. There are three reduction peaks: A, B, and C. Peak A, occurring at potential $E = -0.16$ V, indicates irreversible reaction of reduction of $[Co(NH_3)_6]^{3+}$ complex to $[Co(NH_3)_6]^{2+}$ complex. The complex obtained is soluble and does not precipitate on the electrode surface. This result confirmed monitoring the QCM

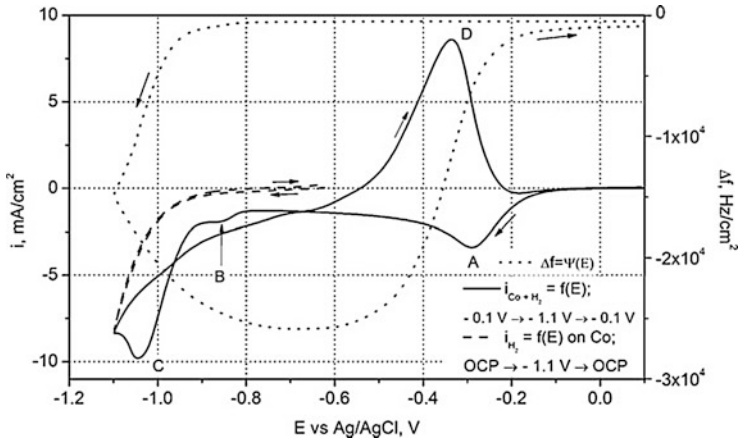

Fig. 9.37 CV registered in the 50 mM $[Co(NH_3)_6]^{3+}$ (Reprinted from [127], https://doi.org/10.1016/j.electacta.2012.07.067, copyright (2012), with permission from Elsevier)

signal which did not show changes of oscillation frequencies of quartz resonator within the potential region of the peak appearance [127].

In a similar study, Zhou et al. [126] have used a QCM to monitor the processes of adsorption of Hg and ethylenediamine tetraacetic Acid (EDTA) formed by a photocatalytic reduction. Heavy metal contaminated wastewater commonly contains chelating agents such as EDTA. Photocatalysis is a technology that facilitates the removal of EDTA complexes; titanium dioxide is a photocatalyst capable of decomposing a variety of pollutants.

In addition, they used cyclic voltammetry (CV) to explain the effect of EDTA on the photocatalytic reduction of Hg [126]. Cyclic voltammetry was done in 0.2 M H_2SO_4 solution of the TiO_2/GC electrode after immersed in certain solutions for 20 min and rinsed with distilled water. The voltage potential range was 0 to 1 V, and the potential sweep rate was 50 mV/s.

And in situ-QCM with TiO2/Au electrode was used to monitor adsorption of Hg and EDTA solutions in different sequences:

- Starting with 0.05 mM EDTA, then applying 0.05 mM EDTA + 0.05 mM Hg (II) while in the dark and finally UV illumination. Control experiment was performed in same way but without UV.
- Starting with 0.05 mM Hg(II), then applying 0.05 mM EDTA + 0.05 mM Hg (II) while in the dark and UV illumination later. Control experiment was also performed without UV.

In both sequences, the frequency response of QCM showed a change in the slope after UV illumination, speeding the frequency decrease as can be seen in Fig. 9.38, showing that UV illumination was effective for the reduction of Hg. Fig. 9.39 shows the results of cyclic voltammetry.

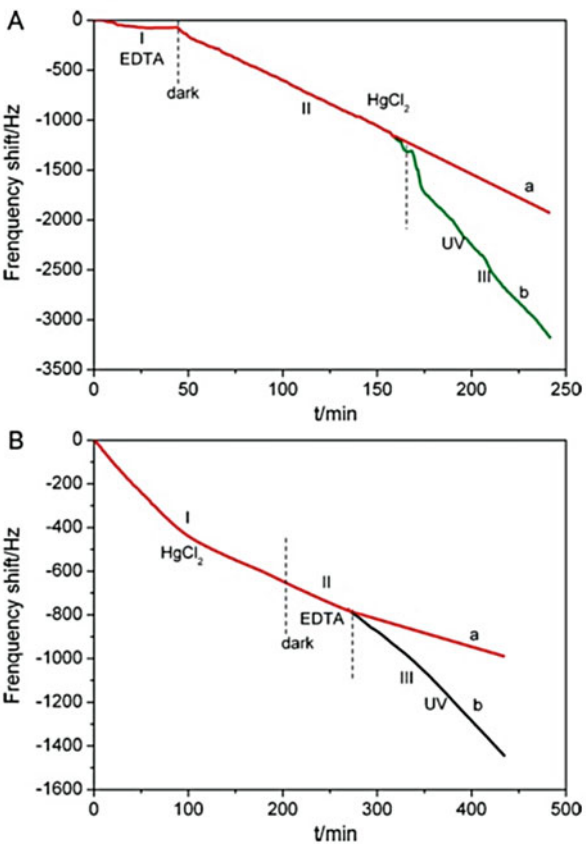

Fig. 9.38 Frequency changes of the QCM electrodes against time under different order of injection solutions. (**a**) Order of components added to cell EDTA (I), Hg(II) + EDTA (II), UV illumination (III); (**b**) Order of components added to cell Hg(II) (I), Hg(II) + EDTA (II), UV illumination (III) (Reprinted from [126], https://doi.org/10.1016/j.electacta.2010.11.047, copyright (2010), with permission from Elsevier)

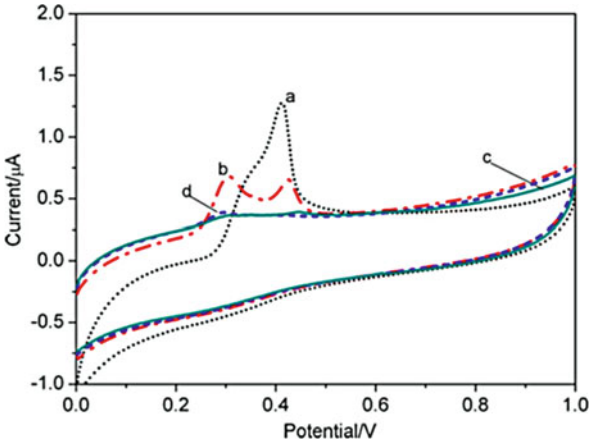

Fig. 9.39 Cyclic voltammograms. (**a**) Solution of Hg(II):HCOOH 1:1 under UV illumination. (**b**) Solution of Hg(II):EDTA 1:1 under UV illumination. (**c**) Solution of Hg(II):HCOOH 1:1 in the dark. (**d**) Solution of Hg(II):EDTA 1:1 in the dark (Reprinted from [126], https://doi.org/10.1016/j.electacta.2010.11.047, copyright (2010), with permission from Elsevier)

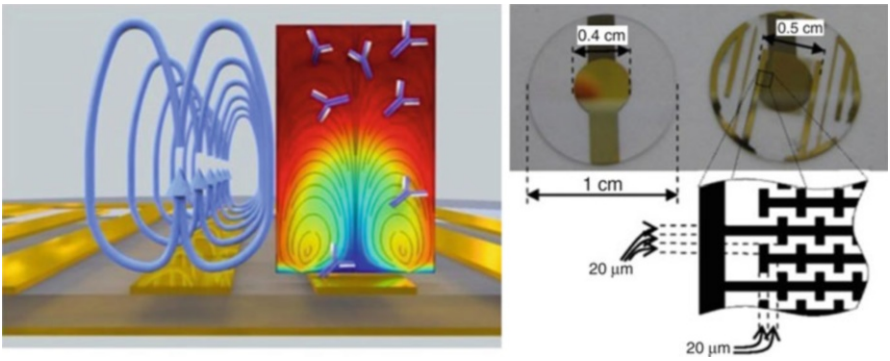

Fig. 9.40 Left: A conceptual diagram of ACEO motion (blue arrows) produced by parallel interdigitated electrodes and its effect on analyte concentration (color map), which is removed from the bulk solution by a reaction at the bottom surface. Right: Image of (left) an unmodified QCM and (right) a QCM that has been modified with a microelectrode pattern. The QCMs used were 1 cm diameter and 167 μm thickness (Reprinted from [130], https://doi.org/10.1016/j.bios.2010.12.038, copyright (2010), with permission from Elsevier)

5.6.4 Electrokinetic QCM (EKQCM)

AC electroosmosis (ACEO) is electrokinetic phenomenon characterized by stable rotational velocity fluid patterns that exist near the surface of microelectrodes supplied with an AC field. These rotational patterns can be used to stir the bulk solution. Stirring antibody-to-surface bound receptor reactions therefore improves transport, by bringing fresh reagent to the surface which replenishes the quickly consumed reactants. Reduction in time often implies an increase in sensitivity. The major drawback of ACEO is that it can only function in low conductivity solutions.

In addition to ACEO, there are two other common AC electrokinetic phenomena: the electrothermal effect (ETE) and dielectrophoresis (DEP). ETE usually exists in high conductivity solutions and is caused by temperature gradients, which induce the movement of free charges. DEP acts directly on submerged particles moving due to electric field gradients. Other groups have worked using different electrokinetic, acoustic, and magnetic methods for stirring.

Hart and coworkers have developed an EKQCM enhancing the output signal 5.6 times. The quality factor was slightly reduced due to the modification of the QCMs to obtain EKQCMs, and the sensitivity to viscosity changes was increased (151%). EKQCMs were obtained by replacing the continuous circular electrode of a QCM with a pair of interdigitated microelectrodes (IDEs), which can generate ACEO (Fig. 9.40). This process is simple and inexpensive. Castellated IDEs were used for this study as they enhance the mixing capability. 10 MHz QCMs were used and they were modified by leaving a side of the QCM completely bare, allowing for a new electrode to be patterned by lift-off [130].

The EKQCM could be operated in two ways: using just one of the top electrode fingers or by shorting the top two electrodes. Single-finger operation shows greater electrical losses at resonance. The resonance frequency shift caused by the

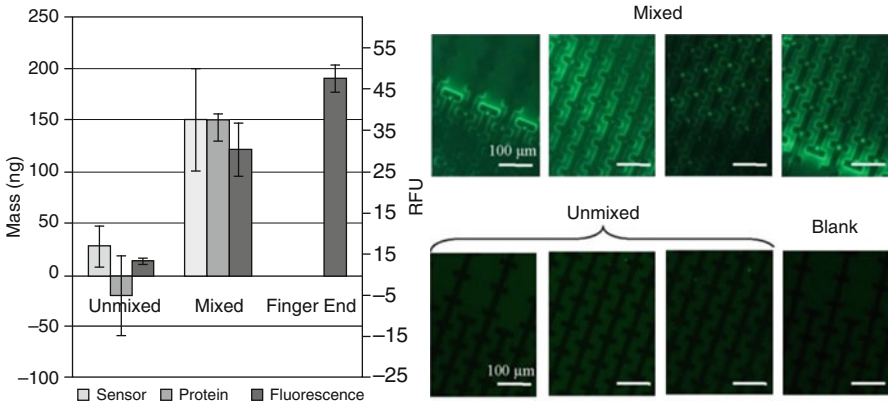

Fig. 9.41 Measurement of directly adsorbed fluorescein-labeled IgG bound to the EKQCM surface. The graph shows the quantity of adsorbed protein using three different measurement approaches. The three techniques are (1) EKQCM, (2) MicroBCA protein quantification assay, and (3) fluorescence microscopy. Note that the fluorescence series uses the secondary axis on the right in relative fluorescence units (RFU) and is the only method that can measure values at the finger end. The others are bulk measurement techniques. The images show mixed samples, unmixed samples, and a blank, which was not subjected to any fluorescent IgG (EKQCM $n = 4$, MicroBCA assay (unmixed $n = 4$, mixed $n = 2$), and fluorescence $n = 10$). (Reprinted from [130], https://doi.org/10.1016/j.bios.2010.12.038, copyright (2010), with permission from Elsevier)

modification of the QCM was predicted using Sauerbrey's equation. The sensitivity of the 10 MHz QCM is about 2.89 Hz/ng. The difference in mass between the original and modified QCM will be about 7.5 µg, which would cause a 21.68 kHz frequency shift. A calibration using aqueous concentrations of glycerin was performed to verify that the interdigitated electrodes did not significantly affect sensor function [130].

Antibody binding to the EKQCM (Immunoglobulin G – IgG as a sample) was measured using the dip-dry technique to demonstrate the proof of concept; this technique compares the resonance frequency of the sensor in the air before and after a period of binding. Sauerbrey's equation was used to derive the mass change from the frequency shift. IgG spatial distribution was studied using FITC-labeled IgG fluorescent microscopy [130]. Antibody function was not significantly degraded by the enhancement technique. To check if using ACEO more protein was adsorbed. The antibody solution was dialyzed to control its conductivity. Antibody orientation was not controlled, and the simplicity of the protocol has been achieved at the cost of reduced binding capacity. By using a self-assembled monolayer (SAM) of protein IgG or by a variety of other conjugation methods, this binding capacity could be improved.

According to Fig. 9.41, mixed and unmixed EKQCMs were incubated in fluorescein-labeled IgG. Data revealed that in the 15 min incubation, the amount of mass adsorbed was increased by a factor of about 5.6 by utilizing ACEO mixing. The antibody was observed to be preferentially adsorbed near the edges of the activated electrodes and toward the ends of each finger, a pattern that usually indicates DEP [130].

Results so far have only indicated the ability of ACEO to enhance nonspecific binding. To selectively detect an antigen, biosensors should be functionalized with a receptor layer. Experiments involved primary and secondary binding were performed. Antibody attachment around edges and at finger ends (enhanced about six times) was much pronounced. However, mixing in the center of the device was much more effective during the primary IgG binding step. To test if the antibodies have retained function after subjection to high electric fields and dialysis assays were performed. Electrode damage at high voltages was checked, and it was discovered to be more likely to happen at higher antibody concentrations. Thus, although ACEO mixing velocity increases with voltage, benefitting performance, attention must be paid when increasing the voltage to avoid damage to the gold and chromium layers of the sensors. In fact, the authors recommend to use voltage no higher than 2Vpp [130].

6 Conclusions and Future Perspective

Despite the QCM started to be used as sensor device more than five decades ago, many of the features of this versatile and low cost system are being maximized. Improving sensitivity, reproducibility, and portability are some of the characteristics with more research and development work nowadays. Health, environment, and food are the industry fields with more potential to increase the massive use of QCM systems in routine processes. QCM has proven to be an effective technology in biosensor applications, and therefore they constitute a promising tool for a great variety of fields.

Medical and environmental monitoring are currently two fields that are greatly benefiting from the use of QCRs due to their reliability, high sensitivity in protein detection, their easy and inexpensive use, and the versatility for their surface coating. A very important feature of this tool in such applications is the response time, which permits to obtain results promptly (real-time technique). As an example, there are applications with response time <60s [80].

In the medical field, QCMs have been successfully used in the detection of diseases such as prostate and pancreatic cancer [82, 84], avian influenza virus [54], or Salmonella [46]. Besides, they have contributed to relevant discoveries that may contribute to the detection of diseases such as Alzheimer [80].

Regarding environmental monitoring, QCMs have been found to be of great utility in applications such as humidity detection, detection of organic compounds (e.g., detection of pollution in liquids [89, 91, 97]), or food quality analysis. As the future for humidity monitoring seems to be on the path of the combination between the measurements made with the QCM and corrections made with neural networks, the key for improving measurements is to develop better training algorithms for neural networks to make more accurate predictions.

Some other fields can benefit from the use of QCMs by combining their use with the traditional detection techniques, as in the case of explosives detection, when

fluorescence quenching is the preferred method, but it can be used in conjunction to QCM to improve selectivity and sensitivity [124].

It can be therefore concluded that QCM has proven to be an effective technology in biosensor applications; however, it is important to understand its limitations when designing a specific sensing solution.

Cyclic voltammetry, differential pulse voltammetry [126], spectrophotometry [127], surface plasmon resonance [39], and spectroscopic ellipsometry [85], among others, are techniques that can be used in combination with QCM in multisensor applications to improve overall response and to provide further information in comparison with single sensor systems.

One of the most relevant problems that QCM-related research must face nowadays is the improper distribution of a given functionalization bioreceptor over a QCR layer electrode, as this may have a high impact over the measurements taken with this technology [122]. This improper distribution cannot be easily exposed, requiring equipment such as an Atomic Force Microscope (AFM) to be detected. The cause of an improper distribution can be inherent to the properties of functionalized substances or due to functionalizing protocols. This inconvenience can cause a lack of results repeatability between researches; hence, future work should be aimed to find new ways to overcome this inconvenience and give a better comprehension of this phenomenon.

Similar inconveniences such as the lack of control over the orientation of immobilized biomolecules for QCR have been reported and addressed with by using self-assembled monolayers (SAMs) [39].

As future perspectives, the integration of sense systems will be at high levels permitting better sensors response, more accuracy, and more portables and cheapers; and the sensors QCR are not the exception. The conjunction of the QCR with other platforms as spectroscopic ellipsometry, surface plasmon resonance, and electrochemical techniques will permit to obtain better sense systems. In addition, the manufacture techniques will continue improving and reducing their costs. Therefore, the MQCRs will replace the conventional QCR as sense element in quartz crystals microbalances.

References

1. Sauerbrey G (1959) Verwendung von Schwingquarzen zur Wägung dünner Schichten und zur Mikrowägung. Z Phys 155(2):206–222
2. Carvajal Ahumada LA, Peña Pérez N, Herrera Sandoval OL, del Pozo Guerrero F, Serrano Olmedo JJ (2016) A new way to find dielectric properties of liquid sample using the quartz crystal resonator (QCR). Sensors Actuators A Phys 239:153–160
3. Keiji Kanazawa K, Gordon JG (1985) The oscillation frequency of a quartz resonator in contact with liquid. Anal Chim Acta 175:99–105
4. Melroy O, Kanazawa K, Gordon JG, Buttry D (1986) Direct determination of the mass of an underpotentially deposited monolayer of lead on gold. Langmuir 2(6):697–700
5. Dixon MC (2008) Quartz crystal microbalance with dissipation monitoring: enabling real-time characterization of biological materials and their interactions. J Biomol Tech 19(3):151–158

6. Cassiède M, Daridon J-L, Paillol JH, Pauly J (2011) Characterization of the behaviour of a quartz crystal resonator fully immersed in a Newtonian liquid by impedance analysis. Sensors Actuators A Phys 167(2):317–326
7. Arnau A (2008) A review of Interface electronic systems for AT-cut quartz crystal microbalance applications in liquids. Sensors 8(1):370–411
8. Johannsmann D (2015) The quartz crystal microbalance in soft matter research, vol 53, 1st edn. Springer, Cham
9. Montagut Y, Narbon J, Jiménez Y, March C, Montoya A, Arnau A (2011) QCM technology in biosensors, Biosensors - Emerging Materials and Applications, Prof. Pier Andrea Serra (Ed.), InTech, DOI: https://doi.org/10.5772/17991. Available from: https://www.intechopen.com/books/biosensors-emerging-materials-and-applications/qcm-technology-in-biosensors
10. Chen Q, Tang W, Wang D, Wu X, Li N, Liu F (2010) Amplified QCM-D biosensor for protein based on aptamer-functionalized gold nanoparticles. Biosens Bioelectron 26(2):575–579
11. Jaruwongrungsee K, Waiwijit U, Wisitsoraat A, Sangworasil M, Pintavirooj C, Tuantranont A (2015) Real-time multianalyte biosensors based on interference-free multichannel monolithic quartz crystal microbalance. Biosens Bioelectron 67:576–581
12. García-Martinez G et al (2011) Development of a mass sensitive quartz crystal microbalance (QCM)-based DNA biosensor using a 50 MHz electronic oscillator circuit. Sensors (Basel) 11(8):7656–7664
13. Cernosek RW, Martin SJ, Hillman AR, Bandey HL (1998) Comparison of lumped-element and transmission-line models for thickness-shear-mode quartz resonator sensors. IEEE Trans Ultrason Ferroelectr Freq Control 45(5):1399–1407
14. Jakoby B, Art G, Bastemeijer J (2005) Novel analog readout electronics for microacoustic thickness shear-mode sensors. IEEE Sens J 5(5):1106–1111
15. Ferreira GNM, da-Silva A-C, Tomé B (2009) Acoustic wave biosensors: physical models and biological applications of quartz crystal microbalance. Trends Biotechnol 27(12):689–697
16. Gu Y, Li Q, Xu B-J, Zhao Z (2014) Vibration analysis of a new polymer quartz piezoelectric crystal sensor for detecting characteristic materials of volatility liquid. Chin Phys B 23(1):17804
17. Kikuchi M, Shiratori S (2005) Quartz crystal microbalance (QCM) sensor for CH 3 SH gas by using polyelectrolyte-coated sol–gel film. Sensors Actuators B Chem 108:564–571
18. Nilsson S, Björefors F, Robinson ND (2013) Electrochemical quartz crystal microbalance study of polyelectrolyte film growth under anodic conditions. Appl Surf Sci 280:783–790
19. Dell'Atti D et al (2007) Development of combined DNA-based piezoelectric biosensors for the simultaneous detection and genotyping of high risk human papilloma virus strains. Clin Chim Acta 383(1–2):140–146
20. Dewar R, Joyce M (2005) The quartz crystal microbalance as a microviscometer for improved rehabilitation therapy of dysphagic patients. Conf Proc IEEE Eng Med Biol Soc 3:2511–2515
21. Höök F, Kasemo B, Nylander T, Fant C, Sott K, Elwing H (2001) Variations in coupled water, viscoelastic properties, and film thickness of a Mefp-1 protein film during adsorption and cross-linking: a quartz crystal microbalance with dissipation monitoring, ellipsometry, and surface plasmon resonance study. Anal Chem 73(24):5796–5804
22. Lucklum R, Hauptmann P (2006) Acoustic microsensors – the challenge behind microgravimetry. Anal Bioanal Chem 384(3):667–682
23. Deng T, Wang H, Li J-S, Shen G-L, Yu R-Q (2005) A novel biosensing interfacial design based on the assembled multilayers of the oppositely charged polyelectrolytes. Anal Chim Acta 532(2):137–144
24. Fatisson J, Azari F, Tufenkji N (2011) Real-time QCM-D monitoring of cellular responses to different cytomorphic agents. Biosens Bioelectron 26(7):3207–3212
25. Lederer T, Stehrer BP, Bauer S, Jakoby B, Hilber W (2011) Utilizing a high fundamental frequency quartz crystal resonator as a biosensor in a digital microfluidic platform. Sens Actuators A Phys 172(1):161–168
26. Wolfbeis OS (2007) Piezoelectric sensors, vol 5. Springer, Berlin/Heidelberg

27. Granstaff VE, Martin SJ (1994) Characterization of a thickness-shear mode quartz resonator with multiple nonpiezoelectric layers. J Appl Phys 75(3):1319
28. Rosenbaum J (1988) Bulk acoustic wave theory and devices. Artech Print on Demand, Boston
29. Lucklum R (2000) The Δf–ΔR QCM technique: an approach to an advanced sensor signal interpretation. Electrochim Acta 45(22–23):3907–3916
30. Calvo EJ, Etchenique R, Bartlett PN, Singhal K, Santamaria C (1997) Quartz crystal impedance studies at 10 MHz of viscoelastic liquids and films. Faraday Discuss 107:141–157
31. Tao W, Lin P, Ai Y, Wang H, Ke S, Zeng X (2016) Multichannel quartz crystal microbalance array: fabrication, evaluation, application in biomarker detection. Anal Biochem 494:85–92
32. Vavra KC, Yu G, Josowicz M, Janata J (2011) Magnetic quartz crystal microbalance: Magneto-acoustic parameters. J Appl Phys 110(1):13905
33. Cho N-J, D'Amour JN, Stalgren J, Knoll W, Kanazawa K, Frank CW (2007) Quartz resonator signatures under Newtonian liquid loading for initial instrument check. J Colloid Interface Sci 315(1):248–254
34. Cassiède M, Paillol JH, Pauly J, Daridon J-L (2010) Electrical behaviour of AT-cut quartz crystal resonators as a function of overtone number. Sensors Actuators A Phys 159(2):174–183
35. Carvajal Ahumada LA, González MXR, Sandoval OLH, Olmedo JJS (2016) Evaluation of hyaluronic acid dilutions at different concentrations using a Quartz Crystal Resonator (QCR) for the potential diagnosis of arthritic diseases. Sensors (Basel) 16(11):1959
36. Chen K, Tan Z, Nie L, Yao S (1995) Principal component analysis applied to admittance spectra of a quartz-crystal microbalance in contact with a liquid phase. Analyst 120(7):1885
37. Ferrari V, Marioli D, Taroni A (2003) ACC oscillator for in-liquid quartz microbalance sensors. In: Proceedings of IEEE sensors 2003 (IEEE Cat. No.03CH37498). pp 849–854. http://ieeexplore.ieee.org/document/1279063/
38. Gerdon AE, Wright DW, Cliffel DE (2007) Quartz crystal microbalance characterization of nanostructure assemblies in biosensing. In: Nanotechnologies for the life sciences. Wiley-VCH Verlag GmbH & Co. KGaA, Weinheim
39. Ansorena P, Zuzuarregui A, Pérez-Lorenzo E, Mujika M, Arana S (2011) Comparative analysis of QCM and SPR techniques for the optimization of immobilization sequences. Sensors Actuators B Chem 155(2):667–672
40. Biolin Scientific Holding AB, "Q-Sense," (2016) [Online]. Available: http://www.biolinscientific.com/q-sense/products/
41. Rodahl M, Kasemo B (1996) A simple setup to simultaneously measure the resonant frequency and the absolute dissipation factor of a quartz crystal microbalance. Rev Sci Instrum 67 (9):3238
42. Rodahl M, Höök F, Kasemo B (1996) QCM Operation in Liquids: an explanation of measured variations in frequency and Q factor with liquid conductivity. Anal Chem 68(13):2219–2227
43. Fredriksson C, Kihlman S, Rodahl M, Kasemo B (1998) The piezoelectric quartz crystal mass and dissipation sensor: a means of studying cell adhesion. Langmuir 14(2):248–251
44. Rodahl M, Kasemo B (1996) On the measurement of thin liquid overlayers with the quartz-crystal microbalance. Sensors Actuators A Phys 54(1–3):448–456
45. Reviakine I, Johannsmann D, Richter RP (2011) Hearing what you cannot see and visualizing what you hear: interpreting quartz crystal microbalance data from solvated interfaces. Anal Chem 83(23):8838–8848
46. Salam F, Uludag Y, Tothill IE (2013) Real-time and sensitive detection of salmonella typhimurium using an automated quartz crystal microbalance (QCM) instrument with nanoparticles amplification. Talanta 115:761–767
47. Su X-L, Li Y (2004) A self-assembled monolayer-based piezoelectric immunosensor for rapid detection of Escherichia coli O157:H7. Biosens Bioelectron 19(6):563–574
48. Hiatt LA, Cliffel DE (2012) Real-time recognition of mycobacterium tuberculosis and Lipoarabinomannan using the quartz crystal microbalance. Sens Actuators B Chem 174:245–252

49. Xi J, Chen JY, Garcia MP, Penn LS (2013) Biochips & tissue chips quartz crystal microbalance in cell biology studies. pp 1–9. https://www.omicsonline.org/open-access/quartz-crystal-microbalance-in-cell-biology-studies-2153-0777-S5-001.php?aid=11310
50. Afonso AS, Zanetti BF, Santiago AC, Henrique-Silva F, Mattoso LHC, Faria RC (2013) QCM immunoassay for recombinant cysteine peptidase: a potential protein biomarker for diagnosis of citrus canker. Talanta 104:193–197
51. Lu CH et al (2012) Sensing HIV related protein using epitope imprinted hydrophilic polymer coated quartz crystal microbalance. Biosens Bioelectron 31(1):439–444
52. Olanya G, Thormann E, Varga I, Makuska R, Claesson PM (2010) Protein interactions with bottle-brush polymer layers: effect of side chain and charge density ratio probed by QCM-D and AFM. J Colloid Interface Sci 349(1):265–274
53. Serro AP, Degiampietro K, Colaço R, Saramago B (2010) Adsorption of albumin and sodium hyaluronate on UHMWPE: a QCM-D and AFM study. Colloids Surf B Biointerfaces 78(1):1–7
54. Wang R, Li Y (2013) Hydrogel based QCM aptasensor for detection of avian influenza virus. Biosens Bioelectron 42(1):148–155
55. Michanek A, Kristen N, Höök F, Nylander T, Sparr E (2010) RNA and DNA interactions with zwitterionic and charged lipid membranes – a DSC and QCM-D study. Biochim Biophys Acta Biomembr 1798(4):829–838
56. Tsortos A, Papadakis G, Gizeli E (2008) Shear acoustic wave biosensor for detecting DNA intrinsic viscosity and conformation: a study with QCM-D. Biosens Bioelectron 24(4):842–847
57. Zhou XC, Huang LQ, Li SF (2001) Microgravimetric DNA sensor based on quartz crystal microbalance: comparison of oligonucleotide immobilization methods and the application in genetic diagnosis. Biosens Bioelectron 16(1–2):85–95
58. Hao RZ et al (2011) DNA probe functionalized QCM biosensor based on gold nanoparticle amplification for bacillus anthracis detection. Biosens Bioelectron 26(8):3398–3404
59. Wang D et al (2013) A reusable quartz crystal microbalance biosensor for highly specific detection of single-base DNA mutation. Biosens Bioelectron 48:276–280
60. Fang J, Zhu T, Sheng J, Jiang Z, Ma Y (2015) Thickness dependent effective viscosity of a polymer solution near an Interface probed by a quartz crystal microbalance with dissipation method. Sci Rep 5:8491
61. Eris G et al (2015) Determination of viscosity and density of fluids using frequency response of microcantilevers. J Supercrit Fluids 105:179–185
62. Jakoby B et al (2010) Miniaturized sensors for the viscosity and density of liquids – performance and issues. IEEE Trans Ultrason Ferroelectr Freq Control 57(1):111–120
63. Dunér G, Thormann E, Dėdinaitė A (2013) Quartz crystal microbalance with dissipation (QCM-D) studies of the viscoelastic response from a continuously growing grafted polyelectrolyte layer. J Colloid Interface Sci 408(1):229–234
64. Sweity A et al (2011) Relation between EPS adherence, viscoelastic properties, and MBR operation: biofouling study with QCM-D. Water Res 45(19):6430–6440
65. Yu GY (2008) Magnetic quartz crystal microbalance. http://aip.scitation.org/doi/10.1063/1.2749448
66. Nakamoto T, Kobayashi T (1994) Development of circuit for measuring both Q variation and resonant frequency shift of quartz crystal microbalance. IEEE Trans Ultrason Ferroelectr Freq Control 41(6):806–811
67. Yao Y, Chen X, Guo H, Wu Z (2011) Graphene oxide thin film coated quartz crystal microbalance for humidity detection. Appl Surf Sci 257(17):7778–7782
68. Kim GH, Rand AG, Letcher SV (2003) Impedance characterization of a piezoelectric immunosensor. Part I: antibody coating and buffer solution. Biosens Bioelectron 18(1):83–89
69. Johannsmann D, Mathauer K, Wegner G, Knoll W (1992) Viscoelastic properties of thin films probed with a quartz-crystal resonator. Phys Rev B Condens Matter 46(12):7808–7815
70. Wessendorf KKO (1993) The lever oscillator for use in high resistance resonator applications. In: 1993 I.E. international frequency control symposium. pp 711–717. http://ieeexplore.ieee.org/document/367466/

71. Wessendorf KO (2001) The active-bridge oscillator for use with liquid loaded QCM sensors. pp 400–407. http://ieeexplore.ieee.org/document/956260/
72. Papez V, Papezova S (2011) Bridge symmetric crystal oscillator. In: 2011 international conference on telecommunications in modern satellite, cable and broadcasting services TELSIKS 2011 – proceedings of papers, vol 2. pp 597–600. http://ieeexplore.ieee.org/document/6143185/
73. Schweyer M, Hilton J, Munson JE, Andle JC, Hammond JM, Lec RM (1997) A novel monolithic piezoelectric sensor. In: Proceedings of international frequency control symposium. pp 32–40. http://ieeexplore.ieee.org/document/638517/
74. Borngräber R, Schröder J, Lucklum R, Hauptmann P (2002) Is an oscillator-based measurement adequate in a liquid environment? IEEE Trans Ultrason Ferroelectr Freq Control 49(9):1254–1259
75. Rodriguez-Pardo L, Farina J, Gabrielli C, Perrot H, Brendel R (2004) Miller oscillators for high sensitivity quartz crystal microbalance sensors in damping media. pp 806–812. http://ieeexplore.ieee.org/document/1418571/
76. Rodriguez-Pardo L, Fariña J, Gabrielli C, Perrot H, Brendel R (2007) Design considerations of miller oscillators for high-sensitivity QCM sensors in damping media. IEEE Trans Ultrason Ferroelectr Freq Control 54(10):1965–1976
77. Ferrari M, Ferrari V, Marioli D, Taroni A, Suman M, Dalcanale E (2006) In-liquid sensing of chemical compounds by QCM sensors coupled with high-accuracy ACC oscillator. IEEE Trans Instrum Meas 55(3):828–834
78. Doerner S, Schneider T, Schroder J, Hauptmann P (2003) Universal impedance spectrum analyzer for sensor applications, vol 1. pp 596–599. http://ieeexplore.ieee.org/document/1279007/
79. Schröder J, Borngräber R, Eichelbaum F, Hauptmann P (2002) Advanced interface electronics and methods for QCM. Sensors Actuators A Phys 97–98:543–547
80. Oberfrank S, Drechsel H, Sinn S, Northoff H, Gehring F (2016) Utilisation of quartz crystal microbalance sensors with dissipation (QCM-D) for a Clauss fibrinogen assay in comparison with common coagulation reference methods. Sensors 16(3):282
81. Sinn S et al (2010) Platelet aggregation monitoring with a newly developed quartz crystal microbalance system as an alternative to optical platelet aggregometry. Analyst 135(11):2930–2938
82. Stefan Sinn MH (2013) Blood coagulation Thromboplastine time measurements on a nanoparticle coated quartz crystal microbalance biosensor in excellent agreement with standard clinical methods. J Biosens Bioelectron 4(4):4–9
83. Hussain M, Northoff H, Gehring FK (2015) QCM-D providing new horizon in the domain of sensitivity range and information for haemostasis of human plasma. Biosens Bioelectron 66:579–584
84. Yao C, Qu L, Fu W (2013) Detection of fibrinogen and coagulation factor VIII in plasma by a quartz crystal microbalance biosensor. Sensors (Basel) 13(6):6946–6956
85. Mustafa MK, Nabok A, Parkinson D, Tothill IE, Salam F, Tsargorodskaya A (2010) Detection of ??-amyloid peptide (1-16) and amyloid precursor protein (APP770) using spectroscopic ellipsometry and QCM techniques: a step forward towards Alzheimers disease diagnostics. Biosens Bioelectron 26(4):1332–1336
86. Wang Y, Moss MA (2016) Effect of resveratrol and derivatives on interactions between Alzheimer's Disease Associated Aβ protein oligomers and Lipid Membranes: a quartz crystal microbalance analysis. Biophys J 110(3, Supplement 1):256a
87. Uludağ Y, Tothill IE (2010) Development of a sensitive detection method of cancer biomarkers in human serum (75%) using a quartz crystal microbalance sensor and nanoparticles amplification system. Talanta 82(1):277–282
88. Nowacki L et al (2014) Real-time QCM-D monitoring of cancer cell death early events in a dynamic context. Biosens Bioelectron 64:469–476
89. Bianco M et al (2013) Quartz crystal microbalance with dissipation (QCM-D) as tool to exploit antigen-antibody interactions in pancreatic ductal adenocarcinoma detection. Biosens Bioelectron 42(1):646–652

90. Kim YJ, Rahman MM, Lee JJ (2013) Ultrasensitive and label-free detection of annexin A3 based on quartz crystal microbalance. Sensors Actuators B Chem 177:172–177
91. Li D et al (2011) A nanobeads amplified QCM immunosensor for the detection of avian influenza virus H5N1. Biosens Bioelectron 26(10):4146–4154
92. Gale AJ (2011) Continuing education course #2: current understanding of hemostasis. Toxicol Pathol 39(1):273–280
93. World Health Organization (2016) Global tuberculosis report 2016. [Online]. Available: http://www.who.int/tb/en/
94. Harbeck M, Erbahar DD, Gürol I, Musluoğlu E, Ahsen V, Öztürk ZZ (2010) Phthalocyanines as sensitive coatings for QCM sensors operating in liquids for the detection of organic compounds. Sensors Actuators B Chem 150(1):346–354
95. Xie J, Wang H, Lin Y, Zhou Y, Wu Y (2013) Highly sensitive humidity sensor based on quartz crystal microbalance coated with ZnO colloid spheres. Sensors Actuators B Chem 177:1083–1088
96. Erbahar DD et al (2012) Pesticide sensing in water with phthalocyanine based QCM sensors. Sensors Actuators B Chem 173:562–568
97. Korposh S, Selyanchyn R, Lee SW (2010) Nano-assembled thin film gas sensors. IV. Mass-sensitive monitoring of humidity using quartz crystal microbalance (QCM) electrodes. Sensors Actuators B Chem 147(2):599–606
98. Mumyakmaz B, Özmen A, Ebeoğlu MA, Taşaltin C, Gürol I (2010) A study on the development of a compensation method for humidity effect in QCM sensor responses. Sensors Actuators B Chem 147(1):277–282
99. Tai H et al (2016) Facile development of high performance QCM humidity sensor based on protonated polyethylenimine-graphene oxide nanocomposite thin film. Sensors Actuators B Chem 230:501–509
100. Zhou X, Zhang J, Jiang T, Wang X, Zhu Z (2007) Humidity detection by nanostructured ZnO: a wireless quartz crystal microbalance investigation. Sensors Actuators A Phys 135(1):209–214
101. Hu W, Chen S, Zhou B, Liu L, Ding B, Wang H (2011) Highly stable and sensitive humidity sensors based on quartz crystal microbalance coated with bacterial cellulose membrane. Sensors Actuators B Chem 159(1):301–306
102. Harbeck M, Erbahar DD, Gürol I, Musluolu E, Ahsen V, Öztürk ZZ (2011) Phthalocyanines as sensitive coatings for QCM sensors: comparison of gas and liquid sensing properties. Sensors Actuators B Chem 155(1):298–303
103. Hu W, Chen S, Liu L, Ding B, Wang H (2011) Formaldehyde sensors based on nanofibrous polyethyleneimine/bacterial cellulose membranes coated quartz crystal microbalance. Sensors Actuators B Chem 157(2):554–559
104. Andreeva N, Ishizaki T, Baroch P, Saito N (2012) High sensitive detection of volatile organic compounds using superhydrophobic quartz crystal microbalance. Sensors Actuators B Chem 164(1):15–21
105. Sakti SP, Chabibah N, Ayu SP, Padaga MC, Aulanni'am A (2016) Development of QCM biosensor with specific cow milk protein antibody for candidate milk adulteration detection. J Sens 2016(2):1–7
106. Lederer T, Stehrer BP, Bauer S, Jakoby B, Hilber W (2011) Utilizing a high fundamental frequency quartz crystal resonator as a biosensor in a digital microfluidic platform. Sensors Actuators A Phys 172(1):161–168
107. Tuantranont A, Wisitsora-at A, Sritongkham P, Jaruwongrungsee K (2011) A review of monolithic multichannel quartz crystal microbalance: a review. Anal Chim Acta 687(2):114–128
108. Liu F, Li F, Nordin AN, Voiculescu I (2013) A novel cell-based hybrid acoustic wave biosensor with impedimetric sensing capabilities. Sensors (Basel) 13(3):3039–3055
109. Hung VN, Abe T, Minh PN, Esashi M (2003) High-frequency one-chip multichannel quartz crystal microbalance fabricated by deep RIE. Sensors Actuators A Phys 108(1–3):91–96
110. Zhao Z, Qian Z, Wang B (2016) Effects of unequal electrode pairs on an x-strip thickness-shear mode multi-channel quartz crystal microbalance. Ultrasonics 72:73–79

111. Nilebäck E, Feuz L, Uddenberg H, Valiokas R, Svedhem S (2011) Characterization and application of a surface modification designed for QCM-D studies of biotinylated biomolecules. Biosens Bioelectron 28(1):407–413
112. Zhou W-H, Tang S-F, Yao Q-H, Chen F-R, Yang H-H, Wang X-R (2010) A quartz crystal microbalance sensor based on mussel-inspired molecularly imprinted polymer. Biosens Bioelectron 26(2):585–589
113. Fan X, Du B (2012) Selective detection of trace p-xylene by polymer-coated QCM sensors. Sensors Actuators B Chem 166–167:753–760
114. Naderi A, Olanya G, Makuska R, Claesson PM (2008) Desorption of bottle-brush polyelectrolytes from silica by addition of linear polyelectrolytes studied by QCM-D and reflectometry. J Colloid Interface Sci 323(2):223–228
115. Ottakam Thotiyl MM et al (2012) Multilayer assemblies of polyelectrolyte-gold nanoparticles for the electrocatalytic oxidation and detection of arsenic(III). J Colloid Interface Sci 383 (1):130–139
116. Su P-G, Cheng K-H (2009) Self-assembly of polyelectrolytic multilayer thin films of polyelectrolytes on QCM for detecting low humidity. Sensors Actuators B Chem 142:123–129
117. Deshmukh PK et al (2013) Stimuli-sensitive layer-by-layer (LbL) self-assembly systems: targeting and biosensory applications. J Controll Release 166(3):294–306
118. Voinova MV, Rodahl M, Jonson M, Kasemo B (1999) Viscoelastic acoustic response of layered polymer films at fluid-solid interfaces: continuum mechanics approach. Phys Scr 59 (5):391–396
119. Marx KA (2003) Quartz crystal microbalance: a useful tool for studying thin polymer films and complex biomolecular systems at the solution-surface interface. Biomacromolecules 4 (5):1099–1120
120. Pejcic B, Myers M, Ranwala N, Boyd L, Baker M, Ross A (2011) Modifying the response of a polymer-based quartz crystal microbalance hydrocarbon sensor with functionalized carbon nanotubes. Talanta 85(3):1648–1657
121. Sayago I et al (2011) Surface acoustic wave gas sensors based on polyisobutylene and carbon nanotube composites. Sensors Actuators B Chem 156(1):1–5
122. Indest T, Laine J, Kleinschek KS, Zemljič LF (2010) Adsorption of human serum albumin (HSA) on modified PET films monitored by QCM-D, XPS and AFM. Colloids Surf A Physicochem Eng Asp 360(1–3):210–219
123. Vashist SK, Vashist P (2011) Recent advances in Quartz CrystalMicrobalance-Based Sensors. J Sens 2011:13
124. Clavaguera S, Montméat P, Parret F, Pasquinet E, Lère-Porte JP, Hairault L (2010) Comparison of fluorescence and QCM technologies: example of explosives detection with a π-conjugated thin film. Talanta 82(4):1397–1402
125. Kim J, Kim S, Ohashi T, Muramatsu H, Chang S-M, Kim W-S (2009) Construction of simultaneous SPR and QCM sensing platform. Bioprocess Biosyst Eng 33(1):39
126. Zhou J, Deng C, Si S, Shi Y, Zhao X (2011) Study on the effect of EDTA on the photocatalytic reduction of mercury onto nanocrystalline titania using quartz crystal microbalance and differential pulse voltammetry. Electrochim Acta 56(5):2062–2067
127. Mech K, Żabiński P, Kowalik R, Fitzner K (2012) EQCM, SEC and voltammetric study of kinetics and mechanism of hexaamminecobalt(III) electro-reduction onto gold electrode. Electrochim Acta 81:254–259
128. Zelinsky AG, Novgorodtseva ON (2013) EQCM study of the dissolution of gold in thiosulfate solutions. Hydrometallurgy 138:79–83
129. Voltammetric, EQCM, and in situ conductance studies of p- and n-dopable polymers based on ethylenedioxythiophene and bithiazole.pdf
130. Hart R, Ergezen E, Lec R, Noh HM (2011) Improved protein detection on an AC electrokinetic quartz crystal microbalance (EKQCM). Biosens Bioelectron 26(8):3391–3397

Quartz Crystal Microbalance Application for Characterization of Nanomaterials In Situ

10

Victor S. Popov and Alexander Sopilniak

Contents

Abbreviations

AFM	Atomic Force Microscopy
CVD	Chemical Vapor Deposition
EQCM	Electrochemical Quartz Crystal Microbalance
GO	Graphene Oxide
IR	Infrared
MWCNT	Multiwalled Carbon Nano Tubes

V. S. Popov (✉)
Department of advanced research and development, Polyus Research Institute of M.F.Stelmakh, Moscow, Russia

Sector for high-temperature and sensor materials, Kurnakov Institute of General and Inorganic Chemistry, The Russian Academy of Sciences, Moscow, Russia
e-mail: popov.chem@gmail.com

A. Sopilniak
The Institute of Chemistry, The Hebrew University of Jerusalem, Jerusalem, Israel

© Springer-Verlag GmbH Germany, part of Springer Nature 2018

C. S. S. R. Kumar (ed.), *In-situ Characterization Techniques for Nanomaterials*,
https://doi.org/10.1007/978-3-662-56322-9_10

NOM	Natural Organic Matter
NP	Nanoparticle
NR	Nanorod
NS	Nanospheres
NW	Nanowires
PVD	Physical Vapor Deposition
QCM	Quartz Crystal Microbalance
QCM-D	Quartz Crystal Microbalance with Dissipation Monitoring
QCR	Quartz Crystal Resonator
QD	Quantum Dot
QMB	Quartz Microbalance
SAM	Self-Assembled Monolayers
SEM	Scanning Electron Microscopy
SPM	Scanning Probe Microscopy
STM	Scanning Tunneling Microscope
SWCNT	Single-Walled Carbon Nano Tubes
TEM	Transmission Electron Microscopy

1 Definition of the Topic

Quartz crystal microbalance (QCM) or quartz microbalance (QMB) as an in situ precise method for mass control allows vast research of many processes of heterophasic mass transfer.

In the current chapter, we discuss the recent research dedicated to the application of QCM to study growth and degradation processes of nanomaterials, as well as interactions of nanomaterials with different compounds and natural systems, including compounds from a biological origin.

2 Overview

It is a common conception that the era of nanoscience began with the development of a measurement device, giving the necessary resolution to identify a nano-object – the scanning tunneling microscope or STM. The development of a high resolution both scanning and transmission electronic microscopy (SEM and TEM, respectively) quickly followed the STM development and surpassed its abilities to receive a clear image of nano-objects. The SEM/TEM images were highly detailed and opened the possibility to study substructures and crystal structures of the objects. The development of new research tools led to the discovery of nano-scale phenomena, which, in turn, explained the unique properties of well-known materials. The systematic study of the reasons behind the appearance of nano-scale phenomena could have been achieved only with the development of specialized tools and precise methods of analytical quantification.

Quartz crystal microbalance (QCM) or quartz microbalance (QMB) as a measurement tool could monitor changes in mass on the scale of nano to pico grams in real time as well as registering precise changes in viscoelastic properties and structures of materials on thin films, even in cases where such accuracy cannot be achieved with atomic force microscopy. It is therefore a highly necessary and desired research tool in the study of nanomaterials.

Here, we look at the application of QCM for the study of processes related to the growth and degradation of nanostructures and ultrathin films, and the detection of molecular analytes by sensor-nanomaterials and nanoparticle-analytes on specialized receptors. Moreover, a large portion of this work is dedicated to the application of QCM in research of nanostructures transport in different ecosystems as well as nanomaterial toxicology.

3 Introduction

The piezoelectric effect is the occurrence of an electrical potential on certain materials due to mechanical deformation (e.g., quartz). The effect was first discovered in 1880 by Paul-Jacques and Pierre Curie [1]. A year later in 1881, a reverse effect was hypothesized by Lippman [2], which was experimentally proven by the Curie brothers later on that year [3]. Nevertheless, the mathematical analysis, connecting the reverse piezoelectric effect with the changes in a resonator's mass, appeared only 77 years later in the work of Sauerbrey [4]. The proposed method allowed conducting measurements of changes in a resonator's mass with very high sensitivity, which was limited only by the nature of the quartz crystal, used for this purpose. The later was the basis of the development of the quartz crystal microbalance (QCM). Modern day piezoelectric quartz crystal resonators (QCR) can detect changes in mass on the scale of 10^{-9}–10^{-12} grams. A disadvantage of the method is the relatively narrow range of measurement.

Due to the high precision and sensitivity, QCM was widely used for different applications: (a) for quality control of layer depositions, to allow evaluating the thickness of the deposited layer; (b) for piezoelectric mass sensors armed with layers of receptors, ensuring selective binding of an analyte; (c) for research purposes of investigating in situ processes of deposition and growth of layers.

The rapid development of nanoscience and nanotechnology in the last decade of the twentieth century renewed the interest of the scientific community in QCM. Foremost, it became apparent that QCM is irreplaceable as an instrument of in situ measurements of thin layer thickness in electronics in both chemical and physical vapor deposition (CVD and PVD, respectively) apparatus [5], even with recent developments in process technology (14–10 nm) [6]. Moreover, it is possible to utilize QCM not only for layer thickness control but also for the studies of nanomaterial growth and aggregation from both gas and liquid phases [7].

Work in the field of nanomaterials introduced the concept of nanomaterials as receptor layers on piezoelectric mass sensors [8, 9].

Finally, as nanomaterials were incorporated into the industry, scientific attention was devoted to questions regarding the influence of these materials on living organisms and the environment, leading to new branches of nanoscience "nanopharmacology" and "nanotoxicology" [10]. For these reasons, QCM became a vital instrument for investigation of interaction processes of nanoparticles with various biomolecules, development of analytical methods for biosensing of and with nanomaterials [11, 12], as well as in biotechnology [13] and toxicology [14].

As a traditional instrument for mass-metric process control, QCM was utilized not only as a research tool but is also utilized for educational purposes. For example, process control of self-assembled monolayers (SAMs) using QCM was suggested in a paper from Cea et al. [15] as an educational experimental work for students of nanoscience and nanomaterials.

The questions of application of QCM were partially discussed in previously published reviews, covering only a narrow spectrum of nanoscience and nanotechnology, for instance, nanosensors and analytics [12, 16–18] or nanomedicine and health care [19–21]. However, no specialized review covers broad practical applications of QCM in the field of nanoscience.

The latest tightly themed review was published in 2016 and focused on the application of QCM in the research of nanoparticle interactions, with emphasis of aggregation and deposition on nanoparticles from colloidal solutions [22]. The authors devoted much attention to the type of works described by the DLVO theory (Derjaguin, Landau, Verwey, and Overbeek theory). During the course of discussing the forces governing the aggregation process, the authors present research works in application of QCM for investigating only aggregation and deposition processes from colloidal solutions, but for different nano-objects (carbon-based, metal, metal oxide and other nanoparticles).

The goal of the present work is to conduct a systematic review, for the first time, of all possible directions of QCM application in the research of nano-objects. This review includes original publications from the last 6 years. A detailed inquiry using databases such as Web of Knowledge and CAS revealed advancements in the application of QCM. Noticeable work was observed in the following directions: nanomaterial-based sensors, nanotoxicology, detection of nanoparticles as analytes, research of ecological aspects of nanoparticle transportation and distribution in the environment, the study of growth and formation of nanostructures during nanomaterial synthesis, and different and unusual applications of QCM for process control of nanostructures deformation because of external influence. Moreover, this review includes studies dedicated to the combinations of QCM with other methodologies for a better in situ characterization of the investigated processes.

Based on the current review of the latest research trends using QCM at their center, the expansion perspectives of QCM and QCM combined methods application for the study of nanostructures were discussed in the concluding section of this chapter.

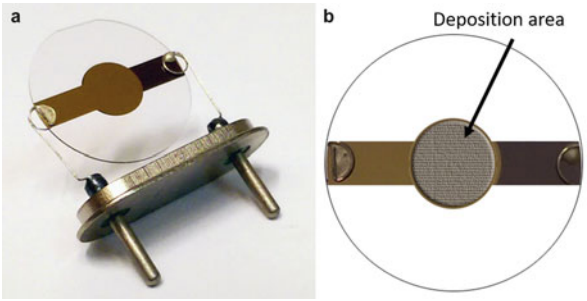

Fig. 10.1 Quartz crystal resonator in holder (**a**) and scheme of deposition area on frontal electrode (**b**)

4 Experimental and Instrumental Methodology

4.1 Working Principle

The core of any quartz microbalance is the piezoelectric quartz crystal (usually with an AT cut) with two adjacent metal electrodes (Au, Pt, Ag), together referred to as the quartz crystal resonator (QCR). Due to the reverse piezoelectric effect, when electrical potential is applied between the two electrodes, the quartz crystal begins to resonate. The frequency of resonance is an internal property of the crystal, as well as all the higher resonance harmonics. The value of the resonance frequency tightly depends on the mass of the crystal (Fig. 10.1).

Relationship between the change of the QCM frequency and the change of the mass can be found from the Sauerbrey model [4]:

$$\Delta f = 2.3 \cdot 10^6 \cdot F_0^2 \cdot \frac{\Delta m}{s} \tag{10.1}$$

where Δf – change the oscillation frequency of quartz resonator at the fundamental harmonic, Hz; F_0 – the natural vibration frequency of the QCR, in MHz; Δm – mass change of the QCR, in gr; s – area of the oscillating part of the QCR (between contacts), in cm^2.

Substitution in (1) the specified values (i.e., F_0, *s and* ΔF) allow to estimate the change of the sample mass as a function of the change in frequency for the first harmonics of quartz crystal:

$$\Delta m = -C\mathrm{m} \cdot \Delta f \tag{10.2}$$

or for harmonics number n [23]:

$$\Delta m = -C\mathrm{m} \cdot \frac{\Delta f}{n} \tag{10.3}$$

where C_m is a constant of the resonator parameters from Eq. 10.1.

The Sauerbrey model gives an accurate description for the cases of deposition for a gas phase or for vacuum, and only for thin rigid films.

For cases of nonrigid films, the Sauerbrey model cannot be applied. These cases use an additional measurement of dissipation energy, which describes the scattering rate of the resonance energy of the crystal to the surroundings. When any material is applied on the QCR surface, the dissipation energy will correlate with the viscoelastic properties of the material. High viscoelastic materials will better dissipate the resonance energy.

The dissipation energy can be evaluated from the dissipation factor D, which can be estimated as follows [24]:

$$D = \frac{1}{\pi F \tau} \tag{10.4}$$

where F is the resonance frequency and τ – decay time constant.

Most cases use the Voigt-based model, described in Eqs. 10.5 and 10.6 [23, 25], which correlates between the density and length of the quartz crystal (ρ_q and h_q), characteristics of the adsorbed film or coating material (h_f – thickness, μ_f – elastic modulus, η_f – viscosity, ρ_f – density), and the bulk-liquid density and viscosity (η_l and ρ_l).

$$\Delta F = \mathrm{Im}\left(\frac{\beta}{2\pi\rho_q h_q}\right) \tag{10.5}$$

$$\Delta D = -\mathrm{Re}\left(\frac{\beta}{2\pi F\rho_q h_q}\right) \tag{10.6}$$

where

$$\beta = \xi_1 \frac{2\pi F\eta_f - i\mu_f}{2\pi F} \frac{1-\alpha e^{2\xi_1 h_f}}{1+\alpha e^{2\xi_1 h_f}},$$

$$\alpha = \frac{\frac{\xi_1}{\xi_2}\frac{2\pi F\eta_f - i\mu_f}{2\pi F\eta_l} + 1}{\frac{\xi_1}{\xi_2}\frac{2\pi F\eta_f - i\mu_f}{2\pi F\eta_l} - 1},$$

$$\xi_1 = \sqrt{-\frac{(2\pi F)^2\rho_f}{\mu_f + i2\pi\eta_f}},$$

$$\xi_2 = \sqrt{i\frac{2\pi F\rho_l}{\eta_l}}.$$

For some cases described in this review, a nonrigid film is formed, especially for deposition from a liquid phase; the full Voigt-based model can be used. However for practical reasons, the signal analysis is limited to measurements of the changes in frequency and dissipation without additional description.

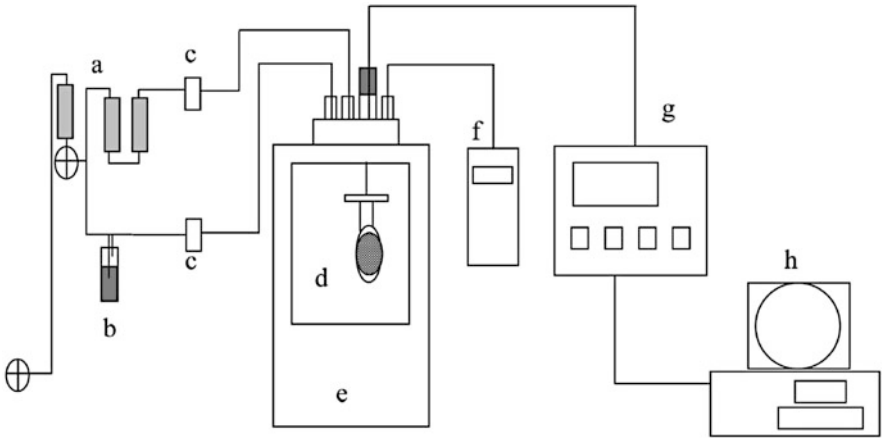

Fig. 10.2 Schematic diagram of experimental setup for the QCM sensor measurement and low humidity atmosphere controller. (**a**) Molecular sieve and desiccating agent; (**b**) water; (**c**) mass flow controller; (**d**) detecting chamber and QCM; (**e**) thermostat; (**f**) low humidity hygrometer; (**g**) oscillator and frequency counter; (**h**) PC [26]

4.2 Tools for Research

4.2.1 Quartz Crystal Microbalance with Dissipation Monitoring (QCM-D)

Quartz crystal microbalance with dissipation monitoring (QCM-D) is the most common and used commercial version of QCM. QCM-D has a hermetic gas/liquid chamber, which can be used for flow experiments. The chamber contains the QCR holder, connecting the electrodes to an electrical circuit (Fig. 10.2). When a QCR sits in the measurement chamber, it is connected to an oscillator and frequency counter. The mass flow controller (Fig. 10.2c), which introduces the gas/liquid sample into the chamber, is connected to the entrance of the detecting chamber (Fig. 10.2d). QCM-D can also be equipped with a thermostat and a humidity hygrometer (Fig. 10.2e–f). QCM can come without the dissipation monitoring system, but the difference between them is in an additional computation block.

4.2.2 In Situ Electrochemical Quartz Crystal Microbalance (EQCM)

In situ electrochemical quartz crystal microbalance (EQCM) is similar in construction to QCM-D with additional electrochemical components in the detecting chamber. The EQCM measuring chamber is integrated with a counter and a reference electrode. The working electrode is the QCR (Fig. 10.3). The electrodes are connected to a potentiostat.

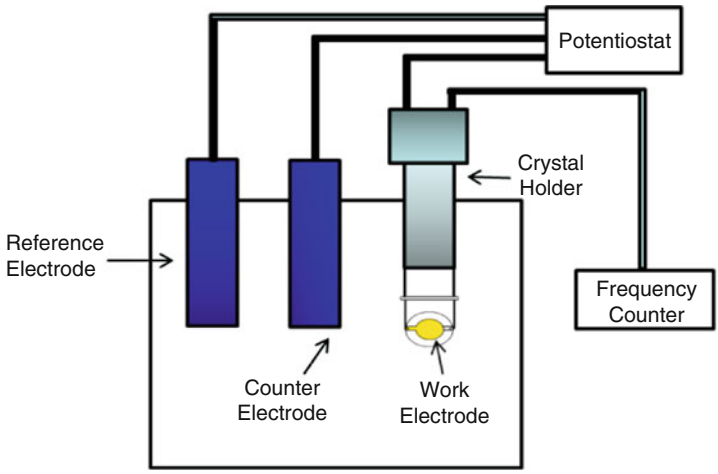

Fig. 10.3 In situ electrochemical quartz crystal microbalance (EQCM) [27]

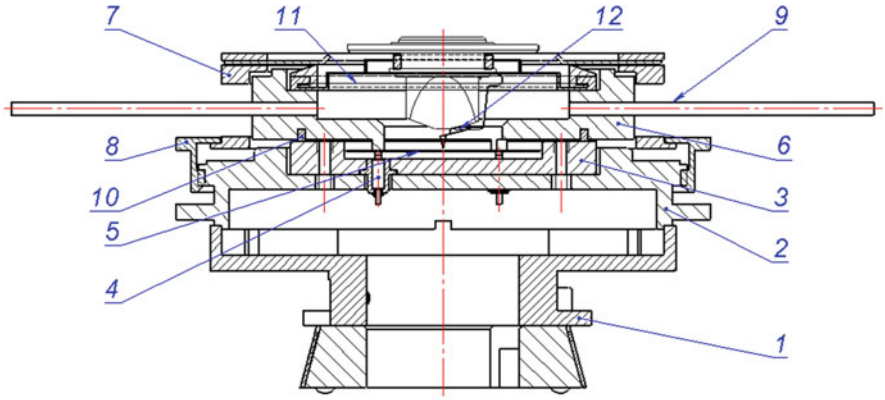

Fig. 10.4 Gas-liquid cell with integrated quartz microbalance [28]

4.2.3 Integrated System Scanning Probe Microscope: Quartz Microbalance

Figure 10.4 shows the design of the gas-liquid cell for an integrated system scanning probe microscope – quartz microbalance: in situ testing of surface potential, topography, and mass of the adsorbed gases [28, 29]. The cell consists of a carriage (1), base (2), bottom cell part (3) with a build-in gold-coated spring contacts (4). Quartz-crystal resonator (QCR) (5) is placed on spring contacts. Fixation of the QCR is carried out by a top cell part (6) with a nozzle (7) and by a screw-nut (8). The gas is supplied through input/output connectors (9). Tightness of the cell is provided by an O-ring (10) between the upper and lower part, and a rubber membrane (11) between

the probe holder and the upper part. An AFM probe (12) is fixed in the probe holder, which allows you to apply electric AC/DC voltage to the probe.

5 Key Research Findings from the Review

5.1 Application of QCM in Studying Nanomaterials for Sensors

Nanomaterials have large surface areas, hence a large number of active centers, which in turn, allow their very broad application as catalysts and highly selective materials for sensors in the gas and liquid phases. Recent works showed promising developments in utilizing nanomaterials as receptors or as matrix for receptor materials for mass sensitive sensors. Recently, carbon nanostructures, such as multiwall carbon nanotubes (MWCNT), MWCNT-COOH (carboxyl functional group), and graphene oxide (GO), were used as receptor materials for sensing water vapor via sorption onto their surface [26]. QCM was used as means to assess the sorption rate and efficiency through measurements of changes in mass. The studied water vapor concentrations were as low as 345 ppm. The authors demonstrated a correlation between the number of functional groups on the surface of MWCNT-COOH and GO (determined using IR spectra) and the sensitivity for low water vapor concentrations. The highest sensitivity to water vapor concentrations was shown for GO based on observations of a larger sorption rate and association constants of water vapor than the corresponding constants for MWCNT-COOH. The authors attribute the difference in sensitivities to the number of -COOH groups on the surface of these materials.

In a paper by Barsan et al. [30], a graphene-based receptor is used as an enzyme biosensor. The activity of the system was demonstrated using QCM as a sensing device for accumulated enzyme (layer deposition). The authors show a rise in deposition of layer containing glucose oxidase enzymes onto the surface of the gold QCM electrode in the presence of nitrogen-doped graphene, used as a template for immobilization of enzymes. The use of nitrogen-doped graphene was shown to increase the sensitivity of the biosensor. Further research is suggested for different nanostructures such as carbon nanotubes/nanorods and fullerenes.

The application of nanostructures as a matrix for receptor materials was successfully shown for a previously developed aptasensor by Du et al. [31]. The binding of microcystin-LR (MC-LR) with the electrochemiluminescence aptasensor, based on three-dimensional boron and nitrogen codoped graphene hydrogels (BN-GHs), was registered using QCM (Fig. 10.5). BN-GHs were applied on a QCR and change in mass was registered due to the binding of the model selective target.

In an interesting research effort, the combination of several in situ techniques, which allow the study of material sensor properties, was proposed by Popov et al. [28]. This idea was demonstrated using a device, integrating both QCM and a scanning probe microscope (SPM), for in situ detection of gas sorption properties on surfaces of nanostructures (Fig. 10.4). Different materials were applied on gold electrode quartz resonators (QCR): SnO_2, palladium-doped tin dioxide (SnO_2-Pd),

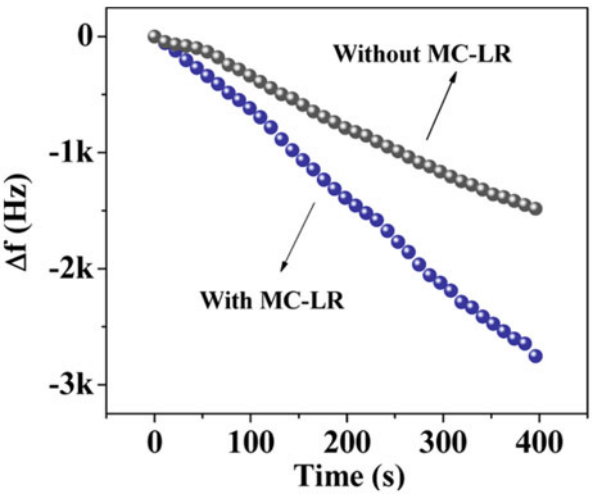

Fig. 10.5 Frequency responses of the aptamer-based QCM biosensor without and with being incubated with 5 pM MC-LR [31]

Table 10.1 Response of QCM and the Kelvin probe at the action of analytes [28]

Sample	Change of the vibration frequency of resonator, Hz (change in the mass, calculated by the Sauerbrey model, ng)			Change of the average surface potential of samples, mV		
	10% (vol) NH_3 in air	0.1% (vol) H_2 in air	0.1% (vol) CH_4 in air	10% (vol) NH_3 in air	0.1% (vol) H_2 in air	0.1% (vol) CH_4 in air
SnO_2	758(2198.2)	420(1218.0)	38(110.2)	189.0	54.7	68.9
SnO_2-Pd	115(333.5)	<1 (−)	70(203.0)	25.8	22.5	30.0
BCP-HfO_2	15(43.5)	1(2.9)	1(2.9)	6.6	15.7	14.1
QCR	12(8.7)	<1(−)	<1(−)	46.3	13.5	6.4

and hafnium dioxide coated with bromocresol purple (HfO_2– BCP). The analyte gases (NH_3, H_2, and CH_4 mixtures with air) were introduced into the measurement chamber, containing one of the nanostructures. Due to gas sorption, frequency shifts were registered with QCM and changes in surface potential were mapped with SPM using a Kelvin probe over an area of 100 × 100 nm. The results are summarized in Table 10.1. These results suggest that sensor properties can be assessed using a single nanocrystal with a surface area of 10^{-8} mm^2.

5.2 Application of QCM for Nanotoxicology and Detection of Nanomaterials as Analytes

The large investment in nanotechnology in the last two decades triggered rapid development of the field of nanoscience and the use of nanomaterials as common analytes. Due to the small scale and high permeability of nanostructures, research effort was devoted to the newly raised question of toxicity of nanomaterials for

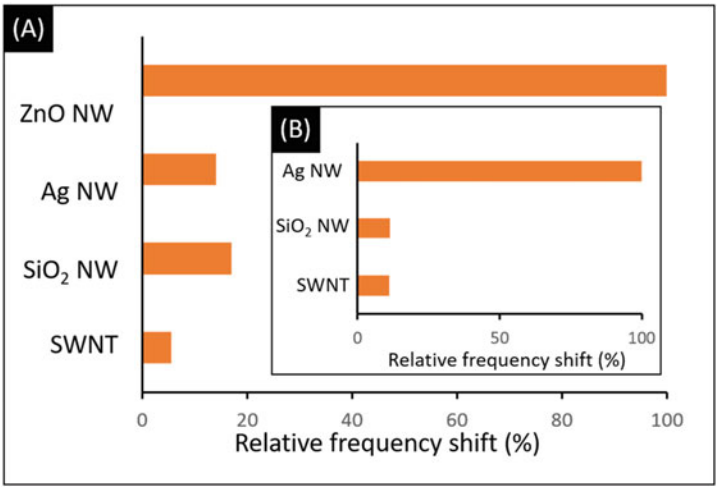

Fig. 10.6 (**a**) Relative frequency shifts for Ag NW, SiO_2 NW, and SWCNT in comparison with ZnO NW; (**b**) relative frequency shifts for SWCNTs and SiO_2 NWs in comparison with Ag NWs. Plot based on data [33, 34], respectively

living organisms. The forecast of size of the global market for nanotoxicology by the year 2019 is expected to reach 64.2 billion dollars [32]. In the last few years, many methods were developed not only for characterizing the toxicity of nanostructures but also for detection of nanostructures as toxic agents, including methods based on QCM.

5.2.1 Application of QCM in Sensor Systems for Detection of Nanomaterials as Analytes

Among the vast number of investigated nanostructures, nano-ZnOs are especially interesting, due to their semiconductive and piezoelectric properties. Jang et al. [33] depicts a method for detection of zinc oxide nanowires (ZnO NWs) based on the covalent interaction between the nanowires, modified with a single-stranded DNA (i.e., linker DNA) using a phosphoric acid group, and the QCM electrode surface, modified with single-stranded DNA containing thiol groups. The authors report a sensitivity level that is 105 times higher than the toxic ZnO NW concentration level in deionized water (limit of detection of 10^{-4} μg/ml).

It should be noted that this method of detection has rather long response times (90% of sensor saturation). For concentrations between 100 pg/mL and 10 ng/mL, as well as for 10 μg/mL, the reported response time was between 10 and 25 min, while for the mid-range concentrations of 100 ng/mL–1 μg/mL, the response time reached 45–50 min.

Other commonly used inorganic materials were also detected using the suggested method (AgNW, SiO_2NW, and single-walled carbon nanotubes (SWCNTs)), and their relative sensitivity compared to ZnO NW detection is depicted in Fig. 10.6a. The low sensitivity to inorganic materials was explained by the absence of interactions with the DNA or by interaction resulting in a low mass difference.

However, a following paper by the same authors reports contradicting results, suggesting high sensitivity for Ag NW in an analogous method, which makes use of the same modifications for NW as well as for the QCM electrodes (Fig. 10.6b) [34]. In 2015, another paper by Jang et al. was released, in which the same methodology was successfully applied for detection of SWCNTs [35].

Unfortunately, the authors did not conduct comparison analysis between their works. Therefore, the selectivity of the suggested method remains to be determined in further research efforts.

5.2.2 Using QCM for Nanotoxicology Research

Developments in the field of nanomedicine increase the human exposure to nanomaterials in the forms of diagnostic and therapeutic agents [36]. Recent QCM-based studies explore the effects of nanostructures on the human body.

The effects of CdTe quantum dots (QD) on the functionality of human blood platelets were demonstrated by Samuel et al. [37] using a QCM-D device. In the course of the study, the QCR was coated with fibrinogen (plasma protein). The changes in frequencies and dissipation response due to platelet deposition were monitored as the QCR was placed in contact with platelet rich plasma (PRP) and platelet poor plasma (PPP) in the presence and absence of CdTe QDs. Measurements were carried out in the third harmonic. The authors did not observe any influence of the CdTe QDs on the deposition of platelets for PPP; however, for PRP, CdTe QDs increased the deposition by 25% due to platelet aggregation. The QCM was reported to be more sensitive to the influence of QDs on the aggregation of platelets than for the commonly used method in such cases, light transmission aggregometry (LTA).

A positive effect to toxicity of nanomaterials was found in a study dedicated to the aggregation of amyloid beta (Aβ) peptides, which cause the amyloid plaques in the brain associated with Alzheimer's disease. The aggregation inhibition with graphene was investigated by Jie Wang et al. [38]. The effects of GO sizes on Aβ (33–42) peptide aggregation were monitored. The shifts in frequencies of a quartz resonator were registered due to precipitation on the surface of its gold electrodes. Various solutions were used with combinations of different GO sizes and Aβ (33–42) peptide (amino acid sequence: NH_2-GLMVGGVVIA-COOH). This experiment illustrates the enhancement of inhibition of Aβ (33–42) peptide aggregation with increasing GO size. These results can become a basis of a new specific inhibition technique for Aβ (33–42) peptide aggregation. Nevertheless, this approach requires additional research on the other effects of GO on a living organism, for instance, toxicity to other proteins.

Toxic effects of deposition of multiwalled carbon nanotubes (MWCNTs) on biological membranes were checked as a function of electrolyte concentration, cation charge, and solution pH [39]. Supported lipid bilayers (SLBs) composed of zwitterionic 1,2-dioleoyl-sn-glyero-3-phosphocholine (DOPC) and vesicles were used as model biological membranes. QCRs were coated with SLBs and vesicles by the method described in Richter et al. [40]. The system was put in different solutions containing the model membranes. The authors show favorable deposition of MWCNTs on biological membranes in acidic conditions (pH 2–3) as well as in the presence of Ca^{2+} ions (Fig. 10.7).

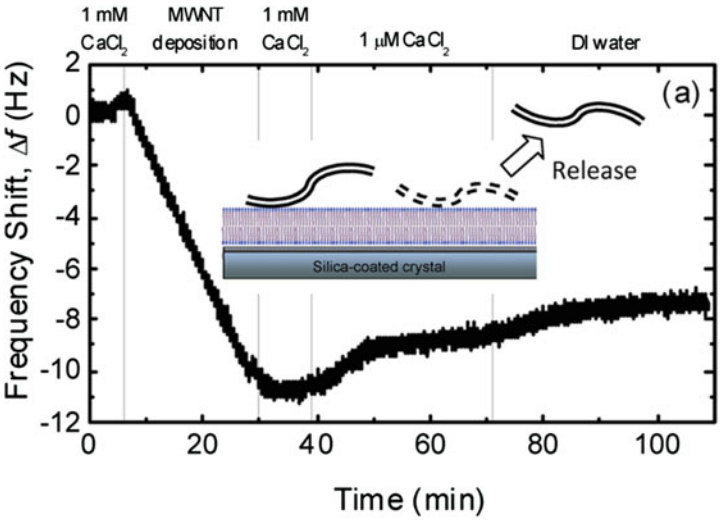

Fig. 10.7 Frequency (blue) and dissipation (red) shifts during the formation of a supported vesicular layer (SVL) and the deposition of MWCNTs on the SVL at 1 mM $CaCl_2$ and pH 7.3. The inset illustrates the deposition of MWCNTs on a SVL (not drawn to scale) [39]

The reversibility of deposition was also observed when rinsing the membranes with low ionic strength solutions at slightly basic conditions (pH 7.3). In addition, a study of the interactions between graphene oxide (GO) sheets of different sizes and small and large liposomes prepared from 1-palmitoyl-2-oleyl-*sn*-glycero-3-phosphocholine (POPC) and 1-palmitoyl-2-oleyl-*sn*-glycero-3-ethyl- phosphocholine (POEPC) [41]. On the surface of a QCR, a layered structure was constructed in the following order: liposomes, GO, small and large unilamellar vesicles (SUVs and LUVs), and GO. QCM-D was used to monitor both frequency shifts (ΔF) due to material adsorption and shifts in dissipation (energy, ΔD). The ΔD-response serves as an indication of viscoelastic coating properties on the QCR. As a result, the lateral dimensions of liposomes and GO were obtained. ΔF and ΔD together allowed the construction of a schematic representation of the process (Fig. 10.8).

Implant integration in the body (soft tissue and osseointegration) can possibly be improved by coating the implant surface with different nanoparticles. In a recent study, the adhesion properties of human gingival fibroblasts were tested on the surface of hydroxyapatite and titanium nanostructures using QCM-D, as materials of interest for dental implant applications [42]. Titanium and hydroxyapatite nanostructures (nanoHA) coated titanium crystals were applied on a surface of a quartz resonator. The authors used a cell suspension, which was introduced into the QCM-D measurement chamber with a constant flow rate. Simultaneously, the adhesion and cell coverage kinetics of the cells were observed in situ while registering shifts in frequencies and dissipation of the resonator. Interestingly, no difference was found in cell spreading rate on titanium and nanoHA, and further studies are advised in order to conclude whether nanoHA and titanium improve soft tissue integration or not.

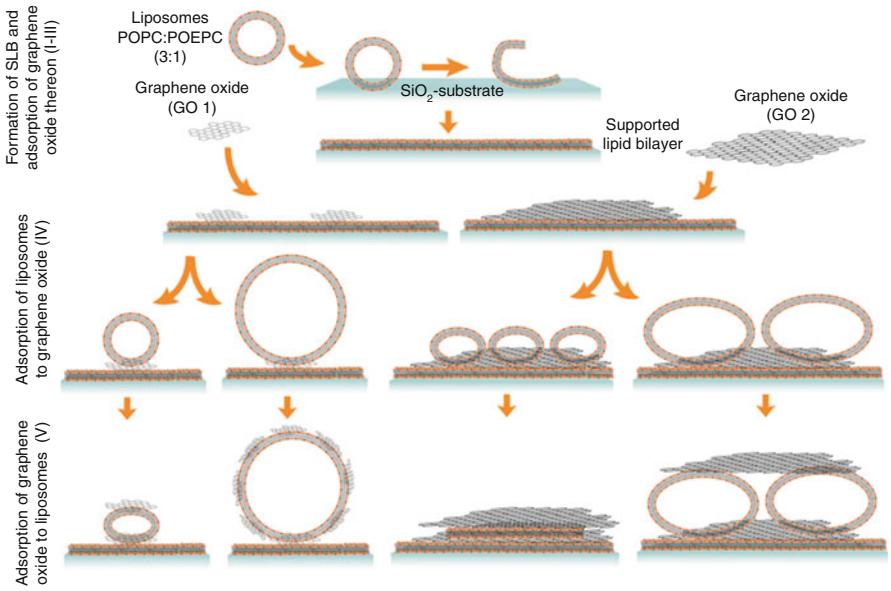

Fig. 10.8 Schematic representation of the GO/lipid membrane (SLB and liposome) interactions, deduced from the data presented in Fig 2.2. The following series of events is illustrated (from the top): (I) addition of liposomes, (II) spontaneous formation of a supported lipid membrane, (III) addition of GO 1 (90 nm) and GO 2 (500–5000 nm, GO sheet sizes in the lower end of this range are dominating), (IV) addition of SUVs and LUVs to adsorbed GO 1 and GO 2, and (V) addition of GO 1 and GO 2 to the adsorbed liposomes. Not drawn to scale [41]

A mechanistic understanding of nanoparticle-induced bacterial toxicity has implications for understanding ecosystem health in general. *Shewanella oneidensis* (metal-reducing bacteria) were chosen as a model system for understanding nanotoxicity (due to their importance for geochemical nutrient cycling) in a study of the influence of TiO_2 nanoparticles on biofilm formation and riboflavin secretion using QCM [43]. In an incubator of 30 °C, a QCR was immersed into a Lysogeny broth (LB), followed by a suspension of bacteria and clean LB. TiO_2 nanoparticles were introduced with the LB or bacteria. The authors used nanoparticles of three kinds: self-synthetized and commercial P25 and T-Eco nanoparticles. The different nanoparticles were used to differentiate between the effects of mass changes due to deposition and biofilm growth. The authors show a decrease in biofilm formation rate in the presence of TiO_2 nanoparticles. Interestingly, riboflavin secretion was increased significantly as a function of present nanoparticles (Fig. 10.9). Both phenomena were attributed to cellular stress response.

5.3 QCM for Study of Environmental Aspects of Nanomaterials

Incorporation of structural and functional nanomaterials in industrial production is a competitive advancement with a substantial profit for any company. This fact let to

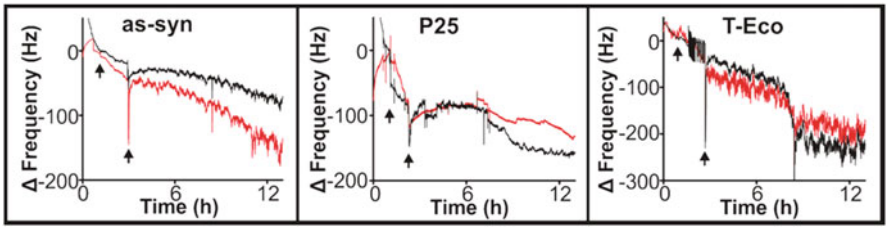

Fig. 10.9 QCM analysis of bacteria exposed to 25 μg/mL as-syn, P25, or T-Eco nanoparticles during bacterial attachment, indicated by the window of time between the arrows. Red = TiO2 exposure and black = control (no nanoparticles) introduced in LB broth [43]

worldwide distribution of products containing nanostructures. Nevertheless, in many cases the producing company does not take under consideration the ecological aspects regarding the effects of nanomaterial on the environment. Therefore, in the last two decades, research in environmental science has become vaster. Not only for the study of toxicity of nanomaterials of living organisms but also for the study of distribution, transport, adsorption, and accumulation as well as biodegradation in the environment. Among the most commonly used nanomaterials in industry, two main groups stand out due to their chemical nature: metal nanoparticles and their binary compounds, including quantum dots, and another large group is the different nanoforms of carbon, such as fullerene, carbon nanotubes, graphene and its derivatives.

5.3.1 Nanoparticles of Metals and Metal Compounds

In a recent paper by Afrooz et al. [44], the influence of the shape of nanoparticles on the nature of aggregation and deposition was studied using QCM with an emphasis on aquatic ecosystems. The authors used gold nanospheres (AuNSs) and nanorods (AuNRs) coated with polyacrylic acid (PAA) as model nanostructures. The deposition rate of the nanoparticles onto a silica-coated quartz crystal was measured using in NaCl solution of concentrations between 10 and 1000 mM (Fig. 10.10). The authors show an increase in deposition rate with increased electrolyte concentration. The observed differences in deposition rates are attributed in the article to unique packing of the nanoparticles as well as to various chemical interfacial properties. In a similar study, Quevedo et al. [45] utilized QCM to study the deposition of commercial quantum dots (QDs) on the surface of Al_2O_3, which is present on aquifer or filter grain, and in the presence of dissolved organic molecules (DOM). CdTe/CdS QDs were stabilized with polyacrylic-acid (PAA) and CdSe/ZnS QDs were coated with poly-ethylene-glycol (PEG) in the form of water suspensions. Carboxyl-functionalized (cPL) and sulfate-functionalized (sPL) polystyrene latex nanospheres were used as control samples.

The model DOMs used were Suwannee River humic acid (SRHA) and JBR215 (10% mixture of the two rhamnolipids RLL ($C_{26}H_{48}O_9$) and RRLL ($C_{32}H_{58}O_{13}$)) as coating material as well as for QD suspension preparation. The alumina-coated QCR was put first in electrolyte-rich solutions (KCl) and afterward in the QD suspensions. Measurements with QCM showed the deposition rate decreases with the increase in

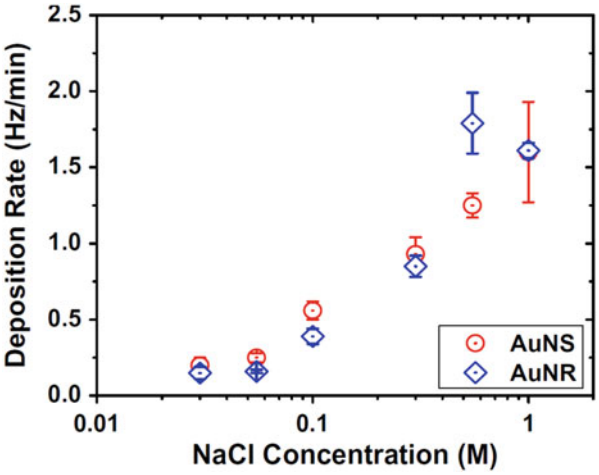

Fig. 10.10 Deposition rates of AuNPs onto a silica-coated quartz crystal in the presence of NaCl. Deposition rates are expressed as the rates of normalized frequency shift at the third overtone. Each data point represents the mean of triplicate measurements conducted at the same experimental conditions, and the error bars represent standard deviations. Measurements were carried out at 20 °C [44]

occupied surface area. The maximum deposition rate was observed in the first minute. The authors note that the deposition rate is affected by modifications of the surface of the QDs and the composition of their solution (Fig. 10.11). The surface-modified QDs had a lower deposition rate on the Al_2O_3 than the model polymer nanoparticles. Coating Al_2O_3 with DOM adds an additional electrostatic barrier (due to charge reversal), which decreases the retention of all QDs. Hence, the deposition of charged QDs is not favorable on adsorbing materials containing DOM in natural systems and filters.

5.3.2 Carbon Nanoforms

The fate and distribution of fullerene C60 in natural systems peaks research interest due to their potential risk to the natural ecosystem and human health. In a study by Tong et al. [46], the influence of biofilms on the transport of fullerene (C60) nanoparticles was studied both using QCM and in soil-like porous media. The biofilms were encapsulated in extracellular polymeric substances (EPS), which was extracted from *E. coli*. QCR with precoated silica surfaces or with EPS was put in solutions of C60 and NaCl, $CaCl_2$ with different environmentally relevant concentrations. Measurements were carried out in a flow system. The authors report that an increased deposition of C60 is observed probably due to the increase in the roughness of SiO_2 in the presence of a biofilm (Fig. 10.12). Hence, biofilms can assist in the inhibition distribution and transport of C60-like materials in the natural ecosystems.

In a parallel study, the thermal dependence of fullerene C60 on the surface of SiO_2 was investigated in the presence and absence of Harpeth humic acids and Harpeth fulvic acids (HHA and HFA), representing the dominant organic components in soils and sediments (soil organic matter (SOM) and attached phase soil organic matter (AP-SOM)) [46].

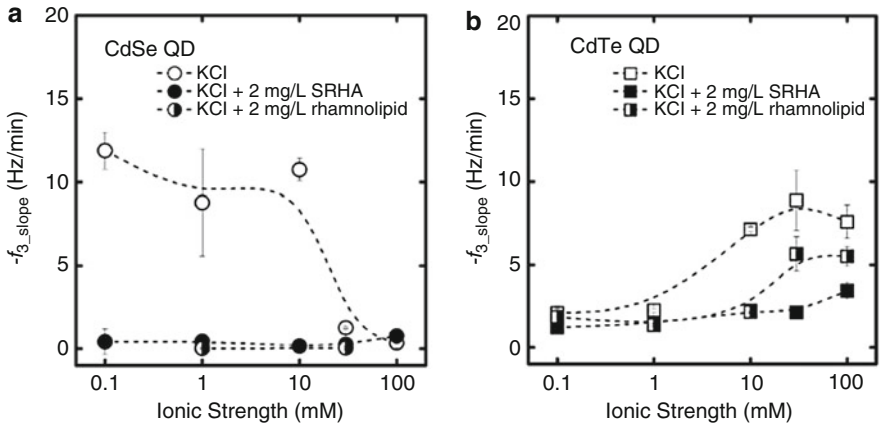

Fig. 10.11 Deposition rates of the QDs over a range of ionic strength (pH 5) onto DOM precoated Al_2O_3 (i.e., SRHA, rhamnolipid) and bare Al_2O_3. The different solution chemistries are represented with full symbols for KCl supplemented with 2 mg/L SRHA, half full symbols for KCl with 2 mg/L rhamnolipid, and open symbols for simple KCl. Data represent the mean ± standard deviation [45]

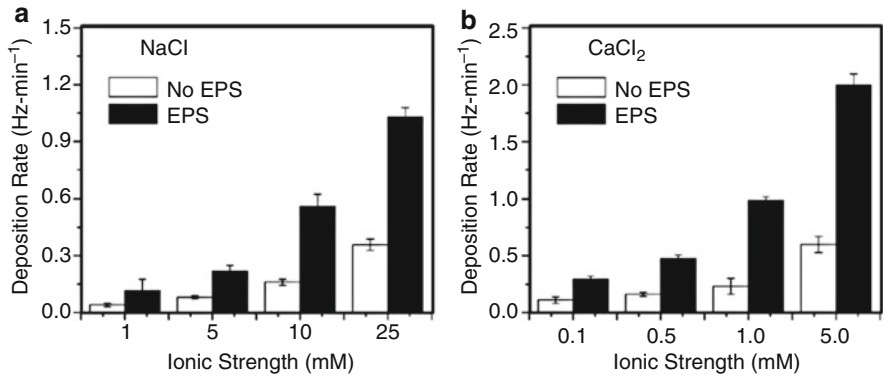

Fig. 10.12 Deposition rate (k_f) of fullerene C60 on bare (white bar) and EPS-coated silica surface (black bar) in NaCl (top) and $CaCl_2$ (bottom) solutions at pH 6.8 (adjusted with 0.1 M NaOH) as a function of ionic strength in QCM-D. Duplicate measurements were conducted over entire ionic strength range, with error bars representing standard deviations [46]

The working electrode of a QCM quartz resonator was used as a model surface. The electrodes were coated with a layer of SiO_2. The study shows a rise in interactions of C60 with immobilized HHA and HFA at higher temperatures, while the interactions with the clean surface of SiO_2 were mostly independent of changes in temperature (Fig. 10.13). The authors attribute this behavior to water-assisted disruption of polar SOM contacts and hydration-induced swelling of AP-SOM matrix. Structures such as C60 are predicted to accumulate in soil and sediments during warm seasons. Further research in this field will be able to predict more

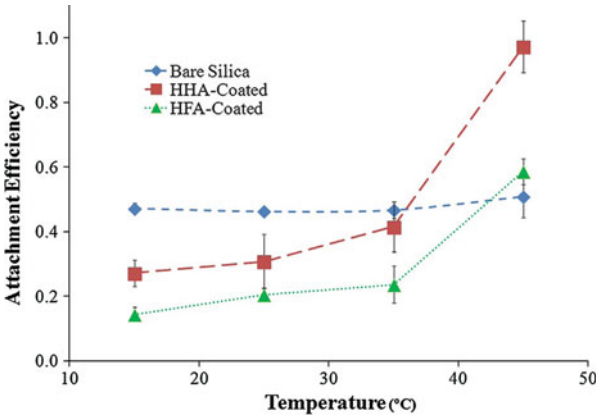

Fig. 10.13 C60 attachment efficiencies onto bare, HHA-coated, and HFA-coated silica sensors as a function of temperature. Error bars represent the standard deviation [47]

accurately the possible anthropological effects on similar ecosystems and to develop the means to counter negative interactions of this sort. A following work by the same authors demonstrated the use of QCM for the study of deposition kinetics of colloidal fullerene C60 particles (nC60) as a result of interaction with HHA in the presence of various electrolyte concentrations [48]. A SiO_2-coated QCR was put into electrolyte solutions with different concentrations and HHA. After reaching equilibrium, the nC60 solution was introduced into the setup. The slope of the linear section in Fig. 10.14f corresponds to the deposition rate (Hz/min) of nC60 onto the surface of the resonator (Fig. 10.15), under experimental conditions, which correlates to transport rate of nC60 in natural systems. The authors observed no dependence of deposition rate for PLL-coated silica with increasing ionic strength. Rise in deposition rate was reported at higher ionic strengths for HHA-coated silica and bare silica. Charge reverse was probably observed for NaCl solutions higher than 50 mM in all cases. It should be noted that the HHA system had higher deposition rates than PLL and bare silica at all NaCl solutions.

The silica-based system was used to model the release conditions of multiwalled carbon nanotubes (MWCNT) from the surface of soil-like systems using QCM-D [49]. Deposition of MWCNTs on a SiO_2-coated resonator was carried out in the presence of 1.5 mM $CaCl_2$ or 600 nm NaCl, both at pH 7.1. The coated resonator with MWCNT was placed in solutions with different concentrations of NaCl and $CaCl_2$ and pH conditions, corresponding to actual concentrations found in aquatic systems. During the experiments, the change in frequency (ΔF) and dissipation response (ΔD) of the crystal sensors were monitored at different harmonics (n = 1, 3, 5, 7, 9, 11, 13). The authors used the Voight-based model, since the values of ΔF and ΔD were significantly different from one another at changing harmonics, and the ΔD/ΔF ratio at all harmonics was high (ca. 0.6×10^{-6}/Hz). The results show that MWCNT will be released from the surface at decreasing concentrations of NaCl and $CaCl_2$ solutions and at increasing pH (pH = 10). These results are believed to assist in further research of the bioavailability of MWCNTs in the environment as well as for construction of possible water treatment systems.

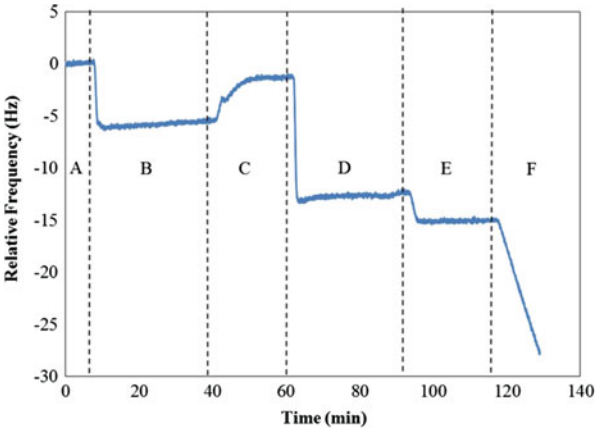

Fig. 10.14 Representative nC60 deposition experiment. The initial baseline was collected in HEPES solution (**a**) before PLL was attached to the silica surface and rinsed in HEPES solution (**b**). The PLL layer was then rinsed in 1 mM NaCl (**c**) before HHA was attached to the PLL surface and rinsed in 1 mM NaCl (**d**). Finally, the HHA layer was rinsed in the electrolyte concentration at which the deposition experiment would take place (100 mM NaCl in this case) (**e**). Once a stable baseline was observed the nC60 was mixed with a premeasured volume of electrolyte to form the desired concentration (100 mM NaCl in this case) and immediately introduced onto the sensor surface (**f**) [48]

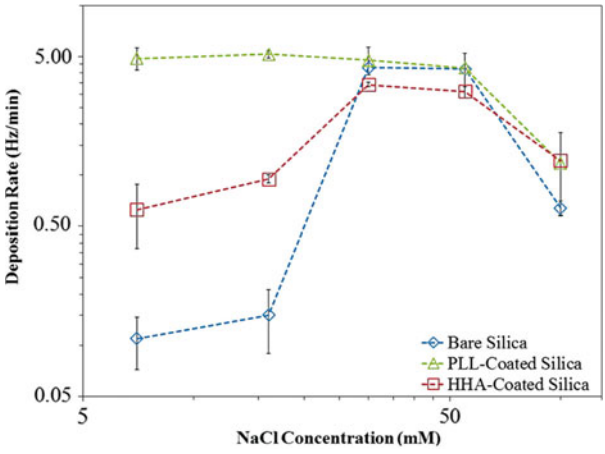

Fig. 10.15 nC60 deposition rates as a function of NaCl concentrations onto three different surfaces [48]

Parallel experiments were carried out for graphene oxide (GO) on the surface of SiO_2 using QCM-D [50]. Changing concentrations of GO were used in the presence of different solutions of NaCl, $CaCl_2$, and $MgCl_2$. A SiO_2-coated QCR was placed in the studied solutions. Measurements were carried out after a lag time of 40 min in order to achieve equilibrium. The deposition attachment efficiency

(α_D) was measured in favorable conditions, achieved by coating the SiO_2 surface with cationic poly-L-lysine hydrobromide. The obtained results for GO deposition in the presence of NaCl and $MgCl_2$ are very similar. These observations fitted the Derjaguin−Landau−Verwey−Overbeek (DLVO) theory, correlating the decreasing deposition rate of GO in high ionic strength conditions. The critical deposition concentration (CDC) for GO exceeds the CDC of carbon nanotubes and fullerenes, showed in prior studies [51, 52]. In the presence of Ca^{2+} ions, GO deposition was negligible, due to the reversible role of Ca^{2+} in the formation of bridges with GO. The release of GO was significantly influenced by the presence of different ions in the solution with an overall trend of NaCl > $MgCl_2$ > $CaCl_2$. In a further research effort, the authors studied the interactions of GO and Al_2O_3 surface in the presence natural organic matter (NOM) [53]. The chosen NOMs were Suwannee River humic and fulvic acids (SRHA and SRFA) and alginate. The experimental method is described above for SiO_2 [50]. The attachment trend of GO to the studied surfaces in a decreasing order was reported as follows: SRFA, SRHA, and aluminum oxide surfaces. The increasing interaction of GO with NOM was attributed to hydroxyl, epoxy, and carboxyl functional groups of GO. In solutions of monovalent and bivalent ions, Na^+ and Ca^{2+}, with concentrations of 10 mM and 1 mM (typical concentrations in aquatic environments), respectively, the rates of deposition of GO on NOM were significantly higher than on Al_2O_3. The authors note that the deposition of GO on NOM and on alumina are highly reversible and, therefore, do not immobilize the distribution of GO in natural aquatic environment.

Following the research of the fate and transport of GO in natural aquatic environmental systems, where the stability of GO against aggregation and deposition was demonstrated, the same authors investigated the possibility of GO transformations and alteration of its properties due to the effect of sunlight [54], since sunlight photolysis is one of the primary routes by which carbonaceous nanomaterials react in natural waters [55, 56]. Moreover, natural organic matter (NOM) can facilitate radical formation under sunlight which can further react with graphene nanomaterials.

Suwannee River humic acid (SRHA) was used as a model NOM. The study was carried out with QCM-D on quartz resonators coated with either clean SiO_2 or with additionally applied SRHA. GO was irradiated with sunlight, prior to any measurements, at different durations (1–187 h) in an/aerobic conditions. The results suggest that on the one hand, photo-induced transformations of GO had slower deposition rate in the presence of NOM and on the other hand, these interactions with NOM were irreversible and no solvation of photo-induced transformations of GO back into water was observed (Fig. 10.16a). It should be noted that photo-induced transformations of GO are faster in anaerobic conditions and therefore have lower mobility in aquatic environments (Fig. 10.16b). The results of this study can be very useful in designing water treatment systems based on irradiation with sunlight or UV.

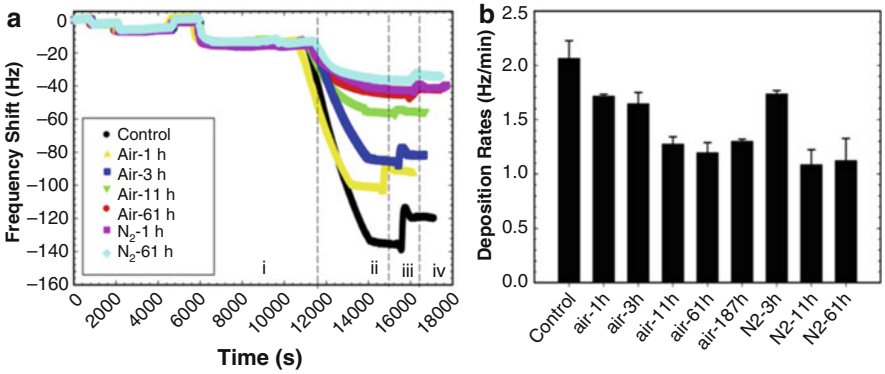

Fig. 10.16 (**a**) Deposition of phototransformed GO on SRHA-coated surface using QCM-D in 30mM NaCl. (A) Frequency shift at the third overtone (Df3) and (**b**) initial deposition rates. Step i: formation of SRHA layer on silica surface; Step ii: injection of phototransformed GO; Step iii: injection of background electrolyte; and Step iv: injection of DI water. GO concentration was maintained 1 mg/L TOC at pH 5.5 ± 0.3 [54]

5.4 Using QCM for Studying of Nanoparticles Deposition and Growth Process

QCM as an in situ tool continues to be one of the most useful and common methods for mass-metric control. QCM is easy to use and can be utilized to study many different processes. The high sensitivity to changes in mass makes this method irreplaceable for investigation of deposition of nanomaterial, their hetero-phasic growth, catalysis on nanoparticles, and finally for processes of modification of nanostructures. The classical application of QCM as a mass-metric device for the study of propagation of different processes continues in recent research.

5.4.1 Application of QCM for Studying Nanostructure Deposition and Interactions with Other Materials

It is well known that the many nanoparticle properties, such as catalytic [57], structural [58], electromagnetic [59, 60], and more, are size dependent. Moreover, the size was shown to effect surface charge properties and due to high surface area and curvature effect of nanoparticles [61–63].

In a recent study, the surface chemistry interactions with a flat SiO_2 surface (curvature ~0) were investigated for three different-sized SiO_2 nanoparticles using QCM-D [64]. Various suspensions of NaCl were used to induce different ionic strengths. The authors monitored the mass changes due to nanoparticle adsorption onto the surface of the quartz resonator, which was coated with a 50 nm layer of SiO_2. The results show that the adsorption of nanoparticles is reduced with the decrease in ionic strength. Almost no adsorption was detected for a solution of 1 mM.

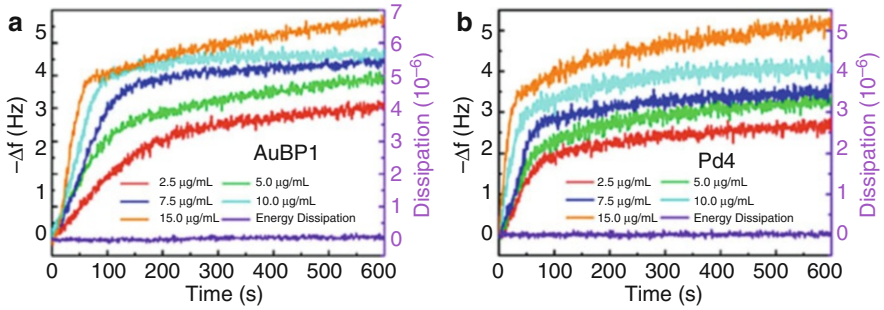

Fig. 10.17 QCM analysis of peptides (**a**) AuBP1 (strongest binder) and (**b**) Pd4 (weakest binder) to obtain ka and kd values [65]

Noncovalent interactions between peptides and gold nanoparticles were investigated using a QCM device, as part of a bionanocombinatorics study, aiming to control the arrangement of the nanocomponents using biomolecules [65].

A standard QCR with a gold electrode was immersed in water solutions of peptides. The authors suggest that equilibrium in the system gold-peptide is achieved after 600 s. The absence of change in dissipation, during these experiments, indicates the presence of a monolayer of peptides on gold, rather than a multilayer (Fig. 10.17). The authors therefore suggest that in such a system, the only favorable interactions are peptide-gold. The change in frequency can be used to characterize the binding interaction between the peptides and the gold nanoparticles and calculate the Gibbs free energy for this interaction.

Unfortunately, the authors do not show the characteristics of the gold electrode, hence it is unclear whether the electrode is composed of nanocrystal gold. The absence of specifications of the gold (particle size, shape, functional groups, etc.) impedes the transfer of the suggested model to other metal particle-peptide systems, even for other gold nanoparticles with other characteristics.

In a recent research effort, QCM was used to monitor mass changes and kinetics of electroless copper deposition (ECD), catalyzed with silver (Ag) nanocubes enclosed by (1 0 0) planes and nanoparticles [66]. The catalyst was applied on the surface of the gold electrode of a QCR. The received electrodes were used for electrochemical deposition of copper. The changes in frequency with time showed that the deposition of copper begins after an incubation period of up to 65 s in the presence of silver (Fig. 10.18). Ag nanoparticles induce a faster deposition than the compared Ag nanocubes.

Silver nanoparticles were used as well to study the silver leaching kinetics from a polysulfone membrane embedded with silver nanoparticles using QCM-D [67]. The nanocomposite solution was applied onto a gold QCR electrode using spin-coating and dried in a desiccator. The authors show the decrease in silver leaching rate with time (Fig. 10.19).

In an attempt to increase the redox activity of carbon electrodes, electrochemical quartz microbalance (EQCM) was used to study the modification process of

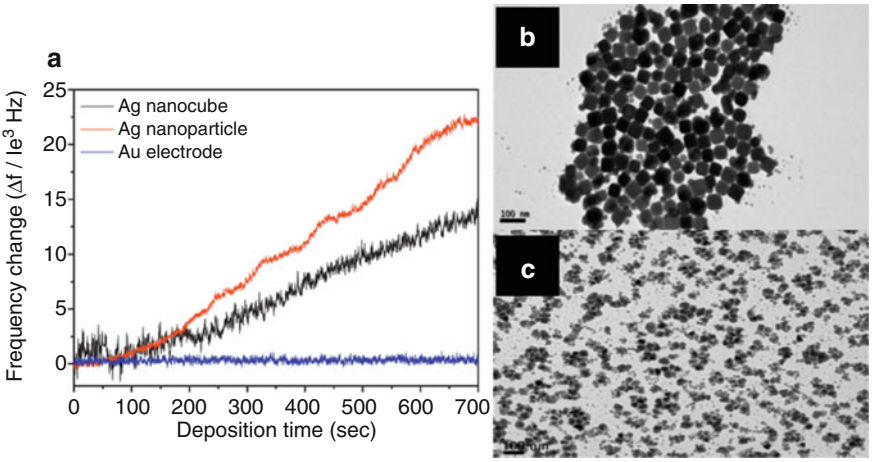

Fig. 10.18 (**a**) Comparison of QCM curves of ECD kinetics in terms of frequency change catalyzed by Ag nanocubes, nanoparticles, and Au electrode, TEM images of Ag catalysts: (**b**) nanocubes and (**c**) nanoparticles [66]

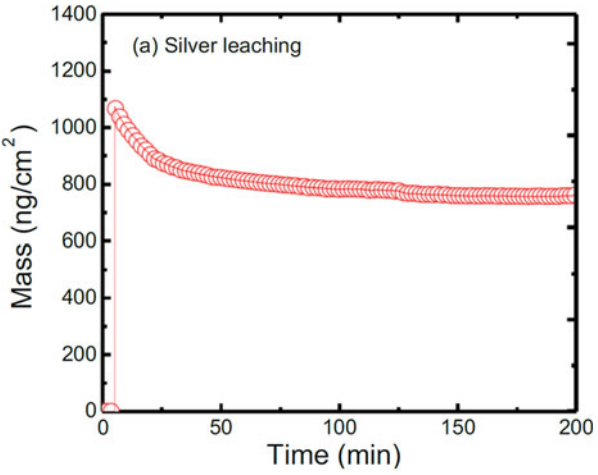

Fig. 10.19 QCM-D measurements of silver leaching from the nanocomposite membrane [67]

multiwalled carbon nanotubes (MWCNT) with quinoline quinones (QLO) for glassy carbon electrodes [68]. The authors suggest a method to obtain highly redox active and stable QLO functionalized MWCNT modified glassy carbon electrode (GCE/MWCNT@QLO) by oxidizing 8-hydroxyquinoline (QL) on GCE/MWCNT. The amount of immobilized QLO on the surface of the MWCNT was determined in situ using EQCM. Changes in mass (Δm) were detected during the process of electrical oxidation in a QL solution when MWCNT modified EQCM-Au electrode (EQCM-Au/MWCNT) was used. The registered amount of passed charge (Q) and Δm allowed the calculation of the molar mass of different intermediate species

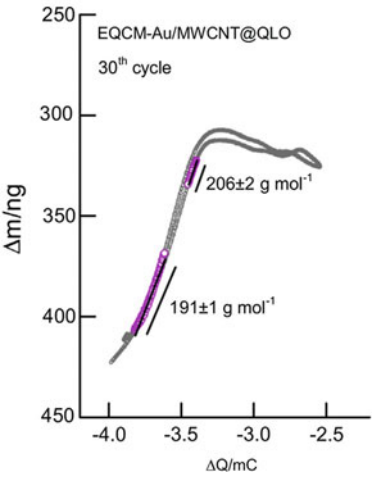

Fig. 10.20 Plot of Δm vs. Q of EQCM-Au/MWCNT@QLO [68]

involved in the electrochemical reactions from the slopes in Fig. 10.20. This method can be useful to study reaction mechanism.

QCM-D was applied for the study of formation of magnetic nanoparticle-vesicle aggregates (MNPVs) as part of the research of transport of proteins and enzymes through phospholipid bilayers via induced magnetic fields [69].

QCM-D confirms the formation of MNPVs when mixing avidin-coated biotinylated APTES ((3-aminopropyl)triethoxysilane)–MNPs and dipalmitoyl phosphatidylcholine vesicles. The authors show that a magnetic impulse can cause the release of proteins and enzymes from within the MNPV into the suspension.

5.4.2 Using QCM for Studying Shape Transformations of Nanostructured Systems

A recent study by Kasputis et al. [70] investigates the formation of new functional nanomaterial through combining organic polymer brushes with gold or silicon slanted columnar thin films (SCTFs) to give unique material properties with potential for applications in chemical and biological sensing, biomaterials, tissue engineering, and nanoelectronics. In situ combinatorial generalized ellipsometry and quartz crystal microbalance with dissipation (GE/QCM-D) were used to demonstrate feasibility of the suggested nanomaterials. The nanomaterial received on the surface of the QCR was shown to swell and deswell under various pH values (Fig. 10.21). These allow to control the geometry of the nanomaterial.

Similar shape transformations as well as changes in viscoelastic properties were induced for Cowpea chlorotic mottle virus (CCMV), used as an active nanomaterial [71]. For this purpose, deposition of CCMVs was carried out on the surface of a gold electrode of a QCR. The change of CCMVs from closed to swollen forms was induced by changing the solution buffer composition. The change in dissipation was the most sensitive parameter to indicate closed and swollen forms due to changes in the viscoelastic properties (Fig. 10.22).

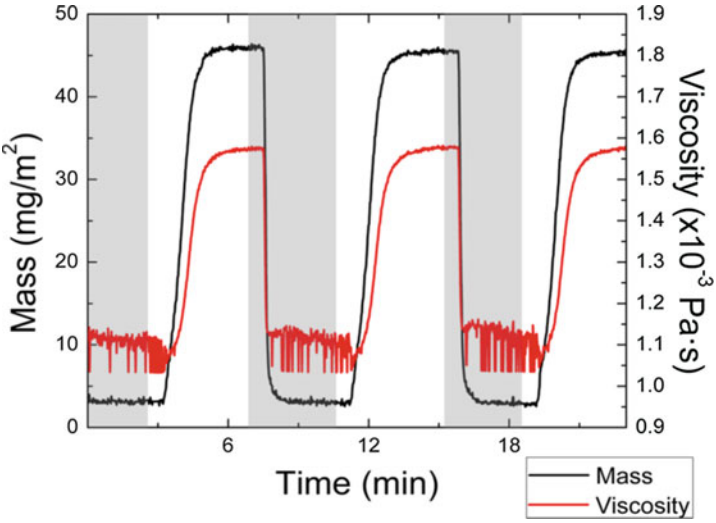

Fig. 10.21 Modeled QCM-D frequency and dissipation data demonstrate the functional swelling characteristics of polymer brushes within SCTFs by changing the pH of the liquid ambient—buffered acetate solution. Changes in pH are indicated by the different shaded background regions on the plots, and changes in pH caused changes in the overall mass (black line) and viscosity (red line) of the thin film, indicative of polymer brush swelling at pH = 7.3 (white background regions) and deswelling at pH = 3.7 (gray-shaded background region) [70]

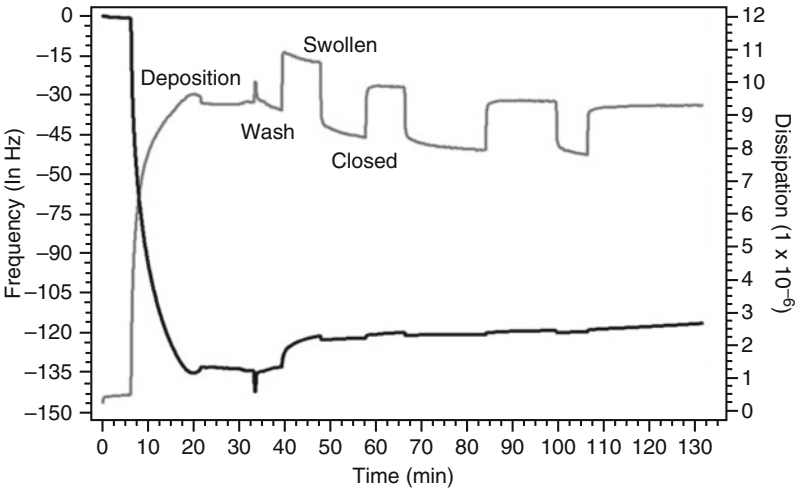

Fig. 10.22 QCM-D analysis of CCMV. Trace shows the frequency (in black, on Y1 axis) and dissipation values (in gray, on Y2 axis) of the third overtone beginning with surface loading of a gold-coated crystal through multiple cycles between swollen and closed conformations. The ratio of frequency to dissipation provides information about the solution phase modulus of the material [71]

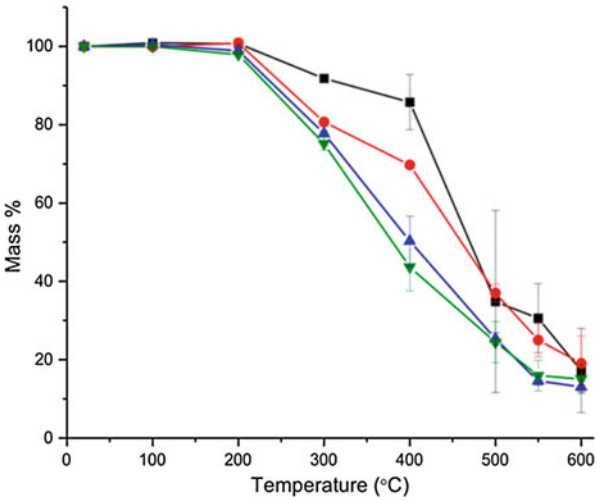

Fig. 10.23 μ-TGA mass % versus temperature thermograms of four layer-by-layer coated Au nanoparticle samples. 30 nm AuNPs + PLL (black), 30 nm AuNPs + PLL + DNA (red), 30 nm AuNPs + PLL + DNA + PLL (blue), and 30 nm AuNPs + PLL + DNA + PLL + DNA (green) [72]

5.4.3 Using QCM for Microscale Thermogravimetric Analysis (μ-TGA)

Mansfield et al. [72] developed the methodology of microscale thermogravimetric analysis (μ-TGA) based on the use of elevated-temperature quartz crystal microbalance. Practically, the authors demonstrate the use of μ-TGA for measurements of nanoparticle purity and presence of any surface coatings of nanomaterials. Samples of nanomaterials in dispersions were applied onto the QCR by drop-cast or by spray-coating. The QCR was then heated for 10 min at 75 °C to remove the water solvent. Layer-by-layer gold nanoparticles (AuNP) were used with a varying number of layers coated by Poly(L-lysine) (PLL) and DNA as well as SiO_2 nanoparticles, coated with polyethylene gycol (SiO_2-PEG) and single-wall carbon nanotubes (SWCNTs). A layer of glass was applied on the QCR prior to carried out experiments with AuNP. μ-TGA was done ex situ: QCR was heated at 10 °C/min to some goal temperature. The QCR was then cooled down and the change in mass registered using QCM. The QCR would then be heated to the next goal temperature up to the desired temperature. A few such cycles were carried out to construct thermogravimetric analysis. Similarly, a QCR with no coatings was heated to the same goal temperatures in order to account for the compensation of the influence of the heating cycles on the quartz crystal. Such compensation is necessary for temperatures above 425°C, where the values of thermal stresses for quartz are not negligible [73].

In addition, mass was recalculated after heating above 100 °C to compensate for the mass of desorbed water. The authors show that their method is sensitive enough to detect mass changes for materials with a difference in one layer for layer-by-layer coated AuNP (Fig. 10.23).

This is by definition an ex situ method; however, the authors are positive that μ-TGA can potentially be used to study nanomaterials in general. This system can involve into an in situ method in condition that the temperature of a QCR could be

changes during the experiment, without the need to interrupt the process. Such a system should also be equipped with a system of signal analysis to compensate for the thermal changes in quartz.

6 Conclusions and Future Perspective

Applying layers of receptor materials on a surface of a QCR is a well-known method that serves as a sensor for detecting various compounds in the gas and liquid phases. In the last decade, these techniques were implemented for nanomaterials, which are used as analytes as well as matrices for applying receptor materials.

Nanomaterials can rarely be used as unique receptor materials for any analyte; hence, nanomaterials can be utilized to assess sensor properties. Important developments in this field are the use of combined methods of research to study complex properties of sensor materials, for instance, QCM and SPM. In this case, QCM can serve as a reliable method of data quantification for integrative properties of a sensor material, which is a complementary data for other specific properties studied by another method.

Researchers who apply layers of receptor materials on QCM to detect nanostructures as analytes experience difficulties similar to the ones described above. The received contradicting results in such cases cannot be used for practical applications. Possible future development in this field can improve the correlations for nanoparticle-receptor interactions and in integration with other methods.

In recent research of nanotoxicology, QCM proved to be more sensitive than other more standard methods. For instance, QCM was reported to be more sensitive to the influence of QDs on the aggregation of human blood platelets than for the commonly used method in such cases, light transmission aggregometry (LTA). The use of QCM to study the influence of nanoparticles on the general and specific bacterial function helped accurately evaluate bacterial secretion functions as well as the decrease in the ability to form biofilms in the presence of TiO_2 nanoparticles. During the study of GO interactions with liposomes, the combined analysis of the change in frequency and dissipation allowed building a possible schematic representation of GO-lipid formation process. This in turn can prove useful for study of environmental aspects of nanomaterials.

Moreover, QCM is a useful tool for the study of nanoparticle interactions with model soil-like materials (alumina, silica) and model DOMs (Suwannee River humic, fulvic acids, Harpeth humic acids, Harpeth fulvic acids), which are essential when assessing processes of distribution, transport, and accumulation of nanomaterials in natural environments. The works presented in this chapter are dedicated primarily to the study of environmental aspects of metal-based nanoparticles: gold nanospheres, gold nanorods, CdTe/CdS and CdSe/ZnS quantum dots, as well as carbon nanoforms: fullerene, carbon nanotubes, and GO. The shift in frequency of QCM can be used to evaluate the deposition rate of nanoparticles in different solution compositions. Based on similar measurements, favorable deposition conditions of nanoparticles can be determined. Such information can prove useful for

predicting the effects of nanostructures on the surrounding environment and for possible water treatment systems.

Many recent works utilized QCM as an in situ tool for mass-metric control of various processes involving nanostructures.

QCM was used to gather essential experimental data to develop general models of noncovalent interactions of nanoparticles with different materials and complexes. Since these papers stand-alone in their line of research and tend to be more exploratory, the presented results in these studies are of a theoretical nature.

The use of the combination of QCM with an electrochemical chamber to study the modification processes of nanotubes allowed determining the composition of intermediate reaction products and to suggest a possible mechanism for the process. This method was validated with techniques such as XPS, FTIR, and GC-MS.

A developed thermogravimetric analysis based on in situ heating of a QCR is of great interest. Unfortunately, this technique was developed for ex situ measurements. If further engineering can solve a line of constructive problems, we could have real-time thermogravimetric resolution.

In the meantime and in the near future, QCM will be utilized for the studies of dependence of material properties as a function of the nanostructure shape in various processes. Moreover, the application of EQCM for the study of electrochemical processes involving nanomaterials can develop in utilizing two QCRs with different electrode materials for simultaneous monitoring of changes in mass on both the electrodes of the electrochemical chamber.

Examples of research progress in the direction of integration of a few analytical methods together can be QCM and IR, as well as the combination of EQCMs. These kinds of study can be proven very useful to investigate nanomaterial sensors and for detection processes of gas analytes.

In conclusion, definite and easily analyzed measurements with QCM can usually be received for the cases of thin rigid films in a gas-filled detection chamber of in vacuum. These kinds of measurements are commonly used for process control in electronics and for study of gas sensors.

The interpretation of QCM measurements for deposition of complex bulky nanostructures, especially deposition from the liquid phase, involves a thorough experiment planning and the use of additional verification methods. The development of the QCM methodology is still in progress. Today QCM can seldom be used as a stand-alone research method; however, as a complementary method, QCM can provide useful and unique information for unfolding processes involving nanomaterials.

Nomenclature

C_m	Constant of the resonator parameters
D	Dissipation factor [−]
F	Resonance frequency [1/T]
F_0	Natural vibration frequency of the QCR [1/T]
h_f	Thickness of film [L]
h_q	Thickness of quartz [L]

n	Number of harmonics [−]
s	Area of oscillation in the QCR [L^2]
ΔD	Change in dissipation [−]
Δf	Change in frequency [1/T]
Δm	Change in mass [M]
η_f	Viscosity of the film [$M{\cdot}L^{-1}{\cdot}T^{-1}$]
η_L	Viscosity of liquid [$M{\cdot}L^{-1}{\cdot}T^{-1}$]
μ_f	Elastic modulus [$M{\cdot}L^{-1}{\cdot}T^{-2}$]
ρ_f	Density of coated film [$M{\cdot}L^{-3}$]
ρ_L	Density of liquid [$M{\cdot}L^{-3}$]
ρ_q	Density of quartz [$M{\cdot}L^{-3}$]
τ	Decay time constant [T]

References

1. Curie J, Curie P (1880) Développement Par Pression de L'électricite Polaire Dans Les Cristaux Hémièdres À Faces Inclinées. Comptes Rendus l'Academie Des Sci 91:294–295
2. Lippman G (1881) Sur Le Principe de La Conservation de L'électricité, Ou Second Principe de La Théorie Des Phénomènes Électriques. Comptes Rendus l'Academie Des Sci. 92:1049–1051
3. Curie J, Curie P (1882) Déformations Électriques Du Quartz. Comptes Rendus l'Académie Des Sci 95:914–917
4. Sauerbrey G (1959) Verwendung von Schvangquarzen Zur Wag-Ung Dunner Schichten Und Zur Mikrowagung. Zeitschrift Fur Phys 155(2):206–222
5. Czanderna AW, Lu C (1984) Applications of Piezoelectric quartz crystal microbalances. In: Lu C, Czanderna AW (eds) Methods phenom, vol 7. Elsevier, Amsterdam, The Netherlands
6. Kim H (2003) Atomic layer deposition of metal and nitride thin films: current research efforts and applications for semiconductor device processing. J Vac Sci Technol B Microelectron Nanometer Struct 21(6):2231
7. Petosa AR, Jaisi DP, Quevedo IR, Elimelech M, Tufenkji N (2010) Aggregation and deposition of engineered nanomaterials in aquatic environments: role of physicochemical interactions. Environ Sci Technol 44(17):6532–6549
8. Wang X, Ding B, Sun G, Wang M, Yu J (2013) Electro-spinning/netting: a strategy for the fabrication of three-dimensional polymer Nano-fiber/nets. Prog Mater Sci 58(8):1173–1243
9. Ding B, Wang M, Wang X, Yu J, Sun G (2010) Electrospun nanomaterials for ultrasensitive sensors. Mater Today 13(11):16–27
10. Radomska A, Leszczyszyn J, Radomski M (2016) The Nanopharmacology and Nano-toxicology of nanomaterials: new opportunities and challenges. Adv Clin Exp Med 25 (1):151–162
11. Li L, Mu Q, Yan B (2010) Analytical strategies for detecting nanoparticle – protein interactions. Analyst 135:1519–1530
12. Ariga K, Yamauchi Y, Ji Q, Yonamine Y, Hill JP (2014) Research update: mesoporous sensor Nanoarchitectonics. APL Mater 2(3):30701
13. Wang L, Sun Y, Li Z, Wu A, Wei G (2016) Bottom-up synthesis and sensor applications of biomimetic nanostructures. Materials (Basel) 9(1):53
14. de la Escosura-Muñiz A, Parolo C, Merkoçi A (2010) Immunosensing using nanoparticles. Mater Today 13(7–8):24–34
15. Cea P, Martín S, González-Orive A, Osorio HM, Quintín P, Herrer L (2016) Nanofabrication and electrochemical characterization of self-assembled monolayers sandwiched between metal nanoparticles and electrode surfaces. J Chem Educ 93(8):1441–1445

16. Hahm J-I (2013) Biomedical detection via macro- and Nano-sensors fabricated with metallic and semiconducting oxides. J Biomed Nanotechnol 9(1):1–25
17. Afzal A, Iqbal N, Mujahid A, Schirhagl R (2013) Advanced vapor recognition materials for selective and fast responsive surface acoustic wave sensors: a review. Anal Chim Acta 787:36–49
18. Bhakta SA, Evans E, Benavidez TE, Garcia CD (2015) Protein adsorption onto nanomaterials for the development of biosensors and analytical devices: a review. Anal Chim Acta 872:7–25
19. Krizkova S, Heger Z, Zalewska M, Moulick A, Adam V, Kizek R (2015) Nanotechnologies in protein microarrays. Nanomedicine 10(17):2743–2755
20. Wark AW, Lee J, Kim S, Faisal SN, Lee HJ (2010) Bioaffinity detection of pathogens on surfaces. J Ind Eng Chem 16(2):169–177
21. Li Z, Yu Y, Li Z, Wu T (2015) A review of biosensing techniques for detection of trace carcinogen contamination in food products. Anal Bioanal Chem 407(10):2711–2726
22. Chen Q, Xu S, Liu Q, Masliyah J, Xu Z (2016) QCM-D Study of nanoparticle interactions. Adv Colloid Interf Sci 233:94–114
23. Höök F, Kasemo B, Nylander T, Fant C, Sott K, Elwing H (2001) Variations in coupled water, viscoelastic properties, and film thickness of a Mefp-1 protein film during adsorption and cross-linking: a quartz crystal microbalance with dissipation monitoring, ellipsometry, and surface plasmon resonance study. Anal Chem 73(24):5796–5804
24. Rodahl M, Kasemo B (1996) On the measurement of thin liquid Overlayers with the quartz-crystal microbalance. Sensors Actuators A Phys 54:448–456
25. Voinova MV, Rodahl M, Jonson M, Kasemo B (1999) Viscoelastic acoustic response of layered polymer films at fluid-solid interfaces: continuum mechanics approach. Phys Scr 59(5):391–396
26. P-G S, Kuo X-R (2014) Low-humidity sensing properties of carboxylic acid functionalized carbon nanomaterials measured by a quartz crystal microbalance. Sensors Actuators A Phys 205:126–132
27. Marrazza G (2014) Piezoelectric biosensors for organophosphate and carbamate pesticides: a review. Biosensors 4(3):301–317
28. Popov VS, Subcheva EN, Shelaev AV, Pavelko RG, Sevastyanov VG, Kuznetsov NT (2014) Scanning probe microscope-quartz crystal microbalances integrated system for in-situ study of sensor properties of microamounts of nanomaterials. Theor Found Chem Eng 48(4):518–523
29. Bykov A, Shelaev A (2008) Scanning probe microscope combined with device for measuring mass and dissipative properties. Patent RU 2407021C2
30. Barsan MM, David M, Florescu M, Ţugulea L, Brett CMA (2014) A new self-assembled layer-by-layer glucose biosensor based on chitosan biopolymer entrapped enzyme with nitrogen doped graphene. Bioelectrochemistry 99:46–52
31. Du X, Jiang D, Hao N, Qian J, Dai L, Zhou L, Hu J, Wang K (2016) Building a three-dimensional Nano–bio Interface for Aptasensing: an analytical methodology based on steric hindrance initiated signal amplification effect. Anal Chem 88(19):9622–9629
32. McWilliams A (2014) Nanotechnology: a realistic market assessment. BCC Research, Wellesley, MA
33. Jang K, You J, Park C, Park H, Choi J, Choi C-H, Park J, Lee H, Na S (2016) Ultra-sensitive detection of zinc oxide nanowires using a quartz crystal microbalance and phosphoric acid DNA. Nanotechnology 27(36):365501
34. Jang K, Park C, You J, Choi J, Park H, Park J, Lee H, Choi C-H, Na S (2016) Highly sensitive, direct and real-time detection of silver nanowires by using a quartz crystal microbalance. Nanotechnology 27(47):475506
35. Jang K, Park J, Lee S, You J, Park C, Lee J, Park W, Yun J, Ahn S, Na S (2015) Situ and fast detection of single-walled carbon nanotubes by using DNA mediated aggregation method and quartz crystal microbalance. J Appl Phys 118(3):34510

36. Dobrovolskaia MA, Aggarwal P, Hall JB, McNeil SE (2008) Preclinical studies to understand nanoparticle interaction with the immune system and its potential effects on nanoparticle biodistribution. Mol Pharm 5(4):487–495
37. Prina-Mello A, Samuel S, Medina C, Jain N, Radomski M, Volkov Y, Santos-Martinez M (2015) CdTe quantum dots induce activation of human platelets: implications for nanoparticle Hemocompatibility. Int J Nanomedicine 10:2723
38. Wang J, Cao Y, Li Q, Liu L, Dong M (2015) Size effect of graphene oxide on modulating amyloid peptide assembly. Chem A Eur J 21(27):9632–9637
39. Yi P, Chen KL (2013) Interaction of multiwalled carbon nanotubes with supported lipid bilayers and vesicles as model biological membranes. Environ Sci Technol 47(11):5711–5719
40. Richter RP, Lai Kee Him J, Tessier B, Tessier C, Brisson AR (2005) On the kinetics of adsorption and two-dimensional self-assembly of Annexin A5 on supported lipid bilayers. Biophys J 89(5):3372–3385
41. Frost R, Svedhem S, Langhammer C, Kasemo B (2016) Graphene oxide and lipid membranes: size-dependent interactions. Langmuir 32(11):2708–2717
42. Westas E, Svanborg LM, Wallin P, Bauer B, Ericson MB, Wennerberg A, Mustafa K, Andersson M (2015) Using QCM-D to study the adhesion of human gingival fibroblasts on implant surfaces. J Biomed Mater Res Part A 103(10):3139–3147
43. Maurer-Jones MA, Gunsolus IL, Meyer BM, Christenson CJ, Haynes CL (2013) Impact of TiO 2 nanoparticles on growth, biofilm formation, and Flavin secretion in Shewanella Oneidensis. Anal Chem 85(12):5810–5818
44. Afrooz ARMN, Sivalapalan ST, Murphy CJ, Hussain SM, Schlager JJ, Saleh NB (2013) Spheres vs. rods: the shape of gold nanoparticles influences aggregation and deposition behavior. Chemosphere 91(1):93–98
45. Quevedo IR, Olsson ALJ, Tufenkji N (2013) Deposition kinetics of quantum dots and polystyrene latex nanoparticles onto alumina: role of water chemistry and particle coating. Environ Sci Technol 47(5):2212–2220
46. Tong M, Ding J, Shen Y, Zhu P (2010) Influence of biofilm on the transport of fullerene (C60) nanoparticles in porous media. Water Res 44(4):1094–1103
47. McNew CP, LeBoeuf EJ (2015) The role of attached phase soil and sediment organic matter physicochemical properties on fullerene (nC60) attachment. Chemosphere 139:609–616
48. McNew CP, LeBoeuf EJ (2016) nC60 deposition kinetics: the complex contribution of humic acid, ion concentration, and valence. J Colloid Interface Sci 473:132–140
49. Yi P, Chen KL (2013) Influence of solution chemistry on the release of multiwalled carbon nanotubes from silica surfaces. Environ Sci Technol 47(21):12211–12218
50. Chowdhury I, Duch MC, Mansukhani ND, Hersam MC, Bouchard D (2014) Deposition and release of graphene oxide nanomaterials using a quartz crystal microbalance. Environ Sci Technol 48(2):961–969
51. Chang X, Bouchard DC (2013) Multiwalled carbon nanotube deposition on model environmental surfaces. Environ Sci Technol 47(18):10372–10380
52. Chen KL, Elimelech M (2008) Interaction of fullerene (C 60) nanoparticles with humic acid and alginate coated silica surfaces: measurements, mechanisms, and environmental implications. Environ Sci Technol 42(20):7607–7614
53. Chowdhury I, Duch MC, Mansukhani ND, Hersam MC, Bouchard D (2014) Interactions of graphene oxide nanomaterials with natural organic matter and metal oxide surfaces. Environ Sci Technol 48(16):9382–9390
54. Chowdhury I, Hou W-C, Goodwin D, Henderson M, Zepp RG, Bouchard D (2015) Sunlight affects aggregation and deposition of graphene oxide in the aquatic environment. Water Res 78:37–46
55. Cheng Y, Yin L, Lin S, Wiesner M, Bernhardt E, Liu J (2011) Toxicity reduction of polymer-stabilized silver nanoparticles by sunlight. J Phys Chem C 115(11):4425–4432
56. Hou W-C, Chowdhury I, Goodwin DG, Henderson WM, Fairbrother DH, Bouchard D, Zepp RG (2015) Photochemical transformation of graphene oxide in sunlight. Environ Sci Technol 49(6):3435–3443

57. Cuenya BR (2010) Synthesis and catalytic properties of metal nanoparticles: size, shape, support, composition, and oxidation state effects. Thin Solid Films 518(12):3127–3150
58. Chen X, Mao SS (2007) Titanium dioxide nanomaterials: synthesis, properties, modifications, and applications. Chem Rev 107(7):2891–2959
59. Lu L, Li L, Wang X, Li G (2005) Understanding of the finite size effects on lattice vibrations and electronic transitions of. J Phys Chem B 109:17151–17156
60. Woldu T, Raneesh B, Reddy MVR, Kalarikkal N (2016) Grain size dependent Magnetoelectric coupling of BaTiO 3 nanoparticles. RSC Adv 6(10):7886–7892
61. Abbas Z, Labbez C, Nordholm S, Ahlberg E (2008) Size-dependent surface charging of nanoparticles. J Phys Chem C 112(15):5715–5723
62. Holmberg JP, Ahlberg E, Bergenholtz J, Hassellöv M, Abbas Z (2013) Surface charge and interfacial potential of titanium dioxide nanoparticles: experimental and theoretical investigations. J Colloid Interface Sci 407:168–176
63. Barisik M, Atalay S, Beskok A, Qian S (2014) Size dependent surface charge properties of silica nanoparticles. J Phys Chem C 118(4):1836–1842
64. Seo J, Kim JH, Lee M, Moon J, Yi DK, Paik U (2016) Size-dependent interactions of silica nanoparticles with a flat silica surface. J Colloid Interface Sci 483:177–184
65. Tang Z, Palafox-Hernandez JP, Law W-C, Hughes ZE, Swihart MT, Prasad PN, Knecht MR, Walsh TR (2013) Biomolecular recognition principles for Bionanocombinatorics: an integrated approach to elucidate Enthalpic and entropic factors. ACS Nano 7(11):9632–9646
66. Lee C-L, Tsai Y-L, Chen C-W (2013) Specific and mass activity of silver Nanocube and nanoparticle-based catalysts for electroless copper deposition. Electrochim Acta 104:185–190
67. Liu Y, Rosenfield E, Hu M, Mi B (2013) Direct observation of bacterial deposition on and detachment from nanocomposite membranes embedded with silver nanoparticles. Water Res 47 (9):2949–2958
68. Swetha P, Devi KSS, Kumar AS (2014) In-situ trapping and confining of highly redox active quinoline quinones on MWCNT modified glassy carbon electrode and its selective electrocatalytic oxidation and sensing of hydrazine. Electrochim Acta 147:62–72
69. Booth A, Pintre IC, Lin Y, Gough JE, Webb SJ (2015) Release of proteins and enzymes from vesicular compartments by alternating magnetic fields. Phys Chem Chem Phys 17 (24):15579–15588
70. Kasputis T, Koenig M, Schmidt D, Sekora D, Rodenhausen KB, Eichhorn K-J, Uhlmann P, Schubert E, Pannier AK, Schubert M, Stamm M (2013) Slanted columnar thin films prepared by glancing angle deposition functionalized with Polyacrylic acid polymer brushes. J Phys Chem C 117(27):13971–13980
71. Rayaprolu V, Manning BM, Douglas T, Bothner B (2010) Virus particles as active nanomaterials that can rapidly change their viscoelastic properties in response to dilute solutions. Soft Matter 6(21):5286–5288
72. Mansfield E, Tyner KM, Poling CM, Blacklock JL (2014) Determination of nanoparticle surface coatings and nanoparticle purity using microscale thermogravimetric analysis. Anal Chem 86(3):1478–1484
73. Mansfield E, Kar A, Quinn TP, Hooker SA (2010) Quartz crystal microbalances for microscale thermogravimetric analysis. Anal Chem 82(24):9977–9982

Tools and Electrochemical In Situ and On-Line Characterization Techniques for Nanomaterials

11

Têko W. Napporn, Laetitia Dubau, Claudia Morais, Mariana R. Camilo, Julien Durst, Fabio H. B. Lima, Frédéric Maillard, and K. Boniface Kokoh

Contents

T. W. Napporn (✉) · C. Morais · K. B. Kokoh
IC2MP UMR 7285 CNRS University of Poitiers, Poitiers, France
e-mail: teko.napporn@univ-poitiers.fr

L. Dubau · J. Durst · F. Maillard
University of Grenoble Alpes, Grenoble, France

CNRS, Grenoble, France

M. R. Camilo · F. H. B. Lima
IQSC, University of São Paulo, São Carlos, SP, Brazil

© Springer-Verlag GmbH Germany, part of Springer Nature 2018

C. S. S. R. Kumar (ed.), *In-situ Characterization Techniques for Nanomaterials*,
https://doi.org/10.1007/978-3-662-56322-9_11

1 Introduction

In the last century, progress in electrochemistry and electrocatalysis was very spectacular due to the remarkable evolution in surface science, chemistry, and physics. Electrochemical study of perfect smooth or bulk materials was the usual way to understand the interaction between the surfaces of such materials with their close environment. Therefore, any modification of the surface structure or composition provides change in the material behavior and the nature of the adsorbed species or near. Usually, the modification of smooth surface consists in the increase of its roughness factor through the deposition of sublayer or layer of metal particles. The deposition can be done on a well-defined surface (model electrode with a known crystallographic structure) [1]. Then, surface modification becomes a way of creating new active sites to enhance the reactivity of molecules. The development of nanoscale materials has changed the approach of studying and identifying active sites in heterogeneous catalysis, and particularly in electrocatalysis. Indeed, electrocatalysis uses the surface of a material, which is submitted to an electrode potential, as the reaction site. Therefore, the material structure, morphology and its composition are the key parameters to control the electrochemical process [2]. The nature of the active site depends on these parameters. Furthermore, the assessment of the nature of the active site before, during, and after the electrocatalytic reaction becomes a huge challenge. Thereby, electrochemical tools like cyclic voltammetry, underpotential deposition of a monolayer of a species [3–5], the specific adsorption of species or molecule, and CO stripping [6] were the first approaches. It is the basic measurement of the electrons flow through the surface per unit of time during the reaction at the surface. Therefore, the electric current per area unit represents the charge transfer reaction that occurs at a metal-solution interface. Since the middle of the last century, an increase in the development of several in situ spectroscopic techniques was observed due to the need of understanding the structure of the interface between electrodes and solutions. Indeed, coupling the electrochemistry measurements to other techniques such as Fourier Transform Infrared Spectroscopy (FTIRS), X-Ray Diffraction (XRD) [7, 8], Transmission Electron Microscopy (TEM) [9], Scanning Tunneling Microscopy (STM) [10], Surface-Enhanced Raman Scattering (SERS) [11] becomes a suitable approach to assess in real time at the electrified interface electrode-solution; some relevant data on electrocatalysts structure, morphology, composition, and stability of materials; and on the reaction intermediates and

products. The identification of the surface state in addition to that of adsorbed species, intermediates, and products of the reaction process have permitted to determine a mechanistic pathway which is essential for enhancing the material performance and selectivity. It appears obvious that the identification of surface state of a nanomaterial under realistic electrochemical reaction conditions represents a noble scientific breakthrough. In the present chapter, for the first time some techniques coupled with electrochemistry able to characterize nanomaterials as electrodes will be extensively addressed. This chapter will also show the progress in in situ and on-line electrochemical approaches. One motivated approach is to be able to characterize electrochemically and experimentally the surface of the nanoparticle. Therefore, in the first part of the chapter, an example of a pure electrochemical tool, which permits to probe the nanoelectrocatalyst surface, is discussed. Although the progress in nanotechnology increases rapidly, various tools have been developed in electrochemistry for understanding the reaction pathway, intermediates, and products formation.

In electrochemistry, the surface structure is often modified by the underpotential deposition (UPD) of a sub- or monolayer of a transition metal for a selective adsorption of molecule; it also permits to enhance the catalytic activity. Furthermore, the underpotential deposition of a monolayer of a metal is discovered as a powerful tool for characterizing the surface structure of an electrode material (bulk or at nanoscale) [4, 5, 12–14]. Indeed, the selective adsorption of the transition metal at different potentials depends on the crystallographic orientation of the material surface. Therefore, the different facets at the nanomaterial surface can be revealed electrochemically. Studying a change in morphology, structure that occurs on a nanomaterial under the operating conditions in electrochemistry is mandatory to approach the reaction mechanisms and to propose mitigation strategies. The modifications of the material are closely related to, for example, the potential range and modulation mode, the nature of the electrolyte, the operating temperature. Any in situ detection of these changes is highly challenging and efforts have been devoted to achieve this goal. The chapter also deals with an additional tool (IL-TEM) used in electrochemistry and different in situ and on-line techniques such as XAS, FTIRS, and DEMS. All these complementary tools and techniques permit to characterize before, during, and after the reaction, the nanomaterial size, morphology, structure, and the products obtained from their surface reactivity and selectivity.

2 Electrochemistry and Nanomaterials: The Challenges

The advent of nanotechnology has created new approaches in the techniques used in surface science. The characterization of a nanomaterial becomes a challenge since it is important to avoid any change in its properties or to be able to explain this change during the experiment or its analysis. Thereby, innovations in characterization techniques have permitted to investigate extensively nanomaterials for understanding their behavior and catalytic activity. In electrochemistry, understanding the intrinsic properties of nanomaterials, their interaction during a reaction in order to

explain their catalytic activity, is a noble objective. At the end of the last century, the development and/or improvement of in situ techniques in the electrochemistry area has taken into account the nanometric scale, which requires several challenges to: (i) be able to observe the nanomaterial in its initial morphology and structure, (ii) keep the morphology and the structure of the nanomaterials during the experiment, (iii) explain any change in this structure and its origin, (iv) determine the active site or be able to suggest the more effective structure and morphology for a desired reaction. The operation conditions of some techniques require high vacuum which is not compatible with the classical aqueous medium used in electrochemistry. The innovation in technology added to the genius of scientists should permit to overcome these challenges in the future.

3 Surface Structure of Nanomaterials by Electrochemical Tools

3.1 Cyclic Voltammetry: Basic and Powerful Tool in Electrochemistry

Cyclic voltammetry is a basic and powerful tool in electrochemistry. It consists in applying a potential (*versus* a reference value) linearly as function of time between two potential limits. Therefore, the variation of the current versus the potential results in the interaction between the polarized surface of the electrode and the species in the electrolyte. This method is a basic measurement in electrochemistry, which gives the profile of the electrode material depending on its nature, surface structure, morphology, the medium, and the species in the electrolyte.

The cyclic voltammogram of unsupported Pt nanoparticles in 0.5 mol L^{-1} H_2SO_4 is shown in Fig. 11.1. Four potential regions can be observed: the hydrogen adsorption-desorption region, the double layer region, and the region where occurs the oxidation of the surface of nanoparticles and after their reduction. The area of each peak indicates the quantity of charge associated with some electrode reactions occurring in the system.

In the hydrogen region three different peaks are observed at 0.11, 0.20, and 0.25 V versus RHE. During the forward scan, they are associated with the hydrogen desorption on the crystallographic planes (110), (100), and (111), respectively. The electrochemical surface area can be assessed from the hydrogen desorption region (blue patterned grid lines). The charge Q_{ex} corresponding to the desorption of adsorbed hydrogen on the electrode can be calculated using the integration approach (e.g., Origin software) with Eq. 11.1. In this equation $E_{initial}$ and E_{end} are the initial and final potentials respectively of the hydrogen desorption reaction: v the scan rate, I the current, and E the potential. It is well known that the charge corresponding to the adsorption of a monolayer of hydrogen on a 1 cm^2 active surface area of Pt is $Q_m = 210$ μC. Therefore, the calculated Q_{ex} is about 600 μC. By considering Eq. 11.2, this charge corresponds to an electrochemically active surface area (EASA) of 2.7 cm^2.

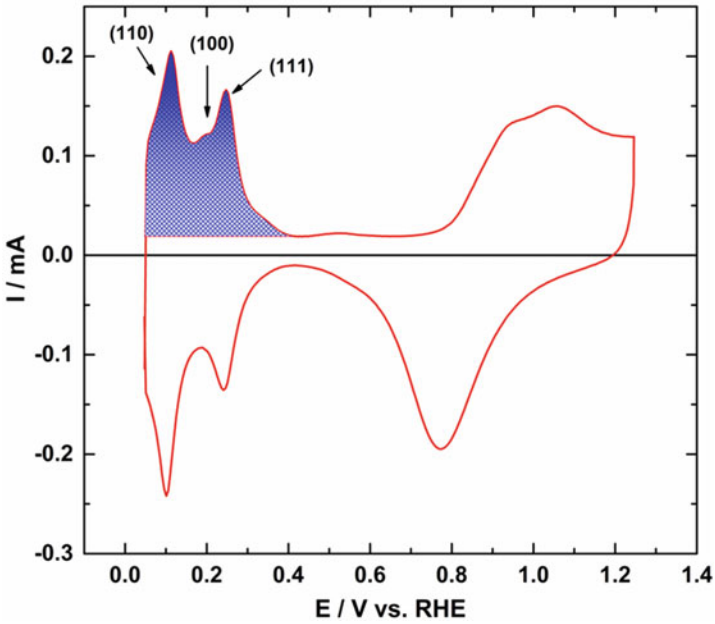

Fig. 11.1 Cyclic voltammogram of unsupported Pt nanoparticles in 0.5 mol L^{-1} H_2SO_4 recorded at 50 mV s^{-1} and 20 °C

$$Q_{\text{ex}} = \frac{1}{v}\left(\int_{E_{\text{initial}}}^{E_{\text{end}}} I(E)\mathrm{d}E\right) \tag{11.1}$$

$$SA\left(\text{cm}^2\right) = \frac{Q_{\text{ex}}}{Q_m} \tag{11.2}$$

Pt surface crystallographic orientation is very sensitive to hydrogen adsorption. However, gold nanoparticles (AuNPs) do not exhibit an affinity with hydrogen (Fig. 11.2). Indeed, during the positive scan, a large capacitive current region which corresponds to the double layer region is observed from 0.05 V to 1.2 V versus RHE followed by the surface oxidation region. The upper potential limit depends on the potential where the surface oxidation starts. Indeed, the oxidation of the gold surface is sensitive to its surface crystallographic planes. This was evidenced by Hamelin on single crystals smooth materials [15]. During the backward scan the reduction of the oxides occurs at a potential range from 1.4 V to 0.8 V with a maximum centered at 1.06 V versus RHE for AuNRs (Fig. 11.2). The profile of the surface oxidation and reduction regions depends on the surface crystallographic structure as well as the size and the shape of the nanoparticles, as evidenced in the literature [4, 5, 16]. This phenomenon was also shown on gold single crystals surfaces [15]. Therefore, assessing the crystallographic orientation of nanoparticles becomes an important target since the activity of a nanomaterial depends thoroughly on its surface.

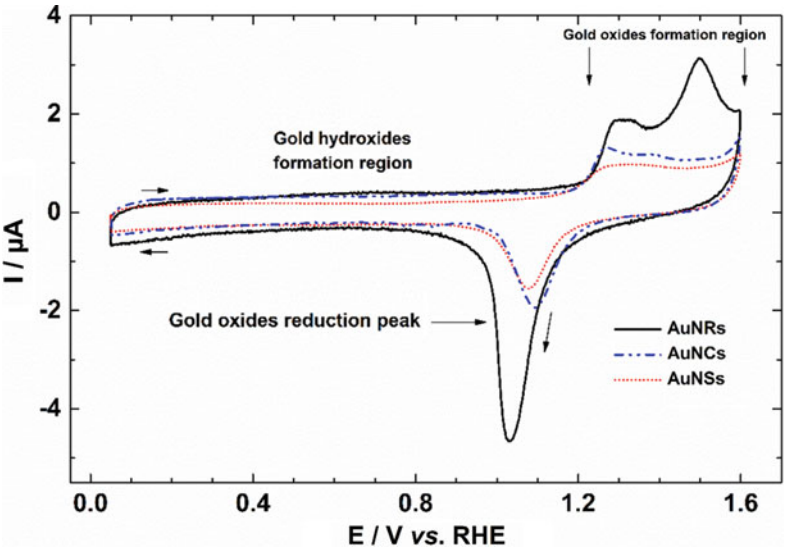

Fig. 11.2 Cyclic voltammograms of shape-controlled gold nanorods (AuNRs), gold nanocubes (AuNCs), and gold nanospheres (AuNSs) electrodes in 0.1 mol L^{-1} NaOH, recorded at 20 mV s^{-1} and at 20 °C (Reprinted and adapted with permission from Ref. [16]; Copyright © 2013, The Author(s))

3.2 Electrochemical Characterization of Gold Nanoparticles Surface by an Underpotential Deposition of Lead (Pb_{UPD}) in Aqueous Media

Assessing electrochemically the crystallographic orientation of the nanoparticles surface is a way to determine a part of their activity. The surface structure of nanomaterials plays a key role in their electroactivity since it represents the reaction site. In catalysis in general, model reactions have permitted to determine specific active sites of a material. In electrocatalysis the underpotential deposition of a metal, CO stripping, adsorption of a specific molecule are some of reactions which have permitted to characterize the surface of the materials. The case of CO stripping will not be discussed in the present chapter because the CO electrooxidation is a simple reaction which depends on experimental conditions (electrode potential, the scan rate, the electrode surface structure and composition). Consequently, the mechanistic approaches for explaining the cyclic voltammogram profile of the interaction of Pt electrode surface with CO demonstrated the complexity of the reaction steps [6, 17–19]. This can explain the discrepancies between different research groups to date. Investigations realized by Urchaga et al. on shape-controlled nanoparticles showed that the multiplicity of the peaks is mostly due to the surface domains (preferentially oriented or disordered) [6, 13, 19]. In the present chapter, we pay attention on the underpotential deposition (UPD) of a metal. This reaction consists in the deposition of a monolayer of a metal M1 on another M2 at a potential higher than the reversible

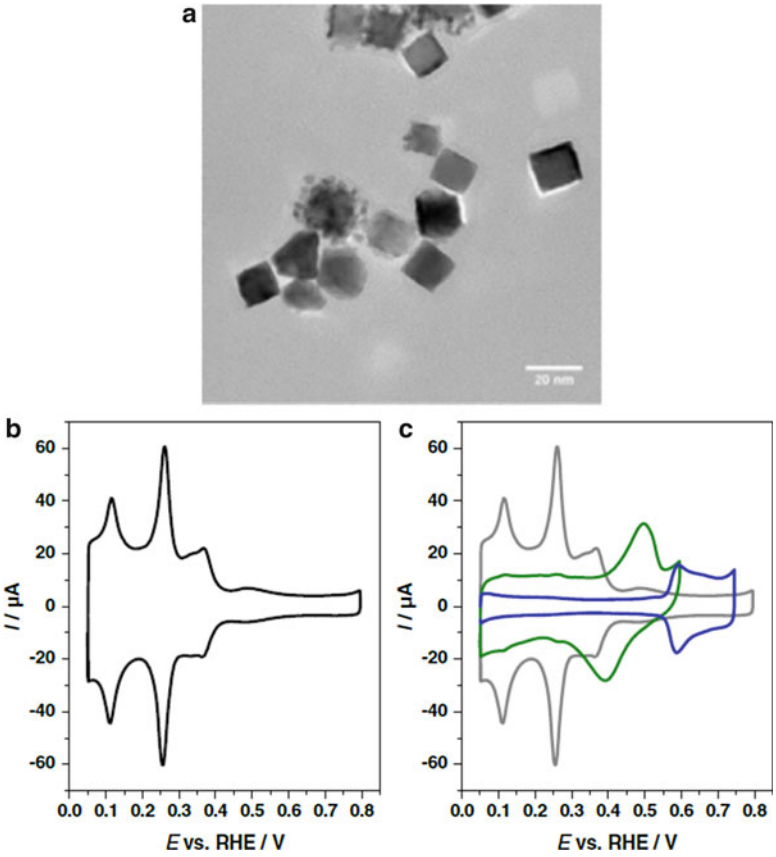

Fig. 11.3 (**a**) Transmission electron microscopy image of Pt nanoparticles obtained by the tetradecyltrimethylammonium bromide method; (**b**) cyclic voltammogram recorded in 0.5 mol L^{-1} H_2SO_4 on cubic Pt nanoparticles recorded at 20 mV s^{-1} and 25 °C; (**c**) cyclic voltammograms after adsorption of germanium on the surface (green line) and after adsorption of bismuth on the platinum surface (blue line), recorded at 50 mV s^{-1} and 25 °C. Copyright 2012 (Reprinted from Ref. [3] with the permission of Springer. Copyright © 2012, Springer Science + Business Media, LLC)

thermodynamic one. One of the usual and friendly UPD is that of hydrogen on platinum, as shown in Fig. 11.1. The adsorption of hydrogen occurs at potential higher than 0 V versus RHE according to the equation:

$$H^+ + e^- + Pt \rightarrow Pt - H_{ads} \tag{11.3}$$

Cyclic voltammogram of Pt nanocubes is shown in Fig. 11.3b. These nanocubes were obtained by the tetradecyltrimethylammonium bromide (TTAB) route. The perfect control of the nanoparticles surface structure during their synthesis is impossible. Therefore, most of the shape-controlled nanoparticles have structure defects that lead to the presence of unexpected crystallographic orientation (e.g., the presence of

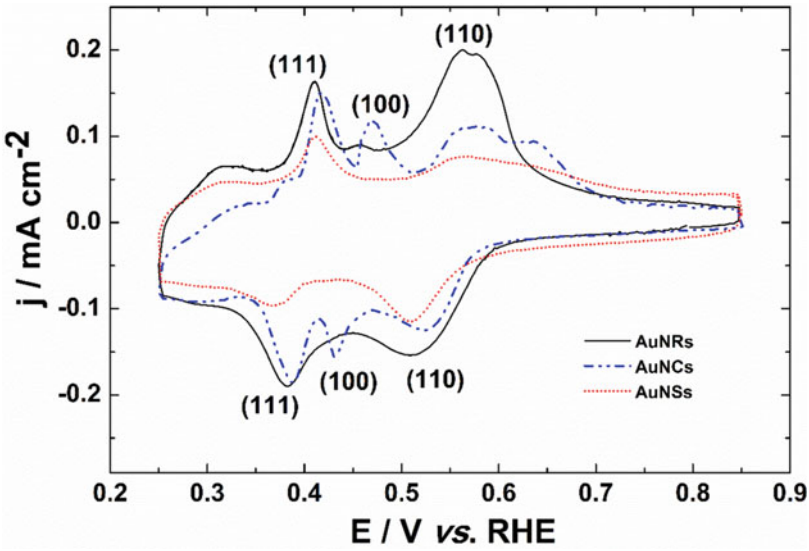

Fig. 11.4 Voltammetric profiles of Pb_{UPD} on the different AuNPs: nanorods (AuNRs), nanocubes (AuNCs), and nanospheres 6 nm (AuNSs)s in 0.1 mol L^{-1} NaOH +1 mmol L^{-1} $Pb(NO_3)_2$ recorded at 20 mV s^{-1} and at controlled temperature of 20 °C. Copyright 2013 (Reprinted from Ref. [16] with the permission of Springer. Copyright © 2013, Springer Science + Business Media, LLC)

the facet (111) on nanocubes). Selective underpotential deposition of germanium and bismuth were performed on these nanoparticles [3]. The authors have determined a total surface domain of 60% which includes 42% and 18% of (100) and (111), respectively.

In the case of gold electrode materials in general, the strong affinity of lead with gold surface structure has been meticulously used to assess the low index facets. Indeed, the underpotential deposition of lead which can involve the deposition of up to one monolayer occurs at different electrode potentials depending of the surface domains [4, 5, 12, 15, 16]. This process occurs at a potential higher than the reversible thermodynamic potential, and is considered as the direct consequence of the high bonding energy of the metal which is deposited at the substrate surface [4, 12]. Thereby, the Pb_{UPD} becomes a sensitive tool for characterizing the gold surface. In this case, the Pb_{UPD} profiles of different gold nanoparticles (nanorods, nanocubes, and nanospheres) in 0.1 mol L^{-1} NaOH +1 mmol L^{-1} $Pb(NO_3)_2$ at 20 mV s^{-1} were presented in Fig. 11.4. During the backward potential scan from 0.8 to 0.25 V versus RHE, the three AuNPs exhibit the first adsorption peak in the potential range from 0.55 to 0.5 V versus RHE. This reduction peak is assigned to the deposition of lead on (110) facets. The difference observed in the potential corresponding to the maximum of the reduction peak is attributed to the length or the stretch of the domain. Two other deposition peaks are observed around 0.44 V and 0.39 V versus RHE, which corresponds to the domains (100) and (111), respectively. The positive potential scan shows three Pb stripping peaks that

correspond to the reversible dissolution of Pb layer on the surface domains (111), (100), and (110). Moreover, in the case of AuNRS and AuNCs, the peak assigned to the lead desorption on the facets (110) was split. This phenomenon can be attributed to the presence of two different domains [4]. For AuNSs, no adsorption peak of lead is observed on the facts (100). Recently, Hebié et al. [14] have reported on the surface domain (100) that appeared with an increase of the particles size. In the literature, it was shown that crystallographic surface structure of nanoparticles depends on synthesis methods [3, 4, 6, 12, 13, 20–22].

4 Using Transmission Electron Microscopy (TEM) to Characterize the Stability of Nanostructured Electrocatalysts

Studying the changes in morphology, structure, and chemistry occurring on a nanomaterial under operating conditions of an electrochemical device is mandatory to identify the degradation mechanisms at stake and to propose mitigation strategies. The material changes are closely related to, for example, the potential range and modulation mode, the nature of the electrolyte, the operating temperature. Monitoring these changes in situ is highly challenging and lots of efforts have been devoted to achieve this goal, X-ray and electron-based techniques being tools of choice.

The characterization of a freshly synthesized nanomaterial by electron-based techniques cannot be overlooked and in that respect, classical microscopy techniques have become routine techniques. They are necessary to provide information on the overall morphology, the shape and the size distribution of the nanoparticles. In addition, global X-ray energy dispersive spectroscopy (EDX) analyses allow to access the chemical nature of the sample both qualitatively and quantitatively. Complementary to conventional transmission electron microscopy (TEM), high resolution TEM (HRTEM) is a powerful tool that provides atomic scale insights. HRTEM is extensively used to determine crystallographic parameters, surface structure but also to unravel lattice imperfections (such as point defects, dislocations, cavities, and voids), which are key to understand the electrochemical reactivity. Using TEM in a scanning mode (STEM) is also of interest. Indeed, focusing the electron beam into a narrow spot which is then scanned along the sample (or the particle) allows mapping the chemical composition of this nanoparticle by EDX or Electron Energy Loss Spectroscopy (EELS). Combining STEM with a high angle detector leads to images containing a chemical information directly visually accessible since the contrast is in first approximation proportional to the atomic number Z (Z-contrast images). The power of the scanning mode is however limited due to the necessity to have an aberration corrected microscope (electron probe with sub-angstroms diameters) to map individual atomic columns.

Using these techniques to characterize the morphology, the structure and the chemical composition of a nanomaterial before operation is not sufficient since it

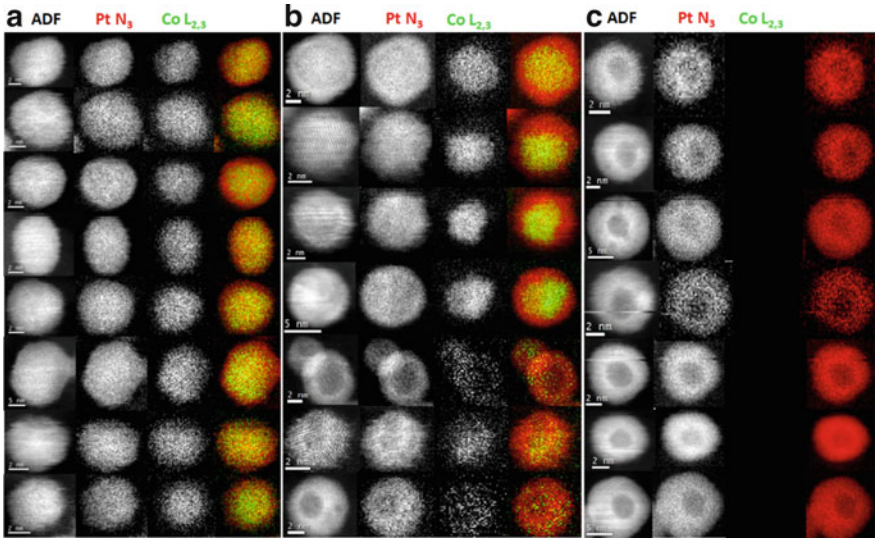

Fig. 11.5 Structural modification of PtCo/C nanoparticles aged in a real PEMFC environment. Annular dark-field images and chemical maps of individual nanoparticles are displayed in (**a**) at the initial state and (**b**–**c**) after PEMFC operation. The spectroscopic maps provide direct evidence of the core-shell nanostructure of the fresh Pt_3Co/C nanoparticles, resulting from acid-leaching and indicate that some aged nanoparticles maintain their core-shell nanostructure, while others display a hollow nanostructure. The Pt N_3 signal is shown in red, and the Co $L_{2,3}$ signal is shown in green (Reprinted from Ref. [38] with the permission of Elsevier)

may evolve under the operating conditions of an electrochemical device. Performing similar observations after aging is first step towards identifying their degradation mechanisms and bridging the structural and chemical changes to their changes in (electro)catalytic activity. In this frame, postmortem analysis of carbon-supported platinum nanoparticles (Pt/C) or platinum-transition metal alloys (PtM/C) electrocatalysts used at the cathode of a Proton Exchange Membrane Fuel Cell (PEMFC) to electrochemically catalyze the electrochemical oxygen reduction reaction (ORR) revealed particularly fruitful [23–38]. From a microscopic point of view, postmortem analysis consists in retrieving the aged nanocatalysts and depositing them on a TEM grid for imaging. Three degradation mechanisms have been evidenced for Pt/C and PtM/C nanoparticles in the harsh environment of a PEMFC cathode: (i) migration and agglomeration of the Pt-based crystallites on the support eventually followed by their coalescence; (ii) dissolution of the mono- or bimetallic nanoparticles and redeposition of ionic species having a standard potential higher than 0 V versus the reversible hydrogen electrode (RHE), resulting in crystallites getting larger in size; and (iii) detachment of the metal nanoparticles from the carbon support. In addition, for PtM/C materials, continuous dissolution of the non-noble metal has also been monitored during operation resulting in severe decay of the catalytic performance. Figure 11.5 shows that, due to preferential dissolution of Co atoms in the operating conditions of a PEMFC cathode, Pt_3Co/C nanoparticles

spontaneously evolve towards Pt_xCo-rich core@Pt-rich shell/C with $x > 3$. After 3422 h of operation at a PEMFC cathode, complete dissolution of the Co atoms was eventually observed yielding the formation of hollow Pt/C nanoparticles [35].

Combining the use of a segmented electrochemical cell with TEM imaging of selected zones of ultramicrotomed membrane electrode assemblies (MEAs) has highlighted the heterogeneities of aging occurring during real PEMFC operation [37, 39]. For example, Fig. 11.6 displays heterogeneities of aging within the thickness of a MEA composed of Pt/C nanoparticles both at the cathode and the anode: the cathode/proton-exchange membrane interface is much more degraded than the diffusion-medium/cathode interface translating into a pronounced shift in the Pt particle size distribution histograms towards larger crystallites close to the proton-exchange membrane [23, 39]. Different extents of degradation have also been reported in the air inlet region (where the atmosphere is rich in oxygen and poor in water) relative to the air outlet area (where the atmosphere is depleted in oxygen and enriched in water) of an MEA after operation in counter-flow mode [40]. Due to different oxygen partially pressures under the channel or under the land of the bipolar plate used to provide oxygen to the cathode, the nanocatalysts used at a PEMFC cathode also degrade at different rates in these regions [37, 41].

Even if the nature of the electrolyte plays a major role on the degradation of the nanocatalyst, [42, 43] durability studies are often performed in liquid electrolyte owing to the better control of the electrochemical aging conditions and to their easiness of implementation. Identical-Location TEM (IL-TEM), which consists in imaging the same zone of the catalyst before and after electrochemical measurements, revealed a tool of choice to establish structure/activity/stability relationships. In this technique first introduced by Mayrhofer et al., [44, 45] a TEM grid onto which the catalyst of interest is deposited is used as working electrode and aged in a classical electrochemical cell. IL-TEM enables to visualize the exact same zones of the sample before and after aging in well-controlled experimental conditions. Furthermore, it allows to discriminate which of the degradation mechanism cited above is predominant as a function of the electrochemical conditions. IL-TEM has shown that the potential window, the way potential is modulated, and the nature of the atmosphere play a major role on the durability of a pure Pt/C catalyst [46]. Under oxygen atmosphere, the detachment of Pt particles induced by the corrosion of the carbon support is predominant (Fig. 11.7). In contrast, neutral atmosphere favors the coexistence of all the pre-cited degradation mechanisms.

This technique has also provided interesting insights into (i) the crucial role of the carbon support (in particular the extent of graphitization) [47], (ii) the influence of stress test conditions (linear vs. square-wave variation of the electrochemical potential) [48], (iii) the impact of temperature, [49] and (iv) the influence of intermediate characterizations [50] on the degradation mechanism. Some interesting declinations of IL-TEM are also proposed in the literature and offer additional characterization tools. This includes Il-EELS, which allows to monitor compositional changes of PtCo/C or PtNi/C due to surface segregation and further dissolution in the acidic environment of a PEMFC cathode and PtNi/C catalysts, respectively [51, 52] (Fig. 11.8).

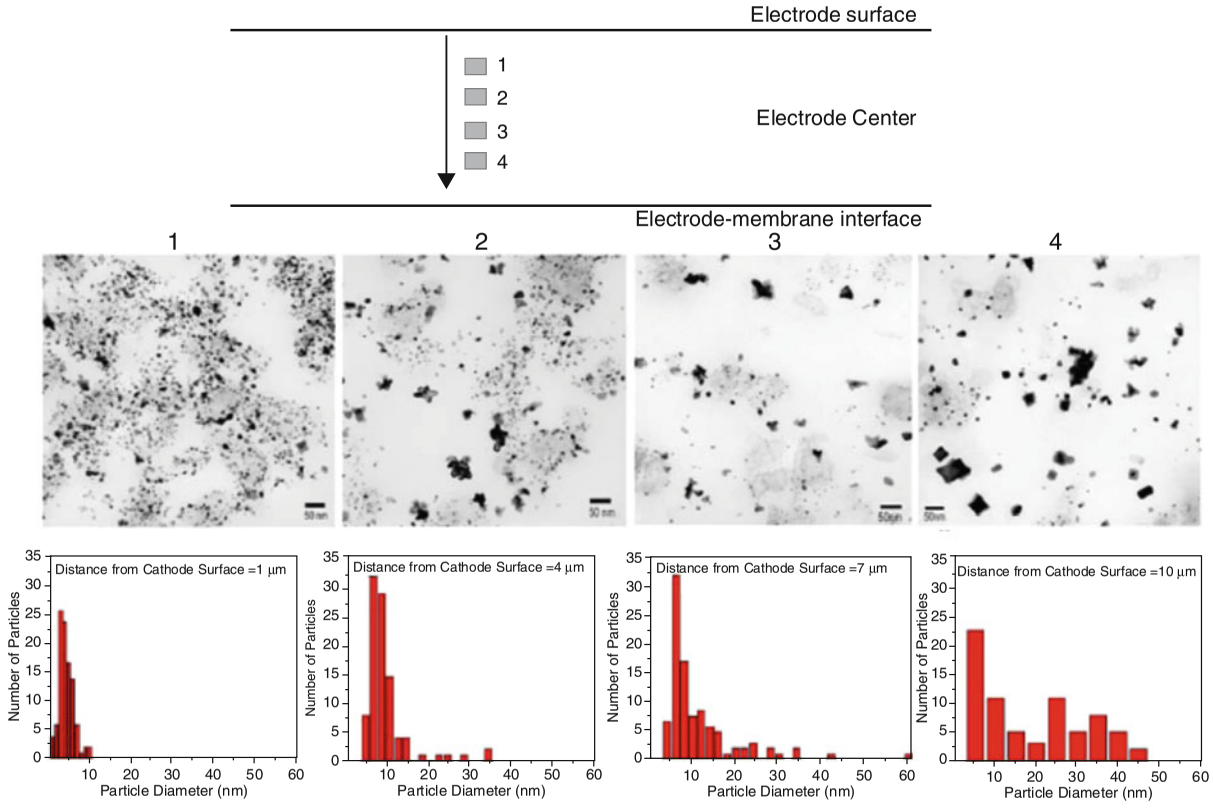

Fig. 11.6 Top: Schematic of the cycled cross-sectional MEA cathode and TEM images were obtained sequentially in the direction perpendicular to the membrane surface from the diffusion medium–cathode interface to the cathode/membrane interface. Middle: (1–4) are corresponding TEM micrographs

Finally, let us emphasize IL-tomography that allows monitoring the collapse of the carbon support architecture upon simulated start-stop conditions of a PEMFC [53] (Fig. 11.9).

5 X-Ray Absorption Spectroscopy

5.1 Principles

We now discuss the basic principles of X-ray absorption (XAS), spectroelectrochemical cells and illustrate the possibilities of XAS with a few didactic examples also related to the lack of stability of Pt_3Co/C nanoparticles at a PEMFC cathode.

X-ray absorption spectroscopy (XAS) is an element-specific characterization technique, which enables determining the geometric and the electronic structure of any material. In XAS, a monochromatic beam of X-ray photons, having an energy E and an intensity I_0, is focused on the sample of interest. Upon absorption, the energy of the X-rays is transferred to core-level electrons (from the K/L/M shell) yielding ejection of photoelectrons that leave behind a highly excited core-hole state.

The excitation of core-level electrons requires energies comprised between $0.1 < E < 100$ keV, hence XAS experiments can only be performed with synchrotron radiation. For light elements, such as those located in the first row of transition metals, one studies core electrons excitations from the K-level: for example, the core electrons of cobalt (electronic structure: [Ar] 3d7 4 s2) require a minimum energy E_0, also called absorption edge, of ca. 7,700 eV to be excited. For heavier atoms, such as platinum (Pt: [Xe] 4f14 5d9 6 s1), excitation of the K edge requires higher energy ($E_0 = 78{,}395$ eV), thus it is more common to excite the electrons that are located within the $2p^{3/2}$ level ($E_0 = 11{,}560$ eV corresponding to the L_3 edge). A XAS spectrum records the absorption intensity as a function of the incoming photon energy, usually varied from close below (−100 eV) to well above (from +60 eV to +1000 eV) the absorption edge.

The interactions of photoelectrons with the neighbors of the absorbing atom lead to a modification of the transmitted photon flux intensity. The absorption coefficient, $\mu_t(E)$, can be determined from the ratio of the flux of incident (I_0) and transmitted (I_t) photons through the sample of a thickness e:

$$\mu_t(E).e = \log \frac{I_0(E)}{I_t(E)} \tag{11.4}$$

Fig. 11.6 (continued) obtained from locations 1, 2, 3, and 4 in the cross-sectional MEA cathode shown in the schematic (top). Bottom: (1–4) Pt particle size histograms measured from TEM micrographs (middle) of the cross-sectional cycled MEA cathode. All four histograms were obtained from a measurement of 100 particles (Reprinted from Ref. [39] with the permission of Springer)

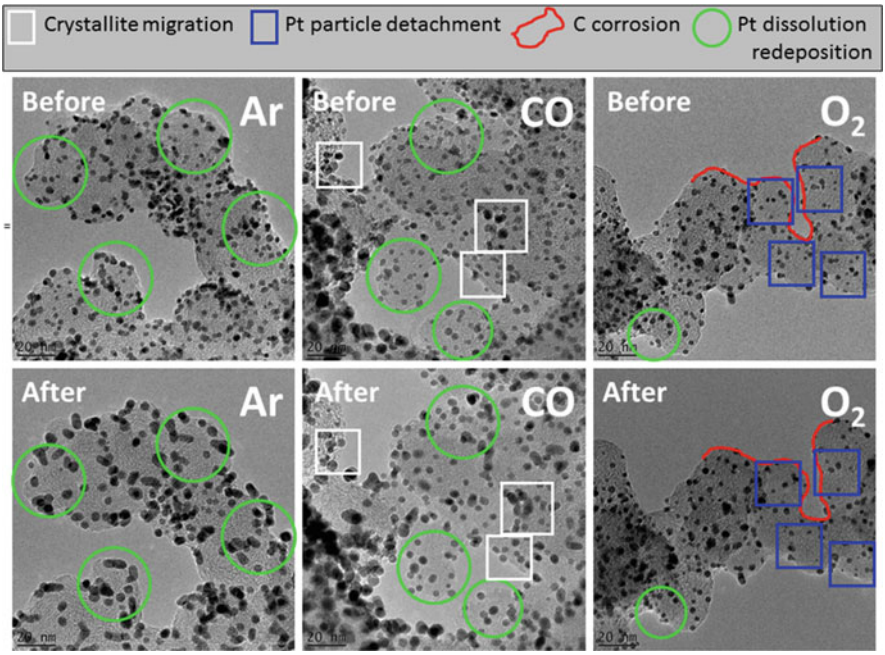

Fig. 11.7 IL-TEM images of Pt/C catalysts before and after 800 potential cycles between 0.05 and 1.23 V versus RHE in solutions containing Ar, CO, or O_2. Electrolyte: 0.1 mol L^{-1} $HClO_4$; $v = 0.200$ V s^{-1}; $T = 20$ °C (Reprinted from Ref. [46] with the permission of Elsevier)

The value of the absorption coefficient depends on the atomic concentration, ρ, and absorption cross-section, σ, as:

$$\mu = \rho.\sigma \tag{11.5}$$

From an experimental point of view, a key to success in XAS experiments is to maximize the edge jump (Δμ), which will ultimately improve the accuracy of the parameters fitted from the signal:

$$\Delta\mu = (\mu(E_2) - \mu(E_1)) \tag{11.6}$$

E_2 and E_1 are the energies below (−20 eV) and above (+20 eV) the absorption edge. Since the absorption cross-section is an element-specific property, [54] the edge jump is controlled by the experimentalist with the atomic concentration of the element of interest [55]. An absorption coefficient can also be deduced from the X-ray fluorescence photon flux intensity I_f:

$$\mu_f(E) \propto {}^{I_f}(E)/_{I_0(E)} \tag{11.7}$$

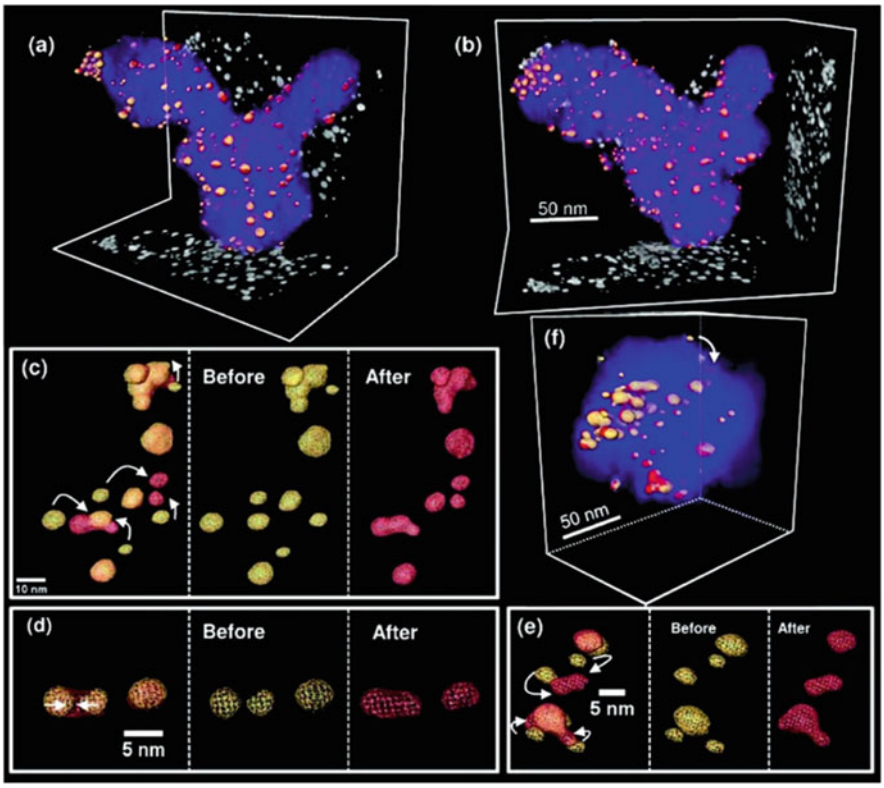

Fig. 11.8 One-to-one correspondence of nanocatalyst particles before (gold) and after (red) electrochemical aging, which is the same color scheme used in all figures. (**a**) A 3D reconstruction of nanocatalyst particles, on the carbon support (violet) with projected 2D images shown at each side. (**b**) Alternate viewing angle. (**c**–**e**) Several instances of nanocatalyst particle coalescence and migration, with particle positions indicated by arrows. (**f**) One example of cropped volume from (**a**, **b**), showing how one nanocatalyst particle moves into the positive curvature (valley) from the negative curvature (summit) of the catalyst support. The arrow points out the trajectory of the particle movement. Violet shading is the carbon support (Reprinted from Ref. [51] with permission of the American Chemical Society)

The fluorescence intensity signal is actually preferred over the transmitted one in the case of diluted samples (biological, environmental, electrocatalytic), due to its linear dependence, and not logarithmic, to the adsorption coefficient. The fluorescence signal originates from filling of core holes with electrons located at a higher energy level, thus it contains similar information than the transmitted signal. In a practical way, the fluorescence signal can be measured at the same time as the transmitted signal by positioning the fluorescence detector perpendicular to the incident beam.

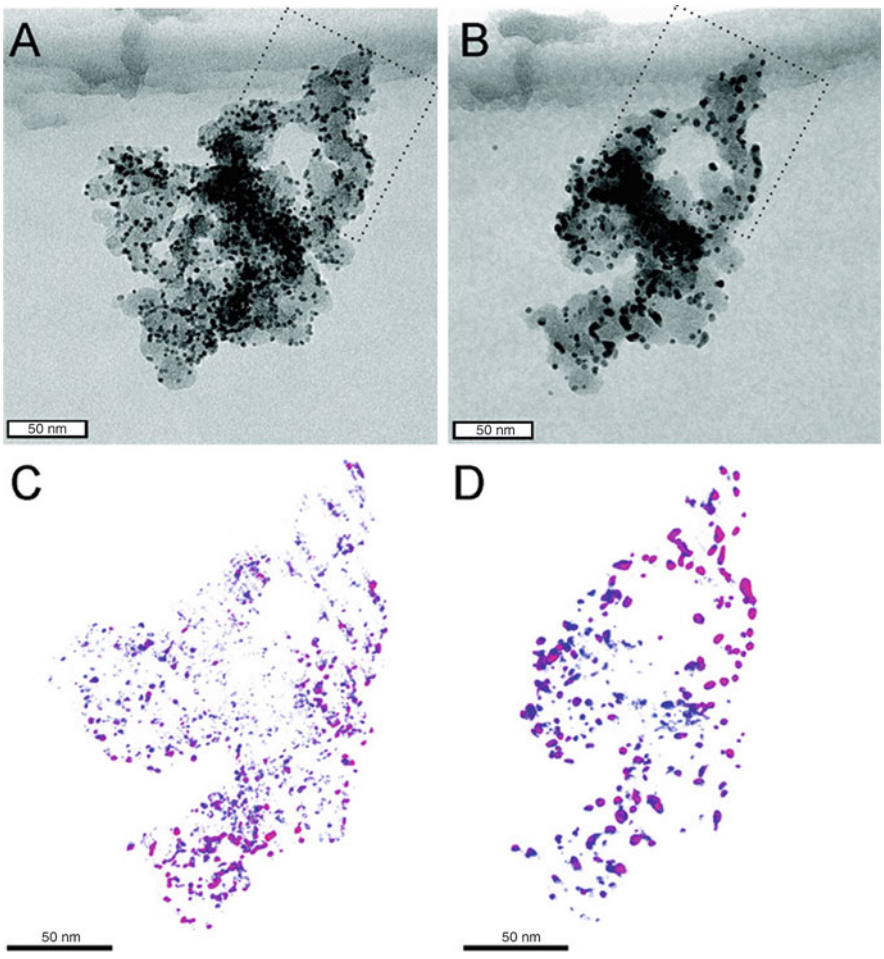

Fig. 11.9 A and B are standard IL-TEM images, C and D are IL-tomography images of the same catalyst location after 0 (A, C) and 3600 (B, D) degradation cycles between 0.4 and 1.4 V versus RHE with a scan rate of 1 V s^{-1} (Reprinted from Ref. [53] with the permission of the American Chemical Society)

5.2 XANES and EXAFS

A XAS spectrum can be divided into three regions (Fig. 11.10a). For X-ray photons energies $E < E_0$, discrete transitions to unoccupied valence states take place. Nevertheless, useful information can be extracted only in the case of a few elements, such as iron (Fe). For X-ray photons energies near the absorption edge, $E_0 \pm 100$ eV, referred to as the X-ray Absorption Near-Edge Spectroscopy (XANES) region, the excited photoelectrons are strongly backscattered by the surrounding atoms. Because of their low kinetic energy, the photoelectrons feature a long mean free

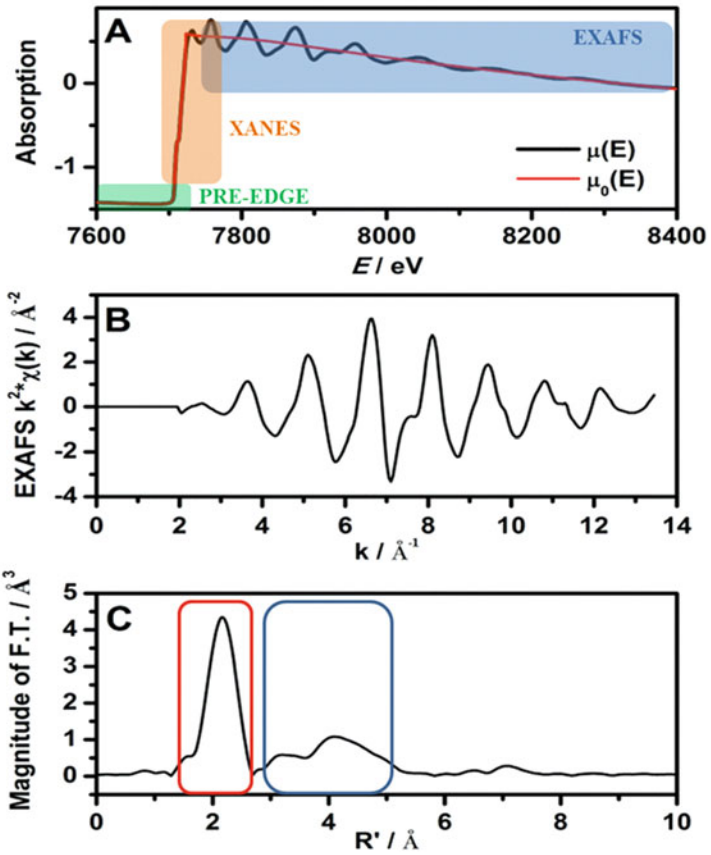

Fig. 11.10 (**a**) Absorption spectrum pattern $\boldsymbol{\mu}(\boldsymbol{E})$ at the K edge of a Co foil (in black). The background function $\boldsymbol{\mu_0}(\boldsymbol{E})$ representing the absorption of an isolated atom is shown in red. The pre-edge, XANES, and EXAFS regions are highlighted in green, orange, and blue, respectively. (**b**) k^2 weighted EXAFS spectrum $\boldsymbol{\chi}(\boldsymbol{k})$. (**c**) Fourier transform of the k^2 weighted EXAFS spectrum. The first and the second atomic shells are circled in red and blue respectively

path allowing them to undergo multiple scattering. Hence, XANES is sensitive to the oxidation state, the orbital occupancy, and the local geometry of the absorbing atom.

Above the absorption edge (up to +1000 eV from the absorption edge), in the so-called Extended X-ray Absorption Fine Structure (EXAFS) region, photoelectrons have high kinetic energy and thus feature a De Broglie wavelength that is comparable to the interatomic distances. EXAFS oscillations are generated by the constructive and destructive interferences between the out-going and the back-scattered photoelectrons (Fig. 11.10b). These $\chi(E)$ oscillations are obtained from the experimental X-ray absorption spectrum $\mu(E)$ after subtraction of an ideal one, $\mu_0(E)$, corresponding to the scattering of a single atom having no neighbor (Fig. 11.10a), according to:

$$\chi(E) = \frac{[\mu(E) - \mu_0(E)]}{\mu_0(E)} \tag{11.8}$$

The determination of $\mu_0(E)$ is a critical step. Nevertheless, even though this term cannot be measured experimentally, many dedicated softwares allow approximating it.

From a practical point of view, EXAFS oscillations are usually expressed as a function of the k wave vector of the photoelectron:

$$k = \sqrt{\frac{2m(E - E_0)}{\hbar^2}} \tag{11.9}$$

Moreover, the EXAFS signal is usually weighted by a factor k^x ($x = 1$, 2 or 3, see Fig. 11.10b) to exalt the oscillations of coming neighboring atoms of different weights. This mathematical operation comes from the fact that interactions of a scattering atom with a light element occurs at low k, while interactions with a heavy element show up at high k.

Going a step further in the analysis, the EXAFS signal $\chi(k)$ is the sum of sinusoidal contributions. Its mathematic description can be obtained after simplification of Fermi's golden rule. In the case of a K edge, the EXAFS signal simplifies as follows:

$$\chi(k) = -\sum_j \frac{1}{kR_j 2} N_j * e^{-\frac{2R_j}{\lambda}} * e^{-2\sigma_j{}^2 k^2} * \left|f_j(k,\pi)\right| \sin\left(2kR_j + \Phi_j(k)\right) \tag{11.10}$$

Equation 11.9 is the sum over j different terms corresponding each to the contribution of one atomic shell. In this sum, there are theoretical parameters $f_j(k, \pi)$, $\Phi_j(k)$, and λ which are the effective backscattering amplitude, the effective scattering phase shift, and the electronic mean free path, respectively, and structural parameters of interest for experimentalists (N_j, σ_j, R_j which are the coordination number in the shell j, the mean squared displacement, and Debye Waller parameter).

The EXAFS signal is then Fourier-transformed to obtain a signal in the R space where each peak corresponds to the contribution of one shell of interaction (see Fig. 11.10c). These interactions can be simple (an ejected photoelectron interacts with one neighboring atom and is then backscattered to its initial position) or multiple. The peaks are then fitted with a dedicated software based on ab initio calculations to extract the structural parameters of interest.

5.3 Spectroelectrochemical Cells

Various cell designs have been developed that allow measuring simultaneously XAS and electrochemical signals. When considering applications in electrocatalysis, most of these designs use a liquid electrolyte (although one can find recently few examples of solid electrolyte PEMFC [56, 57] or battery [58] based designs for operando XAS

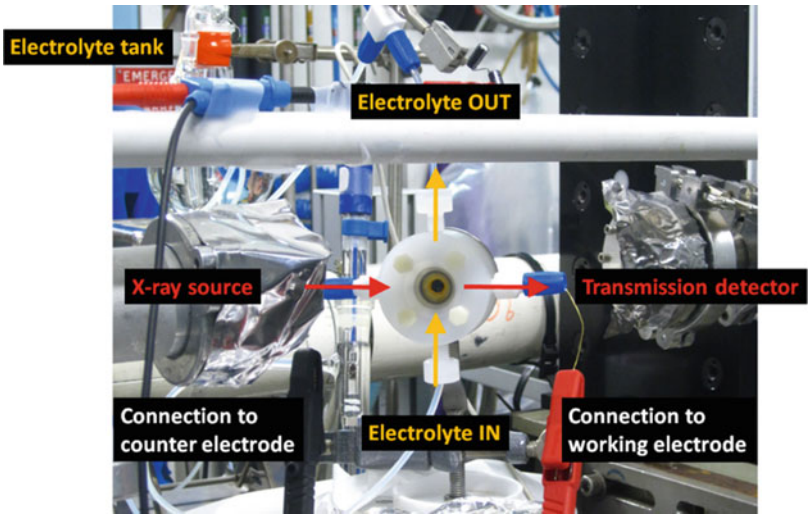

Fig. 11.11 Picture of a spectroelectrochemical cell during in situ XAS measurements at the beamline BM30B of the European Synchrotron Radiation Facility (ESRF)

measurements), hence minimization of the X-ray beam absorption by the electrolyte is of major concern. The quantity of liquid electrolyte should be neither too low, to allow establishment of the electrical potential, and minimize mass-transport limitations, nor too high to maximize the total edge jump [57, 59–64]. A typical spectroelectrochemical cell developed for in situ XAS measurements at the beamline BM30B of the European Synchrotron Radiation Facility (ESRF) is shown in Fig. 11.11.

This cell may be positioned at an angle of 45° with respect to the incident X-ray beam, so as to enable simultaneous measurements in transmission and in fluorescence modes. A gold (Au) ring is used as a current collector on the front-side of the working electrode (here Pt_3Co/C nanoparticles sprayed on a proton-exchange membrane), a Pt wire is used as counter electrode, and a mercury sulfate electrode (MSE), deported from the cell, is used as reference electrode.

5.4 In Situ XAS Measurements on Carbon-Supported Pt-Alloys

5.4.1 Monitoring Adsorption of Surface Oxides on Pt_3Co/C by XANES

To show that XAS is able to capture fine changes in structure (from EXAFS) and adsorbate coverage (from XANES), we take the example of Pt_3Co/C nanoparticles employed to electrocatalyze the ORR at the cathode of a PEMFC. The interest for Pt_xM alloys (M being an early or late transition metal) stems from studies published in the late 1980s–1990s, which have shown that alloying a transition metal to Pt weakens the chemisorption energy of oxygenated species and thus enhances the ORR kinetic current [60, 61, 65–68]. However, dissolution of the element alloyed to Pt in the harsh environment of a PEMFC cathode (low pH, acidic environment, high

electrode potential) leads to a rapid decline in ORR activity, and puts into question the alloying strategy [69, 70].

All XANES and EXAFS spectra presented in the following have been collected on Pt_3Co/C nanoparticles purchased from Tanaka Kikinzoku Kogyo (reference number TEC36E52). These nanoparticles have crystallite size <5 nm (see left column of Fig. 11.5). Before their use, they were first immersed overnight in a stirred 1 M H_2SO_4 solution at $T = 333$ K. As shown by electron energy loss spectroscopy in spectrum-imaging mode (EELS-SI) [38, 71], this procedure caused removal of Co atoms within the first 2–3 monolayers and thus formation of a core@shell structure where a Pt-rich shell covers a PtCo core with a chemical composition close to the nominal. As we will see, this core@shell nanostructure does not ensure stability of the chemical composition of the nanoparticles either in simulated or in real PEMFC operating conditions [34, 35, 38, 70, 72]. A suspension of acid-treated catalyst was mixed with Nafion® ionomer solution, water and isopropanol, ultrasonically treated and then sprayed on a Nafion® XL proton exchange membrane to reach a loading of ca. 5 mgPt_3Co cm^{-2}. Such a high loading is necessary to overcome the absorption from the electrolyte and record enough X-ray photons at both the Co K and Pt L_{III} edges.

Two potential programs were applied to demonstrate the sensitivity of XAS to structural and electronic changes occurring on the Pt_3Co/C nanoparticles with sizes <5 nm. In the first potential program, the potential was linearly increased from 0.60 V to 1.20 V versus the reversible hydrogen electrode (RHE) and then decreased to 0.40 V versus RHE at a sweep rate $v = 0.1$ mV s^{-1}. Meanwhile, quick XANES spectra (30 s each) were continuously recorded first at the Pt L_{III}-edge and then at the Co K edge. In the second potential program, the Pt_3Co/C electrode was polarized at fixed potentials from 0.60 to 1.40 V versus RHE using 0.10 V steps. After each step, the electrode potential was stepped back at 0.60 V versus RHE to ensure that surface oxides were fully reduced and achieve reproducible surface state. During these steps, EXAFS spectra were collected at the Pt L_{III}- and the Co K edges.

Changes of the XANES features at the Pt L_{III} and Co K edges recorded during the potential program #1 are displayed in Fig. 11.12a, b, respectively. Qualitatively, one sees that the Pt L_{III} absorption edge intensity follows well the applied potential profile: first an increase, which signs for an overall oxidation of the Pt atoms, followed by a decrease. Similar results have been observed on pure Pt/C catalysts [60, 61, 73]. In contrast, the XANES features at the Co K edge remain unchanged during the entire potential program, thereby suggesting no oxidation of Co atoms. This set of results confirms the Pt_3Co core@Pt-rich shell nanostructure described above.

A more quantitative analysis can be obtained by superimposing the Pt L_{III} edge intensity and the currents associated to the formation/reduction of surface oxides as displayed in Fig. 11.13a.

The changes in current (increase in current starting from $E > 0.85$ V versus RHE in the positive-going potential sweep and decrease in current below 0.90 V versus RHE in the negative-going potential sweep) indicate that water molecules are dissociated and reduced as:

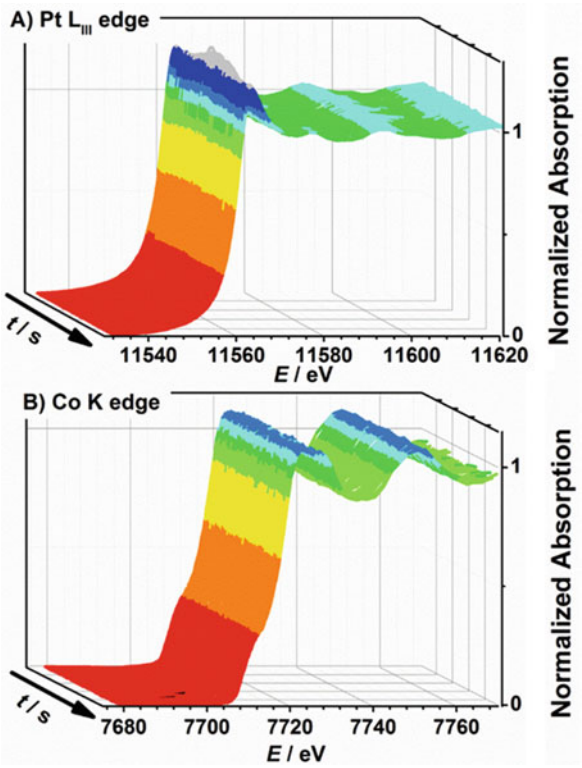

Fig. 11.12 Time-resolved XANES spectra recorded at the (**a**) Pt L_{III} and (**b**) Co K edges during the potential program #1 (potential cycling with linear profile between 0.6 and 1.2 V vs. RHE)

$$H_2O + {}^* \leftrightarrow OH^* + H^+ + e^- \tag{11.11}$$

Here, * denotes a surface site prone to dissociate water molecules yielding adsorbed OH-group (OH*). The variation of the electrochemical charge associated with the formation/reduction of surface oxides was determined from the measured electrochemical currents corrected from pseudo-capacitive processes (see the dashed grey areas in Fig. 11.13a), and is displayed in Fig. 11.13b. In the same plot, the changes in the Pt L_{III} white line intensity with respect to the first spectra collected at 0.6 V versus RHE are reported (Fig. 11.13c). As one can see, changes of the electrochemical charge and the Pt L_{III} white line intensity are clearly correlated, indicating that XANES is sensitive to the adsorption of OH_{ads} in good agreement with literature [62, 74, 75].

5.4.2 Monitoring Structural Changes of Pt_3Co/C Electrodes by EXAFS

Figures 11.14 and 11.15 show the k^2-weighted EXAFS and the Fourier transforms of the k^2-weighted EXAFS oscillations recorded on the Pt_3Co/C electrode during the potential program #2 (stepwise variation of the electrochemical potential between 0.40 and 1.40 V vs. RHE). The EXAFS oscillations were extracted at the Co K

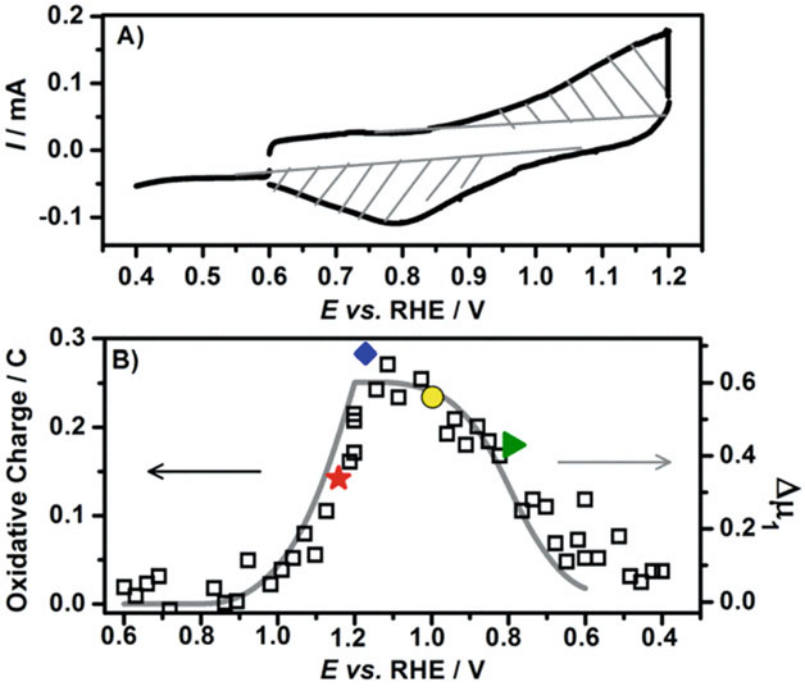

Fig. 11.13 Variation of (**a**) the current, (**b**) the electrical charge, and $\Delta\mu_1$ (open black squares) peak intensity during procedure #1

(Figs. 11.14a and 11.15a) and at the Pt L_{III} (Figs. 11.14b and 11.15b) edges. The insets in Fig. 11.15a, b correspond to the fit of the experimental data in the ranges $2.7 < k < 10.9$ Å^{-1} for Co and $3.2 < k < 11.5$ Å^{-1} for Pt.

From a first qualitative analysis of these results, the Fourier transformed magnitudes of the $k^2\chi$ (k) EXAFS spectra recorded at the Co K edge suggest no oxidation of Co atoms up to $E > 1.30$ V versus RHE (Fig. 11.15a). In order to be more quantitative, the number of closest Pt and Co neighbors ($N_{Co\text{-}Pt}$ and $N_{Co\text{-}Co}$ respectively) and the total coordination number ($N_{Co} = N_{Co\text{-}Pt} + N_{Co\text{-}Co}$) were determined from fitting of EXAFS oscillations at the Co K edge: the increase of these parameters towards those taken by a bulk crystal is another proof that no Co atoms are present in the first monolayers of this catalyst (Fig. 11.16a). In contrast, the $k^2\chi$ (k) EXAFS spectra recorded at the Pt L_{III} edge indicate formation of Pt-O bonds for $E \geq 1.0$ V versus RHE (see Fig. 11.15b with the peak at $R = 1.6$ A). The total coordination number of Pt atoms determined from fitting of EXAFS oscillations at the Pt L_{III} edge is well below 12. This arises from the equal contribution of both surface and bulk atoms (Fig. 11.16b).

Interestingly, one can observe a continuous increase of the N_{Co} and total coordination numbers upon the test which may be rationalized by considering thickening of the Pt-rich shell covering the Pt_3Co core nanostructure during the potential

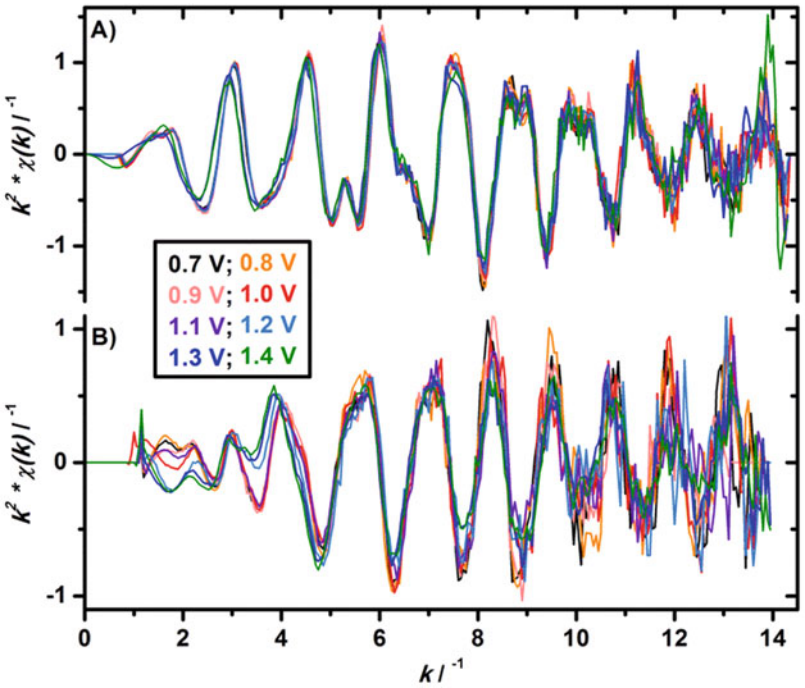

Fig. 11.14 Series of k^2-weighted EXAFS spectra recorded at several electrode potentials at the (**a**) Co K edge and (**b**) at Pt L_{III} edge during the stepwise oxidation protocol

program #2 [71]. Indeed, Co and Pt atoms located in the surface and subsurface regions are prone to dissolve at high electrode potential $E > 1.10$ V versus RHE but only Pt ionic species are thermodynamically allowed to redeposit during potential steps at 0.60 V versus RHE (the standard potential for Co atoms is −0.27 V versus the normal hydrogen electrode [76]). Therefore, during potential cycling, the surface and subsurface regions of the catalyst are depleted in Co, yielding increase of the total coordination number of Co atoms up to $N_{Co} = 11.9 + 1.4$ (Fig. 11.16). No change of the number of closest Pt and Co neighbors ($N_{Pt\text{-}Pt}$ and $N_{Pt\text{-}Co}$ respectively) and the total coordination number ($N_{Pt} = N_{Pt–Pt} + N_{Pt–Co}$) of Pt atoms in the course of the experiment further supports this theory. Moreover, the formation of Pt-O bonds is clearly evidenced (see increase in the F.T. magnitude at 2.5 angstroms in Fig. 11.15b and the resulting increase of $N_{Pt–O}$ in Fig. 11.16b) at electrochemical potentials higher than 1.10 V versus RHE, this process being accompanied by a decrease of $N_{Pt–Pt}$.

5.4.3 Using XANES to Determine Compositional Variations

Since XAS white line intensity scales with the atomic concentrations of the probed element (Eq. 11.5), this parameter could be a guide to follow in situ the chemical composition of the samples [71]. Changes of the chemical composition of the

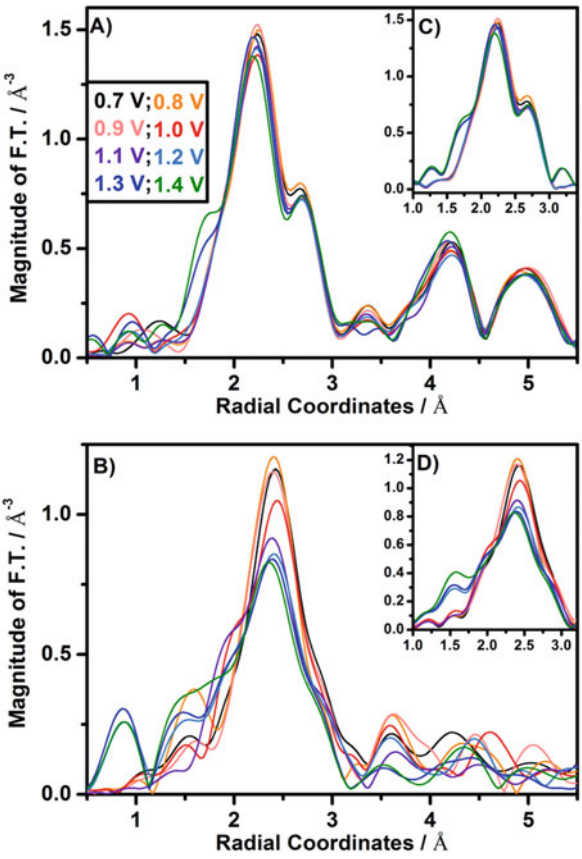

Fig. 11.15 Series of Fourier transformed magnitudes of the $k^2\chi$ (k) EXAFS spectra recorded at several electrode potential at the (**a**) Co K edge and (**b**) Pt L_{III} edge over the course of the stepwise oxidation protocol. The fits of the first shell coordination are displayed in (**c**, **d**) for the Co K and Pt L_{III} edges, respectively

catalyst were followed during potential program #2 and are reported in Table 11.1. The Co content of the catalyst continuously decreases during this protocol. As explained in literature, the higher oxophilicity of Co atoms relative to Pt atoms drives their surface segregation at high electrochemical potentials [34, 35, 72]. Note that each Co atom reaching the surface is instantaneously leached out in the acidic electrolyte.

The same approach was used to determine the atomic composition of Pt_3Co/C catalysts aged at the cathode of a PEMFC during operation in order to gain some insights on the kinetics of Co dissolution. Here, approx. 100 mg of Pt_3Co/C catalyst powder at different life stages was collected on aged gas diffusion electrodes and were then examined by XAS ex-situ. The determined composition of these aged catalysts (Table 11.2) suggests that under this specific aging condition (constant current $j = 0.60$ A cm^{-2} for $t = 3422$ h), the leaching of Co atoms occurs during the first 1000 h of operation, and that an equilibrium composition of $Pt_{83}Co_{17}$ is reached later on. Regarding the fine structure of these materials, this could be indicative of a thickening of their Pt outer shell.

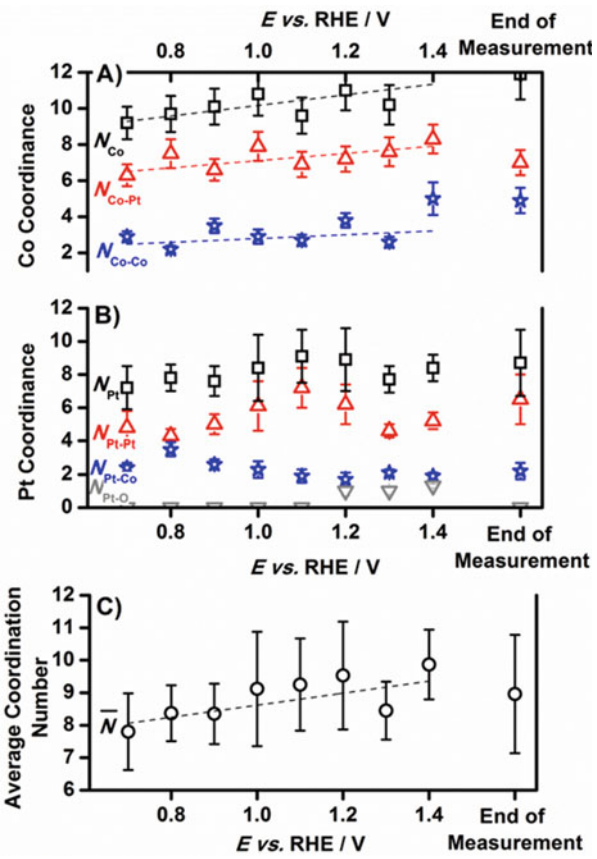

Fig. 11.16 Co and Pt coordination numbers in the Pt_3Co/C sample as a function of the electrode potential, recorded during the stepwise oxidation procedure

Table 11.1 Operando determination of the atomic composition of the nanocatalysts based on the XAS jump intensities measured at the Co K and Pt L_{III} edges in transmission mode during potential program #2 (for more details on atomic composition determination, see Ref. [71])

	0.7 V	0.8 V	0.9 V	1.0 V	1.1 V	1.2 V	1.3 V	1.4. V
At. Comp.	$Pt_{77}Co_{23}$	$Pt_{74}Co_{26}$	$Pt_{72}Co_{28}$	$Pt_{72}Co_{28}$	$Pt_{72}Co_{28}$	$Pt_{71}Co_{29}$	$Pt_{65}Co_{35}$	$Pt_{73}Co_{27}$

Table 11.2 Atomic composition of PtCo/C nanoparticles before and after operation in a real PEMFC stack. The PEMFC stack was operated at constant current $j = 0.60$ A cm^{-2} and temperature $T = 353$ K for $t = 3422$ h. The chemical compositions were determined based on the intensity of the white line at the Pt L_{III} edge (J_{Pt}) and the Co K edge (J_{Co})

	J_{Pt}	J_{Co}	At. Comp. by XAS jump
Fresh	0.06	0.0179	$Pt_{71}Co_{29}$
After conditioning	0.057	0.0187	$Pt_{70}Co_{30}$
After 1163 h	0.06	0.01	$Pt_{82}Co_{18}$
After 2259 h	0.057	0.007	$Pt_{84}Co_{16}$
After 3422 h	0.053	0.008	$Pt_{83}Co_{17}$

6 In Situ Fourier Transform Infrared Spectroscopy (FTIRS)

6.1 Introduction

In situ monitoring of the liquid (electrolyte)-solid (electrode) interface is a crucial point for the successful development of electrochemical devices. Beyond the traditional electrochemical methods that provide valuable potentiometric and amperometric data, in situ infrared spectroscopy at electrochemical interfaces provides accessible means to study both surface and solution electrochemical species. In particular, this technique has found valuable uses on molecular adsorption on electrodes and electrode reactions as it enables the identification of chemical species (adsorbates and reaction intermediates) formed under the influence of electric fields, thereby affording information of interfacial processes. Since the pioneering work of Bewick et al. [77, 78] in situ FTIR spectroscopy coupled to the electrochemical measurement has therefore been extensively used.

Initially, the coupling of infrared reflection techniques and electrochemical measurements was met with uncertainty because it was believed that the strong absorption of aqueous electrolytes in infrared region would prevent the measurement of infrared vibration bands arising from chemical species of interest. To overcome this problem, Bewick and coworkers [77, 78] suggested the electrode to be set very close to the IR window, forming a very thin layer (ca. l–10 μm) of electrolyte solution between electrode and window. Using this idea, the in situ IR method was developed in the late 1970s. The background compensation was undertaken by subtracting two single beam spectra of the sample, collected at two different potentials. The spectra were then obtained by scanning the frequencies while the potential was modulated at ca. 10 Hz. This procedure called Electrochemically Modulated Infrared Spectroscopy (EMIRS) was the first experimental technique to successfully demonstrate the coupling of infrared spectroscopy and electrochemistry. The electro-sorption of different chemical species on platinum electrodes and the electrochemical generation of long-lived intermediates were studied by using a square wave potential modulation applied to the electrode in a thin-electrolyte layer external reflection spectroelectrochemical cell [79–81]. Using dispersive spectrometers infrared absorbance changes on the order of 10^{-4} were then adequately measured for a variety of electrochemical systems by using the fact that band centers for surface features usually shift with changes of the applied potential, while the background features remain unchanged. However, the necessity of using a thin layer configuration introduces the problem of a relatively high resistance in the electrolyte, and hence, an enlarged time response. Moreover, subtracting two spectra obtained using this procedure resulted in bipolar bands for adsorbed species, from which important parameters such as band center frequency, band intensity, and band width could not be properly determined.

Although the point of the signal-to-noise ratio is still considered as one of the challenges to overcome when using infrared spectroscopy for in situ electrochemical studies, the ability of various potential modulation techniques and instrument improvements made it possible to recover small signals in large-amplitude

backgrounds. Examples of potential modulation techniques include single potential alteration infrared spectroscopy (SPAIRS) [82, 83], subtractively normalized interfacial Fourier transform infrared spectroscopy (SNIFTIRS) [84–87], and multistep FTIRS (MS-FTIRS) [88]. Furthermore, the development of Fourier Transform (FT) instruments provided the means to overcome problems caused by potential modulation [84, 86, 89]. Due to the high rate of spectral collection with FT spectrometers, spectra can be obtained by collecting the desired number of interferometer scans at given fixed potentials. Typically, one interferometer scan at 4–8 cm^{-1} resolution takes some tenths of a second. With the advent of Fourier Transform Infrared (FTIR) spectrometers, better detectors and infrared sources, in situ FTIR has become a readily accessible and recognized tool for studying electrochemical interfaces.

6.2 Methods

6.2.1 Internal and External Reflection Infrared In Situ Spectroelectrochemistry

Successful implementation of FTIRS to study the solid-liquid interface requires overcoming the two major experimental problems associated with signal-to-noise ratio:

- The large bulk solvent absorption of infrared radiation. Aqueous solvents are especially problematic as water absorbs strongly throughout the mid-infrared region.
- Sensitivity. The number of molecules under study is typically very small.

Indeed, the reflected IR energy is strongly absorbed by species in the electrolyte solution, but it is also partially lost during reflection at the electrode surface and therefore IR signal arising from the adsorbed species on the electrode surface is very weak. These two problems have motivated the two predominant methodologies for infrared in situ spectroelectrochemistry, internal and external reflection (Fig. 11.17), to overcome the electrolyte absorption problem [90]. In the external reflection configuration (also called infrared reflection-absorption spectroscopy: IRRAS), an incident beam is transmitted through an infrared transparent window (such as a CaF_2 or a ZnSe window) and electrolyte layer and is then reflected off the electrode passing back through the electrolyte and window before being collected at the detector. A very thin layer (1–10 μm) between the IR window and the reflective electrode is typically used to limit the thickness of electrolyte that the infrared radiation must pass through. In practice, electrochemical measurements in such a thin-layer cell become kinetically hindered due to the high resistance of the thin volume of electrolyte and nonuniform accessibility of the electrode (i.e., restricted mass transport). This approach enables nevertheless the simultaneous determination of both adsorbed and solution species although ideal electrochemical behavior has to be sacrificed [83, 91–94]. Besides the potential-induced concentration changes due

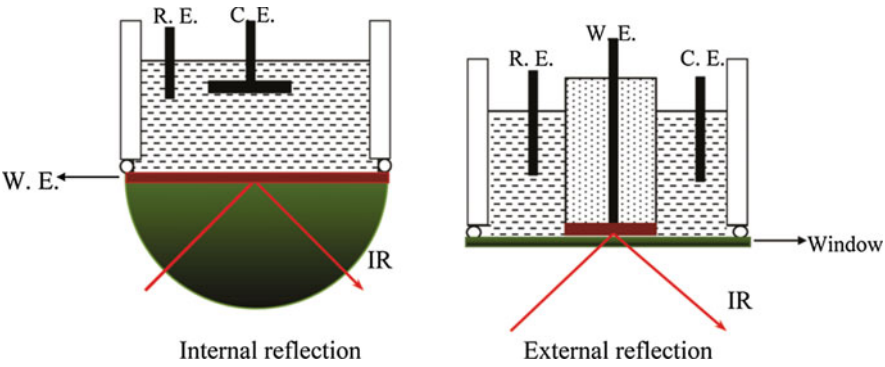

Fig. 11.17 Schematic diagrams of in situ FTIRS cell with internal and external reflection configurations (Reprinted from Ref. [90] with the permission of the American Chemical Society)

to the species under study, surface faradaic reactions of the electrode material contribute to disturb the thin layer. In this configuration the use of highly reflective electrodes coupled with weak signal determination methods such as potential or polarization modulation are used in order to improve the signal-to-noise ratio of spectra.

Internal reflection geometries (also termed attenuated total-internal reflection, ATR), in contrast do not suffer of the same limitations. In ATR, the incident infrared beam is directed onto an infrared transparent crystal (internal reflection element; IRE) with a relatively high refractive index (i.e., Si: 3.4, Ge: 4.0, ZnSe: 2.4). The infrared beam reflects from an internal surface of the crystal and an evanescent wave is produced that projects orthogonally through the reflecting surface. This evanescent wave can interact with the metal film placed on top of the reflecting plane and the returning reflected beam measured at the detector. It is important that the angle of incidence is equal to or greater than the critical angle of the interface. If the critical angle is not met, the resulting spectrum could result only from the external reflectance. Both the angle of incidence and infrared polarization play a crucial role in the optimization of ATR measurements. For completeness, the penetration depth (d_p) of the evanescent wave is often discussed when considering ATR techniques. The wavelength dependence on the depth into the sample is given by the Eq. 11.12:

$$d_p = \frac{\lambda}{2\pi\left(n_1^2 \sin^2\theta - n_2^2\right)^{1/2}} \tag{11.12}$$

where λ is the wavelength of the incident light, θ the angle of incidence, and n_1 and n_2 are the refractive indices of the crystal and sample, respectively. Typical penetration values for mid-infrared radiation are on the order of a few microns and demonstrate some level of surface sensitivity as a result. Materials that are suitable for ATR optical elements must be infrared transparent and have high refractive indices excluding most conductive materials that are commonly used as electrodes

substrates. However, ATR substrates can be modified by the deposition of a thin layer of metal such as gold or platinum. Once the infrared reflection element (IRE) has been suitably modified it is relatively simple to adjust it to a suitable electrochemical cell. ATR techniques are relatively exempt to bulk electrolyte absorption as the infrared radiation does not pass directly through the electrolyte. Furthermore, if the metal film is suitably structured, ATR optical geometry can take advantage of the Surface Enhanced Infrared Absorption Spectroscopy (SEIRAS) [95, 96] giving rise to very low detection limits.

6.2.2 Potential Modulation Techniques

Potential modulation infrared techniques such as EMIRS were limited to the observation of reversible potential-induced spectral changes, resulting from the need to modulate the potential back and forth over the range of interest so as to minimize the bulk-phase spectral interference. Instead, in order to gain information on the possible role of adsorbed species in the irreversible electrooxidation (or electroreduction) pathways it is necessary to employ in situ infrared spectral techniques that can sense irreversible potential-induced changes in the surface composition while the electrode reaction is proceeding. The first proposed technique suitable for this purpose was PM-IRRAS (polarization modulation infrared reflection absorption spectroscopy) [97–99] procedure that achieves the necessary subtraction of bulk-phase spectral interferences by rapid alteration of the polarization of the incident beam. Although less sensitive than potential-difference methods, PM-IRRAS has the important feature of enabling absolute spectra to be obtained at a given electrode potential. Kunimatsu [100] has employed PM-IRRAS to examine the potential-dependent CO coverage in relation to the "steady-state" electrooxidation rate of formic acid and methanol on platinum. This method was shown to be suitable for examining such potential-induced irreversible changes in the surface composition but the time taken to record each spectrum limits its mechanistic utility. Such irreversible electrode processes can be examined conveniently by sweeping or stepping the potential from an initial value where no reaction occurs by using potential-modulation techniques such as SNIFTIRS [84–87] or MS-FTIRS [88]. Potential-modulation FTIR spectra can also be obtained by applying a single potential excursion during the spectral acquisition, which is called the SPAIR procedure [82, 83]. These techniques involve obtaining a sequence of single-beam FTIR spectra at a potential value or during the potential sweep and referencing these to a spectrum obtained at the initial potential or after complete oxidation had occurred. In particular, SPAIR spectra obtained during potential sweep indicate the onset oxidation or reduction of a molecule of interest. The SPAIR procedure is also currently employed to monitor the oxidative removal of adsorbed carbon monoxide.

In addition, the potential-difference procedure is usually employed in order to increase the S/N ratio and to subtract a strong background coming from the electrolyte IR absorption. The interferograms are then collected respectively at reference potential (E_{ref}) and sample potential (E). Usually, E_{ref} is chosen as the potential at which the adsorbates are stable or no reaction occurs, and E is the potential at which oxidation/reduction of adsorbates or reagent stakes place. In order to improve the

S/N, which is proportional to square root of the number of interferograms (n) collected, a large number of interferograms is collected and co-added at each of the two potential values. The Fourier transform of the coadded interferogram yields the single beam spectrum at E_{ref} and E. Finally, the resulting spectrum is then calculated as:

$$\frac{\Delta R}{R} = \frac{R\left(E_{ref}\right) - R\left(E\right)}{R\left(E_{ref}\right)} \tag{11.13}$$

6.2.3 Time-Resolved In Situ FTIR Spectroelectrochemistry

In practice, electrochemical response depends on the configuration of IR electrolytic cell [101, 102]. Thanks to the rapid potential response and free mass transfer, the ATR configuration is currently preponderant in temporal measurements. For example, Osawa et al. [103] have first reported in situ step-scan time-resolved FTIR spectra with sub-millisecond resolution utilizing an IR cell of ATR configuration. Time constants of the IR cell and time resolution of IR spectra through ATR approaches of about 50 μs were reported [104, 105]. A limitation of the ATR configuration consists nevertheless in its application scope as it is inherently limited to electrodes of thin metal film deposited on ATR IRE or some bulk semiconductor material. In contrast, thin-layer IR cell is universally used in static measurements, since any type of material including thin metal films, bulk materials, conductive polymers, and carbon materials, etc., can be employed as electrodes in this configuration. Also, single-crystal electrodes can be employed and the effect of crystallography on the structure of adsorbed layers can be studied. Unfortunately, the large cell time constant (typically several 10 ms) originated from thin layer solution between IR window and electrode has greatly hampered its application in transient investigations. Although some flow cells were proposed to enhance the mass transfer rate [106, 107], the response of electrode potential to alternation remained unsatisfactory for transient studies due to the large time constant of these flow thin-layer IR cells. Some early attempts have also been paid to study dynamic processes of electrochemical reactions by using time-resolved IR techniques employing thin layer IR cells [108, 109] but short-lived intermediates and fast kinetics were hardly investigated until recently due to the still large time constants of IR cells. Zhou et al. have first reported the development of an electrochemical in situ step-scan time-resolved microscope FTIR reflection spectroscopy (in situ SSTR-MFTIRS) [110], which consists of a FTIR spectrometer with step-scan facility, an infrared microscope, a home-made signal synchronizer, and a thin-layer IR cell working with a microelectrode (Fig. 11.18). The employment of microelectrode has overcome successfully the inherent disadvantages of thin-layer IR cell in transient response. The time constant of the thin-layer IR cell could be reduced and the time resolution of IR spectra reached 10 μs. The reported results illustrated that the in situ SSTR-MFTIRS is a suitable tool for studying fast dynamic processes and kinetics of electrochemical reactions at molecular level [111].

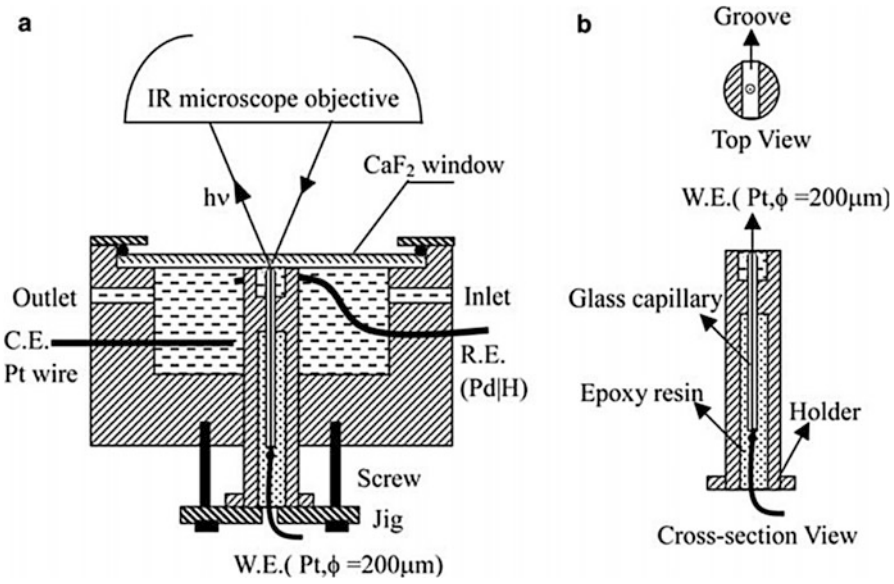

Fig. 11.18 Schematic illustrations in situ spectroelectrochemical cell (**a**) and Pt microelectrode (**b**) (Reprinted from Ref. [110] with the permission of Elsevier)

6.3 In Situ FTIRS Studies of the Electrooxidation Organic Molecules

IR absorption related to the state of the electrode surface or to the electrochemical reactions at a given electrode potential during organic molecules electrooxidation is typically detected by steady-state FTIR methods. Examples of this can be found in the electroxidation of methanol, ethanol, ethylene glycol, glycerol, or glucose (fuel molecules) as in situ FTIRS has been largely used to probe the reaction intermediates and pathways on new kinds of electrocatalysts and fuel molecules and therefore obtain mechanistic insights.

6.3.1 Ethanol Electrooxidation

Ethanol is a molecule which undergoes structure and composition sensitive parallel reactions during its electrooxidation [112]. Breaking of the C-C bond, which is necessary to complete oxidation of the ethanol molecule to CO_2, is the principal challenge for direct ethanol fuel cells but soluble acetaldehyde and acetic acid are the main products in the partial oxidation pathway reactions. It has been reported that Pt and Pd nanoparticles enclosed by high-index-facets exhibit enhanced catalytic activity towards ethanol electrooxidation as they can promote the cleavage of C-C bond and produce therefore more CO_2 than low-index planes nanoparticles [113, 114]. In situ FTIRS experiments were undertaken by Zhou et al. [115] to

Table 11.3 Assignment of IR bands typically observed in the spectra for ethanol oxidation in acidic medium

Wavenumbers (cm^{-1})	Assignment	
1044	ν (C–O)	CH_3CH_2OH
2343	ν_{as} (O=C=O)	CO_2
1720	ν (C=O)	CH_3COOH, CH_3CHO
1392	δ_{as} (CH_3)	
1370	δ_s (CH_3)	
1280	ν (C–O)	CH_3COOH
~2050	ν (CO)	Linearly adsorbed CO **on Pt**

confirm the pathway for ethanol electrooxidation on high index-faceted Pt NPs supported on carbon black catalyst as compared to commercial Pt/C catalyst.

Numerous studies on the electrooxidation of ethanol have been devoted mainly to identifying the adsorbed intermediates and elucidating the reaction mechanism by means of various techniques, including in situ FTIR spectroscopy [116–124]. Briefly, the main FTIR features related to ethanol oxidation products in acidic media, listed in Table 11.3, are: the O=C=O asymmetric stretching at 2343 cm^{-1} reflecting the cleavage of the C-C bond for ethanol oxidation; the CO stretching of adsorbed CO at about 2050 cm^{-1} for CO linearly adsorbed on Pt; the CO stretching at 1720 cm^{-1} attributed to the C=O bond in acetic acid and acetaldehyde; the H–O–H bending from interfacial water present inside the thin layer at 1650 cm^{-1}; the C = O stretching of acetic acid in solution at 1280 cm^{-1}. Furthermore a band at 1044 cm^{-1} corresponding to the signature peak for the C–O stretching vibration of CH_3CH_2OH, confirming its consumption by oxidation, is generally present and CH_3 symmetric and asymmetric vibration modes (at 1370 and 1390 cm^{-1}, respectively) might also be observed. For purposes of following the end-oxidation products, attention is generally focus on the bands centered at 2343 and 1280 cm^{-1}, which are associated to the formation of CO_2 and acetic acid, respectively [116]. Obviously, more CO_2 and less acetic acid are formed on most effective catalysts for ethanol oxidation and consequently the ratio of band intensities of CO_2 to acetic acid should increase. The in situ FTIRS results are therefore suitable to reveal catalysts having enhanced activity for breaking the C-C bond in ethanol.

In recent years studies of ethanol electrooxidation in alkaline media have been undertaken, mostly motivated for the perspective of finding alternative catalysts for the scarce and expensive noble metals. In situ FTIR spectroelectrochemistry was then applied to investigate the dissociation and oxidation of CH_3CH_2OH in alkaline media, aiming to clarify the reaction mechanism with a focus on the crucial intermediate species [119, 121, 124].

Ren et al. studied the H-D kinetic isotope effects on electrooxidation of ethanol on Au, Pd, and Pt electrodes in alkaline solution by combining cyclic voltammetry and in situ FTIRS measurements [125]. They revealed that the cleavage of the α-C–H bond from C–H bond is the rate determining step (RDS) for alcohol electrooxidation on Au electrodes, but not on Pt and Pd electrodes. The authors attributed this

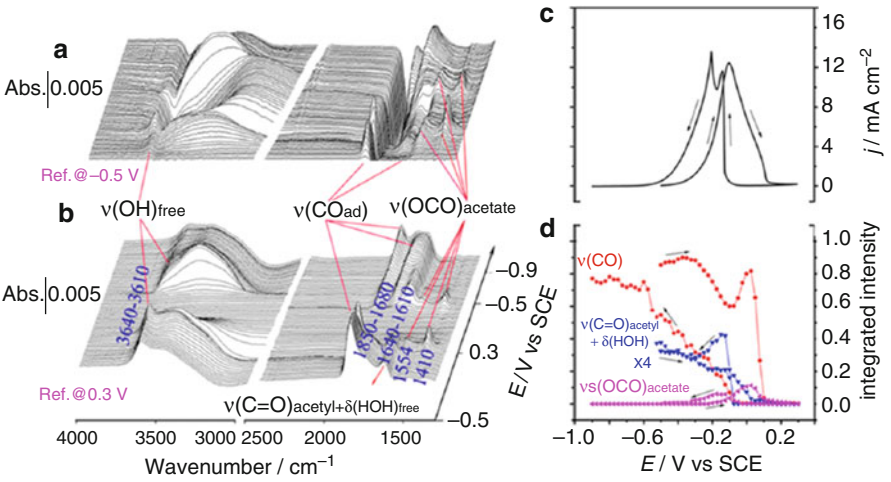

Fig. 11.19 In situ ATR SEIRA spectra obtained with a time resolution of 5 s on a Pd electrode in 0.1 mol L^{-1} NaOH/0.5 mol L^{-1} CH_3CH_2OH solution taking the single-beam spectrum at −0.5 V/SCE (**a**) and −0.3 V/SCE as reference. (**c**) Corresponding cyclic voltammogram recorded at 5 mV/s and (**d**) potential-dependent band intensities for $\nu(CO_{ad})$, $\nu_s(OCO)$ of adsorbed acetate, and $\nu(C{=}O)$ acetyl + δ (HOH) (Reprinted from Ref. [119] with the permission of the American Chemical Society)

difference to the different binding affinity of hydrogen on electrodes surfaces. More recently Yang et al. investigated the ethanol oxidation on Pd electrode with in situ attenuated total reflection (ATR) surface-enhanced infrared absorption spectroscopy coupled with H-D isotope replacement [119]. Real time in situ spectroelectrochemical measurements of ethanol oxidation on Pd electrode in alkaline media revealed that the IR bands appearing within 1 s at 2980, 2120, 2209, 1377, 1452, 1153, and 1046 cm^{-1} correspond to interfacial CH_3CH_2OH or CH_3CD_2OH (Fig. 11.17, Table 11.1 of reference [119]). Then, the band of multiply bonded CO_{ad} species arising from the ethanol dissociation appeared at 1671 cm^{-1}, and its intensity increased with a gradual frequency shift to 1844 cm^{-1} while the band arising at 1625 cm^{-1} and assigned to adsorbed acetyl species was also observed. Their observations suggested that surface ethanol first turns into adsorbed acetyl through fast dehydrogenation on α-C at Pd electrode, and the as-generated acetyl successively dissociates into α-CO_{ad} and carbonaceous fragments by C–C bond cleavage. Potentiodynamic ATR-SEIRA spectra for ethanol electrooxidation at the Pd electrode reported by Yang et al. [119] are shown in Fig. 11.19. On the basis of previous reports, the different observed IR features were assigned as follows: 1410 and 1554 cm^{-1} bands can be attributed to $\nu_s(OCO)$ of bridge-bonded acetate and $\nu_{as}(OCO)$ of solution acetate, respectively; the 1354 cm^{-1} band was assigned to the in-plane bending vibrations of the -CH3 group of the adsorbed acetate [$\delta(CH_3)$], and the 1671–1844 cm^{-1} band is due to CO_{ad} species [$\nu(CO_{ad})$]. As previously stated, the $\nu(C{=}O)$ acetyl vibration is mainly responsible for the observed 1610–1640 cm^{-1} band, in addition to a minor contribution from δ(HOH) of interfacial water.

Taking into account the results obtained by means of in situ FTIR spectroscopic methods the authors concluded that ethanol may undergo dehydrogenation to form adsorbed acetyl followed by a successive decomposition to C1 species, including CO_{ad} and CH_x. As the potential becomes more positive, the adsorbed acetyl is a crucial intermediate that may be converted to either acetate in the C2 pathway or carbonate (IR absorption band at 1390–1420 cm^{-1} that superimposes to ν_s(OCO) of acetate) via the C1 species adsorbed, and CH_x may also be converted to CO_{ad} species at high potentials. Thus, despite different intermediates, the reaction pathways for ethanol electrooxidation on the Pd electrode in alkaline media are more or less similar to that on the Pt electrode in basic and acidic media.

6.3.2 Glycerol Electrooxidation

Glycerol oxidation is made up of complex pathway reactions that can produce a large number of useful intermediates or valuable fine chemicals. Coupling electrochemical methods to analytical and in situ spectroscopic FTIR [126–132] measurements enables to identify the intermediate species and the final reaction products which is helpful to evaluate the activity of an electrode catalyst towards organics and to get insights into the reaction mechanism. This knowledge can also help tailoring a catalyst composition for a selective reaction process to valuable products. During the last years the combination of electrochemical measurements and in situ spectroscopic techniques has been largely reported to study glycerol electrooxidation [128–131, 133–136].

Gomes and Tremiliosi-Filho [130] proposed on the basis of spectroscopic studies that the selectivity of the glycerol oxidation reaction over platinum was not dependent of the pH value. In acidic as well as in alkaline media, tartronic acid (tartronate), glycolic acid (glycolate), glyoxylic acid (glyoxylate), formic acid (formate), and carbon dioxide (carbonate) were formed. Contrarily, Kwon et al. [128] found that the mechanism and the selectivity of glycerol oxidation on platinum depended on the pH value: glycerate produced via glyceraldehyde pathway was shown to be the main product in alkaline media and glyceraldehyde became the main reaction product as the pH value was decreased.

By means of in situ infrared spectroscopy Simoes et al. [133] observed the same absorption bands on Pd/C as on Pt/C electrocatalysts and concluded that the same mechanism was involved on both catalysts. In both cases, an absorption band located at 1335 cm^{-1} and assigned to the presence of dihydroxyacetone species on the electrode or at the vicinity of the electrode were present from the onset of glycerol oxidation to higher potentials (1.15 V vs. RHE), indicating that the carbon bearing the secondary alcohol group could also be oxidized at the platinum and palladium surfaces. In the same work, the authors also claimed the presence of hydroxypyruvate during the electrooxidation of glycerol on gold nanoparticles based on the IR absorption band at 1350 cm^{-1}.

Recently, Holade et al. [136] concluded by means of in situ spectroelectrochemical experiments that the pathway for the electrooxidation of glycerol on Pd-based materials in alkaline medium is the glyceraldehyde one. Figure 11.20 displays the single potential alteration infrared spectra (SPAIRS) obtained for Pd/C and $Pd_{60}Ni_{40}$/C

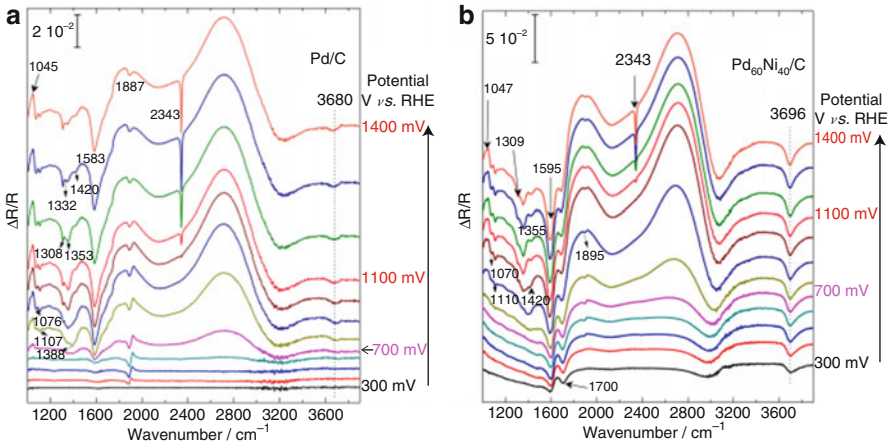

Fig. 11.20 SPAIR spectra recorded during glycerol oxidation in 0.1 mol L^{-1} NaOH electrolyte containing 0.1 mol L^{-1} of glycerol on (**a**) Pd/C and (**b**) $Pd_{60}Ni_{40}/C$ (Reprinted from Ref. [136] with the permission of the American Chemical Society)

catalysts during glycerol oxidation in alkaline medium reported by Holade et al. [136]. The first important result was that adsorbed CO is formed at low potential values (ca. 0.40 V vs. RHE for Pd/C and 0.50 V vs. RHE for PdNi/C) indicating the cleavage of C-C bond as reported in literature [137, 138]. Indeed, the band at about 1887 cm^{-1} on Pd/C and 1895 cm^{-1} on $Pd_{60}Ni_{40}/C$ is attributed to bridged CO (μ_2–(CO)) resulting from the rapid dissociative adsorption of glycerol at low potential values. Another important result was the evidence of CO_2 production on the different nanocatalysts (asymmetric stretching band at 2343 cm^{-1} wavenumber) [130, 131]. This band appears at about 1.0 V versus RHE for bimetallic compositions and at about 1.1 V versus RHE for the monometallic composition and corresponds to the decrease of the absorbed CO band. According to Demarconnay et al. [139] CO_2 appears in alkaline medium as soon as carbonate (1390–1420 cm^{-1} band) [131, 139] could not be further formed due to the lack of OH^-. Indeed, Jeffery and Camara [131] have proved by simple calculation in the thin interfacial layer (IR window-electrode interface) that the depletion of OH^- is enough to justify a sensible pH change during glycerol electro-oxidation in alkaline medium. One can furthermore recognize the O-H stretching vibration band of carboxylic acid towards 3000 cm^{-1} confirming the acidification of the thin layer. It was there clearly shown that (i) adsorbed CO is formed during the oxidation of glycerol for Pd-bases nanocatalysts, which results in poisoning of the catalysts at low potential values, (ii) the main reaction products are glycolate (1076 cm^{-1}, 1326 cm^{-1}, and 1410 cm^{-1} bands) and glycerate (1107 cm^{-1}, 1380 cm^{-1}, and 1416 cm^{-1} bands) and carbonate as shown in the FTIR spectra. These spectra also evidenced small amounts of oxalate (sharp band at 1308 cm^{-1}) and formate (1350, 1382 cm^{-1}). It should be stated that the intense band at 1583 cm^{-1} is characteristic of different carboxylate ions and might also include a contribution of the water bending vibration. For potential values higher than 1.0 V versus RHE CO_2

formation takes place while the amount of glycolate increases. A broad vibration band is also clearly visible between 1650 and 1720 cm^{-1} indicating the presence of adsorbed glyceraldehyde and carbonyl species. Finally, the positive going bands at 1050 and 2700 cm^{-1} are attributed to glycerol and OH^- consumption [131, 133, 137, 139], whereas the band at about 3700 cm^{-1} corresponds to water stretching vibrations. The spectra obtained for the bimetallic catalyst were similar to those obtained for the Pd/C material. The major difference occurs at low potentials values. Indeed, for potentials values ranging from 0.3 to 0.7 V versus RHE two main absorption bands at 1595 and 1700 cm^{-1} (assigned to different carboxylates and adsorbed carbonyl species, respectively) are observed for PdNi/C while for Pd/C the main absorption band corresponds to adsorbed CO.

More recently, Palma et al. [140] reported that changes of the catalyst noble metal (Pd or Pt) makes suitable selectivity towards the glycerol electrooxidation with the possibility of utilizing it in cogeneration processes for renewable energy sources and selective production of added-value molecules. Indeed they provided spectroscopic and analytical evidences that Pt-Ru material has excellent catalytic ability towards a selective oxidation of the secondary alcohol to di-hydroxyacetone, while Pd-Ru anode favors the glycerate production.

6.3.3 In Situ FTIRS Studies of CO_2 Electroreduction

The electrocatalytic reduction of CO_2 has been attracting great interest in the last years. Indeed, CO_2 is a greenhouse gas and its emission has been growing along with the increase in global energy demand. Numerous studies report the development of electrochemical and photochemical metallic or molecular catalysts for efficient CO_2 reduction. For CO_2 electroreduction in situ FTIRS is an efficient approach to get insights on the reaction process as it will help to reveal the mechanism of CO_2 reduction and open the view for designing more effective catalyst. Innocent et al. [141] proposed a reaction mechanism of selective hydrogenation of HCO_3^- to $HCOO^-$ on lead electrode in aqueous media by taking into account the bands of species present in various spectra obtained with in situ IR reflectance spectroscopy. The disappearance of the band ascribed to CO_2 when applying a cathodic electrode potential gave evidence that CO_2 was not absorbed nor is it the electroreducible species on the lead electrode surface. Accordingly, formate was the exclusive organic species identified during chronoamperometry/FTIRS experiments at 1.6 V versus SCE in aqueous or deuterated medium. The same authors also investigated the electroreduction of carbon dioxide at the surface of a Pb electrode in propylene carbonate, an aprotic solvent, by combining a voltammetry study and the in situ FTIR reflectance spectroscopy measurements [142]. In spite of difficulties to differentiate the specific bands of the solvent and those resulting from the adsorption of carbon dioxide, it was shown by FTIR spectroscopy that the main reaction product was oxalate. The chronoamperometry/FTIRS experiment was shown to be a suitable technique to provide evidence of the consumption of carbon dioxide. When applying an electrode potential of −2.5 V versus Ag/AgCl during 300 s, the decrease in the CO_2 IR absorption band intensity (2341 cm^{-1}) was observed, while that attributable to oxalate appearing at 1642 cm^{-1} increased. In addition, the reduction process in a

0.2 mol L^{-1} TEAP-PrC solution at the Pb metallic surface leads selectively to the dimerization of CO_2. The adsorbed species determined by in situ FTIRS measurements supported the proposed mechanism of the reaction in aprotic medium.

On the other hand, Xiang and coworkers [143] reported that 6,7- dimethyl-4-hydroxy-2-mercaptopteridine (PTE) was an effective electrocatalyst for the reduction of CO_2 without the involvement of any metal. They performed bulk electrolysis of a saturated CO_2 solution in the presence of the PTE catalyst and found that it produces methanol with a Faradaic efficiency of 10–23%. FTIR spectroelectrochemistry was used to detect the progression of two-electron reduction products during bulk electrolysis, including formate (1350 and 1370 cm^{-1} IR absorption bands), aqueous formaldehyde (1442 cm^{-1} IR absorption band), and methanol (1466 cm^{-1} IR absorption band). A transient intermediate was also detected by FTIR (at 1625 cm^{-1}) and assigned as a PTE carbamate.

Very recently, Firet and Smith [144] probed surface bound intermediates of the electrocatalytic CO_2 reduction reaction on a Ag thin film catalyst by means of operando ATR-FTIR measurements in an electrochemical cell. The IR signals of the reaction intermediates were large enough to discern as the Ag catalyst was deposited directly on the ATR crystal. They were able to detect both Ag-H and Ag-CO intermediates that lead directly to the formation of H_2 and CO, respectively (Fig. 11.21). In the potential range between −1.40 V and −1.55 V versus Ag/AgCl, COOH* was observed as the only reaction intermediate while at applied potential of −1.6 V versus Ag/AgCl, COO−* intermediate was also observed (Fig. 11.21).

Indeed the large peak at 1288 cm^{-1} observed in spectra of Fig. 11.21 was assigned to the C−OH stretch of COOH. The inverse water peak (H−O−H bend) that was present in the N_2 spectrum at −1.45 V at 1652 cm^{-1} seemed to broaden with the presence of flowing CO_2 at −1.45 V, to show a combination of the H−O−H bend and a C=O asymmetric stretch at 1660 cm^{-1} that was assigned to the COOH* intermediate. Therefore the combined peaks at 1288 and 1660 cm^{-1} indicated that the COOH* intermediate is present during the CO_2 reduction on the Ag film. The peak at 1386 cm^{-1} was more difficult to assign and was shown to correspond to adsorbed COO^-.

Based on their results, the authors proposed that the reaction mechanism of CO_2 reduction to CO on a thin film Ag catalyst is a one-step proton coupled electron transfer when the applied potential is between −1.40 V and −1.55 V versus Ag/AgCl, and at more negative potentials the reaction follows the two-step mechanism where COO−* is formed before COOH*. Besides these results show that operando spectroscopic techniques can be a very valuable tool in elucidating the interplay between the catalyst and the applied potential during the electrochemical CO_2 reduction reaction.

6.4 In Situ FTIRS for Catalysts' Characterization

In situ FTIRS can be also used to characterize electrocatalysts by using a suitable probe molecule. Among the possible probe molecules, CO is definitely the most

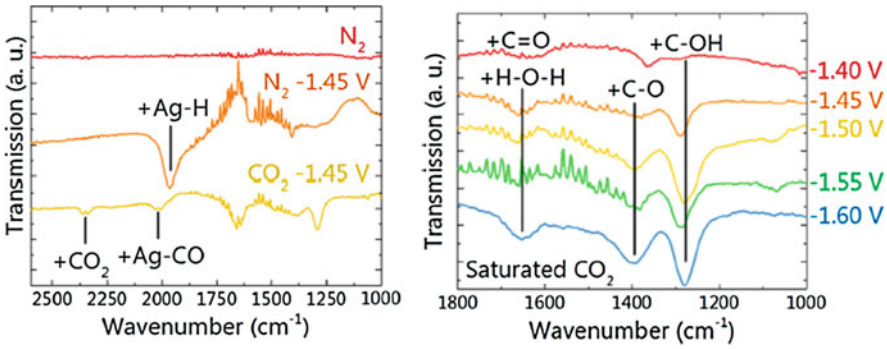

Fig. 11.21 (Left) Assignments of reactants and products present during ATR-FTIR experiments in 0.1 mol L^{-1} KCl. The red line is a spectrum taken during N_2 flow where the background was also taken during N_2. The orange spectrum was taken 20 min after a potential of 1.45 V versus Ag/AgCl is applied, with the red line as background spectrum. The yellow spectrum was taken 20 min after a CO_2 is introduced to the cell. (Right) ATR transmission spectra in saturated CO_2 0.1 mol L^{-1} KCl electrolyte at different potentials showing the peaks that belong to the CO_2 reduction intermediates. The background for these spectra was taken after 30 min at the same potential under a nitrogen purge (Reprinted from Ref. [144] with the permission of the American Chemical Society)

attractive one in electrocatalysis field area for several reasons. The first reason is that CO is the poisonous intermediate involved in oxidation or dissociation of most organic molecules. Secondly, the empty $2\pi^*$ orbital of CO can accept *d*-electrons from transition metals to form d-π^* back-donation bond, enhancing consequently the interaction between CO and transition metals. Finally, CO electrooxidation is a surface structure sensitive reaction. It has been reported that, for CO adsorption on basal planes of Pt single crystal, bridge-bonded CO (CO_B) is favorable on Pt(111) and Pt(100) [145], while linearly bonded CO(CO_L) is dominant on Pt(110) single crystal electrode [146]. Among anode catalysts, Pt-Ru catalyst is one of the best candidates in regard to the CO-tolerance. As proposed by Watanabe and confirmed by in situ FTIRS measurements [147], the oxidation of adsorbed CO at Pt sites is facilitated by oxygen species adsorbed at Ru sites (Ru-OH) in the so-called bifunctional mechanism. Due to the strong IR absorption of the CO stretching mode the in situ FTIRS employing CO as probe molecule has provided invaluable information on characterizing transition metal catalysts.

Ma et al. [148] used in situ FTIRS employing CO as a probe molecule to obtain microscopic level information regarding the interaction between the catalytic site and the probe chemisorbed molecule as it is well stated that the measured vibration frequency (position of the absorption band in the FTIR spectrum) would strongly depend on the electronic properties of the adsorption site, and therefore any eventual shift in this band should be correlated with the modification of the electron density of Pt by Ti or Se atoms. The obtained spectra showed in each case the band characteristic of the stretching of CO linearly bound to Pt (COL) in the 2050–2070 cm^{-1} range. A slight shift (6 cm^{-1} at 0.1 V vs. RHE) of this CO_L band towards higher frequencies was observed for the Pt_xTi_y/C and Pt_xSe_y/C as compared to Pt/C

indicating a weaker CO adsorption. A second band occurring at higher wavenumber values (2072–2085 cm^{-1}) was also clearly visible for the Pt_xTi_y/C catalyst. The occurrence of this higher frequency mode indicates a weaker bound state of CO on Pt nanoparticles (NPs) sites. The obtained CO_L stretching band positions are plotted in Fig. 11.22 as a function of the electrode potential. The inset shows the corresponding spectrum recorded at 0.5 V versus RHE in the CO_L stretching region. It should be noted that a particular band shifts towards higher wavenumbers with the increase of the applied electrode potential at constant CO_{ad} coverage (Stark shift), and it also shifts in a continuous manner to lower frequencies as the coverage decreases. Indeed, as the number of adsorbed molecules decreases, the competition for the electrons of surface atoms also decreases so that there is more charge available to put into each adsorption site with the consequence that the C–O stretching frequency decreases. The obtained band position evolution during the CO electrooxidation can be explained by these two processes. At low potential values, before the beginning of the oxidation the position of a particular band increases therefore linearly with the increase of the potential, and the obtained slope gives an indication of the CO dipole–dipole interaction. In the reported case, the obtained slopes were similar for all the materials and we can therefore conclude that the difference observed in the CO_L band frequency may indeed be explained by the electronic modification of the Pt NPs. Integrated CO_L and CO_2 IR bands' intensities were also depicted in Fig. 11.22 as a function of the electrode potential for the three materials. For the Pt_xTi_y/C it can been seen that the CO electrooxidation to CO_2 starts at the same potential as compared with Pt/C while the maximum of the CO_2 band intensity curve occurs at slightly lower potential values. The negative shift in the oxidation peak potential and the highest C–O stretching frequency obtained for this material indicate that the presence of titanium has an influence on the electronic properties of platinum in a favorable way so as to improve its tolerance towards carbon monoxide.

In another work the same authors provided evidence of the strong interaction between platinum and graphitic domains modifying the electronic properties of platinum nanoparticles by means of CO stripping experiments coupled with in situ FTIR measurements [149].

Finally, in a very recently reported work the effect of the gradual reduction of graphene oxide on the CO tolerance of Pt NPs was studied using several spectroscopic techniques, including in situ FTIR [150]. The authors used the in situ technique to probe the "electronic state" of platinum centers as an eventual shift in the absorption band of CO adsorbed on Pt should indicate their electronic modification resulting from the interaction with the support. Indeed, an electronic influence of the support modifying the electron density nearby the Fermi level should affect the extent of the backdonation of 5d electrons from platinum to the CO antibonding orbitals and therefore the Pt-CO binding. Although there is no straightforward correlation between the adsorbed CO stretching frequency and Pt-CO binding energy it is commonly accepted, as stated before, that the backdonation of metal electrons into CO antibonding orbitals stabilizes the metal-molecule bond and weakens the CO bond resulting therefore in a decreased CO vibration frequency.

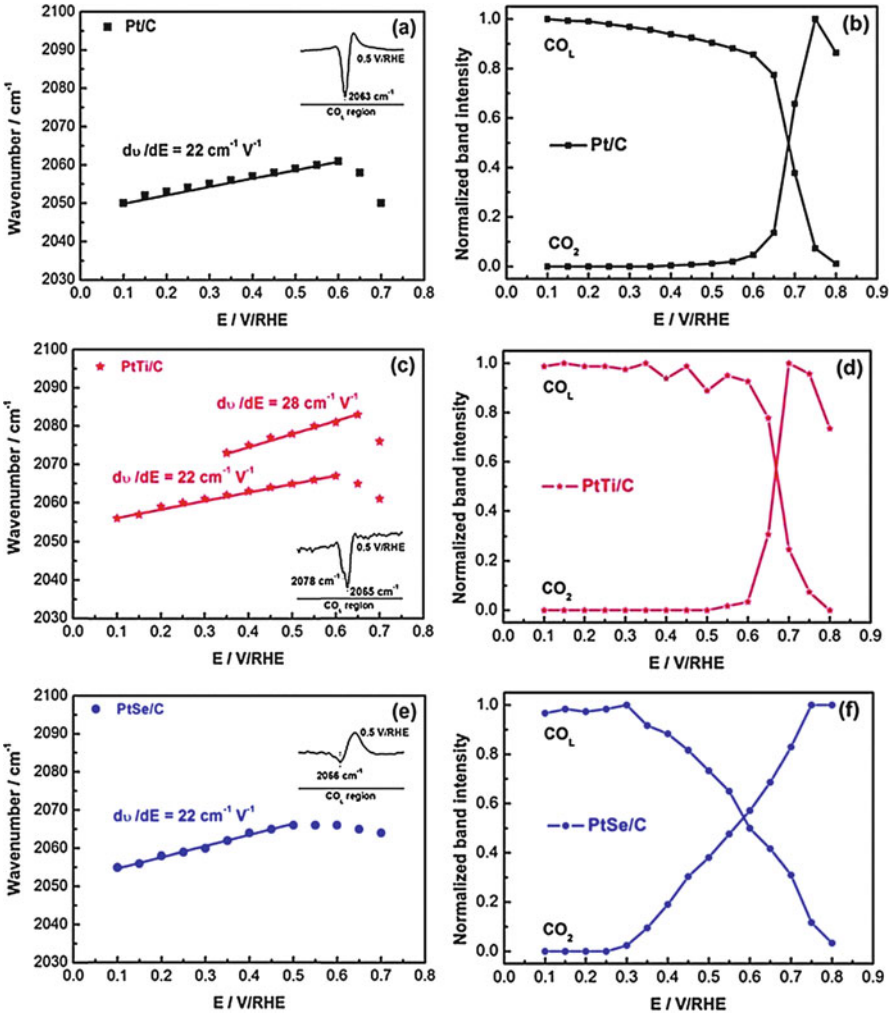

Fig. 11.22 Potential dependence of the C–O stretching wavenumber for on-top CO_L for Pt/C, Pt_xTi_y/C, and Pt_xSe_y/C catalysts (**a**), (**c**), (**e**) (inset curves show the corresponding in situ FTIR spectrum recorded at 0.5 V versus RHE during oxidative stripping of CO absorbed on the investigated catalysts). Normalized CO_L and CO_2 band intensities calculated from FTIR spectra as a function of the electrode potential (**b**), (**d**), (**f**). (Reprinted from Ref. [148] with the permission the Royal Society of Chemistry)

Based on the obtained results the authors concluded that for oxidized carbon-based substrates, a decrease of the p-electron density on the carbon-based materials was responsible for increasing charge transfer between Pt and carbon, engendering the observed increase in the adsorption strength of CO molecule.

Vibration spectra of adsorbed species reflect therefore the state of internal and external bonds, the lateral interactions within the adlayer, as well as the effect of the external electric field on the vibration frequencies and intensities. This information gives valuable data for a molecular picture of the electrochemical double-layer and contributes to an improved understanding of the physicochemical properties of the electrified interface.

7 Composition-Selectivity Correlation of Nanocatalysts for Carbon Dioxide Electroreduction and Ethanol Electrooxidation Determined by On-Line DEMS

7.1 Principle of the Differential Electrochemical Mass Spectrometry (DEMS)

The Differential Electrochemical Mass Spectrometry (DEMS) technique combines electrochemical experiments with mass spectrometry. It allows the on-line detection of gaseous or volatile products from different electrochemical reactions, including nanoparticle-catalyzed electrode reactions.

The study of the electrode reaction pathways may involve not only the investigation of the electrochemical variable such faradaic current, voltage, and charge, but also the nature and quantity of the products generated at the electrode surface. The determination of reaction products can be accomplished by using chromatographic methods, after experiments of bulk electrolysis. However, in this procedure, some reaction intermediates can be reactive with other species in the electrolyte solution or suffer additional steps of readsorption, and this causes a difficulty in the interpretation and distinction of the reaction pathways/mechanism. In order to overcome this limitation, Bruckenstein and Gadde [151] coupled an electrochemical cell with a mass spectrometer by using a porous hydrophobic electrode interface. This apparatus allowed quantitative analysis of volatile and gaseous reaction products, generated during electrochemical reactions. Wolter and Heitbaum [152], also using a porous hydrophobic electrode as the interface, have found that the adaptation of a mass spectrometer with two pumping stages (two turbomolecular pumped vacuum chambers) resulted in fast response times. This enabled on-line and instantaneous analysis of the gaseous or volatile products as a function of the electrode potential, and named this technique as Differential Electrochemical Mass Spectrometry (DEMS).

Different equipment setups can be employed, but in the most of the cases, an adapted electrochemical cell, with a hydrophobic porous electrode interface, is first connected to a pre-chamber (pressure normally at 10^{-4}–10^{-5} mBar during operation), which is connected to a main chamber (pressure normally at 10^{-5}–10^{-6} mBar) via a small hole (ca. 3.0 mm diameter; inducing a pressure difference of a hundred times between both chambers), in which is located the mass selector and detector (usually a quadrupole and a faraday cup or an electron multiplier) [153]. In a typical DEMS experiment, the faradaic current versus potential (or vs. time) is simultaneously collected with the ionic current of the mass fragments (selected values of

mass/charge, *m*/*z*, ratios). Several electrochemical methods can be performed according to the reaction in analysis and the monitored mass fragments can, therefore, be registered synchronized with the potential. Also, different electrochemical cells and working electrode/mass spectrometer interfaces have to be constructed, depending on the reaction under investigation and reaction conditions.

Among the different uses and advantages of this technique, one can mention the on-line and fast detection of products of multiple electron transfer reactions. Nanostructured materials, especially metallic nanocatalysts, have attracted considerable attention due to their specific properties and promising activity for practical applications such as energy storage/conversion systems [154–156]. Several research groups have shown the importance of the performance analysis of these metallic nanocatalysts to produce high-value added products from CO_2 reduction and to catalyze the conversion of chemical to electrical energy on fuel cells. In this part of the chapter, we will present some results obtained for the detection of the reaction products by DEMS of electrocatalytic reactions of CO_2 reduction and ethanol electrooxidation.

7.2 Monitoring the Electrocatalyst Selectivity for the CO_2 Electroreduction to CO Via On-Line DEMS

The electrochemical conversion of CO_2 molecule into useful products can be carried out in aqueous and nonaqueous electrolyte solutions. In aqueous electrolyte, at pH close to 7.0 (in which water is the proton source), the CO_2 electrochemical reduction follows different pathways, producing diverse products, depending on the nature of the nanomaterial used as electrocatalyst. The examples presented in the Eqs. 11.14 and 11.15 are related to the two-electron pathways generating $HCOO^-$ and CO, respectively. More complex pathways are possible, generating hydrocarbons, and they involve multiple steps of hydrogen addition (Eqs. 11.16 and 11.17) [157]. However, by using aqueous electrolyte, the hydrogen evolution reaction (Eq. 11.18, HER) is a possible parallel route, which reduces the faradaic efficiency. Thus, the optimization of electrocatalysts is one of the main challenges for the selective CO_2 electroreduction.

$$CO_2 + H_2O + 2\,e^- \rightarrow HCOO^- + OH^- \qquad -0.43\ V \qquad (11.14)$$

$$CO_2 + H_2O + 2\,e^- \rightarrow CO + 2\,OH^- \qquad -0.52\ V \qquad (11.15)$$

$$CO_2 + 6\,H_2O + 8\,e^- \rightarrow CH_4 + 8\,OH^- \qquad -0.25\ V \qquad (11.16)$$

$$2\,CO_2 + 8\,H_2O + 12\,e^- \rightarrow C_2H_4 + 12\,OH^- \qquad -0.34\ V \qquad (11.17)$$

$$2\,H_2O + 2\,e^- \rightarrow H_2 + 2\,OH^- \qquad -0.41\ V \qquad (11.18)$$

(Potentials vs. standard hydrogen electrode – SHE)

As can be noted, the equilibrium potentials of the electrochemical reduction of CO_2 presented above are close to that of HER. Experimentally, high overpotentials are required and they are related to the high energy associated to the transformation

of linear and stable CO_2 molecule to the bent unstable adsorbed [$CO_2^{\bullet-}$] radical anion. The production of this intermediate, that occurs via 1 e^- transfer ($CO_2 + e^- \rightarrow CO_2^{\bullet-}$, $E = -1.90$ V vs. SHE), is a rate-determining step of the CO_2 electroreduction [157]. Thus, lowering the potential of this initial step is the most challenging aspect for the electrocatalytic CO_2 reduction.

Bulk and/or nanostructured metallic electrocatalysts have been studied as electrocatalysts for the CO_2 electroreduction in aqueous electrolyte [154–156, 158–165]. Basically, the electrocatalysts can be classified according to their hydrogen evolution overpotential and CO adsorption strength [157]: (i) Pb, Hg, In, Sn, Cd, and Bi have high hydrogen overvoltages and negligible CO adsorption strength, producing $HCOO^-$ as the main product; (ii) Au and Ag have medium hydrogen overpotential, and weak CO adsorption properties, producing CO as the main reaction product; (iii) Ni, Fe, and Pt have low hydrogen overpotentials and strong CO adsorption, and, so, the CO_2 electroreduction is negligible compared to the water electroreduction; (iv) Cu has medium hydrogen overvoltages and medium CO adsorption strength, so, it is able to reduce CO_2 to more reduced species such as CH_4 and C_2H_4 [155, 156, 160–165].

Different electrochemical cells and interfaces with the DEMS equipment can be employed for the CO_2 electroreduction study. In a recent work [166], we studied the selective CO_2 electrochemical reduction to CO on metal nanoparticle-catalyzed porous electrode interface in aqueous electrolyte by on-line DEMS. The electrochemical cell was formed by a three-neck round-bottom flask, with a magnetic bar for stirring the electrolyte. The working electrode/mass spectrometer interface consisted of a disk-shaped carbon paper pressed onto a porous (20 nm diameter) polytetrafluoroethylene (PTFE) membrane. This was used as the conductive electrode for the deposition of the powder electrocatalysts. The electrode was positioned onto the top of a stainless steel frit, and two gold ribbons, isolated from the electrolyte, were placed on the electrode edges for the electric contact.

The faradaic and ionic currents for $m/z = 2$ (H_2) and 28 (CO) obtained during DEMS experiments of cyclic voltammetry for the CO_2 electroreduction on synthesized Au/C and Ni/C nanoparticles [167–169] in CO_2-saturated 0.5 mol L^{-1} $KHCO_3$ aqueous electrolyte, at 25 °C, are presented in Fig. 11.23. For both electrocatalysts, it is seen that H_2 (Fig. 11.23b) is produced (via water electroreduction), and it is detected with similar overpotentials. For NiO/C, as the HER is dominant over the CO_2 electroreduction (due to the Ni low HER overpotential and its high CO adsorption) any or insignificant CO is produced. So, the increase in the H_2 signal is accompanied by a decrease of the mass-to-charge ratio 28 (Fig. 11.23c) due to the exhaustion of dissolved CO_2 in the localities of the electrode surface. In the case of the Au/C electrocatalyst, instead, even with parallel H_2 generation, as CO is the major CO_2 reduction product, it is apparent the increase in the ionic current for $m/z = 28$, even with the parallel water reduction, generating H_2.

The CO formation on Au/C was also observed during potentiostatic measurements. Figure 11.24 presents the ionic currents for $m/z = 28$ (CO) and for $m/z = 2$ (H_2), and the imposed electrochemical potential, as a function of time, obtained during DEMS experiments of chronoamperometry for CO_2 electroreduction. As can

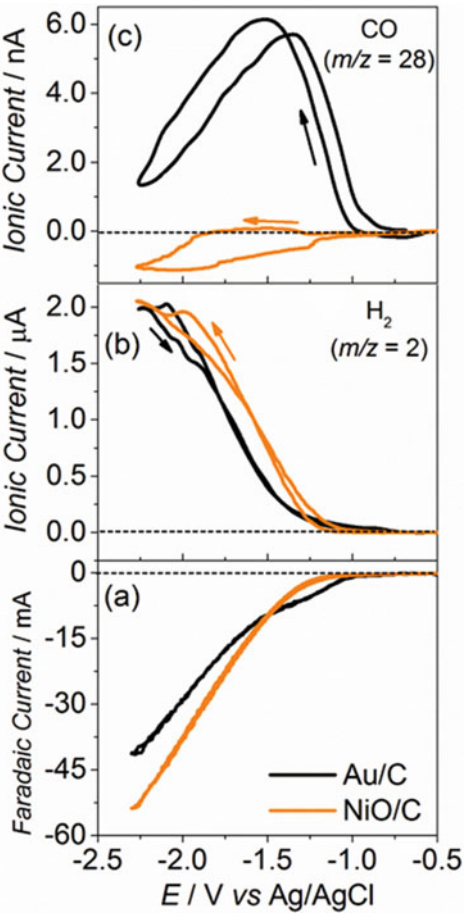

Fig. 11.23 Faradaic and Ionic currents for $m/z = 2$ (H_2) and 28 (CO) acquired during DEMS experiments of cyclic voltammetry at 1.0 mV s^{-1} in CO_2-saturated 0.5 mol L^{-1} $KHCO_3$ electrolyte (25 °C), for the Au/C and NiO/C electrocatalysts (Reproduced with permission from Ref. [166])

be seen, the potential step from OCP to −1.3 V results in a step of the ionic currents due to the CO and H_2 formation originated from the CO_2 and the parallel water electroreduction. The CO signal, nevertheless, undergoes a decrease as a function of time, with the concomitant increase in the signal for H_2 formation ($m/z = 2$), evidencing that the route of CO formation is being suppressed as a function of the time, and further water electroreduction takes place. On the other hand, experimentally, a restoration of the CO signal was observed after potential excursion to higher potential (close to 1.0 V), with the same deactivation behavior in the consecutive measurement of polarization for CO_2 reduction. This deactivation or poisoning of gold during the CO_2 electroreduction to CO was also observed by Kedzierzawski et al. [170], and they stated that an adsorbed reaction intermediate, previous to CO, is likely to be the poisoning species. These results suggest, therefore, that the CO_2 electrochemical reduction studied by the on-line DEMS technique can be used for characterizing the nanoparticle regarding their reactivity for CO adsorption and HER overpotential.

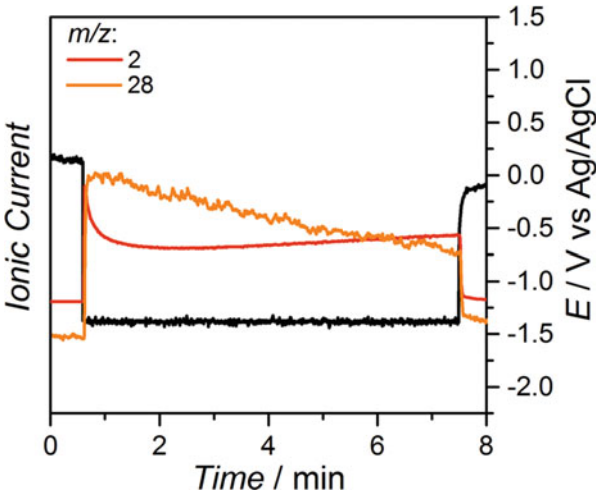

Fig. 11.24 Ionic currents for $m/z = 2$ (H_2) and 28 (CO) and the imposed electrochemical potential (black line), as a function of the time, obtained during DEMS measurements of chronoamperometry in CO_2-saturated 0.1 mol L^{-1} $KHCO_3$ electrolyte at 25 °C for Au/C nanoparticles (Reproduced with permission from Ref. [166])

7.3 Study of the Ethanol Electrooxidation Using DEMS for Indirect Hydrogen Fuel Cells

Ethanol is a renewable fuel and has a high-energy power density. Its direct utilization as fuel in PEMFC (proton exchange membrane fuel cell), however, suffers from a serious drawback related to the sluggish kinetic and low faradaic current efficiency for the complete electrooxidation, lowering the overall fuel cell efficiency [171]. For practical applications, an alternative is its use in indirect hydrogen fuel cells. In this system, the ethanol molecules can be submitted to an external fuel processor, such as a thermal catalytic dehydrogenation and, after a separation step of the by-products (via condensation, for example), the generated H_2 molecules are directed to feed a PEMFC. The dehydrogenation step can be carried out at low temperature (ca. 200 °C) and, by using specific catalysts, be selective to the formation of hydrogen and acetaldehyde or hydrogen and ethyl acetate, for example [172]. Nevertheless, unreacted ethanol and the by-product species might, eventually, not be separated during the condensation step and, so, the PEMFC will be fed with a stream formed by a mixture of H_2 and low quantities of the dehydrogenation by-product vapors. In this case, the fuel cell anode electrocatalyst ought to be active for the H_2 electrooxidation, and tolerant to the presence of the ethanol dehydrogenation by-products. Alternatively, the electrocatalyst can be also active for the electrooxidation of the residual ethanol and of its dehydrogenation by-product (acetaldehyde, for example). Considering that the anode electrocatalyst is based on platinum and that the electrode feed stream will mostly contain H_2, the anode potential during operation will be low. In addition, regular PEMFC, that use Nafion® as electrolyte, will operate at temperatures below 100 °C. On platinum, these conditions will favor the ethanol C-C bond break (C_1-pathway [173]), but the electrooxidative removal of the resulting adsorbed reaction intermediates such as CO and CH_x will not take place (no water activation for the oxygen addition occurs at low potentials). Therefore, the

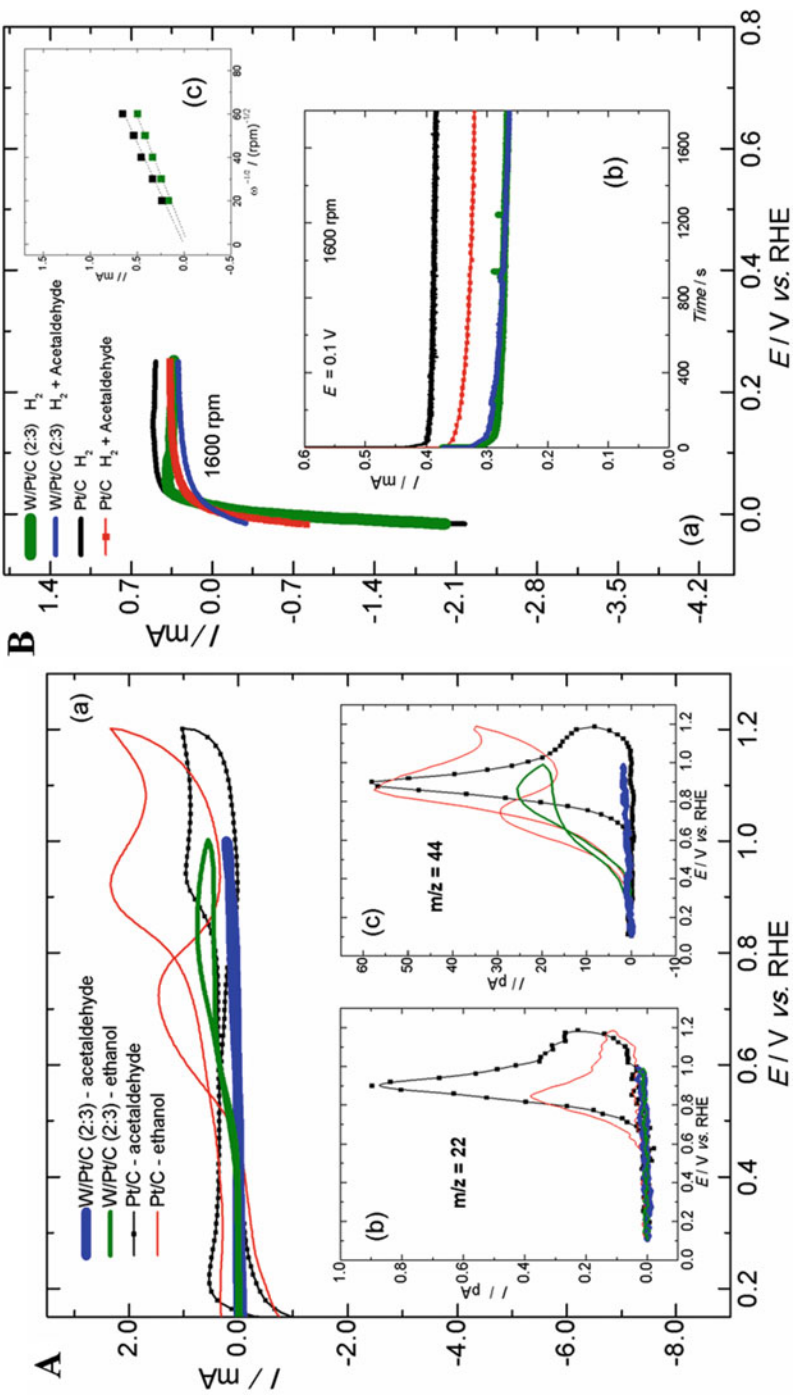

Fig. 11.25 (**a**) Faradaic (*a*) and ionic currents (*b* and *c*) obtained in DEMS measurements during cyclic voltammetry (CV) of ethanol and acetaldehyde electrooxidation catalyzed by W/Pt/C (2:3) Pt/C; $m/z = 22$ (CO_2, CO_2^{2+}) and $m/z = 44$ (CO_2, CO_2^{+} + acetaldehyde, CH_3CHO^{+}) in 0.1 mol L^{-1} ethanol and

use of a nanostructure electrocatalyst that is active for the H_2 electrooxidation and, concomitantly, selectively active for the ethanol (or acetaldehyde, for example) electrooxidation via the C_2-pathway (intact C-C bond) would be viable for such application because it avoids the surface poisoning by CO and or CH_x species.

In view of this scenario, we have synthesized carbon-supported platinum and tungsten-modified platinum nanoparticles, represented here by Pt/C and W/Pt/C (2:3 atomic ratio), respectively. These materials were tested as electrocatalysts for the electrooxidation of ethanol and acetaldehyde, and of H_2 in the presence of these molecules in the electrolyte [174]. The bimetallic material was formed by W-Pt with low W insertion into the Pt lattice (low degree of alloy), superficially decorated by WO_3 nanoclusters, prepared by impregnation methods, followed by thermal treatment in hydrogen atmosphere [175].

Figure 11.25 shows the DEMS results obtained during cyclic voltammetry experiments for the ethanol and acetaldehyde electrooxidation on W/Pt/C in 0.1 mol L^{-1} ethanol or acetaldehyde + in 0.5 mol L^{-1} H_2SO_4 electrolyte, at 25 °C. As can be noted, Pt/C is active for the electrooxidation of both molecules, producing CO_2 (from the electrooxidation of ethanol or acetaldehyde) and acetaldehyde (from the electrooxidation of ethanol) and, therefore, it is not selective for one specific route. W/Pt/C shows lower activity for the ethanol electrooxidation in relation to Pt/C. However, its mass signal for CO_2 ($m/z = 22$) is nearly zero, and acetaldehyde ($m/z = 44$) is the only detectable product (although not shown here, the suppressed C-C bond scission was also evidenced by the absence of methane formation, $m/z = 15$). As mentioned above, the ethanol electrooxidation to CO_2 may involve steps of ethanol adsorption, deprotonation, C-C bond breaking, and oxygen addition. The reaction pathway perturbation brought by the W modification may evidence that the steps of adsorption and deprotonation still occur, but the formation of reactive species such as CH_2CHO_{ads} or $CH_2CH_2O_{ads}$, suggested in a previous work [176], may not occur, suppressing completely the C-C bond dissociation and, consequently, inhibiting the CO_2 production. This result evidences a total deviation from the pathway of CO_2 formation and, so, high selectivity of acetaldehyde formation. Additionally, the W/Pt/C material was barely active for the electrooxidation of acetaldehyde, as noted by the marginal faradaic and ionic signals in Fig. 11.25a. Interestingly, the W/Pt/C electrocatalyst was active for H_2 electrooxidation, and tolerant to the presence of acetaldehyde (due to its inactivity for acetaldehyde electrooxidation), as can be observed in Fig. 11.25b. Contrarily, Pt/C,

Fig. 11.25 (continued) 0.5 mol L^{-1} H_2SO_4 electrolyte at 25 °C. Scan rate of 10 mV s^{-1}. (**b**) Faradaic current obtained during (*a*) CV and (*b*) chronoamperometry in RDE measurements of H_2 or H_2 + 0.1 mol L^{-1} CH_3CHO electrooxidation catalyzed by W/Pt/C (2:3) and Pt/C in 0.5 mol L^{-1} H_2SO_4 electrolyte at 25 °C. The CV measurements were conducted at a scan rate of 10 mV s^{-1} and the chronoamperometric curves were performed at $E = 0.1$ V during 30 min. Rotating rate of 1600 rpm; (*c*) Levich curves for both electrocatalysts showing slight higher inclination for Pt/C, which is ascribed to the electrooxidation of acetaldehyde in parallel to that of H_2 (Reproduced with permission from Ref. [174])

although possessing superior H_2 electrooxidation activity, it suffered a pronounced deactivation of the faradaic current in the presence of acetaldehyde in solution. This is ascribed its low selectivity for the ethanol electrooxidation, producing 1-carbon species, originated from the C-C bond dissociation (of ethanol or acetaldehyde), which poison the electrode surface in the potential domain that the H_2 electrooxidation takes place. Therefore, this material would be useful as a guide or initial point for the development of electrocatalysts for application in the anode of indirect hydrogen PEM fuel cells, as it features the following aspects: (i) is active for H_2 electrooxidation and (ii) is inactive for the C-C bond breaking, which means that it selectively catalyzes the electrooxidation of ethanol and/or acetaldehyde via the C_2-pathway; therefore, it does not suffer the poisoning from 1-carbon intermediate species such as CO and CH_x.

The above-presented results show that the study of the ethanol electrooxidation by on-line DEMS can be utilized as a model study for characterizing the properties of nanostructured electrocatalyst that control the electrochemical reaction activity and selectivity. So, this type of study can be extended to other nanoparticles in order to establish the composition-structure/electrocalytic activity and selectivity correlations.

8 Conclusions and Future Perspective

Electrochemistry offers nowadays various tools and in situ techniques for understanding the surface and morphology of electrode materials at nanoscale. Pure electrochemical tools such as cyclic voltammetry or underpotential deposition of a metallic monolayer are powerful approaches to assess the active surface area and its crystallographic structure. Moreover, IL-TEM is an additional tool which permits to know the morphology of the nanocatalysts before, during, and after the reaction. X-ray absorption spectroscopy is another in situ technique that allows determining (i) the chemical nature and the coverage by specific adsorbates and (ii) the chemical and structural changes occurring under simulated (in situ) or real device (*operando*) operating conditions. Because it allows analysis of the local environment of the different constituents of a multi-element nanomaterial simply by adjusting the beam energy to the specific absorption edge, XAS is also perfectly complementary to electron-based techniques and vibrational spectroscopies. The development of in situ FTIRS allows studying electrooxidation or electroreduction compounds (such as glycerol, ethanol, glucose, CO_2, etc.) on nanocatalysts in order to identify, as function of the electrode potential, the intermediates, the products of reactions and to propose a mechanism. Complementary investigations with on-line DEMS permit the detection of CO during the electroreduction of CO_2 with a strong parallel hydrogen evolution reaction. Additionally, this technique has permitted the on-line and instantaneous monitoring of the ethanol electrooxidation products, and, the selective electrocatalysts for the C_2-pathway, providing evidences of its complementarity with FTIRS in the discrimination of molecules such as CO_2 (m/z = 22; 2343 cm^{-1}) versus CH_3CHO (m/z = 44 or 29; 1720 cm^{-1}). In the near future, the

combination of innovative techniques that provide a molecular level knowledge and the electrochemical interfaces probing appears as a reliable approach to overcome challenges in electrocatalysis.

Acknowledgments T.W. Napporn (IC2MP) thanks Region Poitou Charentes for its financial support for investigating Electrocatalysis of gold nanoparticles. L. Dubau, J. Durst, and F. Maillard (LEPMI) thank Dr. Jean-Louis Hazemann, Dr. Olivier Proux, and all the members of the FAME team for their kind help to the realization of the EXAFS measurements on the beamline BM30B of the European Synchrotron Radiation Facility. F.H.B. Lima and M.R. Camilo (IQSC) acknowledge financial support from FAPESP (Fundação de Amparo à Pesquisa do Estado de São Paulo – Sao Paulo Research Foundation), grants 2016/13323-0, 2013/16930-7, and 2014/26699-3, and CNPq (Conselho Nacional de Desenvolvimento Científico e Tecnológico), grant 306469/2016-2.

References

1. Wadayama T, Todoroki N, Yamada Y, Sugawara T et al (2010) Oxygen reduction reaction activities of Ni/Pt(111) model catalysts fabricated by molecular beam epitaxy. Electrochem Commun 12(8):1112–1115
2. Kang Y, Yang P, Markovic NM, Stamenkovic VR (2016) Shaping electrocatalysis through tailored nanomaterials. Nano Today 11(5):587–600
3. Coutanceau C, Urchaga P, Brimaud S, Baranton S (2012) Colloidal syntheses of shape- and size-controlled Pt nanoparticles for electrocatalysis. Electrocatalysis 3(2):75–87
4. Hernandez J, Solla-Gullon J, Herrero E, Feliu JM et al (2009) In situ surface characterization and oxygen reduction reaction on shape-controlled gold nanoparticles. J Nanosci Nanotechnol 9(4):2256–2273
5. Hebié S, Cornu L, Napporn TW, Rousseau J et al (2013) Insight on the surface structure effect of free gold nanorods on glucose electrooxidation. J Phys Chem C 117(19):9872–9880
6. Urchaga P, Baranton S, Coutanceau C, Jerkiewicz G (2012) Evidence of an eley-rideal mechanism in the stripping of a saturation layer of chemisorbed CO on platinum nanoparticles. Langmuir 28(36):13094–13104
7. Sibert E, Wang L, De Santis M, Soldo-Olivier Y (2014) Mechanisms of the initial steps in the Pd electro-deposition onto Au(111). Electrochim Acta 135(594–603
8. Oliveira VL, Sibert E, Soldo-Olivier Y, Ticianelli EA et al (2016) Borohydride electro-oxidation reaction on Pt(111) and Pt(111) modified by a pseudomorphic Pd monolayer. Electrochim Acta 190:790–796
9. Lopez-Haro M, Guétaz L, Printemps T, Morin A et al (2014) Three-dimensional analysis of Nafion layers in fuel cell electrodes. Nat Commun 5:5229. 1–6
10. Wakisaka M, Asizawa S, Yoneyama T, Uchida H et al (2010) In situ STM observation of the CO Adlayer on a Pt(110) electrode in 0.1 M HClO4 solution. Langmuir 26 (12):9191–9194
11. Li D, Jia SJ, Fodjo EK, Xu H et al (2016) In situ SERS and X-ray photoelectron spectroscopy studies on the pH-dependant adsorption of anthraquinone-2-carboxylic acid on silver electrode. Appl Surf Sci 367:153–159
12. Sánchez-Sánchez CM, Vidal-Iglesias FJ, Solla-Gullón J, Montiel V et al (2010) Scanning electrochemical microscopy for studying electrocatalysis on shape-controlled gold nanoparticles and nanorods. Electrochim Acta 55(27):8252–8257
13. Urchaga P, Baranton S, Coutanceau C (2013) Changes in COchem oxidative stripping activity induced by reconstruction of Pt (111) and (100) surface nanodomains. Electrochim Acta 92 (438–445

14. Hebié S, Napporn TW, Morais C, Kokoh KB (2016) Size-dependent Electrocatalytic activity of free gold nanoparticles for the glucose oxidation reaction. ChemPhysChem 17 (10):1454–1462
15. Hamelin A (1996) Cyclic voltammetry at gold single-crystal surfaces. Part 1. Behaviour at low-index faces. J Electroanal Chem 407(1–2):1–11
16. Hebié S, Kokoh KB, Servat K, Napporn T (2013) Shape-dependent electrocatalytic activity of free gold nanoparticles toward glucose oxidation. Gold Bull 46(4):311–318
17. Maillard F, Savinova ER, Stimming U (2007) CO monolayer oxidation on Pt nanoparticles: further insights into the particle size effects. J Electroanal Chem 599(2):221–232
18. Mayrhofer KJJ, Arenz M, Blizanac BB, Stamenkovic V et al (2005) CO surface electrochemistry on Pt-nanoparticles: a selective review. Electrochim Acta 50(25):5144–5154
19. Urchaga P, Baranton S, Coutanceau C, Jerkiewicz G (2012) Electro-oxidation of COchem on Pt Nanosurfaces: solution of the peak multiplicity puzzle. Langmuir 28(7):3658–3663
20. Wang ZL, Mohamed MB, Link S, El-Sayed MA (1999) Crystallographic facets and shapes of gold nanorods of different aspect ratios. Surf Sci 440(1–2):L809–L814
21. Tollan C, Echeberria J, Marcilla R, Pomposo J et al (2009) One-step growth of gold nanorods using a β-diketone reducing agent. J Nanopart Res 11(5):1241–1245
22. Coutanceau C, Urchaga P, Baranton S (2012) Diffusion of adsorbed CO on platinum (100) and (111) oriented nanosurfaces. Electrochem Commun 22(109–112
23. Ferreira PJ, La O' GJ, Shao-Horn Y, Morgan D et al (2005) Instability of Pt/C electrocatalysts in proton exchange membrane fuel cells. J Electrochem Soc 152(11):A2256–A2271
24. Gasteiger HA, Kocha SS, Sompalli B, Wagner FT (2005) Activity benchmarks and requirements for Pt, Pt-alloy, and non-Pt oxygen reduction catalysts for PEMFCs. Appl Catal B Environ 56(1–2):9–35
25. Sompalli B, Litteer BA, Gu W, Gasteiger HA (2007) Membrane degradation at catalyst layer edges in PEMFC MEAs. J Electrochem Soc 154(12):B1349–B1357
26. Chen S, Gasteiger HA, Hayakawa K, Tada T et al (2010) Platinum-alloy cathode catalyst degradation in proton exchange membrane fuel cells: nanometer-scale compositional and morphological changes. J Electrochem Soc 157(1):A82–A97
27. Xie J, Wood DL, More KL, Atanassov P et al (2005) Microstructural changes of membrane electrode assemblies during PEFC durability testing at high humidity conditions. J Electrochem Soc 152(5):A1011–A1020
28. Borup R, Meyers J, Pivovar B, Kim YS et al (2007) Scientific aspects of polymer electrolyte fuel cell durability and degradation. Chem Rev 107(10):3904–3951
29. Guilminot E, Corcella A, Charlot F, Maillard F et al (2007) Detection of Pt^{z+} ions and Pt nanoparticles inside the membrane of a used PEMFC. J Electrochem Soc 154(1): B96–B105
30. Guilminot E, Corcella A, Iojoiu C, Berthomé G et al (2007) Membrane and active layer degradation upon proton exchange membrane fuel cell steady-state operation – Part I: platinum dissolution and redistribution within the membrane electrode assembly. J Electrochem Soc 154(11):B1106–B1114
31. Iojoiu C, Guilminot E, Maillard F, Chatenet M et al (2007) Membrane and active layer degradation following PEMFC steady-state operation. J Electrochem Soc 154(11): B1115–B1120
32. Chatenet M, Guétaz L, Maillard F (2009) Electron microscopy to study MEA materials and structure degradation. In: Vielstich W, Gasteiger HA, Yokokawa H (eds) Handbook of fuel cells: fundamentals, technology, and applications, vol 5. Wiley, Oxford, pp 844–860
33. Dubau L, Maillard F, Chatenet M, André J et al (2010) Nanoscale compositional changes and modification of the surface reactivity of Pt_3Co/C nanoparticles during proton-exchange membrane fuel cell operation. Electrochim Acta 56(2):776–783
34. Dubau L, Maillard F, Chatenet M, Guétaz L et al (2010) Durability of Pt_3Co/C cathodes in a 16 cell PEMFC stack: macro/microstructural changes and degradation mechanisms. J Electrochem Soc 157(12):B1887–B1895

35. Dubau L, Durst J, Maillard F, Guétaz L et al (2011) Further insights into the durability of Pt_3Co/C electrocatalysts: formation of "hollow" Pt nanoparticles induced by the Kirkendall effect. Electrochim Acta 56(28):10658–10667
36. Dubau L, Lopez-Haro M, Castanheira L, Durst J et al (2013) Probing the structure, the composition and the ORR activity of Pt3Co/C nanocrystallites during a 3422 h PEMFC ageing test. Appl Catal B Environ 142:801–808
37. Durst J, Lamibrac A, Charlot F, Dillet J et al (2013) Degradation heterogeneities induced by repetitive start/stop events in proton exchange membrane fuel cell: inlet vs. outlet and channel vs. land. Appl Catal B Environ 138–139:416–426
38. Lopez-Haro M, Dubau L, Guétaz L, Bayle-Guillemaud P et al (2014) Atomic-scale structure and composition of Pt_3Co/C nanocrystallites during real PEMFC operation: a STEM–EELS study. Appl Catal B Environ 152–153:300–308
39. Shao-Horn Y, Sheng W, Chen S, Ferreira P et al (2007) Instability of supported platinum nanoparticles in low-temperature fuel cells. Top Catal 46(3):285–305
40. Dubau L, Durst J, Maillard F, Chatenet M et al (2012) Heterogeneities of aging within a PEMFC MEA. Fuel Cells 12(2):188–198
41. Lamibrac A, Maranzana G, Dillet J, Lottin O et al (2012) Local degradations resulting from repeated start-ups and shut-downs in proton exchange membrane fuel cell (PEMFC). Energy Procedia 29:318–324
42. Nikkuni FR, Vion-Dury B, Dubau L, Maillard F et al (2014) The role of water in the degradation of Pt3Co/C nanoparticles: an identical location transmission electron microscopy study in polymer electrolyte environment. Appl Catal B Environ 156–157:301–306
43. Nikkuni FR, Dubau L, Ticianelli EA, Chatenet M (2015) Accelerated degradation of Pt_3Co/C and Pt/C electrocatalysts studied by identical-location transmission electron microscopy in polymer electrolyte environment. Appl Catal B Environ 176–177:486–499
44. Mayrhofer KJJ, Meier JC, Ashton SJ, Wiberg GKH et al (2008) Fuel cell catalyst degradation on the nanoscale. Electrochem Commun 10(8):1144–1147
45. Meier JC, Galeano C, Katsounaros I, Witte J et al (2014) Design criteria for stable Pt/C fuel cell catalysts. Beilstein J Nanotechnol 5(1):44–67
46. Dubau L, Castanheira L, Berthomé G, Maillard F (2013) An identical-location transmission electron microscopy study on the degradation of Pt/C nanoparticles under oxidizing, reducing and neutral atmosphere. Electrochim Acta 110:273–281
47. Hartl K, Hanzlik M, Arenz M (2011) IL-TEM investigations on the degradation mechanism of Pt/C electrocatalysts with different carbon supports. Energy Environ Sci 4(1):234–238
48. Zana A, Speder J, Roefzaad M, Altmann L et al (2013) Probing degradation by IL-TEM: the influence of stress test conditions on the degradation mechanism. J Electrochem Soc 160(6): F608–F615
49. Dubau L, Maillard F (2016) Unveiling the crucial role of temperature on the stability of oxygen reduction reaction electrocatalysts. Electrochem Commun 63:65–69
50. Castanheira L, Dubau L, Maillard F (2014) Accelerated stress tests of Pt/HSAC electrocatalysts: an identical-location transmission electron microscopy study on the influence of intermediate characterizations. Electrocatalysis 5(2):125–135
51. Yu YC, Xin HLL, Hovden R, Wang DL et al (2012) Three-dimensional tracking and visualization of hundreds of Pt-Co fuel cell nanocatalysts during electrochemical aging. Nano Lett 12(9):4417–4423
52. Baldizzone C, Gan L, Hodnik N, Keeley GP et al (2015) Stability of dealloyed porous Pt/Ni nanoparticles. ACS Catal 5(9):5000–5007
53. Meier JC, Galeano C, Katsounaros I, Topalov AA et al (2012) Degradation mechanisms of Pt/C fuel cell catalysts under simulated start-stop conditions. ACS Catal 2(5):832–843
54. Mucal. http://csrri.iit.edu/periodic-table.html. Accessed 14 Feb 2017
55. Russell AE, Rose A (2004) X-ray absorption spectroscopy of low temperature fuel cell catalysts. Chem Rev Columbus 104(10):4613–4636

56. Siebel A, Gorlin Y, Durst J, Proux O et al (2016) Identification of catalyst structure during the hydrogen oxidation reaction in an operating PEM fuel cell. ACS Catal 6(11):7326–7334
57. Croze V, Ettingshausen F, Melke J, Soehn M et al (2010) The use of in situ X-ray absorption spectroscopy in applied fuel cell research. J Appl Electrochem 40(5):877–883
58. Wandt J, Freiberg A, Thomas R, Gorlin Y et al (2016) Transition metal dissolution and deposition in Li-ion batteries investigated by operando X-ray absorption spectroscopy. J Mater Chem A 4(47):18300–18305
59. Adora S, Soldo-Olivier Y, Faure R, Durand R et al (2001) Electrochemical preparation of platinum nanocrystallites on activated carbon studied by X-ray absorption spectroscopy. J Phys Chem B 105(43):10489–10495
60. Mukerjee S, McBreen J (1998) Effect of particle size on the electrocatalysis by carbon-supported Pt electrocatalysts: an in situ XAS investigation. J Electroanal Chem 448(2):163–171
61. Murthi VS, Urian RC, Mukerjee S (2004) Oxygen reduction kinetics in low and medium temperature acid environment: correlation of water activation and surface properties in supported Pt and Pt alloy electrocatalysts. J Phys Chem B 108(30):11011–11023
62. Teliska M, Murthi VS, Mukerjee S, Ramaker DE (2007) Site-specific vs specific adsorption of anions on Pt and Pt-based alloys. J Phys Chem C 111(26):9267–9274
63. Dixon D, Habereder A, Farmand M, Kaserer S et al (2012) Space resolved, in operando X-ray absorption spectroscopy: investigations on both the anode and cathode in a direct methanol fuel cell. J Phys Chem C 116(13):7587–7595
64. Melke J, Schoekel A, Dixon D, Cremers C et al (2010) Ethanol oxidation on carbon-supported Pt, PtRu, and PtSn catalysts studied by operando X-ray absorption spectroscopy. J Phys Chem C 114(13):5914–5925
65. Markovic NM, Schmidt TJ, Stamenkovic V, Ross PN (2001) Oxygen reduction reaction on Pt and Pt bimetallic surfaces: a selective review. Fuel Cells 1(2):105–116
66. Wang JX, Markovic NM, Adzic RR (2004) Kinetic analysis of oxygen reduction on Pt(111) in acid solutions: intrinsic kinetic parameters and anion adsorption effects. J Phys Chem B 108:4127–4133
67. Stamenkovic VR, Mun BS, Arenz M, Mayrhofer KJJ et al (2007) Trends in electrocatalysis on extended and nanoscale Pt-bimetallic alloy surfaces. Nat Mater 6(3):241–247
68. Jia Q, Caldwell K, Strickland K, Ziegelbauer JM et al (2015) Improved oxygen reduction activity and durability of dealloyed $PtCo_x$ catalysts for proton exchange membrane fuel cells: strain, ligand, and particle size effects. ACS Catal 5(1):176–186
69. Pourbaix M (1979) Atlas of electrochemical equilibria in aqueous solutions. National Association of Corrosion Engineers, Houston, p 453
70. Jia Q, Li J, Caldwell K, Ramaker DE et al (2016) Circumventing metal dissolution induced degradation of Pt-alloy catalysts in proton exchange membrane fuel cells: revealing the asymmetric volcano nature of redox catalysis. ACS Catal 6(2):928–938
71. Durst J, Lopez-Haro M, Dubau L, Chatenet M et al (2014) Reversibility of Pt-skin and Pt-skeleton nanostructures in acidic media. J Phys Chem Lett 5(3):434–439
72. Maillard F, Dubau L, Durst J, Chatenet M et al (2010) Durability of Pt_3Co/C nanoparticles in a proton-exchange membrane fuel cell: direct evidence of bulk co segregation to the surface. Electrochem Commun 12(9):1161–1164
73. Mukerjee S, Srinivasan S, Soriaga MP, McBreen J (1995) Role of structural and electronic-properties of Pt and Pt alloys on electrocatalysis of oxygen reduction – an in-situ XANES and EXAFS investigation. J Electrochem Soc 142(5):1409–1422
74. Teliska M, O'Grady WE, Ramaker DE (2004) Determination of H adsorption sites on Pt/C electrodes in HClO4 from Pt L23 X-ray absorption spectroscopy. J Phys Chem B 108(7):2333–2344
75. Teliska M, O'Grady WE, Ramaker DE (2005) Determination of O and OH adsorption sites and coverage in situ on Pt electrodes from Pt L23 X-ray absorption spectroscopy. J Phys Chem B 109(16):8076–8084

76. Bard AJ, Faulkner LR (1993) Electrochemical methods. Wiley, Weinheim
77. Bewick A, Kunimatsu K (1980) Infra red spectroscopy of the electrode-electrolyte interphase. Surf Sci 101(1–3):131–138
78. Bewick A, Kunimatsu K, Pons BS (1980) Infrared-spectroscopy of the electrode-electrolyte interphase. Electrochim Acta 25(4):465–468
79. Beden B, Bewick A, Lamy C (1983) A comparative-study of formic-acid adsorption on a platinum-electrode by both electrochemical and emirs techniques. J Electroanal Chem 150(1–2):505–511
80. Bewick A, Kunimatsu K, Pons BS, Russell JW (1984) Electrochemically modulated infrared-spectroscopy (emirs)-experimental details. J Electroanal Chem 160(1–2):47–61
81. Beden B, Bewick A, Lamy C (1983) A study by electrochemically modulated infrared reflectance spectroscopy of the electrosorption of formic-acid at a platinum-electrode. J Electroanal Chem 148(1):147–160
82. Leung LWH, Weaver MJ (1988) Real-time ftir spectroscopy as a quantitative kinetic probe of competing electrooxidation pathways for small organic-molecules. J Phys Chem 92(14):4019–4022
83. Corrigan DS, Weaver MJ (1988) Mechanisms of formic-acid, methanol, and carbon-monoxide electrooxidation at platinum as examined by single potential alteration infrared-spectroscopy. J Electroanal Chem 241(1–2):143–162
84. Davidson T, Pons BS, Bewick A, Schmidt PP (1981) Vibrational spectroscopy of the electrode-electrolyte interface – use of fourier-transform infrared-spectroscopy. J Electroanal Chem 125(1):237–241
85. Pons S, Davidson T, Bewick A (1984) Vibrational spectroscopy of the electrode electrolyte interface .4. Fourier-transform infrared-spectroscopy – experimental considerations. J Electroanal Chem 160(1–2):63–71
86. Pons S, Davidson T, Bewick A (1983) Vibrational spectroscopy of the electrode solution interphase .2. Use of fourier-transform spectroscopy for recording infrared-spectra of radical ion intermediates. J Am Chem Soc 105(7):1802–1805
87. Pons S (1983) The use of fourier-transform infrared-spectroscopy for insitu recording of species in the electrode electrolyte solution interphase. J Electroanal Chem 150(1–2):495–504
88. Lin WF, Sun SG (1996) In situ FTIRS investigations of surface processes of Rh electrode – novel observation of geminal adsorbates of carbon monoxide on Rh electrode in acid solution. Electrochim Acta 41(6):803–809
89. Pons S, Davidson T, Bewick A (1982) Vibrational spectroscopy of the electrode solution interface .3. Use of fourier-transform spectroscopy for observing double-layer reorganization. J Electroanal Chem 140(1):211–216
90. Li JT, Zhou ZY, Broadwell I, Sun SG (2012) In-situ infrared spectroscopic studies of electrochemical energy conversion and storage. Acc Chem Res 45(4):485–494
91. Iwasita T, Nart FC (1990) Bulk effects in external reflection ir spectroscopy- the interpretation of adsorption data for ionic species. J Electroanal Chem 295(1–2):215–224
92. Iwasita T, Nart FC (1997) In situ infrared spectroscopy at electrochemical interfaces. Prog Surf Sci 55(4):271–340
93. Bae IT, Scherson DA, Yeager EB (1990) Infrared spectroscopic determination of ph changes in diffusionally decoupled thin-layer electrochemical-cells. Anal Chem 62(1):45–49
94. Bae IT, Xing XK, Yeager EB, Scherson D (1989) Ionic transport effects in insitu fourier-transform infrared reflection absorption-spectroscopy. Anal Chem 61(10):1164–1167
95. Osawa M (1997) Dynamic processes in electrochemical reactions studied by surface-enhanced infrared absorption spectroscopy (SEIRAS). Bull Chem Soc Jpn 70(12):2861–2880
96. Miki A, Ye S, Osawa M (2002) Surface-enhanced IR absorption on platinum nanoparticles: an application to real-time monitoring of electrocatalytic reactions. Chem Commun 0(14):1500–1501
97. Golden WG, Kunimatsu K, Seki H (1984) Application of polarization-modulated fourier-transform infrared reflection absorption-spectroscopy to the study of carbon-monoxide adsorption and oxidation on a smooth platinum-electrode. J Phys Chem 88(7):1275–1277

98. Golden WG, Saperstein DD, Severson MW, Overend J (1984) Infrared reflection absorption-spectroscopy of surface species – a comparison of fourier-transform and dispersion methods. J Phys Chem 88(3):574–580
99. Golden WG, Dunn DS, Overend J (1981) A method for measuring infrared reflection-absorption spectra of molecules adsorbed on low-area surfaces at monolayer and sub-monolayer concentrations. J Catal 71(2):395–404
100. Kunimatsu K, Kita H (1987) Infrared spectroscopic study of methanol and formic-acid adsorbates on a platinum-electrode .2. Role of the linear co(a) derived from methanol and formic-acid in the electrocatalytic oxidation of ch3oh and hcooh. J Electroanal Chem 218(1–2):155–172
101. Christensen P, Hamnett A (2000) In-situ techniques in electrochemistry – ellipsometry and FTIR. Electrochim Acta 45(15–16):2443–2459
102. Osawa M, Yoshii K (1997) In situ and real-time surface-enhanced infrared study of electrochemical reactions. Appl Spectrosc 51(4):512–518
103. Osawa M, Yoshii K, Ataka K, Yotsuyanagi T (1994) Real-time monitoring of electrochemical dynamics by submillisecond time-resolved surface-enhanced infrared attenuated-total-reflection spectroscopy. Langmuir 10(3):640–642
104. Noda H, Wan LJ, Osawa M (2001) Dynamics of adsorption and phase formation of p-nitrobenzoic acid at Au(111) surface in solution: a combined surface-enhanced infrared and STM study. Phys Chem Chem Phys 3(16):3336–3342
105. Wandlowski T, Ataka K, Pronkin S, Diesing D (2004) Surface enhanced infrared spectroscopy – Au(1 1 1-20 nm)/sulphuric acid – new aspects and challenges. Electrochim Acta 49(8):1233–1247
106. Nichols RJ, Bewick A (1988) Sniftirs with a flow cell – the identification of the reaction intermediates in methanol oxidation at pt anodes. Electrochim Acta 33(11):1691–1694
107. Roth JD, Weaver MJ (1991) The electrooxidation of carbon-monoxide on platinum as examined by surface infrared-spectroscopy under forced hydrodynamic conditions. J Electroanal Chem 307(1–2):119–137
108. Bellec V, De Backer MG, Levillain E, Sauvage FX et al (2001) In situ time-resolved FTIR spectroelectrochemistry: study of the reduction of TCNQ. Electrochem Commun 3(9):483–488
109. Sun SG, Lin Y (1994) Kinetic aspects of oxidation of isopropanol on pt electrodes investigated by in-situ time-resolved ftir spectroscopy. J Electroanal Chem 375(1–2):401–404
110. Zhou ZY, Lin SC, Chen SP, Sun SG (2005) In situ step-scan time-resolved microscope FTIR spectroscopy working with a thin-layer cell. Electrochem Commun 7(5):490–495
111. Kunimatsu K, Yoda T, Tryk DA, Uchida H et al (2010) In situ ATR-FTIR study of oxygen reduction at the Pt/Nafion interface. Phys Chem Chem Phys 12(3):621–629
112. Xia XH, Liess HD, Iwasita T (1997) Early stages in the oxidation of ethanol at low index single crystal platinum electrodes. J Electroanal Chem 437(1–2):233–240
113. Tian N, Zhou ZY, Yu NF, Wang LY et al (2010) Direct electrodeposition of Tetrahexahedral Pd nanocrystals with high-index facets and high catalytic activity for ethanol electrooxidation. J Am Chem Soc 132(22):7580
114. Tian N, Zhou ZY, Sun SG, Ding Y et al (2007) Synthesis of tetrahexahedral platinum nanocrystals with high-index facets and high electro-oxidation activity. Science 316(5825):732–735
115. Zhou ZY, Huang ZZ, Chen DJ, Wang Q et al (2010) High-index faceted platinum nanocrystals supported on carbon black as highly efficient catalysts for ethanol Electrooxidation. Angew Chem Int Ed 49(2):411–414
116. Silva LC, Maia G, Passos RR, de Souza EA et al (2013) Analysis of the selectivity of PtRh/C and PtRhSn/C to the formation of CO_2 during ethanol electrooxidation. Electrochim Acta 112:612–619
117. Soares LA, Morais C, Napporn TW, Kokoh KB et al (2016) Beneficial effects of rhodium and tin oxide on carbon supported platinum catalysts for ethanol electrooxidation. J Power Sources 315:47–55

118. Almeida TS, Palma LM, Morais C, Kokoh KB et al (2013) Effect of adding a third metal to carbon-supported PtSn-based Nanocatalysts for direct ethanol fuel cell in acidic medium. J Electrochem Soc 160(9):F965–F971
119. Yang YY, Ren J, Li QX, Zhou ZY et al (2014) Electrocatalysis of ethanol on a Pd electrode in alkaline media: an in situ attenuated total reflection surface-enhanced infrared absorption spectroscopy study. ACS Catal 4(3):798–803
120. Beyhan S, Uosaki K, Feliu JM, Herrero E (2013) Electrochemical and in situ FTIR studies of ethanol adsorption and oxidation on gold single crystal electrodes in alkaline. J Electroanal Chem 707:89–94
121. Pech-Rodriguez WJ, Gonzalez-Quijano D, Vargas-Gutierrez G, Morais C et al (2017) Electrochemical and in situ FTIR study of the ethanol oxidation reaction on PtMo/C nanomaterials in alkaline media. Appl Catal B Environ 203:654–662
122. Buso-Rogero C, Brimaud S, Solla-Gullon J, Vidal-Iglesias FJ et al (2016) Ethanol oxidation on shape-controlled platinum nanoparticles at different pHs: a combined in situ IR spectroscopy and online mass spectrometry study. J Electroanal Chem 763:116–124
123. Delpeuch AB, Maillard F, Chatenet M, Soudant P et al (2016) Ethanol oxidation reaction (EOR) investigation on Pt/C, Rh/C, and Pt-based bi- and tri-metallic electrocatalysts: a DEMS and in situ FTIR study. Appl Catal B Environ 181:672–680
124. Zhou ZY, Wang QA, Lin JL, Tian N et al (2010) In situ FTIR spectroscopic studies of electrooxidation of ethanol on Pd electrode in alkaline media. Electrochim Acta 55(27):7995–7999
125. Ren J, Yang YY, Zhang BW, Tian N et al (2013) H-D kinetic isotope effects of alcohol electrooxidation on Au, Pd and Pt electrodes in alkaline solutions. Electrochem Commun 37:49–52
126. Allen JB, Faulkner LR (2001) Electrochemical methods: fundamuntals and applications, 2nd edn. Wiley, New York, p 850
127. Scholz F (2010) Electroanalytical methods: guide to experiments and applications. Springer, Berlin/Heidelberg, p 388
128. Kwon Y, Schouten KJP, Koper MTM (2011) Mechanism of the catalytic oxidation of glycerol on polycrystalline gold and platinum electrodes. ChemCatChem 3(7):1176–1185
129. Kwon Y, Koper MTM (2010) Combining voltammetry with HPLC: application to electrooxidation of glycerol. Anal Chem 82(13):5420–5424
130. Gomes J, Tremiliosi-Filho G (2011) Spectroscopic studies of the glycerol electro-oxidation on polycrystalline au and Pt surfaces in acidic and alkaline media. Electrocatalysis 2(2):96–105
131. Jeffery DZ, Camara GA (2010) The formation of carbon dioxide during glycerol electrooxidation in alkaline media: first spectroscopic evidences. Electrochem Commun 12(8):1129–1132
132. Kwon Y, Birdja Y, Spanos I, Rodriguez P et al (2012) Highly selective electro-oxidation of glycerol to dihydroxyacetone on platinum in the presence of bismuth. ACS Catal 2(5):759–764
133. Simões M, Baranton S, Coutanceau C (2011) Enhancement of catalytic properties for glycerol electrooxidation on Pt and Pd nanoparticles induced by Bi surface modification. Appl Catal B Environ 110:40–49
134. Simões M, Baranton S, Coutanceau C (2012) Electrochemical valorisation of glycerol. ChemSusChem 5(11):2106–2124
135. Fernández PS, Martins ME, Camara GA (2012) New insights about the electro-oxidation of glycerol on platinum nanoparticles supported on multi-walled carbon nanotubes. Electrochim Acta 66:180–187
136. Holade Y, Morais C, Servat K, Napporn TW et al (2013) Toward the electrochemical valorization of glycerol: fourier transform infrared spectroscopic and chromatographic studies. ACS Catal 3(10):2403–2411
137. Simões M, Baranton S, Coutanceau C (2010) Electro-oxidation of glycerol at Pd based nanocatalysts for an application in alkaline fuel cells for chemicals and energy cogeneration. Appl Catal B Environ 93(3–4):354–362

138. Sun S-G (1998) Studying electrocatalytic oxidation of small organic molecules with in-situ infra spectroscopy. In: Lipkowski J, Ross PN (eds) Electrocatalysis. Wiley-VCH, Inc., New York, (USA), pp 243–290
139. Demarconnay L, Brimaud S, Coutanceau C, Léger JM (2007) Ethylene glycol electrooxidation in alkaline medium at multi-metallic Pt based catalysts. J Electroanal Chem 601(1–2):169–180
140. Palma LM, Almeida TS, Morais C, Napporn TW et al (2017) Effect of co-catalyst on the selective electrooxidation of glycerol over ruthenium-based nanomaterials. ChemElectroChem 4(1):39–45
141. Innocent B, Pasquier D, Ropital F, Hahn F et al (2010) FTIR spectroscopy study of the reduction of carbon dioxide on lead electrode in aqueous medium. Appl Catal B Environ 94(3–4):219–224
142. Eneau-Innocent B, Pasquier D, Ropital F, Leger JM et al (2010) Electroreduction of carbon dioxide at a lead electrode in propylene carbonate: a spectroscopic study. Appl Catal B Environ 98(1–2):65–71
143. Xiang DM, Magana D, Dyer RB (2014) CO_2 reduction catalyzed by Mercaptopteridine on glassy carbon. J Am Chem Soc 136(40):14007–14010
144. Firet NJ, Smith WA (2017) Probing the reaction mechanism of CO_2 electroreduction over Ag films via operando infrared spectroscopy. ACS Catal 7(1):606–612
145. Chang SC, Weaver MJ (1990) Coverage-dependent and potential-dependent binding geometries of carbon-monoxide at ordered low-index platinum aqueous and rhodium aqueous interfaces – comparisons with adsorption in corresponding metal vacuum environments. Surf Sci 238(1–3):142–162
146. Chang SC, Weaver MJ (1991) Insitu infrared-spectroscopy at single-crystal metal-electrodes – an emerging link between electrochemical and ultrahigh-vacuum surface science. J Phys Chem 95(14):5391–5400
147. Yajima T, Uchida H, Watanabe M (2004) In-situ ATR-FTIR spectroscopic study of electro-oxidation of methanol and adsorbed CO at Pt-Ru alloy. J Phys Chem B 108(8):2654–2659
148. Ma J, Habrioux A, Morais C, Alonso-Vante N (2014) Electronic modification of Pt via Ti and se as tolerant cathodes in air-breathing methanol microfluidic fuel cells. Phys Chem Chem Phys 16(27):13820–13826
149. Ma J, Habrioux A, Morais C, Lewera A et al (2013) Spectroelectrochemical probing of the strong interaction between platinum nanoparticles and graphitic domains of carbon. ACS Catal 3(9):1940–1950
150. Abidat I, Morais C, Pronier S, Guignard N et al (2017) Effect of gradual reduction of graphene oxide on the CO tolerance of supported platinum nanoparticles. Carbon 111:849–858
151. Bruckenstein S, Gadde RR (1971) Use of a porous electrode for in situ mass spectrometric determination of volatile electrode reaction products. J Am Chem Soc 93(3):793–794
152. Wolter O, Heitbaum J (1984) Differential electrochemical mass spectroscopy (DEMS) – a new method for the study of electrode processes. Ber Bunsenges Phys Chem 88(1):2–6
153. Baltruschat H (2004) Differential electrochemical mass spectrometry. J Am Soc Mass Spectrom 15(12):1693–1706
154. Sreekanth N, Phani KL (2014) Selective reduction of CO_2 to formate through bicarbonate reduction on metal electrodes: new insights gained from SG/TC mode of SECM. Chem Commun 50(76):11143–11146
155. Li CW, Kanan MW (2012) CO_2 reduction at low overpotential on Cu electrodes resulting from the reduction of thick Cu_2O films. J Am Chem Soc 134(17):7231–7234
156. Koga O, Hori Y (1993) Reduction of adsorbed co on a Ni electrode in connection with the electrochemical reduction of CO_2. Electrochim Acta 38(10):1391–1394
157. Li W (2010) Electrocatalytic reduction of CO_2 to small organic molecule fuels on metal catalysts. In: Advances in CO_2 conversion and utilization, vol 1056. American Chemical Society, Washington DC, pp 55–76

158. Chen Y, Li CW, Kanan MW (2012) Aqueous CO_2 reduction at very low Overpotential on oxide-derived au nanoparticles. J Am Chem Soc 134(49):19969–19972
159. Hansen HA, Varley JB, Peterson AA, Nørskov JK (2013) Understanding trends in the Electrocatalytic activity of metals and enzymes for CO_2 reduction to CO. J Phys Chem Lett 4(3):388–392
160. Baturina OA, Lu Q, Padilla MA, Xin L et al (2014) CO_2 electroreduction to hydrocarbons on carbon-supported cu nanoparticles. ACS Catal 4(10):3682–3695
161. Ren D, Deng Y, Handoko AD, Chen CS et al (2015) Selective electrochemical reduction of carbon dioxide to ethylene and ethanol on copper(I) oxide catalysts. ACS Catal 5(5):2814–2821
162. Varela AS, Kroschel M, Reier T, Strasser P (2016) Controlling the selectivity of CO_2 electroreduction on copper: the effect of the electrolyte concentration and the importance of the local pH. Catal Today 260:8–13
163. Zhang S, Kang P, Meyer TJ (2014) Nanostructured tin catalysts for selective electrochemical reduction of carbon dioxide to Formate. J Am Chem Soc 136(5):1734–1737
164. Liu Z, Masel RI, Chen Q, Kutz R et al (2016) Electrochemical generation of syngas from water and carbon dioxide at industrially important rates. J CO2 Util 15:50–56
165. Ma M, Trześniewski BJ, Xie J, Smith WA (2016) Selective and efficient reduction of carbon dioxide to carbon monoxide on oxide-derived nanostructured silver Electrocatalysts. Angew Chem Int Ed 55(33):9748–9752
166. Camilo MR, Silva WO, Lima FHB (2017) Investigation of electrocatalysts for selective reduction of CO_2 to CO: monitoring the reaction products by on line mass spectrometry and gas chromatography. J Braz Chem Soc. 28(9):1803–1815
167. Sarkar A, Manthiram A (2010) Synthesis of Pt@Cu Core−Shell nanoparticles by galvanic displacement of Cu by Pt4+ ions and their application as electrocatalysts for oxygen reduction reaction in fuel cells. J Phys Chem C 114(10):4725–4732
168. Zhang J, Lima FHB, Shao MH, Sasaki K et al (2005) Platinum monolayer on nonnoble metal−Noble metal Core−Shell nanoparticle electrocatalysts for O2 reduction. J Phys Chem B 109(48):22701–22704
169. Kiros Y (1996) Electrocatalytic properties of Co, Pt, and Pt-Co on carbon for the reduction of oxygen in alkaline fuel cells. J Electrochem Soc 143(7):2152–2157
170. Kedzierzawski P, Augustynski J (1994) Poisoning and activation of the gold cathode during Electroreduction of CO_2. J Electrochem Soc 141(5):L58–L60
171. Wang H, Jusys Z, Behm RJ (2006) Ethanol electro-oxidation on carbon-supported Pt, PtRu and Pt3Sn catalysts: a quantitative DEMS study. J Power Sources 154(2):351–359
172. Sato AG, Silva GCD, Paganin VA, Biancolli ALG et al (2015) New, efficient and viable system for ethanol fuel utilization on combined electric/internal combustion engine vehicles. J Power Sources 294:569–573
173. Lai SCS, Kleijn SEF, Öztürk FTZ, van Rees Vellinga VC et al (2010) Effects of electrolyte pH and composition on the ethanol electro-oxidation reaction. Catal Today 154(1–2):92–104
174. Queiroz AC, Silva WO, Rodrigues IA, Lima FHB (2014) Identification of bimetallic electrocatalysts for ethanol and acetaldehyde oxidation: probing C2-pathway and activity for hydrogen oxidation for indirect hydrogen fuel cells. Appl Catal B Environ 160–161:423–435
175. Sao-Joao S, Giorgio S, Penisson JM, Chapon C et al (2005) Structure and deformations of Pd−Ni Core−Shell nanoparticles. J Phys Chem B 109(1):342–347
176. Kowal A, Li M, Shao M, Sasaki K et al (2009) Ternary Pt/Rh/SnO_2 electrocatalysts for oxidizing ethanol to CO2. Nat Mater 8(4):325–330

Index

© Springer-Verlag GmbH Germany, part of Springer Nature 2018

C. S. S. R. Kumar (ed.), *In-situ Characterization Techniques for Nanomaterials*,
https://doi.org/10.1007/978-3-662-56322-9